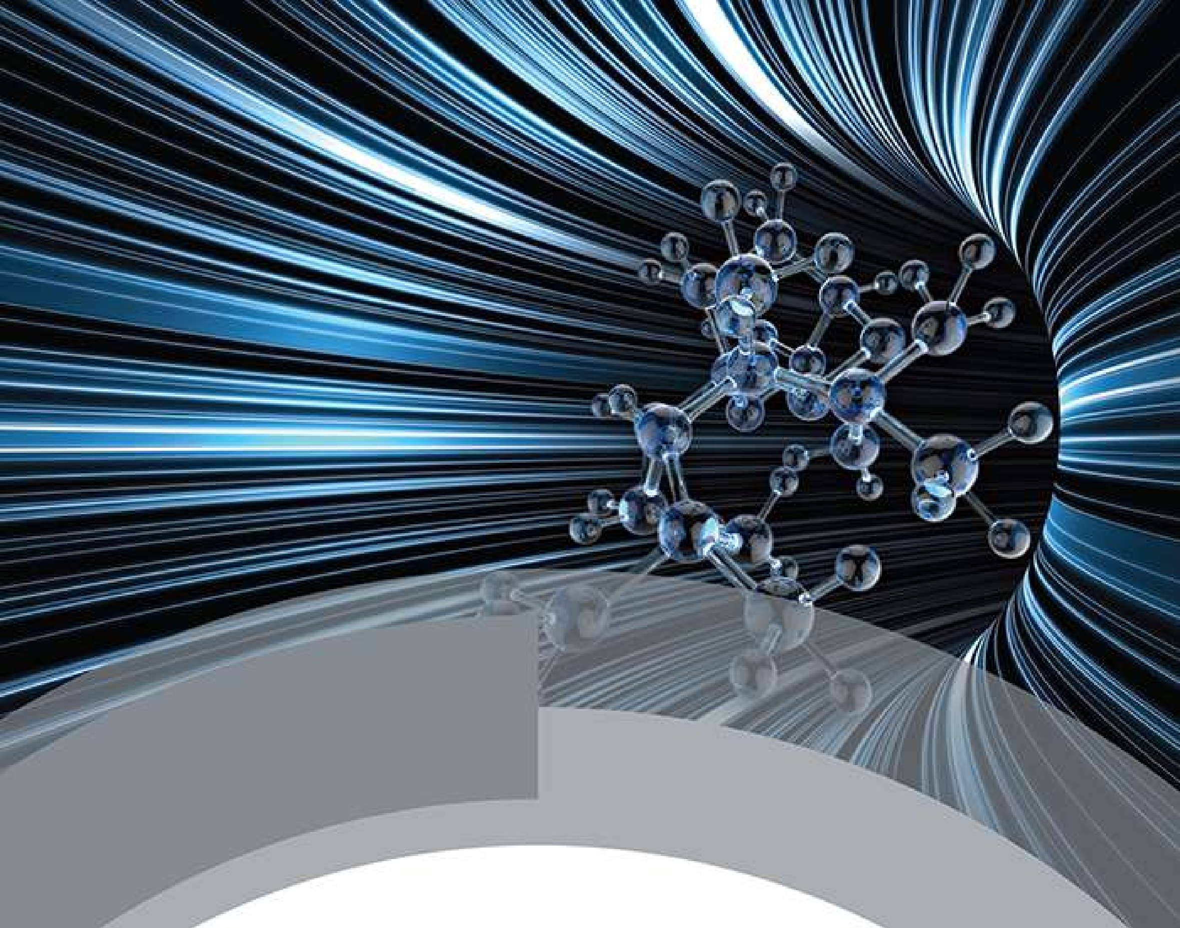

Theoretical and Computational Chemistry Series

Tunnelling in Molecules

Nuclear Quantum Effects from Bio to Physical Chemistry

Edited by Johannes Kästner and Sebastian Kozuch

ROYAL SOCIETY OF CHEMISTRY

Tunnelling in Molecules
Nuclear Quantum Effects from Bio to Physical Chemistry

Theoretical and Computational Chemistry Series

Titles in the series:
1: Knowledge-based Expert Systems in Chemistry: Not Counting on Computers
2: Non-Covalent Interactions: Theory and Experiment
3: Single-Ion Solvation: Experimental and Theoretical Approaches to Elusive Thermodynamic Quantities
4: Computational Nanoscience
5: Computational Quantum Chemistry: Molecular Structure and Properties *in Silico*
6: Reaction Rate Constant Computations: Theories and Applications
7: Theory of Molecular Collisions
8: *In Silico* Medicinal Chemistry: Computational Methods to Support Drug Design
9: Simulating Enzyme Reactivity: Computational Methods in Enzyme Catalysis
10: Computational Biophysics of Membrane Proteins
11: Cold Chemistry: Molecular Scattering and Reactivity Near Absolute Zero
12: Theoretical Chemistry for Electronic Excited States
13: Attosecond Molecular Dynamics
14: Self-organized Motion: Physicochemical Design based on Nonlinear Dynamics
15: Knowledge-based Expert Systems in Chemistry: Artificial Intelligence in Decision Making
16: London Dispersion Forces in Molecules, Solids and Nano-structures: An Introduction to Physical Models and Computational Methods
17: Machine Learning in Chemistry: The Impact of Artificial Intelligence
18: Tunnelling in Molecules: Nuclear Quantum Effects from Bio to Physical Chemistry

How to obtain future titles on publication:
A standing order plan is available for this series. A standing order will bring delivery of each new volume immediately on publication.

For further information please contact:
Book Sales Department, Royal Society of Chemistry, Thomas Graham House,
Science Park, Milton Road, Cambridge, CB4 0WF, UK
Telephone: +44 (0)1223 420066, Fax: +44 (0)1223 420247,
Email: booksales@rsc.org
Visit our website at www.rsc.org/books

Tunnelling in Molecules

Nuclear Quantum Effects from Bio to Physical Chemistry

Edited by

Johannes Kästner
University of Stuttgart, Germany
Email: kaestner@theochem.uni-stuttgart.de

and

Sebastian Kozuch
Ben-Gurion University of the Negev, Israel
Email: kozuch@bgu.ac.il

ROYAL SOCIETY
OF **CHEMISTRY**

Theoretical and Computational Chemistry Series No. 18

Print ISBN: 978-1-78801-870-8
PDF ISBN: 978-1-83916-037-0
EPUB ISBN: 978-1-83916-038-7
Print ISSN: 2041-3181
Electronic ISSN: 2041-319X

A catalogue record for this book is available from the British Library

© The Royal Society of Chemistry 2021

All rights reserved

Apart from fair dealing for the purposes of research for non-commercial purposes or for private study, criticism or review, as permitted under the Copyright, Designs and Patents Act 1988 and the Copyright and Related Rights Regulations 2003, this publication may not be reproduced, stored or transmitted, in any form or by any means, without the prior permission in writing of The Royal Society of Chemistry or the copyright owner, or in the case of reproduction in accordance with the terms of licences issued by the Copyright Licensing Agency in the UK, or in accordance with the terms of the licences issued by the appropriate Reproduction Rights Organization outside the UK. Enquiries concerning reproduction outside the terms stated here should be sent to The Royal Society of Chemistry at the address printed on this page.

Whilst this material has been produced with all due care, The Royal Society of Chemistry cannot be held responsible or liable for its accuracy and completeness, nor for any consequences arising from any errors or the use of the information contained in this publication. The publication of advertisements does not constitute any endorsement by The Royal Society of Chemistry or Authors of any products advertised. The views and opinions advanced by contributors do not necessarily reflect those of The Royal Society of Chemistry which shall not be liable for any resulting loss or damage arising as a result of reliance upon this material.

The Royal Society of Chemistry is a charity, registered in England and Wales, Number 207890, and a company incorporated in England by Royal Charter (Registered No. RC000524), registered office: Burlington House, Piccadilly, London W1J 0BA, UK, Telephone: +44 (0) 20 7437 8656.

For further information see our web site at www.rsc.org

Printed in the United Kingdom by CPI Group (UK) Ltd, Croydon, CR0 4YY, UK

Preface

> *"What we call objective reality...can only be the harmony expressed by mathematical laws. It is this harmony then which is the sole objective reality, the only truth we can attain."*[†]
>
> Henri Poincaré

> *"In so far as theories of mathematics speak about reality, they are not certain, and in so far as they are certain, they do not speak about reality."*[‡]
>
> Albert Einstein

So, what about tunnelling?

Protium, the light hydrogen isotope ^1H, generally reacts noticeably faster than deuterium (^2H); chemical reactions can cross energy barriers close to 0 K; methylhydroxycarbene ($H_3C{-}\ddot{C}{-}OH$) decays to ethanal ($H_3C{-}HC{=}O$), even though its decay to ethanol ($H_2C{=}HC{-}OH$) has a lower activation energy. All these would not happen if atomic nuclei followed the laws of classical mechanics. However, due to the minute length scale of these and many other reactions, quantum mechanics leads to interesting, though sometimes counterintuitive, outcomes. Quantum mechanical tunnelling (QMT) is a mysterious effect that makes possible the seemingly impossible, by making molecules react without enough energy to cross the transition state (even when frozen up to absolute zero!). What would make a molecule react by a QMT mechanism? When, why and how will that occur? How can we detect and predict such an effect? Which strange effects can QMT cause in

---

[†] H. Poincaré, *The Value of Science*, New York, Dover Publications, 1958.

[‡] A. Einstein, in *Geometrie und Erfahrung: Erweiterte Fassung des Festvortrages Gehalten an der Preussischen Akademie der Wissenschaften zu Berlin am 27. Januar 1921*, ed. A. Einstein, Springer, Berlin, Heidelberg, 1921, pp. 2–20.

Theoretical and Computational Chemistry Series No. 18
Tunnelling in Molecules: Nuclear Quantum Effects from Bio to Physical Chemistry
Edited by Johannes Kästner and Sebastian Kozuch

Published by the Royal Society of Chemistry, www.rsc.org

molecular systems? Is there any practical use for such a bizarre effect? Many of these questions, and many more, will be answered in this book. However, in this introduction, we will take the opportunity to give the novice reader a first glimpse into the world of tunnelling of atoms in molecules.

While ‘‘classical’’ chemical reactions exploit the random thermal energy of the medium to reach high vibrational states that will eventually lead to the product, QMT takes advantage of the wave-like nature of atoms (or more accurately of nuclei) to achieve this. Simply put, if a nucleus in a molecule is not a particle located at a specific point in space, but it is represented by a somewhat diffuse ‘‘probability of finding the particle’’ (using Born’s interpretation), then there is always a small but measurable possibility of finding the corresponding atom at the product side of a chemical reaction. Evidently this probability is practically negligible, or it would be impossible to have stable molecules, causing our world to be unrecognizable. However, ‘‘practically negligible’’ does not mean fully negligible. The tiny proportion of chemical reactions driven by QMT brings a fascinating dimension of reactivity to physics, biology, and definitely also to chemistry.

Let us try to understand QMT with basic quantum mechanics. We can consider this the de Broglie wavelength

$$\lambda = \frac{h}{mv} = \frac{h}{\sqrt{2mE_\mathrm{k}}}$$

which gives us a clue about the diffuseness of a particle. Similar to microscopy, where we cannot resolve any particle whose size is smaller than the wavelength of light, in QMT we cannot resolve it if a particle with a de Broglie wavelength larger than the width of the reaction barrier is at the reactant or product side. In this simplistic interpretation, the ‘‘diffuseness’’ of the particle depends on its mass and kinetic energy. Hence, if an electron with a sensible kinetic energy has a λ of, let’s say, ~40 Å (which might mean that it can cross a barrier of such width with a significant probability), then a hydrogen atom with the same E_k will have $\lambda \approx 1$ Å (a typical barrier width for H-tunnelling). What about a heavier atom? Carbon will tunnel, under similar circumstances, through a barrier that is not more than 0.3 Å wide. Therefore, heavy atom tunnelling is an almost impossible cause for a chemical reaction (emphasis on ‘‘almost’’).

Another perspective on QMT is based on the uncertainty principle. As is widely known, it is impossible to know both the position and momentum of a particle (or, at least, not with absolute precision). This is normally written as

$$\Delta x \Delta p = \mathrm{m} \Delta x \Delta v \geq \hbar.$$

Therefore, the lighter the particle is, the less we will know about its position when interacting with a chemical barrier. Thus, there will be a possibility that the position of the atom will be on the product side. How significant would that probability be? Typically, extremely, tremendously small. Low enough to be completely disregarded even by the best kinetic models. However…

The crude explanations given above avoid the analysis of tunnelling through realistic barriers (or at least models of them). As thoroughly explained in this book, the main factors that affect the tunnelling probability in a chemical reaction are the nuclei's masses, the barrier height and the barrier width. In more precise terms, we should consider the reduced mass (since many atoms may move), and an integration over the barrier shape (since a real barrier changes its energy along the reaction coordinate). However, in the simplest case of the well-known rectangular barrier, the probability of tunnelling (also called the transmission coefficient) can be approximated as

$$P \approx \mathrm{e}^{-2w\sqrt{2m(E-E_0)}\big/\hbar}$$

where w is the width of the barrier (the length of the trajectory of the atom during the tunnelling), E is the barrier height, m the mass of the tunnelling particle (the nuclei in chemistry), and E_0 is the energy of the reactant state (usually the zero-point energy). Therefore, the possibility of reactions caused by tunnelling is higher in reactions with lighter atoms, lower activation energies and, most important of all, small atomic movements. This relates to the exponential decrease of a particle's wavefunction with the mass, barrier height and width if the barrier is higher than the particle's energy. Note that since the barrier width is a central feature of the tunnelling probability, it is likely that the reaction crosses *via* a trajectory that avoids the saddle point at the cost of a higher energy path, but maximizes the transmission (*i.e.* minimizes the action), by taking a shorter path. In QMT jargon this is called "cutting corners", an effect almost non-existent in non-QMT dynamics.

If we calculate the tunnelling probability on a rectangular potential using some representative chemical values (*i.e.* the mass of a light atom, sub-Ångström distances and activation energies of some kJ mol^{-1}), we will obtain almost infinitesimal probabilities, of the order of $\sim10^{-14}$. How can such tiny values be relevant? These probabilities are per impact of the particle with the barrier. However, let us not forget that a real molecule is always vibrating due to its zero-point energy, which implicates that the tunnelling atom may collide with the barrier at a rate of the order of $\sim10^{14}$ s^{-1}![§]

Evidently this gives us a very rough approximation of the real QMT probabilities, which can be particularly complicated to evaluate accurately. Several chapters of this book are dedicated to the description of methods for this task. Still, here we want to highlight in simple words another critical aspect of QMT in molecules. As can be seen from the equation of the tunnelling probability in

---

[§] For instance, a hydrogen atom ($m=1$, $u=1.7\times10^{-27}$ kg) crossing a rectangular barrier of 1 Å ($=10^{-10}$ m) and 40 kJ mol^{-1} ($=6.6\times10^{-20}$ J), considering that $\hbar=1.05\times10^{-27}$ J s^{-1} gives $P\approx5\times10^{-13}$. A C–H stretching frequency, as known from IR spectroscopy, is around 3000 cm^{-1}, and considering that $\tilde{\nu}\cdot c=\nu$, this gives us 3000 cm$^{-1}\times3\times10^{10}$ cm s$^{-1}\approx10^{14}$ s^{-1}. Note that the probability changes extremely fast with any change in the conditions (m, w, or E), and therefore these numbers are just for illustration.

a rectangular barrier, QMT is essentially independent of the temperature, which sometimes allows us to detect a reaction entering into the tunnelling regime. However, there is one possibility for how temperature can influence tunnelling: upon raising the temperature, a molecule will begin to populate excited vibrational states. From an excited state the barrier will be lower and even narrower, which results in a markedly faster tunnelling rate. This effect is called thermally (or vibrationally) activated tunnelling, and makes a smooth connection between the exponential temperature dependence of the classical rate constant in the thermal regime and the temperature independence of the ground-state QMT. One interesting outcome of this effect is that if in an ensemble of molecules there is according to classical transition state theory enough energy to cross the barrier, many molecules will be in high vibrational states; if so, the QMT probability of these highly excited individual molecules will be extremely high. In other words, any reacting system will have a strong probability of tunnelling! Why then is QMT usually neglected, if it is actually a universally occurring event in chemistry? The answer is simple. The inclusion of tunnelling will only minimally affect the reaction rate compared to the approximate transition state theory. Still, any dynamical study that aspires to reach ultra-high accuracy must consider QMT. This book deals with reactions where tunnelling is significant, but we are still proud to say that QMT is omnipresent in chemistry.

With this in mind, where can we observe tunnelling in molecular systems? Many hydrogen transfers at room temperature are enhanced by QMT, particularly in biochemistry, combustion chemistry or some specific organic reactions. At this energetic regime, tunnelling is carried out from vibrationally excited states. But when we move to cryogenic temperatures, especially close to 0 K, any point-like particle should be completely at rest; under these extreme conditions QMT, if present, can be detected as the sole culprit of every reactivity pattern, even when considering ‘‘heavy’’ atoms, *i.e.* anything heavier than H. How to experimentally discover these cases is a major methodological challenge, but a very rewarding one.

Beyond the purely chemical aspect of tunnelling such as the rich QMT reactivity observed in frozen matrices (Chapter 1), some possible heavy-atom tunnelling reactions (Chapter 2) and a discussion on biomolecules (Chapter 3), in this book, we delve into different physicomathematical techniques to comprehend, rationalize and predict the different consequences that QMT can cause in the chemical world. The reader will be introduced to quantum dynamics (Chapter 10), instanton theory (Chapter 7), and semiclassical multidimensional tunnelling methods (Chapter 8). The upshots of tunnelling can be very weird: instantaneous reactions (Chapter 12), selectivity that goes beyond the common chemical knowledge (Chapter 4), fluxes of atoms and their electrons (Chapter 5), parity violation (Chapter 6) or unusual spectroscopic signatures (Chapters 9 and 11). All mentioned effects will be reviewed in this book by some of its specialists.

Johannes Kästner and Sebastian Kozuch

Contents

Theoretical and Computational Chemistry Series No. 18
Tunnelling in Molecules: Nuclear Quantum Effects from Bio to Physical Chemistry
Edited by Johannes Kästner and Sebastian Kozuch

Published by the Royal Society of Chemistry, www.rsc.org

Chapter 10 Quantum-dynamical Calculation of Rate Constants in Polyatomic Reactions Employing the Quantum Transition State Concept 328

Ralph Welsch

CHAPTER 1

Direct Observation of Tunnelling Reactions by Matrix Isolation Spectroscopy

CLÁUDIO M. NUNES,*[a] IGOR REVA*[a] AND RUI FAUSTO*[a,b]

[a] University of Coimbra, CQC, Department of Chemistry, 3004-535 Coimbra, Portugal; [b] Department of Chemistry, King Fahd University of Petroleum and Minerals, 31261 Dhahran, Saudi Arabia
*Emails: cmnunes@qui.uc.pt; reva@qui.uc.pt; rfausto@ci.uc.pt

1.1 Introduction

The theoretical foundations for nuclei and electron tunnelling were put forward by Hund,[1] Wigner,[2] Bell,[3] and others,[4,5] following the establishment of quantum mechanics. A more generalized treatment of tunnelling in chemistry appeared almost half a century afterwards in the seminal Bell's monography "*The Tunnel Effect in Chemistry*".[6,7] Indeed, as addressed in several other chapters of this book, theoretical methodologies to treat quantum mechanical tunnelling (QMT) in chemical reactions are still being developed nowadays. In this chapter, QMT in chemistry will be addressed from a more experimental perspective, taking advantage of the conditions typical of a matrix isolation experiment, which allow for direct observation of tunnelling driven processes by steady-state spectroscopic methods.

A simple and common way to portray tunnelling, although not particularly accurate,[8] is to consider it as a phenomenon that arises from the wave–particle duality. If in a chemical reaction the moving distance of a nucleus is comparable to its de Broglie wavelength, then there is a non-negligible probability of

---

Theoretical and Computational Chemistry Series No. 18
Tunnelling in Molecules: Nuclear Quantum Effects from Bio to Physical Chemistry
Edited by Johannes Kästner and Sebastian Kozuch

Published by the Royal Society of Chemistry, www.rsc.org

finding the nucleus on the other side of the reaction barrier, even if the system does not possess enough thermal energy to surmount the barrier. It means that nuclei are able to penetrate through reaction barriers. Of course, such unexpected behavior is framed on a classic perspective, in which all atoms involved in a chemical transformation are assumed to behave as hard spheres.

According to the classic transition state theory (TST), reactants must acquire enough energy to overcome a barrier in order to give rise to products.[9–11] Statistically, as temperature increases, more molecules will have enough energy to traverse the barrier, so that the reaction rate typically increases proportionally. Such temperature dependence of reaction rates was empirically established by Arrhenius in his well-known equation [eqn (1.1)], long before the development of the TST.[11,12]

$$k = A\mathrm{e}^{\left(-\frac{E_a}{RT}\right)} \tag{1.1}$$

In eqn (1.1), A is a pre-exponential constant, E_a the activation energy (J mol^{-1}), R the universal gas constant (8.314 J mol^{-1} K^{-1}), and T (K) is the absolute temperature.

However, deviations from the Arrhenius typical behavior can take place if tunnelling occurs simultaneously with the classic passage over the barrier. In these cases, the QMT contribution to the reaction rate can be incorporated using a tunnelling correction factor Q in the kinetic models, as it is, for instance, shown in eqn (1.2).[6,11,13]

$$k = QA\mathrm{e}^{\left(-\frac{E_a}{RT}\right)} \tag{1.2}$$

The tunnelling correction factor Q takes into account the tunnelling permeability through the barrier, which depends on the mass of the tunnelling particle, as well as on the barrier height and width.[6,13]

The existence of QMT contribution to a chemical reaction is typically detected indirectly by the observation of non-linear Arrhenius plots or abnormal kinetic isotope effects.[14–18] The temperature dependence of k in eqn (1.1) is given by the exponential factor, $\exp(-E_a/RT)$. Consequently, a plot of $\ln(k)$ against $1/T$ results in a straight line (see Figure 1.1). Its slope is $-E_a/R$. For historic reasons, such plots are referred to as Arrhenius plots. On the other hand, contrary to the classical over-the-barrier thermal process, tunnelling rates are approximately independent of the temperature. For a low enough temperature, when the system is in its ground vibrational state, the overall reaction rate is dominated by tunnelling and, consequently, temperature independent (see Figure 1.1).

Working at low temperatures is in fact a very convenient way to search for evidence of tunnelling in chemical reactions. At cryogenic temperatures (*e.g.*, 3–10 K), thermally activated rates become negligible for systems having barriers as low as ∼4 kJ mol^{-1} (∼1 kcal mol^{-1}), so the occurrence of a chemical transformation can only be due to a "pure" tunnelling reaction.[14–18] If such tunnelling transformations span from seconds to days, they can be directly

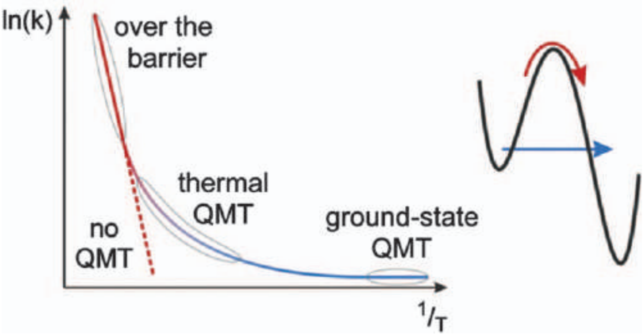

Figure 1.1 Logarithm of the rate constant plotted *versus* the inverse temperature (Arrhenius plot). The classical (thermal) over-the-barrier reaction results in a straight line. The rate becomes constant at low temperature when ground-state quantum-mechanical tunnelling (QMT) dominates. Adapted from ref. 15 with permission from the Royal Society of Chemistry.

observed and monitored using stationary-state spectroscopy methods. Indeed, particularly during the last decade, direct spectroscopic evidence of a variety of tunnelling-driven reactions has been reported using the low-temperature matrix isolation technique coupled to infrared spectroscopy. These observations have contributed significantly to a better understanding of QMT and its role in chemistry.[19]

In this chapter, we will address some representative cases of tunnelling-driven chemical processes, from conformational isomerizations to H-atom and heavy-atom bond-breaking/bond-forming reactions occurring in organic molecules under matrix isolation conditions. Examples of tunnelling reactions at cryogenic temperatures taking place in other than matrix isolation conditions are outside the scope of this chapter.

1.2 Description of Simple Mathematic Models for Tunnelling Computations

The present chapter is not concerned with the theory of tunnelling. There are several recent reviews on the topic.[18,20–22] Here, we shall recall that any occurrence of a tunnelling reaction must always face a barrier to overcome. This section will present simple formulas for the probabilities of tunnelling through two barriers of different shapes.

In a recent review,[22] Borden presents the formula for the energy-dependent probability $P(E)$, of a particle with mass m, tunnelling through a rectangular barrier of width w that is $V_0 - E$ higher than the energy of the particle (see Figure 1.2, left):

$$P(E) = \mathrm{e}^{-4\pi w\sqrt{2m(V_0-E)}/h}. \tag{1.3}$$

A more realistic barrier shape is that of the inverted parabola (as in Figure 1.2, right). The approximate solutions for the equations describing

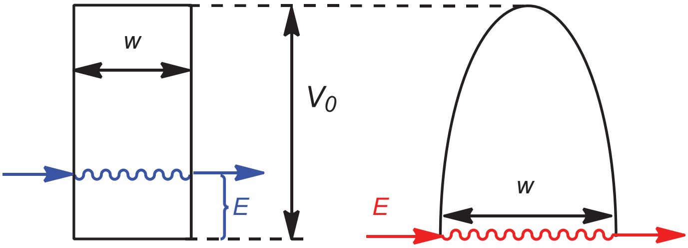

Figure 1.2 Left: tunnelling through a rectangular barrier of width w, at an energy $V_0 - E$ below the top of the barrier. Right: tunnelling through a parabolic barrier of width w, at an energy $V_0 - E$ below the top of the barrier.

the tunnelling of a particle through a parabolic barrier were independently devised by Wentzel, Kramers, and Brillouin in 1926.[23–25] As it is noted by Borden,[22] "*what has become known as the WKB approximate solution*[23–25] *to the calculation of the probability of tunnelling through a parabolic barrier should really be known as the JWKB approximate solution*",[22] because "*earlier Jeffreys*[26] *had published the mathematics necessary to obtain approximate solutions to differential equations of this type*".[22] The probability $P(E)$ of tunnelling through a parabolic barrier in the JWKB approximation can be written as:

$$P(E) = \mathrm{e}^{-\pi^2 w\sqrt{2m(V_0 - E)}/h}. \tag{1.4}$$

where a particle with mass m tunnels through a barrier with height V_0 and width w, $(V_0 - E)$ is the energy deficiency of the particle with respect to the top of the barrier (Figure 1.2, right), and h is Planck's constant.

The exponential eqn (1.3) and (1.4) are very similar; they only differ by a factor of $\pi/4$, related to the different shapes. Tunnelling through a parabolic barrier is more probable than through a rectangular barrier with the same energy deficiency $(V_0 - E)$, and barrier width, w. Both equations show that the probability of tunnelling decreases exponentially with the barrier width, w, times the square root of the particle mass, m, times the square root of the energy deficiency, $(V_0 - E)$. Therefore, the probability of tunnelling is much more sensitive to the width (w) of the barrier than it is to the height (*i.e.*, the energy deficiency), or to the tunnelling mass.

The contemporary methods of quantum chemistry allow for a detailed characterization of potential energy surfaces (PESs). These include not only information about stationary points (local minima and transition states) but also may provide information about the shape of potential energy barriers. In practice, the characterization of the reaction path starts with optimization of a transition state whose initial geometry and the initial force constants are calculated analytically. The intrinsic reaction path is then followed in both directions from that point, for a monomeric molecule in vacuum, typically with the Gaussian set of programs.[27] Note that the intrinsic reaction coordinate (IRC) may be computed either in the default mass-weighted coordinates [expressed in the (amu$^{-\frac{1}{2}}$ Bohr) units] or in non-mass-weighted (Cartesian) coordinates, by using the "IRC = Cartesian" option, expressed in units of Bohr. The latter option was used in this work in order to obtain the barrier width in units of length (Bohr) for tunnelling reactions in systems with OH or SH groups that involve a torsional reaction coordinate (flip by 180°).

An example of such a computed reaction path is presented in Figure 1.3 for the OH torsion connecting two amino-hydroxy conformers of cytosine. This allows for a direct estimation of the barrier width from the computed IRC scan at different relative energies. For example, the distance between the ends of the scan, *i.e.* at the points where the IRC scan converges to the minima, can be considered as the upper limit for the width of the barrier. For the current system, this limit is *ca.* 2.54 Å (from −2.4 to +2.4 Bohr, Figure 1.3). Accounting for the zero-point vibrational energy (ZPE) will reduce the barrier width. In the case of tunnelling from **AH2** to **AH1**, *via* the intramolecular OH torsion, the vibrational mode along the intrinsic reaction coordinate is τ(OH), with a computed frequency of 541 cm^{-1}. Accounting for the ZPE energy of this vibration (3.2 kJ mol^{-1}), the ZPE-corrected barrier width becomes *ca.* 1.77 Å (from −1.72 to +1.62 Bohr, Figure 1.3). Above the ZPE level, the shape of the barrier is very close to the inverted parabola, and the WKB approximation can be used for a rough estimation of the probability of tunnelling.

Using the calculated barrier height of 34.6 kJ mol^{-1} and 1.77 Å width at the ZPE level, the probability of tunnelling (transmission coefficient) of **AH2** can be estimated [using eqn (1.4)] as 1.6×10^{-16}. The tunnelling rate is a product of the transmission coefficient and the frequency of attempts. In this model calculation, assuming that the light H atom of the hydroxyl group of **AH2** conformer

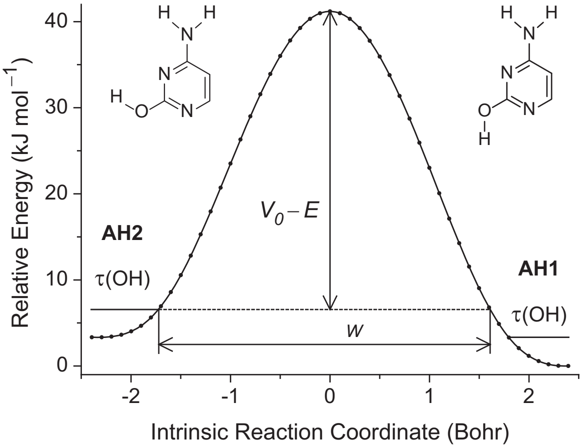

Figure 1.3 Intrinsic reaction coordinate (IRC) profile for rearrangement from **AH2** to **AH1** conformer of cytosine, *via* intramolecular torsion of the OH-group, computed at the B3LYP/6-31++G(d,p) level in Cartesian (non-mass-weighted) coordinates. The vertical arrow ($V_0 - E = 34.6$ kJ mol^{-1}) designates the calculated ZPE-corrected energy of the transition state relative to the reactant (**AH2**, left). The horizontal arrow designates the width ($w = 3.34$ Bohr) of the barrier at the ZPE level of the reactant.

is vibrating at the OH torsional frequency of ~541 cm^{-1} (B3LYP/6-31++G(d,p) computed value), it results in a tunnelling rate of 2.6×10^{-3} s^{-1}, *i.e.* a half-life time of 4.4 min, which is shorter than the experimentally observed lifetime of several hours. We shall note here that tunnelling lifetimes are known to be extremely sensitive to the barrier height and width.[28] Considering that the barrier shape for a molecule in a cryogenic matrix differs from that calculated for a molecule in vacuum,[29] we may carry out another rough estimate of the tunnelling lifetime, introducing a ±15% tolerance interval for the barrier width. With a barrier 2.03 Å wide (*i.e.*, increased by 15%), and all other parameters equal, the tunnelling half-life time of the **AH2** form of cytosine is then estimated to be 17.3 hours, similar to that obtained in the experiment.[30] With a barrier 1.50 Å wide (*i.e.*, reduced by 15%), and all other parameters equal, the estimated tunnelling half-life becomes only 1.1 seconds. This example shows how much sensitive is the probability of tunnelling to the width (w) of the barrier.

In the above example, we have implemented the WKB approximation, which allows defining a minimum-energy tunnelling path by following the intrinsic reaction coordinate. To apply the semi-classical approximation to multidimensional systems, many methods have been developed over the years; they can be classified according to the choice of the tunnelling path. The most likely tunnelling path differs from the minimum-energy path. A classical particle would take the path that requires least energy to proceed from reactant to the product (only the height of the energy barrier is relevant). Such a method is called a zero-curvature tunnelling (ZCT) correction. Unlike the classical particle, a quantum particle proceeds along the path that minimizes the action along the whole path. From a more advanced treatment, it becomes clear that the tunnelling path would cut corners, *i.e.*, that a shorter path on a small expenditure of a higher barrier leads to higher tunnelling rates.[31,32] This is taken into account in the small-curvature tunnelling (SCT) correction,[33] which is a popular and successful method to approximate tunnelling rates. Another advanced method is called instanton theory, which aims at optimization of the tunnelling path, *i.e.*, finding the path with the largest tunnelling probability at a given temperature. These more advanced methods are beyond the scope of this chapter.

1.3 The Matrix Isolation Method: Creating the Conditions for Direct Observation of Tunnelling-driven Chemistry

Matrix isolation is a technique where atoms or molecular species are trapped from the gas phase into an environment of a solidified inert gas at a temperature close to the absolute zero. By combining matrix isolation with different spectroscopic detection methods a powerful research tool has evolved over the time, which is currently being applied in several laboratories worldwide in a considerably large number of research areas. The method was in fact originally designed to study short-lived reaction intermediates, but receives nowadays many other uses, being particularly powerful for investigation of light-induced and tunnelling-driven chemical reactions.

The method was first developed by the groups of Pimentel and Porter, at Berkeley (USA) and Cambridge (UK), respectively,[34,35] and its name coined in the historical single-page report by Pimentel, Whittle and Dows "*Matrix Isolation Method for the Experimental Study of Unstable Species*", published in the Journal of Chemical Physics, in 1954.[34] Interestingly, it took almost two decades until matrix isolation became popular among organic chemists, what happened after its success in allowing generation and characterization of the hitherto elusive cyclobutadiene molecule.[36–38]

Although, as mentioned above, the matrix isolation was invented as a tool for stabilization, detection, and characterization of reactive species, the method has also some advantages over other techniques for the study of stable molecules as well as for investigation of chemical reactions, in particular unimolecular reactions. Most of its main advantages result from the low work temperature (typically of a few Kelvin), low concentration of the trapped species, and rigidity and chemical inertness of the medium. Among these, in the context of the topic of the present chapter we may highlight: (*i*) the fact that interactions between the trapped molecules can be neglected in diluted matrices, thus allowing easy access to the study of unimolecular chemistry, (*ii*) the absence of significant perturbations of the structure of the molecules under study by the matrix environment, (*iii*) the quenching of molecular diffusion and rotation (except in the case of very small molecules), which makes vibrational spectra of matrix-isolated species being essentially pure vibrational spectra, thus enabling a direct and easy comparison with theoretically predicted spectroscopic data, (*iv*) the fact that the trapped molecules are cage-confined, which precludes occurrence of secondary cross-reactions involving species originating from different reactant molecules, and then strongly reducing the number of possible products in comparison with gas phase or solution studies, and last but not the least (*v*) the inhibition of thermally induced over-the-barrier processes (for barriers of just a few kJ mol^{-1}) due to the low work temperature, which opens the gate for the study of tunnelling-driven reactions under favorable experimental conditions.

In spite of its power as an experimental technique to address problems of structure and reactivity, matrix isolation does not require expensive equipment (Figure 1.4). It should also be noted that, while matrix isolation has also some weaknesses, most of these have been overcome over time by the development of more reliable and precise cryostats, sample inlet systems, pressure and temperature controllers, and interfaces to spectrometers and auxiliary instrumentation, like light sources for *in situ* photolysis, pyrolyzers, *etc.* Those less aware of the method may find detailed descriptions of the experimental setups for matrix isolation in the classic books by Meyer,[39] Andrews and Moskovits,[40] Barnes *et al.*,[41] Dunkin,[42] and Fausto,[43,44] which may be used as introductory textbooks to the technique.

An interesting feature resulting from isolation of a given chemical species in a low temperature matrix is the well-known fact that, even under

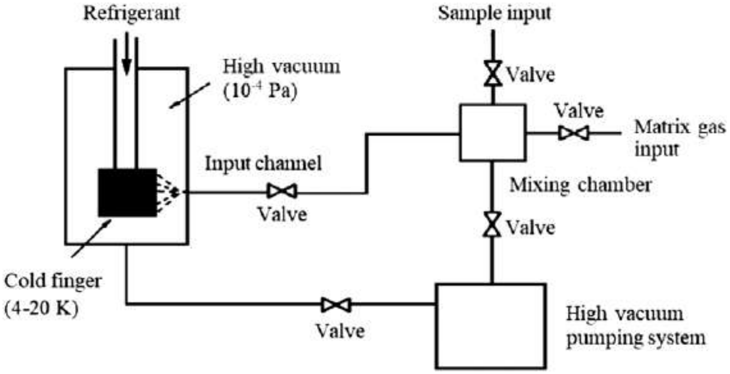

Figure 1.4 Schematic representation of a basic setup for matrix isolation. The cryostat (shown on the left) should have several external windows in order to enable to register the spectra and perform *in situ* irradiation of the sample.

well-controlled matrix deposition conditions, most of the times the produced matrices allow for different local environments around the isolated molecules. The co-existence of these different *matrix sites* leads to slightly different spectral vibrational signatures of molecules, which result in the usual observation of bands with multiplet structure (this is, however, most of the time readily recognized by comparing spectra obtained using different matrix gases). As described in detail in the next sections, the local environment may change considerably the reactivity of the molecules, in particular that resulting from tunnelling, and this must then be taken into account when interpreting the experimental data.

1.4 Interpretation of Kinetic Decays Observed in Cryogenic Matrices

Let us consider again the case of tunnelling decay of the **AH2** amino-hydroxy conformer of cytosine. For convenience, the experimentally observed amount of this form, as a function of time is depicted in Figure 1.5. This decay is rather slow: during 52 hours of observation, some 66% of the initially present **AH2** conformer spontaneously converted into **AH1**. On this time scale, during registration of a single data point (taking some 3 minutes), the conformational distribution practically does not change. This permits fitting of the experimental data using different kinetic models. The tunnelling conversion of **AH2** into **AH1** does not follow a first-order exponential kinetics that could be described with just one classical time constant τ_{clas}, as defined by the equation:

$$[n]_t/[n]_{t=0} = \exp(-t/\tau_{\text{clas}}). \tag{1.5}$$

The fit of eqn (1.5) to the experimentally observed decrease of **AH2** population is presented in Figure 1.5a. Initially, the process is faster than predicted by the best fit to classical single-exponential kinetics eqn (1.5). At

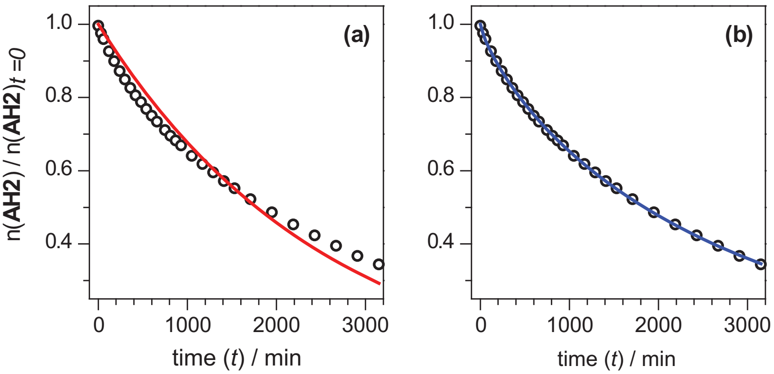

Figure 1.5 Circles: evolution of the abundance of the **AH2** form of cytosine with time of keeping the matrix in the dark at 13 K. The amount of **AH2** form at the beginning of registration ($t = 0$) is normalized to unity. Solid lines represent the best fits: (a) using the equation of classical kinetics [eqn (1.5)]; (b) using the equations of dispersive kinetics [eqn (1.6) and (1.7)]. The optimized classical time constant is $\tau_{\text{clas}} = 2564$ minutes; whereas for dispersive kinetics τ_{disp}, derived from the optimized values of k and $\beta = 0.7955$ using formula eqn (1.7), is $\tau_{\text{disp}} = 2192$ minutes.

later stages, the tunnelling clearly slows down (with respect to the best fit).[30,45] This suggests that the probability of tunnelling depends on time.

Dynamical processes in which many timescales coexist are called dispersive.[46–49] The rate coefficients for dispersive processes depend on time. In the case of a chemical reaction, the time dependence of the rate coefficient, $k(t)$, termed the specific reaction rate, is rationalized in the following way. Reactions by their very nature have to disturb reactivity distributions of the reactants in condensed media, as the more reactive species are the first ones to disappear from the system. The extent of this disturbance depends on the ratio of the rates of reactions to the rate of internal rearrangements (mixing) in the system restoring the initial distribution in reactivity of reactants. If the rates of chemical reactions exceed the rates of internal rearrangements, then the initial distributions in reactant reactivity are not preserved during the course of reactions and the specific reaction rates depend on time. Otherwise the extent of disturbance is negligible and classical kinetics, with a constant specific reaction rate, k, termed the reaction rate constant, may be valid as an approximation. In condensed media dispersive dynamical processes are endemic.

A cryogenic matrix represents exactly such a reaction system where the studied molecules (such as **AH2** conformer of cytosine) are embedded in a variety of different microenvironments (matrix sites), where the probability of rearrangement (*i.e.*, the reaction barrier) slightly differs from one site to another. Moreover, one may assume that the internal structure of different matrix sites in a cryogenic matrix does not change over time, which means that the chemical reaction (such as decay of **AH2** into **AH1**) proceeds on a time scale shorter than rearrangement of the matrix. Under such circumstances, the chemical reactions follow the dispersive kinetics,[50] rather than the classical first-order kinetics expected for unimolecular reactions in the gas phase. The dispersive kinetics is described by an empirical equation.

$$[n]_t/[n]_{t=0} = \exp[-k\,t^{\beta}],\ 0<\beta\leq 1 \tag{1.6}$$

introduced by Siebrand and Wildman.[51] Later Plonka showed[52] that

$$k \equiv \beta/(\tau_{\text{disp}})^{\beta} \tag{1.7}$$

Parameter β can be treated as a measure of inhomogeneity of the matrix. Without environmental effects, $\beta = 1$ should be observed, and the equation of dispersive kinetics [eqn (1.6)] transforms into the equation of classical kinetics [eqn (1.5)]. In matrices, β is reported to lie between 0.5 and 1, depending on the matrix, the temperature, and the time when the measurement of the kinetics is started.[53]

The progress of the **AH2** → **AH1** tunnelling during the experiment is very well reproduced by eqn (1.6), see Figure 1.5b. On that basis, one can conclude that the matrix medium (even within a single, spectroscopically distinguishable site) is to some extent inhomogeneous. The value of $\beta \approx 0.8$, obtained for the **AH2** → **AH1** tunnelling at 13 K, is in accord with the literature.[53,54] It suggests that, although the Ar matrix environment is not very disordered, the inhomogeneous character of this medium cannot be neglected.

It is also instructive to comment on the best fits obtained for the kinetical decays where the spectrometer-induced effect on the reaction rate is not negligible. Examples of such decays are those designated by numbers 1 and 2 in Figure 1.6 (observed for pyruvic acid without filter, or with a filter transmitting up to 4200 cm^{-1}).[55] Very interestingly, such decays (that phenomenologically can be designated as "fast") can be fitted much better with

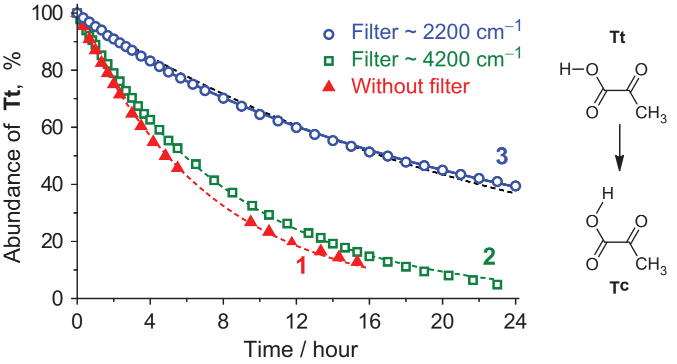

Figure 1.6 Decay kinetics of **Tt** form of pyruvic acid (which converts into **Tc**) in an Ar matrix at 15 K. The spectra recorded: without filter (**1**, triangles); with cutoff filters transmitting only up to 4200 cm^{-1} (**2**, squares), or only up to 2200 cm^{-1} (**3**, circles). The dashed lines (red, green, black) show best fits using the equations of classic single exponential kinetics. The continuous line (blue) shows the best fit using the equations of dispersive kinetics.

eqn (1.5) of the classical single-exponential kinetics, as compared to purely spontaneous decays showing dispersive kinetics (which can be designated phenomenologically as ‘‘slow’’). This means that the observed ‘‘fast’’ reactions induced by the light source of the spectrometer do not depend on the microenvironments (matrix sites). This is another practical hint for an experimentalist: true spontaneous (dark, ‘‘slow’’) tunnelling decays observed for matrix-isolated molecules are expected to show some dispersive character. Still, for practical reasons, it is sometimes useful to fit the dispersive decays using the equations of classical kinetics, and in such a way obtain approximate half-life times for the studied processes.

1.5 NIR and IR-induced Chemistry

To illustrate NIR and IR-induced chemistry, and also how it can interfere with the experimental observation of the tunnelling phenomenon, we start with presenting the very didactic case of the study on matrix-isolated cytosine. The results of the contemporary quantum chemical calculations[56] predict a consistent (and probably correct) energy ordering of cytosine isomers. According to these calculations, carried out at the CCSD(T) or QCISD(T) levels, the most stable tautomer of monomeric cytosine should be the amino-hydroxy (**AH**) form. Of the two **AH** conformers, **AH1** is computed to be more stable by 3.1 kJ mol^{-1} than **AH2** (Figure 1.7). The computed relative energy of the amino-oxo (**AO**) form is 5–6 kJ mol^{-1}, while those of the imino-oxo forms **IO1** and **IO2** are *ca.* 7 and 12 kJ mol^{-1}, all with respect to **AH1** (see ref. 56 and citations therein). Hence, for the gaseous cytosine, the **AH1** and **AH2** isomers should be dominating.

For two conformational structures such as **AH1** and **AH2** differing only by the position of a light particle (hydrogen atom; see Figure 1.7), a transformation of the higher-energy form into the lower-energy conformer can occur by tunnelling. Such spontaneous transformations were observed first for formic and acetic acids isolated in low-temperature matrices kept in the dark, as described later in this chapter in more detail. For cytosine, thermal equilibrium of **AH1** and **AH2** forms (differing in energy by 3.1 kJ mol^{-1}) corresponds to the population ratio **AH1**/**AH2** $= 3\times10^{13}$ at 13 K, and then

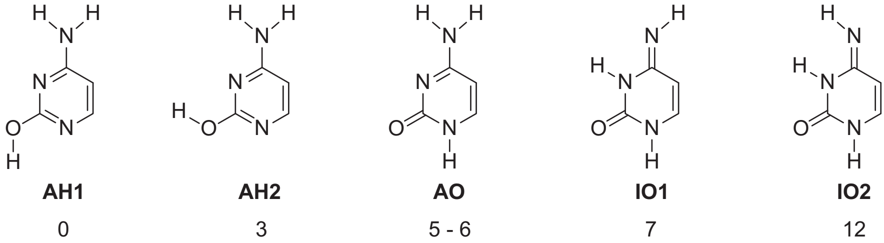

Figure 1.7 Structures of the lowest-energy isomeric forms of cytosine and their relative energies (in kJ mol^{-1}) computed at the CCSD(T) or QCISD(T) levels (see ref. 56 and citations therein).

tunnelling in the dark should lead to total conversion of **AH2** into **AH1**. However, upon trapping cytosine monomers in a cryogenic matrix, the amounts of conformers **AH1** and **AH2** were monitored by IR spectroscopy and found to be approximately equal.[30]

It has been demonstrated[57] that upon narrowband near-infrared (NIR) irradiation at 7013 cm^{-1} the most stable **AH1** form almost totally converts into **AH2** (Figure 1.8a; see band 1428 cm^{-1}), whereas narrowband NIR irradiation at 7034 cm^{-1} induces large-scale changes of population in the opposite direction, converting almost all **AH2** into **AH1** (Figure 1.8d; see band 1439 cm^{-1}).[57]

Starting from matrices enriched with either **AH1** or **AH2** conformers, the populations of the conformers were monitored by periodical registration of spectra in the full mid-infrared range. After 2 hours, the spectrum of the sample initially enriched with **AH2** (Figure 1.8a) transformed into that shown in Figure 1.8b, while for the sample initially enriched with **AH1** (Figure 1.8d), the spectrum after *ca.* 2 hours of monitoring is presented in Figure 1.8e. The striking point is that, independently of the initial **AH1** : **AH2** ratio [very low

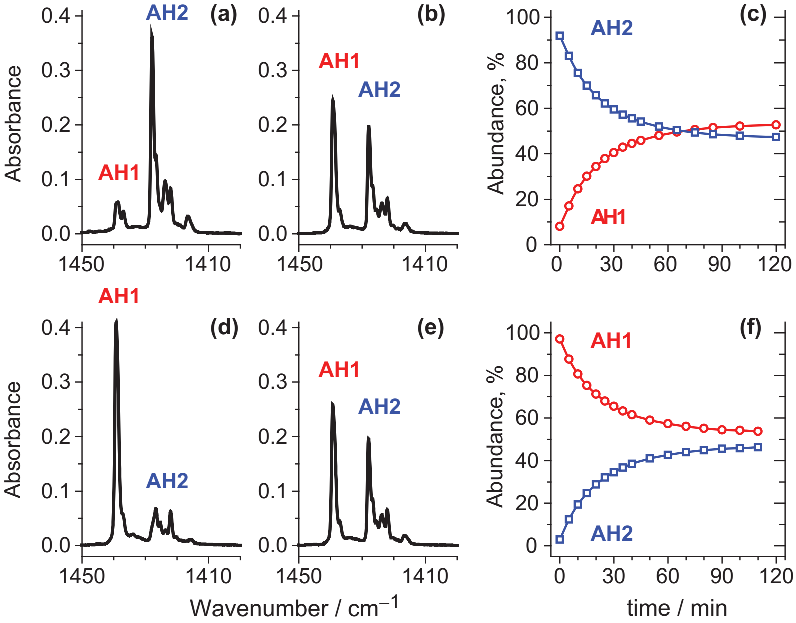

Figure 1.8 Fragment of the IR spectrum of cytosine isolated in an Ar matrix at 13 K: (a) recorded after narrowband irradiation at 7013 cm^{-1}; (b) after subsequent 120 min of exposure to the NIR/IR broadband radiation of the spectrometer source; (c) evolution of abundances of **AH1** and **AH2** conformers with time of broadband NIR/IR irradiation [initial point corresponds to (a) and final point corresponds to (b)]; (d) recorded after narrowband irradiation at 7034 cm^{-1}; (e) after subsequent 110 min of exposure to the NIR/IR broadband radiation of the spectrometer source; (f) evolution of abundances of **AH1** and **AH2** conformers with time of broadband NIR/IR irradiation [initial point corresponds to (d) and final point corresponds to (e)].

(Figure 1.8a) or very high (Figure 1.8d)], the changes induced by the broadband NIR/IR light of the spectrometer source led to the same stationary state.[30] In this state, the total population of the amino-hydroxy tautomer is divided into **AH1** (53%) and **AH2** (47%) forms (see Figure 1.8c and Figure 1.8f). That makes the stationary **AH1**/**AH2** ratio equal to 1.1.

It is easy to prove that the conformational transformations depicted in Figure 1.8, occurring on the time scale of 2 hours at 13 K are not thermally induced. This proof is based on the potential energy profile connecting the **AH1** and **AH2** conformers of cytosine (see Figure 1.3).

If the reaction occurred in a classical way, exclusively as the thermal over-the-barrier reaction, its rate constant could be estimated using the Eyring–Polányi equation,

$$k = \frac{\kappa k_B T}{h} e^{-\frac{\Delta^{\ddagger} G^{\ominus}}{RT}}$$

where k is the reaction rate (in s^{-1}), κ is the transmission coefficient usually assumed to be 1 (no tunnelling and no reflection at the barrier top), k_B is the Boltzmann constant (1.38×10^{-23} J K^{-1}), T is the absolute temperature (in K), h is the Planck constant (6.626×10^{-34} J s), R is the universal gas constant, and $\Delta^{\ddagger} G^{\ominus}$ is the standard Gibbs energy of activation of the studied compound.

For cytosine, the theoretical harmonic vibrational computations at the B3LYP/6-31++G(d,p) level give $\Delta^{\ddagger} G^{\ominus} = 34.6$ kJ mol^{-1}. The half-life of the **AH2**→**AH1** over-the-barrier reaction is calculated to be *ca.* 10^{120} years at 13 K (in contrast, the estimated half-life for the same reaction would be about 130 ns at 298 K).

In order to investigate in more detail the **AH1**↔**AH2** phototransformation induced by broadband NIR/IR light, several bandpass IR filters were employed.[30] Whatever the initial **AH1**:**AH2** ratio, no measurable change in relative populations of these forms was observed (during 10–30 minutes) for matrix-isolated cytosine exposed to the light of the spectrometer source passed through a filter transmitting only below 1750 cm^{-1} (equivalent of 21 kJ mol^{-1}). However, when this IR filter was substituted by another one transmitting light in the spectral range up to 4200 cm^{-1} (50 kJ mol^{-1}), quite rapid changes in the **AH1**:**AH2** population ratio were observed.[30] These observations demonstrate that not only NIR excitation to overtones (at 7013 or 7034 cm^{-1}) but also excitation of the fundamental OH or NH stretching modes (in the 3610–3430 cm^{-1} range) induces mutual conversion of **AH1** and **AH2** conformers. This can be rationalized by considering that the conformational change induced, *e.g.*, by the excitation at 3601 cm^{-1} (to the first excited state of the OH stretching vibration in **AH2**) should be an over-the-barrier process. The energy of this excited vibrational state (3601 cm^{-1} is *ca.* 43 kJ mol^{-1}) is indeed higher than the barrier for the **AH2**→**AH1** conversion, estimated at the B3LYP/6-31++G(d,p) level to be 34.6 kJ mol^{-1}.[30]

For matrix-isolated cytosine kept in the dark and monitored only in the spectral range below 1750 cm^{-1} (with photons of the spectrometer source having energies no more than 21 kJ mol^{-1}), relative populations of **AH1** and

AH2 changed very slowly. Independent of the initial **AH1** : **AH2** ratio, the higher-energy **AH2** conformer always converted into **AH1**. In order to observe the changes of relative populations of **AH1** and **AH2** in a possibly largest scale, in a dedicated experiment, a matrix with very high relative population of **AH2** (with the **AH1** amount close to zero) was prepared by narrowband irradiation at 7013 cm^{-1}. After 35 hours of monitoring, the **AH1** : **AH2** ratio reached the value of 1.1, and continued to grow (Figure 1.9). After 52 hours in the dark, the **AH1** : **AH2** ratio was approximately 2, and the kinetical profiles did not show any sign of reaching a plateau.[30] Such kinetical behavior points out the occurrence of a tunnelling process.

The spectrometer-induced conformational changes and tunnelling effects, similar to those observed for the parent cytosine, were also observed for several 5-substituted cytosines,[58] and these cases by no means constitute an exception. The spectrometer-induced structural changes in matrix-isolated molecules do indeed occur frequently and should be carefully characterized, in order to be able to separate them from the spontaneous changes (that typically occur on a larger time scale). Here we shall provide some more examples.

We have recently studied in detail the conformational behavior of matrix-isolated pyruvic acid.[55] It has two main conformational structures, designated as **Tc** and **Tt** (Figure 1.10). The main **Tc** form of pyruvic acid is almost exclusively present in the gas phase and in freshly deposited cryogenic matrices. Irradiation of the samples at the frequency of the first OH stretching overtone of **Tc** (at 6630 cm^{-1} in Ar matrix) results in conformational isomerization, and up to 75% of the compound is transformed into its

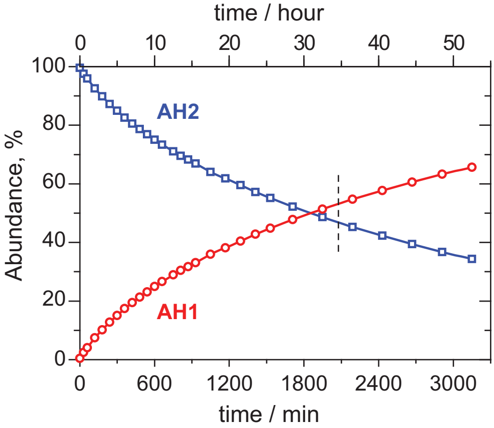

Figure 1.9 Evolution of abundances of **AH1** and **AH2** forms of cytosine with time of keeping the matrix in the dark at 13 K and monitoring only through a filter transmitting below 1750 cm^{-1}; the initial population of **AH1** (near 0%) and **AH2** (near 100%) was induced by narrowband NIR irradiation at 7013 cm^{-1}. The vertical dashed line near 35 hours corresponds to the conformer distribution shown in Figure 1.8b and 1.8e. The continuous lines, connecting the experimental points, are shown to guide the eye.

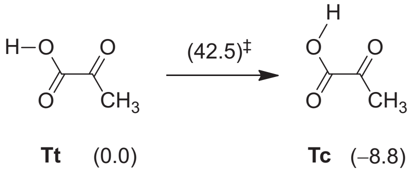

Figure 1.10 Two main conformers of pyruvic acid and their ZPE-corrected relative energies (kJ mol^{-1}) computed at the B3LYP/6-311++G(d,p) level, with respect to the minor **Tt** form. The ZPE-corrected relative energy of the transition state (with respect to **Tt**) for intramolecular torsion of the OH group is shown above the arrow.

higher-energy **Tt** conformer. This allowed for the subsequent studies of kinetics of spontaneous and spectrometer-induced conformational changes. Once the **Tt** form was generated, several independent experiments were performed. In one case, the sample was exposed to the unfiltered IR beam of the spectrometer. In other cases, a long-pass cutoff IR filter was placed between the spectrometer source and the sample. Two different cutoff filters were applied: transmitting only light with wavenumbers up to 4200 cm^{-1} (~50 kJ mol^{-1}) or up to 2200 cm^{-1} (~26 kJ mol^{-1}). In all cases, the **Tt**→**Tc** decay process was followed spectroscopically over the time. The decay rates in these experiments depended on the transmittance range of the applied filter (Figure 1.6, Section 1.4).[55]

In the experiments undertaken without filter or with filter transmitting in the whole mid-IR range (transparent up to 4200 cm^{-1}), a half of the **Tt** form was converted to **Tc** within 5 or 6 hours. In the case of the filter transmitting only light up to 2200 cm^{-1} the decay was considerably slower: it took ~17 h to convert a half of **Tt** form back to **Tc**. The rationalization of the observed differences is the following: when the matrix sample is protected with the long-pass cutoff filter, transmitting only below 2200 cm^{-1}, all accessible energy levels in the system are below the barrier (for each conformer) and isomerization from **Tt** to **Tc** is only feasible *via* tunnelling.[55] With the filter transparent up to 4200 cm^{-1}, or without it, excitation of the OH stretching fundamental modes promotes additional phototransformations. In this case, the stationary state is strongly shifted toward **Tc**. Comparing the present case of pyruvic acid with the case of cytosine discussed earlier, there is similarity: only with a proper filter (having its cut-off below the activation energy) the true tunnelling kinetics can be observed.

Some other interesting cases related to spectroscopic studies of H-atom tunnelling concern cyanophenol[59] and imino-thiol forms of thioacetamide.[60] In cyanophenol (Figure 1.11), the barrier separating the higher energy *trans* form from the conformational ground state *cis* is computed to be near 15 kJ mol^{-1} (1250 cm^{-1}). In agreement with such a low energy barrier, a successful spectroscopic observation of the *trans*→*cis* tunnelling relaxation was only possible by using the longpass cutoff filter transmitting solely below 1170 cm^{-1}.[59]

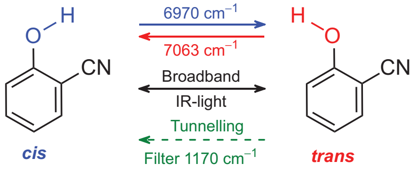

Figure 1.11 Narrowband-induced (top), broadband-induced (middle) and tunnelling isomerizations in matrix-isolated 2-cyanophenol. The observation of a true tunnelling was only possible by using a longpass cutoff filter transmitting solely below 1170 cm^{-1}.

Based on all the cases described above, we propose here an empirically derived "rule of thumb" for spectroscopic observation of tunnelling decays. This rule, to date, has been in agreement with all our experimental observations. According to this rule, the calculated activation energy will approximately define the higher bound of the cutoff value of the longpass filter that should permit spectroscopic characterization of the expected tunnelling reaction, without affecting the kinetics of the spontaneous reaction. It is important to keep in mind that when the relative energies of transition states (with respect to the neighboring minima) fall into the mid-IR range of the spectrum, the possibility of IR-induced photochemistry (during recording of spectra) should not be neglected.

1.6 Conformational Isomerizations by Tunnelling

Numerous investigations on tunnelling-driven reactions of organic molecules observed in low-temperature matrices refer to conformational isomerizations. The prototype reaction was observed for the first time for formic acid (HCOOH; see Figure 1.12).[61–63] The most stable *Z* (*cis*) conformer of this compound was isolated in an argon matrix and vibrationally excited by narrowband NIR light tuned at the frequency of the first overtone of its OH stretching vibration (6934 cm^{-1}), which led to generation of the less stable *E* (*trans*) conformer. The *trans* conformer was then found to convert back to the *cis* form by tunnelling at a rate of *ca.* 4×10^{-3} s^{-1}.[61]

Interestingly, the photogeneration of the *trans* conformer from the *cis* form was observed to take place even when irradiation of the lower energy form was performed with an energy below the energy barrier separating the two conformers (Figure 1.13).[64] This observation implies that, in those cases, vibrational excitation of the *cis* conformer followed by vibrational energy relaxation takes the molecule to a high vibrational excited torsional state, reducing the height and width of the energy barrier for conformational isomerization in such a way that the transformation can then take place by tunnelling.

The selective photogeneration of high-energy conformers that are found in nature in very low amounts (or not found at all) by vibrational excitation of the low-energy and abundant in nature forms has more than academic significance: it also opened the opportunity to investigate the characteristic chemistries of species otherwise not accessible to experimentation, which might be

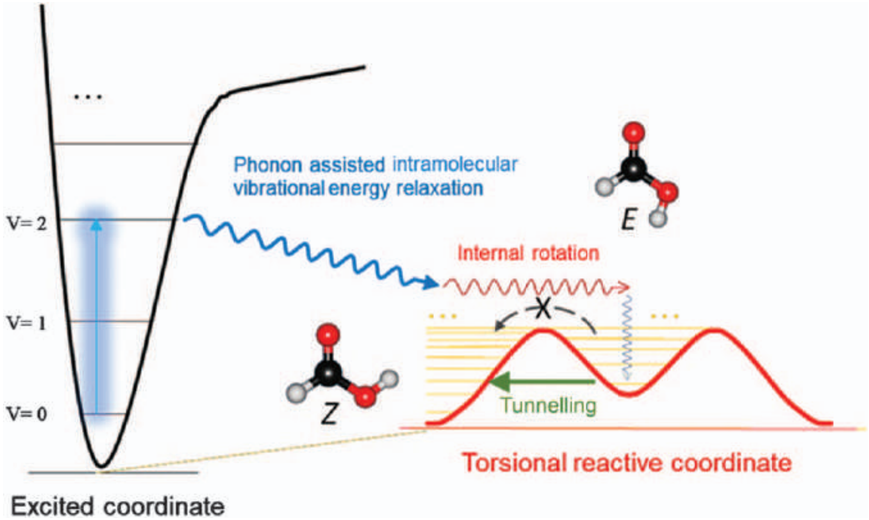

Figure 1.12 Conformers of formic acid and schematic representation of the (N)IR-induced *Z* (*cis*) → *E* (*trans*) isomerization and subsequent decay of the *E* conformer into the more stable *Z* form by tunnelling (green arrow). The photoisomerization involves vibrational excitation of a high-absorption cross-section high-energy mode, followed by phonon-assisted intramolecular vibrational energy relaxation and internal rotation. The over-the-barrier thermal back-isomerization is not accessible. Note that the *cis*/*trans* designation of the conformers does not follow some of the original publications, where the opposite designations are used.

different from those of the low-energy conformers. In the case of formic acid, for example, it was found that, while the more stable *cis* conformer photochemically decomposes predominantly to carbon monoxide and water, the less stable *trans* form dissociates mainly to carbon dioxide and molecular hydrogen.[65] This experimental approach has been evolved over time and, recently, we have introduced the concept of *vibrational antenna* to control the structure of a fragment remotely located in the molecule relative to the group where the energy is introduced (the *antenna*),[66–68] and also presented the first example where excitation of the second OH overtone was used to promote conformational changes,[69] thus demonstrating the feasibility of this type of excitation to promote structural changes in a molecule. Use of higher-order overtones allows for the introduction in a molecule of a large amount of energy (~10 500–9600 cm^{-1}, or ~130–115 kJ mol^{-1} upon excitation of the second OH stretching overtone, *vs.* ~7300–6300 cm^{-1}, or ~87–75 kJ mol^{-1} upon excitation of the first OH stretching overtone), thus opening the gate to the promotion of chemical processes having considerably higher barriers than those accessible hitherto.

Many other molecules containing a carboxylic acid group have been studied following a similar approach to that initially used to investigate the higher energy conformer of formic acid. These include acetic and propionic acids,[70–73]

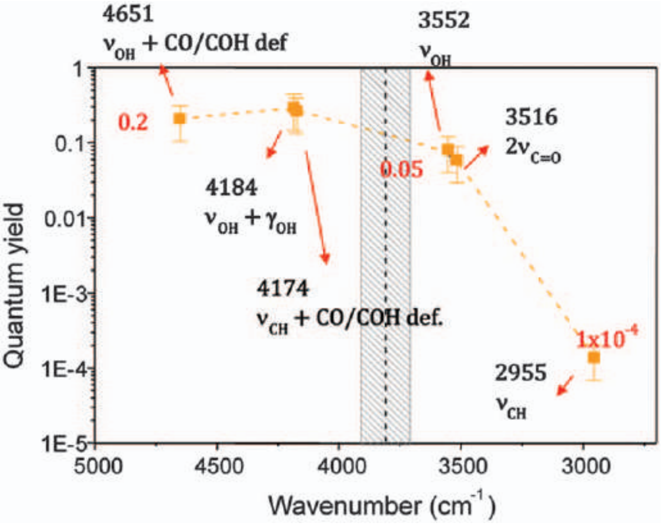

Figure 1.13 Quantum yields for the conversion of the *Z* conformer of formic acid into the *E* form upon vibrational excitation at different frequencies. The quantum yields are indicated in red, while the excitation wavenumbers and description of excited modes are shown in black. The grey area corresponds to the range of energies (in cm^{-1}) of the available data on barrier for $Z \rightarrow E$ internal rotation.
Adapted from ref. 64 with permission of American Chemical Society, Copyright 2003.

halogenated acetic acids,[74–77] α-hydroxyl, α-keto and α, β-unsaturated carboxylic acids,[55,67,78–83] aromatic and other cyclic carboxylic acids,[84–89] dicarboxylic acids,[90–94] and amino acids.[95–101] In most of those cases, the higher-energy conformers generated *in situ* by IR excitation of lower-energy forms were found to relax in the dark, by tunnelling, to the latter forms.

An interesting example of the combined use of selective IR irradiations triggering conformational isomerization and tunnelling decay of the photogenerated higher-energy conformers has been reported as a way to selectively produce the four conformers of propionic acid.[73] Propionic acid has two low-energy conformers, **Cs** and **Cg**$^{\pm}$, where the carboxylic group assumes the *cis* configuration, and two high-energy forms, **Ts** and **Tg**$^{\pm}$, where the conformation of the carboxylic group is *trans* (Figure 1.14). In the vapor of the compound at room temperature, the two low-energy conformers exist in equilibrium. During deposition of the compound in an argon matrix, the **Cg**$^{\pm}$ conformer converts into the lowest energy **Cs** form, in an over-the-barrier process made accessible due to local heating of the cold substrate resulting from the landing of the molecules of the gaseous beam being deposited (conformational cooling).[102,103] This leads to the sole presence of the **Cs** conformer in the initially deposited matrix. Selective NIR irradiation at the frequency of the first OH stretching overtone of this conformer results in production of both **Ts** (through rotation around the C–O bond) and **Cg**$^{\pm}$

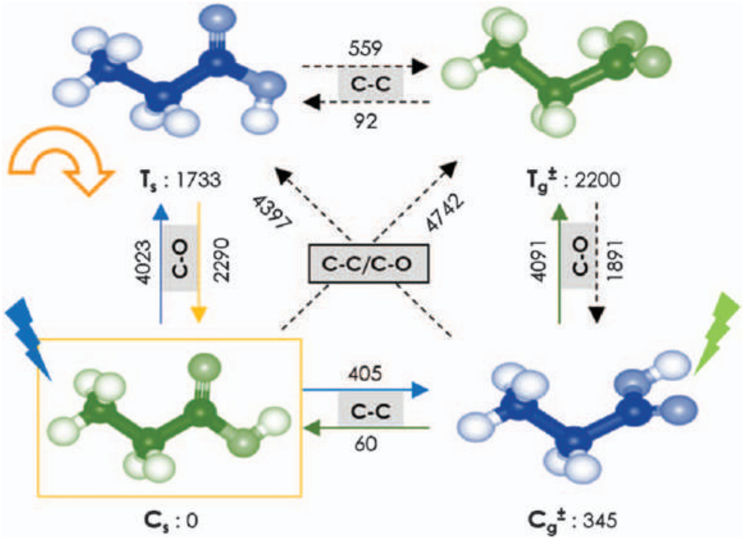

Figure 1.14 Conformers of propionic acid, their relative stabilities and barriers for conformational isomerization (both in units of cm^{-1}) about the C–O and C–C(O) bonds. The figure also illustrates the effect of combination of selective NIR excitation and tunnelling decay processes leading to observation of the four conformers of propionic acid isolated in solid argon. The flash-type arrows indicate NIR irradiations performed at the first OH stretching overtone of the conformer, resulting in the transformations indicated by the solid arrows of the same color. The arch-type arrow indicates tunnelling. Note the different notation of the conformers used here when compared with that used in the original reference.
Adapted from ref. 73 with permission from American Chemical Society, Copyright 2005.

(*via* rotation around the α C–C bond) (Figure 1.14). If subsequently the sample is left in the dark, the **Ts** form relaxes by tunnelling back to the initial conformer (**Cs**) in a few minutes, since this conversion requires only movement of the light hydrogen atom, while the **Cg**$^{\pm}$ form persists in the matrix for several hours (tunnelling to the only conformer with a lower energy than the **Cg**$^{\pm}$ form, *i.e.*, the most stable **Cs** conformer, has a very low probability since it implies movement of a heavy fragment; the slow decay observed for this conformer results from its isomerization to **Cs** over the very low energy barrier (0.7 kJ mol^{-1}) separating these two forms). The population of the **Cg**$^{\pm}$ conformer can then be increased by repeating the procedure making this form the dominant one in the matrix. Subsequently, the **Cg**$^{\pm}$ conformer can be selectively excited, by pumping its OH stretching overtone. Such excitation results partially in regeneration of the **Cs** conformer (*via* rotation about the C–C bond α to the carbonyl) and partially in the production of the highest energy **Tg**$^{\pm}$ conformer (by rotation around the C–O bond). As a whole, these experiments allow selective generation and undertake the experimental characterization of all the four conformational states of propionic acid.

A very interesting phenomenon that has been taken advantage of, in order to investigate high-energy conformers of carboxylic acids, is the fact that the stability of these conformers often strongly increases in matrices made by materials that are able to interact in a specific way with the carboxylic acid group, in particular molecular nitrogen.[55,78,79,104,105] Specific interactions between the matrix N_2 molecules and the OH acid group of the carboxylic fragment have been in fact shown to increase the lifetime of the otherwise short-lived conformers of this type of molecules, by establishing an $OH\cdots N_2$ hydrogen bond type interaction whose interaction energy is typically of *ca.* −5 kJ mol^{-1}.[104,106] This interaction energy may be compared to that associated with the OH···Ar interaction reported by Wawrzyniak *et al.*,[107,108] who found that the latter amounts only to −1.5 to −2.0 kJ mol^{-1}.

The stabilizing effects due to the $OH\cdots N_2$ interaction are in fact frequently very large, while in general the matrix material can considerably influence the tunnelling decay rates, even when we are considering only noble gas matrices. Clearly, in addition to the barrier-height change upon solvation in polarizable media or due to specific interactions with the matrix material (like in the case of N_2), other factors can also influence the tunnelling rates. Among these we can mention the coupling between vibrational levels involved in the energy relaxation process, and the magnitude of the energy gap between the tunnelling levels (which leads to changes in the order of the phonon process providing the required energy dissipation).[62,109,110] For formic acid, the decay rate in a nitrogen matrix is smaller by 5, 30, ~55 and 10 000 times compared to xenon, krypton, argon and neon matrices, respectively.[62,111] For acetic acid, it is slower in N_2 matrices by a factor of ~600 than in both argon and krypton matrices and by a factor of 3000 than in a xenon matrix.[72]

The stabilization of high-energy conformers in an N_2 matrix may even lead to a completely different pattern of reactivity compared to argon or other noble gases. A remarkable case was found for 2-fluorobenzoic acid (2FBA),[84] and very interesting results have also been reported for glycolic acid[82] and β-aminoisobutyric acid.[95] The reader is invited to consult the original articles for details.

The molecule of 2FBA has an asymmetric substitution pattern at the ortho positions (on one side a fluorine atom, and on the other a hydrogen atom). This leads to very different intramolecular interactions when the orientation of the carboxylic group changes. The molecule may exist in four different conformers (Figure 1.15), two of them bearing the carboxylic acid group in the *cis* conformation (the most stable forms) and the other two exhibiting this group in the *trans* conformation. The *cis* conformers (**I** and **II** in Figure 1.15) account for *ca.* 98% of the total population in the gas phase at 25 °C, the calculated **I**:**II** population ratio being ~3.[84] The third conformer on the increasing order of energy (**III**) is stabilized by an intramolecular OH···F hydrogen bond and has an estimated population at 25 °C of *ca.* 2%, while conformer **IV** has a high relative energy (~30 kJ mol^{-1}) and should have a negligible population in the same conditions.[84]

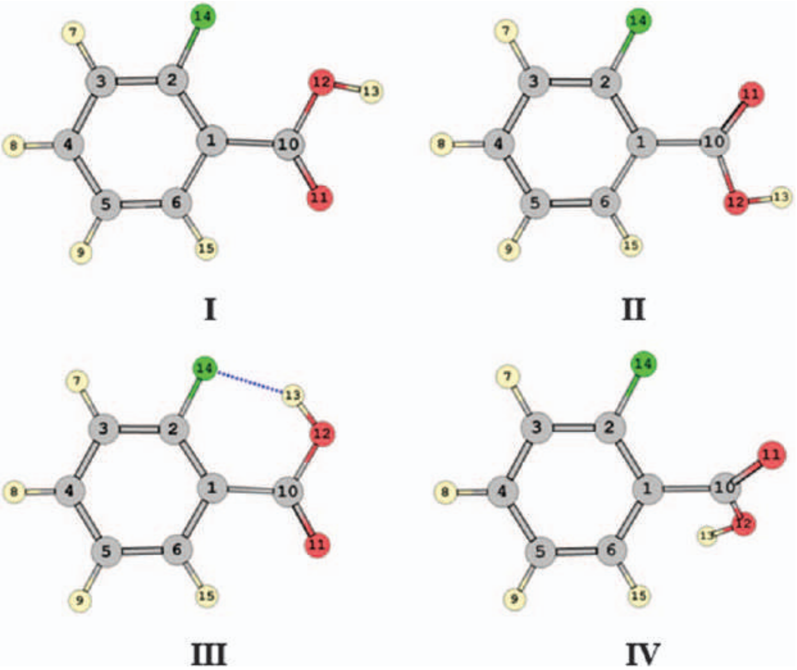

Figure 1.15 Conformers of 2FBA. Conformer **IV** has a non-planar geometry and the represented structure has a symmetry-related counterpart. Reproduced from ref. 84 with permission from the American Institute of Physics, Copyright 2017.

As expected, no bands ascribable to the higher-energy *trans* conformers (**III**, **IV**) were observed in the spectra obtained for the compound in argon or N_2 matrices. Narrowband NIR irradiations at the frequencies of the first overtone of the O–H stretching vibration of conformers **I** and **II** were performed.[84] In the argon matrix, irradiations at the frequencies corresponding to conformer **I** resulted in selective conversion of this form into conformer **III** (rotation around the C–O bond), while those performed at the characteristic frequencies of conformer **II** appeared to be unable to promote any conformational transformation, since no spectral changes could be observed (Figure 1.16). This result was *a priori* unexpected, since one could expect that conformer **II** should convert into conformer **IV** (which differs from **II** by rotation around the C–O bond), in a process similar to that corresponding to the **I** → **III** transformation. The results obtained in the N_2 matrix were also surprising: irradiations at frequencies of the vibrations of conformer **I** yielded identical results as in the argon matrix (conversion of conformer **I** into **III**), but, this time, excitation of conformer **II** resulted in the conversion of this conformer into conformer **III** (Figure 1.16). A point to note is that this last process (**II** → **III**) was found to be considerably less efficient than the **I** → **III** conversion.

The key information to understand these results relates with to relative size of the barriers to internal rotation around the C–O bond in conformers

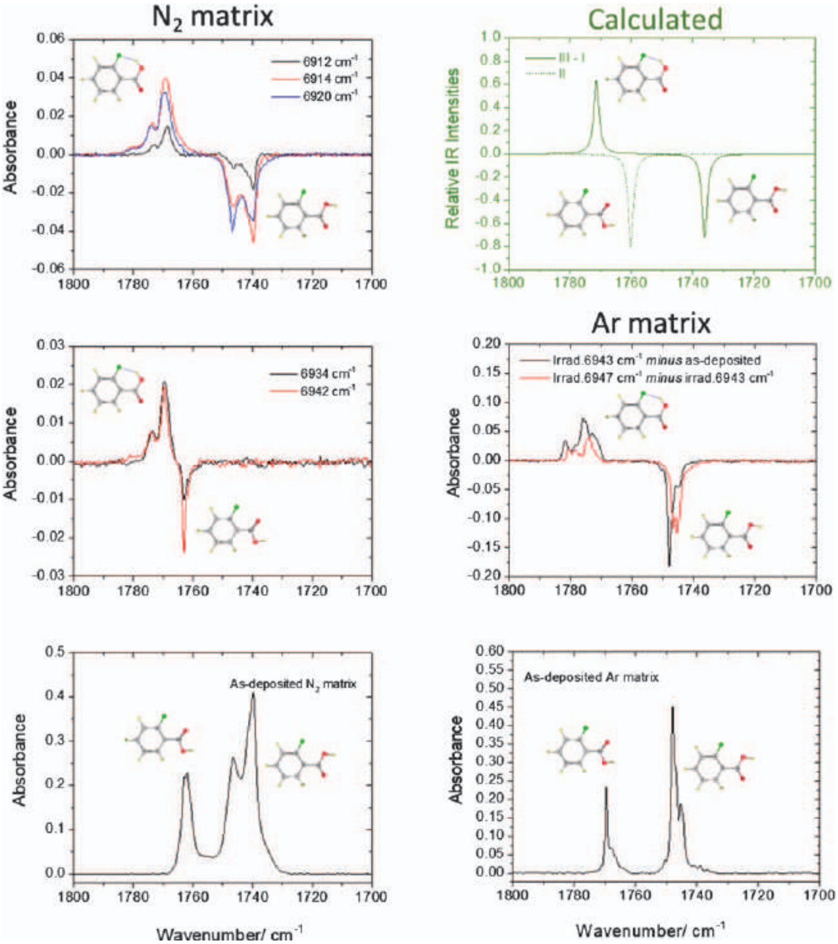

Figure 1.16 Right top; green: simulated IR difference spectrum: B3LYP/6-311++G(d,p) calculated spectrum of conformer **III** *minus* calculated spectrum of conformer **I** (solid line) in the C=O stretching region; the calculated spectrum of conformer **II** in the same spectral region is shown by the dotted line. Right middle: IR difference spectra of 2FBA showing the results of the performed irradiation experiments carried out in an argon matrix. Right bottom: spectrum of the as-deposited 2FBA argon matrix. Left top and middle: IR difference spectra of 2FBA showing the results of the performed irradiation experiments carried out in solid N_2, by irradiating at frequencies of bands of conformer **I** and **II**, respectively Left bottom: spectrum of the as-deposited 2FBA N_2 matrix.
Reproduced from ref. 84 with permission from the American Institute of Physics, Copyright 2017.

III and **IV** (the first is three times higher than the second (40.4 kJ mol^{-1} *vs.* 13.9 kJ mol^{-1}) due to the presence in conformer **III** of the stabilizing O–H$\cdots$F intramolecular H-bond interaction that is absent in conformer **IV**) and the very small energy barrier associated with the **IV**→**III** isomerization (2.6 kJ mol^{-1}),[84] besides the stabilization of high-energy conformers resulting from the O–H···N_2 interaction in the nitrogen matrix.

In the argon matrix the low energy barrier for the **IV**→**II** process allows the fast tunnelling conversion of **IV** into **II** to take place once the higher energy conformer (**IV**) is produced by vibrational excitation of **II**. It shall be noticed that conformer **IV** has a non-planar geometry, with the COOH group twisted out of conjugation with the ring. This means that the H-atom tunnelling within the carboxylic group has to be followed by a relaxation of the geometry leading to the planar conformer **II**. This structural relaxation involves movement of heavy atoms, so that tunnelling is not favored. Nevertheless, the required structural relaxation is barrierless, so that it takes place promptly following the hydrogen tunnelling. In this way, observation of **IV** is precluded. On the other hand, the high-energy barrier associated with the **III**→**I** conversion makes this process inaccessible and allows the observation of conformer **III**. In contrast, in the N_2 matrix, the stabilization of the initially formed conformer **IV** after pumping of **II** resulting from OH···N_2 specific interactions allows this conformer to survive long enough to allow the **IV**→**III** over-the-barrier conversion to be competitive with the **IV**→**II** tunnelling. Hence, while part of the initially formed conformer **IV** still converts back to **II** by tunnelling (justifying the low efficiency of the observed **II**→**III** transformation), the remaining fraction of **IV** converts to **III**, explaining the observed neat conversion of the NIR excited conformer **II** into form **III** in the N_2 matrix.

Another way to promote stabilization of otherwise short-lived conformational species of carboxylic acids is to quench the tunnelling by making associates with other molecules or forming dimers of the compound. There are two different approaches to perform this type of studies. In one type of experiments, the compound to be studied is deposited together with the molecule chosen to form the complex and the higher-energy conformers are then produced *in situ* by selective NIR irradiation of the stable precursor conformers. Thermal mobilization by annealing of the matrix at higher temperatures allows for diffusion of the molecules and formation of the associates containing the high-energy forms. The alternative procedure involves co-deposition of the compound under investigation and the complexing molecule in such conditions that they associate (for example depositing the matrix at a higher temperature or preparing concentrated matrices). The associates will have the molecule under study in one of its low-energy conformers, which is initially present in the gaseous mixture being deposited. Then, selective NIR irradiation of the associates may be used to generate complexes where the compound adopts one of its high-energy conformational states. In the case of dimers, the ligand molecule is, obviously, the molecule under study itself, but the experimental procedures are similar. Both approaches were used very successfully to generate a plethora of new dimers of formic acid and acetic acid containing the higher-energy *trans* conformer of these molecules,[105,112,113] as well as associates of these acids with water.[114,115]

All complexes where the OH carboxylic moiety is involved in the intermolecular interaction that gives rise to the associate were found to be stable or at least considerably more stable than the corresponding monomeric species, clearly demonstrating that the probability of tunnelling strongly reduces upon association. For example, the *trans* formic acid complex with water in an argon matrix is stable for months, in contrast with the *trans* formic acid monomer, whose lifetime is only about 9 minutes.[114] Also, dimers of either formic or acetic acid bearing a *trans* unit in their structures participating in an intramolecular H-bond were found to be stable.[113–115] The main factor responsible for reducing the tunnelling probability is the increase in the barrier height for internal rotation around the C–O bond resulting from the participation of the carboxylic group in a specific H-bond interaction with the ligand. However, also when the OH fragment does not participate directly in the intermolecular bonding, complexation was observed to decrease the tunnelling probability, and dimers of formic acid and acetic acid matching this condition were found to have tunnelling decay rates considerably lower than the corresponding monomers under the same experimental conditions.[113–115] In these cases, it is clear that a stabilization due to the increase of the barrier height cannot explain the observations. We can speculate that, since the tunnelling barrier is influenced by the matrix environment (as pointed out in Section 1.4, tunnelling in general obeys a dispersive type kinetics and molecules trapped in different sites may decay at considerably different rates), the dissimilar morphologies of the matrix-sites required to accommodate the monomer and the dimers are such that they tend to favor the tunnelling in the monomer case, but an accurate description of this effect is a complicated theoretical task and a convincing explanation for the experimental observations is still missing.

Conformational isomerization by tunnelling can also occur for molecules other than carboxylic acids, but a large number of the reported cases involve the rotamerization of the O–H moiety. In previous sections, the case referring to the amino-hydroxy conformers of cytosine[58] has already been discussed in some detail, and this phenomenon has also been observed for some cytosine derivatives[58] and, recently, for 9-methylguanine.[116] Other types of molecules where conformational isomerization by tunnelling has been reported are asymmetrically substituted phenols,[59,117–121] and derivatives of carbonic acid.[122] However, recently, we have reported the first case where the conformational transformation involves rotamerization, by tunnelling, of an S–H moiety.[60] Such possibility could be expected based on the structural similarity between the molecules containing the O–H fragment and their sulfur analogues, but it had never been observed experimentally before our study.

In order to observe conformational transformations by tunnelling, as explained above, one has to generate the higher-energy conformers that can then decay to more stable forms. In the examples given in this section for carboxylic acids, the production of such higher-energy conformers was achieved by *in situ* selective vibrational excitation of lower energy forms. An alternative possibility is to generate these conformers as result of UV irradiation either of a lower energy conformer of the same molecule or of a different precursor molecule. In the first case, the rotamerization may take place either in an excited state or in the vibrationally hot electronic ground state after electronic relaxation. Though these two possibilities are not easy to distinguish, the observation of the same conformational transformation upon both UV and IR excitation in keeping the experimental conditions similar, points to the occurrence of the transformation in the ground electronic state, while the opposite is valid for those transformations that occur only upon UV excitation, *i.e.*, the rotamerization with all probability takes place in an excited electronic state. The situation for the cases where the high-energy conformers result from a rearrangement of different precursor molecules are more complex because they frequently involve a multistep mechanism, *e.g.* bond-breaking leading to formation of radical pairs followed by recombination of the radicals at the same atoms (but with an orientation different from the original one) or involving different atoms, after spin redistribution in one or both radicals undergoing recombination. All the cases mentioned above fit one or other of these possibilities. A common pattern is, naturally, the subsequent decay of the initially generated high-energy conformers into lower-energy forms through the tunnelling mechanism.

The conformational transformation we have recently reported as the first experimentally observed tunnelling rotamerization of an S–H moiety[60] involved the initial photogeneration of the imino-thiol isomeric forms of thioacetamide as a result of UV-induced rearrangement of the most stable amino-thione form of the compound. Four different imino-thiol forms were generated, corresponding to the *cis* or *trans* thiol (C/T) conformers of the two imino isomers (*syn* and *anti*; s/a) (Figure 1.17).

The *syn-cis* (**sC**) imino-thiol form was found to convert by tunnelling to the *syn-trans* (**sT**) form with a half-life of 80 minutes. On the other hand, the photogenerated *anti* conformers (**aC** and **aT**) were found to be stable under the same experimental conditions. Computations grounded on the WKB formalism and using the energy data obtained from B3LYP/6-311++G(3df,3pd) calculations (Figure 1.17) were used to rationalize the results and predicted a tunnelling half-life for the S–H rotamerization of **sC** to **sT** on the time scale of minutes, in agreement with the experimental observations. On the other hand, the calculations predict the putative **aT**→**aC** tunnelling half-life as being ~2.6 days, but after 18 hours of experiment, there was no discernible evidence for such a process (after 18 hours, ~18% conversion could be expected). This may be either caused by different interaction of the matrices with the *anti*- and *syn*-imines, which may change the shape of the barriers, or by the different energy gaps between the starting (in the reactant) and final (in the product) vibrational levels, which may favor or disfavor the two processes in a considerably different way, as well as by the assumptions made by the applied tunnelling computational method (see Section 1.2). This also indicates that imino-thiol systems need further, more advanced, theoretical investigations to be completely understood.

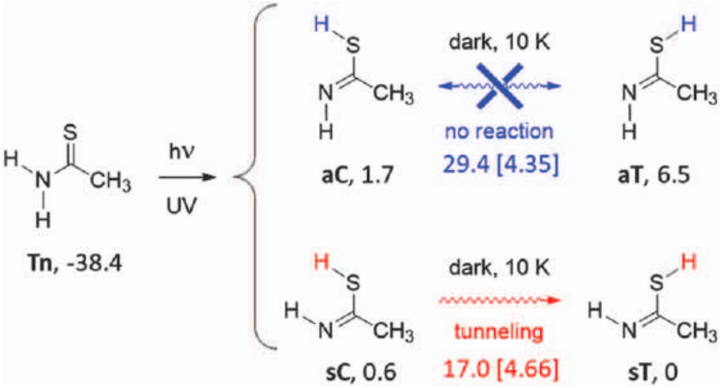

Figure 1.17 Isomers of thioacetamide with summary of transformations observed upon UV irradiation of the amino-thione form **Tn** isolated in an argon matrix, and subsequent observed tunnelling conformational isomerization (**sC** → **sT**). The names of the isomers are shown in bold, followed by relative energies with respect to the **sT** thiol isomer. The numbers in blue and red represent the relative energies of the first-order TSs (with respect to **sT**) for the indicated reactions, as well as the barrier widths (in Bohr) along the respective intrinsic reaction paths (in square brackets). Energies of all the stationary points (in kJ mol^{-1}) include the zero-point vibrational energy corrections, computed at the B3LYP/6-311++G(3df,3pd) level of theory.
Adapted from ref. 60 with permission from the PCCP Owner Societies.

1.7 Bond-breaking/Bond-forming H-atom Tunnelling (H-shifts)

In the previous section, we discussed tunnelling-induced conformational isomerizations, *i.e.* reactions where the chemical bonding in the reactant and the product has the same topology. In this section we shall discuss other type of tunnelling transformations: H-atom shifts, *i.e.* reactions where chemical bonds are broken, formed, and rearranged from single to double bonds or *vice versa*. Here we shall skip the tunnelling reactions where the structures of the reactant and the product are equivalent by symmetry (such as H-atom shifts in tropolone,[123] malonaldehyde,[124–126] or acetylacetone[124,127]) and will focus on tunnelling reactions where the reactant and product are chemically distinct.

Intramolecular hydrogen migrations are frequently associated with reactivity of carbenes. Considerable theoretical and experimental attention has been focused on the activation energies, geometrical requirements (orientation), and spin multiplicities involved in such processes. Despite the current interest in carbene reaction dynamics, the tremendously facile nature of intramolecular hydrogen shifts in these species makes direct experimental studies at normal conditions difficult. However, generation, stabilization, and spectroscopic observation of carbenes, as well as observation of their rearrangements under cryogenic conditions, make low-temperature techniques very attractive for such studies.[128,129] Early reports, by Chapman[130] and Platz,[131] on application of cryogenic techniques for studies of carbenes, are dated forty years back. Starting from those early works, the carbene intermediates were generated in matrices photochemically from diazo compounds. This way of generation of carbenes is widely used up to date. Here we shall provide some paradigmatic examples involving carbenes.

In 1987, McMahon and Chapman reported on an intramolecular [1,4]-hydrogen shift in a matrix-isolated carbene, which was observed directly by IR and UV spectroscopy.[132] Triplet *o*-tolylmethylene ^{3}**2a** decayed to singlet *o*-xylylene **3a** in an Ar matrix at 4.6 K (Figure 1.18). The small temperature dependence and non-Arrhenius behavior of the decay rate implicated a tunnelling mechanism.[132] The reaction was blocked by H/D substitution as expected for a tunnelling reaction.

In contrast, and as example of exception, triplet 1-phenylethylidene ^{3}**5** is thermally stable in argon or xenon matrices at 10 K (Figure 1.19). Warming ^{3}**5** to 65 K in a xenon matrix produced styrene **6**, *via* an intramolecular [1,2] hydrogen shift. Thermal rearrangement of triplet ^{3}**5a** to styrene **6a** likely occurs upon thermal population of the first excited singlet state of **5** at 65 K. The carbene ^{3}**5** disappearance was observed directly by IR spectroscopy[132] and followed a first-order kinetics. This allowed estimating an upper limit of *ca.* 19.7 kJ mol^{-1} for the singlet–triplet energy gap in **5a**.[132] Such a relatively small singlet–triplet energy gap is characteristic of majority of carbenes.

Nitrenes are typically generated in matrices from azide precursors, by photochemical elimination of molecular nitrogen from the N_3 group. One

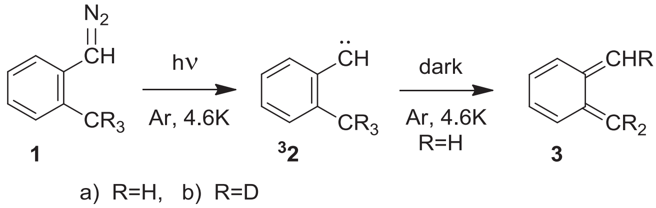

Figure 1.18 Tunnelling decay of triplet *o*-tolylmethylene ^{3}**2a** to singlet *o*-xylylene **3a**, reported in ref. 132. The deuterated analogue ^{3}**2b** is thermally stable in argon at 19 K and in xenon at 59 K.[132]

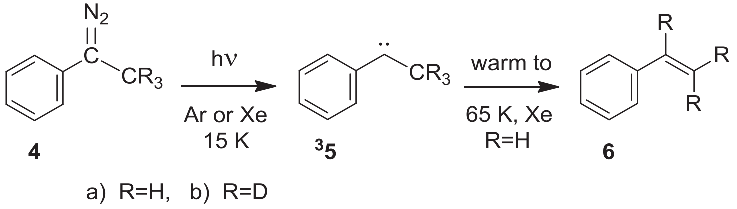

Figure 1.19 Triplet carbene 1-phenylethylidene ^{3}**5** is thermally stable in argon or xenon matrices at 10 K. Warming the sample to 65 K in a xenon matrix produces styrene **6**. See ref. 132 for details.

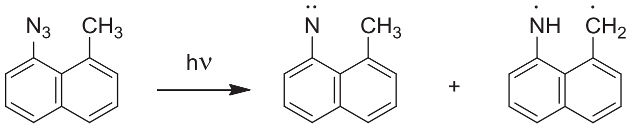

7 ^{3}**8** ^{3}**9**

Figure 1.20 Photolysis of azide **7** in 2-methyltetrahydrofuran glass at 77 K produces electron spin resonance (ESR) absorptions characteristic of randomly oriented triplet states and are assigned to triplet 1-methyl-8-nitrenonaphthalene ^{3}**8** and triplet biradical 1-imino-8-naphthoquinomethane ^{3}**9**. See ref. 134 for details.

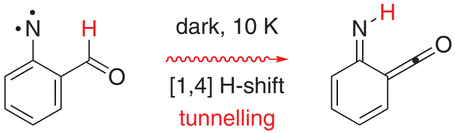

^{3}**10**-*h* **11**-*h*

Figure 1.21 Intramolecular tunnelling reaction of triplet protium 2-formyl phenylnitrene ^{3}**10-*h*** into imino ketene **11-*h***. See ref. 54 for details.

might expect nitrenes to display reactivity similar to their isoelectronic carbene analogues. This has not been true in the systems studied thus far.

Platz *et al.* observed both triplet nitrene ^{3}**8** and triplet biradical ^{3}**9** upon photolysis of 1-azido-8-methylnaphthalene **7** (Figure 1.20).[133,134] Nitrene ^{3}**8** does not produce biradical ^{3}**9** either thermally or photochemically. At 77 K the nitrene ESR spectrum did not interconvert into that of the biradical; both species were indefinitely stable at 77 K,[133,134] and the H-atom abstraction by the nitrene center did not occur.

The lack of reactivity of triplet nitrenes toward H-abstraction, even for intramolecular reactions, contrasts with the reactivity of triplet carbenes.[135] This unique behavior has been interpreted as a result of thermodynamic and electronic factors. Triplet nitrenes are ~165 $\mathrm{kJ\,mol^{-1}}$ more stable than the comparably substituted triplet carbenes.[136] Moreover, the singlet–triplet gap ($\Delta E_{\mathrm{S-T}}$) in nitrenes is generally much larger than in carbenes. The $\Delta E_{\mathrm{S-T}}$ in phenylnitrenes is ~75 $\mathrm{kJ\,mol^{-1}}$ and, therefore, the intersystem crossing (ISC) in phenylnitrenes to their triplet ground-state is often considered irreversible. In phenylcarbenes $\Delta E_{\mathrm{S-T}}$ is less than 20 $\mathrm{kJ\,mol^{-1}}$,[137,138] and consequently the triplet ground-state phenylcarbenes can serve as a reservoir for the highly reactive singlet phenylcarbene.

Recently, we have succeeded in the observation of a first intramolecular H-abstraction reaction in a nitrene.[54] Triplet 2-formyl phenylnitrene **10-*h*** (Figure 1.21) was generated by photolysis of 2-formyl phenylazide isolated in Ar, Kr, and Xe matrices. The identity of **10-*h*** was confirmed by IR, UV–vis, and EPR spectroscopies. Upon generation, the triplet nitrene spontaneously rearranged at 10 K in the dark to singlet 6-imino-2,4-cyclohexadien-1-ketene

11-*h* on the time scale of several hours. This was the first direct evidence of a tunnelling reaction in nitrene chemistry.

Several experimental tests were carried out in order to confirm that the transformation of ^{3}**10-*h*** into **11-*h*** was a true tunnelling reaction. As expected for tunnelling, the reaction is independent of temperature (and in this case also of the matrix material). The calculated barrier for this reaction is above 70 kJ mol^{-1}, which clearly rules out the possibility of an over-the-barrier thermal reaction at 10 K. However, conditions for the occurrence of quantum tunnelling are satisfied: the barrier width is rather narrow, no more than 2.1 Å,[54] and the reaction is associated with the movement of the light H atom. Indeed, considering this hypothesis, the H-formyl (^{3}**10-*h***) and D-formyl (^{3}**10-*d***) phenylnitrenes were generated in matrices, and the kinetics of the transformations were studied for both isotopes. The deuterated analogue was found to be indefinitely stable (Figure 1.22).

The absence of tunnelling in D-formyl phenylnitrene is also confirmed by WKB computations. The life time of ^{3}**10-*d*** was estimated to be on the order of 150 000 years.[54]

Note that a direct transformation of ^{3}**10-*h*** into **11-*h*** is spin-forbidden. We propose that the intramolecular H-shift tunnelling initially occurs on the triplet manifold, giving initially an excited triplet state of imino-ketene ^{3}**11**, which is marginally more stable than ^{3}**10**. After the actual H-shift, the singlet electronic ground state **11** is formed by means of intersystem crossing (Figure 1.23).

Interestingly, Fisher and Michl were able to observe external and internal heavy-atom effects, leading to an increased rate of a spin-forbidden proton

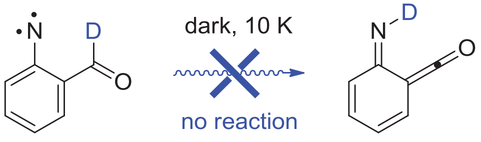

^{3}**10**-*d* **11**-*d*

Figure 1.22 Lack of spontaneous decay of triplet deuterated 2-formyl phenylnitrene ^{3}**10-*d***. See ref. 54 for details.

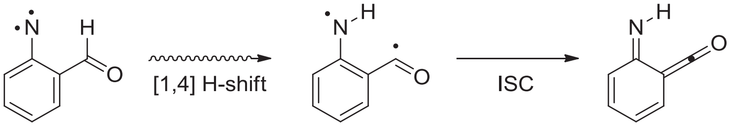

^{3}**10** (2.0) ^{3}**11** (0.0) ^{1}**11** (–104.6)

Figure 1.23 Mechanism of formation of singlet imino-ketene **11** from triplet nitrene ^{3}**10**, *via* triplet biradical ^{3}**11**. Numbers in parentheses show relative electronic energies, in kJ mol^{-1}, computed at the B3LYP/6-311++G(d,p) level of theory. ISC stands for intersystem crossing. See ref. 54 for details.

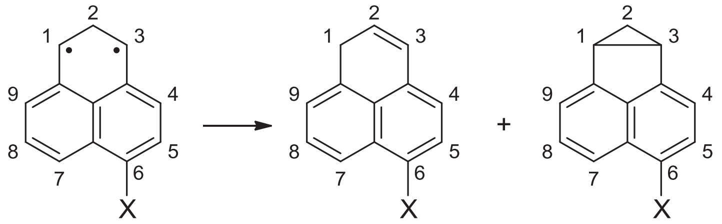

^{3}**12**, X=H ^{1}**13**, X=H **14**, X=H

^{3}**15**, X=Br ^{1}**16**, X=Br

Figure 1.24 Tunnelling in 1,3-perinaphthadiyl triplet biradical (^{3}**12** and ^{3}**15**) to singlet phenalene. See ref. 139 for details.

tunnelling reaction. They studied the rearrangement of the 1,3-perinaphthadiyl triplet biradical ^{3}**12** generated by UV-irradiation of cyclopropane **14**. It was found that biradical ^{3}**12** decays to singlet phenalene ^{1}**13** and that the reaction below 100 K proceeds at a temperature-independent rate.[139] This was attributed to quantum mechanical tunnelling (by [2,1]-hydrogen shift) from the triplet ground state of ^{3}**12** to the singlet ground state of ^{1}**13** (Figure 1.24). The support for a tunnelling mechanism also was obtained from a deuterium kinetic isotope effect of 1300.[139]

Direct evidence of the spin-forbidden nature of the rate-determining tunnelling step was obtained by varying the matrix host.[139] The tunnelling reaction rate increased by a factor of 10 by going from argon to xenon matrix. Fisher and Michl claimed that an external heavy-atom effect on the tunnelling rate for a ground state process had not been observed until then,[139] but mentioned such effects to be well known[140] "to enhance the rate of intersystem crossing from an excited triplet state T_1 to the singlet ground state S_0". An internal heavy-atom effect on the hydrogen-shift reaction was also observed upon introducing a bromine substituent at position 6 (Figure 1.24). Fisher and Michl concluded that "the observation of external and internal heavy-atom effects on the temperature-independent rate of tunnelling from ^{3}**12** to ^{1}**13** and from ^{3}**15** to ^{1}**16** provided conclusive evidence for its spin-forbidden nature".[139]

Two decades after reports of McMahon and Chapman,[132] and Fisher and Michl,[139] studies on tunnelling reactions involving H-atom migration in carbenes gained a considerable renewed attention when Schreiner and co-authors generated and captured methylhydroxycarbene in noble gas matrices at temperatures of around 10 K (reported in 2011).[28] The potential energy surface around methylhydroxycarbene was characterized computationally and large activation enthalpies (over 90 kJ mol^{-1}) were found for two putative [1,2] H atom shifts leading to either acetaldehyde or vinyl alcohol (Figure 1.25).

With such high barriers, and under cryogenic conditions, methylhydroxycarbene should not react at all. Still, a first-order reaction consuming

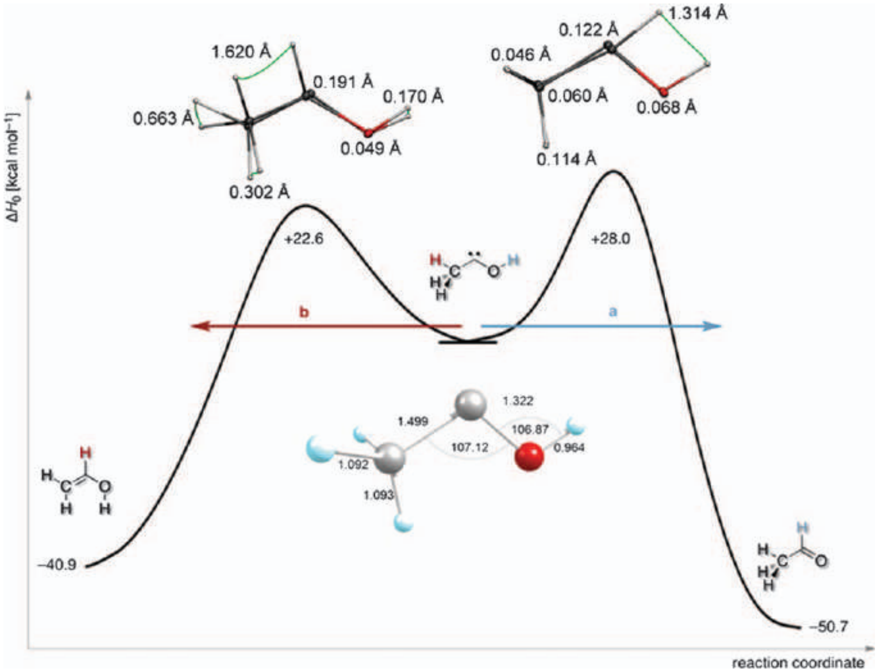

Figure 1.25 Computed potential energy surface of methylhydroxycarbene (middle: carbon = grey, oxygen = red, hydrogens = light blue) and tunnelling paths **a** and **b** to the thermodynamic product acetaldehyde (right) or the kinetic product vinyl alcohol (left). The paths are intrinsic reaction coordinates that depict the proper heights and widths of the barriers for a fair visual assessment of the potential reactivity. Focal point energies are extrapolated to fully account for electron correlation and an infinitely large basis set using AECCSD(T)/cc-pCVQZ geometries.
Reprinted from ref. 19 with permission from American Chemical Society, Copyright 2017.

methylhydroxycarbene, with a half-life of about 1 hour was observed, a transformation that was found to be largely temperature independent.[28] That finding, and the fact that the OD-deuterated methylhydroxycarbene was stable, had led to the conclusion that the reaction exclusively occurred *via* the tunnelling mechanism. Among the two possible [1,2] H-shifts, the reaction in the dark proceeded exclusively to acetaldehyde. This was the first experimental demonstration of the principle of tunnelling control, whereby the reaction proceeded only to a product with a higher tunnelling probability, albeit facing a higher (but narrower) barrier (Figure 1.25).[28]

The study on tunnelling in methylhydroxycarbene was followed by preparation and experimental characterization of a series of other long-elusive hydroxycarbenes (Figure 1.26). Schreiner *et al.* found tunnelling control[15] to prevail also for *tert*-butyl-, phenyl-, cyclopropyl-, and trifluoromethylhydroxycarbene by giving the thermodynamic products from [1,2] H-shift tunnelling reactions of large but narrow barriers similar to the depiction of Figure 1.26. The tunnelling

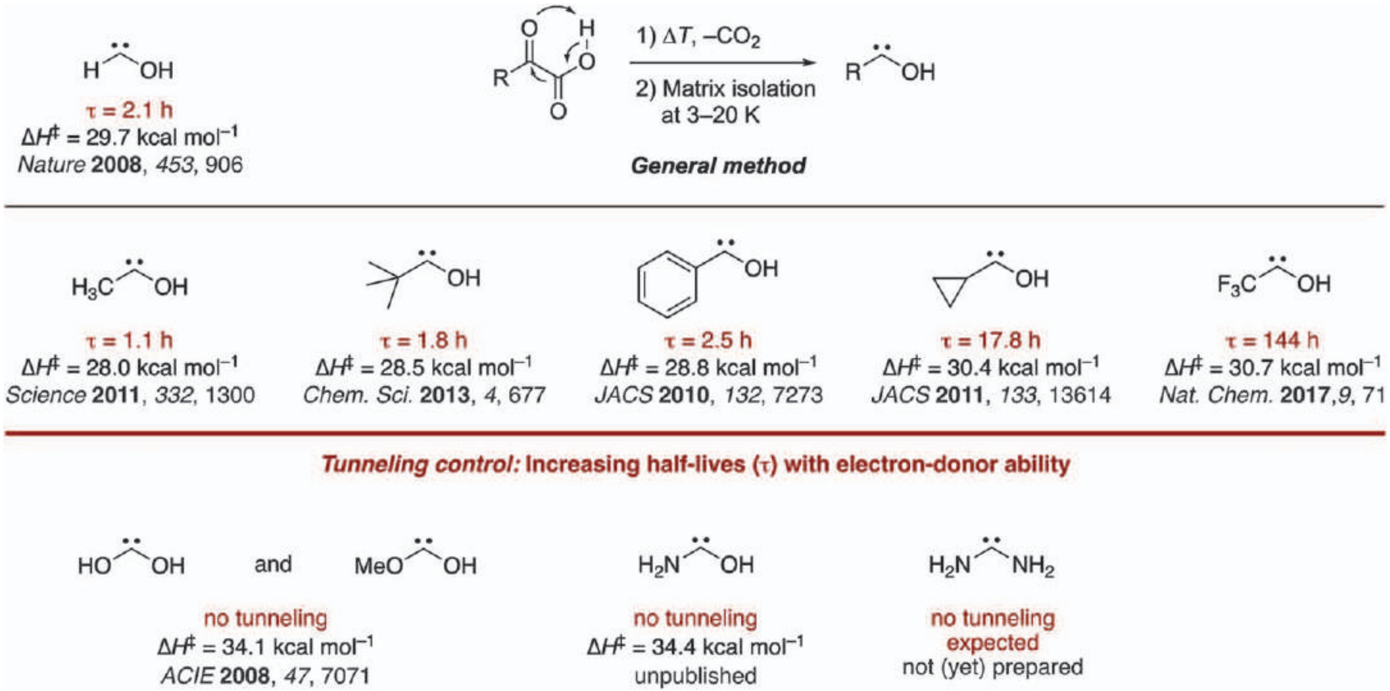

Figure 1.26 Family of hydroxycarbenes with HCOH as the parent species (top left)[141] and the general way of preparation through thermal extrusion of CO_2 from α-ketocarboxylic acids. Middle: tunnelling half-lives τ and [1,2] H-shift barriers for the associated tunnelling process computed at the coupled cluster level of theory with at least triple-ζ basis sets.[28,142–145] Bottom: related diheteroatom-substituted carbenes that do not show tunnelling.[146]
Reprinted from ref. 19 with permission from American Chemical Society, Copyright 2017.

half-lives correlate well with the stereoelectronic properties of the R group and depend on the absolute barrier height (with very similar overall shapes).[15] Also, when the carbene carbon atom was stabilized by another π-donor heteroatom (N or O), tunnelling was not observable at laboratory time scales.[15]

The research on H-atom tunnelling in carbenes actively continues.[147,148] Very recently, a new member was added to the family of hydroxycarbenes. Eckhardt *et al.* reported the gas-phase preparation of cyanohydroxycarbene by high-vacuum flash pyrolysis of ethyl 2-cyano-2-oxoacetate and subsequent trapping of the pyrolysate in an inert argon matrix at 3 K (Figure 1.27).[149] After a few seconds of irradiation of the matrix with green light, singlet *trans*-cyanohydroxycarbene **17t** rearranges to its *cis*-conformer **17c**.

Cis- and *trans*-cyanohydroxycarbene were characterized by IR and UV–vis spectroscopy. *Trans*-cyanohydroxycarbene **17t** undergoes a conformer-specific [1,2] H-tunnelling reaction through a 139.3 kJ mol^{-1} barrier (the highest penetrated barrier of all H-tunnelling reactions observed to date) to cyanoformaldehyde **18** with a half-life of 23.5 days; this is the longest half-life reported for an H tunnelling process to date. During the tunnelling reaction the *cis*-conformer **17c** remains unchanged over the same period of time (see Figure 1.27).[149]

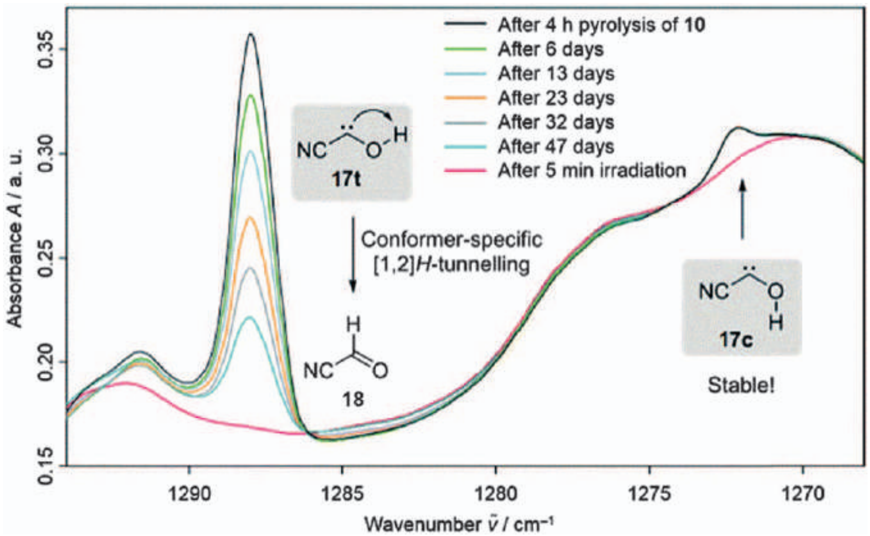

Figure 1.27 Conformer-specific [1,2] H-tunnelling of *trans*-cyanohydroxy-carbene (**17t**) with a tunnelling half-life of 23.5 days over a time period of 47 days monitored by the signal decay at 1288 cm^{-1}. The amount of the *cis*-conformer **17c** remained unchanged over the same period (band at 1272 cm^{-1}). After 5 min irradiation of the matrix with a light of 520 nm, both carbene signals are completely depleted (red spectrum).
Adapted from ref. 149 with permission from the Royal Society of Chemistry.

One of the interesting questions is: what if the oxygen atom of the hydroxycarbene was substituted by either a sulfur or a selenium atom? Do the mercaptocarbene (H–C–S–H) and selenocarbene (H–C–Se–H) congeners of hydroxycarbene (H–C–O–H) also undergo [1,2] H-tunnelling? Schreiner and co-authors addressed this question theoretically.[150] Comparison of the computed intrinsic reaction paths of the reactions *trans*-HC*X*H to H_2CX ($X = O$, S, Se) indicated that the energetic characteristics of the paths are very similar (126–139 kJ mol^{-1}). For the three [1,2] H-shift reactions investigated, the barrier is considerably narrower for the parent [H, H, C, O] system than those for [H, H, C, S] and [H, H, C, Se]. It was then concluded that the tunnelling half-lives for the $X = S$ and $X = Se$ unimolecular isomerization reactions are expected to be much longer than that for the *trans* $HCOH \rightarrow H_2CO$ reaction. This means that unlike for the parent hydroxymethylene (HCOH), at the low temperatures of matrix isolation experiments no tunnelling will be observable for the *trans*-HCSH and *trans*-HCSeH systems. The most intriguing fact is that, despite numerous experimental attempts to synthesize *trans*-HCSH or *trans*-HCSeH *via* routes similar to those that resulted in the formation of the parent hydroxymethylene, these [H, H, C, S] thiol or [H, H, C, Se] selenol isomers have thus far remained inaccessible under matrix isolation conditions.

There are, however, reports on trapping thiol (SH) and selenol (SeH) compounds under matrix isolation conditions and experimental observation of the respective tunnelling isomerizations into their thione (C=S) or selenone (C=Se) congeners. Rostkowska and co-authors trapped the amino-thione form of thiourea in argon matrices (Figure 1.28) and, by using UV-irradiation ($\lambda > 270$ nm), they generated *in situ* two imino-thiol isomers (**20tl** and **21tl**).[151] They observed that the *anti*-imino-thiol **21tl** isomer converted back to the **19tn** form at 10 K, and in the dark, with a time constant of 52 hours (Figure 1.28). The molecules in the *syn*-imino-thiol **20tl** conformation remained unchanged. The authors concluded that "the only possible mechanism of the ground-state thiol→thione transformation at low temperature is hydrogen tunnelling through the very high energy barrier (108 kJ mol^{-1}, as calculated at the MP2/6-31++G(d,p) level)".[151]

Fifteen years later, the same group of authors reinvestigated the reactions for the thiourea molecules isolated in Ar, Ne, *n*-H_2 and *n*-D_2 matrices at

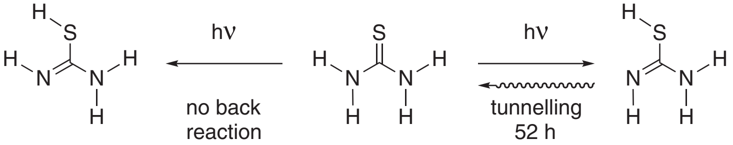

20tl **19tn** **21tl**

Figure 1.28 Photochemical generation of imino-thiol forms (**20** and **21**) of thiourea **19** isolated in an Ar matrix and spontaneous thiol→thione tunnelling for one of the imino-thiol isomers. See ref. 151 and 152 for details.

3.5 K.[152] The less stable thiol form of the compound was photochemically generated by UV irradiation of the matrix, and after that, a spontaneous thiol → thione conversion was studied as a function of matrix material or matrix temperature. The authors did not find any drastic dependence of the tunnelling rate either on the matrix environment (measured time constants between 52 and 94 hours in four different hosts), or on the matrix temperature (between 3.5 and 15 K in Ar).[152]

Rostkowska *et al.* also studied H-atom transfer processes for selenourea isolated in Ar matrices.[153] Initially, the monomers of selenourea adopt exclusively the selenone tautomeric form **22** (Figure 1.29). UV irradiation of the matrix-isolated compound led to generation of the selenol tautomer **23**. For the matrix kept at 10 K and in dark, an H-atom tunnelling reaction transforming the photoproduced selenol *anti* form **23a** back into the initial selenone tautomer **22** was observed[153] (Figure 1.29). Interestingly, the selenol → selenone tunnelling reaction in selenourea was considerably quicker (16 h)[153] than the analogous thiol → thione tunnelling in thiourea (52 h)[151] despite the computed barriers being rather similar: 95 kJ mol^{-1} [MP2/6-311++G(2d,p)][153] and 108 kJ mol^{-1} [MP2/6-31++G(d,p)].[151] The difference in observed tunnelling rates must be related with the barrier widths that were not reported.

The experimental observations of tunnelling in imino-thiol and imino-selenol compounds means in the first place that these high-energy forms can be successfully generated. On the other hand, Schreiner and co-authors suggest that part of the reason for not being able to synthesize in matrices carbene-thiol (and carbene-selenol) isomers is that *trans*-HCSH is not a true carbene but is better represented as an ylide with a negatively charged carbon atom and a positively charged sulphur.[150]

The thiol → thione proton tunnelling in thiourea (and selenourea) can also be compared with structurally similar molecule of thioacetamide. Similarly to thiourea, matrix-isolated molecules of thioacetamide initially exist exclusively as amino-thione tautomer. The imino-thiol isomer can be generated in cryogenic matrices by means of UV-irradiation (see Figure 1.30).[60,154] The lack of thiol → thione tunnelling transformation in thioacetamide is consistent with its relatively high barrier. Calculated at the MP2/6-31++G(d,p) level, it equates to 123 kJ mol^{-1}.[154] This is higher than

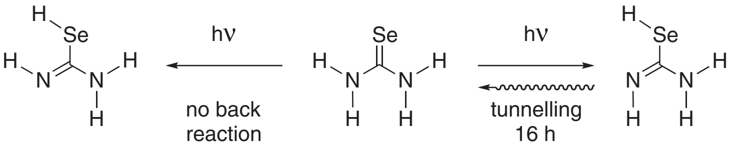

23s **22** **23a**

Figure 1.29 Photochemical generation of imino-selenol forms of selenourea isolated in an Ar matrix and spontaneous selenol → selenone tunnelling for one of the imino-selenol isomers. See ref. 153 for details.

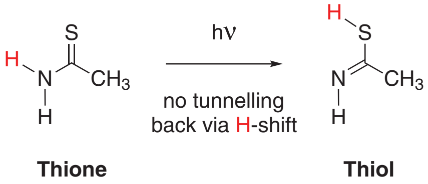

Figure 1.30 UV-induced generation of imino-thiol tautomer of thioacetamide. The imino-thiol can exist in four isomeric structures, but only the "tunnelling-ready" isomer is shown in the figure. Reverse thiol → thione proton tunnelling in thioacetamide was not observed. See ref. 60 and 154 for details.

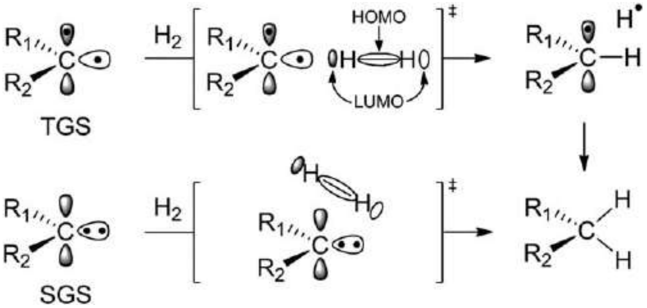

Figure 1.31 Reactions of singlet ground state (SGS) and triplet ground state (TGS) carbenes with molecular hydrogen. See ref. 156 for details.

the MP2-computed barriers for the thiol → thione transformation in thiourea (108 kJ mol^{-1})[151] or selenourea (95 kJ mol^{-1}).[153]

The barrier for thiol → thione proton tunnelling in thioacetamide was also calculated at the B3LYP/6-311++G(3df,3pd) level, and the obtained value was 108.5 kJ mol^{-1}.[60] Considering this barrier height, and also the barrier width (1.29 Å) of the calculated intrinsic reaction path, a tunnelling half-life of 100 days (8.63×10^6 s) for thiol → thione isomerization was computed using the WKB approximation.[60] This would imply a tunnelling reaction too slow to be observed within the time limits achievable in our experiments.

Carbenes are among the few metal-free molecules that are able to activate molecular hydrogen. The reactivity patterns of carbenes depend on the substituents at the carbene center. Closed-shell singlet carbenes can be described as 1,1-zwitterions, bearing both nucleophilic and electrophilic regions at the carbene center. Singlet carbenes insert in concerted reactions with considerable activation barriers, and are thus poorly reactive towards H_2 at cryogenic temperatures. In contrast, triplet carbenes exhibit radical-like reactivity, such as atom abstractions.[155] They quickly yield radical pairs that rapidly undergo secondary reactions (Figure 1.31).[156] These properties of carbenes can be used for activation of molecular hydrogen, a topic actively studied by Sander *et al.*[156] A paradigm in carbene chemistry is that reactions of carbenes are spin specific and occur from equilibrated spin states, depending on the temperature.

4-Oxocyclohexa-2,5-dienylidene **24** has a triplet ground state (TGS) carbene that is highly reactive toward solid H_2, HD, and D_2 at 3 K. Sander *et al.* investigated the mechanism of the insertion of this carbene into dihydrogen by IR and EPR spectroscopy and by kinetic studies.[157] The hydrogenation showed a very large kinetic isotope effect and remarkable isotope selectivity, as could be expected for a tunnelling reaction. H or D atoms were observed as products of the reaction with H_2 or D_2, respectively, whereas HD produces exclusively D atoms (Figure 1.32).[157] The experiments of Sander *et al.*, therefore, provide clear evidence for both hydrogen tunnelling and the rare deuterium tunnelling in an intermolecular reaction.[157]

The activation barrier for the reaction of 4-oxocyclohexa-2,5-dienylidene **24** (Figure 1.32) with hydrogen was calculated to be 22.6 kJ mol^{-1}, which is higher than the thermal energy available at 30 K.[157] Similar barriers were found for the other triplet ground state carbenes, such as cyclopentadienylidene studied by Zuev and Sheridan.[158] Therefore, these carbenes should not react thermally with hydrogen at very low temperatures, which suggests that the reaction rates are governed by quantum chemical tunnelling. For tunnelling reactions, large kinetic isotope effects (KIE) are expected, and indeed, with D_2 no reaction was observed by Sander *et al.*, under conditions in which H_2 rapidly reacts.[157] Zuev and Sheridan concluded that the "most likely pathway is single H abstraction by tunnelling to give a triplet radical pair, which then combines following intersystem crossing".[158]

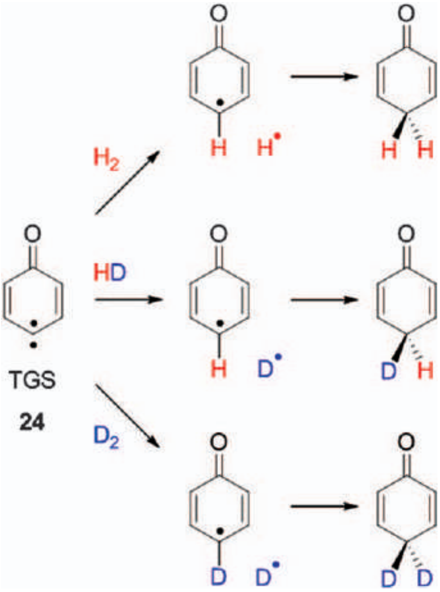

Figure 1.32 Reaction of 4-oxocyclohexa-2,5-dienylidene **24**, which is a carbene characterized by triplet ground state (TGS), with H_2, HD, and D_2. See ref. 157 for details.

Recently, Henkel *et al.* reported that 1-azulenylcarbene **25** has a singlet ground state (SGS), in contrast to most other arylcarbenes that show triplet ground states.[159] Carbene **25** can be generated by photolysis of 1-azulenyldiazomethane **26** (Figure 1.33), but even at 3 K it is kinetically unstable and quickly rearranges to the strained allene **27** through QMT.[159] The tunnelling reaction can be completely blocked by deuteration at position 8 in the seven-membered ring (Figure 1.33). Upon studying neat noble gas matrices,[159] Henkel and Sander reported their investigations on the reaction of singlet carbene **25** with molecular hydrogen.[160] To suppress the rearrangement of **25** through QMT, only the dideuterated isotopomer **d_2-25** (Figure 1.34) was used in their experiments.[160] It was demonstrated that 1-azulenylcarbene **25** with a singlet ground state readily inserts into H_2, and slowly into D_2, proving that QMT governs the insertion into both H_2 and D_2 (Figure 1.34). This was the first example showing that QMT can also be important for singlet carbenes inserting into dihydrogen.[160]

As a culmination of their research on activation of molecular hydrogen, Sander *et al.* very recently discovered a magnetically bistable carbene (3-methoxy-9-fluorenylidene **28**), and reported on its photochemically induced conformational spin switching and spin-selective hydrogenation.[161] 3-Methoxy-9-fluorenylidene **28** was generated in cryogenic matrices both in

Figure 1.33 Photochemical generation and quantum mechanical tunnelling (QMT) rearrangement of 1-azulenylcarbene **25**, which is a carbene characterized by a singlet ground state (SGS). QMT occurs only for R=H. See ref. 159 for details.

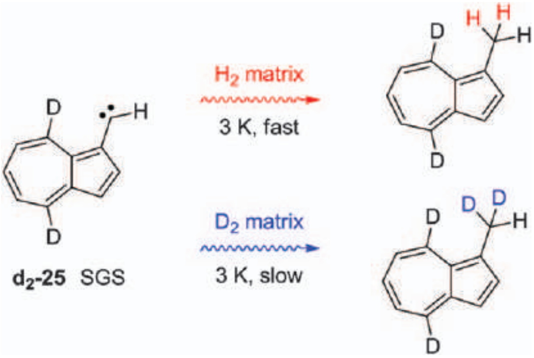

Figure 1.34 Reactivity of singlet dideuterated 1-azulenylcarbene **d_2–25** with hydrogen and deuterium in neat H_2 and D_2 matrices. See ref. 160 for details.

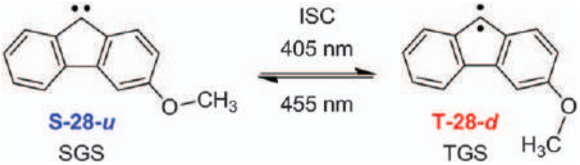

Figure 1.35 The unique spin switching of carbene **28** induced by conformational change of a remote functional group. ISC: intersystem crossing; SGS: singlet ground state, TGS: triplet ground state. Suffixes "u" and "d" designate "up" and "down" conformations of the methoxy group. See ref. 161 for details.

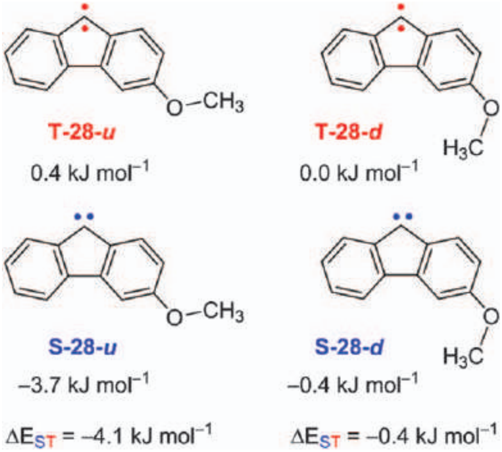

Figure 1.36 Two conformers were considered with respect to the orientation of the methoxy group in singlet **S-28** and triplet **T-28**, denoted as "up" (**u**) and "down" (**d**) conformers. Geometries were optimized at the B3LYP-D3/def2-TZVP level and energies were refined by single point CCSD(T)/cc-pVTZ calculations. See ref. 161 for details.

its lowest energy singlet and triplet states, and the ratio of these states was shifted by selective irradiation (Figure 1.35).[161] The interconversion of the nearly degenerate spin states was achieved by a conformational change of the methoxy group: "up" position results in the singlet state and switching into the "down" position yields the triplet state (Figure 1.36).[161] The spin control *via* a remote functional group makes this carbene unique for the study of spin-specific reactions, which is demonstrated for the hydrogenation reaction. Sander *et al.* suggest that the control of the spin states opens the path to tuning selectivity in chemical reactions and to developing novel magnetically switchable materials.[161]

The experiments clearly demonstrated that the insertion of carbene **28** into D_2 is both spin and conformation specific. Only triplet carbene **T-28-d** (Figure 1.36) reacts with D_2 to produce the "down" fluorene conformer exclusively, whereas the singlet carbene **S-28-u** is indefinitely stable in solid

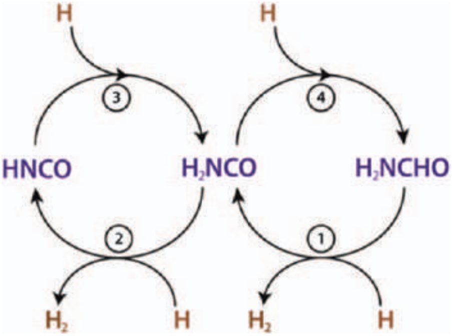

Figure 1.37 Dual-cyclic mechanism of H-abstraction and H-addition reactions connecting H_2NCHO, H_2NCO, and HNCO.
Reprinted from ref. 162 with permission from American Chemical Society, Copyright 2019.

deuterium. Conformational spin switching by a remote functional group, a new phenomenon discovered by Sander *et al.*, could be utilized beyond tracing spin states in mechanistic studies. They propose that ‘‘the introduction of a bulkier or conformationally restricted ether, amino, or similar groups should allow to manipulate spin states, and thus the magnetic properties, of molecular materials. Such switchable molecular materials have potential applications in information recording’’.[161]

Finally, Haupa *et al.* recently demonstrated that hydrogen abstraction/addition tunnelling reactions elucidate the interstellar H_2NCHO/HNCO ratio and explain the H_2 formation.[162] Interstellar observations show a strong correlation between the abundance of formamide (H_2NCHO) and isocyanic acid (HNCO), indicating that they are likely to be chemically related, but no experiment or theory could explain this correlation satisfactorily.[162]

Haupa *et al.* studied reactions of formamide in a *p*-H_2 matrix and identified production of H_2NCO and HNCO from hydrogen-abstraction reactions.[162] Haupa *et al.* observed temporal profiles of H_2NCHO, H_2NCO, HNCO, and their deuterium isotopologues, and showed that a dual-cycle consisting of hydrogen abstraction and hydrogen addition (Figure 1.37) can satisfactorily explain the quasi-equilibrium between H_2NCHO and HNCO and explain other previous experimental results.[162] In the proposed mechanism, it was assumed that the H atoms produced in the reaction cycle can move efficiently through the lattice on continuously breaking and formation of neighboring H–H bonds *via* quantum tunnelling.[162]

1.8 Heavy-atom Tunnelling

As shown in the previous sections of this chapter, H-atom tunnelling is a common phenomenon. Its relevance in chemistry has been stressed long ago, in particular when Bell published his seminal theoretical paper demonstrating the need to consider tunnelling for a correct description of reactions involving the motion of a hydrogen atom or a proton.[3] Interestingly enough, he also predicted that under normal conditions heavier atoms should behave classically. Because, as discussed before, tunnelling probabilities decrease exponentially with the square root of the moving mass, tunnelling of a carbon atom, 12 times heavier than hydrogen, can indeed be predicted to be much less likely. According to the expectations, for almost half-century, Bell's claim was practically unchallenged. The paradigm only shifted when experimentalists published the first examples of heavy-atom tunnelling in the mid-1970s/1980s. Nonetheless, 40 years after the first examples were reported, the number of experimental observations of heavy-atom tunnelling reactions is still small. Considering that a hydrogen atom can tunnel across a barrier of around 1 Å, a carbon atom can be expected to tunnel through a barrier with a width of $12^{-\frac{1}{2}} \approx 0.3$ Å with the same probability (assuming a barrier of similar height and shape).[163] Such very narrow barriers are expected to occur only in processes involving very reactive species or, as Kozuch *et al.* highlighted,[163] in strongly exothermic reactions or some symmetrical isothermic transformations. Indeed, these conditions have been matched in almost all of the heavy-atom tunnelling reactions observed so far.

One of the first experimental evidence of heavy-atom tunnelling was reported by Buchwalter and Closs in 1975,[164] namely for the ring-closure of triplet 1,3-cyclopentanediyl **30** to bicyclopentane **31** (Figure 1.38). The triplet 1,3-diradical ^{3}**30** was generated by UV irradiation of a matrix-isolated diazo precursor **29** and characterized by EPR spectroscopy. The EPR signals assigned to ^{3}**30** were found to diminish in intensity with a half-life of 30 minutes, and the reaction rate was observed to be essentially the same between 1.3 and 20 K. Based on this temperature independence, it was suggested that the reaction takes place by tunnelling.[164,165]

Additional evidence of heavy-atom tunnelling in the ring-closure of triplet 1,3-diradicals was reported later by Dougherty *et al.* (Figure 1.39).[50] They observed that the EPR signals of methyl and ethyl substituted triplet 1,3-cyclobutanediyls ^{3}**32** decay at temperatures as low as 3.8 K. The kinetic treatment of the measured rate constants between 4 and 20 K gave non-linear Arrhenius plots. These observations clearly suggest the occurrence of tunnelling.

In their studies, Closs, Dougherty and coworkers noted that the observed decay kinetics were complicated by the existence of a distribution of rate constants resulting from different matrix sites[50,164,165] (see also Section 1.4). It is also interesting to note that, in both studied cases,[50,164,165] triplet 1,3-diradicals must undergo intersystem crossing (ISC) to form the singlet products. However, it is not yet clear (even today) if tunnelling takes place on

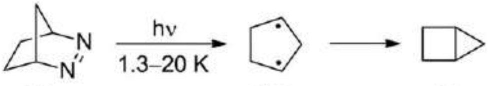

29 ^{3}**30** **31**

Figure 1.38 Ring-closure of triplet 1,3-cyclopentanediyl ^{3}**30** to bicyclopentane **31**.

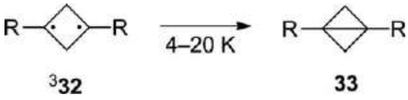

Figure 1.39 Ring-closure of triplet 1,3-cyclobutanediyls ^{3}**32** to bicyclobutanes **33**.

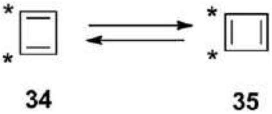

Figure 1.40 Valence isomerization between 1,4-labeled-cyclobutadiene **34** and 1,2-labeled-cyclobutadiene **35**.

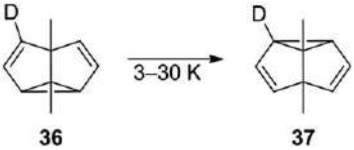

Figure 1.41 Cope rearrangement of 1,5-dimethylsemibullvalene-4-d_1 **36** to 1,5-dimethylsemibullvalene-2-d_1 **37**.

the triplet surface, to a geometry that then undergoes ISC to the singlet surface, or if tunnelling occurs concomitantly with the ISC process.[22]

The studies on the interconversion between valence isomers of cyclobutadiene (Figure 1.40) can be considered a milestone among the investigations on heavy-atom tunnelling reactivity. About 40 years ago, Whitman and Carpenter investigated, using variable temperature NMR spectroscopy, the isomerization rate of cyclobutadiene-1,4-d_2 **34** (selectively generated *in situ* from a precursor) to cyclobutadiene-1,2-d_2 **35**, concomitantly with the rate of trapping **34** and **35** in a cycloaddition reaction.[166] The unexpected negative entropy value found for the isomerization of cyclobutadiene was interpreted as an evidence that the reaction was taking place by carbon tunnelling.[166,167] Afterwards, Michl *et al.* reported polarized IR and ^{13}C NMR spectra of cyclobutadiene and its vicinal ^{13}C-dilabeled derivative, photogenerated in rare-gas matrices.[168] Based on the spectroscopic observations, it was determined that the two valence isomers **34** and **35** were rapidly interconverting (at a rate $> 10^{-3}$ s^{-1}) in the matrices at 25 K. They concluded that the observed isomerization had to be due to tunnelling, since the reaction barrier (estimated as ~40 kJ mol^{-1}) cannot be overcome at the temperatures of the experiments.

A recent case of heavy-atom tunnelling in an almost symmetrical isothermic reaction was reported by Sander and coworkers (Figure 1.41).[169] Interestingly, this experimental work was inspired by an earlier theoretical study carried by Borden *et al.*,[170] where the authors, using computations performed at the B3LYP/6-31G(d) level within the small-curvature tunnelling (SCT) methodology, predicted that the Cope rearrangement of semibullvalene (and some

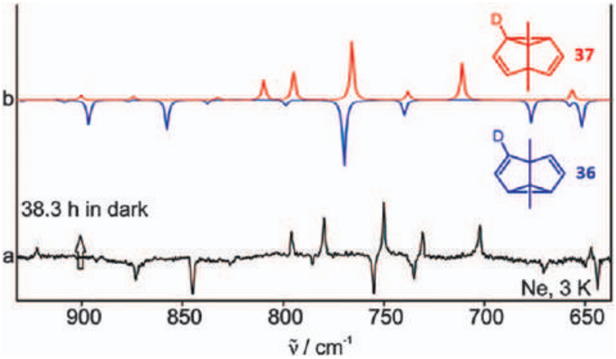

Figure 1.42 (a) IR difference spectrum showing the Cope rearrangement of **36** to **37** after keeping a neon matrix containing a mixture of **36** and **37** in the dark for 38.3 h at 3 K. (b) Computed B3LYP/6–311G(d,p) IR spectra of **36** (pointing downwards) and **37** (pointing upwards).
Adapted from ref. 169 with permission from John Wiley and Sons, © 2017 Wiley-VCH Verlag GmbH & Co. KGaA, Weinheim.

derivatives) should take place by tunnelling at cryogenic temperatures. In their article, they recommended to perform experiments on 1,5-dimethylsemibullvalene substituted with one deuterium atom to break symmetry. The presence of the deuterium atom either at position 4 or 2 (corresponding to the isotopomers **36** and **37** in Figure 1.41, respectively) leads to an energy difference between the two isomers of ≈0.7 kJ mol^{-1}, with **36** being separated by a barrier of *ca.* 23 kJ mol^{-1} from the most stable isotopomer **37**.

In the experiments performed by Sander and coworkers, the room temperature equilibrium mixture (≈1 : 1) of isotopomers **36** and **37** was deposited in a matrix at 3 K and both species characterized by their mid-IR spectrum.[169] Subsequently, the matrix was kept in the dark for several hours. They observed that the intensity of the IR signals assigned to **36** decreased, whereas those due to **37** increased (Figure 1.42). Because the barrier between the isotopomers cannot be overcome at the cryogenic temperature used in the experiments, the observed Cope rearrangement from **36** to **37** can only take place by heavy-atom tunnelling, thus confirming the theoretical predictions.[170]

The reaction kinetics was also measured as a function of the temperature, although it is complicated by its dispersive character. The rate of the Cope rearrangement in argon matrix was then found to increase only by a factor 3 on increasing the temperature by a factor of 10 (3–30 K), providing additional support for the existence of heavy-atom tunnelling. The noticed small increase in the rate of the process can be justified by changes in the medium resulting from the matrix softening.

Two puzzling observations related to the studies reported by Sander and coworkers that still do not have a clear explanation shall be mentioned here: (i) the Cope rearrangement tunnelling does not take place in solid xenon nor in the absence of a matrix, whereas in neon, argon, nitrogen, and para-hydrogen the rates were comparable, and (ii) after very long reaction time,

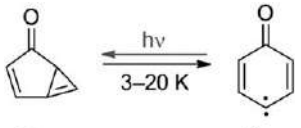

38 **^{3}24**

Figure 1.43 Ring-expansion reaction of 1H-bicyclo[3.1.0]-hexa-3,5-dien-2-one **38** to 4-oxocyclohexa-2,5-dienylidene **^{3}24**.

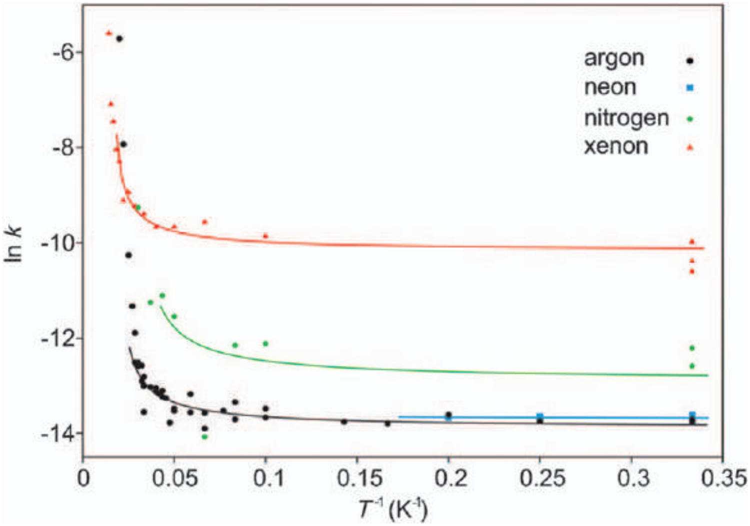

Figure 1.44 Arrhenius plots for the ring-expansion of **38** to **^{3}24** in neon, argon, nitrogen, and xenon matrices.
Reproduced from ref. 53 with permission from John Wiley and Sons, © 2014 WILEY-VCH Verlag GmbH & Co. KGaA, Weinheim.

the Cope rearrangement tunnelling resulted in a ratio between the isotopomers far from the expectations (*e.g.*, in argon at 5 K: *initial ratio* = 1 : 1.3; *final ratio* (16.1 h) = 1 : 1.5, *final ratio expected* = 1 : 10^{-5}).

Another example of heavy-atom tunnelling reported by Sander's group was the ring-expansion of the fused cyclopropene **38** to triplet carbene **^{3}24** (Figure 1.43).[53,171] Cyclopropene derivative **38** was generated by irradiation of triplet carbene **^{3}24**, which in turn was obtained in cryogenic matrices by the photolysis of a quinone diazo derivative. It was found that the intensities of the IR bands of **38** decrease in the dark, while those of **^{3}24** increase. A detailed kinetic study of this transformation showed that the Arrhenius plots between 3 and 20 K are temperature independent (in matrices of several different host gases), clearly indicating that the ring-expansion was taking place through heavy-atom tunnelling (Figure 1.44).[53] At temperatures above 25 K, the rates increase rapidly (independent of the matrix host), which was interpreted as a result of occurrence of thermally activated tunnelling. The different reaction rates observed for different matrix host gases were a consequence of the matrix influence on the barrier width and height. Particularly noticeable was the acceleration at 3 K of the tunnelling rates in xenon ($\tau_{\frac{1}{2}} \approx 5$ hours) compared to those observed in argon ($\tau_{\frac{1}{2}} \approx 7$ days). Nevertheless, these matrix effects are not yet clearly understood.

An interesting feature of this ring-expansion reaction is the existence of an ISC step, since cyclopropene **38** has a singlet ground state and carbene **24** has a triplet ground state. Multi-configurational calculations revealed further that carbene **24** has an open-shell singlet state (OSS) as the lowest singlet state, which is energetically more stable ($\approx$16 kJ mol^{-1}) than cyclopropene **38**. Therefore, the proposed mechanism for the formation of triplet carbene ^{3}**24** at cryogenic temperatures involves the ring-expansion of **38** to OSS **24** by heavy-atom tunnelling, followed by ISC of OSS **24** to ^{3}**24**. CASPT2 computations were carried out,[53] and the activation energy for the ring-expansion of **38** to OSS **24** was estimated as being 29–33 kJ mol^{-1}. This energy barrier should result in a rate of effectively zero for the over-the-barrier reaction at the used cryogenic temperatures. Then, the rate constants were evaluated using the small-curvature tunnelling (SCT) approximation. The performed calculations led to rate constants which were independent of the temperature up to 50 K, thus indicating that the only tunnelling contribution to the ring-expansion of **38** to OSS **24** should originate from the ground vibrational level. The predicted rate of 2×10^{-6} to 2×10^{-8} s^{-1} (depending on the basis set used) was found to reasonably agree with the experimental rate of 1.2×10^{-6} s^{-1} measured in an Ar matrix at 3 K.

Two other examples of heavy-atom tunnelling involving ring-expansion reactions were reported for benzazirine rearrangement to a cyclic ketenimine: the first, discovered by McMahon's group for the reaction of **39** to **40**,[172] and the second discovered by our group for the reaction of **41** to **42** (Figure 1.45).[173]

The McMahon group showed that irradiation of 4-methylthiophenylazide in argon matrix with 365 nm light mainly leads to the corresponding arylnitrene.[172] The irradiation of this arylnitrene at 313 or > 415 nm leads to its rearrangement to the cyclic ketenimine **40** [ν(C=C=N) = 1889 cm^{-1}], which

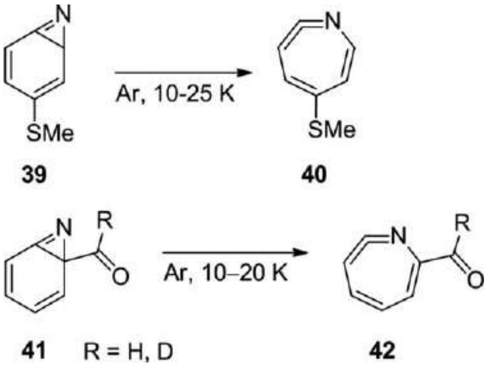

Figure 1.45 Ring-expansion reaction of benzazirines **39** and **41** to cyclic ketenimines **40** and **42**, respectively.

then slowly converts to benzazirine **39** [ν(C=N) = 1717 cm^{-1}] upon irradiation at >415 nm. They found that ring-expansion of benzazirine **39** to ketenimine **40** takes place spontaneously in the dark, with a rate constant that shows almost no temperature dependence from 10 K (1.5×10^{-5} s^{-1}) to 25 K (1.8×10^{-5} s^{-1}), which clearly suggests heavy-atom tunnelling. B3LYP/6-31G(d) calculations estimated an activation barrier of 14 kJ mol^{-1} for the reaction of **39** to **40**, indicating that it cannot occur as a thermally activated process, because a rate constant to surmount this barrier at 10 K would be around 2.0×10^{-63} s^{-1} (based on the Eyring equation).

When the methylthio moiety was replaced by a methoxy group, the corresponding benzazirine was found stable under the low-temperature matrix conditions; no evidence for tunnelling was observed. The different behavior of the two compounds was rationalized in terms of the height and width of the associated energy barriers, which were found to be greater for the methoxy-substituted benzazirine (Figure 1.46).

In our study,[173] we showed that benzazirine **41**, generated *in situ* upon 530 nm irradiation of protium and deuterated triplet 2-formylphenylnitrene, spontaneously undergoes ring-expansion to ketenimine **42** under cryogenic

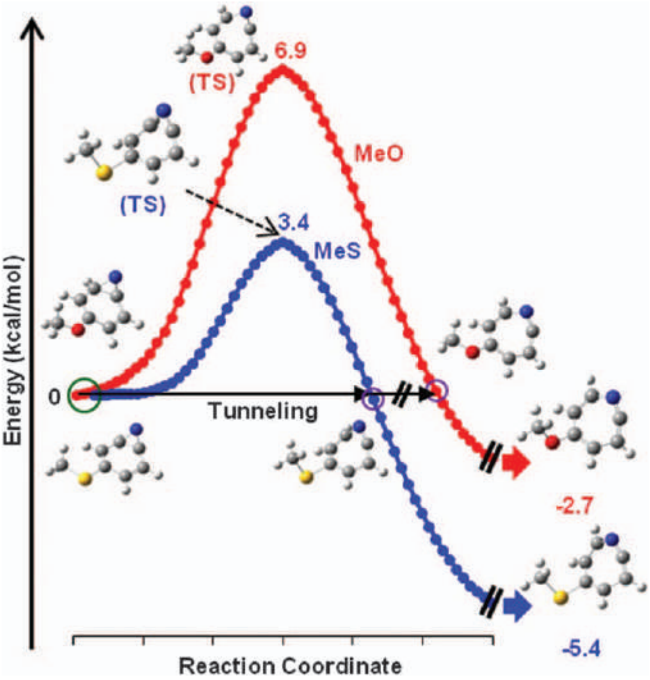

Figure 1.46 B3LYP/6-31G(d) computed intrinsic reaction path for the transformation of benzazirine **39** to ketenimine **40** (blue) and the corresponding methoxy substituted derivative (red).
Adapted from ref. 172 with permission from the American Chemical Society, Copyright 2013.

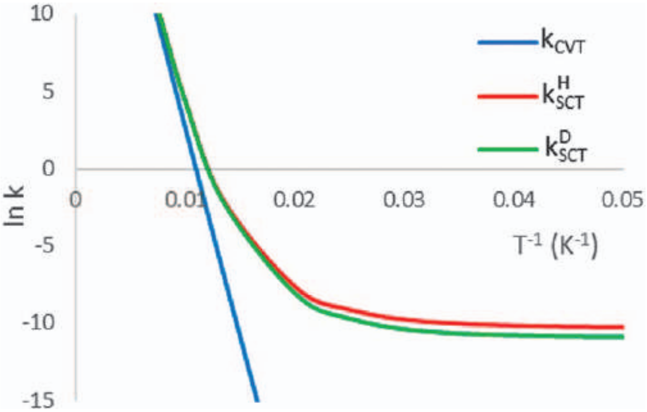

Figure 1.47 Arrhenius graph for the ring-expansion of benzazirine **41** to cyclic ketenimine **42** reaction without (CVT) and with (SCT) tunnelling corrections, computed at the M06-2X/6-311+G(2d,p) level.
Adapted from ref. 173 with permission from American Chemical Society, Copyright 2017.

conditions (see Figure 1.45). In an argon matrix at 10 K and under dark, ~25% of **41**-d rearranges to **42**-d after 5 days. Using IR spectroscopy, we determined a rate constant of ~7.4×10^{-7} s^{-1} (a half-life time of ~260 hours) for this process. Upon increasing the absolute temperature the reaction rate hardly show any increase (~8.9×10^{-7} s^{-1} at 20 K), which provides a strong evidence for the occurrence of heavy-atom tunnelling.

Computed rate constants without and with tunnelling consideration [using canonical variational transition state theory (CVT) and small curvature tunnelling (SCT), respectively], confirm that the observed process can only take place by tunnelling from the ground state (Figure 1.47).[173] The estimated CVT rate constant at 10 K was 1.8×10^{-177} s^{-1}, which indicates that it is impossible for a thermal reaction to occur, whereas the estimated SCT rate constant was 3.5×10^{-5} s^{-1} (half-life time of ~6 hours), which is comparable to the experimental result. The difference (computed around 40 times faster) is justifiable considering errors resulting from the used DFT/M06-2X computations [*e.g.*, M06-2X gives an energy barrier of 30 kJ mol^{-1} for the ring-expansion of **41** to **42**, which is about 5 kJ mol^{-1} lower than that calculated at the more precise CCSD(T) level]. A small secondary kinetic isotopic effect, resulting in the acceleration of the reaction upon substitution of deuterium by protium in the formyl group of benzazirine **41**, was also predicted theoretically and measured experimentally. Very interestingly, it was also observed that the reaction rate for the ring-expansion of **41** to **42** is one order of magnitude larger (faster) when the sample at 10 K is exposed to the radiation of the spectrometer IR globar source. This suggests the possibility of occurrence of IR-induced photochemistry or IR-assisted tunnelling.

Direct spectroscopic evidence of heavy-atom tunnelling under low-temperature matrix isolation conditions was also reported for cases

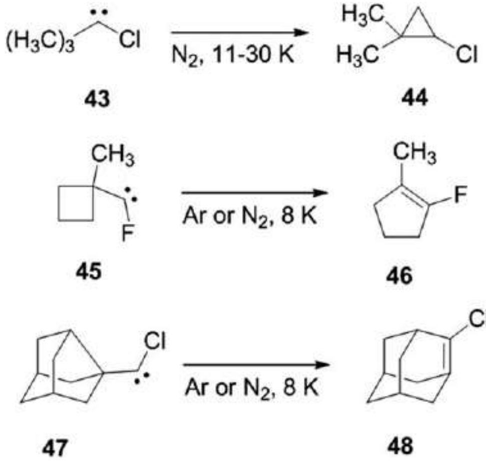

Figure 1.48 Rearrangement reaction of carbenes **43**, **45** and **47** to species **44**, **46** and **48**, respectively.

involving singlet carbene species (Figure 1.48).[174–176] Zuev and Sheridan found that upon irradiation (334 nm) of *tert*-butylchlorodiazirine in an N_2 matrix at 11 K, the IR bands associated with the photogenerated carbene **43** slowly disappeared, while the IR bands of cyclopropane **44** simultaneously increased.[174] The rate constant for the decay of **43** varied from 4×10^{-4} s^{-1}, initially, to 3×10^{-5} s^{-1}, at one-half of the conversion (a typical dispersive kinetics behavior). The rate of the reaction was observed to be insensitive to temperature on warming the matrix from 11 to 30 K, which signals the existence of tunnelling. Interestingly, it was found that perdeuterated carbene **43** was stable under the matrix isolation conditions. This extremely large kinetic isotope effect reflects the expected significant role that the H-atom movement plays in the tunnelling reaction. Nonetheless, the 1,3-CH insertion reaction of carbene **43** implies formation of a C–C bond during the process leading to **44**, and therefore, carbon-atom tunnelling must also be involved.

Later, the same authors published another example of tunnelling involving carbenes trapped in cryogenic matrices.[175] Fluorocarbene **45** and fluorocyclopentene **46** were generated in a nitrogen matrix at 8 K by irradiation of a diazo precursor with visible light (>550 nm). Subsequent irradiation at 436 nm caused rapid disappearance of the IR bands of carbene **45** and simultaneous growth of those of cyclopentene **46**. Even under exclusion of light, a slow rearrangement of **45** to **46** was observed at 8 K. In an N_2 matrix at 8 K under dark, the most reactive conformer of **45** was observed to decay following a first order kinetics, in the first 20% of conversion, with a rate constant of 4×10^{-6} s^{-1}. In an Ar matrix at 8 K, carbene **45** was found to undergo ring-expansion with a rate one order of magnitude faster, *ca.* 4×10^{-5} s^{-1}. When the Ar matrix was warmed to 16 K, the ring-expansion rate of **45** increases only by a factor of 2, to *ca.* 9×10^{-5} s^{-1} (in the N_2 matrix tripling the temperature accelerates the ring-expansion of **45** by a factor of about 100). These findings were interpreted as an indication that ring-expansion of **45** occurs by carbon-atom tunnelling.

To confirm that carbon-atom tunnelling provides an explanation for the experimental results, tunnelling reaction rates were calculated.[175] At the MPW1K/6-31+G(d,p) level, the ring-expansion of carbene **45** to cyclopentene **46** was computed to have a barrier of 27 kJ mol^{-1} and to be 328 kJ mol^{-1} exothermic. Arrhenius plots for the rate constants of the **45**→**46** transformation, calculated using the SCT approximation as well as the CVT theory, predict a rate constant of 9×10^{-6} s^{-1} at the low-temperature limiting ($T<20$ K) when tunnelling is included and a classical rate constant 2×10^{152} times smaller. The reaction coordinate mode was calculated to have a frequency of 69 cm^{-1}, and therefore, at 8 K tunnelling should occur almost exclusively from the $\nu=0$ vibrational ground state. At 16 K, the fraction of reaction occurring out of the $\nu=1$ vibrational level can be estimated to increase to 6%. Theory predicts that this will produce a negligible change in rate, so the observed increase in the rate constant upon the temperature increase was interpreted as due to environmental effects resulting from the matrix softening.

The last known example reported of heavy-atom tunnelling in a singlet carbene species involves the ring-expansion of a noradamantylchlorocarbene. In a collaborative effort, Moss *et al.*[176] described the generation of carbene **47** upon irradiation (334 nm) of a diazirine precursor in an N_2 matrix at 8 K. Product **47** was characterized using IR and UV–vis spectroscopies with the support of B3LYP/6-31+G(d,p) computations. In the absence of light, matrix-isolated carbene **47** was found to slowly rearrange to **48**. Following the evolution of the IR spectra along the transformation, it was determined that 15% of **47** was converted into **48** after 3 days ($k\approx2.3\times10^{-7}$ s^{-1}). The rearrangement rate of **47** was a bit faster (35% conversion over the same time) at 23 K. The experimentally observed behavior was similar to that found for carbene **45** ring-expansion to **46**, which led the authors to propose that rearrangement of **47** to **48** also proceeds *via* heavy-atom tunnelling.

B3LYP/6-31+G(d,p) computations predict a barrier of 22 kJ mol^{-1} for the **47**→**48** rearrangement, which precludes the possibility of a classical over-the-barrier reaction at the used cryogenic temperatures. The lower exothermicity for the reaction of **47** comparing with that of **45** (86 *vs.* 328 kJ mol^{-1}) probably makes the width of the barrier larger and explains the slower tunnelling rate for **47**→**48** in comparison with that for **45**→**46**, despite the smaller barrier height for the former transformation (22 *vs.* 27 kJ mol^{-1}).

The first case of heavy-atom tunnelling involving a nitrene species was reported in 2017 by Zeng *et al.* (Figure 1.49).[177] They generated triplet

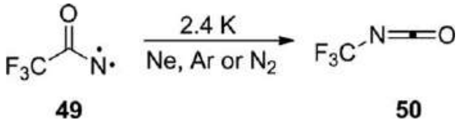

Figure 1.49 Rearrangement reaction of triplet nitrene ^{3}**49** to isocyanate **50**.

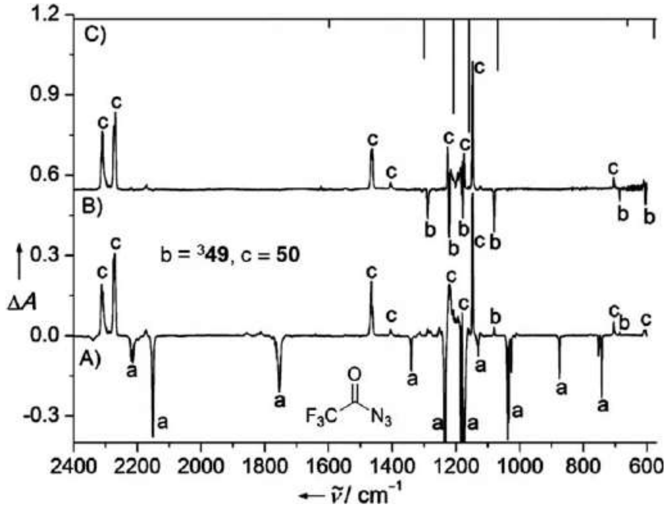

Figure 1.50 (A) IR difference spectrum showing the change upon the 193 nm laser photolysis of azide precursor (a) in solid Ar at 2.8 K. (B) IR difference spectrum showing the conversion from triplet nitrene **49** (b) to singlet isocyanate **50** (c) after standing the sample in the dark for 60 minutes at 2.8 K. (C) Computed IR spectrum of ^{3}**49**.
Reproduced from ref. 177 with permission from John Wiley and Sons, © 2017 Wiley-VCH Verlag GmbH & Co. KGaA, Weinheim.

trifluoroacetyl nitrene ^{3}**49** by irradiating the corresponding azide precursor in solid matrices (Ar, Ne, and N_2) with a 193 nm laser. Isocyanate **50** was the main product observed. The weak IR bands assigned to ^{3}**49** were found to vanish quickly even at 2.8 K and while keeping the matrix in the dark (Figure 1.50). Concomitantly, the intensity of the IR bands of **50** increased. First-order kinetics for the ^{3}**49**$\rightarrow$**50** rearrangement were studied in various matrices and at different temperatures. Noteworthy, temperature independent rate constants were observed in the 2.8–23.0 K range. For instance, rate constants of 11.9×10^{-4} and 12.8×10^{-4} s^{-1} (half-life time of <10 min) were obtained in Ar matrices at 2.8 and 19.0 K, respectively. The fast and temperature independent rearrangement of nitrene ^{3}**49** at extremely low temperatures can only take place by a mechanism of heavy-atom tunnelling. The unexpectedly observed large $^{14}N/^{15}N$ kinetic isotopic effect (1.18–1.33) indicates that the tunnelling rearrangement does not occur solely by shift of the CF_3 fragment, but that the nitrogen atom also plays a significant role in the reaction.

As expected, calculations indicate that the triplet state of **49** is lower in energy than the singlet state (by 50 and 30 kJ mol^{-1}, at M06-2X/6-311+G(3df,3pd) and CASPT2(10,10)/6-311G** levels, respectively). One minimum energy crossing point (MECP) connecting the triplet **49** and the singlet **50** product was located 58.5 kJ mol^{-1} above ^{3}**49** [at the B3LYP/6-311+G(3df,3pd) level]. This estimated rearrangement barrier reinforces the conclusion that only tunnelling can

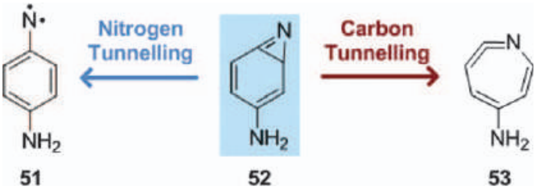

Figure 1.51 Competitive ring-open *vs.* ring-expansion reaction of benzazirine **52** to triplet nitrene ^{3}**51** and cyclic ketenimine **53**, respectively.

explain the observed reaction at cryogenic temperatures. In less inert organic matrices, like 2-methyltetrahydrofuran or toluene, the tunnelling transformation was dramatically influenced (the kinetics was considerably reduced), implying that for this system intermolecular interactions can have a huge effect on the tunnelling probability.

The most recent example (2019) of heavy-atom tunnelling observed in cryogenic matrix conditions was reported by our group in collaboration with Schreiner's group (Figure 1.51).[178] Triplet arylnitrene ^{3}**51** was first generated by photolysis (254 nm) of *p*-azidoaniline in an Ar matrix at 3 K and its vibrational signature was obtained. Subsequently, nitrene ^{3}**51** was depleted by irradiation at $\lambda = 435$ nm, resulting in the formation of the cyclic ketenimine **53** and a small amount of benzazirine **52**. Ketenimine **53** was selectively converted to nitrene ^{3}**51** by irradiation at $\lambda = 350$ nm, and a clear spectroscopic IR signature of these two species was obtained. In Ar at 3 K in the dark, benzazirine **52** was found to spontaneously decay, and surprisingly the rearrangement reaction simultaneously yielded two products, namely triplet nitrene ^{3}**51** and singlet ketenimine **53** (Figure 1.52).

A detailed assignment of the IR spectrum of **52** was performed with the support of the B3LYP/6-311+G(2d,p) computed IR spectrum. Under these conditions, a rate constant of $\sim 5.5 \times 10^{-5}$ s^{-1} was obtained (half-life time of ~210 minutes) and the product ^{3}**51** : **53** ratio was found to be roughly 15 : 85. Kinetic measurements were also performed at 10 and 18 K, and resulted in rate constants of $\sim 6.0 \times 10^{-5}$ and $\sim 7.0 \times 10^{-5}$ s^{-1}, respectively, *i.e.*, the rearrangement rate of **52** barely shows an increase upon increasing the absolute temperature by a factor up to five. Moreover, the product ^{3}**51** : **53** ratio practically did not change with the increase of temperature (18 : 82 at 10 K and 17 : 83 at 18 K). Therefore, it became evident that the rearrangements of **52** in cryogenic conditions, leading to the formation of ^{3}**51** and **53**, were not due to thermally activated processes but to two independent and competitive heavy-atom tunnelling reactions.

The formation of ^{3}**51** conceivably involves the ring-opening of **52** to open-shell singlet (OSS) **51** followed by fast ISC. Because OSS **51** can only be adequately described using a multi-configurational wave function, the ring-opening **52** → OSS **51** was computed at the NEVPT2(8,8) level, and an energy barrier of 10 kJ mol^{-1} was obtained. For the ring-expansion **52** → **53**, computations at the CCSD(T) level were found more reliable, and an energy barrier of

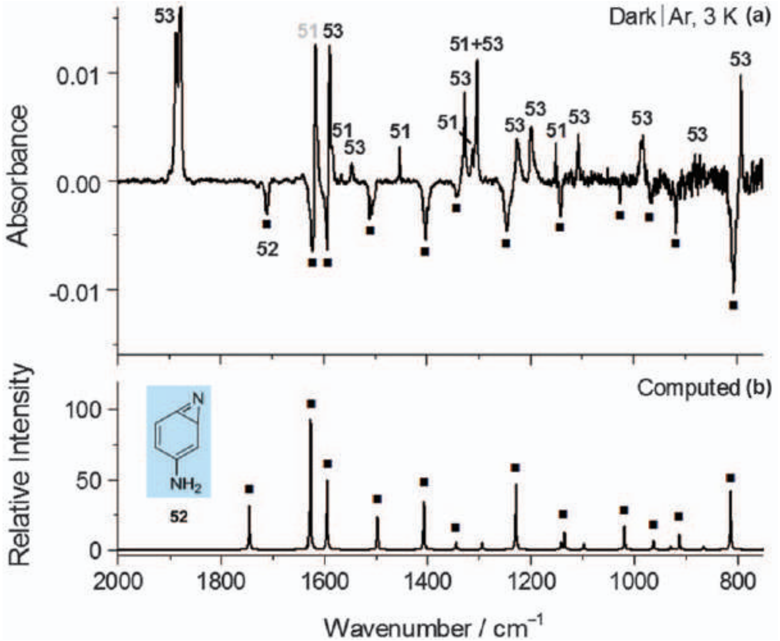

Figure 1.52 (a) Experimental difference IR spectrum showing changes after keeping the sample at 3 K (argon matrix) in the dark for 24 hours, subsequent to depletion of nitrene ^{3}**51** at $\lambda = 435$ nm. The downward bands are due to the consumption of benzazirine **52**. The upward bands are due to the formation of both ^{3}**51** and **53**. (b) IR spectrum of **52** computed at B3LYP/6-311+G(2d,p) level of theory.
Adapted from ref. 178 with permission from American Chemical Society, Copyright 2019.

30 kJ mol^{-1} was obtained. Even a smaller barrier of ~10 kJ mol^{-1} is prohibitive at the cryogenic temperatures of the experiment, and according to the classic rate theory, **52** should be stable (a half-life of ~10^{162} years at 3 K is predicted). In addition, the observed major product **53** is separated by a higher computed energy barrier than the minor product ^{3}**51**. This contradicts the rules inferred from classical TST and can only be explained considering the occurrence of heavy-atom tunnelling reactions and tunnelling control of the global chemical reactivity exhibited by benzazirine **52**.[19]

Computed tunnelling half-lives using the one-dimensional WKB formalism do indeed predict the existence of two competitive tunnelling reactions from **52**, in accordance with the experimental observations.[178] Moreover, computations also showed that in the ring-opening **52** → OSS **51**, the nitrogen atom in the three-membered ring is the heavy atom having by far the largest displacement (a traversed arc of ~0.56 Å), making the case for a predominant nitrogen-atom tunnelling. Regarding the ring-expansion **52** → **53**, the two carbon atoms in the three-membered ring are clearly the heavy atoms with the largest displacements (a traversed arc of ~0.32 Å each), making the case for a predominant carbon atom tunnelling. With this discovery, we unveiled a new reactivity paradigm in this area, by demonstrating that a well-defined chemical starting material decays spontaneously at cryogenic temperature into two different products that arise from competitive heavy-atom carbon *vs.* nitrogen tunnelling reactions.

Author Contributions

CMN wrote the first version of Sections 1.1 and 1.8; IR wrote the first version of Sections 1.2, 1.4, 1.5, and 1.7; RF wrote the first version of Sections 1.3 and 1.6. All authors contributed to the preparation of the final version of all sections.

Acknowledgements

This work was supported by Projects POCI-01-0145-FEDER-028973 and POCI-01-0145-FEDER-016617 (PTDC/QEQ-QFI/3284/2014), funded by FEDER *via* Portugal 2020-POCI, by National Funds *via* the Portuguese Foundation for Science and Technology (FCT), by bilateral project for scientific cooperation between FCT (Portugal) and DAAD (Germany), and by bilateral project for scientific cooperation between FCT (Portugal) and PHC Pessoa (France). The Coimbra Chemistry Centre is supported by the FCT through the project UID/QUI/0313/2019, cofunded by COMPETE. CMN and IR acknowledge the FCT for an Auxiliary Researcher grant and an Investigador FCT grant, respectively.

References

1. F. Hund, *Z. Phys.*, 1927, **43**, 805–826.
2. E. P. Wigner, *Z. Phys. Chem.*, 1932, **19B**, 203–216.
3. R. P. Bell, *Proc. R. Soc. A: Math. Phys. Eng. Sci.*, 1933, **139**, 466–474.
4. S. Roginsky and L. Rosenkewitsch, *Nature*, 1930, **125**, 347–348.
5. D. G. Bourgin, *Proc. Natl. Acad. Sci. U. S. A.*, 1929, **15**, 357–362.
6. R. P. Bell, *The Tunnel Effect in Chemistry*, Springer, Boston, MA, 1980.
7. Form more recent books addressing tunnelling effects in chemistry see(a) H. Nakamura and G. Mil'nikov, *Quantum Mechanical Tunnelling in Chemical Physics*, CRC Press, 2013; (b) *Quantum Tunnelling in Enzyme-Catalysed Reactions*, ed. R. K. Allemann and N. S. Scrutton, RSC, Cambridge, 2009; (c) *Atom Tunnelling Phenomena in Physics, Chemistry and Biology*, ed. T. Miyazaki, Springer, Berlin, 2004.
8. P. Ball, *Beyond Weird: Why Everything You Thought You Knew About Quantum Physics Is Different*, University of Chicago Press, Chicago, **ch. 3**, 2018, pp. 38–57.
9. H. Eyring, *J. Chem. Phys.*, 1935, **3**, 107–115.
10. K. J. Laidler and C. King, *J. Phys. Chem.*, 1983, **87**, 2657–2664.
11. D. A. Dougherty and V. A. Eric, *Modern Physical Organic Chemistry*, University Science Books, Sausalito, CA, 2006.
12. S. Arrhenius, *Z. Phys. Chem.*, 1889, **4**, 226–248.

13. E. F. Caldin, *Chem. Rev.*, 1969, **69**, 135–156.
14. R. S. Sheridan, Quantum Mechanical Tunneling in Organic Reactive Intermediates, in *Reviews of Reactive Intermediate Chemistry*, ed. R. A Moss, M. S. Platz and M. J. Jones, John Wiley & Sons, 2006, pp. 415–463.
15. D. Ley, D. Gerbig and P. R. Schreiner, *Org. Biomol. Chem.*, 2012, **10**, 3781–3790.
16. E. M. Greer, K. Kwon, A. Greer and C. Doubleday, *Tetrahedron*, 2016, **72**, 7357–7373.
17. J. Meisner and J. Kästner, *Angew. Chem., Int. Ed.*, 2016, **55**, 5400–5413.
18. J. Kästner, *Wiley Interdiscip. Rev.: Comput. Mol. Sci.*, 2014, **4**, 158–168.
19. P. R. Schreiner, *J. Am. Chem. Soc.*, 2017, **139**, 15276–15283.
20. R. J. Le Roy, H. Murai and F. Williams, *J. Am. Chem. Soc.*, 1980, **102**, 2325–2334.
21. D. G. Truhlar, *J. Phys. Org. Chem.*, 2010, **23**, 660–676.
22. W. T. Borden, *Wiley Interdiscip. Rev.: Comput. Mol. Sci.*, 2016, **6**, 20–46.
23. G. Wentzel, *Z. Phys.*, 1926, **38**, 518–529.
24. H. A. Kramers, *Z. Phys.*, 1926, **39**, 828–840.
25. L. Brillouin, *C. R. Hebd. Seances Acad. Sci.*, 1926, **183**, 24–26.
26. H. Jeffreys, *Proc. London Math. Soc.*, 1925, **23**, 428–436.
27. M. J. Frisch, G. W. Trucks, H. B. Schlegel, G. E. Scuseria, M. A. Robb, J. R. Cheeseman, G. Scalmani, V. Barone, B. Mennucci, G. A. Petersson, H. Nakatsuji, M. Caricato, X. Li, H. P. Hratchian, A. F. Izmaylov, J. Bloino, G. Zheng, J. L. Sonnenberg, M. Hada, M. Ehara, K. Toyota, R. Fukuda, J. Hasegawa, M. Ishida, T. Nakajima, Y. Honda, O. Kitao, H. Nakai, T. Vreven, J. A. Montgomery, Jr., J. E. Peralta, F. Ogliaro, M. Bearpark, J. J. Heyd, E. Brothers, K. N. Kudin, V. N. Staroverov, T. Keith, R. Kobayashi, J. Normand, K. Raghavachari, A. Rendell, J. C. Burant, S. S. Iyengar, J. Tomasi, M. Cossi, N. Rega, J. M. Millam, M. Klene, J. E. Knox, J. B. Cross, V. Bakken, C. Adamo, J. Jaramillo, R. Gomperts, R. E. Stratmann, O. Yazyev, A. J. Austin, R. Cammi, C. Pomelli, J. W. Ochterski, R. L. Martin, K. Morokuma, V. G. Zakrzewski, G. A. Voth, P. Salvador, J. J. Dannenberg, S. Dapprich, A. D. Daniels, Ö. Farkas, J. B. Foresman, J. V. Ortiz, J. Cioslowski and D. J. Fox Gaussian, *09, Revision D.01*, Gaussian, Inc., Wallingford, CT, 2013.
28. P. R. Schreiner, H. P. Reisenauer, D. Ley, D. Gerbig, C. H. Wu and W. D. Allen, *Science*, 2011, **332**, 1300–1303.
29. M. Tsuge and L. Khriachtchev, *J. Phys. Chem. A*, 2015, **119**, 2628–2635.
30. I. Reva, M. J. Nowak, L. Lapinski and R. Fausto, *J. Chem. Phys.*, 2012, **136**, 064511.
31. R. A. Marcus and M. E. Coltrin, *J. Chem. Phys.*, 1977, **67**, 2609–2613.
32. D. G. Truhlar and A. Kuppermann, *J. Am. Chem. Soc.*, 1971, **93**, 1840–1851.
33. R. T. Skodje, D. G. Truhlar and B. C. Garrett, *J. Phys. Chem.*, 1981, **85**, 3019–3023.
34. E. Whittle, D. A. Dows and G. C. Pimentel, *J. Chem. Phys.*, 1954, **22**, 1943.

35. I. Norman and G. Porter, *Nature*, 1954, **174**, 508–509.
36. C. Y. Lin and A. Krantz, *J. Chem. Soc., Chem. Commun.*, 1972, 1111–1112.
37. O. L. Chapman, C. L. McIntosh and J. Pacansky, *J. Am. Chem. Soc.*, 1973, **95**, 244–246.
38. R. G. S. Pong and J. S. Shirk, *J. Am. Chem. Soc.*, 1973, **95**, 248–249.
39. B. Meyer, *Low Temperature Spectroscopy*, American Elsevier Publishers Company, New York, 1971.
40. *Chemistry and Physics of Matrix Isolated Species*, ed. L. Andrews and M. Moskovits, Elsevier, Amsterdam, 1989.
41. *Matrix Isolation Spectroscopy*, ed. A. Barnes, W. J. Orville-Thomas, R. Gaufrès and A. Müller, Springer, 1981.
42. I. R. Dunkin, *Matrix Isolation Techniques: A Practical Approach*, Oxford University Press, 1998.
43. *Low Temperature Molecular Spectroscopy*, ed. R. Fausto, NATO-ASI Series C483, Kluwer, Amsterdam, 1996.
44. R. Fausto, *Photogeneration of Rare Molecules in Cryogenic Matrices: Spectroscopists' Adventures in Wonderland, in Frontiers and Advances in Molecular Spectroscopy*, ed. J. Laane, Elsevier, Amsterdam, **ch. 19**, 2018, pp. 631–666.
45. S. Góbi, I. Reva, I. P. Csonka, C. M. Nunes, G. Tarczay and R. Fausto, *Phys. Chem. Chem. Phys.*, 2019, **21**, 24935–24949.
46. A. Plonka, *Radiat. Phys. Chem.*, 1991, **37**, 411–415.
47. A. Plonka, W. Lefik and J. Kroh, *Chem. Phys. Lett.*, 1979, **62**, 271–274.
48. A. Plonka and A. Paszkiewicz, *J. Chem. Phys.*, 1992, **96**, 1128–1133.
49. A. Plonka and A. Paszkiewicz, *Chem. Phys.*, 1996, **212**, 1–8.
50. M. B. Sponsler, R. Jain, F. D. Coms and D. A. Dougherty, *J. Am. Chem. Soc.*, 1989, **111**, 2240–2252.
51. W. Siebrand and T. A. Wildman, *Acc. Chem. Res.*, 1986, **19**, 238–243.
52. A. Plonka, *Annu. Rep. Prog. Chem., Sect. C: Phys. Chem.*, 1988, **85**, 47–75.
53. M. Ertelt, D. A. Hrovat, W. T. Borden and W. Sander, *Chem. – Eur. J.*, 2014, **20**, 4713–4720.
54. C. M. Nunes, S. N. Knezz, I. Reva, R. Fausto and R. J. McMahon, *J. Am. Chem. Soc.*, 2016, **138**, 15287–15290.
55. I. Reva, C. M. Nunes, M. Biczysko and R. Fausto, *J. Phys. Chem. A*, 2015, **119**, 2614–2627.
56. L. Lapinski, I. Reva, M. J. Nowak and R. Fausto, *Phys. Chem. Chem. Phys.*, 2011, **13**, 9676–9684.
57. L. Lapinski, M. J. Nowak, I. Reva, H. Rostkowska and R. Fausto, *Phys. Chem. Chem. Phys.*, 2010, **12**, 9615–9618.
58. L. Lapinski, I. Reva, H. Rostkowska, R. Fausto and M. J. Nowak, *J. Phys. Chem. B*, 2014, **118**, 2831–2841.
59. A. J. Lopes Jesus, C. M. Nunes, I. Reva, S. M. V. Pinto and R. Fausto, *J. Phys. Chem. A*, 2019, **123**, 4396–4405.
60. S. Góbi, C. M. Nunes, I. Reva, G. Tarczay and R. Fausto, *Phys. Chem. Chem. Phys.*, 2019, **21**, 17063–17071.

61. M. Pettersson, J. Lundell, L. Khriachtchev and M. Räsänen, *J. Am. Chem. Soc.*, 1997, **119**, 11715–11716.
62. M. Pettersson, E. M. S. Maçôas, L. Khriachtchev, J. Lundell, M. Räsänen and R. Fausto, *J. Chem. Phys.*, 2002, **117**, 9095–9098.
63. E. M. S. Maçôas, J. Lundell, M. Pettersson, L. Khriachtchev, R. Fausto and M. Räsänen, *J. Mol. Spectrosc.*, 2003, **219**, 70–80.
64. M. Pettersson, E. M. S. Maçôas, L. Kriachtchev, R. Fausto and M. Räsänen, *J. Am. Chem. Soc.*, 2003, **125**, 4058–4059.
65. L. Khriachtchev, E. M. S. Maçôas, M. Pettersson and M. Räsänen, *J. Am. Chem. Soc.*, 2002, **124**, 10994–10995.
66. A. J. Lopes Jesus, C. M. Nunes, R. Fausto and I. Reva, *Chem. Commun.*, 2018, **54**, 4778–4781.
67. B. Kovács, N. Kuş, G. Tarczay and R. Fausto, *J. Phys. Chem. A*, 2017, **121**, 3392–3400.
68. A. J. Lopes Jesus, I. Reva, C. Araujo-Andrade and R. Fausto, *J. Chem. Phys.*, 2016, **144**, 124306.
69. C. M. Nunes, I. Reva and R. Fausto, *Phys. Chem. Chem. Phys.*, 2019, **21**, 24993–25001.
70. E. M. S. Maçôas, L. Khriachtchev, M. Pettersson, R. Fausto and M. Räsänen, *J. Am. Chem. Soc.*, 2003, **125**, 16188–16189.
71. E. M. S. Maçôas, L. Kriachtchev, R. Fausto and M. Räsänen, *J. Phys. Chem. A*, 2004, **108**, 3380–3389.
72. E. M. S. Maçôas, L. Kriachtchev, M. Pettersson, R. Fausto and M. Räsänen, *J. Chem. Phys.*, 2004, **121**, 1331–1338.
73. E. M. S. Maçôas, L. Khriachtchev, M. Pettersson, R. Fausto and M. Räsänen, *J. Phys. Chem. A*, 2005, **109**, 3617–3625.
74. R. F. G. Apóstolo, R. R. F. Bento, G. Tarczay and R. Fausto, *J. Mol. Struct.*, 2016, **1125**, 288–295.
75. R. F. G. Apóstolo, R. R. F. Bento and R. Fausto, *Croat. Chem. Acta*, 2015, **88**, 377–386.
76. R. F. G. Apóstolo, G. Bazsó, G. O. Ildiz, G. Tarczay and R. Fausto, *J. Chem. Phys.*, 2018, **148**, 044303.
77. G. Bazsó, S. Góbi and G. Tarczay, *J. Phys. Chem. A*, 2012, **116**, 4823–4832.
78. S. Lopes, T. Nikitin and R. Fausto, *J. Phys. Chem. A*, 2019, **123**, 1581–1593.
79. N. Kuş and R. Fausto, *J. Chem. Phys.*, 2014, **141**, 234310.
80. I. D. Reva, S. Stepanian, L. Adamowicz and R. Fausto, *J. Phys. Chem. A*, 2001, **105**, 4773–4780.
81. I. D. Reva, S. Jarmelo, L. Lapinski and R. Fausto, *J. Phys. Chem. A*, 2004, **108**, 6982–6989.
82. A. Halasa, L. Lapinski, I. Reva, H. Rostkowska, R. Fausto and M. J. Nowak, *J. Phys. Chem. A*, 2014, **118**, 5626–5635.
83. D. Gerbig and P. R. Schreiner, *J. Phys. Chem. B*, 2015, **119**, 693–703.
84. N. Kuş and R. Fausto, *J. Chem. Phys.*, 2017, **146**, 124305.
85. L. Lapinski, I. Reva, H. Rostkowska, R. Fausto and M. J. Nowak, *J. Phys. Chem. A*, 2013, **117**, 5251–5259.

86. A. Halasa, L. Lapinski, I. Reva, H. Rostkowska, R. Fausto and M. J. Nowak, *J. Phys. Chem. A*, 2015, **119**, 1037–1047.
87. L. L. G. Justino, I. Reva and R. Fausto, *J. Chem. Phys.*, 2016, **145**, 014304.
88. S. Amiri, H. P. Reisenauer and P. R. Schreiner, *J. Am. Chem. Soc.*, 2010, **132**, 15902–15904.
89. S. Nishino and M. Nakata, *J. Phys. Chem. A*, 2007, **111**, 7041–7047.
90. E. M. S. Maçôas, R. Fausto, M. Pettersson, L. Khriachtchev and M. Räsänen, *J. Phys. Chem. A*, 2000, **104**, 6956–6961.
91. E. M. S. Maçôas, R. Fausto, J. Lundell, M. Pettersson, L. Khriachtchev and M. Räsänen, *J. Phys. Chem. A*, 2000, **104**, 11725–11732.
92. E. M. S. Maçôas, R. Fausto, J. Lundell, M. Pettersson, L. Khriachtchev and M. Räsänen, *J. Phys. Chem. A*, 2001, **105**, 3922–3933.
93. A. Halasa, I. Reva, L. Lapinski, M. J. Nowak and R. Fausto, *J. Phys. Chem. A*, 2016, **120**, 2078–2088.
94. P. R. Schreiner, J. P. Wagner, H. P. Reisenauer, D. Gerbig, D. Ley, J. Sarka, A. G. Császár, A. Vaughn and W. D. Allen, *J. Am. Chem. Soc.*, 2015, **137**, 7828–7834.
95. N. Kuş, A. Sharma, I. Peña, M. C. Bermúdez, C. Cabezas, J. L. Alonso and R. Fausto, *J. Chem. Phys.*, 2013, **138**, 144305.
96. C. M. Nunes, L. Lapinski, R. Fausto and I. Reva, *J. Chem. Phys.*, 2013, **138**, 125101.
97. G. Bazsó, G. Magyarfalvi and G. Tarczay, *J. Phys. Chem. A*, 2012, **116**, 10539–10547.
98. G. Bazsó, E. E. Najbauer, G. Magyarfalvi and G. Tarczay, *J. Phys. Chem. A*, 2013, **117**, 1952–1962.
99. G. Bazsó, G. Magyarfalvi and G. Tarczay, *J. Mol. Struct.*, 2012, **1025**, 33–42.
100. E. E. Najbauer, G. Bazsó, R. Apóstolo, R. Fausto, M. Biczysko, V. Barone and G. Tarczay, *J. Phys. Chem. B*, 2015, **119**, 10496–10510.
101. E. E. Najbauer, G. Bazsó, S. Góbi, G. Magyarfalvi and G. Tarczay, *J. Phys. Chem. B*, 2014, **118**, 2093–2103.
102. I. D. Reva, S. G. Stepanian, L. Adamowicz and R. Fausto, *Chem. Phys. Lett.*, 2003, **374**, 631–638.
103. I. D. Reva, A. J. Lopes Jesus, M. T. S. Rosado, R. Fausto, M. E. Eusébio and J. S. Redinha, *Phys. Chem. Chem. Phys.*, 2006, **8**, 5339–5349.
104. S. Lopes, A. V. Domanskaya, R. Fausto, M. Räsänen and L. Khriachtchev, *J. Chem. Phys.*, 2010, **133**, 144507.
105. S. Lopes, A. Domanskaya, M. Räsänen, L. Khriachtchev and R. Fausto, *J. Chem. Phys.*, 2015, **143**, 104307.
106. J. Lundell, M. Räsänen and Z. Latajka, *Chem. Phys.*, 1994, **189**, 245–260.
107. P. K. Wawrzyniak, J. Panek, J. Lundell and Z. Latajka, *J. Mol. Model.*, 2005, **11**, 351–361.
108. P. K. Wawrzyniak, J. Panek, Z. Latajka and J. Lundell, *J. Mol. Struct.*, 2004, **704**, 297–304.
109. L. Khriachtchev, *J. Mol. Struct.*, 2008, **880**, 14–22.

110. A. Domanskaya, K. Marushkevich, L. Khriachtchev and M. Räsänen, *J. Chem. Phys.*, 2009, **130**, 154509.
111. K. Marushkevich, L. Khriachtchev and M. Räsänen, *J. Chem. Phys.*, 2007, **126**, 241102.
112. K. Marushkevich, M. Siltanen, M. Räsänen, L. Halonen and L. Khriachtchev, *J. Phys. Chem. Lett.*, 2011, **2**, 695–699.
113. L. Khriachtchev, A. Domanskaya, K. Marushkevich, M. Räsänen, B. Grigorenko, A. Ermilov, N. Andrijchenko and A. Nemukhin, *J. Phys. Chem. A*, 2009, **113**, 8143–8146.
114. K. Marushkevich, L. Khriachtchev and M. Räsänen, *J. Phys. Chem. A*, 2007, **111**, 2040–2042.
115. S. Lopes, R. Fausto and L. Khriachtchev, *J. Chem. Phys.*, 2016, **144**, 084308.
116. M. J. Nowak, I. Reva, A. J. Lopes Jesus, L. Lapinski and R. Fausto, *Phys. Chem. Chem. Phys.*, 2019, **21**, 22857–22868.
117. S. Nanbu, M. Sekine and M. Nakata, *J. Mol. Struct.*, 2012, **1025**, 69–73.
118. S. Nanbu, M. Sekine and M. Nakata, *J. Phys. Chem. A*, 2011, **115**, 9911–9918.
119. N. Akai, S. Kudoh and M. Nakata, *J. Phys. Chem. A*, 2003, **107**, 3655–3659.
120. N. Akai, S. Kudoh, M. Takayanagi and M. Nakata, *J. Phys. Chem. A*, 2002, **106**, 11029–11033.
121. N. Akai, S. Kudoh, M. Takayanagi and M. Nakata, *Chem. Phys. Lett.*, 2002, **356**, 133–139.
122. M. M. Linden, J. P. Wagner, B. Bernhardt, M. A. Bartlett, W. D. Allen and P. R. Schreiner, *J. Chem. Phys. Lett.*, 2018, **9**, 1663–1667.
123. R. L. Redington, *J. Chem. Phys.*, 2000, **113**, 2319–2335.
124. A. S. Trivella, S. Coussan, T. Chiavassa, P. Theulé, P. Roubin and C. Manca, *Low Temp. Phys.*, 2006, **32**, 1042–1049.
125. N. O. B. Lüttschwager, T. N. Wassermann, S. Coussan and M. A. Suhm, *Mol. Phys.*, 2013, **111**, 2211–2227.
126. F. Wu, Y. H. Ren and W. S. Bian, *J. Chem. Phys.*, 2016, **145**, 074309.
127. A. Gutiérrez-Quintanilla, M. Chevalier and C. Crépin, *Phys. Chem. Chem. Phys.*, 2016, **18**, 20713–20725.
128. H. Tomioka, *Res. Chem. Intermed.*, 1994, **20**, 605–634.
129. C. Wentrup, *Angew. Chem., Int. Ed.*, 2018, **57**, 11508–11521.
130. O. L. Chapman, *Pure Appl. Chem.*, 1979, **51**, 331–339.
131. M. S. Platz, *J. Am. Chem. Soc.*, 1979, **101**, 3398–3399.
132. R. J. McMahon and O. L. Chapman, *J. Am. Chem. Soc.*, 1987, **109**, 683–692.
133. M. S. Platz, *J. Am. Chem. Soc.*, 1980, **102**, 1192–1194.
134. M. S. Platz and J. R. Burns, *J. Am. Chem. Soc.*, 1979, **101**, 4425–4426.
135. M. C. Biewer, M. S. Platz, M. Roth and J. Wirz, *J. Am. Chem. Soc.*, 1991, **113**, 8069–8073.
136. C. R. Kemnitz, C. W. L. Karney and W. T. Borden, *J. Am. Chem. Soc.*, 1998, **120**, 3499–3503.

137. A. Admasu, A. D. Gudmundsdottir and M. S. Platz, *J. Phys. Chem. A*, 1997, **101**, 3832–3840.
138. W. T. Borden, N. P. Gritsan, C. M. Hadad, W. L. Karney, C. R. Kemnitz and M. S. Platz, *Acc. Chem. Res.*, 2000, **33**, 765–771.
139. J. J. Fisher and J. Michl, *J. Am. Chem. Soc.*, 1987, **109**, 583–584.
140. J. C. Koziar and D. O. Cowan, *Acc. Chem. Res.*, 1978, **11**, 334–341.
141. P. R. Schreiner, H. P. Reisenauer, F. C. Pickard IV, A. C. Simmonett, W. D. Allen, E. Mátyus and A. G. Császár, *Nature*, 2008, **453**, 906–909.
142. D. Ley, D. Gerbig and P. R. Schreiner, *Chem. Sci.*, 2013, **4**, 677–684.
143. D. Gerbig, H. P. Reisenauer, C. H. Wu, D. Ley, W. D. Allen and P. R. Schreiner, *J. Am. Chem. Soc.*, 2010, **132**, 7273–7275.
144. D. Ley, D. Gerbig, J. P. Wagner, H. P. Reisenauer and P. R. Schreiner, *J. Am. Chem. Soc.*, 2011, **133**, 13614–13621.
145. A. Mardyukov, H. Quanz and P. R. Schreiner, *Nat. Chem.*, 2017, **9**, 71–76.
146. P. R. Schreiner and H. P. Reisenauer, *Angew. Chem., Int. Ed.*, 2008, **47**, 7071–7074.
147. A. Nandi, D. Gerbig, P. R. Schreiner, W. T. Borden and S. Kozuch, *J. Am. Chem. Soc.*, 2017, **139**, 9097–9099.
148. A. K. Eckhardt, D. Gerbig and P. R. Schreiner, *J. Phys. Chem. A*, 2018, **122**, 1488–1495.
149. A. K. Eckhardt, F. R. Erb and P. R. Schreiner, *Chem. Sci.*, 2019, **10**, 802–808.
150. J. Sarka, A. G. Császár and P. R. Schreiner, *Collect. Czech. Chem. Commun.*, 2011, **76**, 645–667.
151. H. Rostkowska, L. Lapinski, A. Khvorostov and M. J. Nowak, *J. Phys. Chem. A*, 2003, **107**, 6373–6380.
152. H. Rostkowska, L. Lapinski and M. J. Nowak, *Phys. Chem. Chem. Phys.*, 2018, **20**, 13994–14002.
153. H. Rostkowska, L. Lapinski, A. Khvorostov and M. J. Nowak, *Chem. Phys.*, 2004, **298**, 223–232.
154. L. Lapinski, H. Rostkowska, A. Khvorostov and M. J. Nowak, *Phys. Chem. Chem. Phys.*, 2003, **5**, 1524–1529.
155. B. B. Wright, V. P. Senthilnathan, M. S. Platz and C. W. McCurdy Jr., *Tetrahedron Lett.*, 1982, **23**, 833–836.
156. E. Mendez-Vega, M. Maehara, A. H. Raut, J. Mieres-Perez, M. Tsuge, Y. P. Lee and W. Sander, *Chem. – Eur. J.*, 2018, **24**, 18801–18808.
157. S. Henkel, M. Ertelt and W. Sander, *Chem. – Eur. J.*, 2014, **20**, 7585–7588.
158. P. S. Zuev and R. S. Sheridan, *J. Am. Chem. Soc.*, 2001, **123**, 12434–12435.
159. S. Henkel, Y. A. Huynh, P. Neuhaus, M. Winkler and W. Sander, *J. Am. Chem. Soc.*, 2012, **134**, 13204–13207.
160. S. Henkel and W. Sander, *Angew. Chem., Int. Ed.*, 2015, **54**, 4603–4607.
161. I. Trosien, E. Mendez-Vega, T. Thomanek and W. Sander, *Angew. Chem., Int. Ed.*, 2019, **58**, 14855–14859.
162. K. A. Haupa, G. Tarczay and Y.-P. Lee, *J. Am. Chem. Soc.*, 2019, **141**, 11614–11620.

163. S. Kozuch, A. Nandi and A. Sucher, *Chem. – Eur. J.*, 2018, **24**, 16348–16355.
164. S. L. Buchwalter and G. L. Closs, *J. Am. Chem. Soc.*, 1975, **97**, 3875–3878.
165. S. L. Buchwalter and G. L. Closs, *J. Am. Chem. Soc.*, 1979, **101**, 4688–4694.
166. D. W. Whitman and B. K. Carpenter, *J. Am. Chem. Soc.*, 1982, **104**, 6473–6474.
167. B. K. Carpenter, *J. Am. Chem. Soc.*, 1983, **105**, 1700–1701.
168. A. M. Orendt, B. R. Arnold, J. G. Radziszewski, J. C. Facelli, K. D. Malsch, H. Strub, D. M. Grant and J. Michl, *J. Am. Chem. Soc.*, 1988, **110**, 2648–2650.
169. T. Schleif, J. Mierez-Perez, S. Henkel, M. Ertelt, W. T. Borden and W. Sander, *Angew. Chem., Int. Ed.*, 2017, **56**, 10746–10749.
170. X. Zhang, D. A. Hrovat and W. T. Borden, *Org. Lett.*, 2010, **12**, 2798–2801.
171. W. Sander, W. Müller and R. Sustmann, *Angew. Chem., Int. Ed.*, 1988, **27**, 572–574.
172. H. Inui, K. Sawada, S. Oishi, K. Ushida and R. J. McMahon, *J. Am. Chem. Soc.*, 2013, **135**, 10246–10249.
173. C. M. Nunes, I. Reva, S. Kozuch, R. J. McMahon and R. Fausto, *J. Am. Chem. Soc.*, 2017, **139**, 17649–17659.
174. P. Zuev and R. D. Sheridan, *J. Am. Chem. Soc.*, 1994, **116**, 4123–4124.
175. P. S. Zuev, R. S. Sheridan, T. V. Albu, D. G. Truhlar, D. A. Hrovat and W. T. Borden, *Science*, 2003, **299**, 867–870.
176. R. A. Moss, R. R. Sauers, R. S. Sheridan, J. Tian and P. S. Zuev, *J. Am. Chem. Soc.*, 2004, **126**, 10196–10197.
177. Z. Wu, R. Feng, H. Li, J. Xu, G. Deng, M. Abe, D. Bégué, K. Liu and X. Zeng, *Angew. Chem., Int. Ed.*, 2017, **56**, 15672–15676.
178. C. M. Nunes, A. K. Eckhardt, I. Reva, R. Fausto and P. R. Schreiner, *J. Am. Chem. Soc.*, 2019, **141**, 14340–14348.

CHAPTER 2

Tunnelling Instability in Molecular Systems. An Exercise in Computational Chemistry Prediction Power

H. AMLANI, A. FRENKLAH AND S. KOZUCH*

Department of Chemistry, Ben-Gurion University of the Negev,
Beer-Sheva 841051, Israel
*Email: kozuch@bgu.ac.il

2.1 Introduction and Motivation

One of the hardest, but also most rewarding tasks in chemistry consists in the generation of any molecule we can envision. This includes industrial or pharmaceutical fine chemicals of high economic value or, more relevant to this book chapter, small but intricate molecules of high academic[1] (or even aesthetic[2]) significance. In fact, the possibility of synthesizing complex molecular structures starting from bulk chemicals through the manipulation of atoms and bonds has been considered as one of the ‘‘holy grails in chemistry’’.[3,4] This urge to produce unique and extreme molecules was elegantly summarized by Hoffmann,[1] when stating that

> *‘‘. . .the literature of organic chemistry has contained characterizations of molecules as unstable, strained, distorted, sterically hindered, bent and battered. Such molecules are hardly seen as dull; on the contrary, they are*

Theoretical and Computational Chemistry Series No. 18
Tunnelling in Molecules: Nuclear Quantum Effects from Bio to Physical Chemistry
Edited by Johannes Kästner and Sebastian Kozuch

Published by the Royal Society of Chemistry, www.rsc.org

> *perceived as worthwhile synthetic goals, and their synthesis, or evidence of their fleeting existence, acclaimed. What is going on here? Why this obsession with abnormal molecules? Is this molecular science sadistic at its core?*''

This raises the question: is it even in the realm of possibilities to generate all those extreme molecules? It is epistemologically impossible to determine only by experimental means that an inexistent, hypothetical molecule can or cannot be synthesized. At most, guided by rules of thumb it is possible to guesstimate their viability. On this matter computational chemistry has the upper hand: it can predict with high confidence the stability of any system whether in kinetic or thermodynamic terms. Therefore, *in silico* studies can signal if trying to synthesize certain molecules can be an impossible endeavour and/or a waste of resources. This idea is not novel,[1–8] but there is one critical aspect that has never been considered: can quantum mechanical tunnelling (QMT) be the reason why certain hypothetical molecules cannot be prepared? Which molecules people are actively trying to synthesize, when they are unstable even close to absolute zero? In light of this, the motivation for this chapter is to discuss the viability of computational chemistry in the prediction of the impossibility to create certain molecules in a real-life laboratory.[9]

Special emphasis will be given, obviously, to the QMT stability challenge, an effect which we named ''quantum tunnelling instability'' (QTI[†]). This molecular instability can, in principle, be driven by hydrogen tunnelling. However, in most cases when speaking about strained molecules we mean that the heavy-atom framework (mostly carbon–carbon bonds) is stressed, while light hydrogen is only saturating their valences. Therefore, this chapter is a practical exercise as well as a pedagogical and semi-philosophical exposition on heavy-atom tunnelling,[10,11] a relatively new field that we are only starting to scratch its surface.

2.1.1 Stability in the Eye of the Beholder?

Beyond the technical difficulties in the total synthesis of organic and inorganic molecules, the most evident problem resides in their kinetic stability. Any single internal bond-breaking reaction can completely destroy the molecule. Therefore, the system must be checked for its weak points (*e.g.* stretched C–C bonds) whose lability can kickstart the molecular decomposition. Herein we will use the nomenclature introduced by Hoffmann, Schleyer and Schaefer to distinguish the scope of the kinetic stability of any particular chemical entity:[7]

> *'''Viable'' might be a label attached to a molecule that meets computational criteria of persistence appropriate to ambient conditions in a typical chemical laboratory environment.*

[†] pronounced as /kjuːti/.

> *"Fleeting" molecules might be claimed legitimately based on computations in which the sole energetic criterion is a vibrational analysis. That a molecule is a local minimum, with barriers, albeit small ones, preventing escape from its local basin.'*

We can add the obvious term of "unstable" to a molecular geometry that is not even a real minimum in the potential energy surface (PES), and therefore will distort or be shattered without any external influence. So, if we would like to physically create a new molecule, we will have to be sure that it is viable, or at least that it is fleeting. In this case we must know at which temperature "preventing escape from its local basin" is a sensible outcome: would it be stable for a year in liquid nitrogen ($\Delta G^{\ddagger} \approx 30$ kJ mol^{-1} according to transition state theory)? Maybe for a century in liquid helium ($\Delta G^{\ddagger} \approx 1.4$ kJ mol^{-1})? Clearly the conditions of stability have to be stated, or the synthesis will be futile.

Still, one more situation must be considered. What if the barrier of the fleeting molecule can be surmounted by going not over the barrier, but *through* the barrier, in a QMT mechanism? If the reaction barrier is exceptionally narrow (not uncommon in exothermic bond-breaking reactions), the activation energy is relatively low (not uncommon for strained systems), and the atoms are reasonably light (*i.e.* up to second row elements), going to deeper temperatures might not prevent the decomposition. The QTI might be the death sentence of such molecule, and that is an aspect that has to be included into the definition of "fleeting".

2.2 A Primer: Computational Design of an Impossible Molecule

One human obsession is trying to find the harder, better, faster, stronger; to reach the extremes and win a Guinness world record certificate. This also fits chemistry and chemists.[12] In this sense, some years ago Martínez-Guajardo *et al.* computationally designed an organic molecule with the shortest C–C σ bond.[13] This caged tetrahedryl-tetrahedrane (**TT**, Figure 2.1) accomplishes such a

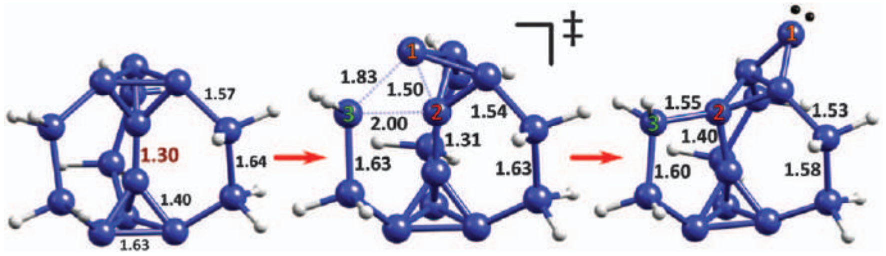

Figure 2.1 Computationally designed caged tetrahedryl-tetrahedrane (**TT**), with the shortest known theoretical C–C σ bond (bond distances in Å), and its cage-opening mechanism.
Adapted from ref. 15 with permission from American Chemical Society, Copyright 2014.

short bond due to the "iron maiden" effect[14] of the external chains plus the enhanced s character of the carbons at the vertex of the tetrahedra thanks to its forced angles.

The stability of **TT** was subsequently studied by the method of Markopoulos and Grunenberg,[16] which analyses the strength of individual bonds. The conclusion was that the decomposition of the molecule should occur by the rupture of one tetrahedrane from the shackles that maintained the molecule in a forced equilibrium, followed by the opening of the tetrahedra, ending in a carbene product. The activation energy of such process is *circa* 30 $\mathrm{kJ\,mol^{-1}}$. Undoubtedly it would be tremendously complicated to synthesize this molecule, but even if having the technical skills for such a feat, would this fleeting molecule withstand the test of time?

A simple calculation under transition state theory [TST, eqn (2.1)]

$$k = \frac{k_\mathrm{B}T}{h}\mathrm{e}^{-\Delta G^{\ddagger}/RT} \tag{2.1}$$

gives a first order half-life ($t_{\frac{1}{2}} = \ln 2/k$) of approximately some nanoseconds for this reaction at room temperature, clearly not a stable system. However, if we go to liquid nitrogen temperature the classical $t_{\frac{1}{2}}$ reaches years, and therefore **TT** can be considered fleeting, and can be preserved *ad infinitum* at the right conditions. Or can it?

The tunnelling process of **TT** decomposition was studied computationally (see below and in the original article for the methodology),[15] with unexpected results. The maximum predicted half-life of this caged tetrahedryl-tetrahedrane is of the order of milliseconds due to a QTI process; no matter at which temperature we would like to keep it, it will swiftly decompose; any attempt to synthesize this molecule would be futile!

Some other observations of the computational study, which are typical of many tunnelling processes, were that:

- Below ~50 K the rate of decomposition is constant since QMT is, in principle, a temperature independent process (tunnelling from the ground state, see Scheme 2.1).
- From ~50 K and up to ~150 K the rate grows with raising temperatures. Although QMT is formally invariable, that does not preclude other processes from being temperature dependent. In this case, it is the occupation of vibrationally excited states that makes for a lower and narrower effective barrier (*vide infra*), in what is called thermally (or vibrationally) activated tunnelling (Scheme 2.1).[17,18]
- The carbon kinetic isotope effect (KIE) is huge, reaching values higher than 2 at cryogenic conditions (compare to the expected value of 1.04 for the classical first-order KIE at room temperature). The change of slope is a clear indication of change in the kinetic regime (classical, thermally activated tunnelling, and ground-state QMT, Figure 2.2 and Scheme 2.1).
- The magnitude of the KIE is a direct clue of which atom hinders the most the QMT process (the "tunnelling determining atom",[15,20,21]

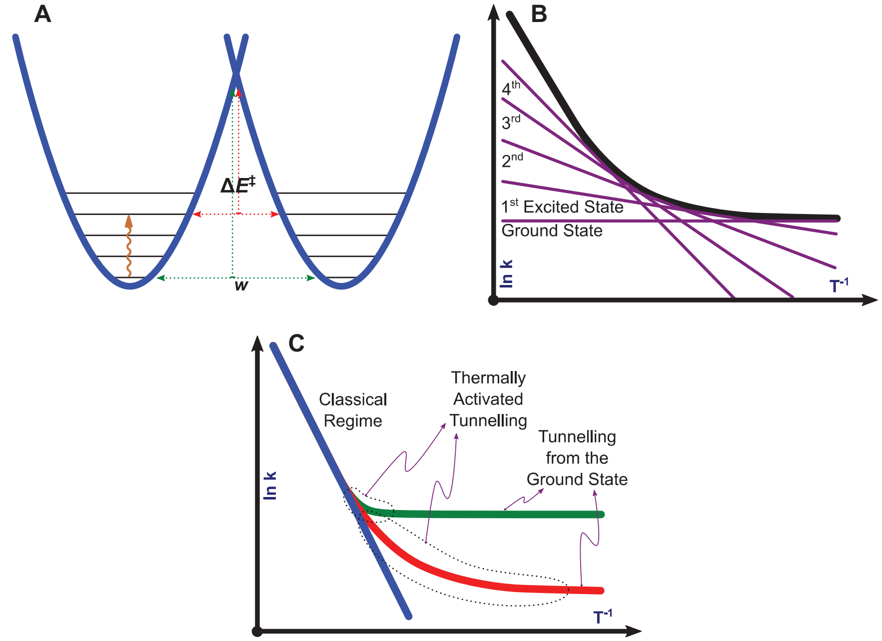

Scheme 2.1 (A) Thermally activated tunnelling occurring by occupation of excited vibrational states, producing a lower and narrower effective barrier. (B) While tunnelling from a specific state is temperature independent, the occupation of excited states follows a Boltzmann distribution, and therefore QMT from excited states are temperature dependent. The superposition between all the states' profiles form the traditional tunnelling curve in the Arrhenius plot.[19] (C) Systems with small gaps between vibrational levels, typical of heavy-atom stretching modes, form a wide curvature with temperature dependence starting at low temperatures (red line). Hydrogen tunnelling, with large zero-point energy (ZPE) and gaps between states, tend to have sharper curves (green line).

carbon 1 in **TT**). This correlates with the length of the trajectory of each atom across the reaction, as large displacements reduce the probability of tunnelling. Since in heavy-atom QMT the reaction usually involves many atoms moving through the least-action pathway,[22–24] then it is common to observe high KIEs for many atoms (in contrast to H QMT, where this light atom tends to be the sole determining one).

- If the impact of each individual isotopic substitution is fairly independent of other substitutions, then the KIE after multiple substitutions is roughly equal to the product of the individual substitutions ($\text{KIE}_{\text{total}} \approx \Pi_i\ \text{KIE}_i$, see the blue curve in Figure 2.2). This approximation mostly works in heavy-atom tunnelling; in hydrogen QMT the large effect of H or D on the zero-point energy (ZPE) breaks the independency of the different substitutions.

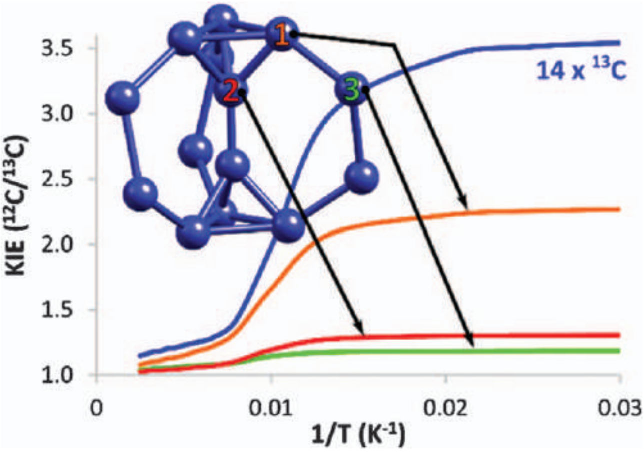

Figure 2.2 Three main $^{12}C/^{13}C$ kinetic isotope effects on the decomposition of **TT**, and the total KIE (in blue) after substituting all the fourteen carbons together. Reproduced from ref. 15 with permission from American Chemical Society, Copyright 2014.

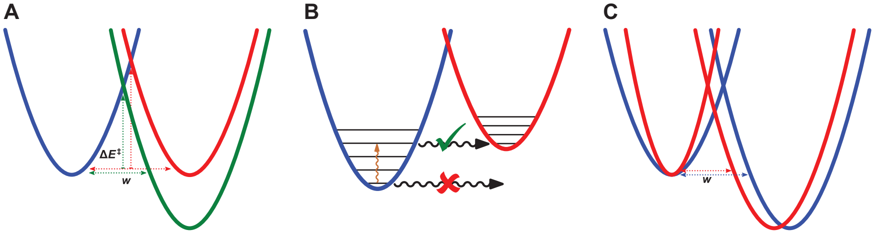

Scheme 2.2 (A) A strongly exothermic reaction tends to produce, according to the Hammond principle, a lower activation energy, but it may also generate a narrower barrier.[10] (B) Endothermic reactions cannot tunnel, unless there is enough thermal energy to populate high vibrational states. (C) A stronger bond in terms of the force constant (higher stretching frequency, red profile) may produce a narrower barrier.

- The reaction involves very large movement of the atoms, especially of C1. This should make QMT impossible. However, the reaction is deeply exothermic, which makes the effective tunnelling distance quite short (see Scheme 2.2).
- The degradation of a molecule can be a concerted, single-step reaction (see the pericyclic reactions below), or it can comprise many steps, since the intermediates might be unstable as well. In the case of **TT**, after the opening of the first tetrahedron, the second one will open in a similar fashion by QMT with almost the same half-life, in a kind of "domino tunnelling".[25]

TT is an example of a computationally designed molecule that will never see the light due to being a QTI. Many other hypothetical molecules can also be proven to be only computational exercises, but a much worse-case scenario is when experimentalists actually try to prepare such systems. Before recounting some of them, we will describe some computational techniques to predict the QTI effect.

2.3 Theoretical and Computational Digression

2.3.1 Quantum Tunnelling: Theoretical and Practical Considerations

Many chapters of this book already provide thorough expositions of the diverse methods to calculate or compute the rate constants of molecular QMT reactions. Therefore, we will bring here only a short introduction of the basic concepts and methodologies used to compute the rates of the relevant systems of this chapter.

For a tunnelling particle, the transmission probability depends approximately on the dimensionless *action* (s), according to:[10,21,26–28]

$$P \underset{\sim}{\propto} \mathrm{e}^{-xs} \quad s = w\sqrt{\Delta E^{\ddagger} m}/\hbar \tag{2.2}$$

where $\Delta E^{\ddagger}$ is the activation energy, m the mass of the tunnelling atom, w the barrier width, and x is the barrier shape factor. For example, for a rectangular barrier $x = 2\sqrt{2}$, and for an inverted parabolic barrier $x = \pi/\sqrt{2}$ (with w considered at the maximum width). Evidently real barriers have their own unique shape and therefore a unique x value (which can vary depending on where we take the barrier width[21]), but for didactical purposes we can assume here that the shape factor is similar in most reactions. Undoubtedly, from the three factors that shape the transmission probability by QMT (barrier height and width, and particle mass), the most critical is the barrier width. This means that a "heavy" atom can tunnel as long as its trajectory is extremely narrow.[10,11,29] For instance, if H can tunnel through a barrier of 1 Å with a certain probability, a carbon atom will do so through a barrier of ~0.3 Å with the same probability. Not impossible, but it is quite rare to have a reaction with such narrow path. Because of this, the myth of the impossibility of heavy-atom tunnelling was born.

Beyond the mass issue, the difficulties of massive atoms to tunnel can be worsened by their longer bonds, which make wider trajectories in chemical reactions. Therefore, extremely heavy (in a QMT sense) but strongly electronegative atoms like F or O may still tunnel,[19,30] given that atomic radii shrinks when going to the right in the periodic table. We can say that for chemical tunnelling purposes there is the "fluorine wall", beyond which QMT is probably impossible.

As it happens, due to the short nature of covalent bonds, bond-breaking reactions usually have short trajectories, as long as the reaction is strongly exothermic (Scheme 2.2A). If it were not exothermic, there would be no state to tunnel to (unless the molecule was standing in a high vibrational state, for which we need high temperature, see Scheme 2.2B). But why would a more exothermic reaction, a thermodynamic effect, affect the kinetics? In classical reactions this is roughly explained by the Hammond principle (similar in spirit to other relationships like the Marcus equation or the Bell–Evans–Polanyi principle): a lower energy product brings down the activation energy, since the transition state gets more similar to the reactant. However, what is less known is that it also makes the barrier narrower, and therefore it affects twice the tunnelling chances (Scheme 2.2A). This significant factor does not appear in classical (TST) kinetics.

Note that eqn (2.2) is an approximation for a sole particle tunnelling, while in real molecules several atoms move synchronously, especially in heavy-atom tunnelling. While in H tunnelling systems it is basically the hydrogen moving, the mass-weighted coordinates on carbon-based reactions is a function of the whole system (or at least of several atoms), as was seen in Figure 2.2. Therefore, the tunnelling mass is generally not as simple as the mass of one atom (think of the π-bond shifting on cyclobutadiene,[31] where the four carbons move identically). Furthermore, what we might consider the "tunnelling determining atom" according to our chemical intuition might be an oversimplification of a holistic movement of the molecule through barriers of arbitrary shapes.[21,32] Therefore, for realistic tunnelling corrections there is no simple analytical equation that can universally provide accurate results. Ballpark estimations are always possible, but expect errors of many orders of magnitude on the rate.

Some of these general approximations for QMT include the transmission estimation through different barrier shapes, such as the rectangular and parabolic profiles, or the popular Eckart function.[26] If a "fast and dirty" calculation of QMT is required, the tunnelling limit (T_L), which is nothing more than the calculation of the action [eqn (2.2)], taking the barrier width as the half-height width of the minimum energy pathway (MEP) curve,[21,30] may be sufficient. A more advanced methodology that fits the shape of any barrier is the WKB approximation, which basically integrates the permeability as infinite points on the MEP,[26,28,33] thus providing more accurate results when the barrier does not have a regular shape.[34] These approximations do not require costly computations, but they typically lack a thermally activated tunnelling correction (with higher occupied vibrational states the barrier becomes lower and narrower), the possibility to "cut corners" (see below), and other factors such as the inclusion of zero-point energy and vibrational level quantization into the MEP.

QMT corrections that take thermal effects into account include, for instance, the renowned but inaccurate Wigner correction (taking as parameters the temperature and the imaginary frequency of the transition state),[26,28] the Bell method based on a truncated parabolic potential,[26,35] the correction of Skodje and Truhlar,[36,37] and the correction of Fermann and Auerbach.[38] A much more advanced method that includes canonical variational transition state theory for an arbitrary shape barrier is the zero-curvature tunnelling

(ZCT) method,[23,24,39] which, combined with the canonical variational transition state theory (CVT),[23,39,40] is arguably the most accurate technique that runs through the MEP. These methods are not always more accurate than simpler methods such as the use of Eckart's function, but that comes through accidental error compensation.[41]

The main missing factor resides in the multidimensional nature of the PES, which raises the possibility of cutting corners to pass through the least-action pathway [*i.e.* maximizing the tunnelling probability, eqn (2.2)].[22–24] The trajectory through the transition state usually requires reorganization of the whole system, entailing a large sum of masses moving collectively, hindering the tunnelling process. Thus, the QMT calculation across the MEP (used by all the previous techniques) underestimates the tunnelling contribution. A highly accurate method that can cut corners (*i.e.* going through shorter pathways than the MEP) but at the cost of being extremely demanding computationally is the small curvature tunnelling (SCT) correction.[23,24,39] Based on ZCT, the SCT correction has the added capability of mapping the MEP with multidimensional contributions by calculating second derivatives of the energy all along the valley. Noteworthy, SCT (and ZCT) can find the rate of a reaction including tunnelling both from the ground state and from vibrationally excited states (aka "thermally activated tunnelling"). As such, the SCT method will be our method of choice here to provide accurate tunnelling rates, as provided by Polyrate17[42] in combination with Gaussian16[43] for the DFT computations. When combined with a good choice of functional and basis set, this methodology proved to be a very successful choice.[30,44–46] We must also mention here the also popular instanton method, which has proven itself to be the best alternative to SCT; for more information on this method we refer the reader to Chapter 7.[24]

The question of the use of the large-curvature tunnelling (LCT) method instead of SCT for heavy-atom tunnelling has been raised in the past. LCT uses a much shorter trajectory than SCT,[23,24] even if it involves much higher energies, which is useful when extreme corner-cutting is necessary. This arises when the least-action pathway involves keeping the heavy atoms almost immobile, and therefore it is more significant for H transfer reactions than for heavy-atom tunnelling. In practice, if the difference between the ZCT and SCT rates is not large (say, an order of magnitude), then LCT is probably unnecessary.

2.3.2 Electronic Structure Methods and Methodological Challenges

The idea of predicting, helped by computational means, that a molecule is unsynthesizable opens an epistemological question: how scientific would this prediction be?

Let us say that the lifetime of molecule **A** is predicted to be milliseconds at zero K, after which we will obtain product **B**. This will make the process of creation and detection of **A** absolutely impossible within the current experimental capabilities (and for the foreseeable future). The fact that the molecule cannot be experimentally detected can be ascribed to its inherent instability or, alternatively, to the faulty techniques used to synthesize it. Since we cannot know if the computations were accurate enough, we can only *disprove* our prediction if we experimentally detect **A**. At maximum, if we see signs of **B**, we can presuppose that it came from **A**, but this is a much weaker proof of its fleeting nature. Moreover, if we predicted that **A** is an impossible molecule, who will make the expensive effort of trying to synthesize it? In other words, we cannot strictly falsify our prediction of the instability of **A** *vis à vis* the alternative hypothesis that **A** is just too difficult to synthesize; this renders our instability hypothesis as ''non-scientific'' from a Popperian perspective.[47] The only way out of this epistemological conundrum is to be sure that our computations are sufficiently accurate, either by using extremely high-level methods, or by using cheap methods validated *vis à vis* high-level methods (or matching experimental methods, *vide infra*). In such a case, we partially cover the Popperian complication with an ''*a proxy*'' solution.

Since accurate SCT values are costly, we usually have to settle for DFT with a judicious basis set. Therefore, our best chance to produce trustworthy computational results is by selecting an inexpensive quantum chemical method through proper benchmarking. Bear in mind that different functionals can produce wildly different results, so benchmarking is a must (do not trust any paper that blindly employs a functional without proper testing in similar systems with similar properties). Benchmarks are typically carried out by comparison with high-accuracy computational methods, typically CCSD(T) or some approximation to it[48,49] with a complete basis set, but sometimes multireference methods are required. Alternatively, comparison with tunnelling reactions with experimentally known rates can be used. Both approaches have ups and downs.

Computational benchmarks can only be carried out on small molecules, but in an almost limitless number. This gives a veil of validation to any DFT or similarly cheap method that matches the results of most of these cases (even if it is by error compensation). But here is the deal: we will only obtain an accurate functional/basis set combination for *gas phase energies*. We hardly consider the accuracy of geometries (since good geometries are easy to obtain), and it will probably not include free energy corrections (neglecting errors in the frequencies, entropy and solvation). However, most important for our current purposes, it does not contemplate tunnelling rate constants as the target measurement.

It might be a small leap of faith, but there are reasons to believe that SCT provides a highly accurate technique to compute QMT corrections, as long as the PES is accurate.[23,39] Since a chain is only as strong as its weakest link, finding a good functional/basis set that agrees in terms of activation energies with the benchmark values will then be the best single step to achieve reliable results. On the other hand, there is a clever trick to reshape the PES by applying a dual-level method,[42,50] where individual energies obtained by a high-level method [typically of the reactant, transition state and product, obtained with CCSD(T)], can fix to some extent the energy profile obtained with a lower-level method (typically DFT).

In addition, we must discuss the elephant in the room: molecules are seldom obtained in sterile, gas-phase conditions, and solvent and other extra-molecular interactions are extremely hard to mimic. No coupled cluster benchmark can withstand the computation of the non-covalent interactions of the reactive molecule with its surrounding, while continuum solvent models,[51] with all their attractiveness as a simple correction for tunnelling,[30] can have errors larger than the functional inaccuracies. Since it is known that the medium can severely affect the tunnelling perspectives,[26,29,52] this is an ongoing and unfinished debate.

Yet, when we argue that experimental tunnelling results are more accurate than computational ones, what kind of experiment are we speaking about? Room temperature QMT can be detected by kinetic isotope effects, rate constant anomalies (low activation energy and pre-exponential factor in an Arrhenius graph) or other methodologies,[26] but in most cases the reactions are carried out in solvent phase. When we test for low-temperature QMT (where most heavy-atom tunnelling reactions are found, as they can be easily distinguished in those conditions from classical thermal reactions), we have a much more limited number of chemical media. It is hard to find convenient liquid solvents at liquid nitrogen temperature, let alone at liquid helium conditions. Therefore, if we are not checking interstellar reactions *in situ*, we are left with a small assortment of experimental methods to set up and isolate the molecules to study, with abysmal differences between them, such as:

- Supersonic expansion[53] (gas phase-like media)
- He nanodroplet[54] (liquid-like media)
- Matrix isolation[29] (weakly interacting amorphous solid-like media, including noble gases, H_2, N_2, *etc.*)
- Glassy matrices[55–57] (moderately interacting amorphous solid-like media, such as organic molecules)
- Doped crystals[58] (very strongly interacting crystal-like media).

The interaction with the different media (or lack thereof) will make significantly disparate tunnelling rates. Therefore, how can we speak of an "experimental value" to take as a benchmark? Furthermore, when due to the variability of interactions in amorphous matrices we have a range of rates,[25] then the best we can do is to compare the computational results with specific experimental methods and to consider an average of the random interactions. This can produce a different "best functional" compared to the hypothetical selection based on computational gas-phase benchmarks.[45]

Summing up, the stability of any molecule will be associated, to a certain extent, with the medium. Still, it is highly unlikely that a molecule will undergo tunnelling in one case while being stable in another (except for the case where the system is encapsulated inside a crystal or a host molecule that completely hinders the decomposition). Therefore, when selecting the method to carry out the electronic structure computations, we have to be aware that it can show accuracy compared to a specific type of experiment (possibly due to a happy coincidence or error compensation[45]), but we cannot expect foolproof precision under every possible circumstance. What computations can give is a highly educated semi-quantitative prediction of molecular stability. In the end, if we do not know if a molecule can be stable for a microsecond or a millisecond, we will not split hairs about such a difference.

For this chapter all the reactions were computed with similar techniques (SCT and DFT). We direct the reader to the original articles to check the methodology details of the already published systems, while for the reactions considered here for the first time we will specify the quantum method, with the understanding that all the rates are ballpark predictions.

2.4 Quantum Tunnelling Instability: Past and Future

2.4.1 Some Published Examples

As said before, QTI implicates mostly heavy-atom tunnelling,[10,11] of which many examples were cited in this same book. Between the systems that show instability, we can mention the photochemically obtained carbene systems that are designed to be reactive:[45,59–62] the surprise here is not that they can react, but the fact that in some cases the QMT is slow enough to prove their fleeting existence (Scheme 2.3A).[10,21,29,59–63] However, our focus is not to study molecules that are deliberately reactive but to find the molecules that are supposed to be stable, and therefore appropriate synthetic targets.

2.4.1.1 Ozone

A personal favourite of such a system is the cyclic, meta-stable D_{3h} ozone (Scheme 2.3B and Figure 2.3). This geometry is ~120 kJ mol^{-1} higher than the known bent C_{2h} O_3, with an interconversion "forbidden"[65] barrier of ~105 kJ mol^{-1}, enough to stabilize it forever and ever (these values are so difficult to obtain that the reaction is used as a trial by fire to test the accuracy of quantum methods).[66] The spectroscopic characteristics of cyclic ozone are theoretically known,[67,68] so if one day the molecule is created, we already know how to detect it. And yet, after many tries (we do not know how many, since negative results are virtually unpublishable), nobody has seen a

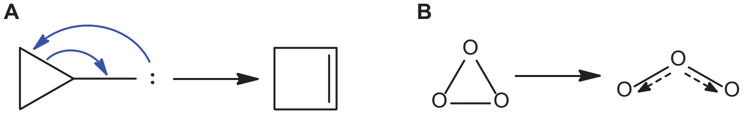

Scheme 2.3 (A) Ring expansion of cyclopropylcarbene, a prototypical example of carbon tunnelling.[64] (B) Ring opening of cyclic ozone.[19]

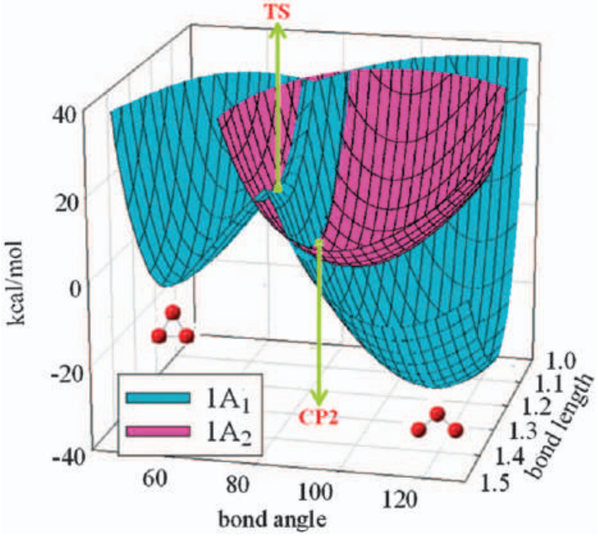

Figure 2.3 Potential energy surfaces of ozone ring opening. Reproduced from ref. 19 with permission from American Chemical Society, Copyright 2011.

naked ring of O_3,[65] in spite of having a more intuitive Lewis structure than the dative bond stabilized bent ozone.[69] The closest we were to seeing it was a three-oxygen ring stabilized by an MgO surface[70] (maybe a transition metal complex can do the trick as well[71]). However, are we ever going to see pure cyclic ozone? Probably not, unless a transient species with a half-life of a minute counts. Chen and Hu[19] "proved" computationally that below 100 K the rate of ring opening is temperature independent, that is QMT from the ground state. Therefore, unless stabilized by strong chemical interactions (which in our view should be considered as a different species), cyclic ozone cannot be obtained as a fleeting species in a flask under any conditions. At maximum, it might be fortuitously observed and accidentally characterized as a very short-lived intermediary in the path to create regular ozone. We will therefore put cyclic ozone in the QTI category.

2.4.1.2 CMe_5^+

Cyclic O_3 does not really decompose, it just switches to a not so different geometry with an altered connectivity. However, there are other studied systems whose hypothetical decomposition is much more drastic. For instance, some years ago McKee *et al.* studied the possibility of having an "impossible" pentamethyl carbocation (CMe_5^+, Figure 2.4).[72] This molecule should actually be a fleeting system, with a real minimum at the PES, albeit with an extremely low activation energy leading to its decomposition (6.9 and 5.7 kJ mol^{-1} $(E+ZPE)^{\ddagger}$ for pathways 1 and 2, respectively). With such low barriers nobody would dare to take the challenge to synthesize it, but from a theoretical

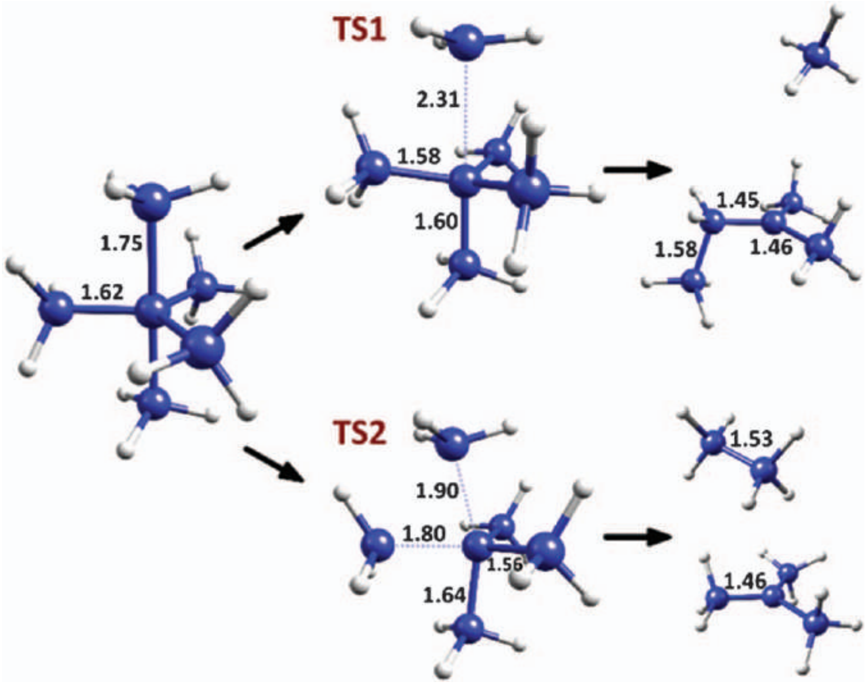

Figure 2.4 CMe_5^+ and the two most probable decomposition mechanisms (distances in Å).[44,72]
Reproduced from ref. 44 with permission from the PCCP Owner Societies.

perspective at liquid He conditions the molecule should be stable for many times the age of the universe. At least if we neglect the QTI possibility.

SCT computations pointed to a completely different conclusion.[44] The $t_{\frac{1}{2}}$ of CMe_5^+ was of the order of microseconds, with temperature independence (aka ground state QMT) up to ~50 K. Therefore, the unlikelihood of experimentally detecting this molecule comes not only from technical organic synthetic complications, but also from the impossibility to keep the molecule "alive" for a sensible time, at least to obtain any type of spectroscopic characterization. In this sense, this is a clear QTI.

CMe_5^+ has some other interesting effects up its sleeve. First, from the barriers' heights pathway 1 (C–C bond stretching of the axial methyl group, see TS1 in Figure 2.4) should be slower than pathway 2 (C–C–C bond bending, TS2 in Figure 2.4), and therefore the product of the latter (ethane and trimethylcarbenium) should be in higher concentration than that of the former (methane and ethyl-dimethylcarbenium), with the ratio depending on the temperature (approximately 1 : 10 at liquid N_2). However, due to the narrower barrier of mechanism 1, the selectivity is inverted *via* a tunnelling control effect,[62,63,73] which penalizes reactions with longer atomic trajectories. Close to absolute zero, the ratio of products would be 8 : 1 in favour of the higher energy barrier path.

Also interesting is a technique to improve the stability of CMe_5^+. In principle, we can reduce the QTI by buffing up the mass of the tunnelling determining atoms (upper axial carbon in the first mechanism of Figure 2.4). However, a change from ^{12}C to ^{13}C makes the reaction only half as fast, with a half-life going from 6 μs to 12 μs; still a clear QTI. In contrast, substituting all the H with D has a much more striking effect, with $t_{\frac{1}{2}} = 4$ ms. Still a QTI, but three orders of magnitude more stable. However, this occurs despite substituting mostly immobile atoms! How does this tunnelling heretical paradox transpire? The answer is that QMT is not the sole quantum effect in play, since the zero-point energy is significantly reduced in the isotopic substitution of this molecule, producing an approximately 30% higher effective barrier when having an all deuterated molecule.[44] As a note, this large isotopic effect is only valid for reactions with very low barriers and lots of hydrogens close to the reactive position.

2.4.1.3 Pericyclic Reactions

Pericyclic reactions are a fascinating type of organic reactions where the transition state has a "cyclic array of continuously bonded atoms",[74] even if the reactant and/or product does not.[75,76] They are concerted, in many cases with little atomic movement, which favours QMT chances. The big exception is when having a rotation of larger than hydrogen substituents, as in the "conrotatory/disrotatory" reactions described by Woodward–Hoffman rules, which can severely hinder the tunnelling transmission.[46,77] The rearrangement is an electronic game of bond breaking and forming, which is usually considered to be a synchronized cyclic movement of p atomic orbitals switching from σ to π molecular orbitals and *vice versa* (see Schemes 2.5–2.6 for some examples that can occur by QMT from the ground state). Interestingly, whether the reaction is synchronous or asynchronous may depend on whether the reaction goes through an over the barrier or through a tunnelling mechanism.[78]

From a reactivity perspective, we can divide these reactions between exothermic and isothermic. The latter, except for fortuitous cases, involve degenerate rearrangements (aka automerizations) with a symmetric double or multiwell PES. Starting from the breakthrough discovery of the π-bond shifting in cyclobutadiene[31,79] many other degenerate pericyclic reactions have been found experimentally or theoretically.[10,11] These are not of interest in a QTI chapter, but since they are excellent examples of heavy-atom tunnelling, we show some examples in Scheme 2.4.

From the known exothermic pericyclic reactions, we can first cite the ring expansion of benzazirine (Scheme 2.5A).[29,32,81,82] The reactant can be created photochemically from aryl azides, and, depending on the substitutions on the ring, the reactions can occur in a measurable time (*i.e.* in a matter of days) even close to absolute zero. This means that we can have certainty of the existence of the benzazirine by spectroscopical analysis, and therefore this system does not really count as a QTI. Interestingly, an alternative and competitive pathway involves the opening of the azirine cycle, forming

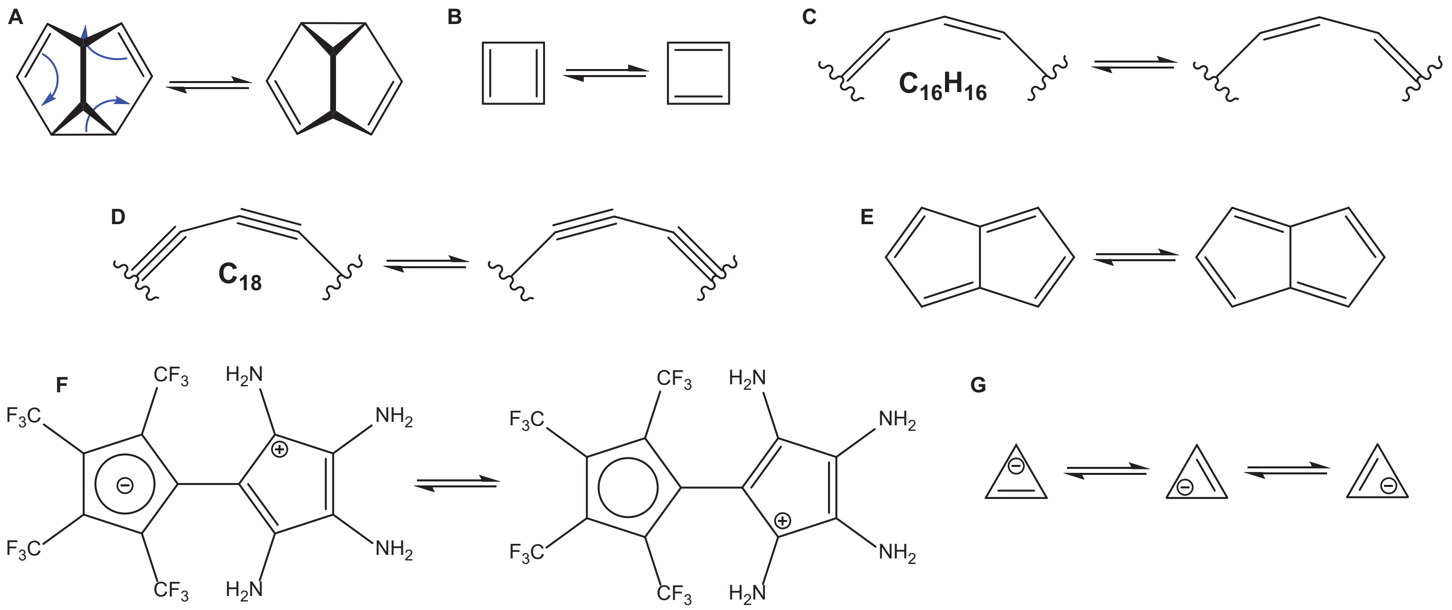

Scheme 2.4 Degenerate pericyclic reactions that can proceed through heavy-atom tunnelling from the ground state.[10,11] (A) Semibullvalene.[78,80] (B) Cyclobutadiene.[32,81,82] (C) [16]Annulene.[83] (D) Cyclo[18]carbon.[84] (E) Pentalene.[77] (F) Substituted pentafulvalene.[20] (G) Cyclopropenyl anion.[46]

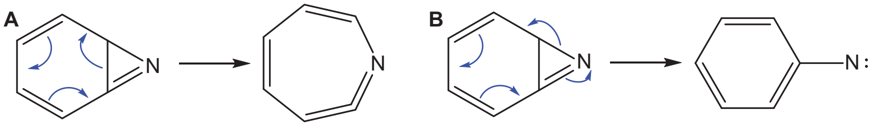

Scheme 2.5 (A) Benzazirine to keteneimine.[32,81,82] (B) Benzazirine to phenylnitrene.[82]

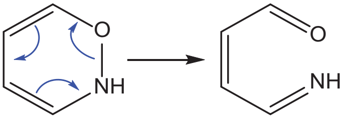

Scheme 2.6 Cyclic hydroxylamine ether to linear 4-iminobut-2-enal.[85]

phenylnitrene (Scheme 2.5B). While the six-membered ring opening involves mostly carbon tunnelling, the three-membered ring opening is based on nitrogen tunnelling.[82] The final outcome depends on the kinetic control of the tunnelling effect.[62,73]

Several other pericyclic reactions have been computationally proven to react with significant tunnelling from excited vibrational states.[17,18] Although they are interesting cases, they would be completely stable at low temperature and therefore not exactly suffering from QTI. A real, and maybe the first, case of QTI came with the analysis of a cyclic hydroxylamine ether (Scheme 2.6) as an intermediate in a complex series of reactive species.[85] In spite of having a barrier of 26 kJ mol^{-1}, this molecule was predicted to undergo an extremely fast electrocyclic ring opening no matter the temperature. With a computed half-life of some microseconds, it would be completely impossible to isolate such a ring. The molecule can be synthesized, but not observed. The only proof of its super-fleeting existence would be the detection of the iminobutenal product.

As Borden states in his key review on reactions that involve carbon tunnelling:[10]

> "*Thus, if [the cyclic hydroxylamine ether] were ever prepared, even at cryogenic temperatures, Dr Chen's calculations predict that it would probably not be observed; and only its rearrangement product would be isolated... Dr Chen was, therefore, very surprised to find a paper in which Mark Lautens and coworkers reported the synthesis, isolation, and characterization of a dimethyl derivative of [the hydroxylamine ether].*[86] *When informed that his purported reaction product could not exist for more than about* 10^{-4} *s, even at 30 K, Professor Lautens reinvestigated the* ^{13}C *NMR spectrum of the compound that he had isolated. The compound turned out not to be a dimethyl derivative of [the hydroxylamine ether], but, instead, 2,4-dimethylhydroxypyrrole!*"

Is there a more joyous moment for a computational chemist than to correct an experimental result?

2.4.2 Some Unpublished Examples: Pericyclic Deazatation

At the present time the number of unknown molecules with known QTI adversities is extremely small, but there is a large number of unknown strained molecules that are actively pursued experimentally, or those that are hypothesized to be ‘‘worthwhile synthetic goals’’.[1] These systems usually have one thing in common: they comply with Lewis structures, but their bond angles and lengths are less than optimal (see above the tetrahedryltetrahedrane case in Section 2.2). Some other systems suffer from instability only due to their exothermicity (as in the cyclic hydroxylamine ether, Section 2.4.1.3), which makes a lower and narrower barrier following the Hammond postulate (Scheme 2.2). Of this last category are the systems we are going to discuss as a final exercise in heavy-atom tunnelling.

One of the most famous families of organic reactions is the pericyclic cycloadditions (such as the Diels–Alder case) or, more relevant to this work, their reverse case, the cycloreversions. In this, the molecule breaks down into two fragments through a pericyclic bond rearrangement, as shown in Scheme 2.7. If the products are particularly stable, for instance an aromatic system and N_2 (the ‘‘leaving group’’), then Hammond might be on our side. It must be noted that Woodward–Hoffmann rules, critical to define if a pericyclic reaction is allowed or forbidden (that is, thermally of photochemically reactive, respectively), might bear little responsibility for the tunnelling rates here; not only it is hard to determine the barrier width according to these rules but also the extreme exothermicity and relatively eccentric bonding blurs any hint of prediction based on them.

We decided to test several hypothetical compounds that can degrade by a cycloreversion mechanism, all of them having N_2 as the leaving group (a deazatation), and therefore producing exothermic reactions (Scheme 2.8 and Figure 2.5). All of them have an early transition state, an important factor for QTI, as it helps in making narrow tunnelling trajectories. As a reminder, the full displacement of atoms through the complete reaction is irrelevant, as only the movement from the reactant to the state of same energy in the product side determines the barrier width (Scheme 2.2).

A couple of the selected reactions have an open-shell singlet transition state (reactions **3** and **5** in Scheme 2.8). This is not particularly surprising, considering that breaking bonds can easily produce diradicals. On the contrary, the surprise is that most of these reactions go through a closed-shell transition state. The symmetry of the reactions and the fact that two C–N bonds must be

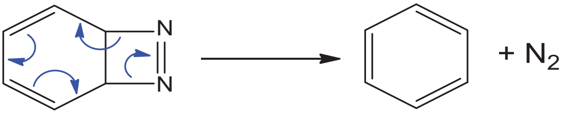

Scheme 2.7 Prototypical cycloreversion reaction. The stability of the products, especially the triple bond of N_2, creates its driving force and low activation energies.

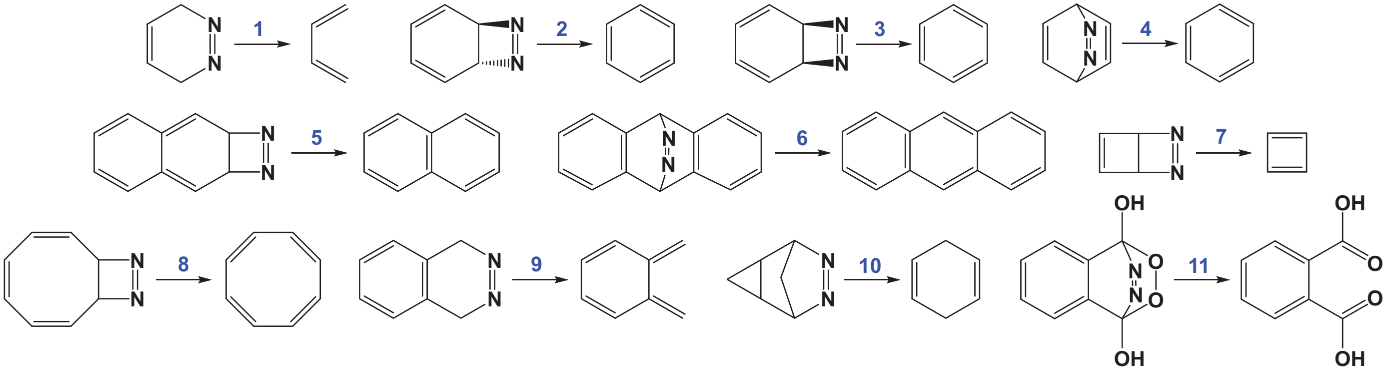

Scheme 2.8 Series of pericyclic cycloreversion deazatation reactions studied for QTI. The N_2 leaving group is not shown. As an exercise for the reader, guess which one might have QTI or not.

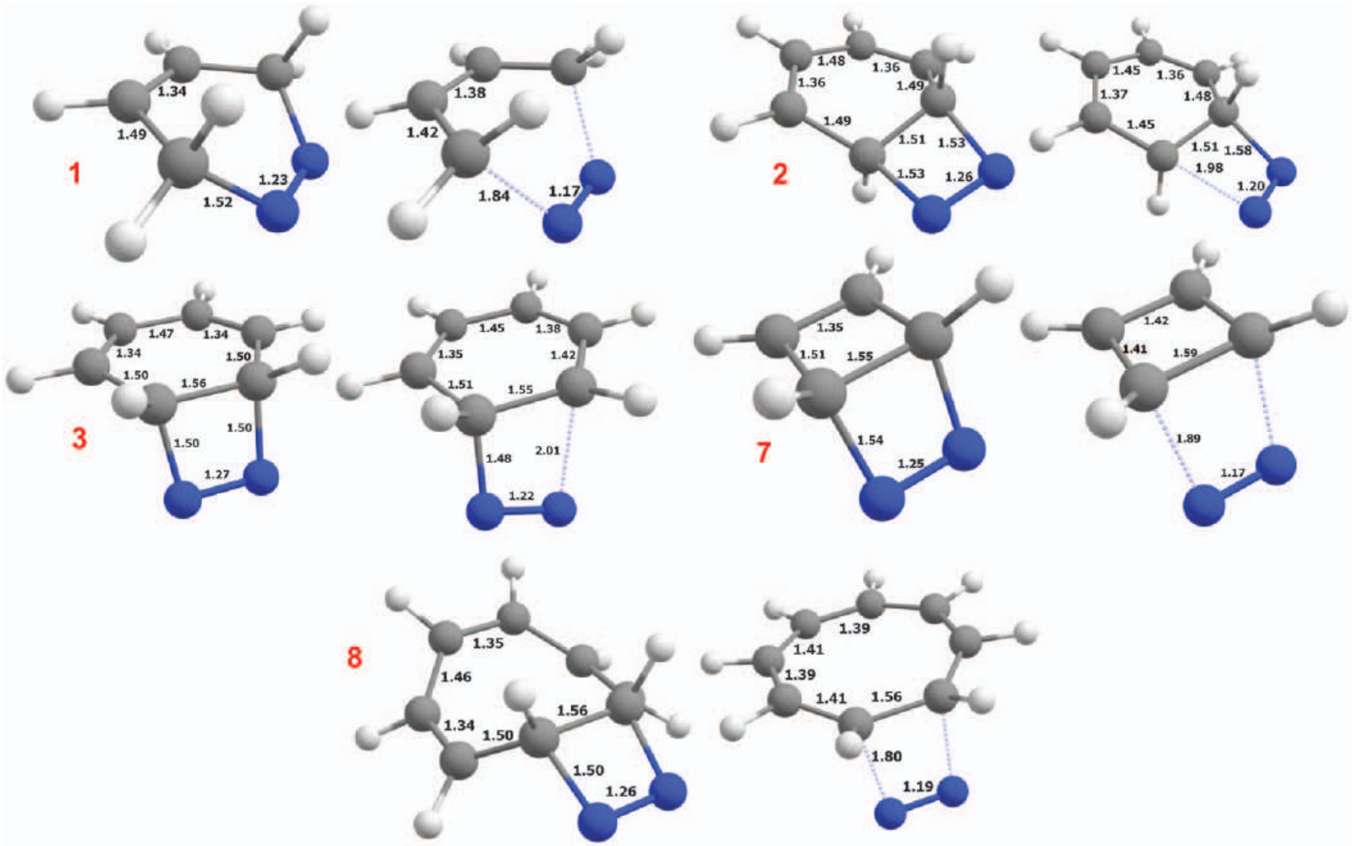

Figure 2.5 Reactant and transition state geometries for selected cycloreversion reactions.

broken helps to maintain the orbitals fully occupied in synchronous reactions. As can be seen in the cases of benzene formation from a *cis*-diazenediyl group (reaction **3**) compared to a strained *trans* system (reaction **2**), the open or closed-shell nature of the path is connected with Woodward–Hoffmann rules and the antara or suprafacial mechanisms (we leave to organic chemists the analysis of this reactivity pattern). What we must emphasize here is that for this type of reaction a study of the stability of the wave function is a must, or we can fail in finding the proper decomposition pathway. Unrestricted DFT might lower the accuracy, since we require, in principle, a real multireference method. However, while unrestricted DFT has some unphysical artefacts (such as huge spin contamination and unrealistic α–β spin differences), the energies provided by this method are actually not that bad, especially if proper benchmarking was carried out.

We show here the results obtained with (u)B3LYP/6-31G(d), since this inexpensive functional-basis set combination actually provided excellent accuracies compared to experimental results in cryogenic noble gas matrices.[45] For comparison, M06, a more accurate functional compared to CCSD(T) benchmarks (that is, probably better compared to gas-phase reactions), provides slightly higher barriers with QMT rates larger by one, two or up to three orders of magnitude. As described before, these differences can also be seen in different experimental set-ups (Section 2.3.2), and therefore it is not an exclusive problem of theoreticians. For reference, we carried out all the QMT computations using Polyrate software,[42] Gaussian for the DFT computations,[43] and Gaussrate for communication between them.[87] For the SCT we used a small step of 0.001 and the quantized reactant state tunnelling (QRST) option.[88]

Table 2.1 and Figure 2.6 show the most relevant information for these eleven systems. Let us extract some conclusions from them.

Except for compound **4**, which has no minimum and decomposes with a barrierless reaction, at extremely low temperatures (below 10 K) all these molecules should be stable under a semi-classical mechanism (if they can be

Table 2.1 SCT rate constants (s^{-1}) and half-lives (s) at 4 K, transition state imaginary frequencies (cm^{-1}), threshold and reaction energies ($\Delta E^{\ddagger}$ and ΔE_{rx}, kJ mol^{-1}) for the deazatation decompositions of the eleven systems of Scheme 2.8.

Compound	$\Delta E^{\ddagger}$	ΔE_{rx}	ν	k	$t_{\frac{1}{2}}$
1	36.2	−131.3	524	0.02	32
2	41.8	−482.0	413	3×10^{-9}	2×10^{8}
3	85.3	−378.0	858	5×10^{-13}	1×10^{12}
4	Unstable				
5	52.5	−432.1	899	2	0.4
6	7.8	−232.9	398	6×10^{9}	1×10^{-10}
7	44.7	−63.7	547	2×10^{-4}	4×10^{3}
8	54.0	−233.0	719	2×10^{-49}	3×10^{48}
9	76.4	−26.6	475	3×10^{-30}	2×10^{29}
10	95.8	−234.0	621	1×10^{-21}	7×10^{20}
11	72.1	−571.3	477	3×10^{-25}	3×10^{24}

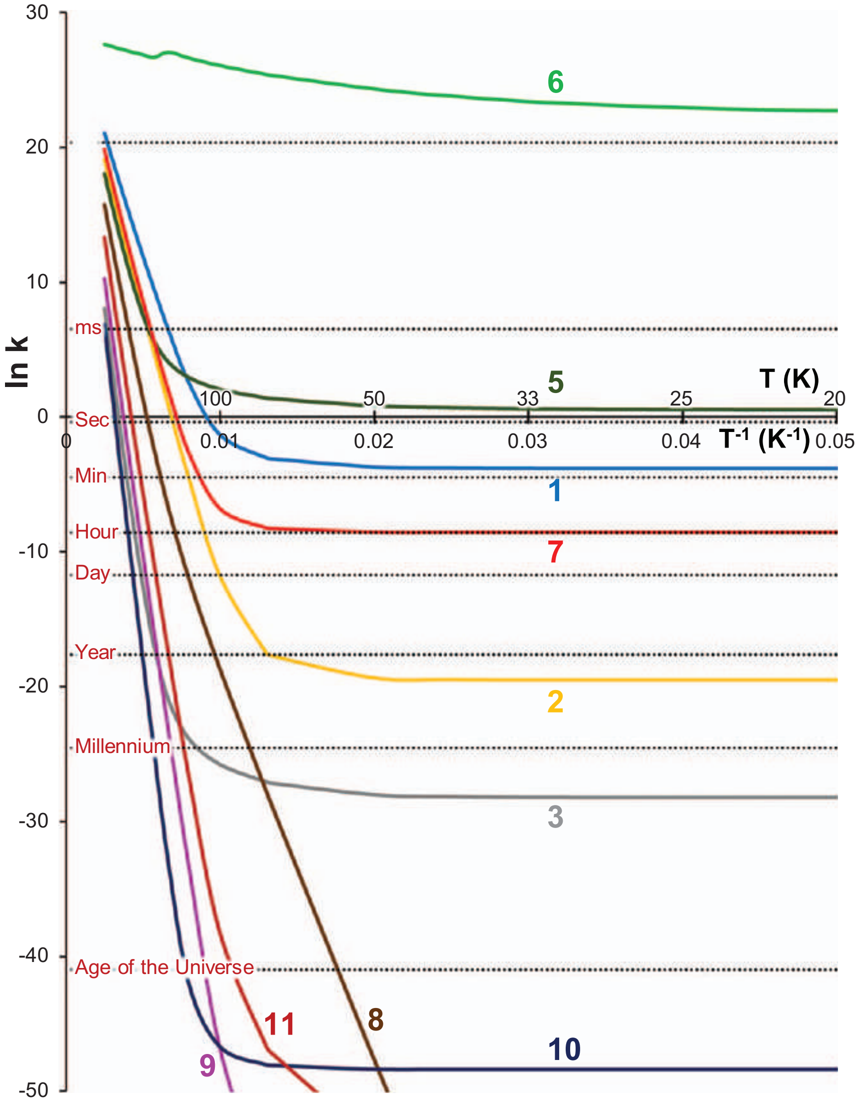

Figure 2.6 Arrhenius plot of the QMT included decomposition rates of the eleven systems of Scheme 2.8. Horizontal dotted lines show, for reference, selected half-lives.

synthesized in the first place). However, compounds **6**, **5** and **1** will decompose even approaching absolute zero due to heavy atom QTI from the ground vibrational state ($t_{\frac{1}{2}}$ of the order of nanoseconds, seconds and minutes, respectively). **7** would be stable for around an hour, and therefore an extremely fast and efficient organic chemist might still detect it by some spectroscopic method.[29] As explained before, these predictions are extremely sensitive to the method, so they must be taken with some sensible scepticism; remember that semi-accurate rate results require highly accurate computational work.

The correlation between the activation energy and the logarithm of the QMT rate for this series of deazatation reactions is very weak ($R^2 \approx 0.3$), a fact that emphasizes the importance of the barrier width and shape. However, if we take out reaction **8**, a clear outlier with a huge movement of the ring (going from a "tub-shaped" to planar geometries and back, see Figure 2.5), R^2 grows to ≈ 0.7, indicating that knowing the activation energy can still provide a hint on the likelihood of having QMT. Yet, since each reaction has its particularities, it might be very tricky to make *a priori* rate estimations. Or as Sherlock Holmes said, "*It is a capital mistake to theorize before you have all the evidence. It biases the judgment*."

2.5 Final Words

Beyond a couple of ground-breaking exemplars,[31,57,89] heavy-atom tunnelling is undoubtedly a 21st century phenomenon.[10,11] In this context it is understandable that the concept of quantum tunnelling instability has not been thoroughly considered. But in this day and age we have the insight to discern which unknown molecules might have the potential to rupture by a QTI mechanism, and, more importantly, we have the computational tools to predict their lifetime. This information is invaluable for those seeking to synthesize unusual and exceptional molecules. Clearly most hypothetical molecules that live only on paper but comply with Lewis structures would exist if taken to low enough temperatures. However, it would be a serious misuse of resources to hunt for those particular systems where nuclear quantum effects give a pathway to their decomposition.

In this chapter we have discussed several hypothetical organic molecules that, under current capabilities, will be impossible to detect or synthesize. We analyzed the characteristics that such molecules must have to react in a QTI manner, some methodologies to compute their rates, and we debated on the validity of such computations and predictions. In this sense, this chapter was partly a review, a road map, and a manual to understand heavy-atom tunnelling. In addition, as an exercise, we managed to include some new results within the family of pericyclic reactions that provide a general overview of the topic.

One can only wonder how many other fleeting systems have been theoretically predicted but will not pass the tunnelling test. Or, quoting the title of the essay of Hoffmann, Schleyer and Schaeffer,[7] we may say: "*Predicting Molecules—More Realism, Please!*"

Abbreviations

CVT	Canonical variational transition state theory
DFT	Density functional theory
KIE	Kinetic isotope effect
MEP	Minimum energy pathway

PES	Potential energy surface
QMT	Quantum mechanical tunnelling
QTI	Quantum tunnelling instability
SCT	Small curvature tunnelling
TST	Transition state theory
ZPE	Zero-point energy

References

1. R. Hoffmann and H. Hopf, *Angew. Chem., Int. Ed.*, 2008, **47**, 4474–4481.
2. *Molecular Aesthetics*, ed. P. Weibel, L. Fruk and Zentrum für Kunst und Medientechnologie Karlsruhe, MIT Press, Cambridge, MA, 2013.
3. A. J. Bard, G. M. Whitesides, R. N. Zare and F. W. McLafferty, *Acc. Chem. Res.*, 1995, **28**, 91.
4. C. J. Burrows, *Acc. Chem. Res.*, 2017, **50**, 445.
5. C. Poree and F. Schoenebeck, *Acc. Chem. Res.*, 2017, **50**, 605–608.
6. E. G. Lewars, *Modeling Marvels: Computational Anticipation of Novel Molecules*, Springer Netherlands, 2008.
7. R. Hoffmann, P. V. R. Schleyer and H. F. Schaefer, *Angew. Chem., Int. Ed.*, 2008, **47**, 7164–7167.
8. A. Meijere and S. Blechert, *Strain and Its Implications in Organic Chemistry: Organic Stress and Reactivity*, Springer Netherlands, Dordrecht, 1989.
9. H. Amlani, MSc Thesis, Ben-Gurion University of the Negev, 2019.
10. W. T. Borden, *WIREs Comput. Mol. Sci.*, 2015, **6**, 20–46.
11. C. Castro and W. L. Karney, *Angew. Chem., Int. Ed.*, 2020, **59**, 8355–8366.
12. The Chemical Record – Record of Records, http://onlinelibrary.wiley.com/journal/10.1002/(ISSN)1528-0691/homepage/records/index.html.
13. G. Martínez-Guajardo, K. J. Donald, B. K. Wittmaack, M. A. Vazquez and G. Merino, *Org. Lett.*, 2010, **12**, 4058–4061.
14. R. A. Pascal, *Eur. J. Org. Chem.*, 2004, **2004**, 3763–3771.
15. S. Kozuch, *Org. Lett.*, 2014, **16**, 4102–4105.
16. G. Markopoulos and J. Grunenberg, *Angew. Chem., Int. Ed.*, 2013, **52**, 10648–10651.
17. E. M. Greer, K. Kwon, A. Greer and C. Doubleday, *Tetrahedron*, 2016, **72**, 7357–7373.
18. C. Doubleday, R. Armas, D. Walker, C. V. Cosgriff and E. M. Greer, *Angew. Chem., Int. Ed.*, 2017, **56**, 13099–13102.
19. J.-L. Chen and W.-P. Hu, *J. Am. Chem. Soc.*, 2011, **133**, 16045–16053.
20. E. Solel and S. Kozuch, *J. Org. Chem.*, 2018, **83**, 10826–10834.
21. S. Kozuch, *Phys. Chem. Chem. Phys.*, 2014, **16**, 7718–7727.
22. B. C. Garrett and D. G. Truhlar, *J. Chem. Phys.*, 1983, **79**, 4931.
23. A. Fernandez-Ramos, B. A. Ellingson, B. C. Garrett and D. G. Truhlar, in *Reviews in Computational Chemistry*, ed. K. B. Lipkowitz and T. R. Cundari, John Wiley & Sons, Inc., Hoboken, NJ, USA, vol. 3, 2007, pp. 125–232.

24. V. Zaverkin and J. Kästner, in *Tunnelling in Molecules*, ed. J. Kästner and S. Kozuch, Royal Society of Chemistry, Cambridge, 2020.
25. P. R. Schreiner, J. P. Wagner, H. P. Reisenauer, D. Gerbig, D. Ley, J. Sarka, A. G. Császár, A. Vaughn and W. D. Allen, *J. Am. Chem. Soc.*, 2015, **137**, 7828–7834.
26. R. P. Bell, *The Tunnelling Effect in Chemistry*, Chapman and Hall, London, 1980.
27. J. Manz, A. Schild, B. Schmidt and Y. Yang, *Chem. Phys.*, 2014, **442**, 9–17.
28. M. Razavy, *Quantum Theory of Tunnelling*, World Scientific, River Edge, NJ, 2003.
29. C. M. Nunes, I. Reva and R. Fausto, in *Tunnelling in Molecules*, ed. J. Kästner and S. Kozuch, Royal Society of Chemistry, Cambridge, 2020.
30. A. Nandi, A. Sucher and S. Kozuch, *Chem. – Eur. J.*, 2018, **24**, 16348–16355.
31. B. K. Carpenter, *J. Am. Chem. Soc.*, 1983, **105**, 1700–1701.
32. C. M. Nunes, I. Reva, S. Kozuch, R. J. McMahon and R. Fausto, *J. Am. Chem. Soc.*, 2017, **139**, 17649–17659.
33. H. Quanz and P. R. Schreiner, *J. Comput. Chem.*, 2019, **40**, 543–547.
34. J. Basran, S. Patel, M. J. Sutcliffe and N. S. Scrutton, *J. Biol. Chem.*, 2001, **276**, 6234–6242.
35. R. P. Bell, *J. Chem. Soc., Faraday Trans.*, 1959, **55**, 1.
36. R. T. Skodje and D. G. Truhlar, *J. Phys. Chem.*, 1981, **85**, 624–628.
37. E. C. Sherer and C. J. Cramer, *Organometallics*, 2003, **22**, 1682–1689.
38. J. T. Fermann and S. Auerbach, *J. Chem. Phys.*, 2000, **112**, 6787–6794.
39. J. Lucas Bao and D. G. Truhlar, *Chem. Soc. Rev.*, 2017, **46**, 7548–7596.
40. D. G. Truhlar and B. C. Garrett, *Annu. Rev. Phys. Chem.*, 1984, **35**, 159–189.
41. B. Sirjean, E. Dames, H. Wang and W. Tsang, *J. Phys. Chem. A*, 2012, **116**, 319–332.
42. J. Zheng, J. L. Bao, R. Meana-Pañeda, S. Zhang, B. J. Lynch, J. C. Corchado, Y.-Y. Chuang, P. L. Fast, W.-P. Hu, Y.-P. Liu, G. C. Lynch, K. A. Nguyen, C. F. Jackels, A. Fernandez Ramos, B. A. Ellingson, V. S. Melissas, J. Villà, I. Rossi, E. L. Coitiño, J. Pu, T. V. Albu, A. Ratkiewicz, R. Steckler, B. C. Garrett, A. D. Isaacson and D. G. Truhlar, *POLYRATE 17*.
43. M. J. Frisch, G. W. Trucks, H. B. Schlegel, G. E. Scuseria, M. A. Robb, J. R. Cheeseman, G. Scalmani, V. Barone, B. Mennucci, G. A. Petersson, H. Nakatsuji, M. Caricato, X. Li, H. P. Hratchian, A. F. Izmaylov, J. Bloino, G. Zheng, J. L. Sonnenberg, M. Hada, M. Ehara, K. Toyota, R. Fukuda, J. Hasegawa, M. Ishida, T. Nakajima, Y. Honda, O. Kitao, H. Nakai, T. Vreven, J. A. Montgomery Jr., J. E. Peralta, F. Ogliaro, M. Bearpark, J. J. Heyd, E. Brothers, K. N. Kudin, V. N. Staroverov, R. Kobayashi, J. Normand, K. Raghavachari, A. Rendell, J. C. Burant, S. S. Iyengar, J. Tomasi, M. Cossi, N. Rega, J. M. Millam, M. Klene, J. E. Knox, J. B. Cross, V. Bakken, C. Adamo, J. Jaramillo, R. Gomperts, R. E. Stratmann, O. Yazyev, A. J. Austin, R. Cammi, C. Pomelli, J. W. Ochterski, R. L. Martin, K. Morokuma, V. G. Zakrzewski, G. A. Voth, P. Salvador, J. J. Dannenberg, S. Dapprich, A. D. Daniels, Ö. Farkas,

J. B. Foresman, J. V. Ortiz, J. Cioslowski and D. J. Fox, *Gaussian16 Revision A.03*.
44. S. Kozuch, *Phys. Chem. Chem. Phys.*, 2015, **17**, 16688–16691.
45. A. Nandi, D. Gerbig, P. R. Schreiner, W. T. Borden and S. Kozuch, *J. Am. Chem. Soc.*, 2017, **139**, 9097–9099.
46. S. Kozuch, *J. Chem. Theory Comput.*, 2015, **11**, 3089–3095.
47. K. R. Popper, *The Logic of Scientific Discovery*, Routledge, London, 2009th edn, 1935.
48. C. Riplinger and F. Neese, *J. Chem. Phys.*, 2013, **138**, 034106.
49. F. Neese, *WIREs Comput. Mol. Sci.*, 2012, **2**, 73–78.
50. J. Meisner and J. Kästner, *J. Chem. Theory Comput.*, 2018, **14**, 1865–1872.
51. B. Mennucci, *WIREs Comput. Mol. Sci.*, 2012, **2**, 386–404.
52. A. K. Eckhardt, D. Gerbig and P. R. Schreiner, *J. Phys. Chem. A*, 2018, **122**, 1488–1495.
53. J. Jankunas and A. Osterwalder, *Annu. Rev. Phys. Chem.*, 2015, **66**, 241–262.
54. M. Y. Choi, G. E. Douberly, T. M. Falconer, W. K. Lewis, C. M. Lindsay, J. M. Merritt, P. L. Stiles and R. E. Miller, *Int. Rev. Phys. Chem.*, 2006, **25**, 15–75.
55. M. Abe, *Chem. Rev.*, 2013, **113**, 7011–7088.
56. G. Kaupp, *J. Mol. Struct.*, 2006, **786**, 140–156.
57. S. L. Buchwalter and G. L. Closs, *J. Am. Chem. Soc.*, 1975, **97**, 3857–3858.
58. P. L. W. Tregenna-Piggott, C. J. Noble and M. J. Riley, in *Vibronic Interactions and the Jahn-Teller Effect*, Springer Netherlands, 2012.
59. P. S. Zuev, R. S. Sheridan, T. V. Albu, D. G. Truhlar, D. A. Hrovat and W. T. Borden, *Science*, 2003, **299**, 867–870.
60. R. A. Moss, R. R. Sauers, R. S. Sheridan, J. Tian and P. S. Zuev, *J. Am. Chem. Soc.*, 2004, **126**, 10196–10197.
61. S. Kozuch, X. Zhang, D. A. Hrovat and W. T. Borden, *J. Am. Chem. Soc.*, 2013, **135**, 17274–17277.
62. P. R. Schreiner, H. P. Reisenauer, D. Ley, D. Gerbig, C.-H. Wu and W. D. Allen, *Science*, 2011, **332**, 1300–1303.
63. A. G. Császár and C. Fábri, in *Tunnelling in Molecules*, ed. J. Kästner and S. Kozuch, Royal Society of Chemistry, Cambridge, 2020.
64. D. Gerbig, D. Ley and P. R. Schreiner, *Org. Lett.*, 2011, **13**, 3526–3529.
65. R. Hoffmann, *Am. Sci.*, 2004, **92**, 23–26.
66. D. Theis, J. Ivanic, T. L. Windus and K. Ruedenberg, *J. Chem. Phys.*, 2016, **144**, 104304.
67. Z.-W. Qu, H. Zhu and R. Schinke, *J. Chem. Phys.*, 2005, **123**, 204324.
68. R. Siebert and R. Schinke, *J. Chem. Phys.*, 2003, **119**, 3092–3097.
69. A. Nandi and S. Kozuch, *Chem. – Eur. J.*, 2019, **26**, 759–772.
70. R. Plass, K. Egan, C. Collazo-Davila, D. Grozea, E. Landree, L. D. Marks and M. Gajdardziska-Josifovska, *Phys. Rev. Lett.*, 1998, **81**, 4891–4894.
71. B. Flemmig, P. T. Wolczanski and R. Hoffmann, *J. Am. Chem. Soc.*, 2005, **127**, 1278–1285.

72. W. C. McKee, J. Agarwal, H. F. Schaefer and P. V. R. Schleyer, *Angew. Chem., Int. Ed.*, 2014, **53**, 7875–7878.
73. D. Ley, D. Gerbig and P. R. Schreiner, *Org. Biomol. Chem.*, 2012, **10**, 3781.
74. IUPAC Gold Book., http://goldbook.iupac.org.
75. F. A. Carroll, *Perspectives on Structure and Mechanism in Organic Chemistry*, John Wiley & Sons, 2011.
76. I. Fleming, *Molecular Orbitals and Organic Chemical Reactions*, John Wiley & Sons, 2011.
77. S. Kozuch, *RSC Adv.*, 2014, **4**, 21650–21656.
78. T. Bredtmann and J. Manz, *Angew. Chem., Int. Ed.*, 2011, **50**, 12652–12654.
79. D. W. Whitman and B. K. Carpenter, *J. Am. Chem. Soc.*, 1982, **104**, 6473–6474.
80. T. Schleif, J. Mieres-Perez, S. Henkel, M. Ertelt, W. T. Borden and W. Sander, *Angew. Chem., Int. Ed.*, 2017, **56**, 10746–10749.
81. H. Inui, K. Sawada, S. Oishi, K. Ushida and R. J. McMahon, *J. Am. Chem. Soc.*, 2013, **135**, 10246–10249.
82. C. M. Nunes, A. K. Eckhardt, I. Reva, R. Fausto and P. R. Schreiner, *J. Am. Chem. Soc.*, 2019, **141**, 14340–14348.
83. C. S. Michel, P. P. Lampkin, J. Z. Shezaf, J. F. Moll, C. Castro and W. L. Karney, *J. Am. Chem. Soc.*, 2019, **141**, 5286–5293.
84. S. Kozuch, A. Nandi and E. Solel, *Chem. – Eur. J.*, 2020, **26**, 625–628.
85. B. Chen, M. E. Scott, B. A. Adams, D. A. Hrovat, W. T. Borden and M. Lautens, *Org. Lett.*, 2014, **16**, 3930–3933.
86. M. E. Scott, Y. Bethuel and M. Lautens, *J. Am. Chem. Soc.*, 2007, **129**, 1482–1483.
87. J. Zheng, J. L. Bao, S. Zhang, J. C. Corchado, R. Meana-Pañeda, Y.-Y. Chuang, E. L. Coitiño, B. A. Ellingson and D. G. Truhlar, *GAUSSRATE 2017-B*.
88. J. G. Lauderdale and D. G. Truhlar, *Surf. Sci.*, 1985, **164**, 558–588.
89. I. B. Bersuker, *Coord. Chem. Rev.*, 1975, **14**, 357–412.

CHAPTER 3

Proton Tunnelling and Proton-coupled Electron Transfer in Biological Systems: Theory and Experimental Analysis

PAUL M. CHAMPION* AND ABDELKRIM BENABBAS

Department of Physics and Center for Interdisciplinary Research on Complex Systems, Northeastern University, Boston, Massachusetts 02115, USA
*Email: champ@neu.edu

3.1 Introduction

Proteins are key elements in nearly all biological systems and the transport of electrons and protons within the protein environment is both ubiquitous and fundamental to biological function. The measurement and analysis of electron and proton transfer rates can pose unique challenges to experimentalists, particularly when the rates are governed by tunnelling processes.[1–23] Because of the many degrees of freedom and timescales associated with protein motions, a precise theoretical analysis can become quite complicated. The large size of protein macromolecules, along with their (sometimes slowly) interconverting conformational sub-states, make a full quantum chemical calculation intractable, particularly in enzyme systems where a wide range of protein conformations is often associated with substrate binding and release. This situation can

Theoretical and Computational Chemistry Series No. 18
Tunnelling in Molecules: Nuclear Quantum Effects from Bio to Physical Chemistry
Edited by Johannes Kästner and Sebastian Kozuch

Published by the Royal Society of Chemistry, www.rsc.org

be approached theoretically with modern computational techniques that span regions governed primarily by classical dynamics and interface with the regime undergoing the quantum mechanical (QM) tunnelling reaction.[24–30] Within this context, there have been various theoretical developments over the years that include path integral approaches and empirical valence bond potentials (EVB) used to probe the role of nuclear quantum effects,[31–34] multidimensional tunnelling,[35,36] variational transition state theory,[37,38] approximate quantum trajectories,[39,40] wave packet dynamics on dynamic hybrid density functional theory potentials,[41] and ring polymer molecular dynamics[42] to name a few. However, a complete review of this extensive literature reaches far beyond the scope of this chapter, which is focused on simple analytical models that may be of use to experimentalists.

Generally, there are many variables and interactions embedded within these more theoretically complete models and the computations can sometimes be quite time consuming, creating an obstacle to experimentalists who often want a simple and straightforward method for analyzing and characterizing their experimental data. Thus, it is useful to have relatively simple analytical expressions at hand that can sequester some of the fundamental aspects of proton tunnelling into a minimal set of parameters that can be used for comparison with experiments as well as with the more elaborate theoretical approaches.

Building on past work,[14–18,22,43–52] the intent of this chapter is to outline some useful analytical approaches, as well as a few of the associated pitfalls, which may prove helpful to experimentalists when analyzing proton (and proton-coupled electron) tunnelling kinetics. Two prototypical examples will be emphasized, both of which can be treated using a "golden rule" type of analysis in what is sometimes referred to as the vibronically non-adiabatic regime.[52] Within this regime, the two fundamentally different situations that will be examined are the electronically non-adiabatic and the electronically adiabatic limits. For these two limits, the electronic response time is either slow or fast, respectively, relative to the proton tunnelling process.[18,50,53] For the electronically non-adiabatic case, the off-diagonal coupling between the reactant (R) and product (P) electron–proton vibronic states involves a (usually very small) vibronic coupling, which is defined as the product of the Franck–Condon overlap for the reactant and product proton vibrational wavefunctions and an electronic matrix element, V_{RP}, that couples R and P.

In contrast, for proton tunnelling in the electronically adiabatic limit, the off-diagonal coupling involves the splitting of the symmetric and antisymmetric proton vibrational wavefunctions within a single double well electronic potential energy surface. This "tunnel splitting" is also usually much less than $k_{\mathrm{B}}T$ ($k_{\mathrm{B}}T_0 \cong 200\ \mathrm{cm}^{-1}$ for $T_0 = 298$ K), so long as the proton energy levels are located well below the barrier between the two potential wells (this is the so-called "deep tunnelling" regime). The golden rule expressions can be used with reasonable confidence in both the electronically non-adiabatic and adiabatic cases so long as these off-diagonal vibronic coupling terms remain small (*i.e.*, weak coupling $\lesssim k_{\mathrm{B}}T$). However, for the electronically adiabatic case there is, in principle, the possibility that the heavy donor (D) and acceptor (A) atoms are so tightly compressed that the barrier between the reactant and product states is lowered and the tunnel splitting starts to approach or exceed k_BT. This strong coupling regime is referred to as the adiabatic proton transfer limit[16,45] and, under this condition, the golden rule no longer applies. We will briefly discuss the adiabatic proton transfer limit in Section 3.3.3.2 in the context of anharmonic donor–acceptor potentials and the external forces between the donor and acceptor atoms that help to facilitate proton-tunnelling-based catalysis in enzymes.

In Section 3.2, we will present some of the basic concepts and define the various classical and quantum subsystems and timescale separations that are used to reduce the tunnelling rate expressions into a tractable analytical form. We emphasize the importance of analyzing and predicting rates on an absolute scale using either the quantum or the classical model for the D–A motions. A discussion of the normal modes comprising the donor and acceptor subsystem is presented in Section 3.2.4, along with methods to properly assign an effective reduced mass and frequency to the D–A oscillator. To do this, we present a specific example, using the well-structured green fluorescent protein (GFP) and show how the low-frequency spectral density that contributes to the relative donor–acceptor motion, which is of crucial importance in vibrationally assisted tunnelling reactions, can be captured using an Einstein oscillator model. In Section 3.2.5, we also consider the experimentally observed rate in the context of enzyme conformational interconversions that may be occurring on timescales that compete with the inherent tunnelling rate.

In Section 3.3, the electronically non-adiabatic proton tunnelling and proton coupled electron transfer rate expressions are discussed for the fully quantized, and Duschinsky mixed, sub-system composed of the D–A and the light atom (H or D) oscillators. These exact expressions can then be compared to the results obtained using the Born–Oppenheimer approximation that separates the heavy and light atom motions (an approximation that is also needed for the electronically adiabatic treatment in Section 3.4). A model that applies near room temperature, where the D–A oscillator is treated classically, is also presented. In addition, the often used[13–16,18,22,43,45,49,52,54–57] "linear approximation" for the exponential coupling of the D–A distance to the tunnelling rate (initially presented in Section 3.2.4.3) is further scrutinized and corrective action is recommended for enzymes and proteins,[58,59] which tend to have relatively broad, rather than highly constrained,[60] D–A distance distributions. The effect of using anharmonic potentials for the D–A and light atom oscillators is also discussed in the context of both the absolute rate calculations and the kinetic isotope effect (KIE) analysis. Finally, calculations of the KIE and its temperature dependence are applied to proton-coupled electron transfer (PCET) in the enzyme system soybean lipoxygenase (SLO). In order to account for the experimental measurements, we find that a ∼1 nN electrostatic force, which is much stronger than realistic protein conformational forces, must act to reduce the D–A tunnelling distance below the expected van der Waals limit.

In Section 3.4, we turn to the case of electronically adiabatic deep proton tunnelling in the well-structured green fluorescent protein (GFP) where the measurement and calculation of absolute proton and deuteron tunnelling rates are exploited to derive a set of theoretical parameters that are subject to confirmation and constraint by independent measurements or analysis. The only truly unconstrained (or truly free) parameter is the reaction barrier along the environmental coordinate, which is dependent upon the charge transport ''reorganization energy'' and the free energy of the reaction.

Overall, this chapter will examine some of the main issues that are important to address when developing suitable expressions for the analysis of biological proton tunnelling experiments. These include the appropriate use of electronically adiabatic or electronically non-adiabatic limits, as well as role of harmonic and/or anharmonic approximations to the D–A and the proton coordinate motion. The issue of quantum *vs.* classical treatment of the D–A coordinate, which depends on both the temperature and the D–A oscillator frequency, will also be explored. We note that, for the case of softer anharmonic D–A potentials, which are associated with conformationally flexible enzymes, the classical approach should suffice for experiments near room temperature. A simple Morse approximation to the anharmonic D–A potential allows for both a ''hard'' potential that includes van der Waals repulsion at short D–A distance as well as a ''softer'' potential at longer distances that recognizes the very weak hydrogen bonding that is typically present (often involving a CH···O interaction) in enzyme systems. In addition, the local electric field, associated with the enzyme active-site, and its interaction with (or polarization of) the substrate, is also considered. The resulting D–A compressive force needs to be included in the model expressions in order to explain how an enzyme overcomes the van der Waals repulsion energy between the donor and acceptor atoms. Such effects are necessary in order to account for the measured tunnelling-based catalytic rates in SLO as well as their isotope dependence. It turns out that the magnitude of these electric field forces can be deduced using a relatively simple analytic approach.

Finally, we note that, based on experimental measurements, the inherent proton tunnelling rates for both the ''proton wire'' of GFP and the PCET enzymatic reaction of SLO turn out to be surprisingly rapid and fall in the sub-nanosecond or nanosecond regime. In enzyme reactions, the observed catalytic rate involves conformational interconversion processes.[61] These processes can compete with, and sometimes partially obscure, the underlying tunnelling reaction. The probability for finding the tunnelling active conformation (which is found to be very small for SLO) can also be estimated when the theoretical model is required to account for the absolute rate along with ''relative'' observables such as the KIE and its temperature dependence. In contrast to enzymes, the well-structured proton wire in the GFP system does not involve a conformational selection process and this allows its room-temperature tunnelling time constant of ~400 ps to be directly revealed. The rapid room-temperature tunnelling rates, found for both the prototypical proton ''wire'' in GFP and for the SLO enzyme system, suggest that proton tunnelling may be a more ubiquitous and essential transport process in biology than is currently assumed.

3.2 Basic Rate Expressions and Time Scale Separations

3.2.1 Time Scale Separations

As noted in the introduction, the analytical approaches presented here are limited to the conditions under which the golden rule (GR) rate expression is applicable. For most analytical models there are simplifications that involve sequestering (or factoring) our lack of detailed knowledge into separate sub-systems where vibrational and/or conformational motions take place on very different timescales. For proton tunnelling in proteins, there are four basic sub-systems that will be considered here: (1) the high-frequency (and always quantized) vibrational motion of the tunnel particle (ω_{L} with $L = \mathrm{H}$ or D), which typically falls in the 2800–3600 cm^{-1} region for OH and CH bonds (and is lowered by deuteron substitution); (2) the somewhat lower frequency ($\tilde{\nu}_{\mathrm{DA}} = \omega_{\mathrm{DA}}/2\pi c \sim 200$–$300\ \mathrm{cm}^{-1}$) "heavy" atom D–A motions, where D and A are typically hydrogen bonded oxygen and/or carbon atoms; (3) the low-frequency motions of the surrounding environment (ω_s), which are defined to include the protein residue fluctuations and solvent reorientations that are separable from the tunnel particle and D–A subsystems and which "reorganize" to accommodate the altered charge distribution of the product state; and (4) the very slow protein conformational interconversions that can affect the *equilibrium position* of the D–A subsystem, as opposed to the much faster timescale D–A vibrations that occur relative to a specific equilibrium position associated with a given protein conformation.

3.2.2 Rate Expression for Electronically Adiabatic and Vibrationally Non-adiabatic Proton Transfer with a Fixed Donor–Acceptor Distance

For simplicity, this section considers that proton tunnelling occurs between the zero-point energy levels of a single one-dimensional (1D) double well potential energy surface along a proton coordinate with a fixed D–A distance and a constant tunnelling distance, ℓ. (Note: the reader is referred to the appendix for a table of parameter definitions that may be helpful for interpretation of the various formulas and equations that appear throughout the text.) For the electronically adiabatic (A) and vibrationally non-adiabatic case, the off-diagonal coupling depends only on the energy splitting, $\Delta_0(\ell)$, between the symmetric and anti-symmetric proton vibrational wave-functions at the transition state. The rate, k_ℓ^A, for tunnelling distance, ℓ, can then be written as:[15,59]

$$k_\ell^A = \frac{2\pi}{\hbar}\left|\frac{\Delta_0(\ell)}{2}\right|^2 \frac{1}{\hbar\omega_s}\frac{\hbar\omega_s}{\sqrt{4\pi\lambda_s k_{\mathrm{B}}T}}\exp\left[-\frac{\Delta G_s^{\ddagger}}{k_{\mathrm{B}}T}\right] \tag{3.1}$$

where the role of the surrounding environment is treated semi-classically in an Einstein approximation[62–64] using a generalized reaction coordinate,

q_s, with frequency $\omega_s \ll k_B T/\hbar$. The thermalized Franck–Condon factor associated with the R to P transition for the environmental mode includes a factor of $\hbar\omega_s$ that cancels the density-of-states in eqn (3.1). This frequency is also related to the environmental reorganization energy, $\lambda_s = S_s\hbar\omega_s$, which depends on the Huang–Rhys factor, S_s, describing the linear coupling (reorganization) of the surrounding environment upon going from the reactant to the product state. The term $\Delta G_s^{\ddagger} = (\Delta G^0 + \lambda_s)^2/4\lambda_s$ includes the reaction free energy, ΔG^0, and quantifies the thermal energy along the environmental coordinate that is needed to bring the system to the transition state where the vibrational proton energy levels become degenerate. This environmental configuration is depicted by a red dot in Figure 3.1.

The generalization of eqn (3.1) to include the D–A vibrational motion will be discussed in Section 3.4.1. The very-low-frequency conformational interconversions of the protein environment can also couple to, and affect the equilibrium separation of, the important D–A sub-system. These slow interconversions and their effect on eqn (3.1) will be discussed in Section 3.2.5 in the context of the observed kinetic rate and the possibility of kinetic inhomogeneity within the ensemble. Finally, it is important to note that, because there is no electronic matrix element to evaluate for the electronically adiabatic case, the GR expression facilitates a direct comparison of the analytic theory with the experimentally determined absolute rates. This places an important additional constraint on the parameter space, which goes beyond the usual relative measurements that typically involve the kinetic isotope effect (KIE) and its temperature dependence.

3.2.3 Rate Expression for Electronically Non-adiabatic PCET with Fixed Donor–Acceptor Distance

PCET can occur sequentially or in a concerted fashion. In this chapter, we only consider concerted PCET in the electronically non-adiabatic (NA) limit. There are usually two clearly accessible electronic states in this case and, for biological systems, these states often correspond to electron relocation between reactant and product orbitals that are spatially separated from the proton tunnelling location, leading to a significant charge redistribution.[52,65] This type of PCET reaction is referred to as electron–proton transfer (EPT) in order to differentiate it from another common PCET reaction, hydrogen atom transfer (HAT), which has been shown to be an electronically adiabatic form of PCET.[52,65] Thus, for the non-adiabatic EPT reaction between a pair of zero-point proton (or deuteron) vibrational states, belonging to two distinct diabatic R and P electronic potential surfaces, we can write a simplified GR rate expression for a specific tunnel distance, ℓ:

$$k_\ell^{\mathrm{NA}} = \frac{2\pi|V_{\mathrm{RP}}|^2}{\hbar}\frac{|\langle 0_{\mathrm{DL}}|0_{\mathrm{AL}}\rangle|^2}{\sqrt{4\pi k_{\mathrm{B}} T\lambda_s}}\,\mathrm{e}^{-\frac{\Delta G_s^{\ddagger}}{k_{\mathrm{B}}T}} \tag{3.2}$$

where the off-diagonal vibronic (electronic + vibrational) coupling between reactant and product states has been separated using the Born–Oppenheimer

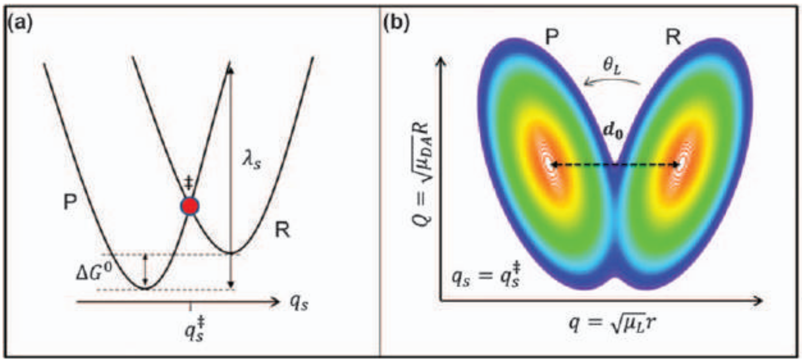

Figure 3.1 Coordinate system for the analytic factorized electronically adiabatic model used to fit the GFP kinetics data. Panel a depicts the environmental coordinate, q_s, which represents the surrounding protein. Panel b shows the two key quantum coordinates in mass-weighted space at the transition state configuration ($q_s = q_s^\ddagger$), where the reactant and product vibrational states are brought into degeneracy so that tunnelling can occur. The *x*-axis represents the mass-weighted tunnelling coordinate ($q = \sqrt{\mu_L}r$ with $L = \mathrm{H, D}$) and the *y*-axis represents the mass-weighted D–A coordinate ($Q = \sqrt{\mu_{DA}}R$) where μ represents the reduced mass. The normal modes of the reactant and product states are rotated relative to one another by a mass-dependent angle, $\theta_L \cong \sqrt{\mu_L / \mu_{DA}}$, and this Duschinsky mixing allows an exact solution for the thermally weighted Franck–Condon factor needed to describe the electronically non-adiabatic transition. The mass-weighted equilibrium tunnel distance is given by $d_0 = \sqrt{\mu_L}\ell_0$. Reproduced from ref. 71 with permission from Springer Nature, Copyright 2016.

approximation. The electronic coupling, V_{RP}, between R and P is exposed along with the one-dimensional Franck–Condon (FC) vibrational overlap, $\langle 0_{DL}|0_{AL}\rangle$, between the tunnel particle ($L = \mathrm{H}$ or D) zero-point wavefunctions in the donor and acceptor states. Here, for simplicity, we have chosen to consider only the zero-point vibrational states of the tunnel particle wave-function because the energy of the first vibrational excited state is much larger than k_BT_0. We note that there are certain circumstances, for highly exothermic or endothermic reactions, where the excited tunnel particle vibrational states must be considered;[15] however, these circumstances will not be treated here. For the more general case where the D–A motion is included and treated quantum mechanically, the vibrational overlap integral becomes two dimensional and involves a Duschinsky rotation of the D–A and tunnel particle modes.[59] This more complicated case will be discussed in Section 3.3.

For harmonic potentials separated by a tunnel distance ℓ, the one-dimensional overlap between the donor and acceptor tunnel particle wavefunctions can be written very simply as:

$$|\langle 0_{DL}|0_{AL}\rangle|^2 \equiv |\langle 0|0_\ell\rangle|^2 = \exp[-S_L], \quad \text{with} \quad S_L = \frac{\mu_L\omega_L}{2\hbar}\ell^2, \tag{3.3}$$

where μ_L is the reduced mass of the light particle oscillator involving mass m_L ($L = \mathrm{H}$ or D) and $\mu_L \cong m_L$. On the other hand, for anharmonic tunnel particle wave functions, described using back-to-back Morse oscillators of the form $V_R(r) = D_e[1 - \exp(-ar)]^2$ and $V_P(r) = D_e[1 - \exp(-a(\ell - r))]^2$, the Franck–Condon overlap factor is still tractable, but a bit more complicated:

$$\left|\langle 0|0\rangle_\ell\right|^2 = \frac{4(2\Lambda_L - 1)^2 (2\Lambda_L)^{2(2\Lambda_L - 1)}}{[\Gamma(2\Lambda_L)]^2} \left\{ \exp\left[-\frac{a\ell}{2}(2\Lambda_L - 1)\right] K_0\left((2\Lambda_L)\exp\left[-\frac{a\ell}{2}\right]\right)\right\}^2 \tag{3.4}$$

where $\Lambda_L = \frac{1}{a}\left(\frac{\sqrt{2\mu_L D_e}}{\hbar}\right) = \frac{2D_e}{\hbar\omega_L}$ and $K_\nu(z)$ is the modified Bessel function of the third kind.

In eqn (3.4), the value of D_e is typically set to 80 kcal mol^{-1}, which is the average value for the C–H and O–H bonds (77 kcal mol^{-1} and 82 kcal mol^{-1}, respectively). The proton vibration, $\omega_H/2\pi c$, is often set to 3200 cm^{-1}, which is the average oscillator frequency for C–H and O–H bonds (2900 cm^{-1} and 3500 cm^{-1}, respectively). Although this is a somewhat restrictive approximation, it is used in many analytical models. When more accuracy is desired, numerical methods can be used to evaluate the vibrational wave-function overlap. The above values of D_e and $\omega_H/2\pi c$ result in $a = 2.3$ Å^{-1}, which is typically used to treat tunnelling reactions in enzymes. More details regarding the anharmonic FC overlap can be found in S2 of ref. 58.

3.2.4 Basic Properties of the D–A Sub-system

3.2.4.1 Coordinate Space and Duschinsky Mixing

Because of its significance, we emphasize the properties of the D–A sub-system and give some explicit examples in this section. At lower temperatures the D–A mode must be treated quantum mechanically; however, near room temperature, it can sometimes be treated classically.[44,46,49,59] A good model for the D–A motion, when treated either quantum mechanically or classically, is crucial to the tunnelling rate calculation because thermal excitations (*i.e.*, thermal broadening of the D–A wave-function and/or a thermally driven classical D–A distance distribution) increase the probability of sampling shorter tunnelling paths between the initial- and final-state proton wave-functions. These shorter paths increase the tunnelling rate super-exponentially.

An important issue is the assumption that allows description of the D–A motion using a single "mode". The underlying assumption is analogous to the treatment of the environmental coordinate, where an Einstein oscillator approximation is also used.[62] In principle, there can be many internal protein vibrational modes, particularly within the mid-frequency range (~200–300 cm^{-1}). Several of these modes can couple to the D–A motion and can be involved in the thermal excitation that drives this key "oscillator". A specific example of this situation will be given below.

Although, in this work, we must hold to relatively simple potentials in order to maintain an analytic perspective, it should be emphasized that such potentials can only offer an approximation to parameterized potentials with improved accuracy that are able to more realistically reflect hydrogen bonded systems. Some examples include the Lippincott–Schroeder potential[66] and potentials based on empirical valence bond theory[67,68] as well as London–Eyring–Polanyi–Sato (LEPS) models[69] that have been widely used in gas phase and strongly hydrogen bonded systems. It is also possible to use quantum methods to characterize hydrogen bonded biological systems[70] and a simple example of such an approach will be given in Section 3.3.3.2.

In order to give more perspective to the simple factorized analytical model being treated here, we refer to Figure 3.1, which shows an electronically adiabatic potential surface involving the D–A and the tunnelling particle coordinates in panel (b). The two-dimensional (2D) double-well electronic ground-state surface is symmetrized at the red dot in panel (a), due to thermal motion along the classical environmental coordinate, q_s representing sub-system 3. This generalized environmental coordinate brings the proton levels of the reactant and product into degeneracy at a transition state ($q^{\ddagger}$) so that tunnelling can occur.[45] It is noteworthy that when a quantized D–A oscillator is used in the factorized treatment, there are many combinations of D–A vibrational states that can lead to proton level degeneracy[15] between the proton levels of R and P. Thus, the 2D QM treatment must average over all thermally occupied initial states (n) and sum over all final D–A vibrational states (m) in order to properly calculate all channels contributing to the rate. Because the tunnel splitting depends upon the D–A coordinates, it must be integrated over each pair of initial and final state wavefunctions, as discussed in Section 3.4.

The coordinates along the axes in panel (b) correspond to the symmetrized Cartesian and mass-weighted normal modes of a three-body system composed of the donor, acceptor, and the proton or deuteron. The upper-case coordinates (Q and R) are associated with the heavy-atom D–A motion and the lower-case coordinates (q and r) are associated with the light atom (tunnel particle) motion. The mass-weighted tunnel distance at the D–A equilibrium position is denoted by $d_0 = \sqrt{\mu_L}\ell_0$, where ℓ_0 is the actual equilibrium tunnel distance and the reduced mass μ_L is very close to the mass of the tunnel particle, m_L. Typically, $\ell_0 \sim 0.8$ Å for an OH···O hydrogen bonding situation. We also note that the tunnel distance, ℓ, and its equilibrium, ℓ_0, is directly related to the distance between the fluctuating and vibrating donor and acceptor atoms, R, by using a fixed average covalent bond length, $\bar{l}_c = \frac{l_{cD} + l_{cA}}{2}$, so that:

$$R = \ell + 2\bar{l}_c \tag{3.5a}$$

$$R_0 = \ell_0 + 2\bar{l}_c \tag{3.5b}$$

and $\bar{l}_c \cong 0.99$ Å for a typical pair of OH covalent bond lengths.

Because the Hessian matrix of the three-body system is mixed by off-diagonal terms, the potential surfaces in Figure 3.1b are rotated by an angle θ_L in going from the reactant to the product configuration. Such a coordinate rotation can be understood intuitively, based on eqn (3.5), because the tunnel distance becomes shorter as the D–A distance is compressed (*e.g.*, by moving to smaller Q in the figure the horizontal distance along the tunnelling coordinate between R and P is reduced). The rotation angle in the mass-weighted normal mode coordinate space can be shown to be generally dependent on the masses of the particles and the force constants between them (see ref. 59, supplement SI3, for more details). However, for reasonable choices of the force constant and mass parameters the expression for the rotation angle can be simplified and for a symmetric D–A system it is approximated by:

$$\tan\left(\frac{\theta_L}{2}\right) \cong \sqrt{\frac{m_L}{2M + m_L}} \quad \text{or for small angles,} \quad \theta_L \approx \sqrt{\frac{\mu_L}{\mu_{DA}}} \tag{3.6}$$

where m_L is the mass of the tunnel particle and M is the heavy-atom donor and acceptor mass (16 amu for oxygen). This expression allows direct calculation of the rotation angles associated with tunnelling of a proton or deuteron from the reactant to the product potential surface. For oxygen-based D–A systems we find:

$$\theta_H = 19.7^\circ \text{ and } \theta_D = 27.3^\circ \tag{3.7}$$

Because these angles fundamentally quantify the rotation (or Duschinsky mixing) of the harmonic normal modes upon moving from the reactant to the product potential energy surface, a time correlator approach allows exact calculation of the thermally averaged two-dimensional electronically non-adiabatic vibrational overlap integral needed for the tunnelling rate calculation. This will be discussed further in Section 3.3.1.1.

The exact expressions for the eigenfrequencies of a three-body system connected by three spring constants, along with a detailed normal mode analysis, which explicitly includes the hydrogen bonding force, can be found in the supplementary material (S3) of ref. 59. For now, we simply note that the D–A mode frequency, ω_{DA}, can be viewed in terms of an effective vibrational force constant when $M \gg m_L$ so that:

$$\omega_{DA}^2 = \frac{K_{vib}}{\mu_{DA}} = \frac{2K_{vib}}{M} \tag{3.8}$$

with

$$K_{vib} \cong \frac{k_1 k_{HB}}{k_1 + k_{HB}} + K_p \approx k_{HB} + K_p. \tag{3.9a}$$

K_{vib} acts as a single effective vibrational force constant that includes a sum of the H-bonding (k_{HB}) and protein (K_p) forces that act to constrain the relative vibrations of the donor and acceptor atoms (k_1 is the very large force constant associated with the high-frequency tunnel particle oscillator). In a classical limit for the D–A vibrational motion we can write the mean square displacement (MSD) as

$$\sigma^2_{\mathrm{DA}}(T) = \frac{k_{\mathrm{B}}T}{K_{\mathrm{vib}}} \quad \text{(classical)} \tag{3.9b}$$

3.2.4.2 Einstein Approximation for the D–A Mode Frequency

A more detailed approach for extracting the frequency and reduced mass of the D–A motion involves the use of an explicit Einstein oscillator approximation. As an example, we have considered[71] the situation in a well-structured protein (GFP), which has minimal conformational flexibility and is one of the most compact and stable proteins known.[72] It has a beta-barrel structure that contains an endogenous chromophore connected to a short proton transport chain composed of OH···O hydrogen-bonded oxygen atoms. These include a tyrosine associated with the chromophore, a water molecule, a serine and a glutamic acid residue.[73] Because there is very little protein flexibility, the H-bonded residues form a wire that has a stable structure, and the D–A motion is strongly influenced by what is sometimes called a "hydrogen bond stretching" vibration. However, because the various residues are intimately connected by the protein structure it is instructive to utilize a full protein normal mode analysis that is based on a hybrid ONIOM(QM/MM) approach.[74] The full normal mode analysis allows us to calculate a "power spectrum" for the mode-specific relative mean square displacements associated with each pair of donor–acceptor oxygen atoms in the GFP proton transport chain.[71] The supplementary discussion in reference[71] presents the details of the method for transforming the normal modes of a protein, each with frequency ω_α, into the thermally averaged mean square displacement along the unit vector ($\hat{u}_{ij}$) between a given pair of adjacent donor and acceptor atoms. The result for arbitrary donor (M_i) and acceptor (M_j) atom masses can be used to cast their thermally averaged relative motion into the form of a diatomic oscillator driven by the normal modes of the system:

$$\sigma^2_{\mathrm{Tot}(ij)} = \sum_\alpha \frac{\hbar}{2\mu_{ij}\omega_\alpha}(2\bar{n}_\alpha + 1)\left[\hat{u}_{ij}\cdot\left(M_i^{1/2}\vec{\boldsymbol{e}}_{i\alpha} - M_j^{1/2}\vec{\boldsymbol{e}}_{j\alpha}\right)\right]^2/(M_i + M_j) \tag{3.10}$$

where the thermal occupation number of each normal mode is $\bar{n}_\alpha(\omega_\alpha,T) = [\mathrm{e}^{\hbar\omega_\alpha/k_{\mathrm{B}}T} - 1]^{-1}$ and the diatomic reduced mass is given by $\mu_{ij} = \dfrac{M_iM_j}{M_i + M_j}$. The orthonormal character of the transformation matrix[75] between the normal modes and Cartesian displacements has the required property $\sum_\alpha \vec{\boldsymbol{e}}_{i\alpha}\vec{\boldsymbol{e}}_{j\alpha} = \overset{\leftrightarrow}{\mathrm{I}}\,\delta_{ij}$. When the donor and acceptor atoms have the same mass, as for GFP, where $M_i = M_j = 16$ amu, eqn (3.10) reduces to:

$$\sigma^2_{\mathrm{Tot}(ij)} = \sum_\alpha \frac{\hbar}{2\mu_{ij}\omega_\alpha}[2\bar{n}_\alpha + 1]\left[\hat{u}_{ij}\cdot\left(\vec{\boldsymbol{e}}_{i\alpha}/\sqrt{2} - \vec{\boldsymbol{e}}_{j\alpha}/\sqrt{2}\right)\right]^2 \equiv \sum_\alpha \sigma^2_\alpha(T), \tag{3.11}$$

which reveals the contributions to the relative MSD between atoms i and j from each of the 13 092 GFP normal modes[74] with frequency, ω_α. When $\sigma^2_\alpha(T_0)$ is plotted for each normal mode frequency, a "power spectrum" emerges that depicts the contributions to the total thermally averaged relative MSD for the chosen pair of D–A atoms [labelled as i and j in eqn (3.10) and (3.11)]. As shown in Figure 3.2, the average Einstein oscillator mode frequency, $\bar{\omega}_E$, for each of the three D–A oxygen pairs in GFP can be defined by using the amplitudes $\sigma^2_\alpha(\mathrm{T})$ as weighting factors:

$$\bar{\omega}_E = \sum \sigma^2_\alpha(T)\omega_\alpha / \sum \sigma^2_\alpha(T) \tag{3.12}$$

Although, in principle, there can be a temperature dependence in $\bar{\omega}_E$, we find the thermal down-shift over the region 160–298 K to be only ~8% for the O_{Ser}–O_{H_2O} pair, and slightly larger for O_{H_2O}–O_{Tyr} (9%) and O_{Glu}–O_{Ser} (12%). A frequency shift of this magnitude has a negligible effect and its small size is due to the relatively tight grouping of the participating normal modes. This is an independent measure of the quality of the Einstein approximation being utilized. If we now associate the sum in eqn (3.11) with the mean square displacement of the single quantized Einstein D–A oscillator with frequency, $\bar{\omega}_E$, and effective reduced mass, μ_{DA}, we find for the quantum mechanical (QM) limit:

$$\sigma^2_{DA}(T) \equiv \frac{\hbar}{2\mu_{DA}\bar{\omega}_E}[2\bar{n}(\bar{\omega}_E)+1] = \frac{\hbar\coth(\hbar\bar{\omega}_E/2k_BT)}{2\mu_{DA}\bar{\omega}_E} = \sum_\alpha \sigma^2_\alpha(T) \quad \text{(QM)} \tag{3.13}$$

Using the calculated numerical sum, $\sum_\alpha \sigma^2_\alpha(T)$, along with $\bar{\omega}_E$ from eqn (3.12), we find an expression for μ_{DA}:

$$\mu_{DA} = \frac{\hbar\coth(\hbar\bar{\omega}_E/2k_BT)}{2\bar{\omega}_E \sum_\alpha \sigma^2_\alpha(T)}. \tag{3.14}$$

As shown in Figure 3.2, the effective reduced masses from eqn (3.14) for each of the D–A pairs in GFP yields values that are very close to the simple two-atom reduced mass of 8 amu, as might be expected. This indicates that the very large reduced masses, sometimes used for the D–A oscillator in proteins,[46,47,54,60,76] are probably unphysical and somewhat misleading.

3.2.4.3 Linear Approximation for D–A Coupling to the Tunnelling Rate

One potential reason for the use of a large reduced mass for the D–A oscillator may be due to the linear approximation that is commonly used for coupling the D–A motions to the tunnelling rate.[18,22,45,49,52] To illustrate this most simply we consider the D–A motions from a classical point of view and examine the Franck–Condon overlap of harmonic 0-point tunnel particle wavefunctions in the D-H and A-H states, $|\langle 0_{DL}|0_{AL}\rangle|^2$. We do this as a function of the variation $\delta\ell = \ell - \ell_0$ away from the most probable

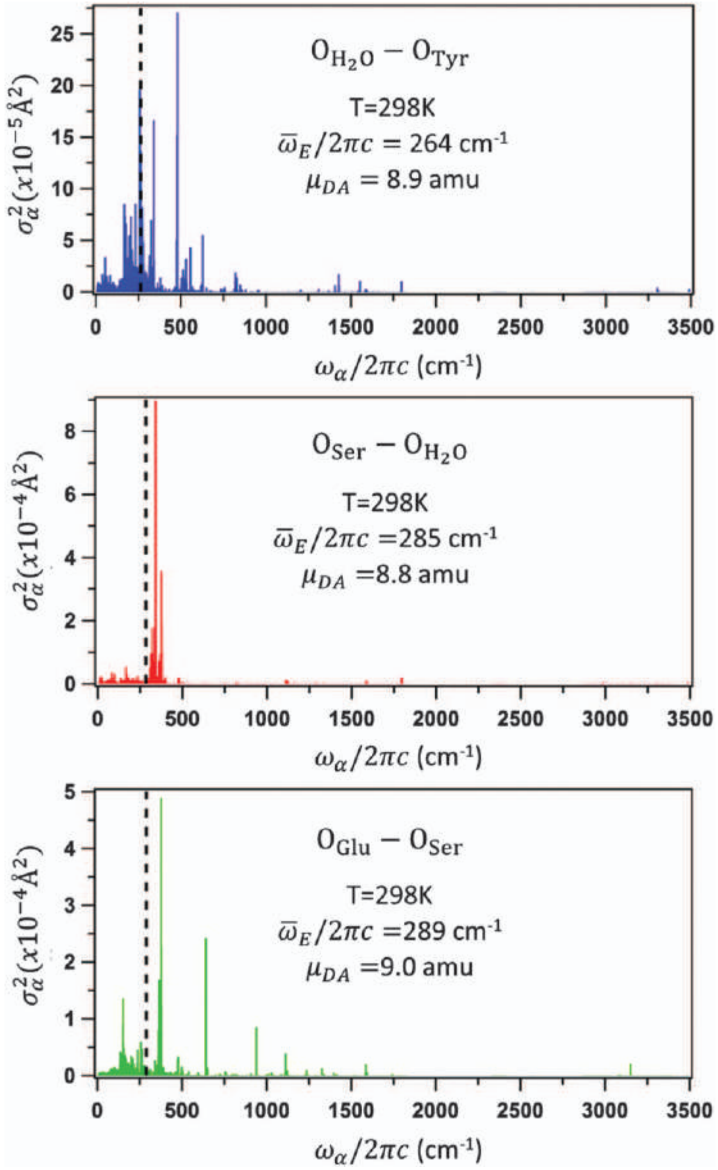

Figure 3.2 Normal mode analysis of GFP oxygen motions in the proton wire are derived using a QM/MM analysis. The mode-specific relative mean square displacement (σ_α^2) of the oxygen atoms participating in the proton transport wire of GFP are determined from eqn (3.11) and the GFP normal modes. The vertical dashed line is the average frequency, $\bar{\omega} = \sum \omega_\alpha \sigma_\alpha^2 / \sum \sigma_\alpha^2$. We find: $\mu_{DA} = 8.9$, 8.8, and 9.0 amu for the O_{H_2O}–O_{Tyr}, O_{Ser}–O_{H_2O}, and O_{Glu}–O_{Ser} atom pairs with σ_{DA} values of 0.11 Å, 0.10 Å, and 0.10 Å, respectively.
Reproduced from ref. 71 with permission from Springer Nature, Copyright 2016.

equilibrium tunnel length, ℓ_0. The D–A coupling to the tunnelling reaction can be determined by using eqn (3.3) with

$$S_L = \frac{\mu_L \omega_L}{2\hbar}\ell^2 = \frac{\mu_L \omega_L}{2\hbar}(\ell_0 + \delta\ell)^2. \tag{3.15a}$$

If only the linear terms in $\delta\ell$ are retained in a Taylor expansion of the exponent in eqn (3.3), the linear approximation to the coupling emerges as:

$$|\langle 0|0\rangle_\ell|^2 = C(\ell) = e^{-\bar{S}_L}\exp[-\alpha_L\delta\ell \ -\beta_L(\delta\ell)^2] \approx e^{-\bar{S}_L}\exp[-\alpha_L\delta\ell] \tag{3.15b}$$

where the average Huang–Rhys factor is given by $\bar{S}_L = \frac{\mu_L \omega_L}{2\hbar}\ell_0^2$ with $\alpha_L = \mu_L\omega_L\ell_0/\hbar$ and $\beta_L = \mu_L\omega_L/2\hbar$. Upon averaging over the distribution of tunnel length fluctuations, $P(\delta\ell)$, it can be seen that compressive fluctuations, where $\delta\ell < 0$, lead to an unconstrained exponential increase in $C(\ell)$ when the approximation in eqn 3.15b is used. Because this is where most of the tunnelling amplitude is found, it generates an exponential divergence and a serious overestimate of the tunnelling rate unless the fluctuations are tightly confined[60] around ℓ_0. Thus, for a given ω_{DA}, the improper use of a large reduced mass will generate a larger K_{vib}, which confines the oscillator and may (incorrectly) appear to help justify the linear approximation. A much better approach[58–60] is to always include the positive definite quadratic term ($\delta\ell^2$).

When a large reduced mass is (arbitrarily) chosen for the D–A oscillator,[46,54,60,76] the restoring force constant from eqn (3.9) can be made large enough that the rms D–A fluctuations (σ_R) and, equivalently, the tunnelling length fluctuations (σ_ℓ) become more tightly constrained. This arbitrary constraint on σ_ℓ can lead to an improvement in the linear approximation, but the calculated tunnelling rates still usually exceed the full quadratic expression by at least an order of magnitude.[58] The magnitude of the tunnelling rate overestimate when using the linear approximation also depends to some extent on the tunnelling particle potentials being used. For harmonic tunnelling particle potentials, the deviation from the exact (quadratic) calculation reaches an order of magnitude or more when $\sigma_\ell \gtrsim 0.05$ Å and, for anharmonic tunnelling particle potentials, the order of magnitude breakdown threshold is reached when $\sigma_\ell \gtrsim 0.09$ Å.[58]

Because proteins and biomolecules can fluctuate over a variety of length scales, the existence of a confined D–A distribution is relatively unlikely. Thus, it is generally important to keep the quadratic $\delta\ell^2$ term in eqn (3.15), which acts to control the exponential growth of the tunnel rate when decreased tunnel distances are sampled. We will consider the role of anharmonic D–A potentials in more detail in Section 3.3.3, both in the context of the linear approximation and to explore how the rate calculation is affected by the anharmonic van der Waals repulsion between D and A.

3.2.5 The Observed Rate and the Role of Protein Conformational Interconversions

For enzyme systems, which need conformational flexibility to accommodate substrate binding and product release, it is important to recognize that the ensemble contains a variety of conformations that are interconverting on timescales that may be faster than, slower than, or comparable to the tunnelling rate. In the simplest picture, we can assume there are only two sets of relevant reactant conformations. One, the tunnelling active reactant, will be denoted as $\langle r^* \rangle$ with a well-defined H-bond interaction and average D–A equilibrium distance, while the other will be denoted as $\langle r \rangle$ with such large distances between D and A that no H-bond interaction exists and no tunnelling occurs. The brackets around the state index denote the fact that within each of these generalized conformations, there exists a lower hierarchy of substates that carries its own specific distribution of D–A distances. The distance fluctuations within the conformation $\langle r^* \rangle$ involve small fluctuations in the equilibrium distance between D and A, along with the D–A vibrational motion about a given equilibrium. These fluctuations (and/or vibrations) take place on a more fine-grained and faster timescale than the larger conformational interconversions that take place between $\langle r \rangle$ and $\langle r^* \rangle$.

Assuming that these smaller scale fluctuations and vibrations are fast compared to the tunnelling rate and, if the D–A oscillator is treated classically (so that only a probability distribution of the tunnelling distance is required for the rate calculation), we can modify eqn (3.9a) to explicitly include the D–A equilibrium distance fluctuations within $\langle r^* \rangle$. We assume a temperature-dependent Gaussian distribution for the substates within $\langle r^* \rangle$, which yields a set of D–A equilibrium positions (R_0) governed by a harmonic force constant, K_{R_0}. Upon including the vibrational motion around each equilibrium position [as governed by K_{vib} in eqn (3.9a)], the overall effective force constant can be written as:[77]

$$K_{\text{eff}} = \frac{K_{\text{vib}} K_{R_0}}{K_{\text{vib}} + K_{R_0}} \tag{3.16a}$$

with

$$\sigma_{\text{DA}}^2(T) = \frac{k_{\text{B}} T}{K_{\text{eff}}} \quad \text{(classical)}. \tag{3.16b}$$

In the limit of a very sharp distribution for the substate-specific D–A equilibrium positions (large K_{R_0}) we recover eqn (3.9a), while for a more flexible enzyme conformation associated with $\langle r^* \rangle$, the value of K_{R_0} could be reduced to the point that $K_{\text{eff}} \cong K_{R_0}$. In this situation, the fluctuations between the substates within $\langle r^* \rangle$, having differing D–A equilibrium positions, rather than the still more localized D–A (H-bond) vibrations dominate the D–A distance distribution. The resulting broader distribution can be functional, for example, if an enzyme needs to access rare substate conformations. The potential for such a broadened distribution re-emphasizes the fact that it is perilous to apply the linear approximation to a D–A distance distribution associated with proton tunnelling in biomolecules. It is also noteworthy that, at low temperature, the substates associated with conformations having differing D–A equilibrium distances can, in principle, be "frozen out" leading to a non-ergodic ensemble with a static distribution of D–A equilibrium positions. Under this condition, the linear temperature dependence in eqn (3.16b) is no longer valid and kinetic inhomogeneity sets in, leading to non-exponential kinetics.[78–80]

However, even at room temperature the timescales for conformational interconversions, which allow the enzyme to reach the tunnelling-active conformation, can sometimes be entropically or enthalpically challenged and, therefore, can be relatively slow. In order to treat such a case, we again consider the simple bimodal (two-state) limit where the D–A distance distribution of the reacting enzyme has a set of inactive conformational substates, $\langle r \rangle$, and a separate set of tunnelling-active conformational substates, $\langle r^* \rangle$. In this case, we need to write a more general expression for the observed reaction rate. For the moment, we denote $\langle k^L_{\mathrm{r}^*} \rangle_\ell$ as an irreversible tunnelling rate, where the brackets imply an appropriate average over the tunnelling distances associated with the tunnelling-active reactant conformation, $\langle r^* \rangle$. If we denote the product state as P, a simple three-state kinetic scheme is given by eqn (3.17)

$$\langle r \rangle \underset{k_-}{\overset{k_+}{\rightleftarrows}} \langle r^* \rangle \xrightarrow{\langle k^L_{r^*} \rangle_\ell} P \tag{3.17}$$

where the conformational interconversion rates between $\langle r \rangle$ and $\langle r^* \rangle$ are given by k_+ and k_-. Within such a kinetic scheme, the observed kinetic rate for product formation is simply:

$$k^L_{\mathrm{obs}} = \frac{k_+}{k_- + \langle k^L_{r^*} \rangle_\ell} \langle k^L_{r^*} \rangle_\ell. \tag{3.18}$$

It is clear that if the enzyme conformational interconversion rate, k_-, is fast compared to the thermally averaged tunnelling rate, the experimentally observed tunnelling rate will be directly proportional to $\langle k^L_{r^*} \rangle_\ell$. However, the experimentally observed rate will be scaled down by the thermodynamic equilibrium population, $p_{\langle r^* \rangle} = k_+/k_-$. On the other hand, if the rate k_- is similar to $\langle k^L_{r^*} \rangle_\ell$ (but both rates are still much slower than the picosecond thermal equilibration timescale, so that the GR can still be applied to the $\langle r^* \rangle \to P$) a situation ensues where the "prefactor" to $\langle k^L_{r^*} \rangle_\ell$ in eqn (3.18) begins to develop isotope dependence. This intermediate limit can lead to complications in the analysis of experiments, particularly the temperature dependence of the KIE. Finally, we see that if $\langle k^L_{r^*} \rangle_\ell$ significantly exceeds the rate (k_-) for converting from $\langle r^* \rangle$ to $\langle r \rangle$, the tunnelling process is "conformationally masked" (*i.e.*, $k^L_{\mathrm{obs}} = k_+$). This means that observables such as the KIE will not reveal the fundamental tunnelling process that underlies the enzymatic reaction. A different, but analogous, type of masking occurs, not from slow enzyme conformational interconversions, but rather when the overall biochemical rate measurement involves product formation *via* additional (non-tunnelling) chemical reactions, one of which is rate limiting.

The recent observation[71] of 400 ps room-temperature deep proton tunnelling in GFP (Section 3.4) and the calculation of a similar rapid inherent rate for the tunnelling active state of SLO (Section 3.3.4) suggests that "conformational masking" of the enzymatic KIE may occur more often than commonly thought. Thus, proton tunnelling could be much more widespread in the biological world than is currently appreciated.

3.3 Electronically Non-adiabatic Proton-coupled Electron Transfer in Biomolecules

3.3.1 Theoretical Treatment of D–A Motion in the Quantum and Classical Limits

3.3.1.1 Two-dimensional Quantum Treatment of the D–A and H/D Coordinates

When performing tunnelling rate measurements that span the low temperature regime, it is important to acknowledge that the D–A coordinate must be treated in the quantum limit, along with the proton (or deuteron) coordinate (which, for simplicity, is maintained in its zero-point level). In general, this is a difficult problem to solve exactly, but it is possible for the electronically non-adiabatic case in the harmonic limit using the time correlation function for Duschinsky mixing. The thermally averaged Franck–Condon vibrational overlap that is needed for the rate calculation can be evaluated using optical lineshape theory[59,63,81–85] by setting the optical frequency (Ω) to zero, which generates the reactant and product vibrational overlap in the absence of a photon but in the presence of the thermal bath. The environmental coordinate ($\hbar\omega_s \ll k_B T$) is treated using the short-time approximation so that it folds in the usual temperature-dependent Gaussian lineshape, which upon normalization and evaluation at zero frequency equates to:

$$\begin{aligned}\lim_{\Omega\to 0}\frac{\hbar\omega_s}{\sqrt{4\pi\lambda_s k_B T}}\exp\left[-\frac{(\Delta E^0+\Delta E_{nm}+\lambda_s-\Omega)^2}{4\lambda_s k_B T}\right]\\ =\frac{\hbar\omega_s}{\sqrt{4\pi\lambda_s k_B T}}\exp\left[-\frac{(\Delta G^0+\Delta E_{nm}+\lambda_s)^2}{4\lambda_s k_B T}\right]\end{aligned} \tag{3.19a}$$

where the reaction free energy, ΔG^0, takes the place of the R and P state zero-point separation and the terms in the exponent can be identified with the "environmental barrier":

$$\Delta G^{\ddagger}_{nm} = (\Delta G^0 + \Delta E_{nm} + \lambda_s)^2/4\lambda_s \tag{3.19b}$$

for reaching the various *n*–*m* degenerate transition states between R and P *via* the D–A oscillator where $\Delta E_{nm} = (m - n)\hbar\omega_{DA}$. In Figure 3.1, the 2D quantum subsystem (Q and q) is depicted for only one such degenerate situation where $n = m$. Because of the thermal accessibility of the various D–A oscillator levels, we must average over the initial states and sum over the final states for all possible degenerate transitions. This can be a very tedious calculation in the energy domain, but it becomes much more tractable in the time domain where the optical time correlator approach naturally keeps track of all such pathways at a given temperature.[59,81–86]

For the electronically non-adiabatic case in the harmonic limit, we can evaluate the normal mode rotation angle, which to a good approximation is given by eqn (3.6) and (3.7), and then use the Duschinsky mixing correlation function (see supplement S4 in ref. 59) to evaluate an exact 2D quantum expression for the thermally averaged Franck–Condon factor between R and P, $\langle FC \rangle_{\mathrm{cf}}$. Thus, in the electronically non-adiabatic limit:

$$k_{\ell_0}^{NA} = \frac{2\pi |V_{\mathrm{RP}}|^2}{\hbar} \frac{\langle FC \rangle_{\mathrm{cf}}}{\hbar \omega_s} \tag{3.20}$$

The inverse frequency of the environmental mode, associated with the density of states, is cancelled by an equivalent frequency factor for the environmental mode in the short-time correlation function [(*e.g.*, see eqn (3.19a)] so, for a given rotation angle, the surviving variables associated with the Franck–Condon factor are the equilibrium tunnel distance, ℓ_0, the frequencies of the two oscillators, ω_{L} and ω_{DA}, and the environmental barriers, $\Delta G_{nm}^{\ddagger}$. Because they depend on the reorganization energy, λ_s, and the reaction free energy, ΔG^0, as seen in eqn (3.19b), these ubiquitous parameters also contribute to $\langle FC \rangle_{\mathrm{cf}}$.

A more traditional approach to the vibrational overlap calculation in the electronically non-adiabatic limit invokes the Born–Oppenheimer (B–O) approximation to separate the timescales of the heavy and light nuclei. Because the reduced mass of the D–A oscillator for oxygen atoms, compared that of a bound proton, is only about 8 : 1, it is not immediately obvious that this is good approximation. Thus, in order to test it, we can evaluate the thermalized 2D Frank–Condon factor for harmonic oscillators using a B–O approximation and compare it with $\langle FC \rangle_{\mathrm{cf}}$. This somewhat tedious, but instructive, calculation is discussed in detail in previous work.[59] The result for the rate is the same as eqn (3.20) except that the Franck–Condon factor is replaced by

$$\langle FC \rangle_{\mathrm{BO}} = \sum_n \sum_m P_n I_{nm}^2 \frac{\hbar \omega_s}{\sqrt{4\pi \lambda_s k_{\mathrm{B}} T}} \exp\left[-\frac{\Delta G_{nm}^{\ddagger}}{k_{\mathrm{B}} T} \right] \tag{3.21}$$

where the probability of being in the initial D–A state, n, is given by:

$$P_n = \mathrm{e}^{-\frac{n\hbar\omega_{\mathrm{DA}}}{k_{\mathrm{B}}T}} \left[1 - \mathrm{e}^{-\frac{\hbar\omega_{\mathrm{DA}}}{k_{\mathrm{B}}T}} \right] \tag{3.22}$$

and $\Delta G_{nm}^{\ddagger}$ is defined in eqn (3.19b). The B–O overlap integral I_{nm} can be expressed as:

$$I_{nm} = \langle n | I(Q) | m \rangle = \int \chi_n^R \,(Q) I(Q) \chi_m^P(Q) \mathrm{d}Q \tag{3.23a}$$

with

$$I(Q) = \int \varphi_0^R(q, Q)\, \varphi_0^P(q, Q) \mathrm{d}q \tag{3.23b}$$

where the tunnel particle vibrational wavefunction, $\varphi_0^{R,P}(q, Q)$, remains in its zero-point state and the D–A wave-functions, $\chi_{n,m}^{R,P}(Q)$ are allowed to explore all accessible vibrational states. The relevant coordinate transformations that account for the rotation between the reactant and product state mass-weighted normal modes (Q and q), as well as the analytic evaluation of I_{nm} factors have been given previously[59] and will not be reproduced here.

In Figure 3.3a we set the D–A oscillator reduced mass to 8 amu and its force constant to 30 $\mathrm{N\,m^{-1}}$ (which generates a room-temperature rms relative displacement of $\sigma_{\mathrm{DA}} \sim 0.11$Å) and then plot the quantities $\langle FC \rangle_{\mathrm{cf}}$, $\langle FC \rangle_{\mathrm{BO}}$, and its linear approximation, $\langle FC \rangle_{\mathrm{BO}}^{\beta \to 0}$, on a logarithmic scale as a function of temperature. It can be seen that the exact correlation function and the B–O FC values converge near room temperature. Although there are some differences at lower temperature, they are much less than an order of magnitude. This gives reasonable confidence that use of the B–O approximation is warranted when performing tunnelling calculations involving the D–A oscillator. As a result, we will use the B–O method when evaluating the electronically adiabatic proton tunnelling rates in Section 3.4. We note that, if the D–A oscillator reduced mass is increased, the B–O approximation can be improved further[59] and this may also have partially motivated the use of a large D–A reduced mass in prior work.[46,54,60,76] However, based on the full normal mode treatment for GFP, as discussed in Section 3.2.4 [see eqn (3.14)], we see no obvious reason that the D–A reduced mass should be taken to be significantly larger than the values derived from the donor and acceptor atomic masses. Figure 3.3a also displays (as a dashed line) the effect of the linear approximation for D–A coupling by setting β_H in eqn (3.15b) to zero in the $\langle FC \rangle_{\mathrm{BO}}$ calculation. The extreme deviation from the exact result emphasizes the necessity of retaining the quadratic terms.

3.3.1.2 Classical Treatment of the D–A Coordinate

When experiments are being performed at or near room temperature, as is often the case for enzymatic systems,[2,3,7,12] there is an important simplification that can be made by treating the D–A oscillations and equilibrium fluctuations classically, using an effective force constant as given by eqn (3.16). The MSD given by eqn (3.16b) for a classical D–A harmonic oscillator (along with eqn (3.5a), which yields $\sigma_{\mathrm{DA}} \equiv \sigma_\ell$) generates a temperature dependent Gaussian distribution of tunnelling distances, $P(\ell)$. This distribution can be used to find the statistically averaged Franck–Condon factor for the tunnelling particle ($L = \mathrm{H, D}$). The electronically non-adiabatic rate can then be written as:

$$\langle k^L \rangle_\ell = \frac{2\pi |V_{\mathrm{RP}}|^2}{\hbar} \frac{\langle |\langle 0_{\mathrm{DL}} | 0_{\mathrm{AL}} \rangle|^2 \rangle_\ell}{\sqrt{4\pi k_{\mathrm{B}} T \lambda_s}} e^{-\Delta G_s^\ddagger / k_{\mathrm{B}} T} \tag{3.24}$$

where the brackets $\langle \cdots \rangle_\ell$ denote the average over $P(\ell)$ and the one-dimensional Franck–Condon overlap of the tunnel particle wavefunction

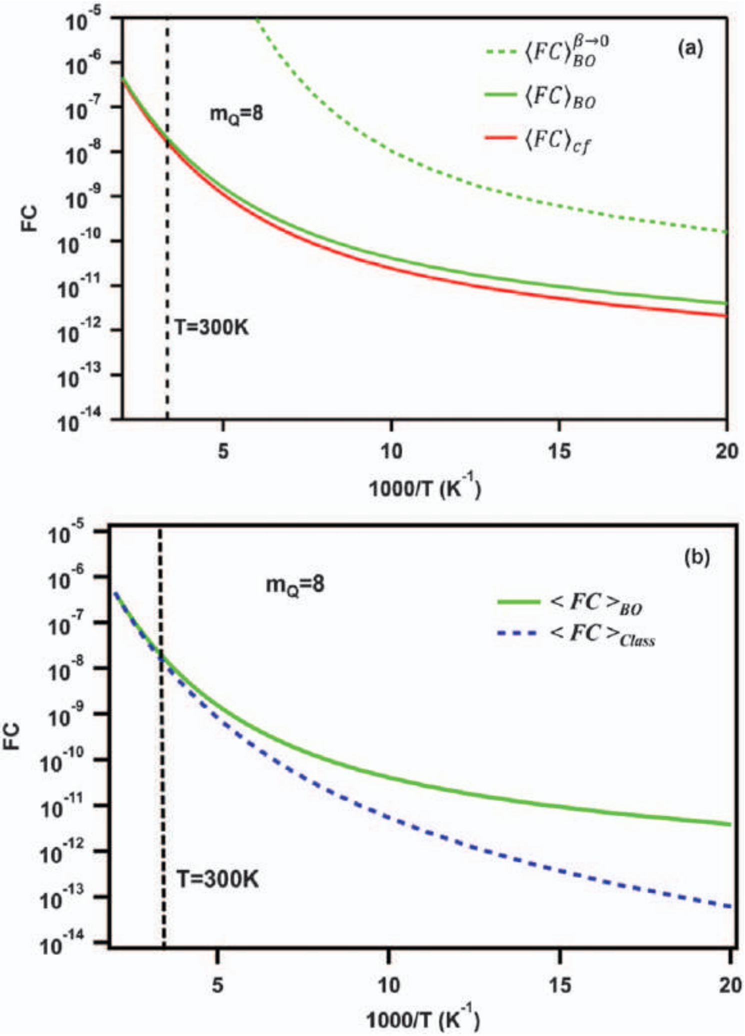

Figure 3.3 Part (a) displays the thermally weighted Franck–Condon (FC) factors for the quantum analytic B–O approximation, eqn (3.21), and for the exact correlation function, eqn (3.20). The limit for the linear approximation, where $\beta_H \rightarrow 0$, is also shown in the upper panel. The effective force constant for ω_{DA} is fixed at $K_{vib} = 30$ N m^{-1} and $m_H = 8$ amu, so that $\theta_H = 19.7^\circ$ and $\omega_{DA}/2\pi c = 250$ cm^{-1}. Part (b) shows the temperature dependent FC factor for the quantum analytic B-O approximation compared to the classical D–A approximation. Other parameters used in the figure are: $\omega_H/2\pi c$ 3200 cm^{-1}, $\ell_0 = 0.8$ Å, $\Delta G^0 = -600$ cm^{-1}, $\lambda_s = 1200$ cm^{-1} ($\Delta G^{\ddagger}_{nn} = 75$ cm^{-1}), and $\omega_s/2\pi c = 33$ cm^{-1}. As the temperature approaches and falls below ~50 K, the classical assumption for the solvent obviously breaks down.

Part (a) reproduced from ref. 59 with permission from AIP Publishing, Copyright 2015.

between the donor and acceptor zero-point states is given by $|\langle 0_{\mathrm{DL}}|0_{\mathrm{AL}}\rangle|^2$. This overlap can be evaluated for either harmonic oscillators [eqn (3.3)] or back-to-back anharmonic Morse oscillators [eqn (3.4)]. It is also relatively easy to generalize eqn (3.16) to account for the anharmonic forces that are associated with the D–A oscillator. In such a case, the classical anharmonic probability distribution for the tunnel distance can be found using a more general D–A anharmonic potential surface, $V_{\mathrm{DA}}(R)$ along with eqn (3.5) (which relates $P(R)$ to $P(\ell)$ by a simple coordinate shift). The result, now written in terms of the D–A distance, R, is given by:

$$P_{\mathrm{DA}}^{\langle i\rangle}(R) = N\,\exp\left\{\frac{-V_{\mathrm{DA}}^{\langle i\rangle}(R)}{k_{\mathrm{B}}T}\right\} \tag{3.25}$$

where N is set to normalize the distribution so that it integrates to unity over the domain of R at temperature T and $\langle i\rangle$ denotes a specific protein conformation (*e.g.*, $\langle r\rangle$ or $\langle r^*\rangle$).

3.3.2 KIE Analysis in the Classical Harmonic Limit

Turning to the evaluation of the KIE, it is instructive to first proceed using harmonic potentials for both the D–A motion and the tunnel particle. In this limit the integral $\langle|\langle 0_{\mathrm{DL}}|0_{\mathrm{AL}}\rangle|^2\rangle_\ell = \int P(\ell)\mathrm{e}^{-S_{\mathrm{L}}}\mathrm{d}\ell$ with $P(\ell) = \frac{1}{\sqrt{2\pi}\sigma_{\mathrm{DA}}}\exp\left[-\frac{(\ell-\ell_0)^2}{2\sigma_{\mathrm{DA}}^2}\right]$ is easily solved, leading to a particularly simple result[44] for the electronically non-adiabatic tunnelling rate:

$$\langle k^L\rangle_\ell = \frac{2\pi|V_{\mathrm{RP}}|^2}{\hbar}\frac{\mathrm{e}^{-\bar{S}_{\mathrm{L}}\rho_{\mathrm{L}}(T)}}{\sqrt{4\pi k_{\mathrm{B}}T\lambda_s/\rho_{\mathrm{L}}(T)}}\mathrm{e}^{-\Delta G_s^{\ddagger}/k_{\mathrm{B}}T} \tag{3.26a}$$

where $\bar{S}_{\mathrm{L}} = \frac{\mu_{\mathrm{L}}\omega_{\mathrm{L}}\ell_0^2}{2\hbar}$ and the average tunnelling distance is given by ℓ_0. The quantity

$$\rho_{\mathrm{L}}(T) = \frac{\sigma_{\mathrm{L}}^2}{\sigma_{\mathrm{L}}^2 + \sigma_{\mathrm{DA}}^2(T)} \tag{3.26b}$$

depends on $\sigma_{\mathrm{DA}}^2(T)$, which is given by eqn (3.16b), while $\sigma_{\mathrm{L}}^2 = \frac{\hbar}{\mu_{\mathrm{L}}\omega_{\mathrm{L}}}$ is defined as the square of the zero-point Gaussian variance of the tunnelling particle *probability density*, which differs by a factor of two from the square of the position *probability amplitude* of the wave-function, $\frac{\hbar}{2\mu_{\mathrm{L}}\omega_{\mathrm{L}}}$. Thus, a proton with $\tilde{\nu}_H = 3300\ \mathrm{cm}^{-1}$ has a variation in position probability amplitude of ~0.07 Å when $\sigma_H \cong 0.1$ Å. Eqn (3.26) is identical to the well-known electronically non-adiabatic result given by Kuznetsov and Ulstrup,[44] but it is written in a more compact and intuitive form by using the temperature-dependent ratio, $\rho_{\mathrm{L}}(T)$. Notice that the effective Huang–Rhys coupling, $\bar{S}_{\mathrm{L}}\rho_{\mathrm{L}}(T)$, is scaled downward as the width of the D–A excursions broadens at higher temperatures. This increases the tunnelling rate and is effectively a measure of how the thermally averaged tunnelling distance is reduced as the temperature increases.

It is important to note that eqn (3.26) and the related expressions presented below, are based on the simplifying assumption that the zero-point proton and deuteron vibrational states play a dominant role in the tunnelling process. If the magnitude of the reaction free energy is large enough, this assumption breaks down and vibrational overlaps involving the excited vibrational states of the tunnelling particle can begin to affect the KIE as quantified previously within the confines of the linear approximation.[46] However, for the specific examples treated here (SLO and GFP), the reaction free energies (-5.4 kcal mol^{-1} and -2 kcal mol^{-1}, respectively) should be small enough that the zero-point assumption for the tunnelling particles is reasonably accurate.

If we now proceed to utilize eqn (3.26a) and factor out a term $\frac{2\pi|V_{\mathrm{RP}}|^2}{\hbar^2\omega_s}$, it allows the residual expression, $\langle FC\rangle_{\mathrm{class}} = \frac{\hbar\omega_s \mathrm{e}^{-\bar{S}_{\mathrm{L}}\rho_{\mathrm{L}}(T)}}{\sqrt{4\pi k_{\mathrm{B}}T\lambda_s/\rho_{\mathrm{L}}(T)}}\mathrm{e}^{-\Delta G_s^{\ddagger}/k_{\mathrm{B}}T}$, to be compared with the FC factors where the D–A mode is treated at the quantum level. This comparison is shown in Figure 3.3b where it can be seen that the agreement is still very good near room temperature and $\langle FC\rangle_{\mathrm{class}} \cong \langle FC\rangle_{\mathrm{BO}}$, with the exact $\langle FC\rangle_{\mathrm{cf}}$ (in panel a) also falling slightly below $\langle FC\rangle_{\mathrm{BO}}$ (but above $\langle FC\rangle_{\mathrm{class}}$) near 300 K. Thus, when the experiments measure the tunnelling rates only near room temperature, it appears to be well justified to use a classical approach to account for the vibrations and fluctuations of the heavy D–A atoms.

Eqn (3.26) can be used to evaluate other experimental observables such as the KIE and the temperature dependence of the H and D tunnelling rates. For the KIE, we take $\mu_D = 2\mu_H$ and $\omega_D = \omega_H/\sqrt{2}$ to find:

$$\mathrm{KIE}(T) = \frac{\langle k^H\rangle_\ell}{\langle k^D\rangle_\ell} = \sqrt{\rho_H(T)\left\{1-\sqrt{2}\right\}+\sqrt{2}}\,\exp\left[-\bar{S}_H\left(\frac{\rho_H^2(T)\left\{1-\sqrt{2}\right\}}{\rho_H(T)\left\{1-\sqrt{2}\right\}+\sqrt{2}}\right)\right] \tag{3.27}$$

Although tunnelling rates are sometimes plotted in an Arrhenius form (*i.e.*, $\ln\langle k^L\rangle_\ell$ *vs.* $1/T$), we do not expect the simple linear Arrhenius form to hold for tunnelling over a wide range of temperatures. However, when only a narrow temperature range is probed, the results can be approximated by a linear function[5]. Thus, we use eqn (3.26) to take the derivative of $\ln\langle k^L\rangle_\ell$ with respect to $1/k_{\mathrm{B}}T$, focusing on the exponential terms and picking $T_0 = 298$ K as a practical reference temperature. This yields an "Arrhenius" slope for the tunnel particle ($L = \mathrm{H}$ or D):

$$-E_a^L(T_0) = -\frac{d\ln\langle k^L\rangle_\ell}{d(1/k_{\mathrm{B}}T)} \sim \left[\Delta H_s^{\ddagger} + \frac{k_{\mathrm{B}}T_0\ell_0^2\sigma_{\mathrm{DA}}^2(T_0)}{2(\sigma_{\mathrm{DA}}^2(T_0)+\sigma_{\mathrm{L}}^2)^2}\right]. \tag{3.28}$$

The D–A distribution-dependent term carries the isotope dependence:

$$E_{\mathrm{DA}}^{L}(T_0) = \frac{k_{\mathrm{B}}T_0\ell_0^2\sigma_{\mathrm{DA}}^2(T_0)}{2(\sigma_{\mathrm{DA}}^2(T_0)+\sigma_{\mathrm{L}}^2)^2} = \frac{k_{\mathrm{B}}T_0\ell_0^2}{2\sigma_{\mathrm{L}}^2}\rho_{\mathrm{L}}(T_0)[1-\rho_{\mathrm{L}}(T_0)]. \tag{3.29}$$

The temperature dependence of the KIE (sometimes referred to as the "Arrhenius slope" of the KIE) in the vicinity of T_0 is given by the difference in eqn (3.28) for the deuteron and proton:

$$\Delta E_a = E_a^D(T_0) - E_a^H(T_0) = E_{\mathrm{DA}}^D(T_0) - E_{\mathrm{DA}}^H(T_0) \tag{3.30a}$$

and, since $\Delta H_s^{\ddagger}$ does not depend on the mass of the tunnelling particle, the temperature-dependent KIE is solely dependent on the D–A contribution given by eqn (3.29). Thus, upon substituting $\sigma_D^2 = \sigma_H^2/\sqrt{2}$ (*i.e.*, using $\mu_D = 2\mu_H$ and $\omega_D = \omega_H/\sqrt{2}$), we find:

$$\Delta E_a(T_0) = \frac{k_{\mathrm{B}}T_0\ell_0^2\ \sigma_{\mathrm{DA}}^2(T_0)}{2\left(\sigma_{\mathrm{DA}}^2(T_0)+\sigma_H^2/\sqrt{2}\right)^2} - \frac{k_{\mathrm{B}}T_0\ell_0^2\ \sigma_{\mathrm{DA}}^2(T_0)}{2(\sigma_{\mathrm{DA}}^2(T_0)+\sigma_H^2)^2} \tag{3.30b}$$

Examining eqn (3.27)–(3.30), it is apparent that, in principle, the three relevant unknown physical parameters, ℓ_0, $\sigma_{\mathrm{DA}}(T_0)$, and $\Delta H_s^{\ddagger}$, can be extracted from the experimental tunnelling measurements near room temperature. Specifically, knowing the KIE and its temperature-dependent slope, ΔE_a, allows determination of the parameters ℓ_0 and $\sigma_{\mathrm{DA}}(T_0)$. However, there are two possible values of $\sigma_{\mathrm{DA}}(T_0)$ that will generally be consistent with a given ΔE_a (these correspond to a "hard" or a "soft" D–A force constant). It is noteworthy that, within the "linear approximation" (*cf.* eqn (3.15), only a single value of $\sigma_{\mathrm{DA}}(T_0)$ is possible, which corresponds to a "hard" localizing force constant that tightly constrains the D–A distribution. The more general double-valued nature of σ_{DA} *vs.* ΔE_a can readily be seen when eqn (3.30b) is plotted[58] and the singular point where $\Delta E_a(\sigma_{\mathrm{DA}},\ell_0)$ reaches a maximum can be denoted as $\Delta E_a^{\max}(\sigma_{\mathrm{DA}}^{\max})$. In general, this maximum occurs in the region $\sigma_{\mathrm{DA}}^{\max}(T_0) \sim [0.65-1.0]\ \sigma\mathrm{H} \sim [0.065-0.1]$ Å, depending somewhat on the potentials that are used for both the tunnel particle and the D–A motion. Thus, on either side of $\sigma_{\mathrm{DA}}^{\max}$, we find two values of $\sigma_{\mathrm{DA}}(T_0)$, corresponding to the "hard" and "soft" force constant, and either of which is consistent with a given experimentally determined $\Delta E_a \leq \Delta E_{\mathrm{a}}^{\max}$). If these two possibilities can be differentiated using other experimental information (*e.g.*, certain electron-nuclear double resonance experiments may be helpful[87]), eqn (3.28) and (3.29) can be used to unambiguously find $\Delta H_s^{\ddagger} \cong E_a^L - E_{\mathrm{DA}}^L(T_0)$.

3.3.3 Effect of Anharmonic D–A Interactions and Local Electric Fields

3.3.3.1 *Background*

The effect of anharmonic interactions between D and A can play an important role in the determination of the tunnelling rate. This is particularly true for enzyme systems where PCET facilitates a fundamental catalytic process that involves transfer of both an electron and a proton from an aliphatic carbon substrate donor atom (C–H) to an acceptor that is often an activated oxygen atom bound to a transition metal (usually iron) in the enzyme active site. When isolated, the CH···O hydrogen bond tends to be very weak, having an equilibrium D–A distance of ~3.6–3.7 Å. However, when proton tunnelling mediated enzymatic catalysis is involved, additional forces can act to move the CH···O donor–acceptor subsystem into closer proximity so the proton is able to tunnel more effectively. Such forces can even move the donor and acceptor atoms inside their respective van der Waals radii where anharmonic repulsion terms become significant.

As an example, we consider a PCET reaction, where the catalytic active site iron atom is reduced by the electron while the proton tunnels from the substrate carbon to the iron-bound oxygen. This leaves behind a very reactive carbon radical on the substrate that immediately re-hybridizes and becomes available for the ensuing catalytic activity. Numerous studies have focused on the role of proton tunnelling in such reactions[88] and one enzymatic system (soybean lipoxygenase, SLO) has received particular attention because of its very large KIE.[3,89,90] In this system, a hydroxyl group is bound to an active site ferric iron and the proton is removed from C_{11} of the linoleic acid substrate.[87] Figure 3.4 shows the active site of the SLO system and we will discuss more details of this system in Section 3.3.4.

Because the proton tunnelling reaction takes place predominantly in the short distance tail of the D–A probability distribution (or during the compressive part of a D–A vibrational cycle), it is crucial to properly model the compressive region of the D–A interaction. Generally, attention to anharmonic interactions in analytic models have been focused on the tunnelling

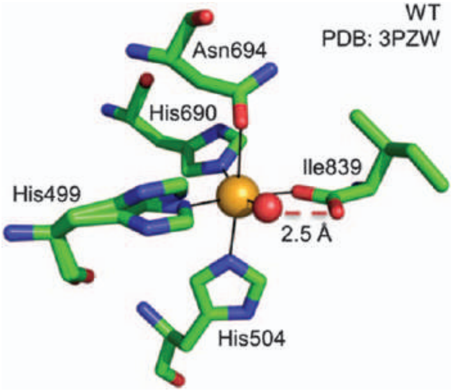

Figure 3.4 The active site of wild type SLO from the crystal structure (PDB: 3PZW). The red sphere is the acceptor oxygen of the iron bound hydroxyl, which is strongly hydrogen bonded to Ile 839. The donor atom is the C_{11} of the linoleic acid substrate, which is not shown.
Reproduced from ref. 77, https://doi.org/10.1021/acs.jpcb.7b05570, with permission from American Chemical Society, Copyright 2015.

particle wave-functions where back-to-back Morse oscillators, with Franck–Condon overlaps described by eqn (3.4) are used. While this level of anharmonicity has an important effect on the KIE, the importance of the anharmonic D–A repulsion in the compressive region is equally, if not more, important. It is crucial for correctly predicting the absolute tunnelling rate because the long tail associated with a harmonic (*i.e.*, Gaussian) probability distribution offers up too much amplitude in regions where the tunnelling lengths are small. This can lead to significant overestimates of the tunnelling rate. This problem is particularly acute when the D–A coordinate is treated harmonically while the tunnelling coordinate is treated anharmonically as implemented in several prior treatments.[46,55] It turns out that there is a fortuitous cancellation of errors in the rate calculation when both coordinates are treated in the harmonic limit.[77] This occurs because, compared to the respective anharmonic potentials, the use of a harmonic D–A potential increases the rate while the use of harmonic tunnel particle potentials decreases the rate. Thus, using anharmonic tunnel particle potentials increases the rate and exacerbates the error of a rate calculation that is based on a harmonic D–A potential.

In order to analyze the relative magnitude of the cancellation, a systematic comparison has been carried out with the tunnelling particle and D–A coordinates treated as either harmonic or anharmonic. For the tunnelling particle coordinate, back-to-back Morse potentials were used to simulate the anharmonic case. For the D–A coordinate, the anharmonic treatment uses the Morse potential discussed below and comparisons are made by appropriately matching the harmonic force constant with the effective force constant found for small amplitude motions within the anharmonic potential. The nearly perfect cancellation of error in the context of the OH$\cdots$O hydrogen-bonded system is discussed quantitatively elsewhere (ref. 77 in S6 of the supporting information).

3.3.3.2 A Simple Anharmonic Donor–Acceptor Model

In order to quantitatively treat the anharmonic repulsion between the substrate CH donor and the activated (*i.e.*, charged) oxygen acceptor, we construct a simple quantum model system that mimics the basic CH$\cdots$O^q interaction (where q is the net charge on the oxygen atom). Examples of this model system are shown in Figure 3.5 where we use a simple density functional theory (DFT) calculation to map out the ‘‘bare’’ potential energy as the D and A atoms approach each other for different values of the net charge on the oxygen atom.[77] We control the level of ‘‘activation’’ (*i.e.*, value of q) on the oxygen by artificially *increasing* the charge of the hydroxyl proton so that the absolute value of the total negative charge on the OH group, $[\mathrm{OH}]^{\delta-}$, is reduced from $-e$ to $-\delta e$, where $\delta \leq 1$. As δ is reduced, it decreases the charge, q, on the oxygen atom from its maximal value ($q \cong -1.2e$ for $\delta = 1$). The value of charge, q, on the oxygen of the model complex in Figure 3.5, as well as on the larger model complex shown in Figure 3.4, can

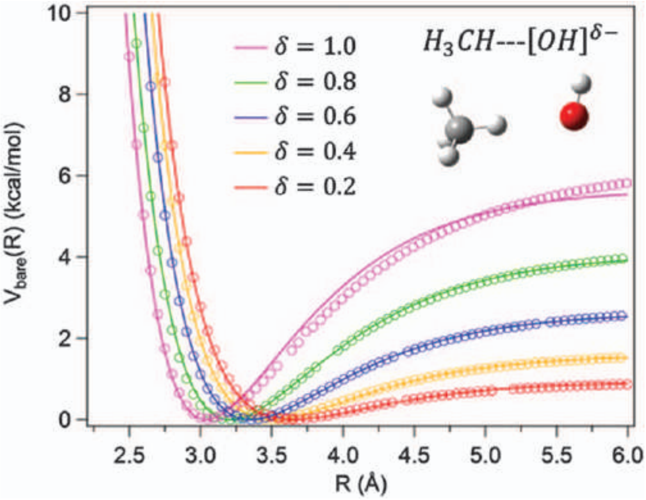

Figure 3.5 Results of DFT test calculations plotting the potential energy, $V_{\mathrm{bare}}(R)$, as a function of distance, R, between methane (donor carbon) and hydroxyl (acceptor oxygen). The charge on the acceptor oxygen is modulated by adjusting the charge of the embedded hydroxyl proton, which also determines the value of δ. The Morse potential fitting parameters, b_{DA}, D_{DA}, and R_0^{DA}, for the various charge states can be found elsewhere.[77] For SLO, a much larger scale DFT calculation finds the charge on the acceptor oxygen to be approimately $\sim -0.9e$ and this correlates to $\delta = 0.6$ in the model calculation shown in the figure, which makes the oxygen atom charge equivalent to what is found in the full SLO active site DFT calculation. Reproduced from ref. 77, https://doi.org/10.1021/acs.jpcb.7b05570, with permission from American Chemical Society, Copyright 2015.

be found using a grid based method[91] in conjunction with the DFT model calculation.[77]

Although this is a very simplistic model, the essential D–A repulsion forces can be found easily as a function of the D–A distance and oxygen charge. We can see from Figure 3.5 that, as the charge on the oxygen is decreased (smaller δ), the D–A minimum energy and the repulsive region of the ‘‘bare’’ model potential, $V_{\mathrm{bare}}(R)$, move out to longer D–A distances and the CH···O binding energy is reduced, as expected. The solid lines through the DFT data points correspond to a simple Morse oscillator fit, which mimics the energetics very well, particularly at short distance where it is most important to maintain accuracy for the tunnelling calculation. Thus, we use

$$V_{\mathrm{bare}}(R) = D_{\mathrm{DA}}[1 - \exp\left(-b_{\mathrm{DA}}(R - R_0^{\mathrm{DA}})\right)]^2 \tag{3.31}$$

as the effective anharmonic D–A bare potential interaction. The anharmonic D–A Morse binding potentials that fit the different CH···O^q interactions are shown in Figure 3.5 and the parameters using eqn (3.31), as well as the correlations between q and δ, are tabulated in supplementary information that can be found elsewhere.[77]

Once the value of q is determined for a given enzymatic active site, by employing just a *single* large scale DFT calculation, the bare Morse potential associated with that specific value of q can be combined with additional external forces acting on the D–A subsystem [*e.g.*, see eqn (3.32)]. In the case of the active site of SLO, shown in Figure 3.4, the value of $q \sim -0.9\text{e}$. The overall potential governing the D–A motion facilitates a classical evaluation of the distribution of tunnelling distances by using eqn (3.25) along with

$$V_{\text{DA}}(R) = V_{\text{bare}}(R) + V_{\text{Ext}}(R). \tag{3.32}$$

The added potential, $V_{\text{Ext}}(R)$, reflects the action of forces, external to the D–A subsystem, that are primarily due to electric fields and/or protein conformational effects. The classical distribution, $P_{\text{DA}}(R)$, in eqn (3.25) is fundamental to the tunnelling rate calculation and when paired with eqn (3.31) and (3.32), it takes into account the anharmonic D–A repulsion at short distance as well as additional compressive forces, external to the simple model system in Figure 3.5, that may be needed to bring the donor carbon and acceptor oxygen into close enough proximity that effective tunnelling can occur.

The simplest example of an external force is an electric field with a component along the R-coordinate axis, *i.e.*, $F_{\text{field}} = -qE_R$. When the external field, E_R, points toward the negatively charged oxygen acceptor, there will be an additional strengthening of the $\text{CH}\cdots\text{O}^q$ interaction. This shifts the location of the D–A equilibrium position to smaller values that depend on the magnitude of the electric field. In principle, such an external field can originate from nearby atomic or molecular polarizations or from charged groups within the protein. Because of the very small distance over which the D–A repulsive interaction takes place, combined with our desire to minimize the number of adjustable parameters in the model, we do not consider spatial variation of the electric field within the interaction region. For example, we note that for a nearby polarizable residue or substrate that interacts with the electric field from the negatively charged oxygen atom, there will be an ion-induced dipole field that points back at the oxygen and this field should scale approximately as $1/r^5$. However, the resulting force from this dipole field acts in such a localized region at the negatively charged oxygen, that the assumption of a nearly constant external field may be considered reasonable. In terms of the bare Morse potential parameters, a simple classical calculation (see S5.3 in ref. 77) yields the relationship between the external electric field strength, E_R, and the relative shift, ΔR_0, in the D–A equilibrium position:

$$E_R = E_R^0 \exp\{-b_{\text{DA}}\Delta R_0\}[1 - \exp\{-b_{\text{DA}}\Delta R_0\}] \tag{3.33}$$

with $E_R^0 = \dfrac{2D_{\text{DA}}b_{\text{DA}}}{q}$. As an example, we take $\delta = 0.6$ in Figure 3.5, where $D_{\text{DA}} = 2.7\ \text{kcal mol}^{-1}$, $b_{\text{DA}} = 1.45\ \text{Å}^{-1}$, and the charge on the oxygen is $q \cong -0.9e$. This leads to $\Delta R_0 \cong -0.4$ Å for an applied field of 75 MV cm^{-1} (*i.e.*, the applied field compresses the D–A equilibrium position from 3.3 to 2.9 Å). When this simple classical approach is tested against a full quantum calculation,[77] it is seen to provide an excellent approximation for fields below about 40 MV cm^{-1}. Even when the field strength reaches ~80 MV cm^{-1} there is only a ~ 10% underestimate of the equilibrium position shift and, at this point, the electric field-induced compressive force on the D–A subsystem is ~1.1 nN.

Another interaction, which is external to the D–A subsystem, involves the protein conformational force. These compressive forces are significantly weaker than what can be achieved by the action of electric fields. Based on single molecule force–extension studies,[92–94] protein conformational forces, at a maximum, can only reach a few hundred pN. Thus, when attempting to simulate a catalytic proton tunnelling reaction in an enzyme, the application of an electric field external to the $CH\cdots O^q$ sub-system appears to be the most effective way to bring the D–A atoms together in order to significantly counteract the anharmonic repulsion forces.

As discussed further in the following sub-section, a "bare" anharmonic Morse potential specific to SLO can be constructed using the small $CH\cdots O^q$ model system shown in Figure 3.5. This allows DFT calculations to be carried out as a function of D–A separation in order to approximate the D–A interaction energy. Such calculations are efficient because the model system is so small, but the effective charge on the catalytically active oxygen atom should be determined independently using a larger scale DFT calculation of the SLO active site. However, the large scale calculation only needs to be performed once using a simplified substrate (in this case CH_4) at its equilibrium position (see S2 in ref. 77 for a detailed example). The small (~0.1 Å) length scale of the fluctuations around the $CH\cdots O^q$ equilibrium help to make the fixed effective charge approximation reasonable.

The effective charge approximation bypasses the need for a large scale DFT iterative procedure and allows the data to be considered using a simple analytic approach with a well-defined D–A probability distribution. Moreover, when a constant external force, F_{Ext}, is applied to compress the D–A equilibrium distance to generate the tunnelling-active reactant conformation, $\langle r^* \rangle$, it becomes the only adjustable parameter needed to determine the anharmonic potential, $V_{\text{DA}}^{\langle r^* \rangle}(R)$, which generates the tunnelling-active reactant conformational distribution, $P_{\text{DA}}^{\langle r^* \rangle}(R)$. From a data analysis point-of-view, this approach effectively reduces the number of free parameters needed to simulate the experimental measurements. Thus, a simple Morse function fit to the DFT-calculated anharmonic "bare" potential, along with a constant external compressive force, F_{Ext}, offers the experimentalist a significantly improved treatment. This approach includes the D–A repulsion energy and introduces only a single adjustable parameter, F_{Ext}, to fit the tunnelling kinetic data. In comparison, the simple harmonic model has two adjustable parameters, since both the D–A force constant and its equilibrium position are unknown.

3.3.4 Application to Soybean Lipoxygenase

As noted above, when enzymes are involved in CH bond catalysis, there is generally only a very weak interaction between the largely unpolarized

CH bond and a neutral oxygen acceptor atom. The enzyme active site has therefore evolved to "activate" the oxygen atom by helping to build up negative charge on the oxygen so that a stronger $\mathrm{CH}\cdots\mathrm{O}^q$ interaction can be established. For the SLO system, a ferric iron atom binds a hydroxyl group with its proton separately hydrogen bonded to Ile839 (see Figure 3.4). Upon successful PCET from the lipoic acid substrate, the iron is reduced to the Fe^{2+} state and a proton is transferred from C_{11} of the substrate, converting the bound hydroxyl to a water molecule. The activated C_{11} carbon radical on the lipoic acid substrate then undergoes rearrangement into a different pi-bonding carbon radical structure which facilitates a subsequent dioxygenation reaction. Although the negative charge on the iron-bound hydroxyl oxygen ($q \cong -0.9e$) leads to a stronger interaction with the substrate CH group, the ~3.3 Å equilibrium D–A separation of the bare potential (*e.g.*, see $V_{\mathrm{bare}}(R)$ for $\delta = 0.6$ in Figure 3.5) is still too large to simultaneously reproduce the magnitude of the KIE and the temperature dependence of the H/D tunnelling rates.[77,90] On the other hand, by introducing an external compressive force from an electric field that originates outside of the simple D–A subsystem, the data can be explained without resorting to unrealistic effective masses or high D–A frequencies.[77] In earlier work on the SLO system, using a harmonic model for the D–A motion, such accommodations were possibly introduced to help compensate for the linear approximation.[46,54,60,76]

It should also be pointed out that, in order to "fit" the experimental tunnelling data for SLO, the KIE and the temperature dependence of both the H and D tunnelling rates must be duplicated. In addition, the absolute magnitude of the rate should be considered but, in the electronically non-adiabatic limit for enzyme reactions, there are at least two unknown scaling parameters. However, if we use the previously calculated[51] value for $V_{\mathrm{RP}} \sim 1600\ \mathrm{cm}^{-1}$ in SLO, the only remaining adjustable parameter for scaling the absolute rate, is the probability for being in the tunnelling-active reactant conformation, $\langle r^* \rangle$. Because of the large observed KIE ~ 80, we can assume a fast exchange model with a probability factor characterized by $p_{\langle r^* \rangle} = k_+/k_-$. Eqn (3.18), (3.24), and (3.25) can be combined for the $\langle r^* \rangle$ conformation, leading to $k^H_{\mathrm{obs}} = p_{\langle r^* \rangle} \langle k^H_{r^*} \rangle_\ell \cong 300\ \mathrm{s}^{-1}$ for the measured room temperature SLO tunnelling rate.[3] Upon fitting the KIE and its temperature dependence, we find[77] a value for the inherent tunnelling rate for the wild type (WT) SLO enzyme that falls in the range, $\langle k^H_{r^*} \rangle_\ell \cong 3\times10^8 - 3\times10^9\ \mathrm{s}^{-1}$ with $p_{\langle r^* \rangle} \sim 10^{-6}$–$10^{-7}$. Thus, the inherent time constant associated with the tunnelling-active $\langle r^* \rangle$ conformation must be on the order of 0.3–3 ns in order to be consistent with not only the KIE and its temperature dependence, but also with the observed room-temperature rate of $\sim 300\ \mathrm{s}^{-1}$. We conclude that, even for the SLO enzyme system, which has a relatively slow experimentally observed rate constant, the fundamental underlying electronically non-adiabatic tunnelling rate is remarkably fast at room temperature.

The application of a simple anharmonic Morse potential to describe the D–A motion using an adjustable oxygen charge and an external force results in a relatively simple and intuitive method for data analysis. A single DFT calculation that includes a larger active site quantum region can be used to independently evaluate and fix the oxygen charge, allowing the data to be fit by application of a constant external force, $V_{\mathrm{Ext}}(R) = -F_{\mathrm{Ext}}R + \mathrm{const}$. This single additional parameter (F_{Ext}) generates the final D–A subsystem potential and the tunnelling distance distribution needed to fit the kinetic data. In the case of SLO, the charge on the oxygen atom is found by using a quantum region that includes the iron atom and the surrounding amino acids as seen in Figure 3.4, along with a CH_4 donor molecule representing the substrate (more details can be found in the supporting information S2 of ref. 77). When this system is analyzed using DFT, it is found that the net charge on the acceptor oxygen is close to $q \cong -0.9e$. This corresponds to $\delta \cong 0.6$ in the bare model system, $H_3CH\text{–}[OH]^{\delta-}$, where δ is set by altering the proton charge so that the simple model potential for the D–A subsystem mimics the larger SLO active site so that it also carries an oxygen charge of $q \cong -0.9e$.

To go beyond the simple constant external force, a harmonic restoring force can also be applied to the bare D–A Morse oscillator. Such a force can be used to represent the effect of the protein conformation.[77] However, it is important to recognize that the details of the potential, $V_{\mathrm{DA}}^{\langle r^{*}\rangle}(R)$, at larger values of R are not of critical importance in determining the KIE and temperature dependence of the H/D tunnelling rates. This is because nearly all of the tunnelling amplitude is carried in the short-distance tail of the $P_{\mathrm{DA}}^{\langle r^{*}\rangle}(R)$ distribution given by eqn (3.25). (However, one should keep in mind that the absolute rate can be affected to some extent by the behavior of $V_{\mathrm{DA}}^{\langle r^{*}\rangle}(R)$ at larger distances *via* the normalization factor, N, which depends upon the entire distribution).

In the case of wild-type (WT) SLO, it was found that a compressive force in the range of ∼1–2 nN was needed to generate a $P_{\mathrm{DA}}^{\langle r^{*}\rangle}(R)$ distribution consistent with the tunnelling measurements.[77] An example of the bare SLO potential (with $\delta = 0.6$ and $q \cong -0.9e$) along with the application of such a compressive force is given in Figure 3.6 where it can be seen how the $P_{\mathrm{DA}}^{\langle i\rangle}(R)$ distribution can be moved as different external compressive forces (red and blue dashed curves) are applied. A stronger ∼nN force from the electric field (red dashed curve) is needed to generate the $P_{\mathrm{DA}}^{\langle r^{*}\rangle}(R)$ distribution. When fitting the details of the WT SLO tunnelling data, it was concluded that a total compressive force of about 1.3 nN generated the best overall fits to the data[77] and this corresponded to an external electric field magnitude of ∼90 MV cm^{-1}.

Such a force is assigned to an electric field because it is much larger than the maximum (<300 pN) that can be expected from protein conformational forces.[92–94] Thus, depending on the size of a potential protein conformational force that may also be present, an electric field of 60–100 MV cm^{-1}, external to the D–A subsystem that defines the bare potential, is necessary to initiate tunnelling catalysis in SLO. It is tempting to suggest that this field is associated with the active site of SLO because of its consistency with Stark shifts that have been observed within the active sites of other enzymes.[95] On the other hand, it turns out that the charge on the oxygen can also induce a dipole in the polarizable linoleic acid substrate and the resulting dipole can also generate an electric field that acts to compress the D–A equilibrium distance.

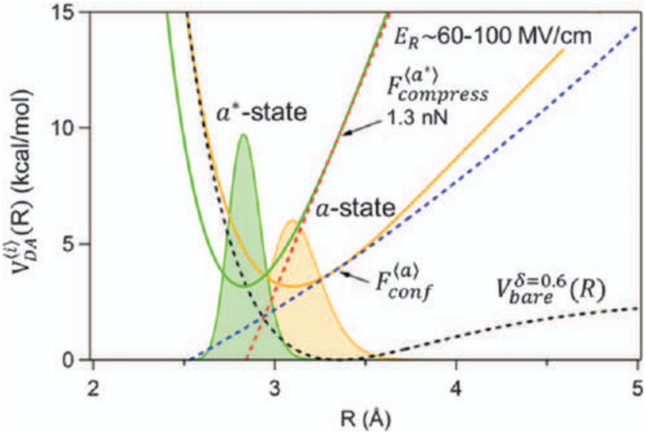

Figure 3.6 An example of a D–A probability distribution for wild type SLO that is consistent with the tunnelling kinetics. The tunnelling-active reactant state distribution (green) is labelled as the a*-state (note that the tunnelling active reactant conformation, $\langle r^* \rangle$, described in the text is labelled as the a*-state in the figure). A representative tunnelling inactive $\langle r \rangle$-state distribution (orange) is labelled in the figure as the a-state. The distributions in the figure are normalized, but if they were weighted with their relative thermodynamic probability, $p_{\langle a^* \rangle}$, the a*-state population would be very much smaller than that of the a-state. A protein conformational force, $F_{\text{conf}}^{\langle a \rangle} \sim 300$ pN, is shown by the blue dashed curve acting in concert with the $V_{\text{bare}}^{\delta=0.6}$ potential (black dashed curve), to generate the inactive a-state distribution. A much stronger compressive force, $F_{\text{compress}}^{\langle a^* \rangle} \sim 1.3$ nN, that arises primarily from an electric field external to the small $\text{CH}\cdots\text{O}^q$ quantum region (as characterized by the bare potential) is shown as the red dashed line. This force acts to "dress" the bare potential, generating the tunnelling-active reactant state distribution that is associated with $\langle a^* \rangle$. The electric field strength is $E_R \sim 90\ \text{MV cm}^{-1}$, and this leads to an average donor acceptor distance, $R = 2.84$ Å, for the $\langle a^* \rangle$ substate distribution of wild type SLO.
Reproduced from ref. 77, https://doi.org/10.1021/acs.jpcb.7b05570, with permission from American Chemical Society, Copyright 2015.

This latter possibility is based on the results of an alternative approach, which utilizes a more complete, large scale, quantum mechanical/molecular mechanical (QM/MM) simulation.[27] Although such an approach is very computer time intensive, it generates important insights into the source of the electrostatic forces that help to reduce the D–A distance, which leads to tunnelling-based catalysis in the SLO system. It is of interest that, when the potential of mean force (PMF) is calculated for the SLO system using a quantum region that encompasses 122 atoms, including the π-backbone of the linoleic acid substrate,[27] there are some encouraging similarities with the bare SLO potential depicted in Figure 3.6. The equilibrium positions for both potentials are found near 3.3 Å and both potentials seem to have a relatively soft structure, at least over the first 0.7 Å of compression. Upon compression from equilibrium, the energy increases to 4.0 kcal mol^{-1} at 2.8 Å and 10.4 kcal mol^{-1} at 2.6 Å for the $V_{\text{bare}}(R)$ potential. The calculated[27]

PMF shows a very similar level of increase upon compression with energies of ∼5 kcal mol^{-1} at 2.8 Å and ∼10 kcal mol^{-1} at 2.6 Å. However, as the D–A compression continues down to ∼2.4 Å there is a distinct hardening of $V_{\text{bare}}(R)$ relative to the PMF calculation.

One of the main insights from this large scale QM/MM calculation[27] is that the π-backbone of the substrate appears to play an important role as a source of the electric field that softens the potential surface as the D–A compression takes place. However, because the defined quantum region of the QM/MM calculation includes the substrate, there is no need to invoke an "external field" because the electrostatic interactions from the substrate π-backbone are already included within the QM boundary. It is noteworthy that when the electric field at the proton between the C_{11} and the iron bound oxygen is computed using the full QM/MM simulation,[27] it is found to be ∼100 MV cm^{-1}, which is very close to the external field of ∼90 MV cm^{-1} that would be required in Figure 3.6 if the protein conformational force was set to zero and the entire external compressive force was attributed to the electric field from the polarized substrate.

The most obvious interpretation of the simple anharmonic model calculation shown in Figure 3.6 is that the ∼90 MV cm^{-1} external electric field results from an ion-induced dipole originating at the substrate that acts to pull it closer to the negatively charged oxygen atom. Essentially, the two pairs of π-bonding carbons, sitting on either side of the aliphatic C_{11} of the linoleic acid, act to make the substrate polarizable and the ensuing electric field (which is external to $V_{\text{bare}}(R)$, the quantum calculated anharmonic bare potential) arises from the induced dipole on the substrate that is created by the negatively charged oxygen atom. Thus, it appears that nature has found an elegant and very efficient solution to implement catalysis. Namely, it uses the substrate polarizability to generate a reactive electric field, rather than having to design and build an evolutionarily expensive active site with a difficult-to-implement charge distribution within the hydrophobic interior of a protein. The charge ($q \cong -0.9e$) on the activated oxygen, combined with the substrate polarizability, evidently generates enough attractive electric field strength to facilitate a sub-van der Waals D–A equilibrium distance in the $\langle r^* \rangle$ conformation. This is what allows the proton tunnelling reaction to proceed and what triggers catalysis in the SLO system.

3.4 Electronically Adiabatic and Vibrationally Non-adiabatic Proton Tunnelling in Biomolecules

3.4.1 Proton Tunnelling Rate Expression Using a Quantized D–A Oscillator

When proton or deuteron tunnelling from D to A occurs along a single double-well ground-state potential energy surface, the theoretical analysis is based on the GR in the electronically adiabatic limit, as expressed by eqn (3.1). The off-diagonal matrix elements that couple the reactant and product states are found when vibrational level degeneracies are accessed along the environmental coordinate, q_s. These matrix elements are characterized as tunnel splittings (Δ_0^{nm}) between the reactant and product vibrational eigenstates (n and m) of the D–A oscillator and, so long as $\Delta_0^{nm} \lesssim k_BT$, the GR can be applied. This criterion is sometimes termed[45] the "proton vibrational non-adiabatic regime", which is commensurate with the so-called "deep tunnelling" process. In the event that electron repulsion is somehow overcome and the tunnelling distance between D and A becomes small enough that the tunnel-splitting starts to exceed k_BT, the adiabatic proton transfer limit is reached where the GR no longer applies.[45] This limit has been discussed elsewhere for the OH···O bond, where it is estimated that the adiabatic regime is accessed when the tunnelling length is on the order 0.4 Å or less (more details can be found in supplementary information S1 of ref. 59 and S8B of ref. 71).

It is important to recognize the differences between the two limits presented by eqn (3.1) and (3.2) as well as to note that a more general treatment, which bridges these two limits, can be found elsewhere.[53] A key point is that there is no electronic coupling term, V_{RP}, that appears in the off-diagonal matrix element in eqn (3.1). This means that the temperature-dependen absolute rate for tunnelling between D and A can be uniquely defined by the nuclear coordinate potentials alone. That is, the experimental observables can be expressed in terms of an equilibrium tunnel distance, the D–A and tunnel particle frequencies and masses, and the environmental coordinate. Because many of these quantities are constrained to a narrow range of possible values for a given type of hydrogen bond in the deep tunnelling regime (*e.g.*, for OH···O), fitting the experimental data on an absolute scale can help to unambiguously determine, or confirm, the remaining parameters.

In eqn (3.1) the GR is expressed in terms of the critically important tunnelling distance, $\ell = R - \bar{l}_c$, as defined by eqn (3.5). While it is certainly possible to average over the D–A coordinate using a classical distribution, as discussed above for the electronically non-adiabatic case, here we will invoke a quantum treatment of the D–A motion using the Einstein oscillator approach (*cf.* Section 3.2.4). In this approach, the D–A quantum oscillator is fully determined by its frequency, $\bar{\omega}_E \equiv \omega_{DA}$, and its reduced mass, μ_{DA}. Thus, the superscript on Δ_0^{nm} in the above paragraph anticipates the fact that the tunnel splitting will depend on both the initial (n) and final (m) vibrational state wavefunctions of the DA quantum oscillator. Our choice of the quantum harmonic treatment, rather than a classical anharmonic treatment, is based on the need to describe the tunnelling kinetics over a very wide range of temperatures. Obviously, at low temperature, the classical picture for D–A motion will fail. Moreover, we use a fully harmonic 2D quantum treatment, where the tunnel particle is also treated harmonically. As noted in Section 3.3.3.1, we do this because of the fortuitous cancellation of errors that is indicated for the OH···O hydrogen bonding situation, where a fully harmonic model has minimal error compared to using an anharmonic potential for the proton vibrational states in combination with a harmonic model for the D–A motion (details can be found in supplementary information S6 of ref. 77).

In Figure 3.1 we show the Duschinsky rotated ground-state potential surfaces that can be solved exactly in the electronically non-adiabatic limit. However, for the adiabatic case, we must solve for the D–A vibrational state-specific tunnel splittings. To do this, the B–O approximation must be invoked as discussed in Section 3.3.1.1, where it is verified by comparison to the exactly soluble electronically case in the electronically non-adiabatic limit. Although the details are presented elsewhere,[59,71] the essence of the calculation is discussed below and refers to Figure 3.1.

In order to find the Q-dependent tunnel splitting, we use the method of Wentzel–Kramers–Brillouin (WKB) at an arbitrary degeneracy for the n and m vibrational states of the D–A oscillator and for the zero-point transition of the high-frequency tunnelling particle oscillator (thus, we are again neglecting the high-frequency vibrational excitations of the tunnelling particle oscillators). The degeneracies occur as dictated by eqn (3.19b) and the state-specific tunnel splitting for the D–A states are found using:

$$\Delta_0^{nm} = \langle n|\Delta_0(Q)|m\rangle = \int \chi_n^R(Q)\Delta_0(Q)\chi_m^P(Q)\mathrm{d}Q \tag{3.34a}$$

with

$$\Delta_0(Q) = \frac{\hbar\omega_q}{\sqrt{e\pi}}\exp\left[-\int_{-a'}^{a'}\frac{|p(Q)|}{\hbar}\mathrm{d}q\right]. \tag{3.34b}$$

where $\pm a'(Q)$ are the Q-dependent turning points along q (for a fixed Q) where the tunnelling begins and ends (see Figure 3.1). For the symmetric R and P potentials, the integral can be halved and solved on either the reactant or the product side. When $V_P(q, Q)$ defines the product side potential, we have:

$$|p(Q)| = \sqrt{2V_P(q,Q) - E_0(Q)} \tag{3.35a}$$

$$V_P(q,Q) = \frac{1}{2}\omega_q^2(q - a(Q))^2 + \frac{1}{2}\Omega_Q^2(Q - Q_0)^2 \tag{3.35b}$$

$$a(Q) \approx \frac{d_0}{2} + (Q - Q_0)\tan\left(\frac{\theta_L}{2}\right)$$

$$E_0(Q) = \frac{\hbar\omega_q}{2} + \frac{1}{2}\Omega_Q^2(Q - Q_0)^2 \tag{3.35c}$$

with $\omega_q \cong \omega_L\cos(\theta_L/2)$ and $\Omega_Q \cong \omega_{DA}$.

Upon performing the tunnel splitting integration for either a potential with a cusp, or with an inverted parabola continuously attached to the top of the barrier, we arrive at an expression for $\Delta_0(Q)$ with two terms. The first term, $\Delta_0^{(1)}(Q)$, is dominant and the second term, $\Delta_0^{(2)}(Q)$, provides a second order correction. For the first term we have:

$$\Delta_0^{(1)}(Q) = \Delta_{eq}\exp[-\alpha(Q - Q_0) - \beta(Q - Q_0)^2] \tag{3.36a}$$

with

$$\alpha \approx \frac{d_0 \omega_q \tan(\theta_\mathrm{L}/2)}{\hbar} \quad \text{and} \quad \beta \approx \frac{\omega_q \tan^2(\theta_\mathrm{L}/2)}{\hbar} \tag{3.36b}$$

$$S_q = \frac{\omega_q d_0^2}{2\hbar} \quad \text{and} \quad \Delta_\mathrm{eq} = \hbar\omega_q \sqrt{\frac{2S_q}{\pi}}\,\mathrm{e}^{-\frac{S_q}{2}}. \tag{3.36c}$$

Note that the mass-weighted equilibrium ($Q = Q_0$) tunnel distance is $d_0 = \sqrt{\mu_\mathrm{L}}\ell_0 \cong \sqrt{m_\mathrm{L}}\ell_0$ and that additional mass dependence is contained within the mixing angle θ_L and the frequency that is defined along q-axis, $\omega_q \cong \omega_\mathrm{L}\cos(\theta_\mathrm{L}/2)$. The use of the continuously attached inverted parabola at the top of the potential barrier between R and P will not be discussed in detail here because, to first order, it simply scales the terms in eqn (3.36b) and S_q in eqn (3.36c) by a factor of $1 - \frac{2b_0^2}{d_0^2}$, where $\pm b_0$ are the transition points between the harmonic potential and the inverted parabola (see supplementary information S7 in ref. 59 for details). Note that, if we take $\frac{b_0}{d_0} = 0.1$, which reduces the harmonic barrier by 20%, the scaling factor is only 0.98. If a quartic potential is used,[59] the calculation leads to a similar expression for $\Delta_0(Q)$, but the parameters α, β, and S_q in eqn (3.36b) and (3.36c) are scaled down by a factor of 2/3, while Δ_eq is scaled by a factor of $\sqrt{6}$. This leads to a much larger tunnelling rate for a given equilibrium tunnel distance, ℓ_0.

After performing a Boltzmann thermal average over initial states (P_n) and summing over final states (m), the result for the factorized 2D QM electronically adiabatic rate is expressed as:

$$k^A_{\ell_0,\omega_\mathrm{DA}} = \sum_n \sum_m P_n \frac{2\pi}{\hbar} \left|\frac{\Delta_0^{nm}}{2}\right|^2 \frac{1}{\sqrt{4\pi\lambda_s k_\mathrm{B} T}} \exp\left[-\frac{\Delta G^\dagger_{nm}}{k_\mathrm{B} T}\right]. \tag{3.37}$$

The final expression for Δ_0^{nm} involves the integration in eqn (3.34a) and (as noted above) it can be written as two terms, $\Delta_0^{nm} = \Delta_0^{nm}(1) + \Delta_0^{nm}(2)$, that are found in the supplementary information of ref. 59. In terms of the mass unweighted zero-point widths of the D–A and tunnel particle wave functions, $\sigma_0^\mathrm{DA} \approx \sqrt{\frac{\hbar}{2\mu_\mathrm{DA}\omega_\mathrm{DA}}}$ and $\sigma_0^L \approx \sqrt{\frac{\hbar}{2\mu_\mathrm{L}\omega_\mathrm{L}}}$, and making the small mixing angle approximation, $\frac{\theta_\mathrm{L}}{2} \approx \sqrt{\frac{\mu_\mathrm{L}}{4\mu_\mathrm{DA}}}$, we define

$$y_0 = \frac{-\eta\sigma_0^\mathrm{DA}\ell_0}{4\sqrt{2}(\sigma_0^L)^2} \quad \text{with} \quad \eta = \sqrt{\frac{4(\sigma_0^L)^2}{4(\sigma_0^L)^2 + (\sigma_0^\mathrm{DA})^2}} \tag{3.38}$$

so that to a good approximation:

$$\Delta_0^{nm}(1) = \frac{\Delta_{\text{eq}}\eta e^{y_0^2}}{\sqrt{2^{n+m}n!\,m!}}\left\{\sum_{k=0}^{\min(n,m)} 2^k k!\binom{m}{k}\binom{n}{k}(1-\eta^2)^{\frac{m+n}{2}-k}H_{m+n\pm 2k}\left[\frac{-\eta\ell_0}{4\sqrt{2}\sigma_0^L}\right]\right\} \tag{3.39}$$

where $H_n(x)$ are the Hermite polynomials and $\binom{n}{k} = \frac{n!}{k!(n-k)!}$ are the generalized binomial coefficients.

In Figure 3.7 we display some examples of the temperature-dependent electronically adiabatic proton tunnelling rate for parameters that might be considered typical for a OH···O hydrogen bond. Here it can be seen that the rate for the quartic potential is very much larger than the rate for the harmonic potential, either with a cusp or with a continuously attached inverted parabola spanning 20% of the intersection region. For the quartic potential, a much longer equilibrium tunnel distance (~1 Å) is needed to reduce the tunnelling rate to the level that is found using the harmonic or quasi-harmonic potential.

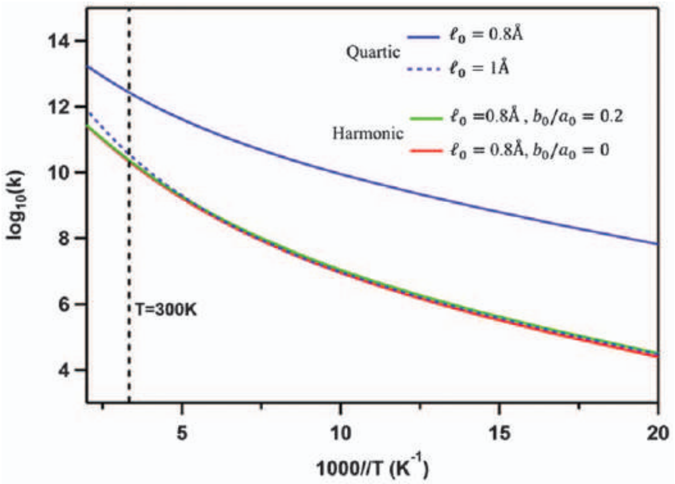

Figure 3.7 Comparison of electronically adiabatic rates using different potentials to describe the proton tunnelling coordinate: harmonic with cusp (red), harmonic with an inverted parabola (green), and the quartic (blue). The parameters common to all curves are $\omega_H/2\pi c = 3200$ cm^{-1}, $\omega_H/2\pi c = 200$ cm^{-1}, $\mu_{DA} = 8m_H$, $K_{\text{vib}} = 19$ N m^{-1}, $\lambda_s = 2000$ cm^{-1}, $\Delta G^0 = -500$ cm^{-1}, $\Delta G_{nn}^{\ddagger} = 280$ cm^{-1}. The solid curves all use $\ell_0 = 0.8$ Å, while the dashed curve for the quartic potential uses $\ell_0 = 1$ Å in order to decrease the PT rate so that it is similar to the results from the harmonic potentials (the longer ℓ_0 compensates for the lower barrier). For the harmonic potential with an inverted parabola, $b_0/a_0 = 0.2$. The use of the quartic potential with $\ell_0 = 0.8$ Å may enter into the proton-level adiabatic regime during D–A compression.
Reproduced from ref. 59 with the permission of AIP Publishing, Copyright 2015.

The details of the calculations of the tunnel splitting in various potentials can be found elsewhere[59] in the supplementary material.

3.4.2 Kinetic Isotope Effect in the Electronically Adiabatic Limit

We can use eqn (3.36) and include both terms, $\Delta_0^{nm} = \Delta_0^{nm}(1) + \Delta_0^{nm}(2)$, to find the dependence of the 2D tunnelling rate on the mass of the tunnelling particle in order to generate the KIE. The room-temperature KIE values for the electronically adiabatic 2D quantum model of the OH$\cdots$O bond are calculated as a function of the equilibrium tunnel distance and the D–A force constant (or, alternatively, the DA frequency $\omega_{\mathrm{DA}} \equiv 2\pi c\tilde{\nu}_2$) and this information is presented in Figure 3.8a. The bottom panel shows the temperature dependence of the KIE for several combinations of the equilibrium tunnel distance and the D–A force constant. In addition to the obvious mass dependence of the tunnel particle frequency, ω_{L}, the KIE also depends upon μ_{DA} because this reduced mass affects the values of θ_H and θ_D (where $\theta_{\mathrm{L}} \approx \sqrt{\mu_{\mathrm{L}}/\mu_{\mathrm{DA}}}$). The KIE will be reduced for larger angles (smaller μ_{DA}) because shorter tunnel distances become accessible, making the rate less sensitive to the mass of the tunnelling particle. It should be noted that we are assuming a fixed protein conformation in this analysis so, in the classical limit for D–A motion, this would correspond to $K_{R_0} \gg K_{\mathrm{vib}}$ in eqn (3.16a) so that $K_{\mathrm{eff}} = K_{\mathrm{vib}}$.

Notice that, for a tunnel distance of $\ell_0 = 0.8$ Å, a KIE of $\lesssim 10$ is found when the force constant, K_{vib}, is in the range below ~25 N m^{-1} (for $\mu_{\mathrm{DA}} = 8\mu_H$ the upper axis shows the D–A frequency is $\lesssim 230$ cm^{-1} in this region). This occurs because a softer D–A force constant allows for greater thermally induced sampling of shorter tunnel distances. This increases the energy splitting and tunnelling probability, making it less sensitive to the mass of the tunnelling particle. It is also worth noting the large magnitude of the room-temperature tunnelling rates ($\gtrsim 10^{10}$ s^{-1}) shown in Figure 3.7, where $K_{\mathrm{vib}} = 19$ N m^{-1} and the D–A separation is ~2.8 Å and $\ell_0 \cong 0.8$ Å. This suggests that kinetically rapid deep proton tunnelling at room temperature may be a relatively common occurrence, even though very large KIEs are not necessarily observed.

Finally, the explosive growth of the room-temperature KIE can be seen in the upper panel of Figure 3.8 as a function of the D–A frequency and $K_{\mathrm{eff}} = K_{\mathrm{vib}}$. For $\ell_0 = 0.8$ Å, a D–A frequency shift from only 220 cm^{-1} to 290 cm^{-1} (as K_{vib} varies from about 23 to 42 N m^{-1}) reduces the thermal excitation of the D–A oscillator and narrows the spread of its wave-function enough that the KIE is increased from ~10 to ~50.

3.4.3 Application of the Electronically Adiabatic 2D Quantum Model to the Ground State Proton Transfer in GFP

As a final example of the measurement and analysis of proton tunnelling in a biological system, we turn to recent observations of the ground-state thermally activated proton "reset" reaction in GFP. GFP provides an excellent

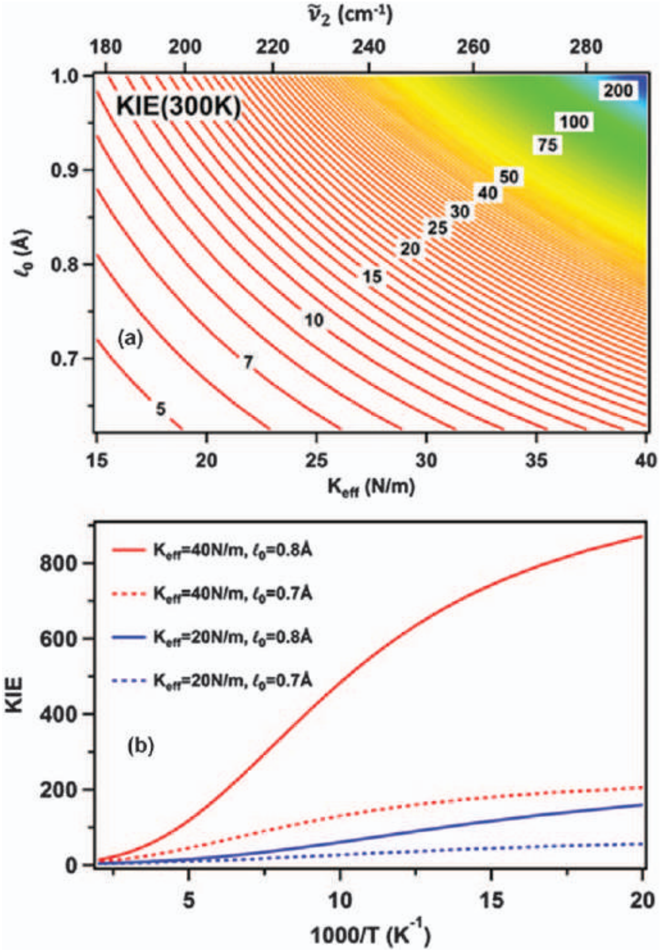

Figure 3.8 The KIE (k_H/k_D) for the electronically adiabatic QM model using eqn (3.37) with parameters $\omega_H/2\pi c = 3330\ \text{cm}^{-1}$, $k_1 = 659\ \text{N m}^{-1}$, $\mu_{\text{DA}} = 8m_H$, $b_0 = 0$, $\lambda_s = 1200\ \text{cm}^{-1}$, $\Delta G^0 = -600\ \text{cm}^{-1}$, and $\Delta G^{\ddagger}_{\text{nn}} 75\ \text{cm}^{-1}$ [from eqn (3.19b)]. Panel (a) presents the KIE at $T = 300$ K as a function of ℓ_0 within a single conformation where $K_{\text{eff}} = K_{\text{vib}} = \mu_{\text{DA}}\omega_{\text{DA}}^2$. The upper axis depicts $\tilde{\nu}_2 \equiv \omega_{\text{DA}}/2\pi c$. Panel (b) shows the temperature dependent KIE for several combinations of $K_{\text{eff}}(=K_{\text{vib}})$ and ℓ_0. For $K_{\text{eff}} = 40\ \text{N m}^{-1}$, we have $\omega_{\text{DA}}/2\pi c = 290\ \text{cm}^{-1}$; and for $K_{\text{eff}} = 20\ \text{N m}^{-1}$, $\omega_{\text{DA}}/2\pi c = 205\ \text{cm}^{-1}$. Reproduced from ref. 59 with the permission of AIP Publishing, Copyright 2015.

model system for experimental study because the reaction can be triggered by a laser light pulse, which initiates ultrafast excited state proton transport from the excited A*-state to the fluorescent I*-state. However, after the relatively rapid (~3 ns) spontaneous radiative population transfer from I* back to the ground-state (I) surface, the protons in the short transport chain return to their initial donors *via* a I → A ground-state reaction (the GFP I-state proton configuration can be seen in Figure 3.10A). Because this cycle is completed on the ns-μs timescale, it can be pumped repetitively, which leads to very accurate pump–probe averaging using high-frequency lock-in methods.[96] This approach allows the time-dependent populations of the entire photocycle to be interrogated as a function of temperature.[71]

Figure 3.9 presents the population kinetics of GFP as the system moves through the photocycle at 200 K. The solid red lines represent global fits to the kinetic progress for the protonated and deuterated reactions. In order to extract accurate time constants and amplitudes, it is important to perform the fit across the complete logarithmic timescale as described elsewhere (supplementary discussion S1 of ref. 71). Following the 0.15 ps pump pulse at 405 nm in Figure 3.9, the initial A-state moves to the A* photoexcited state; however, the ~3 ps probe pulse is located at 420 nm, the isosbestic point between A and A*, so no change is apparent in the first few picoseconds. Note that time-zero, t_0, has also been arbitrarily shifted by 3 ps in order to depict the probe-before-pulse ($t < 0$) data on the log time axis. Additional

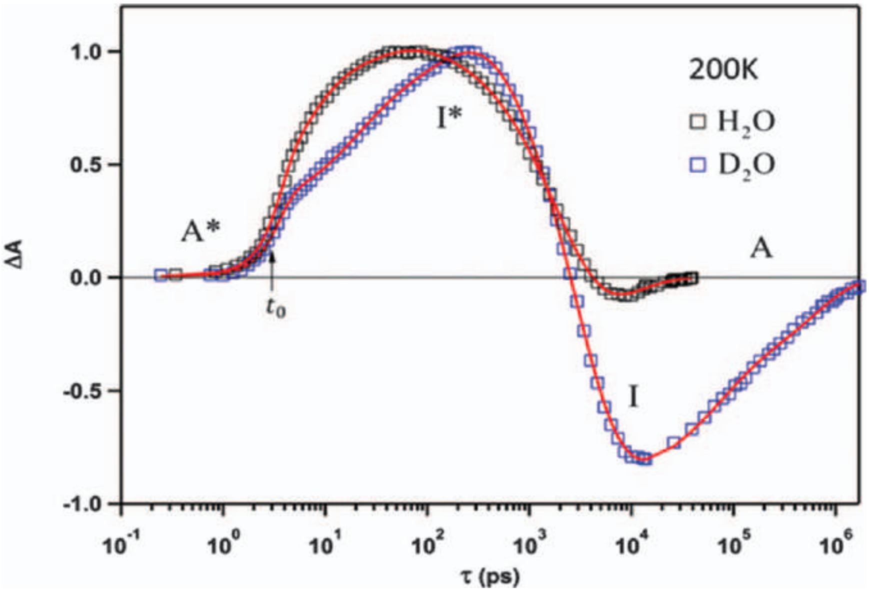

Figure 3.9 Comparison of the full proton transfer cycle kinetics of GFP using H_2O and D_2O probed at 420 nm and 200 K. The solid red lines are global fits to the data and the time axis is $\tau = t + (3ps - t_0)$. The arrow locates the time-zero, t_0, which is arbitrarily shifted to 3 ps to reveal the data at negative times. This verifies that the probe before pump signal is zero. The isosbestic point between states A and A* is located at 420 nm so there is no contribution to $\Delta A(t)$ from this transition, however the kinetic progress through the rest of the photocycle, from A* to I*, from I* to I, and from I back to A can be seen in the log–time figure.
Reproduced from ref. 71 with permission from Springer Nature, Copyright 2016.

experiments probing at the isosbestic point between A and I* reveal the same kinetic time constants (supplementary discussion S3 of ref. 71).

The growth of the I* excited state in Figure 3.9 can be seen to take place in a few tens of picoseconds for the H_2O sample and it is slowed by a factor of 5–10 after exchange with D_2O. The ensuing I* → I population transfer, measured using the pump–probe absorption technique, is in very good agreement with the independent measurements of the lifetime that directly monitor the fluorescence. In addition, the n^2 index of refraction correction to the local field and the radiative rate, upon going from an aqueous to a 50% glycerol solvent, is also determined with very good accuracy, indicating that the error in the kinetic rate determinations falls within the range of ~5%.

The process that is of most relevance to the development presented here is the final, thermally driven, ground-state reaction associated with proton reset from the I-state to the A-state where the protons on O_2, O_3, and O_4 move to O_1, O_2, and O_3, respectively (as can be discerned from Figure 3.10A). At 200 K, the ground-state rates involving proton *vs.* deuteron transport are found to vary by about a factor of 70. Although it is difficult to see in Figure 3.9, there is a residual overlap between the I* → I and I → A kinetics (particularly in H_2O at $T \geq 200$ K) and this re-emphasizes the need for a global kinetic fitting process. At room temperature, the I → A proton reaction speeds up to the point that it completely underlies the I* → I reaction and therefore it becomes unobservable, so long as the spontaneous emission process governs the I* → I population transfer. This limitation was overcome by Kennis *et al.*[97] who used a pump-dump-probe protocol and stimulated emission to bypass the spontaneous I* → I transition at 298 K. This early experiment revealed a room temperature I → A kinetic rate of $(400\ \mathrm{ps})^{-1}$ for proton transport but, for technical reasons, it was unable to reliably measure the much slower deuteron transport, which would have revealed the tunneling reaction.

Although there are three protons and three pairs of donors and/or acceptors in the GFP reset reaction, all of the donors and acceptors, except the serine 205 residue, naturally support a proton ionization reaction. The ionization resistant hydroxyl of S205 in the GFP system has a pK_a of ~16 and is hydrogen bonded to a neutral water molecule that must accept the S205 proton in the reset step. There is such a high classical barrier for the transport of this proton that the tunnelling channel between S205 and water offers the fastest route. Thus, the tunnelling reaction from O_3 to O_2 (Figure 3.10A) becomes the rate-limiting step that initiates a three-proton *asynchronous* concerted transport process in GFP.

Various two- and three-proton *synchronous* concerted tunnelling scenarios have also been considered, but such scenarios call for an effective tunnelling path length that is longer, leading to predicted rates that are many orders of magnitude slower than the experimentally observed absolute rates (details can be found in supplementary discussion S7 of ref. 71). A schematic of the GFP proton wire showing the I-state is depicted in Figure 3.10A along with the Einstein frequencies in Figure 3.10B that are extracted from the normal mode analysis using an approach analogous to eqn (3.10) and (3.11).

A calculation of the "power spectrum" for correlated three-atom motion (*e.g.*, defined using the symmetric compression shown at the bottom of Figure 3.10C) is needed to evaluate a synchronous vibrationally assisted tunnelling model. In this approach, we extracted the normal modes with components that supply the required simultaneous compression of the three selected oxygen atoms labelled (i, j, k) as depicted in Figure 3.10C. The mode-specific MSDs are then used to generate a power spectrum. As might be expected, the Einstein oscillator for such motion is found at a much lower frequency than for the simple one-proton vibrationally assisted tunnelling process (Figure 3.2) where the frequency accurately predicts the T-dependence of the tunnelling rate (Table 3.1). The frequency associated with two-

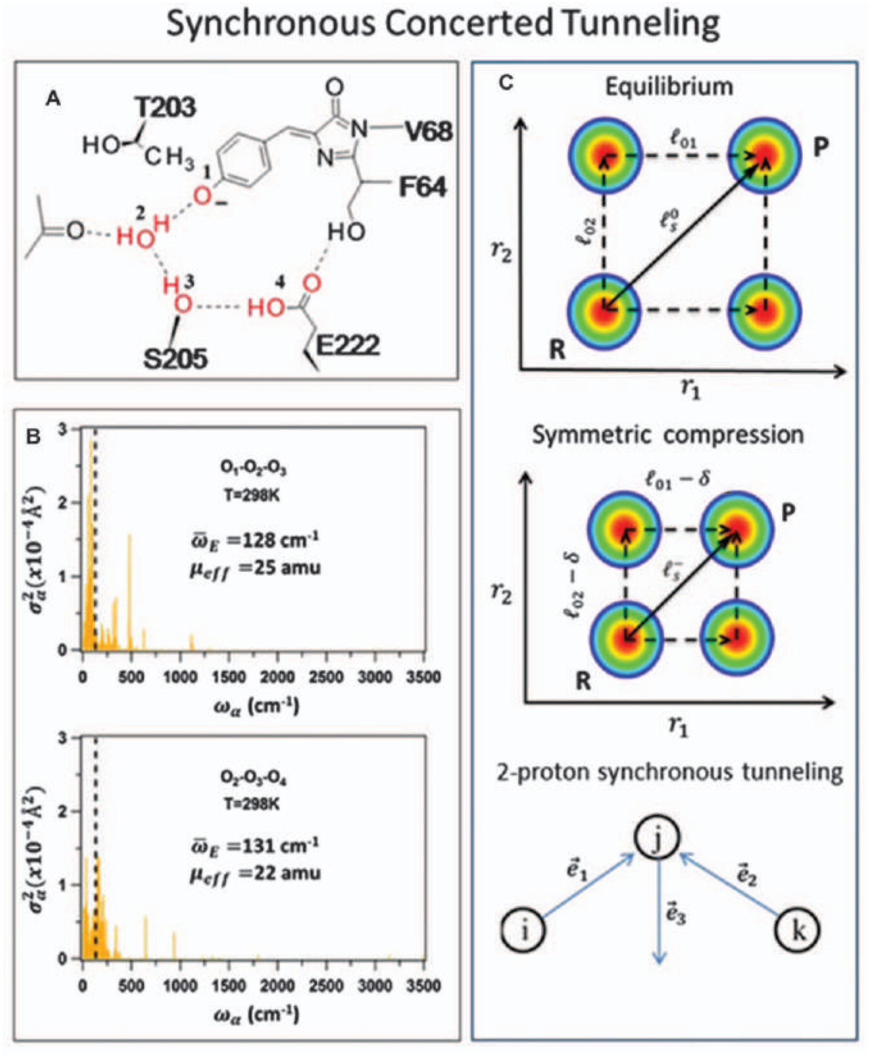

proton synchronous tunnelling will be further depressed by inclusion of the three-atom bending motions, and the three-proton synchronous tunnelling frequency will be depressed still further. These considerations indicate that such models will involve a much stronger temperature dependence in the kinetics than is observed experimentally. Moreover, as also depicted in Figure 3.10C, the effective synchronous tunnelling path length, ℓ_s^0, is also be expected to be significantly larger than the ~0.7 Å individual tunnel lengths (ℓ_{01} and ℓ_{02}) determined from the oxygen–oxygen distances in the I-state.[74] In addition, the longer charge transport distance associated with a synchronous two- or three-proton tunnelling reaction would be expected to generate a large reorganization energy. Thus, we conclude that, although the three-proton transport reaction likely involves *concerted* over-barrier proton hopping of the other protons in the wire, the observed kinetic rate is slaved to the single-proton tunnelling event between the serine (O_3) and water (O_2) oxygen atoms. Such a scenario is consistent with asynchronous nuclear motion of the remaining atoms in the proton wire.

It should also be noted that a suggestion has been made[98] concerning the possibility of water molecules entering the active site of GFP at room temperature and bypassing the important serine residue shown in Figure 3.10A. However, this suggestion is based on molecular dynamics (MD) simulations

Figure 3.10 (A) The schematic arrangement of the GFP chromophore and the amino acids that comprise its ''proton wire''. The protons are shown in the I-state, prior to transfer to the A-state. The four oxygen atoms that play the role of donor and acceptor are labelled 1–4 and the dynamics of these atomic positions can be analyzed using the full set of GFP normal modes.[59,74] This allows extraction of the MSD-based ''power spectrum'' that moves the various oxygen atoms together in a manner that allows for one-proton asynchronous or multiple-proton synchronous concerted proton tunnelling. (B) The effective Einstein frequencies that offer the possibility of the synchronous tunnelling of two protons between three oxygens (1–3 or 2–4) are shown as the vertical dashed lines and are found to be much lower than the vibrational frequency needed to fit the experimental kinetic data. (C) A schematic showing a symmetric vibrational compression, involving three oxygen atoms and (implicitly) two protons, as would be needed to vibrationally assist a two-proton synchronous tunnelling process. Here, it can be seen that the effective pathway from R to P leads to an overall tunnel length (ℓ_s^0) that is elongated relative to a single proton tunnelling event (ℓ_{01} or ℓ_{02}). A more realistic symmetric mode can be used to define unit vectors for compressive enhancement, as shown at the bottom of panel C. This allows the transformed Cartesian vibrational motions of each normal mode of GFP to be projected onto the compression, generating the MSD power spectrum for vibrationally assisted two-proton *synchronous* concerted tunnelling (panel B). In contrast, for the case of one-proton *asynchronous* concerted tunnelling, the other (non-tunnelling) protons are able to follow the tunnelling proton in a concerted fashion *via* a very rapid over-barrier hopping process. In this case, the rate-limiting step and the KIE depend only on the tunnelling between a single hydrogen bonded pair of oxygen atoms.

that do not consider tunnelling and cannot allow a residue such as serine to participate in a water-based proton wire. Moreover, it is important to emphasize that the putative water wire (*i.e.*, where the serine residue is bypassed) is not consistent with either the large KIE that is experimentally observed or with the Laue crystal structures that show no evidence of additional waters in the vicinity of the GFP proton wire at room temperature (J. van Thor, private communication).

The use of the absolute rate measurement in the above analysis again points to the importance of recognizing that, for electronically adiabatic tunnelling reactions, there is no electronic coupling parameter, V_{RP}, available to scale the rate. This helps to place tighter constraints on the remaining model parameters. More generally, the parameter that typically has the most freedom in these models is the environmental barrier height, $\Delta G_s^{\ddagger}$ or, alternatively, the environmental reorganization energy in conjunction with the reaction free energy [*e.g.*, see the expression for $\Delta G_s^{\ddagger}$ following eqn (3.1)]. The other parameters needed to predict the electronically adiabatic proton-tunnelling rate are generally well constrained. For example, the average tunnel distance for the $\mathrm{OH}\cdots\mathrm{O}$ bond is typically $\ell_0 \sim 0.7$–0.8 Å and the OH oscillator frequency is $\omega_H \sim 3200$–$3400\ \mathrm{cm}^{-1}$ and its correlation with H-bond length (and therefore the tunnelling distance) has been measured experimentally.[99] This means that ℓ_0 and ω_L are not independent parameters. In addition, the frequency and reduced mass of the Einstein oscillator governing the D–A motion can be constrained by the calculation discussed in Section 3.2.4 and shown in Figure 3.2. The reduced mass of the tunnel particle oscillator is, to a good approximation, given by $\mu_L \cong m_L$ so, along with μ_{DA}, the Duschinsky rotation angles are well determined. Finally, the free energy of the reaction, ΔG^0, has been found independently for GFP,[71] so there are essentially no other free parameters needed to predict the proton tunnelling rate for this $\mathrm{OH}\cdots\mathrm{O}$ system.

In Figure 3.11 we present the kinetic data for the I → A proton reset reaction in GFP over a very wide temperature range. The red lines through the data are the result of a global fit using eqn (3.36) (more detail of the fitting process can be found in the supplementary discussion S6 of ref. 71) with parameters listed in Table 3.1. The tunnel particle oscillator frequency ($\omega_H/2\pi c = 3330\ \mathrm{cm}^{-1}$) was fixed to the experimentally determined[99] correlation with $\bar{\ell}_0 = 0.78$ Å (supplementary information S1 in ref. 59 also displays a fitted plot of the frequency and tunnel–distance correlation[99]). A very small global distribution in the tunnel length distribution, $\sigma_{R_0} = \sigma_{\ell_0} = 0.02$ Å, was also allowed[71] in order to account for the small deviation of the I → A kinetics from a pure exponential response (details of the fits to experimental data can be found in supplementary discussion S6 of ref. 71). Because GFP has such a rigid beta-barrel structure, it is one of the most stable proteins known.[72] Thus, the very small disorder and relatively slow conformational exchange times ($\tau \gtrsim \mu$s) are both reasonable and expected. This highly ordered property also allows us to set $p_{\langle r^* \rangle} \cong 1$ for GFP, in contrast to the situation encountered with enzymes.

A key parameter derived from the fitting procedure is $\omega_{DA}/2\pi c = 273 \pm 7\ \mathrm{cm}^{-1}$, which is very close to the value found for the Ser-OH—OH_2 Einstein oscillator discussed in Section 3.2.4. The uncertainty given for this frequency derives ultimately from our choice of the reduced mass for the D–A subsystem. We have noted the weak temperature dependence of μ_{DA} and used the values found at 160 K (8.1 amu) and at 298 K (8.8 amu) as uncertainty limits. Thus, we set a generous error margin for $\mu_{DA} = 8.5 \pm 0.5$ amu and, upon fitting the data by fixing μ_{DA} at either 8 amu or 9 amu, the various error limits emerge for the other parameters denoted in Table 3.1.

Generally, the fits are very satisfying and we emphasize that the magnitude of the absolute rate has not been artificially scaled for either the proton or deuteron kinetics. The grey zone in Figure 3.11 depicts the region of temperatures that are normally probed in biologically relevant proton tunnelling reactions, so it can be appreciated that the experiments presented in the figure span a much wider temperature range than previously examined. The experimental details for performing such experiments at cryogenic temperatures are given elsewhere.[71] The open diamond in Figure 3.11 represents the room-temperature

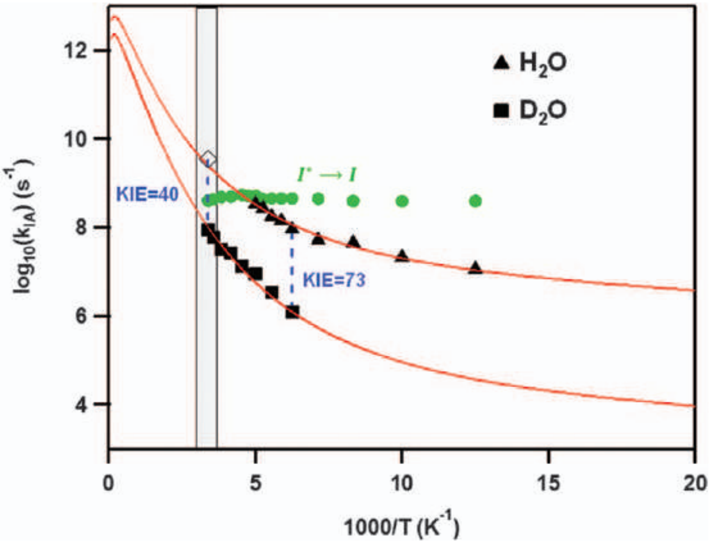

Figure 3.11 Arrhenius plot of the ground-state ($I \rightarrow A$) proton transfer kinetics of GFP. The typical temperature range for studies of biological proton transport is shaded in grey. The rate for the H_2O samples (in 50% glycerol buffer) increases at higher temperature and becomes inseparable from the 3 ns $I^* \rightarrow I$ population transfer due to fluorescence decay (green dots). The apparent decrease of these $I^* \rightarrow I$ rates at higher temperature in H_2O is due to the underlying oppositely signed $I \rightarrow A$ process. A measurement at room temperature using the pump-dump-probe method is shown with the open diamond. The experimental KIEs of 73 (160 K) and 40 (298 K), are depicted by the blue dashed lines. The global fits to the kinetic data, using the two-dimensional QM model, described in Section 3.4.1 [eqn (3.37)], are shown as the red lines. The fitting parameters are listed in Table 3.1.
Reproduced from ref. 71 with permission from Springer Nature, Copyright 2016.

Table 3.1 Parameters for ground-state proton-tunnelling kinetics in GFP.

Parameter	Value	Description
Unconstrained		
$\Delta G^{\ddagger}_{nn}$	54 ± 3 cm^{-1}	Environmental barrier
Constrained[a]		
$\omega_{DA}/2\pi c$	273 ± 7 cm^{-1}	D–A mode frequency (fit)
$\bar{\ell}_0$	0.78 Å ($\sigma_{\ell_0} =$ 0.02 Å)	Equilibrium tunnel distance
Fixed[b]		
$2b_0/d_0$	<0.2	Width of inverted parabola
ΔG^0	-665 cm^{-1}	Free energy of $I \rightarrow A$ reaction
$\omega_H/2\pi c$	3330 cm^{-1}	OH mode frequency
μ_{DA}	8.5 ± 0.5 amu	Reduced mass of D–A mode
θ_H	$19.2^\circ \pm 0.5^\circ$	Duschinsky rotation for H
θ_D	$26.5^\circ \pm 0.7^\circ$	Duschinsky rotation for D
χ^2_{red}	8.0×10^{-3}	Reduced chi-squared

[a] The value of $\bar{\ell}_0$ is constrained by X-ray data and I-state ONIOM minimization and σ_{ℓ_0} is the width of $\bar{\ell}_0$ distribution. The value of $\omega_{DA} \cong \bar{\omega}_E$, is constrained to 264–289 cm^{-1} as calculated and shown in Section 3.2.4.

[b] The O–H frequency of the proton, ω_H was correlated[99] to the O–O distance and fixed by the value of $\bar{\ell}_0$. The parameter b_0 locates the attachment of a continuous inverted parabola at the top of the barrier. The effect is negligible on the other fitting parameters if $2b_0/d_0 < 0.25$. The measurements of $\Delta G^0 \equiv \Delta G^0_{IA}$ are presented elsewhere[71] and yield $\lambda_s = 1165$ cm^{-1}. The effective mass for the D–A oxygen motion is $\mu_{DA} \cong 8.5 \pm 0.5$ amu (Section 3.2.4). The rotation angles are given by $\theta_L \cong \sqrt{\mu_L/\mu_{DA}}$. The uncertainty in μ_{DA} generates uncertainty in the other parameters as noted in the table.

I → A proton transport rate found using pump-dump-probe protocol.[97] Finally, the green dots show the extracted rates for the I* → I spontaneous radiative population transfer in H_2O. This rate is expected to be independent of temperature with a time constant of $\tau_{I^*I} \cong 3$ ns. However, near room temperature the rate constants found using the global fitting procedure, begin to show slightly depressed values as seen in the figure. This is due to the oppositely signed I → A absorbance change in H_2O that underlies, and begins to interfere with, the I* → I absorbance change at these higher temperatures. Because of this problem we cannot extract reliable I → A proton rates for temperatures above ~200 K. Similarly, at very low temperatures ($\lesssim$160 K), it becomes difficult to extract the I → A deuteron rate because it becomes too slow to measure with a pump–probe system operating at 200 kHz (~5 μs).

However, even given the experimental limitations and the relatively simple theoretical model that is being applied, there appears to be solid agreement between the analytic theory and the GFP kinetics experiment, which is very encouraging. The results indicate that room-temperature deep tunnelling in the charge neutral OH···O system, using typical values for H-bonding distances and frequencies, leads to a surprisingly rapid (~400 ps) room-temperature tunnelling process. In the case of GFP, this involves proton tunnelling between the ionization resistant serine residue and a neutral water molecule.

Given that serine and threonine residues are often found in the vicinity of proton ''wires'' in proteins,[28,100–104] we have suggested that they are likely participants in such wires, even though these residues are often modeled out of classically based proton transport calculations. Because the classical MD calculations are not able to include the QM tunnelling process, the energetically expensive classical ionization potential improperly precludes such residues as active participants in water wires. On the other hand, the ∼400 ps room-temperature tunnelling time constant, while much slower than a typical picosecond timescale proton hopping rate, is still fast enough to be relevant for many biological processes.

This has led to the suggestion[71] that neutral residues like serine and threonine should be considered as active tunnelling elements in certain biologically relevant proton wires,[28,105,106] particularly where pumping against a proton gradient is required. The presence of serine in the proton wire is established for the GFP system, where both the wire structure[73] and the tunnelling process[71] have been observed experimentally. Residues such as serine and threonine can act to stabilize water-based proton wires in proteins but potentially, and more importantly, by participating as active elements in the ''wire'', they can also maintain proton pumping directionality *via* kinetic trapping processes that involve tunnelling. This latter attribute emerges when (over a given timescale) the tunnelling rate in one direction is significantly larger relative to the tunnelling rate in the opposite direction. Such a scenario is depicted in Figure 3.12 and relies on the fact that the two water molecules, located on either side of a putative serine residue in such a wire, must act separately as donor and/or acceptor in the forward and reverse tunnelling directions. This offers the possibility that a small (∼tenths of Å) difference in the forward (ℓ_d) and reverse (ℓ_u) tunnelling distances will lead to rate limiting forward and reverse asynchronous concerted tunnelling processes that can differ by *orders of magnitude*. This will generate a kinetic trap that helps to move the protons in a preferred direction. Moreover, such a distance differential would also help to drive a H-bonding reorientation reaction, involving the serine and the water molecules, as indicated by the blue arrows in Figure 3.12c. The H-bond reorientation will be enabled because the serine H-bond will prefer the shorter (more energetically stable) of the two H-bonding possibilities offered by the adjacent water molecules. The reorientation reaction will also act to definitively trap the proton on the downstream side of the serine residue. This reorientation process is crucial because it is needed to fulfill the fundamental ''reset'' requirement that must occur in order to allow repetitive and quasi-continuous proton pumping along water-based proton wires.[71]

3.5 Conclusion

This chapter has attempted to outline several different analytic approaches to help experimentalists analyze kinetic data sets that involve the tunnelling of protons. The relatively straightforward (and mostly analytic) calculations presented here predict surprisingly fast ground-state proton-tunnelling rates for biological systems at room temperature, and this is borne out by the experimental measurements. Both the electronically adiabatic tunnelling in the GFP proton wire and the electronically non-adiabatic tunnelling in the SLO enzymatic reaction indicate that proton tunnelling takes place with inherent time constants that fall within the nanosecond or sub-nanosecond regime. The relatively slow *experimentally observed* rate for SLO is a consequence of eqn (3.18) and the very small probability for the enzyme to occupy the tunnelling-active reactant conformation, $\langle r^{*}\rangle$. Further inspection of eqn (3.18) illustrates the point that for very rapid tunnelling rates, $\langle k_{r^*}{}^{L}\rangle_{\ell} \gg k_{-}$, there is a significant possibility for the masking of tunnelling processes due to slow conformational interconversions. More traditional masking occurs in biological systems when there are additional rate limiting biochemical reactions that control the observed experimental rates. The possibility of "conformational masking" suggests that the proton tunnelling step in many biologically relevant reactions may not be detected by isotopic

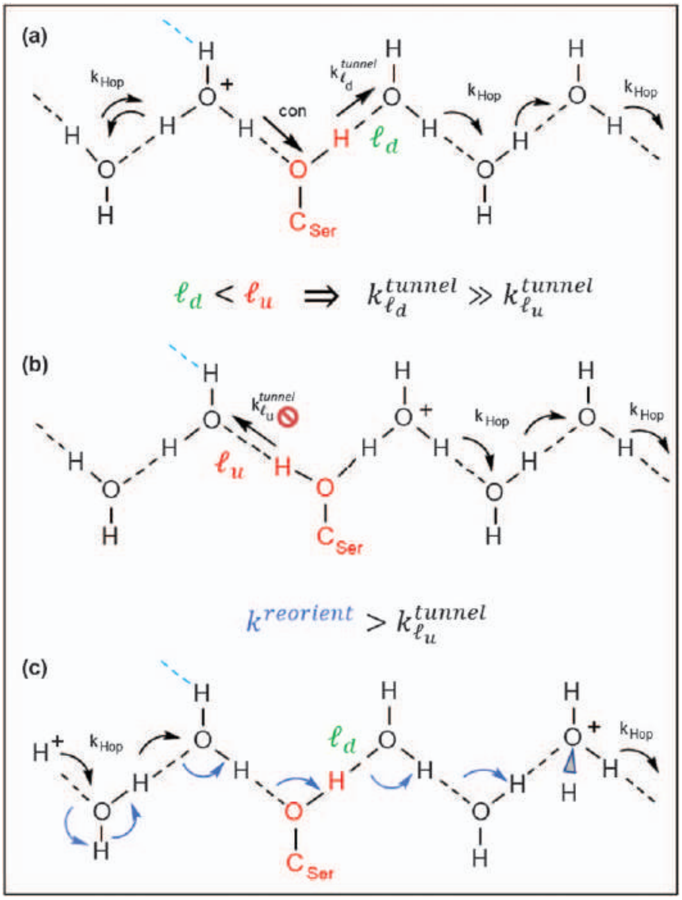

substitution and that much more proton tunnelling may be taking place in biological systems than is currently appreciated.

One new and important area where proton tunnelling on such a rapid timescale could play a crucial role involves proton pumping against a pH gradient along water wires within proteins that are embedded in membranes. Because proton tunnelling is super-exponentially sensitive to the

---

Figure 3.12 A schematic showing how protons undergoing picosecond hopping on a protein water wire can be controlled and biased by insertion of an ionization-resistant OH group of serine (or threonine) into the wire, as found in GFP. For example, if (on average) the "downstream" tunnelling distance, ℓ_d, is only slightly shorter than the "upstream" tunnelling distance, ℓ_u, it will lead to significant differences in the upstream and downstream tunnel splittings, $\Delta_0(\ell)$, which will affect the relative tunnelling rates by orders of magnitude. Such a small distance differential, on the order of $\lesssim 0.1$ Å could arise from protein architecture that induces steric constraints or supplies an additional H-bond to the upstream water molecule (*e.g.*, blue dashed lines in the figure). Such a situation can lead to kinetic trapping and bias the direction of proton flow "downstream" over relatively long timescales. In (a), the proton on the hydronium ion sits upstream of the serine residue (C_{Ser}–OH) where it can take part in an asynchronous concerted tunnelling process (arrows denote the rate-limiting $k_{\ell_d}{}^{\mathrm{tunnel}}$ and the concerted H^+ hop, labelled "con"). This moves the proton (hydronium ion) to the downstream side of the serine residue as shown in part (b). The hydrogen bonding direction is then reversed so the serine proton now points upstream. The proton (hydronium ion) will be trapped downstream of the serine because the upstream tunnelling distance ($\ell_u > \ell_d$) significantly slows the upstream tunnelling rate as denoted by the red "not allowed" symbol. In addition to slowing the upstream tunnelling rate, this condition also dictates that the stronger serine hydrogen bond occurs when it points downstream (*i.e.*, because it is shorter). The system is therefore stabilized for the downstream orientation and this property aids the reorientation (k^{reorient}) of the H-bonding in the proton wire as schematically depicted by the blue arrows in part (c). This reorientation reaction is a necessary condition for repetitive proton pumping even if the wire is composed only of water molecules. It is also worth noting that the water wire in cytochrome oxidase terminates at the propionic acid side chain of the heme, which is an important conduit for non-radiative dissipation from heme excited states. Thus, excess heat from the exothermic oxygen splitting reaction might act to help in re-orienting the H-bonds associated with the proton wire. In any case, when $k^{\mathrm{reorient}} > k_{\ell_u}{}^{\mathrm{tunnel}}$, the system will reorient from (b) to (c) and this re-establishes the state shown in part (a), but with a *new* proton ready to transit across the serine "gate", rather than by allowing the original proton to tunnel back upstream from (b) to (a). The reorientation shown in (c) effectively locks the proton (hydronium ion) on the downstream side of the serine residue where it rapidly hops further downstream. Such an effect involves only small distance fluctuations, but when tunnelling is involved, a small distance differential can strongly bias the proton pumping kinetics in a preferred direction.

tunnelling distance, very small deviations between the forward and reverse tunnelling distances in a water wire containing a serine (or a threonine) residue can lead to an efficient method for kinetic trapping. This property could facilitate transport of protons along water wires in a preferred direction as well as help with the reorientation of the serine–water hydrogen bonding, which is necessary to ''reset'' the proton wire for the continued pumping of additional protons (*e.g.*, see Figure 3.12).

We want to stress that the simple theoretical expressions presented here are clearly approximations; however, they have the advantage of exposing some of the key underlying parameters that help to account for experimental measurements of tunnelling kinetics. The main observables in most experiments involving biological systems include the KIE and its temperature dependence in the vicinity of room temperature. However, as we have emphasized, the absolute tunnelling rate provides another important independent experimental observable that should also be used to constrain the parameters in theoretical modeling.

For the electronically adiabatic tunnelling reaction of GFP, where we treated the D–A sub-system quantum mechanically rather than classically, the harmonic oscillator frequency (ω_{DA}) and average tunnelling distance (ℓ_0) are the two key unknown factors. In contrast, the high-frequency tunnelling particle oscillator parameters can be modeled using well-known covalent and H-bonding properties. Moreover, when the D–A oscillator is quantized, the environmental barriers are characterized by a single basic quantity, $\Delta G^{\ddagger}_{00} = \Delta G^{\ddagger}_{nn}$, with the other n–m transition barriers fully determined by $\hbar\omega_{DA}$ within the harmonic approximation [*e.g.*, see eqn (3.19b)]. These barriers represent the thermal energy needed to bring the reactant and product vibrational states into a degenerate condition that allows tunnelling. The independent measurement of the reaction free energy, ΔG^0, can then be used to extract the environmental reorganization energy once $\Delta G^{\ddagger}_{nn}$ is found from the fits to the tunnelling kinetics. Because there are only three basic underlying theoretical parameters that are unknown in this approach, the model is, in principle, fully constrained by the experimental data. The data includes the temperature dependence of both the H and D tunnelling rates, which are used to generate the temperature-dependent KIE. In addition, the absolute rates must be correctly predicted. Given that the OH···O hydrogen bond length is known to be very close to 2.8 Å, the value for ℓ_0 is tightly constrained. These conditions place stringent limits on the analytical model and the fact that it performs so well in fitting the GFP data is remarkable. However, this success is at least partially due to the fortuitous cancellation of errors that takes place for the OH···O system when moving between a fully anharmonic model and a fully harmonic model (*e.g.*, see supporting information S4 and S6 in ref. 77).

In the case of the electronically non-adiabatic formulation used for PCET in the SLO enzyme, the D–A oscillator is treated classically as discussed in Section 3.3.2. In this case, there are three key parameters that can be found from the KIE and the slopes of the Arrhenius rate plots near room temperature. Two of these parameters describe the first two moments of the D–A probability distribution, *i.e.*, $R_0 = \ell_0 + 2\bar{l}c$ and $\sigma_{\mathrm{DA}}(T_0)$, while the third describes the environmental barrier, $\Delta G_s^{\ddagger}$. This latter parameter is linked to the reorganization energy, λ_s, by the independently measured reaction free energy, ΔG^0. Each of these parameters can be found, in principle, because the KIE and the temperature-dependent rates for H and D provide three independent experimental observables. However, there is a caveat because the second moment of the D–A distribution, $\sigma_{\mathrm{DA}}(T_0)$, generally offers two possibilities[58,77] that are both consistent with a given temperature-dependent KIE. The absolute rate provides another (often neglected) independent experimental observable. In the electronically non-adiabatic limit it depends on two additional parameters: (1) the electronic coupling, V_{RP}, and (2) the statistical probability for being in the tunnelling-active reactant conformation, $p_{\langle r^* \rangle}$. However, if the value for V_{RP} can be calculated independently,[51] then $p_{\langle r^* \rangle}$ can be estimated by scaling the theoretical prediction so that it matches the measured absolute rate.

Finally, we note that extracting a detailed expression for the D–A potential, which is consistent with the tunnelling kinetics, should be considered only as a partially resolvable problem. The result obviously depends upon the specific assumptions that are made regarding the functional form taken for the potential (*e.g.*, harmonic or anharmonic). More importantly, the full D–A potential is generally not uniquely determined because, in the classical limit, only the short distance tail of the temperature-dependent D–A distribution determines the experimentally measured tunnelling observables. However, the use of a simple Morse potential (determined using quantum-chemical methods such as DFT), acting in conjunction with an applied force that compresses the distance between the donor and acceptor atoms, appears to be sufficient to define a reasonably realistic tunnelling-active D–A potential and its associated temperature-dependent distribution of tunnelling distances.

Such an approach offers a simple intuitive picture (*e.g.*, Figure 3.6) and allows the external force to be estimated by fitting the tunnelling data. The ~1–2 nN magnitude of the external compressive force that is found, in the case of SLO, suggests that an electric field must act to overcome the basic van der Waals repulsion between the substrate carbon and the catalytically active oxygen atom at the active site. Such an electric field probably originates from an induced dipole on the polarizable linoleic acid substrate that arises from the charge on the active site oxygen atom. More generally, electric fields from various sources within an active site (*e.g.*, charged or polarizable amino acid residues or a polarizable substrate), along with the much weaker protein conformational forces, can all contribute to the D-A compression. Such forces are needed to overcome the inherent van der Waals repulsion between the proton donor and acceptor atoms in order to facilitate tunnelling-based enzyme catalysis.

Appendix: Table of Parameters

Parameter	Description
ℓ	Tunnelling length for proton or deuteron.
ℓ_0	Equilibrium (or average) tunnelling length for a specific distribution, $P(\ell)$, associated with a given protein sub-state, $\langle i \rangle$. If it is necessary to specify the sub-state, $P(\ell)$ is denoted as $P^{\langle i \rangle}(\ell)$
$\bar{\ell}_0$	The average value of the equilibrium tunnelling length within a hierarchical ensemble of conformational sub-states having different tunnelling length equilibria (ℓ_0). The distribution of tunnelling length equilibria is denoted as $P(\ell_0)$ and has a width σ_{ℓ_0}.
R	Donor–cceptor distance: $R = \ell + 2\bar{l}_c$ and $R_0 = \ell_0 + 2\bar{l}_c$.
$\bar{l}_c$	Average covalent bond distance for D–H and A–H.
$P_{\mathrm{DA}}(R)$	Probability distribution for the donor–acceptor distance (R) that is related to $P(\ell)$ by the simple shift between R and ℓ. $P_{\mathrm{DA}}(R) = N \exp\left\{\frac{-V_{\mathrm{DA}}(R)}{k_{\mathrm{B}}T}\right\}$.
$V_{\mathrm{DA}}(R)$	The potential energy between the donor and acceptor atoms as a function of their separation, R.
$V_{\mathrm{bare}}(R)$	The DFT-determined anharmonic Morse potential that mimics the bare interaction between the CH donor and activated O^q acceptor in an enzyme active site. A charge q resides on the acceptor oxygen atom.
$V_{\mathrm{Ext}}(R)$	The potential describing compressive forces external to the atomic level DFT-determined Morse potential. In the simplest case this is a linear function with a slope proportional to q and the local electric field.
$V_{\mathrm{DA}}^{\langle r* \rangle}(R)$	The D–A potential associated with the tunnelling active conformation, $\langle r* \rangle$. This conformation is expected to have a strong local electric field.
$\Delta_0(\ell)$	Tunnel splitting between symmetric and anti-symmetric zero-point proton wave-functions.
k_ℓ^A	Electronically adiabatic tunnelling rate for a specific value of ℓ.
S_{L}	Huang–Rhys factor of the light particle vibrational coordinate $S_{\mathrm{L}} = \frac{\mu_{\mathrm{L}}\omega_{\mathrm{L}}}{2\hbar}\ell^2$ $(L = H \text{ or } D)$.
$\bar{S}_{\mathrm{L}}$	Average Huang–Rhys factor $\bar{S}_{\mathrm{L}} = \frac{m_{\mathrm{L}}\omega_{\mathrm{L}}}{2\hbar}\ell_0^2$ within the $P(\ell)$ distribution.
ω_s	Low frequency Einstein approximation for the frequency of the environmental modes surrounding the charge transport sub-system.
S_s	Huang–Rhys factor of the environmental coordinate.
λ_s	Reorganization energy of the environment surrounding the charge transport sub-system $\lambda_s = S_s\hbar\omega_s$.

Parameter	Description
$\Delta G_s^{\ddagger}$	Free energy barrier associated with the environmental coordinate that brings reactant (R) and product (P) states into degeneracy in the classical treatment for D–A motion $\Delta G_s^{\ddagger} = (\Delta G^0 + \lambda_s)^2/4\lambda_s$
ΔG^0	Free energy of the overall tunnelling reaction.
$\Delta H_s^{\ddagger}$	Enthalpic barrier associated with the environmental coordinate. This barrier contributes an isotope-independent term to the "effective Arrhenius slope", $E_a^L(T_0)$, found from the log of tunnelling rate *vs.* $1/T$.
$\Delta G_{nm}^{\ddagger}$	Free energy barrier associated with the environmental coordinate that brings the quantized D–A vibrational states (n, m) of the reactant (R) and product (P) into degeneracy, $\Delta G_{nm}^{\ddagger} = (\Delta G^0 + \Delta E_{nm} + \lambda_s)^2/4\lambda_s$.
ΔE_{nm}	Energy separation between the initial (n) and final (m) vibrational states in the quantum treatment of D–A motion. $\Delta E_{nm} = (m - n)\hbar\omega_{\mathrm{DA}}$.
Δ_0^{nm}	The vibrationally state-specific tunnel splitting for the 0-point light particle (H or D dependent) oscillator. $\Delta_0^{nm} = \langle n\vert\Delta_0(Q)\vert m\rangle$ in the B–O approximation.
ω_{L}	Vibrational frequency of the light particle oscillator ($L = H$ or D).
μ_{L}	Reduced mass of the light particle vibrational oscillator. ($\mu_{\mathrm{L}} \cong m_{\mathrm{L}}$ with m_{L} the mass of the tunnelling particle).
ω_{DA}	Heavy atom D–A vibrational frequency obtained from fits to the data using quantum approach to D–A motion.
$\bar{\omega}_E$	Theoretically calculated average Einstein oscillator frequency for motion between D–A heavy atoms. $\bar{\omega}_E \approx \omega_{\mathrm{DA}}$
μ_{DA}	Reduced mass of the D–A vibrational oscillator ($\mu_{\mathrm{DA}} \cong M/2$ with M the average mass of the heavy atoms).
$k^{A}{}_{\ell_0,\omega_{\mathrm{DA}}}$	Electronically adiabatic two-dimensional quantized tunnelling rate. Depends upon ℓ_0, ω_{L}, μ_{L} ω_{DA}, μ_{DA}, λ_s and ΔG^0.
k_{ℓ}^{NA}	One dimensional electronically non-adiabatic tunnelling rate for a specific value of ℓ in the absence of a D–A oscillator or a D–A thermal distribution.
$k_{\ell_0}^{NA}$	Electronically non-adiabatic tunnelling rate using quantum treatment for D–A oscillator that depends on ℓ_0, ω_{L}, μ_{L} ω_{DA}, μ_{DA}, λ_s, ΔG^0, and V_{RP}.
$\langle k^L\rangle_{\ell}$	Electronically non-adiabatic tunnelling rate thermally averaged over a classical D–A distribution. ($L = H$ or D). This expression depends on ℓ_0, σ_{L}, $\sigma_{\mathrm{DA}}(T)$, λ_s, ΔG^0, and V_{RP}.
V_{RP}	Non-adiabatic electronic matrix element that couples the diabatic electronic states R and P.
$\langle 0_{\mathrm{DL}}\vert 0_{\mathrm{AL}}\rangle$	Franck–Condon overlap of light particle ($L = H$ or D) zero-point vibrational wave-functions localized on the donor (D) and acceptor (A).

Parameter	Description
d	Mass-weighted tunnelling length $d=\sqrt{\mu_{\mathrm{L}}}\ell$ ($d_0=\sqrt{\mu_{\mathrm{L}}}\ell_0$ at equilibrium).
$\pm b_0$	Mass-weighted points of attachment (relative to the midpoint) of inverted parabola along double-well harmonic tunnelling particle potential.
k_1	The force constant for the high-frequency tunnel particle oscillator.
K_{vib}	Effective vibrational force constant binding D and A, including H-bonding and protein forces.
K_{R_0}	Force constant determining a Gaussian distribution of conformational sub-states where different conformations have different values of R_0.
K_{eff}	Effective force constant determining overall distribution of D–A distances in the classical fast exchange limit: $K_{\mathrm{eff}}=\dfrac{K_{\mathrm{vib}}K_{R_0}}{K_{\mathrm{vib}}+K_{R_0}}$.
$\sigma_{\mathrm{DA}}(T)$	Temperature-dependent width of D–A distribution in classical harmonic model: $\sigma_{\mathrm{DA}}^2(T)=k_{\mathrm{B}}T/\mathrm{K}_{\mathrm{eff}}$. Note that $\sigma_{\mathrm{DA}}(T)=\sigma_\ell(T)$ from eqn (3.5).
$\sigma_{\mathrm{DA}}(T)$	Temperature-dependent width of D–A distribution in quantum harmonic model: $\sigma_{\mathrm{DA}}^2(T)=\dfrac{\hbar}{2\mu_{\mathrm{DA}}\bar{\omega}_E}[2\bar{n}(\bar{\omega}_E)+1]$.
$\sigma_\alpha(T)$	Contribution of an individual protein normal mode to the D–A distribution width.
$\rho_{\mathrm{L}}(T)$	Ratio of the square of the variance of the tunnel particle probability density to the summed total MSD: $\rho_{\mathrm{L}}(T)=\dfrac{\sigma_{\mathrm{L}}^2}{\sigma_{\mathrm{L}}^2+\sigma_{\mathrm{DA}}^2(T)}$.
σ_{L}	Zero-point Gaussian variance of the tunnelling particle *probability density*. $\sigma_{\mathrm{L}}^2=\dfrac{\hbar}{\mu_{\mathrm{L}}\omega_{\mathrm{L}}}$. Note, this is twice the value of the vibrational wave function probability amplitude.
$\langle FC\rangle_{cf}$	Exact, thermally averaged, Franck–Condon factor for the Duschinsky rotated vibrational wave functions in the two-dimensional quantum model as determined by the correlation function method.
$\langle FC\rangle_{\mathrm{BO}}$	Thermally averaged Franck–Condon factor for the Duschinsky rotated vibrational wave functions in the two-dimensional quantum model as determined using the Born–Oppenheimer approximation that separates the heavy and light atom motion.
$\langle FC\rangle_{\mathrm{BO}}^{\beta\to 0}$	Same as $\langle FC\rangle_{\mathrm{BO}}$ except terms that are quadratic in the D–A fluctuations from equilibrium have been dropped. This is the "linear approximation".
$\langle FC\rangle_{\mathrm{class}}$	Thermally averaged Franck–Condon factor using a classical Gaussian probability distribution for the D–A distance as well as the environmental coordinate.

Parameter	Description
$-E_a^L(T_0)$	Effective “Arrhenius” slope for the tunnel particle (L) at a reference temperature, T_0, usually taken to be 295 K, using a classical D–A model.
ΔE_a	Difference in effective “Arrhenius” slopes for D and H. Approximates the T-dependence of the KIE. $\Delta E_a = E_a^D(T_0) - E_a^H(T_0) = E_{\mathrm{DA}}^D(T_0) - E_{\mathrm{DA}}^H(T_0)$.
$E_{\mathrm{DA}}^L(T_0)$	The term in $E_a^L(T_0)$ that carries the tunnelling rate dependence on the isotope as well as the thermal properties of the D–A distribution.
R,r	Vibrational coordinates for the heavy and light particle oscillators, respectively.
Q,q	Mass-weighted coordinates for heavy and light particle oscillators, respectively.
$\langle r^* \rangle$,$\langle r \rangle$	An enzyme conformational state that carries its own distribution of reactant (r) sub-states, within a hierarchal model. The tunnelling-length distribution is active in the state, $\langle r^* \rangle$, and inactive in $\langle r \rangle$.
k_{obs}^L	Observed kinetic rate for an enzyme undergoing a conformational forward (rate k_+) and reverse (rate k_-) search for the tunnelling-active conformation $\langle r^* \rangle$: $$k_{\mathrm{obs}}^L = \frac{k_+}{k_- + \langle k_{r^*}^L \rangle_\ell} \langle k_{r^*}^L \rangle_\ell.$$
$p\langle r^* \rangle$	Probability for being in conformation $\langle r^* \rangle$ in the fast exchange model. $p_{\langle r^* \rangle} = k_+/k_-$ so that $k_{\mathrm{obs}}^L = p_{\langle r^* \rangle} \langle k_{r^*}^L \rangle_\ell$.
θ_{L}	The Duschinsky rotation angle for the two-dimensional fully quantized treatment for either the correlation function or the B–O approximation treatment. $\theta_{\mathrm{L}} \approx \sqrt{\frac{\mu_{\mathrm{L}}}{\mu_{\mathrm{DA}}}}$.
σ_0^{DA}	Zero-point width of D–A vibrational wave-function. $$\sigma_0^{\mathrm{DA}} \approx \sqrt{\frac{\hbar}{2\mu_{\mathrm{DA}}\omega_{\mathrm{DA}}}}.$$
σ_0^L	Zero-point width of tunnel particle vibrational wave-function. $$\sigma_0^L \approx \sqrt{\frac{\hbar}{2\mu_{\mathrm{L}}\omega_{\mathrm{L}}}}$$

Acknowledgements

This work is supported by the NSF CHE-1764221. The authors thank Bridget Salna, Jasper van Thor, and Tim Sage for their contributions to this work.

References

1. H. H. Limbach, J. M. Lopez and A. Kohen, *Philos. Trans. R. Soc. London, Ser. B*, 2006, **361**, 1399–1415.

2. A. Kohen, R. Cannio, S. Bartolucci and J. P. Klinman, *Nature*, 1999, **399**, 496.
3. M. J. Knapp, K. Rickert and J. P. Klinman, *J. Am. Chem. Soc.*, 2002, **124**, 3865–3874.
4. J. P. Klinman and A. Kohen, *Annu. Rev. Biochem.*, 2013, **82**, 471–496.
5. J. P. Klinman and A. R. Offenbacher, *Acc. Chem. Res.*, 2018, **51**, 1966–1974.
6. M. J. Sutcliffe, L. Masgrau, A. Roujeinikova, L. O. Johannissen, P. Hothi, J. Basran, K. E. Ranaghan, A. J. Mulholland, D. Leys and N. S. Scrutton, *Philos. Trans. R. Soc. London, Ser. B*, 2006, **361**, 1375–1386.
7. L. Masgrau, A. Roujeinikova, L. O. Johannissen, P. Hothi, J. Basran, K. E. Ranaghan, A. J. Mulholland, M. J. Sutcliffe, N. S. Scrutton and D. Leys, *Science*, 2006, **312**, 237–241.
8. L. O. Johannissen, S. Hay, N. S. Scrutton and M. J. Sutcliffe, *J. Phys. Chem. B*, 2007, **111**, 2631–2638.
9. C. R. Pudney, L. O. Johannissen, M. J. Sutcliffe, S. Hay and N. S. Scrutton, *J. Am. Chem. Soc.*, 2010, **132**, 11329–11335.
10. L. O. Johannissen, N. S. Scrutton and M. J. Sutcliffe, *Angew. Chem., Int. Ed.*, 2011, **50**, 2129–2132.
11. J. Rittle and M. T. Green, *Science*, 2010, **330**, 933–937.
12. G. Bhabha, J. Lee, D. C. Ekiert, J. Gam, I. A. Wilson, H. J. Dyson, S. J. Benkovic and P. E. Wright, *Science*, 2011, **332**, 234–238.
13. D. C. Borgis, S. Y. Lee and J. T. Hynes, *Chem. Phys. Lett.*, 1989, **162**, 19–26.
14. P. M. Kiefer and J. T. Hynes, *Solid State Ionics*, 2004, **168**, 219–224.
15. P. M. Kiefer and J. T. Hynes, *J. Phys. Chem. A*, 2004, **108**, 11793–11808.
16. P. M. Kiefer and J. T. Hynes, *J. Phys. Chem. A*, 2004, **108**, 11809–11818.
17. S. Hammes-Schiffer, *Acc. Chem. Res.*, 2006, **39**, 93–100.
18. S. Hammes-Schiffer and A. A. Stuchebrukhov, *Chem. Rev.*, 2010, **110**, 6939–6960.
19. Y. P. Liu, D. H. Lu, A. Gonzalezlafont, D. G. Truhlar and B. C. Garrett, *J. Am. Chem. Soc.*, 1993, **115**, 7806–7817.
20. D. G. Truhlar, J. L. Gao, M. Garcia-Viloca, C. Alhambra, J. Corchado, M. L. Sanchez and T. D. Poulsen, *Int. J. Quantum Chem.*, 2004, **100**, 1136–1152.
21. R. Davydov, S. Chemerisov, D. E. Werst, T. Rajh, T. Matsui, M. Ikeda-Saito and B. M. Hoffman, *J. Am. Chem. Soc.*, 2004, **126**, 15960–15961.
22. D. Borgis and J. T. Hynes, *Chem. Phys.*, 1993, **170**, 315–346.
23. D. Antoniou and S. D. Schwartz, *Proc. Natl. Acad. Sci. U. S. A.*, 1997, **94**, 12360–12365.
24. Q. Cui and M. Karplus, *J. Am. Chem. Soc.*, 2002, **124**, 3093–3124.
25. M. Garcia-Viloca, J. Gao, M. Karplus and D. G. Truhlar, *Science*, 2004, **303**, 186–195.
26. D. G. Truhlar, *J. Phys. Org. Chem.*, 2010, **23**, 660–676.
27. P. Li, A. V. Soudackov and S. Hammes-Schiffer, *J. Am. Chem. Soc.*, 2018, **140**, 3068–3076.
28. P. Goyal, S. Yang and Q. Cui, *Chem. Sci.*, 2015, **6**, 826–841.
29. J. S. Kretchmer and T. F. Miller, *J. Chem. Phys.*, 2013, **138**, 134109.

30. J. Gao and D. G. Truhlar, *Annu. Rev. Phys. Chem.*, 2002, **53**, 467–505.
31. M. H. M. Olsson, P. E. M. Siegbahn and A. Warshel, *J. Am. Chem. Soc.*, 2004, **126**, 2820–2828.
32. S. C. L. Kamerlin and A. Warshel, *J. Phys. Org. Chem.*, 2010, **23**, 677–684.
33. D. T. Major, A. Heroux, A. M. Orville, M. P. Valley, P. F. Fitzpatrick and J. Gao, *Proc. Natl. Acad. Sci. U. S. A.*, 2009, **106**, 20734.
34. J. Mavri, H. Liu, M. H. M. Olsson and A. Warshel, *J. Phys. Chem. B*, 2008, **112**, 5950–5954.
35. I. Tejero, M. Garcia-Viloca, À. González-Lafont, J. M. Lluch and D. M. York, *J. Phys. Chem. B*, 2006, **110**, 24708–24719.
36. J. Z. Pu, J. L. Gao and D. G. Truhlar, *Chem. Rev.*, 2006, **106**, 3140–3169.
37. J. L. Bao and D. G. Truhlar, *Chem. Soc. Rev.*, 2017, **46**, 7548–7596.
38. E. Pollak, *J. Phys. Chem. B*, 2012, **116**, 12966–12971.
39. J. Mazzuca, S. Garashchuk and J. Jakowski, *Chem. Phys. Lett.*, 2012, **542**, 153–158.
40. J. W. Mazzuca, S. Garashchuk and J. Jakowski, *Chem. Phys. Lett.*, 2014, **613**, 104–109.
41. S. S. Iyengar, I. Sumner and J. Jakowski, *J. Phys. Chem. B*, 2008, **112**, 7601–7613.
42. S. Habershon, D. E. Manolopoulos, T. E. Markland and T. F. Miller, *Annu. Rev. Phys. Chem.*, 2013, **64**, 387–413.
43. L. I. Trakhtenberg, V. L. Klochikhin and S. Y. Pshezhetsky, *Chem. Phys.*, 1982, **69**, 121–134.
44. A. M. Kuznetsov and J. Ulstrup, *Can. J. Chem.*, 1999, **77**, 1085–1096.
45. P. M. Kiefer and J. T. Hynes, *J. Phys. Org. Chem.*, 2010, **23**, 632–646.
46. S. J. Edwards, A. V. Soudackov and S. Hammes-Schiffer, *J. Phys. Chem. A*, 2009, **113**, 2117–2126.
47. E. Hatcher, A. V. Soudackov and S. Hammes-Schiffer, *J. Am. Chem. Soc.*, 2004, **126**, 5763–5775.
48. J. P. Layfield and S. Hammes-Schiffer, *Chem. Rev.*, 2014, **114**, 3466–3494.
49. A. Soudackov, E. Hatcher and S. Hammes-Schiffer, *J. Chem. Phys.*, 2005, **122**, 014505.
50. A. V. Soudackov and S. Hammes-Schiffer, *J. Phys. Chem. Lett.*, 2014, **5**, 3274–3278.
51. A. K. Harshan, T. Yu, A. V. Soudackov and S. Hammes-Schiffer, *J. Am. Chem. Soc.*, 2015, **137**, 13545–13555.
52. S. Hammes-Schiffer, *J. Am. Chem. Soc.*, 2015, **137**, 8860–8871.
53. Y. Georgievskii and A. A. Stuchebrukhov, *J. Chem. Phys.*, 2000, **113**, 10438–10450.
54. S. J. Edwards, A. V. Soudackov and S. Hammes-Schiffer, *J. Phys. Chem. B*, 2010, **114**, 6653–6660.
55. S. Hammes-Schiffer, E. Hatcher, H. Ishikita, J. H. Skone and A. V. Soudackov, *Coord. Chem. Rev.*, 2008, **252**, 384–394.
56. S. Hammes-Schiffer and A. V. Soudackov, *J. Phys. Chem. B*, 2008, **112**, 14108–14123.

57. E. Hatcher, A. Soudackov and S. Hammes-Schiffer, *Chem. Phys.*, 2005, **319**, 93–100.
58. B. Salna, A. Benabbas and P. M. Champion, *J. Phys. Chem. A*, 2017, **121**, 2199–2207.
59. A. Benabbas, B. Salna, J. T. Sage and P. M. Champion, *J. Chem. Phys.*, 2015, **142**, 114101.
60. A. V. Soudackov and S. Hammes-Schiffer, *J. Chem. Phys.*, 2015, **143**, 194101.
61. M. Karplus, *Angew. Chem., Int. Ed.*, 2014, **53**, 9992–10005.
62. J. Jortner, *J. Chem. Phys.*, 1976, **64**, 4860.
63. J. J. Hopfield, *Proc. Natl. Acad. Sci. U. S. A.*, 1974, **71**, 3640.
64. R. A. Marcus and N. Sutin, *Biochim. Biophys. Acta*, 1985, **811**, 265–322.
65. A. Sirjoosingh and S. Hammes-Schiffer, *J. Phys. Chem. A*, 2011, **115**, 2367–2377.
66. E. R. Lippincott and R. Schroeder, *J. Chem. Phys.*, 1955, **23**, 1099–1106.
67. D. E. Sagnella and M. E. Tuckerman, *J. Chem. Phys.*, 1998, **108**, 2073–2083.
68. A. Warshel and R. M. Weiss, *J. Am. Chem. Soc.*, 1980, **102**, 6218–6226.
69. D. G. Truhlar and C. A. Parr, *J. Phys. Chem.*, 1971, **75**, 1844–1860.
70. S. Scheiner, *J. Phys. Chem. B*, 2006, **110**, 18670–18679.
71. B. Salna, A. Benabbas, J. T. Sage, J. van Thor and P. M. Champion, *Nat. Chem.*, 2016, **8**, 874–880.
72. B. T. Andrews, S. Gosavi, J. M. Finke, J. N. Onuchic and P. A. Jennings, *Proc. Natl. Acad. Sci. U. S. A.*, 2008, **105**, 12283–12288.
73. J. J. van Thor, G. Y. Georgiev, M. Towrie and J. T. Sage, *J. Biol. Chem.*, 2005, **280**, 33652–33659.
74. L. M. Thompson, A. Lasoroski, P. M. Champion, J. T. Sage, M. J. Frisch, J. J. van Thor and M. J. Bearpark, *J. Chem. Theory Comput.*, 2014, **10**, 751–766.
75. J. T. Sage, C. Paxson, G. R. A. Wyllie, W. Sturhahn, S. M. Durbin, P. M. Champion, E. E. Alp and W. R. Scheidt, *J. Phys.: Condens. Matter*, 2001, **13**, 7707–7722.
76. A. V. Soudackov and S. Hammes-Schiffer, *Faraday Discuss.*, 2016, **195**, 171–189.
77. B. Salna, A. Benabbas, D. Russo and P. M. Champion, *J. Phys. Chem. B*, 2017, **121**, 6869–6881.
78. V. Srajer, L. Reinisch and P. M. Champion, *J. Am. Chem. Soc.*, 1988, **110**, 6656–6670.
79. A. Benabbas, V. Karunakaran, H. Youn, T. L. Poulos and P. M. Champion, *J. Biol. Chem.*, 2012, **287**, 21729–21740.
80. A. Benabbas, Y. Sun, T. L. Poulos and P. M. Champion, *J. Am. Chem. Soc.*, 2017, **139**, 15738–15747.
81. D. L. Tonks and J. B. Page, *J. Chem. Phys.*, 1988, **88**, 738–760.
82. V. Srajer, K. T. Schomacker and P. M. Champion, *Phys. Rev. Lett.*, 1986, **57**, 1267–1270.
83. K. T. Schomacker and P. M. Champion, *J. Chem. Phys.*, 1989, **90**, 5982–5993.

84. Y. J. Yan and S. Mukamel, *J. Chem. Phys.*, 1986, **85**, 5908–5923.
85. Y. J. Yan and S. Mukamel, *J. Phys. Chem.*, 1989, **93**, 6991–6996.
86. J. Tang, M. T. Lee and S. H. Lin, *J. Chem. Phys.*, 2003, **119**, 7188–7196.
87. M. Horitani, A. R. Offenbacher, C. A. M. Carr, T. Yu, V. Hoeke, G. E. Cutsail, S. Hammes-Schiffer, J. P. Klinman and B. M. Hoffman, *J. Am. Chem. Soc.*, 2017, **139**, 1984–1997.
88. Z. D. Nagel and J. P. Klinman, *Chem. Rev.*, 2010, **110**, PR41–PR67.
89. J. P. Klinman, A. R. Offenbacher and S. Hu, *J. Am. Chem. Soc.*, 2017, **139**, 18409–18427.
90. S. Hu, S. C. Sharma, A. D. Scouras, A. V. Soudackov, C. A. M. Carr, S. Hammes-Schiffer, T. Alber and J. P. Klinman, *J. Am. Chem. Soc.*, 2014, **136**, 8157–8160.
91. C. M. Breneman and K. B. Wiberg, *J. Comput. Chem.*, 1990, **11**, 361–373.
92. J. O. L. Andreasson, S. Shastry, W. O. Hancock and S. M. Block, *Curr. Biol.*, 2015, **25**, 1166–1175.
93. M. Rief, M. Gautel, F. Oesterhelt, J. M. Fernandez and H. E. Gaub, *Science*, 1997, **276**, 1109–1112.
94. I. Popa, R. Berkovich, J. Alegre-Cebollada, C. L. Badilla, J. A. Rivas-Pardo, Y. Taniguchi, M. Kawakami and J. M. Fernandez, *J. Am. Chem. Soc.*, 2013, **135**, 12762–12771.
95. S. D. Fried and S. G. Boxer, *Acc. Chem. Res.*, 2015, **48**, 998–1006.
96. A. C. Yu, X. Ye, D. Ionascu, W. X. Cao and P. M. Champion, *Rev. Sci. Instrum.*, 2005, **76**, 114301.
97. J. T. M. Kennis, D. S. Larsen, I. H. M. van Stokkum, M. Vengris, J. J. van Thor and R. van Grondelle, *Proc. Natl. Acad. Sci. U. S. A.*, 2004, **101**, 17988–17993.
98. A. Shinobu and N. Agmon, *J. Chem. Theory Comput.*, 2017, **13**, 353–369.
99. A. Novak, *Struct. Bonding*, 1974, **18**, 177–216.
100. M. Y. Okamura and G. Feher, *Annu. Rev. Biochem.*, 1992, **61**, 861–896.
101. M. Y. Okamura, M. L. Paddock, M. S. Graige and G. Feher, *Biochim. Biophys. Acta*, 2000, **1458**, 148–163.
102. M. Wikstrom, V. Sharma, V. R. I. Kaila, J. P. Hosler and G. Hummer, *Chem. Rev.*, 2015, **115**, 2196–2221.
103. B. Ginovska-Pangovska, M. H. Ho, J. C. Linehan, Y. H. Cheng, M. Dupuis, S. Raugei and W. J. Shaw, *Biochim. Biophys. Acta, Bioenerg.*, 2014, **1837**, 131–138.
104. K. Saito, A. W. Rutherford and H. Ishikita, *Proc. Natl. Acad. Sci. U. S. A.*, 2014, **110**, 954–959.
105. I. Belevich, M. I. Verkhovsky and M. Wikström, *Nature*, 2006, **440**, 829–832.
106. R. Liang, J. M. J. Swanson, Y. Peng, M. Wikström and G. A. Voth, *Proc. Natl. Acad. Sci. U. S. A.*, 2016, **113**, 7420–7425.

CHAPTER 4

From Tunnelling Control to Controlling Tunnelling

ATTILA G. CSÁSZÁR* AND CSABA FÁBRI

Laboratory of Molecular Structure and Dynamics, Institute of Chemistry,
ELTE Eötvös Loránd University and MTA-ELTE Complex Chemical Systems
Research Group, Pázmány Péter sétány 1/A, H-1117 Budapest, Hungary
*Email: csaszarag@caesar.elte.hu

4.1 Introduction

Quantum mechanical tunnelling (QMT), transmission of particles through a potential barrier of finite width and height in cases when the energy of the particle does not allow an over-the-barrier passage, has a fascinating history.[1] Hund[2,3] was the first to consider, in 1926, the possibility of tunnelling in a ''reacting'' chemical system; Hund treated the enantiomeric interconversion of molecules without the ''classical'' over-the-barrier passage. Interestingly, the term tunnelling was introduced only somewhat later, perhaps the first time by Schottky[4] in 1931. Unusually, the paper of Hund, addressing a chemical problem, precedes the clear identification of the role of tunnelling in physics, as it was in 1928 that Gamow,[5,6] and independently Gurney and Condon,[7] interpreting experimental observations[8] foregoing the new quantum mechanics, described the ''quantum theory of nuclear disintegration''; in modern language the α-decay of heavy atomic nuclei, providing the first great triumph of QMT. Despite its more than 90 years of history and its origin, the microscopic, purely quantum phenomenon of tunnelling[9,10] is still considered by many to be more relevant for physics than for chemistry, although there is growing realization that tunnelling is

Theoretical and Computational Chemistry Series No. 18
Tunnelling in Molecules: Nuclear Quantum Effects from Bio to Physical Chemistry
Edited by Johannes Kästner and Sebastian Kozuch

Published by the Royal Society of Chemistry, www.rsc.org

indeed important for certain areas of transformative chemistry and spectroscopy. QMT plays a definite role, for example, in the case of reactions hindered by barriers and taking place at low temperatures.[11–16] Nevertheless, as this and other chapters of this book prove, there are several other interesting chemical systems and phenomena that are related to tunnelling and, in particular, its control. The role of QMT in chemistry[9,10,14,16–21] simply cannot be overstated.

This chapter addresses two fundamental issues related to QMT of small chemical systems. First, it considers cases where the outcome of a chemical transformation (a reaction) can only be understood if tunnelling is assumed to be the main reaction mechanism (in other words, the reaction goes "through" the barrier instead of "above" it), and discusses how a reaction controlled by tunnelling will be different from "ordinary" chemical reactions, assumed to proceed under kinetic or thermodynamic control (see Figure 4.1). Second, this chapter considers how to control QMT, a reaction

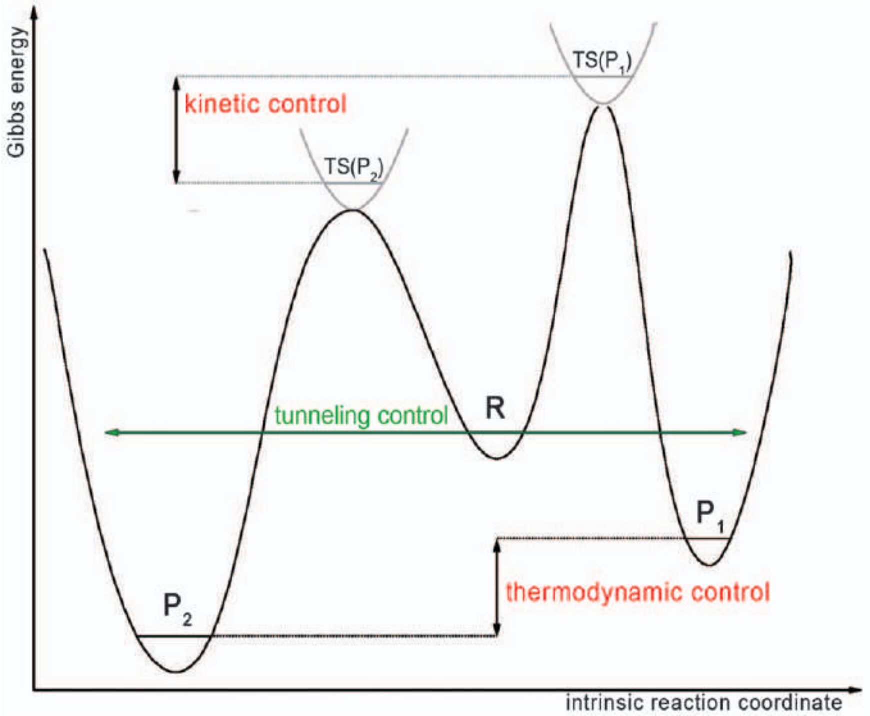

Figure 4.1 Characteristics of kinetic, thermodynamic, and tunnelling control based on a simplified one-dimensional picture involving reactant R and possible products P_1 and P_2, and two distinct transition states (TS) sitting on top of barriers of significantly different widths. In this figure both kinetic and thermodynamic control results in product P_2; only tunnelling control yields product P_1.
Image courtesy of Dr Tibor Furtenbacher.

type itself, and explains how tunnelling can be controlled either internally, *via* nuclear motions (vibrations as well as rotations) or isotopic substitutions, or externally, *via* shaped laser fields, providing coherent control.

Chemists, in particular synthetic organic chemists, successfully utilize several ''rules of thumb'' in their everyday research when synthesis of certain chemical species and reactions leading to them are designed, utilized, and refined. One of these ''rules of thumb'', borrowed from physical chemistry, is that chemical reactions proceed under either kinetic or thermodynamic control. One of the earliest examples of this principle was presented in ref. 22. Kinetic control of chemical reactions is built around the notion of reaction paths,[23–26] some of minimum energy (MEP),[23] some of minimum action (MAP),[24,27] and some neither of these two,[28,29] and of reaction barriers[30–33] along the reaction paths (note that there are also barrierless chemical reactions, *e.g.*, those involving charged species, but they are not considered here). Kinetic control means that among possible reaction paths the one with the lowest reaction barrier will be the dominant one. Thus, within this framework, control of the reaction means a change in the height of the barrier (Figure 4.1). Note that according to the Bell–Evans–Polanyi (BEP) theorem,[32,33] within the same family of reactions the difference in barrier heights is considered to be proportional to the difference in reaction enthalpies. It is important to emphasize that there are factors other than the barrier height affecting the magnitude of rate coefficients. According to classical transition state theory, the rate coefficient is proportional to the ratio of partition functions of the transition state and reactants, which can give rise to statistical-mechanical contributions. Tunnelling corrections can also influence the value of the rate coefficient along with other dynamical factors. Thermodynamic control means that among the possible products of a reaction the most stable one, the one with the lowest Gibbs energy, will be dominant. Both of these control ideas utilize only the energies of the chemical species involved in the reactions (reactants and products) and on the reaction path(s) (transition states). The actual shape of the barrier(s) characterizing reaction paths explaining kinetic control is not part of the simple picture chemists created about elementary reactions; it is used neither in the enhancement (catalysis) nor in the inhibition of chemical reactions. Nevertheless, the shape and the width of the barrier becomes an important issue when tunnelling is considered not merely as a correction to rates of chemical reactions[34] but when it is the rate-determining process.[35] Thus, one needs to emphasize the extension of the calculation of reaction barriers to the determination or the modeling of its shape when the feasibility of tunnelling is considered.

If the barrier hindering a reaction along a given path turns out to be ''narrow'', tunnelling becomes a feasible ''driving force'' of a barrier-hindered elementary reaction[35,36] (the width of the barrier is defined as the width of the classically forbidden region at the energy of the tunnelling system; moreover, the mass of the ''tunnelling particle'' should also be considered). This is surprising from a classical point of view as in the macroscopic world we got accustomed to not being able to go ''through'' barriers, just above them. To explain tunnelling and develop a simple picture about it we note that in the quantum world we are not able to define exactly the position and the momentum of a particle for any instant of its motion (Heisenberg's uncertainty principle) and that wave functions (and thus their probability densities) extend for the whole available configuration space. In relation to the mass dependence of tunnelling we note that interesting cases have been identified where the ''tunnelling particle'' is a heavy atom (heavy-atom or non-hydrogen tunnelling).[37–42]

The two fundamental issues this chapter is concerned with, namely tunnelling control of reactions and internal or external control of tunnelling dynamics, can be associated with two kinds of spectroscopy: low and high resolution. To follow the temporal evolution of chemical reactions determined by tunnelling, for example that of reactions taking place in cryogenic inert-gas matrices, it is straightforward to utilize low-resolution vibrational spectroscopy, usually infrared (IR) spectroscopy. Low-resolution IR spectroscopy allows the detection of tunnelling on the time-scale of a few seconds to several days.[43] These tunnelling reactions, when the reactants and the products are different, can be modeled through reduced-dimensional treatments (even a one-dimensional intrinsic-reaction coordinate (IRC)[25] approach will often suffice). While the temporal evolution of transformative tunnelling reactions has considerable importance, usually it is not necessary to invoke the time-dependent formalism of quantum chemistry to understand these reactions. When tunnelling does not result in a product substantially different energetically from the reactant, tunnelling can be detected experimentally *via* splittings in the rovibrational energy-level set characterizing the molecule. For the observation and characterization of this manifestation of tunnelling it is necessary to use high-resolution spectroscopy.[44] Tunnelling splittings, which are often (exceedingly) small, can be computed *via* solving the time-independent nuclear Schrödinger equation utilizing various variational techniques of the fourth age[45] of quantum chemistry.

Once tunnelling is identified in a chemical system, the question arises how to control it. In fact, there are several ways one can influence tunnelling and its rate(s). These opportunities can be divided into internal and external ones. The ''internal'' controlling possibilities considered here include isotopic substitution and rovibrational excitation. If the tunnelling particle is the hydrogen atom, H/D exchange has a huge kinetic isotope effect (KIE), as expected based on the simplest modeling arguments.[35] One can also modify the composition of the chemical system *via* asymmetric substitution, not affecting the ''tunnelling particle''. Although within the Born–Oppenheimer (BO) separation[46] of nuclear and electronic degrees of freedom this will result in no change for the electronic potential energy surface (PES) governing the dynamics of the system, it will have an effect on the effective PES felt by the nuclei and on the corresponding nuclear dynamics. Such an asymmetric substitution has been demonstrated to cause symmetry breaking in double-well systems that have two symmetry-equivalent potential wells in the non-substituted case and lead to significant changes in the tunnelling behavior, as the asymmetrically susbtituted molecule shows low-energy eigenstates localized in one of the potential wells and higher-energy eigenstates delocalized over the asymmetric double-well potential due to tunnelling switching.[47–51] The concept of tunnelling switching is crucial in the field of molecular parity violation[47,48] and might be used to construct molecular quantum switches.[52] Another ''internal'' control is provided by the internal motions (vibrations and rotations) of the molecule. It is of general interest to know how the different internal motions of a molecule influence and are influenced by tunnelling. Among the ''external'' controlling possibilities we discuss the control of tunnelling *via* shaped laser fields and present results for both the enhancement and the inhibition of tunnelling in ammonia isotopomers,[53] as it is of considerable interest to understand how one can either enhance (''accelerate'')[54] or inhibit (''destruct'')[55] tunnelling by judiciously chosen shaped laser fields.

In relation to high-resolution spectroscopy and observable ''tunnelling splittings'' one must note that there are molecular systems where the energy levels are split but the splittings have nothing to do with tunnelling. These cases include molecules where one must include versions[56] of the structures in the Longuet–Higgins sense[57] to interpret the observed spectra as well as molecular motions (mostly torsions) close to the free-motion limit. Molecular systems that can be mentioned as relevant examples include H_5^+[58,59] and CH_5^+,[60–62] as well as their deuterated isotopomers.[61,63]

The remainder of this chapter is organized as follows. In Section 4.2 we present an overview of the tunnelling control of chemical reactions, where consideration of tunnelling through different pathways is needed to understand the outcome of a reaction. Section 4.3 discusses the promotion and inhibition of tunnelling *via* nuclear motions, employing the tetratomic $^{14}NH_3$ molecule as an example. Section 4.4 provides an example of controlling tunnelling *via* isotopic substitution in the case of double-well potentials, namely tunnelling switching in the asymmetrically D-substituted vinyl radical, $CHD{=}CH$.[64] In Section 4.5, the molecule of choice is once again ammonia, and here we discuss the external coherent control of tunnelling with shaped laser pulses.[53] Section 4.6 summarizes and concludes this chapter.

4.2 Tunnelling Control in Chemical Reactions

The concept of ''tunnelling control of chemical reactions'' was defined by Allen, Schreiner, and their co-workers.[14,43,65] Introduction of this reaction-control type to the chemistry literature in 2011[65] was based on the recognition that in certain chemical reactions, with barriers along at least two feasible reaction path(s), product formation is governed neither by the lowest activation barrier (kinetic control) nor by the highest Gibbs energy gain (thermodynamic control) but by the most facile tunnelling process. Due to its very nature, the tunnelling rate depends much more directly on the width of the barrier, defining in a simplified sense the tunnelling-path (minimum-action-path) length, than on the height of the barrier.[35,36] Thus, for reactions governed by tunnelling control, one must investigate barrier widths and not (only) barrier heights, as usual during kinetic-control studies. Therefore, while tunnelling control could indeed be considered as a subclass of kinetic control, for practical purposes it appears to be useful to distinguish the two control mechanisms and handle tunnelling control as the "third reactivity paradigm".[14]

As reviewed recently by Schreiner,[14] the number of chemical systems where tunnelling control has been recognized as the determining factor governing which chemical transformation takes place is quite large by now. The conceptually simplest cases of this type of reaction selectivity concern reactants and products in low-temperature inert-gas matrices, where the temperature of the environment, actually around 10 K, is so low that no reactions characterized by barriers can proceed *via* incoherent thermal excitation. If a reaction is observed under such cold conditions, it can safely be assumed that the reaction proceeds *via* tunnelling. For example, in the case of *trans*-hydroxymethylene, *t*-HCOH, a unimolecular isomerization reaction, taking place under matrix-isolation conditions, leads to the product, formaldehyde, H_2CO, *via* a [1,2]H-shift with a tunnelling half-life of about two hours.[66]

Although it is not usual to consider reaction barrier shapes along reaction paths in the chemistry literature (a notable early exception is ref. 35), these characteristics of barriers become essential for reactions driven by tunnelling. The associated modeling choices are discussed here in the order of their increasing sophistication. These models effectively lead to different definitions of the barrier width and thus the tunnelling path length.

First, one can assume a harmonic model for the vibrations at the transition state (TS). Despite its considerable simplicity, similar to a minimum-energy structure and harmonic vibrations around it, the parabolic model[67] is highly useful. Since tunnelling is enhanced by a decrease in the width of the barrier, facile tunnelling is expected if the imaginary harmonic frequency at the TS is large. In fact, a large imaginary frequency at the TS is a clear indicator of enhanced tunnelling. As an example, we note that for *t*-HCOH the harmonic imaginary wavenumber corresponding to the transition state (TS) leading from *t*-HCOH to H_2CO is as large as $\omega_{TS} = 2174\,\mathrm{i\,cm^{-1}}$,[66] and this promotes facile tunnelling with a half-life of only two hours, while the barrier height itself is in excess of 30 $\mathrm{kcal\,mol^{-1}}$. For the S and Se congeners of *t*-HCOH the harmonic imaginary wavenumbers are $\omega_{TS} = 1869\,\mathrm{i}$ and $1773\,\mathrm{i\,cm^{-1}}$, respectively, and neither for *t*-HCSH nor for *t*-HCSeH tunnelling is expected to be observable.[68] Second, the asymmetric Eckart-barrier model[69–71] is considered, especially applicable for the cases of deep tunnelling. This is a one-dimensional model potential, whereby the corresponding time-independent Schrödinger equation can be solved analytically and a simple formula can be derived for the transmission probability through a potential-energy barrier. There are only a few quantities determining the tunnelling lifetimes within this approach, all referring to the three stationary points characterizing the isomerization path. These are the two barrier heights measured on the reactant and product sides, the imaginary harmonic frequency at the TS, related to the curvature at the top of the barrier, and the frequency of the normal mode closest resembling the tunnelling (reaction) mode. Additional data for the Eckart-barrier calculation are the zero-point vibrational energy (ZPVE) estimates of the three stationary points, excluding the reaction mode. This simple model provided surprisingly good tunnelling rates and lifetimes for the rearrangement of hydroxymethylene to formaldehyde under matrix isolation conditions.[66] Third, the intrinsic reaction path (IRP)[23,72] or the minimum-energy path (MEP) can be computed *via* techniques of electronic-structure theory and sophisticated algorithms.[28] The IRP is traced in the $3N$-dimensional configuration space of mass-weighted Cartesian coordinates of the atoms of an N-atomic molecule. The underlying non-local intrinsic reaction coordinate (IRC) minimizes the barrier height by design but does not take into account the length of the tunnelling path. Nevertheless, this approach, combined with the JWKB (Jeffreys–Wentzel–Kramers–Brillouin) semiclassical theory,[10,73] has been used quite successfully[65,66] to model deep-tunnelling cases. Fourth, one can employ the so-called instanton theory[24,36,74] to model tunnelling phenomena. This is the most sophisticated approach to model tunnelling decay rates as this is the only model that provides the optimum tunnelling path, called the instanton path, which is simply the MAP. The instanton model also provides the temperature dependence of the tunnelling decay rate. For a qualitative understanding of whether tunnelling needs to be considered or not, the first two, simple modeling attempts appear to be satisfactory. For a quantitative assessment of tunnelling the last two approaches should be followed.

After this brief introduction into the topic of tunnelling control of chemical reactions, the third reactivity paradigm,[14] the next task is to find cases where there are at least two distinct possibilities for chemical transformation *via* tunnelling and thus tunnelling control can be identified *via* detecting the reaction product(s). A simple case is that of methylhydroxycarbene, CH_3–C–OH,[65] where there are two transformation possibilities and reaction paths and two associated barriers for a [1,2]H-shift, and tunnelling under matrix-isolation conditions could lead to two products: acetaldehyde, CH_3–CHO, where the [1,2]H-shift goes along the CO bond, and vinylalcohol, $CH_2{=}CHOH$, when the shift goes through the CC bond. Experiments proved that, due to tunnelling control, the reaction proceeds, at the temperature of about 10 K of inert-gas matrices, *via* the higher but narrower barrier, resulting in a single product, acetaldehyde.

In another related study,[75] carefully executed matrix-isolation experiments demonstrated that the higher-energy rotamers of oxalic acid (OA), $(COOH)_2$, similarly to other organic acids studied previously, undergo a (relatively slow) tunnelling rotamerization, even at 3 K in solid Ne. In OA, two independent tunnelling processes interconvert the higher-energy rotamers, tTt and cTt (see Scheme 1 of ref. 75 for the notation of the rotamers with different relative OH orientations (*trans*, t, *vs. cis*, c), while the rotamers possess an s-*trans* (T) orientation of the carbonyl groups) to the overall minimum-energy structure, cTc. The sequence of two tunnelling events was termed[75] domino tunnelling. Based on the experiments, it was deduced *via* multistate models and the related dispersive kinetics[75] that in the Ne matrix the cTt → cTc isomerization of OA is considerably faster than its tTt → cTt counterpart, even though the barrier for the former isomerization is 0.8 kcal mol^{-1} larger than for the latter. These experiments also show convincingly that tunnelling favors the chemical transformation with the higher but narrower barrier, *i.e.*, tunnelling control is in effect during the domino tunnelling involving OA rotamers.

Several further examples for tunnelling control are given in ref. 14, the interested reader should consult this paper.

4.3 Promoting and Inhibiting Tunnelling *via* Nuclear Motion in $^{14}NH_3$

In this section, our attention is turned to non-transformative tunnelling, which can be investigated experimentally *via* high-resolution rovibrational spectroscopy. In order to investigate how nuclear motions (vibrations and rotations), affect the tunnelling rate and the related tunnelling splittings, one must choose molecules for which a considerable number of rovibrational transitions have been measured and assigned. An almost perfect molecule for this purpose is ammonia,[76] for which promotion and inhibition of tunnelling are discussed in the forthcoming paragraphs. Note that similar investigations using purely *ab initio* data were carried out for another tetratomic molecule, H_2O_2, by Quack and co-workers.[77,78]

The MARVEL (Measured Active Rotational-Vibrational Energy Levels) approach[79–81] enables the conversion of a set of assigned experimental rovibronic transitions to *empirical* rovibronic energy levels, with associated uncertainties propagated from the input transition data to the output energy levels. This conversion relies on the construction of an experimental spectroscopic network (SN)[80–85] formed by the measured and assigned transitions, facilitating an improved characterization of the high-resolution spectroscopic information. The MARVEL approach has been used to analyze the experimental rovibrational transitions of $^{14}NH_3$,[76,86] resulting in about 5000 highly accurate empirical energy levels of rovibrational states. The height of the one-dimensional electronic barrier of $^{14}NH_3$ is 1773 ± 13 cm^{-1} (5.1 kcal mol^{-1}), increasing to 2021 ± 20 cm^{-1} (5.8 kcal mol^{-1}) when the effect of zero-point vibrations is considered.[87,88] The empirical (MARVEL) coverage of vibrational band origins (VBO) of $^{14}NH_3$ is complete up to 3500 cm^{-1}; the first missing VBO, of E'' symmetry of the $D_{3h}(M)$ molecular symmetry group,[56] is at 3502 cm^{-1}. Up to this energy the set of rovibrational energies is basically complete. The availability of this large set of empirical rovibrational energy levels is what allows the investigation of the effect of nuclear motions on tunnelling in the case of $^{14}NH_3$.

Nuclear motions, *i.e.*, vibrations and rotations, can have a significant effect on the effective tunnelling barrier height and width and consequently the tunnelling splittings characterizing the rovibrational spectrum of ammonia. Nuclear-motion effects can be monitored extremely sensitively by the differences, the so-called tunnelling splittings, of the corresponding pairs of symmetric (s) and antisymmetric (a) energy levels. The results of this monitoring are provided in the remainder of this section.

The umbrella mode, ν_2, is unique among the vibrational modes of ammonia as it corresponds to the tunnelling mode. Therefore, with increasing number of vibrational quanta in the ν_2 mode, the system approaches the top of the inversion barrier, the tunnelling paths between the "left" and "right" wells become shorter and the corresponding tunnelling splittings increase. As known from accurate variational computations, the splittings corresponding to the $n\nu_2$ vibrational eigenstates of $^{14}NH_3$ are 0.8, 36, 282, 511, 600, 665, 708, and 747 cm^{-1} for $n = 0$–7. The magnitude of the splittings grows fast while the excitation remains below the top of the barrier. The splittings increase slowly and the separation of the averages of the "s" and "a" state pairs decrease slowly above the top of the barrier, *i.e.*, from $n = 3$.

Vibrational modes other than ν_2 have a less pronounced effect on the tunnelling splitting of the corresponding antisymmetric and symmetric eigenstates. Both the symmetric (ν_1) and the antisymmetric (ν_3) stretching motions decrease the observed splittings. For example, symmetric stretching of the N–H bonds (ν_1) results in a quenching of the splitting, from 35.7 cm^{-1} for the ν_2 fundamental to 25.5 cm^{-1} for the $\nu_1 + \nu_2$ combination band. This can be rationalized by a corresponding increase in the tunnelling-path length. "Antisymmetric" bending promotes tunnelling but to a much smaller extent than its symmetric counterpart.

Next, let us turn our attention to rovibrational states, where we assume, in line with the fact that ammonia is basically a semirigid molecule, that each rovibrational state has a well-defined vibrational parent.[89] Let J be the quantum number corresponding to overall rotations and let K correspond to the projection of the rotational angular momentum on the body-fixed z axis. For the rotational states $(J, K) = (J, J)$, *i.e.*, for what one can call "parallel" rotations, the tunnelling splitting increases quadratically as J increases. The effect is especially pronounced for the $n\nu_2$ states. As given above, the tunnelling splitting characterizing the ν_2 fundamental is 35.7 cm^{-1}. A similar "extra" splitting, yet unobserved, is reached by about $J = 25$, a substantial but perfectly feasible rotational excitation.

The other limiting case concerns the $(J, K) = (J, 1)$ states (note that for non-degenerate VBOs the $K = 0$ states are missing due to nuclear spin statistics), what one may call "perpendicular" rotation. Perpendicular rotation motion inhibits tunnelling rather effectively. The inhibition is so effective that for the ground vibrational state, for example, the splitting decreases basically to zero by about $J = 25$.

All the results noted, concerning $^{14}NH_3$, are relevant not only for this simple and thoroughly studied molecule but for many others, and serve to increase our general understanding of controlling tunnelling *via* nuclear dynamics.

4.4 Tunnelling Switching

Interesting possibilities to control tunnelling internally are offered through isotopic substitutions. Although every atom of the molecule is involved in the tunnelling process, it is often possible to regard tunnelling as a local phenomenon, identify the ''tunnelling atom'', and make a simple isotopic substitution for this atom. Most dramatic in this sense is an H/D substitution, as this factor-of-two change in the tunnelling mass leads to a reduction in the tunnelling rate of several orders of magnitude (to the best of our knowledge, apart from a few exceptions, *e.g.*, ref. 90, neither tritium, $T \equiv {}^3H$, a radioactive isotope of H, nor its light cousin, muonium ($Mu \equiv \mu^+ e^-$), have been used in tunnelling experiments). As an example for the effect of H/D substitution, in the case of *t*-HCO(H/D)[66] the KIE is several orders of magnitude, as the tunnelling half-life is two hours (measured and computed) for *t*-HCOH and over 1200 years (computed result) for *t*-HCOD. In fact, tunnelling rates are expected to decrease exponentially with the square root of the effective tunnelling mass.[9]

It is perhaps even more interesting to point out that, in the case of a potential-energy surface (PES) characterized by a symmetric double well, one may be able to introduce an asymmetric isotopic substitution into the molecule, changing the tunnelling behavior in a drastic, clearly observable way. An asymmetric substitution, breaking the symmetry characterizing the effective tunnelling potential of the non-substituted isotopomer, results in low-energy eigenstates localized in one of the potential wells, while higher-energy eigenstates are delocalized due to the occurrence of tunnelling switching.[47–51] Quack[47] was the first to provide a detailed theoretical analysis of tunnelling switching in slightly asymmetric double-well potentials in relation to the measurement of the parity-violating energy difference between enantiomers of chiral molecules. In fact, tunnelling switching can be easily understood by a simple two-state model.[47,51] Experimental observation of tunnelling switching in *meta*-D-phenol by high-resolution spectroscopic measurements was reported in ref. 51. In this chapter we use the case of the vinyl radical (VR), $H_2C_\beta{=}C_\alpha H$, to provide an example for the tunnelling switching behavior as breaking the equivalence of the two wells can be achieved by a non-symmetric deuteration, *i.e.*, in the case of the CHD=CH species.[64]

The VR is the simplest open-shell olefinic radical and its structure and (ro)vibrational quantum dynamics, as well as the related (high-resolution) spectra, have been the subject of a considerable number of experimental (spectroscopic)[91–95] and computational (quantum-chemical)[64,96–98] studies. Based on its structure, the VR is expected to show a $C_\alpha H$ rocking tunnelling motion, governed by a double-well potential, leading to considerable splitting for all rovibrational states of the VR. As detailed quantum-chemical computations[64] show, a barrier of 1641(25) cm^{-1} (4.7 kcal mol^{-1}) leads to substantial splittings; for the ground vibrational state it is measured to be 0.542 770 2(2) cm^{-1}.[92] The same rovibrational nuclear-motion computations also reveal a somewhat less expected feature of the tunnelling motion of the

VR: the $C_\alpha H$ and $C_\beta H_2$ bending motions are strongly coupled. This is true both at the harmonic and the fully anharmonic levels.

For CHD=CH the delocalized ground-state pair of CH_2=CH is combined into *syn* and *anti* localized (unistructural) states, with an energy separation as large as 30 cm^{-1}, almost an order of magnitude larger than for the bistructural ground state of CH_2=CH. Some of the higher-lying vibrational states are again delocalized (bistructural), as expected when the splitting of the unperturbed states becomes (much) larger than the perturbation causing the effective asymmetry of the double-well potential.

4.5 Coherent Control of Tunnelling with Laser Fields

The problem of *driven tunnelling*, *i.e.*, tunnelling through a barrier in the presence of time-dependent external fields, is of considerable importance in various scientific disciplines, *e.g.*, in the coherent control of chemical reactions by shaped laser pulses,[99–108] as well as in solid-state,[109,110] ultracold,[111] and attosecond physics,[112] where driven tunnelling is vital for understanding the mechanism of high harmonic generation.[113–115]

The methods presented in the early 1990s in ref. 54 and 55 were designed to enhance and inhibit tunnelling in double-well potentials and they were applied to one-dimensional model problems in the original publications. Recently we have shown that the strategies of ref. 54 and 55 can be adapted to achieve the coherent control of tunnelling in molecular systems.[53] Our computations for the ammonia isotopomers treated all vibrational and rotational degrees of freedom as well as all the couplings between them in a numerically exact way and employed the GENIUSH code[116,117] extended with time-dependent quantum-dynamical features.[53] Inhibition and enhancement of tunnelling are based on the application of Floquet's theorem[118] and the concept of light-dressed states.[119–121] As an alternative to the light-dressed state formalism, a quasi-stationary effective Hamiltonian (both with the Floquet and quasiresonant approximations) was suggested in ref. 122. The Floquet formalism not only provides a detailed qualitative understanding of the underlying physical processes but also facilitates the design of the carrier frequency, as well as the intensity and the envelope of the laser fields used to control tunnelling.

The control involving the chiral NHDT isotopomer of ammonia is particularly interesting as it allows the study of a chemical reaction, namely enantiomerization by stereomutation tunnelling. As seen below, in the example of NHDT we can investigate both the enhancement and the inhibition of tunnelling.

First, let us investigate how to inhibit tunnelling *via* coherent control. Let us assume an initial state localized in one of the two equivalent potential wells, corresponding to one of the enantiomers of NHDT. Since this localized initial state is a superposition of the delocalized symmetric and antisymmetric ground-state tunnelling eigenstates of NHDT, it shows a periodic time evolution with the time period $T = h/\Delta E_\pm = 292.8$ ps, where

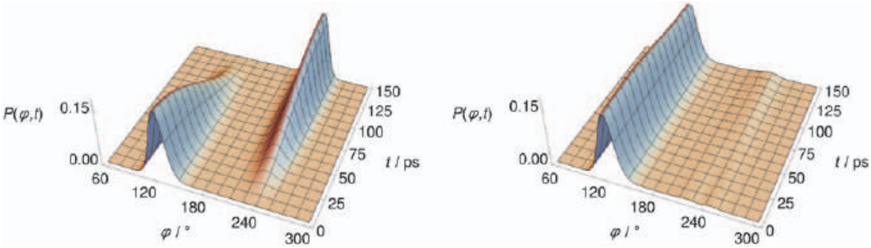

Figure 4.2 Reduced probability density as a function of the inversion coordinate φ and time t for NHDT (after ref. 53). The left and right panels show reduced probability densities for the field-free and tunnelling inhibition dynamical schemes, respectively.

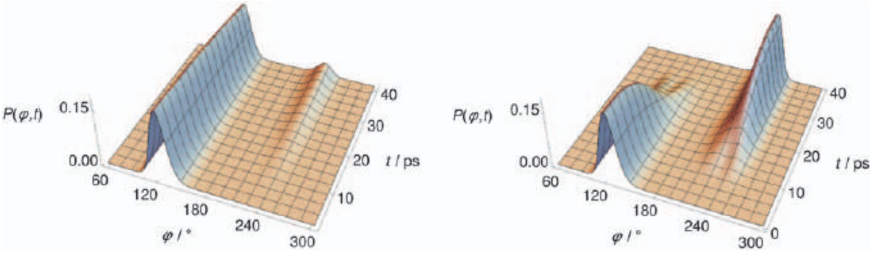

Figure 4.3 Reduced probability density as a function of the inversion coordinate φ and time t for NHDT (after ref. 53). The left and right panels show reduced probability densities for the field-free and tunnelling enhancement dynamical schemes, respectively.

$\Delta E_{\pm} = 0.114$ cm^{-1} is the ground-state tunnelling splitting of NHDT.[53] The periodic motion of the wavepacket is apparent in the left panel of Figure 4.2, where the reduced probability density (probability density integrated over all coordinates but φ, where the inversion coordinate φ corresponds to the angle between the NHD and NHT planes) is shown for a half period for the case of an isolated molecule. Indeed, the wavepacket that is initially localized in the left potential well tunnels through the barrier and becomes localized in the right potential well at $t = T/2 = 146.4$ ps. However, if the molecule interacts with a continuous-wave laser field with a carrier wavenumber of $\omega_0 = 780$ cm^{-1} and an intensity of $I = 7.56$ GW cm^{-2}, the wavepacket remains mainly localized in the left potential well and tunnelling is almost completely suppressed, as shown in the right panel of Figure 4.2.

Next, let us discuss how one can enhance tunnelling with an external laser field. In fact, tunnelling in NHDT can be enhanced by an off-resonant laser pulse with a $\sin^2(\pi t/t_p)$ envelope function and a duration of $t_p = 40$ ps ($\omega_0 = 793.5$ cm^{-1} and $I = 3.15$ GW cm^{-2}). Figure 4.3 shows that the population from the left potential well is completely transferred to the right potential well by the laser pulse, so the field-free tunnelling time of $T/2 = 146.4$ ps is shortened to 40 ps by the laser pulse.

For a detailed description of the theoretical and technical details of coherent control of tunnelling, the reader is referred to ref. 53. The results presented in ref. 53 not only confirm the applicability of the tunnelling enhancement and inhibition schemes to realistic molecular systems but also complement earlier studies of tunnelling control in ammonia isotopomers treating only the vibrational degrees of freedom[123–125] and help clarify the role of the rotational degrees of freedom in quantum dynamics.

4.6 Summary and Conclusions

This chapter dealt basically with two fundamental issues related to tunnelling in molecular systems, both important to chemistry and relevant in several different fields, in particular, reaction dynamics and low- and high-resolution spectroscopy.

First, it was demonstrated that tunnelling control of chemical reactions takes over traditional kinetic control when the reaction, due to insufficient extra energy, must proceed ''through'' the barrier instead of going above it. This means in turn that it is not the height of the barrier but its width that determines the efficiency of the tunnelling reaction, the tunnelling decay of a reactant perhaps through a unimolecular isomerization reaction.

Second, we discussed how to control tunnelling, either internally or externally. Two internal control possibilities were discussed: isotopic substitution and rovibrational excitation. Isotopic substitution of the tunnelling atom is well known and it is a well-utilized concept, as when the mass of the tunnelling atom increases, imagine a H/D substitution, the tunnelling rate decreases. Isotopic substitution becomes extremely interesting when it is done in a non-symmetric fashion for a molecule characterized by a double-well potential, as it leads to the effect of tunnelling switching. Rovibrational excitation has a substantial effect on tunnelling. The effect is especially large for the ''tunnelling mode'' but it is also significant for all modes. The effect is discussed on the experimental energy levels and tunnelling splittings of $^{14}NH_3$, a molecule for which a large number of experimental data are available. Concerning the external control of tunnelling, computational strategies, based on Floquet's theorem and light-dressed states, were explored to achieve either the inhibition or the enhancement of tunnelling in molecules by laser fields. As shown, it is feasible to treat all rotational and vibrational degrees of freedom in a numerically exact way and it is not necessary to assume either the alignment or the orientation of the molecule under investigation. Results were presented for the coherent control of a quantum state initially localized in one of the potential wells of ammonia isotopomers, in particular NHDT.

Acknowledgements

The authors are grateful for the financial support received from NKFIH, through grants K119658 (AGC) and PD124699 (CF), and for the VEKOP-2.3.2-16-2017-00014 program supported by the European Union and the State of Hungary and co-financed by the European Regional Development Fund. The authors would like to acknowledge the significant contributions of and the numerous discussions with Drs Wesley D. Allen, Roberto Marquardt, Martin Quack, János Sarka, Peter R. Schreiner, and Jan Šmydke, shaping the joint publications referred to in this chapter and upon which most of this chapter is built. Dr Tibor Furtenbacher is gratefully acknowledged for preparing Figure 4.1.

References

1. E. Merzbacher, The early history of quantum tunneling, *Phys. Today*, 2002, **69**, 44–49.
2. F. Hund, Zur Deutung der Molekelspektren. I, *Z. Phys.*, 1927, **40**, 742–764.
3. F. Hund, Zur Deutung der Molekelspektren. III, *Z. Phys.*, 1927, **43**, 805–826.
4. W. Schottky, Conduction and photoelectric effects in blocking layers, *Phys. Z.*, 1931, **32**, 833.
5. G. Gamow, The quantum theory of nuclear disintegration, *Nature*, 1928, **122**, 805.
6. G. Gamow, Zur Quantentheorie des Atomkernes, *Z. Phys.*, 1928, **51**, 204–212.
7. R. W. Gurney and E. U. Condon, Quantum mechanics and radioactive disintegration, *Nature*, 1928, **122**, 439–440.
8. E. Rutherford, Radioactive substance emitted from thorium compounds, *Philos. Mag.*, 1900, **49**, 1.
9. R. P. Bell, *The Tunnel Effect in Chemistry*, Chapman and Hall, New York, 1980.
10. M. Razavy, *Quantum Theory of Tunneling*, World Scientific, New Jersey, 2003.
11. G. Bazsó, S. Góbi and G. Tarczay, Near-infrared radiation induced conformational change and hydrogen atom tunneling of 2-chloropropionic acid in low-temperature Ar matrix, *J. Phys. Chem. A*, 2012, **116**, 4823–4832.
12. F. M. Mutunga, S. E. Follett and D. T. Anderson, Communication: H-atom reactivity as a function of temperature in solid parahydrogen: The $H + N_2O$ reaction, *J. Phys. Chem. A*, 2012, **116**, 4823–4832.
13. L. O. Paulson, F. M. Mutunga, S. E. Follett and D. T. Anderson, Reactions of atomic hydrogen with formic acid and carbon monoxide in solid parahydrogen I: Anomalous effect of temperature, *J. Phys. Chem. A*, 2014, **118**, 7640–7652.
14. P. R. Schreiner, Tunnelling control of chemical reactions: The third reactivity paradigm, *J. Am. Chem. Soc.*, 2017, **139**, 15276–15283.
15. M. E. Balabanoff, M. Ruzi and D. T. Anderson, Signatures of a quantum diffusion limited hydrogen atom tunneling reaction, *Phys. Chem. Chem. Phys.*, 2018, **20**, 422–434.

16. K. A. Haupa, G. Tarczay and Y. P. Lee, Hydrogen abstraction/addition tunneling reactions elucidate the interstellar $H_2NCHO/HNCO$ ratio and H_2 formation, *J. Am. Chem. Soc.*, 2019, **141**, 11614–11620.
17. P. O. Löwdin, Proton tunneling in DNA and its biological implications, *Rev. Mod. Phys.*, 1963, **35**, 724–732.
18. Z. X-Liang and J. P. Klinman, Structural basis of hydrogen tunneling in enzymes: progress and puzzles, *Curr. Opin. Struct. Biol.*, 1963, **14**, 648–655.
19. J. P. Klinman and A. Kohen, Hydrogen tunneling links protein dynamics to enzyme catalysis, *Annu. Rev. Biochem.*, 2013, **82**, 471–496.
20. T. Firmino, R. Marquardt, F. Gatti and W. Dong, Diffusion rates for hydrogen on Pd(111) from molecular quantum dynamics calculations, *J. Phys. Chem. Lett.*, 2014, **5**(24), 4270–4274.
21. G. Seyfang and M. Quack, Trendbericht Physikalische Chemie 2017: Atomare und molekulare Tunnelprozesse, *Nachr. Chem.*, 2018, **66**, 307–315.
22. R. B. Woodward and H. Baer, Studies on diene-addition reactions. II.1 The reaction of 6,6-pentamethylenefulvene with maleic anhydride, *J. Am. Chem. Soc.*, 1944, **66**(4), 645–649.
23. K. Fukui, A formulation of the reaction coordinate, *J. Phys. Chem.*, 1970, **74**, 4161–4163.
24. W. H. Miller, Semiclassical limit of quantum mechanical transition state theory for nonseparable systems, *J. Chem. Phys.*, 1975, **62**, 1899–1906.
25. K. Fukui, The path of chemical reactions – The IRC approach, *Acc. Chem. Res.*, 1981, **14**, 363–368.
26. J. Villa and D. G. Truhlar, Variational transition state theory without the minimum-energy path, *Theor. Chem. Acc.*, 1997, **97**, 317–323.
27. M. I. Freidlin and A. D. Wentzell, *Random Perturbations of Dynamical Systems*, Springer, New York, 1998.
28. M. A. Collins, The interface between electronic structure theory and reaction dynamics by reaction path methods, *Adv. Chem. Phys.*, 1996, **93**, 389–453.
29. W. D. Allen, A. Bodi, V. Szalay and A. G. Császár, Adiabatic approximations to internal rotation, *J. Chem. Phys.*, 2006, **124**, 224310.
30. H. Eyring, The activated complex in chemical reactions, *J. Chem. Phys.*, 1935, **3**, 107–115.
31. M. G. Evans and M. Polanyi, Some applications of the transition state method to the calculation of reaction velocities, especially in solution, *Trans. Faraday Soc.*, 1935, **31**, 875.
32. R. P. Bell, The theory of reactions involving proton transfers, *Proc. R. Soc. London, Ser. A*, 1936, **154**, 414.
33. M. G. Evans and M. Polanyi, Inertia and driving force of chemical reactions, *J. Chem. Soc., Faraday Trans.*, 1936, **32**, 1333.
34. H. S. Johnston and J. Heicklen, Tunnelling corrections for unsymmetrical Eckart potential energy barriers, *J. Phys. Chem.*, 1962, **66**, 532–533.

35. M. Simonyi and I. Mayer, Barrier width: a powerful parameter for hydrogen transfer reactions, *J. Chem. Soc., Chem. Commun.*, 1975, 695–696.
36. J. Kästner, Path length determines the tunneling decay of substituted carbenes, *Chem. – Eur. J.*, 2013, **19**, 8207–8212.
37. D. Gerbig, D. Ley and P. R. Schreiner, Light- and heavy-atom tunneling in rearrangement reactions of cyclopropylcarbenes, *Org. Lett.*, 2011, **13**(13), 3526–3529.
38. W. T. Borden, Reactions that involve tunneling by carbon and the role that calculations have played in their study, *WIREs Comput. Mol. Sci.*, 2016, **6**, 20–46.
39. Z. Wu, R. Feng, H. Li, J. Xu, G. Deng and M. Abe, *et al.*, Fast heavy-atom tunneling in trifluoroacetyl nitrene, *Angew. Chem., Int. Ed. Engl.*, 2017, **56**(49), 15672–15676.
40. C. M. Nunes, I. Reva, S. Kozuch, R. J. McMahon and R. Fausto, Photochemistry of 2-formylphenylnitrene: A doorway to heavy-atom tunneling of a benzazirine to a cyclic ketenimine, *J. Am. Chem. Soc.*, 2017, **139**(48), 17649–17659.
41. A. Nandi, D. Gerbig, P. R. Schreiner, W. T. Borden and S. Kozuch, Isotope-controlled selectivity by quantum tunneling: Hydrogen migration versus ring expansion in cyclopropylmethylcarbenes, *J. Am. Chem. Soc.*, 2017, **139**(27), 9097–9099.
42. C. M. Nunes, A. K. Eckhardt, I. Reva, R. Fausto and P. R. Schreiner, Competitive nitrogen versus carbon tunneling, *J. Am. Chem. Soc.*, 2019, **141**(36), 14340–14348.
43. D. Ley, D. Gerbig and P. R. Schreiner, Tunneling control of chemical reactions – the organic chemist's perspective, *Org. Biomol. Chem.*, 2012, **19**, 3781–3790.
44. *Handbook of High-Resolution Spectroscopy*, ed. M. Quack and F. Merkt, Wiley, Chichester, 2011.
45. A. G. Császár, C. Fábri, T. Szidarovszky, E. Mátyus, T. Furtenbacher and G. Czakó, Fourth age of quantum chemistry: Molecules in motion, *Phys. Chem. Chem. Phys.*, 2012, **13**, 1085–1106.
46. M. Born and J. R. Oppenheimer, Zur Quantentheorie der Molekeln, *Ann. Phys.*, 1927, **389**, 457–484.
47. M. Quack, On the measurement of the parity violating energy difference between enantiomers, *Chem. Phys. Lett.*, 1986, **132**, 147–153.
48. M. Quack, Fundamental Symmetries and Symmetry Violations from High-resolution Spectroscopy, in *Handbook of High-resolution Spectroscopy*, ed. M. Quack and F. Merkt, Wiley, Chichester, 2011, pp. 659–722.
49. M. Quack and M. Willeke, Stereomutation tunneling switching dynamics and parity violation in chlorineperoxide, Cl–O–O–Cl, *J. Phys. Chem. A*, 2006, **110**, 3338–3348.
50. S. Albert, P. Lerch, R. Prentner and M. Quack, Tunneling and tunneling switching dynamics in phenol and its isotopomers from high-

resolution FTIR spectroscopy with synchrotron radiation, *Angew. Chem., Int. Ed.*, 2013, **52**, 346–349.

51. S. Albert, Z. Chen, C. Fábri, P. Lerch, R. Prentner and M. Quack, A combined Gigahertz and Terahertz (FTIR) spectroscopic investigation of meta-D-phenol: observation of tunneling switching, *Mol. Phys.*, 2016, **114**, 2751–2768.
52. C. Fábri, S. Albert, Z. Chen, R. Prentner and M. Quack, A molecular quantum switch based on tunneling in meta-d-phenol C_6H_4DOH, *Phys. Chem. Chem. Phys.*, 2018, **20**, 7387–7394.
53. C. Fábri, R. Marquardt, A. G. Császár and M. Quack, Controlling tunneling in ammonia isotopomers, *J. Chem. Phys.*, 2019, **150**, 014102.
54. M. Holthaus, Pulse-shape-controlled tunneling in a laser field, *Phys. Rev. Lett.*, 1992, **69**, 1596–1599.
55. F. Grossmann, T. Dittrich, P. Jung and P. Hänggi, Coherent destruction of tunneling, *Phys. Rev. Lett.*, 1991, **67**, 516–519.
56. P. R. Bunker and P. Jensen, *Molecular Symmetry and Spectroscopy*, NRC Research Press, Ottawa, 1998.
57. H. C. Longuet-Higgins, The symmetry groups of non-rigid molecules, *Mol. Phys.*, 1963, **6**, 445–460.
58. C. Fábri, J. Sarka and A. G. Császár, Communication: Rigidity of the molecular ion H_5^+, *J. Chem. Phys.*, 2014, **140**, 051101.
59. J. Sarka, C. Fábri, T. Szidarovszky, A. G. Császár, Z. Lin and A. B. McCoy, Modelling rotations, vibrations, and rovibrational couplings in astructural molecules – A case study based on the H_5^+ molecular ion, *Mol. Phys.*, 2015, **113**, 1873–1883.
60. C. Fábri, M. Quack and A. G. Császár, On the use of nonrigid-molecular symmetry in nuclear-motion computations employing a discrete variable representation: A case study of the bending energy levels of CH_5^+, *J. Chem. Phys.*, 2017, **147**, 134101.
61. C. Fábri and A. G. Császár, Vibrational quantum graphs and their application to the quantum dynamics of CH_5^+, *Phys. Chem. Chem. Phys.*, 2018, **20**, 16913–16917.
62. J. I. Rawlinson, Quantum graph model for rovibrational states of protonated methane, *J. Chem. Phys.*, 2019, **151**, 164303.
63. J. Sarka and A. G. Császár, Interpretation of the vibrational energy level structure of the astructural molecular ion H_5^+ and all of its deuterated isotopomers, *J. Chem. Phys.*, 2016, **144**, 154309.
64. J. Šmydke, C. Fábri, J. Sarka and A. G. Császár, Rovibrational quantum dynamics of the vinyl radical and its deuterated isotopologues, *Phys. Chem. Chem. Phys.*, 2019, **21**, 3453–3472.
65. P. R. Schreiner, H. P. Reisenauer, D. Ley, D. Gerbig, C. H. Wu and W. D. Allen, Methylhydroxycarbene: Tunneling control of a chemical reaction, *Science*, 2011, **332**, 1300–1303.
66. P. R. Schreiner, H. P. Reisenauer, F. C. Pickard, A. C. Simmonett, W. D. Allen and E. Mátyus, *et al.*, Capture of hydroxymethylene and its fast disappearance through tunneling, *Nature*, 2008, **453**, 906–909.

67. R. P. Bell, The tunnel effect correction for parabolic potential barriers, *Trans. Faraday Soc.*, 1959, **55**, 1.
68. J. Sarka, A. G. Császár and P. R. Schreiner, Do the mercaptocarbene (H–C–S–H) and selenocarbene (H–C–Se–H) congeners of hydroxycarbene (H–C–O–H) undergo 1,2-H-tunneling? *Collect. Czech. Chem. Commun.*, 2011, **76**, 645–667.
69. C. Eckart, The penetration of a potential barrier by electrons, *Phys. Rev.*, 1930, **35**, 1303–1309.
70. H. S. Johnston, *Gas Phase Reaction Rate Theory*, Ronald Press, New York, 1966.
71. W. H. Miller, Tunneling corrections to unimolecular rate constants, with application to formaldehyde, *J. Am. Chem. Soc.*, 1979, **101**, 6810–6814.
72. C. Gonzalez and H. B. Schlegel, An improved algorithm for reaction path following, *J. Chem. Phys.*, 1989, **90**, 2154.
73. N. Fröman and P. O. Fröman *JWKB Approximation. North-Holland*, Amsterdam, 1965.
74. J. S. Langer, Theory of the condensation point, *Ann. Phys.*, 1967, **41**, 108–157.
75. P. R. Schreiner, J. P. Wagner, H. P. Reisenauer, D. Gerbig, D. Ley and J. Sarka, *et al.*, Domino tunneling, *J. Am. Chem. Soc.*, 2015, **137**, 7828–7834.
76. A. G. Császár and T. Furtenbacher, Promoting and inhibiting tunneling via nuclear motions, *Phys. Chem. Chem. Phys.*, 2016, **18**, 1092–1104.
77. B. Fehrensen, D. Luckhaus and M. Quack, Stereomutation dynamics in hydrogen peroxide, *Chem. Phys.*, 2007, **338**, 90–105.
78. B. Fehrensen, D. Luckhaus and M. Quack, Mode selective stereomutation tunneling in hydrogen peroxide isotopomers, *Chem. Phys. Lett.*, 1999, **300**(3), 312–320.
79. T. Furtenbacher, A. G. Császár and J. Tennyson, MARVEL: measured active rotational-vibrational energy levels, *J. Mol. Spectrosc.*, 2007, **245**, 115–125.
80. A. G. Császár and T. Furtenbacher, Spectroscopic networks, *J. Mol. Spectrosc.*, 2011, **266**, 99–103.
81. T. Furtenbacher and A. G. Császár, MARVEL: measured active rotational-vibrational energy levels. II. Algorithmic improvements, *J. Quant. Spectrosc. Radiat. Transfer*, 2012, **113**, 929–935.
82. A. G. Császár, T. Furtenbacher and P. Árendás, Small molecules – Big data, *J. Phys. Chem. A*, 2016, **120**, 8949–8969.
83. R. Tóbiás, T. Furtenbacher and A. G. Császár, Cycle bases to the rescue, *J. Quant. Spectrosc. Radiat. Transfer*, 2017, **203**, 557–564.
84. R. Tóbiás, T. Furtenbacher, J. Tennyson and A. G. Császár, Accurate empirical rovibrational energies and transitions of $H_2{}^{16}O$, *Phys. Chem. Chem. Phys.*, 2019, **21**, 3473–3495.
85. T. Furtenbacher and A. G. Császár, The role of intensities in determining characteristics of spectroscopic networks, *J. Mol. Struct.*, 2012, **1009**, 123–129.

86. A. R. Al Derzi, T. Furtenbacher, J. Tennyson, S. N. Yurchenko and A. G. Császár, MARVEL analysis of the measured high-resolution spectra of $^{14}NH_3$, *J. Quant. Spectrosc. Radiat. Transfer*, 2015, **161**, 117–130.
87. A. G. Császár, W. D. Allen and H. F. Schaefer III, In pursuit of the *ab initio* limit for conformational energy prototypes, *J. Chem. Phys.*, 1998, **108**, 9751–9764.
88. W. Klopper, C. C. M. Samson, G. Tarczay and A. G. Császár, Equilibrium inversion barrier of NH_3 from extrapolated coupled-cluster pair energies, *J. Comput. Chem.*, 2001, **22**, 1306–1314.
89. E. Mátyus, C. Fábri, T. Szidarovszky, G. Czakó, W. D. Allen and A. G. Császár, Assigning quantum labels to variationally computed rotational-vibrational eigenstates of polyatomic molecules, *J. Chem. Phys.*, 2010, **133**, 034113.
90. D. M. Garner, D. G. Fleming, D. J. Arseneau, M. Senba, I. D. Reid and R. J. Mikula, Muonium addition reasctions in the gas phase: Quantum tunneling in $Mu + C_2H_4$ and $Mu + C_2D_4$, *J. Chem. Phys.*, 1990, **93**, 1732–1740.
91. K. Tanaka, M. Hayashi, M. Ohtsuki, K. Harada and T. Tanaka, Ortho-para mixing interaction in the vinyl radical detected by millimeter-wave spectroscopy, *J. Chem. Phys.*, 2009, **131**, 111101.
92. K. Tanaka, M. Toshimitsu, K. Harada and T. Tanaka, Determination of the proton tunneling splitting of the vinyl radical in the ground state by millimeter-wave spectroscopy combined with supersonic jet expansion and ultraviolet photolysis, *J. Chem. Phys.*, 2004, **120**, 3604.
93. H. Tanskanen, L. Khriachtchev, M. Räsänen, V. I. Feldman, F. F. Sukhov and A. Y. Orlov, *et al.*, Infrared absorption and electron paramagnetic resonance studies of vinyl radical in noble-gas matrices, *J. Chem. Phys.*, 2005, **123**, 064318.
94. F. Dong, M. Roberts and D. J. Nesbitt, High-resolution infrared spectroscopy of jet-cooled vinyl radical: Symmetic CH_2 stretch excitation and tunneling dynamics, *J. Chem. Phys.*, 2008, **128**, 044305.
95. P. L. Raston, T. Liang and G. E. Douberly, Infrared spectroscopy and tunneling dynamics of the vinyl radical in ^4He nanodroplets, *J. Chem. Phys.*, 2013, **138**(17), 174302.
96. D. J. Nesbitt and F. Dong, Ab initio large-amplitude quantum-tunneling dynamics in vinyl radical: a vibrationally adiabatic approach, *Phys. Chem. Chem. Phys.*, 2008, **10**, 2113–2122.
97. A. R. Sharma, J. M. Bowman and D. J. Nesbitt, Large-amplitude dynamics in vinyl radical: The role of quantum tunneling as an isomerization mechanism, *J. Chem. Phys.*, 2012, **136**, 034305.
98. H. G. Yu, H. Song and M. Yang, A rigorous full-dimensional quantum dynamics study of tunneling splitting of rovibrational states of vinyl radical C_2H_3, *J. Chem. Phys.*, 2017, **146**(22), 224307.
99. C. Brif, R. Chakrabarti and H. Rabitz, Control of quantum phenomena: past, present and future, *New J Phys*, 2010, **12**, 075008.

100. T. Baumert and G. Gerber, Fundamental interactions of molecules (Na_2, Na_3) with intense femtosecond laser pulses, *Isr. J. Chem.*, 1994, **34**(1), 103–114.
101. T. Brixner and G. Gerber, Quantum control of gas-phase and liquid-phase femtochemistry, *ChemPhysChem*, 2003, **4**(5), 418–438.
102. C. Horn, M. Wollenhaupt, M. Krug, T. Baumert, R. de Nalda and L. Bañares, Adaptive control of molecular alignment, *Phys. Rev. A*, 2006, **73**, 031401.
103. R. N. Zare, Laser control of chemical reactions, *Science*, 1998, **279**(5358), 1875–1879.
104. P. Brumer and M. Shapiro, Control of unimolecular reactions using coherent light, *Chem. Phys. Lett.*, 1986, **126**(6), 541–546.
105. M. Shapiro and P. Brumer, *Quantum Control of Molecular Processes*, Wiley-VCH Verlag GmbH & Co. KgaA, 2012.
106. R. J. Gordon and S. A. Rice, Active control of the dynamics of atoms and molecules, *Annu. Rev. Phys. Chem.*, 1997, **48**(1), 601–641.
107. P. Král, I. Thanopulos and M. Shapiro, Colloquium: Coherently controlled adiabatic passage, *Rev. Mod. Phys.*, 2007, **79**, 53–77.
108. J. Martin and D. Braun, Coherent control of atomic tunneling, *J. Phys B*, 2008, **41**(11), 115502.
109. J. M. Villas-Bôas, A. O. Govorov and S. E. Ulloa, Coherent control of tunneling in a quantum dot molecule, *Phys. Rev. B*, 2004, **69**, 125342.
110. L. G. C. Rego, L. F. Santos and V. S. Batista, Coherent control of quantum dynamics with sequences of unitary phase-kick pulses, *Annu. Rev. Phys. Chem.*, 2009, **60**(1), 293–320.
111. V. Averbukh, S. Osovski and N. Moiseyev, Controlled tunneling of cold atoms: From full suppression to strong enhancement, *Phys. Rev. Lett.*, 2002, **89**, 253201.
112. P. Ranitovic, C. W. Hogle, P. Rivière, A. Palacios, X. M. Tong and N. Toshima, *et al.*, Attosecond vacuum UV coherent control of molecular dynamics, *Proc. Natl. Acad. Sci. U. S. A.*, 2014, **111**(3), 912–917.
113. F. Krausz and M. Ivanov, Attosecond physics, *Rev. Mod. Phys.*, 2009, **81**, 163–234.
114. H. J. Wörner and P. B. Corkum, in *Attosecond Spectroscopy*, ed. M. Quack and F. Merkt, John Wiley & Sons, Ltd, **vol. 3**, 2011, pp. 1781–1804.
115. L. Gallmann and U. Keller in *Femtosecond and Attosecond Light Sources and Techniques for Spectroscopy*, ed. M. Quack and F. Merkt, John Wiley & Sons, Ltd, **vol. 3**, 2011, pp. 1805–1836.
116. E. Mátyus, G. Czakó and A. G. Császár, Toward black-box-type full- and reduced-dimensional variational (ro)vibrational computations, *J. Chem. Phys.*, 2009, **130**, 134112.
117. C. Fábri, E. Mátyus and A. G. Császár, Rotating full- and reduced-dimensional quantum chemical models of molecules, *J. Chem. Phys.*, 2011, **134**, 074105.
118. G. Floquet, Sur les équations différentielles linéaires à coefficients périodiques, *Ann. Sci. École Norm. Supér.*, 1883, **12**, 47–88.

119. C. Cohen-Tannoudji, B. Diu and F. Laloë, *Mécanique Quantique*, Hermann, 1973.
120. S. Haroche, L′atome habillé: une étude théorique et expérimentale des propriétés physiques datomes en interaction avec des photons de radiofréquence (*) - Première partie (**), *Ann. Phys.*, 1971, **14**(6), 189–326.
121. S. Haroche, L′atome habillé: une étude théorique et expérimentale des propriétés physiques datomes en interaction avec des photons de radiofréquence - Deuxième partie (*), *Ann. Phys.*, 1971, **14**(6), 327–387.
122. M. Quack, Theory of unimolecular reactions induced by monochromatic infrared radiation, *J. Chem. Phys.*, 1978, **69**, 1282–1307.
123. R. Marquardt, M. Quack, I. Thanopulos and D. Luckhaus, Tunneling dynamics of the NH chromophore in NHD_2 during and after coherent infrared excitation, *J. Chem. Phys.*, 2003, **118**(2), 643–658.
124. M. Sala, S. Guérin, F. Gatti, R. Marquardt and H. D. Meyer, Laser-induced enhancement of tunneling in NHD_2, *J. Chem. Phys.*, 2012, **136**, 194308.
125. M. Sala, F. Gatti and S. Guérin, Coherent destruction of tunneling in a six-dimensional model of NHD_2: A computational study using the multi-configuration time-dependent Hartree method, *J. Chem. Phys.*, 2014, **141**(16), 164326.

CHAPTER 5

From Nuclear Fluxes During Tunnelling to Electronic Fluxes During Charge Migration

DONGMING JIA,[a] JÖRN MANZ,*[a,b,c] AXEL SCHILD,[d]
VÍT SVOBODA[d] AND YONGGANG YANG[a,c]

[a] State Key Laboratory of Quantum Optics and Quantum Optics Devices, Institute of Laser Spectroscopy, Shanxi University, 92 Wucheng Road, Taiyuan 030006, China; [b] Institut für Chemie und Biochemie, Freie Universität Berlin, Takustrasse 3, 14195 Berlin, Germany; [c] Collaborative Innovation Center of Extreme Optics, Shanxi University, 92 Wucheng Road, Taiyuan 030006, China; [d] Laboratorium für Physikalische Chemie, Eidgenössische Technische Hochschule, Vladimir-Prelog-Weg 2, 8093 Zürich, Switzerland
*Email: jmanz@chemie.fu-berlin.de

5.1 Introduction

The purpose of this chapter is to manifest a quantum dynamical analogy of intramolecular nuclear tunnelling and electronic charge migration, with special emphasis on the corresponding nuclear and electronic fluxes. On first glance, the two processes may appear so different that one may not expect any analogy between them: on the one hand, nuclear tunnelling is a reactive process that transforms a ‘‘reactant’’ isomer into a ‘‘product’’ isomer by means of large-amplitude motions of the nuclei, in typical time domains of picoseconds (ps) or even much longer. Reactants and products are centred

---

Theoretical and Computational Chemistry Series No. 18
Tunnelling in Molecules: Nuclear Quantum Effects from Bio to Physical Chemistry
Edited by Johannes Kästner and Sebastian Kozuch

Published by the Royal Society of Chemistry, www.rsc.org

at two different minima of the potential energy surface (PES) of the molecular system in its electronic ground state, and they are separated from each other by the barrier of the PES. The system's energy is below the barrier, which means the reaction from the reactant to the product is classically forbidden – it proceeds by quantum mechanical tunnelling through the barrier. On the other hand, electronic charge migration is a non-reactive process at much higher energies that involves not just the electronic ground state. This allows the electronic charge to flow from one molecular site to another, in typical time domains from few hundred attoseconds (as) to few femtoseconds (fs); by comparison, nuclear motions appear to be nearly frozen in this time domain.

The quantum dynamics of nuclear tunnelling has been investigated from the early days of quantum mechanics[1] up to today; for an outstanding example of the present state-of-the-art, see the work by Fábri *et al.* on tunnelling isomerization of ammonia and its isotopomers, including stereomutation of NHDT;[2] see also the complementary chapters of this book.[3] For comparison, the first presentation of the quantum dynamics of charge migration is in the 1944 textbook on quantum chemistry by Eyring *et al.*;[4] however, this was largely forgotten[5] so the first experimental signatures of the process[6] came as a rediscovery that launched the renaissance of the field, see for example ref. 7–12 and the surveys of the literature in ref. 13 and 14. A prominent example is the first joint experimental and theoretical reconstruction of charge migration in the iodoacetylenic cation $HCCI^+$.[14,15] We call special attention to the two recent papers by Fábri *et al.* on tunnelling of NH_3 and NHDT,[2] and by Kraus *et al.* on charge migration in $HCCI^+$,[15] because they serve as important references for the subsequent quantum dynamics simulations of similar processes in similar model systems, the stereomutation of the CHFBr radical by nuclear tunnelling, and electronic charge migration in the bromoacetylenic cation $HCCBr^+$. The results will be used to illustrate the analogy of nuclear tunnelling and electronic charge migration.

The general quantum theory for the analogous processes, nuclear tunnelling and electronic charge migration, will be presented in Section 5.2, with special focus on the nuclear and electronic fluxes, *cf.* ref. 16. In order to emphasize the analogy, Section 5.2 uses common notations for both processes. Illuminating applications with more special notations for the two examples are given in Sections 5.3 and 5.4. Specifically, for the case of nuclear tunnelling, we consider the umbrella inversion of the CHFBr radical, as illustrated by the cartoon in Figure 5.1. Important properties of the system have been discovered and analysed recently; see the joint experimental and theoretical ref. 17 and 18. Section 5.3 presents the results that are essential for the present purpose. Section 5.4 presents analogous new results for the case of charge migration in $HCCBr^+$, as illustrated by the cartoon in Figure 5.2. The analogy of the results for nuclear tunnelling of CHFBr (Section 5.3) and for charge migration in $HCCBr^+$ of (Section 5.4) is discussed in Section 5.5. The conclusions are given in Section 5.6.

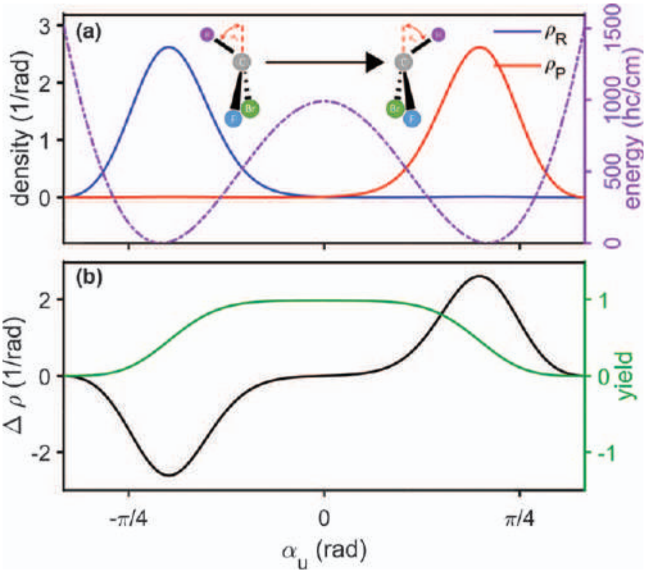

Figure 5.1 Periodic stereomutation of the CHFBr radical by nuclear tunnelling, from the reactant S-enantiomer (left) to the product R-enantiomer (right) along the angle α_u for umbrella inversion, and back. (a) Illustration of the stereomutation. The symmetric double-well potential energy curve $V(\alpha_u)$ with two equivalent minima which support the two enantiomers is shown as purple dashed line. The horizontal line is at the mean energy of the two vibrational levels E_g and E_e for the ground and excited states of the lowest tunnelling doublet – they coincide within graphical resolution. The level splitting is $\Delta E = E_e - E_g = 3.16\ \mathrm{h\,c\,cm^{-1}}$; the corresponding tunnelling period is $\tau_{\mathrm{stereo}} = h/\Delta E = 10.57$ ps. The horizontal line serves as baseline for the densities $\rho_R(\alpha_u)$ and $\rho_P(\alpha_u)$ of the reactant (R, blue) and product (P, red). The horizontal arrow symbolizes the nuclear flux from R to P during the first half period, $0 \leq t \leq \tau_{\mathrm{stereo}}/2$. (b) Density difference $\Delta\rho(\alpha_u) = \rho_P(\alpha_u) - \rho_R(\alpha_u)$ (black) and the resulting yield $y(\alpha_u)$ (green). The yield serves as spatial profile of the flux, *cf.* eqn (5.28) and (5.29) and Figure 5.3(c).

5.2 Quantum Theory

In order to establish the analogy of nuclear tunnelling and electronic charge migration, we employ simple models. Examples will be presented in Sections 5.3 and 5.4, respectively. Refinements and extensions will be discussed in the conclusions in Section 5.6. To begin with, we employ two-state models, with two vibrational states for applications to nuclear tunnelling, and with two electronic states for electronic charge migration. For convenience, we consider the scenarios where one of the two states is the ground (g) state and the other one is the next vibrationally or electronically excited (e) state. The two states are represented by the corresponding quantum mechanical wave functions Ψ_g and Ψ_e with energies E_g and E_e. To emphasize the analogy, we employ the same notations for the two different phenomena, which means in the cases of nuclear tunnelling and electronic charge migration, Ψ_g, Ψ_e and

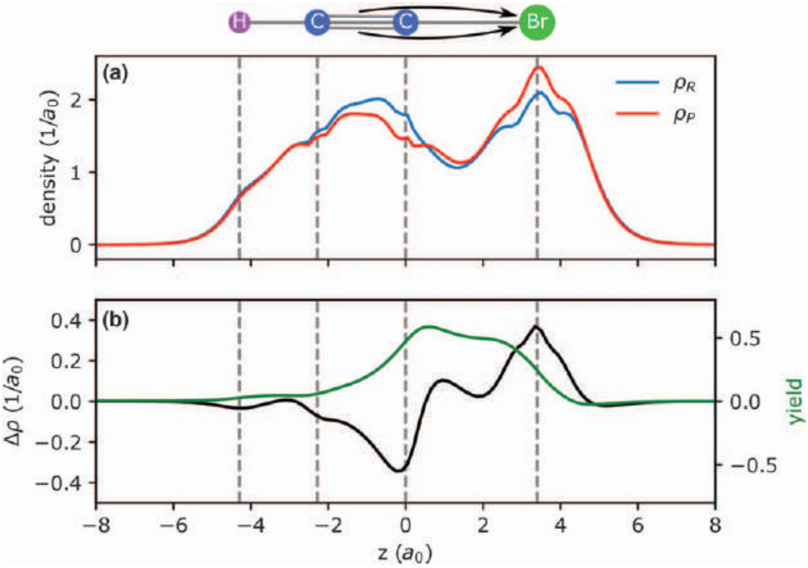

Figure 5.2 Periodic electronic charge migration in the linear HCCBr$^+$ cation along its axis z. (a) Cartoon of HCCBr$^+$ with the nuclei fixed at the global minimum structure of the precursor molecule HCCBr in the electronic ground state ($\tilde{X}^+\ ^1\Sigma^+$). Initially, the cation is prepared in the reactant (R) superposition state $1/\sqrt{2}(\Psi_g + \Psi_e)$ of the electronic ground state Ψ_g ($g = \tilde{X}^+\ ^2\Pi$) and the first-excited state Ψ_e ($e = \tilde{A}^+\ ^2\Pi$). The corresponding electronic eigenenergies are E_g and E_e, with energy gap $\Delta E = E_e - E_g = 2.74$ eV. The reactant (R) state evolves periodically to the product (P) superposition state, which is represented by $1/\sqrt{2}\ (\Psi_g - \Psi_e)$ (except for an irrelevant phase factor), and then back to R. The period for one cycle R→P→R is $\tau_{chm} = h/\Delta E = 1.51$ fs. Also shown are the one-dimensional axial densities of the valence electrons $\rho_R(z)$ (blue) of the initial state ("reactant" R) and $\rho_P(z)$ (red) for the corresponding "product" (P) state; they are obtained by integrating the related 3D one-electron densities of the valence electrons over the planes (x, y) perpendicular to the molecular axis (z). The curved, nearly horizontal arrows symbolize the flux of the valence electrons during the first half period $0 \le t \le \tau_{chm}/2$, mainly from the acetylenic moiety to the domain close to the bromine nucleus. (b) The density difference $\Delta\rho(z) = \rho_P(z) - \rho_R(z)$ (black) and the resulting yield $y(z)$ (green). The yield serves as spatial profile of the electronic flux that is shown in Figure 5.4(c), *cf.* eqn (5.28) and (5.29).

E_g, E_e represent nuclear and electronic wave functions and energies, respectively. The wave functions depend on the specific coordinates of the molecule (or the molecular radical or ion, or in general the molecular "model system"). For the time being, these coordinates will not be written down explicitly. For simplicity, we consider scenarios of oriented model systems.

The wave functions Ψ_g, Ψ_e and energies E_g, E_e are evaluated as eigenfunctions and eigenenergies of the time-independent Schrödinger equation (TISE)

$$H\ \Psi_j = E_j\ \Psi_j,\ j = g,\ e \tag{5.1}$$

where H denotes the system's model Hamiltonian. In the case of tunnelling, the two states belong to the lowest tunnelling doublet of the molecular system in its electronic ground state, embedded in a symmetric double-well potential. Effects of nuclear and electronic couplings are assumed to be negligible, *i.e.* the nuclear wave functions and energies Ψ_g, Ψ_e and E_g, E_e may be evaluated in the frame of the Born–Oppenheimer approximation (BOA).[19,20] Likewise, in the case of charge migration, the electronic wave functions and energies Ψ_g, Ψ_e and E_g, E_e of the system are evaluated using the approximation of fixed nuclei, *i.e.* again in the frame of the BOA, without consideration of the couplings between electrons and the nuclei. The effects of the couplings will also be discussed in the conclusions.

For special cases, the wave functions Ψ_g, Ψ_e are real-valued, but in general they are complex,

$$\Psi_j = \psi_j \exp(i\ \delta_j),\ j = \mathrm{g},\ \mathrm{e}, \tag{5.2}$$

with real-valued functions ψ_j and phases δ_j that depend on the coordinates.

We consider the scenario where the initial state of the system is prepared as superposition state

$$\Psi(t=0) = C_g\ \Psi_g + C_e\ \Psi_e. \tag{5.3}$$

The coefficients C_g and C_e may be real, and they may be equal to each other (*e.g.* $C_g = C_e = 1/\sqrt{2}$), but in general they are complex and not equal to each other,

$$C_j = c_j \exp(i\ \eta_j),\ j = \mathrm{g},\ \mathrm{e} \tag{5.4}$$

with real-valued amplitudes $c_j \geq 0$ and phases η_j. The corresponding initial populations (or occupation probabilities) of the ground and excited states,

$$P_g(t=0) = {c_g}^2,\ P_e(t=0) = {c_e}^2 \tag{5.5}$$

are normalized,

$$P_g(t=0) + P_e(t=0) = {c_g}^2 + {c_e}^2 = 1. \tag{5.6}$$

The system's time evolution is described in terms of the time dependent wave function $\Psi(t)$. It is evaluated as solution of the time-dependent Schrödinger equation (TDSE)

$$i\ \hbar\ \mathrm{d}/\mathrm{d}t\ \Psi(t) = H\ \Psi(t) \tag{5.7}$$

with initial value (5.3). The result is

$$\Psi(t) = C_g \exp(-i\ E_g\ t/\hbar)\ \Psi_g + C_e \exp(-i\ E_e\ t/\hbar)\ \Psi_e. \tag{5.8}$$

The corresponding populations of states g and e are time independent,

$$P_g(t) = P_g(t=0) = {c_g}^2,\ P_e(t) = P_e(t=0) = {c_e}^2. \tag{5.9}$$

This means that, for our scenarios, there are no transitions that transfer the population between states g and e – the system evolves adiabatically.

The time evolution of the system's density is

$$\sigma(t) = |\Psi(t)|^2 = P_g\ \sigma_g + P_e\ \sigma_e + 2\ c_g\ c_e\ \psi_g\ \psi_e \cos\left(\Delta E\ t/\hbar - \Delta\delta - \Delta\eta\right). \tag{5.10}$$

Here

$$\sigma_g = \psi_g{}^2,\ \sigma_e = \psi_e{}^2 \tag{5.11}$$

denote the time-independent densities of the ground and excited states,

$$\Delta E = E_e - E_g \tag{5.12}$$

is the energy gap between the states, and

$$\Delta\delta = \delta_e - \delta_g,\ \Delta\eta = \eta_e - \eta_g \tag{5.13}$$

are the phase differences. Apparently, the density evolves periodically, with period[1]

$$\tau = h/\Delta E \tag{5.14}$$

where h denotes Planck's constant.

In the applications below, we consider the scenarios where the eigenfunctions are real-valued, such that $\Delta\delta = 0$ in eqn (5.10) and (5.13). Moreover, the results do not depend on the absolute phase of the wave function $\Psi(t)$, which means we may set $\eta_g = 0$ and $\Delta\eta = \eta_e$ in eqn (5.4), (5.10) and (5.13). Eqn (5.10) then simplifies to

$$\sigma(t) = |\Psi(t)|^2 = P_g\ \sigma_g + P_e\ \sigma_e + 2\ c_g\ c_e\ \Psi_g\ \Psi_e \cos\left(\Delta E\ t/\hbar - \Delta\eta\right). \tag{5.15}$$

For the present purposes, it is convenient to rewrite eqn (5.15) in the way laid out in ref. 21, with proper adaption of the notation. Accordingly, we employ the variable

$$t' = t - t_{\Delta\eta} \tag{5.16}$$

which denotes the time shifted by

$$t_{\Delta\eta} = \Delta\eta\ \hbar/\Delta E = \tau\ \Delta\eta/2\pi. \tag{5.17}$$

The densities at times $t' = 0$ and $t' = \tau/2$ when the cos term in eqn (5.15) achieves its maximum and minimum values are labelled by R ("reactant") and P ("product"),

$$\sigma_R = P_g\ \sigma_g + P_e\ \sigma_e + 2\ c_g\ c_e\ \Psi_g\ \Psi_e \tag{5.18}$$

$$\sigma_P = P_g\ \sigma_g + P_e\ \sigma_e - 2\ c_g\ c_e\ \Psi_g\ \Psi_e, \tag{5.19}$$

respectively. Let us take a minute here to discuss the definitions of the "reactant" and "product" in eqn (5.18) and (5.19). From a formalistic point of view, the assignments of the right-hand sides of eqn (5.18) and (5.19) to "R" and "P" are arbitrary, because the signs of the real-valued wave functions Ψ_g and Ψ_e are arbitrary – both Ψ_g, Ψ_e and $-\Psi_g$, $-\Psi_e$ are solutions of the TISE [eqn (5.1)]. By convention, the sign of the wave function of the ground state is set such that Ψ_g is dominantly positive, but for Ψ_e, there is no such rule. That means that we are free to determine the sign of Ψ_e such that the assignment of "R" in eqn (5.18) conforms to the experimental preparation of the "reactant". The definition of the "product" in eqn (5.19) then follows automatically. Applications will be demonstrated in Sections 5.3 and 5.4.

Using the density difference

$$\Delta\sigma = \sigma_P - \sigma_R = -4\ c_g\ c_e\ \Psi_g\ \Psi_e \tag{5.20}$$

the time evolution of the density (5.15) can be rewritten in compact form,

$$\sigma(t) = \sigma_R + \Delta\sigma\ \sin^2(\pi t'/\tau). \tag{5.21}$$

The first term in eqn (5.21) is the (time-independent) density of the reactant, which serves as a reference. The second term accounts for the deviation of the density at time t from the reference. The periodicity of the $\sin^2$-function implies that the density alternates between $\sigma(t) = \sigma_R$ for $t = 0, \tau, 2\tau, \ldots$ and $\sigma(t) = \sigma_P$ for $t = \tau/2, 3\tau/2, 5\tau/2, \ldots$. Furthermore, eqn (5.20) and (5.21) show that efficient periodic shifts of the density from the reactant to the product and back call for good overlap of the wave functions Ψ_g and Ψ_e, or turning the table, there is neither tunnelling nor charge migration if Ψ_g and Ψ_e do not overlap. Eqn (5.20) and (5.21) also tell us that for the given wave functions Ψ_g and Ψ_e of the ground and excited states, the most efficient shift of the density is obtained if the product of the coefficients achieves its maximum value

$$\max\ c_g\ c_e = \tfrac{1}{2} \text{ for } c_g = c_e = 1/\sqrt{2}, \tag{5.22}$$

cf. eqn (5.6). That means, in the ideal case, the superposition state (5.3) should be prepared with equal populations of the ground and excited states, $P_g = P_e = \frac{1}{2}$.[21]

In principle, the wave functions Ψ_g, Ψ_e and the densities $\sigma(t)$, σ_g, σ_e and $\Delta\sigma$ in eqn (5.15) and (5.21) depend on all coordinates of the system. It is helpful to reduce these high-dimensional (high-D) densities to low-D ones, for example to 3D or even to 1D ones. In the subsequent applications to nuclear tunnelling and to electronic charge migration, we shall employ 1D densities which depend on the corresponding nuclear or electronic coordinate q, respectively. The 1D densities will be denoted by the letter "ρ", in order to distinguish them from the high-D densities that are denoted by "σ". Thus eqn (5.21) is reduced to

$$\rho(q, t) = \rho_R(q) + \Delta\rho(q)\ \sin^2(\pi\ t'/\tau). \tag{5.23}$$

Various methods for reducing high-D to 1D densities are detailed in ref. 16. Two examples will be demonstrated in Sections 5.3 and 5.4.

Next, we determine the nuclear or electronic fluxes $F(q, t)$ during tunnelling and charge migration, respectively. Fluxes and densities are complementary to each other, which means at a given time t, the density $\rho(q, t)$ of the system tells us where it is, whereas the flux $F(q,\, t)$ quantifies its temporal rate and direction of change. In 3D models, the flux $F(q,\, t)$ at time t determines the number of particles that flow through a surface perpendicular to the coordinate q per time, at the instant t. Positive and negative values of $F(q,\, t)$ mean that the particles flow along q, or in the opposite direction, respectively.

In 1D models, the fluxes $F(q,\, t)$ are equal to the 1D flux densities $j(q,\, t)$.[16] They are related to the corresponding densities $\rho(q,\, t)$ by means of the 1D continuity equation,

$$\partial\rho(q,\, t)/\partial t + \partial j(q,\, t)/\partial q = 0 \tag{5.24}$$

with boundary conditions that depend on the system.[16] In the present applications, we consider scenarios where both the density as well as the flux are negligible for values of q smaller than some minimum value, $q_{\min}$,

$$\rho(q,\, t) = 0,\ F(q,\, t) = j(q,\, t) = 0 \text{ for } q \leq q_{\min}. \tag{5.25}$$

The 1D flux can then be evaluated by integration of the continuity eqn (5.24), with the boundary conditions (5.25). The result is

$$F(q,t) = j(q,t) = -\int_{q_{\min}}^{q} \mathrm{d}q'\ \partial\rho(q',t)/\partial t. \tag{5.26}$$

We re-emphasize that the densities and flux (densities) carry complementary information about the system. For example, in applications where one has complete knowledge about the time evolution of the density $\rho(q,\, t)$, this still does not suffice to calculate the flux $F(q,\, t)$ or the flux density $j(q,\, t)$, because one also needs boundary conditions such as in eqn (5.25).[22] Turning the tables, two identical or practically indistinguishable densities $\rho(q,\, t)$ may be associated with two entirely different fluxes or flux densities, depending on the boundary conditions.[23]

For the present 1D two-state models with time evolutions of the density specified by eqn (5.23), the time derivative in eqn (5.26) can be carried out analytically. As a result, the boundary condition (5.25) yields the 1D flux or flux density

$$F(q,t) = j(q,t) = -\int_{q_{\min}}^{q} \mathrm{d}q' \Delta\rho(q')\pi/\tau \sin(2\pi t'/\tau). \tag{5.27}$$

Accordingly, the flux depends exclusively on the time-dependent part of the density, eqn (5.15) or (5.23). It evolves periodically, with the same period τ as the density, eqn (5.14), but with phase shift $\pi/2$. As a consequence, maximum or minimum shifts of the density at the times when $\cos(2\pi t'/\tau) = \pm 1$ correlate with zero fluxes, and *vice versa.*

Finally, it is instructive to consider the yield $y(q)$ of the flux,[13,24] which means the time integrated number of particles that pass *via* q when they flow from the domain $q_{\mathrm{min}} \leq q' \leq q$ to the complementary domain $q \leq q'$ during the half period $0 \leq t' \leq \tau/2$,

$$y(q) = \int_0^{\tau/2} \mathrm{d}t' j(q, t') = -\int_{q_{\mathrm{min}}}^{q} \mathrm{d}q' \Delta\rho(q'). \tag{5.28}$$

The 1D flux or flux density (5.27) can, therefore, also be expressed as

$$F(q,\ t) = j(q,\ t) = y(q)\ \pi/\tau\ \sin\ (2\pi t'/\tau). \tag{5.29}$$

Eqn (5.29) tells us that the 1D flux or the 1D flux density evolves with robust spatial profile $y(q)$, and this is modulated by the periodic time evolution factor, sin $(2\pi t'/\tau)$. Alternating maximum and minimum values of the fluxes in forward and backward directions from R to P and from P to R are achieved at times $t' = \tau/4$, $5\tau/4$, $9\tau/4, \ldots$ and $t' = 3\tau/4$, $7\tau/4$, $11\tau/4, \ldots$, respectively. The maximum absolute values of the fluxes are reciprocal to the period τ, or they are proportional to the energy gap ΔE between the levels of the excited and ground states, *cf.* eqn (5.14).

5.3 Application to the Stereomutation of CHFBr by Nuclear Tunnelling

Our first application of the general quantum theory for the analogy of nuclear tunnelling and electronic charge migration is to the stereomutation of the CHFBr radical; as an example of nuclear tunnelling, see Figure 5.1. There are several motivations for the choice of this system:

Experimentally, the stereomutation of CHFBr is initiated by enantiomer selective preparation of the precursor (*S*)-CHFBrI, and by photo-dissociating it according to the scheme[17,18]

$$\begin{aligned} &(S)\text{-CHFBrI} \rightarrow (S)\text{-CHFBrI}^* \rightarrow (S)\text{-CHFBr} - \text{I} \rightarrow (R)\text{-CHFBr} - \text{I} \\ &\qquad \rightarrow (S)\text{-CHFBr} + \text{I} \rightarrow (R)\text{-CHFBr} + \text{I} \rightarrow (S)\text{-CHFBr} + \text{I} \rightarrow \ldots. \end{aligned} \tag{5.30}$$

Specifically, an ultrashort UV laser pump-pulse (wavelength 266 nm, full temporal width at half maximum, FWHM = 70 fs) excites the educt (*S*)-CHFBrI from its electronic ground state $\tilde{X}^{+1}$A to the dissociative state $\tilde{A}^{+}\ {}^{1}$E(1). This induces two processes, namely C–I bond breaking as well as stereomutation from the (*S*)-enantiomer to the (*R*)-enantiomer, and back. The two processes are launched simultaneously, which means the first cycle of stereomutation starts during photodissociation. After photodissociation, the stereomutation persists in the CHFBr radical. Experimental details are presented in ref. 17 and 18. Suffice it here to say that the bond breaking is measured by means of time-resolved photo-ion yield spectroscopy (TR-PIS) as well as photo-electron pump (266 nm)–probe (133 nm) spectroscopy (TR-PES). The stereomutation is monitored by means of a new technique: time-resolved photoelectron circular dichroism (TR-PECD). Accordingly, the photodissociation is completed after about 70 fs, whereas the first cycle of stereomutation ("(*S*)-CHFBr − I → (*R*)-CHFBr − I → (*S*)-CHFBr + I" in eqn (5.30)) takes about 200 fs; subsequently, it slows down to the ps time domain. The experimental TR-PECD spectra suggest stereomutation of the CHFBr radical by tunnelling,

$$(S)\text{-CHFBr} \rightarrow (R)\text{-CHFBr} \rightarrow (S)\text{-CHFBr} \rightarrow \ldots \tag{5.31}$$

[compare with the second line of eqn (5.30)], with tunnelling period $\tau_{\text{stereo}} \approx 10$ ps, for a full cycle from R to P and back to R. The results presented in ref. 17 and 18 provide the first experimental observation of stereomutation in the fs-to-ps time domain. This attracts our attention to the model system, calling for its quantum dynamics simulation.

The present investigation of the stereomutation of CHFBr by tunnelling, eqn (5.31), is encouraged furthermore by recent quantum dynamical simulations of the analogous stereomutation of the isotopically substituted ammonia molecule[2]

$$(S)\text{-NHDT} \rightarrow (R)\text{-NHDT} \rightarrow (S)\text{-NHDT} \rightarrow \ldots. \tag{5.32}$$

Here the representative nuclear wave function was propagated in full dimensionality (full-D) on the PES of ammonia in the electronic ground state, without considerations of any couplings to more excited states. The PES was evaluated by means of quantum chemistry state-of-the-art *ab initio* methods. Similar quantum dynamics simulations were also performed for the umbrella inversion of the non-substituted ammonia by tunnelling.[2] The results for the full-D nuclear fluxes of $^{14}NH_3$ were then compared with our previous quantum dynamical results based on a two-state model[25] with empirical 1D model potential.[26] The full-D and 1D results agree with each other almost quantitatively.[2] This supports the present 1D quantum dynamical two-state model simulation of the stereomutation (5.31) by nuclear tunnelling.

Thus, we perform a quantum dynamics model simulation of the stereomutation of the CHFBr radical (5.31). Specifically, we employ a 1D model for the nuclear tunnelling along the angle α_u for the umbrella (u) inversion of CHFBr, as illustrated in Figure 5.1(a). The angle α_u thus takes the role of the generic coordinate which is called "q" in Section 5.2. The corresponding 1D model Hamiltonian is

$$H(\alpha_u) = -\hbar^2\, \partial^2/2\, I\, \partial\, {\alpha_u}^2 + V(\alpha_u). \tag{5.33}$$

The first term accounts for the kinetic energy of the angular nuclear motion along α_u, with moment of inertia $I = m_H\, {R_{CH}}^2$, where $m_H = 1.0079$u is the mass of the hydrogen atom, and R_{CH} is the C–H bond length which is approximately constant during the umbrella inversion, $R_{CH} = 1.08$ Å. This expression for the kinetic energy is equivalent to the term used in ref. 25. The details of the construction of this kinetic energy operator, by reduction of the full-D expression to the 1D model, are presented in ref. 18, based on the general approach of ref. 27 to applications in terms of arbitrary curvilinear coordinates.

The second term in eqn (5.33) is the potential energy curve along α_u, illustrated in Figure 5.1(a). It is a symmetric double-well potential. The "left" and "right" potential wells support the reactant (*R*) and product (P) enantiomers, which are centred at the potential minima at $\alpha_{uR} = -38°$ and at $\alpha_{uP} = -\alpha_{uR} = +0.66$ rad ($+38°$), respectively. For convenience, we define corresponding domains of R ($\alpha_u < 0$) and P ($\alpha_u > 0$). These domains are separated from each other by the potential barrier at $\alpha_u = \alpha_{ub} = 0$, also called the transition state, $\ddagger$. The corresponding cartoons of R and P in Figure 5.1(a) are mirror images of each other, with the mirror plane in vertical orientation perpendicular to the paper plane. The potential curve $V(\alpha_u)$ has been calculated by means of the ORCA program package,[28] by performing a relaxed scan at the Møller–Plesset-2 level of quantum chemistry, with the correlation consistent valence basis set from the Karlsruhe basis set family, specifically valence triple-zeta and two sets of polarization functions and a set of diffuse functions def2-TZVPPD for use with the Stuttgart–Dresden–Bonn relativistic effective core potentials on all atoms,[29] see ref. 18 for the details.

The TISE (5.1) with model Hamiltonian (5.33) is solved for the two real-valued eigenfunctions Ψ_g and Ψ_e and for the energies E_g and E_e of the ground and first excited vibrational states by means of the discrete variable representation (DVR) method[30] on a fine, regularly spaced grid in the angular range $-\pi/3 \text{ rad} \leq \alpha_u \leq +\pi/3$ rad ($-60° \leq \alpha_u \leq +60°$). The resulting energies and the tunnelling splitting $\Delta E = E_e - E_g = 3.16 \text{ h c cm}^{-1}$ are illustrated in Figure 5.1(a). The corresponding time for one cycle $R \rightarrow P \rightarrow R$ of the stereomutation (5.33) is $\tau_{\text{stereo}} = h/\Delta E = 10.57$ ps. The general notation "τ" of Section 5.2 is thus specified as "τ_{stereo}", for the present application to stereomutation of CHFBr. (Note that the value 5.285 ps that is given in ref. (18) applies to the half cycles $R \rightarrow P$ and $P \rightarrow R$.) The symmetry of the double-well potential $V(\alpha_u)$ implies that $\Psi_g(\alpha_u) = \Psi_g(-\alpha_u)$ and $\Psi_e(\alpha_u) = -\Psi_e(-\alpha_u)$ are symmetric and antisymmetric with respect to the umbrella inversion angle α_u, respectively; these symmetry relations for the wave functions impose various symmetry properties on the nuclear densities and the nuclear fluxes and these are specified below. The signs of the wave functions are chosen such that they are consistent with the experimental preparation of the reactant enantiomer [=(*S*)-CHFBr], see the discussion after eqn (5.18) and (5.19). Specifically, we set $\Psi_g(\alpha_u) > 0$, in accord with the standard convention, and $\Psi_e(\alpha_u)$ is positive in the domain of the reactants ($\alpha_u < 0$) but negative in the domain of the products ($\alpha_u > 0$).

The resulting nuclear angular densities $\rho_R(\alpha_u)$ and $\rho_P(\alpha_u)$ of the reactant (R, red) and product (P, blue) embedded in the left and right wells of $V(\alpha_u)$ are also illustrated in Figure 5.1(a). For symmetry reasons, $\rho_P(\alpha_u) = \rho_R(-\alpha_u)$. Both $\rho_R(\alpha_u)$ and $\rho_P(\alpha_u)$ have single maxima that are located close to the left and right minima of the double minimum potential at α_{uR} and α_{uP}, respectively. The values of $\rho_R(\alpha_u)$ and $\rho_P(\alpha_u)$ at $\alpha_u = 0$, *i.e.* at the barrier of the potential curve, are negligible.

Figure 5.1(b) has the nuclear density difference $\Delta\rho(\alpha_u) = \rho_P(\alpha_u) - \rho_R(\alpha_u)$ (black) and the nuclear yield $y(\alpha_u)$ (green), *cf.* eqn (5.20) and (5.28). For symmetry reasons, $\Delta\rho(\alpha_u) = -\Delta\rho(-\alpha_u)$, $\Delta\rho(\alpha_u = 0) = 0$ and $y(\alpha_u) = y(-\alpha_u)$. The value of $\Delta\rho(\alpha_u)$ is negative in the reactant domain but positive in the product domain. The yield is always positive. A significant property of the yield $y(\alpha_u)$ – with important consequences for the nuclear fluxes $F(\alpha_u, t)$ – is that it has a plateau in the domain of the potential barrier, with maximum value at the top of the barrier ($\alpha_u = 0$).

In accord with the experimental initiation of the stereomutation of the CHFBr radical,[17,18] and also for convenience, we set the time $t = 0$ when the nuclear tunnelling starts from the reactant (*S*)-enantiomer. This means that the initial superposition of the wave function (5.3) is prepared with equal coefficients, $C_g = C_e = 1/\sqrt{2}$, and the phases in eqn (5.4) are equal to zero. This scenario simplifies the application of the general theory of Section 5.2. In particular, the time shift in eqn (5.17) is equal to zero, such that $t' = t$ in all subsequent equations for the densities and for the fluxes or the 1D flux densities.

The resulting time evolution of the nuclear angular density $\rho(\alpha_u, t)$ during the first cycle ($0 \leq t \leq \tau_{\text{stereo}} = 10.57$ ps) of the periodic stereomutation (5.31) of CHFBr by umbrella inversion is illustrated in Figure 5.3(a). For symmetry reasons, $\rho(\alpha_u, t) = \rho(-\alpha_u, \tau_{\text{stereo}}/2 - t) = \rho(-\alpha_u, \tau_{\text{stereo}}/2 + t) = \rho(\alpha_u, \tau_{\text{stereo}} - t)$. This implies the special symmetry relation $\rho(\alpha_u, \tau_{\text{stereo}}/4) = \rho(-\alpha_u, \tau_{\text{stereo}}/4) = \rho(\alpha_u, 3\tau_{\text{stereo}}/4) = \rho(-\alpha_u, 3\tau_{\text{stereo}}/4)$. Accordingly, the initial density of the reactant ($t = 0$) tunnels to the product ($t = \tau_{\text{stereo}}/2$) and then back to the reactant ($t = \tau_{\text{stereo}}$). At the intermediate times $t = \tau_{\text{stereo}}/4$ and $t = 3\tau_{\text{stereo}}/4$, the total nuclear density is separated into two equivalent parts for the reactant and for the product. Thus, during the first half period ($0 \leq t \leq \tau_{\text{stereo}}/2$), the nuclear density grows for the product at the expense of the reactant, without any significant appearance at the potential barrier, and *vice versa* during the second half period ($\tau_{\text{stereo}}/2 \leq t \leq \tau_{\text{stereo}}$).

Figure 5.3(b) illustrates the corresponding changes of the nuclear angular density $\rho(\alpha_u, t)$ compared to the initial density $\rho(\alpha_u, t = 0) = \rho_R(\alpha_u)$. For symmetry reasons, $\Delta\rho(\alpha_u, t) = \rho(\alpha_u, t) - \rho_R(\alpha_u) = -\Delta\rho(-\alpha_u, t) = \Delta\rho(\alpha_u, \tau_{\text{stereo}} - t) = -\Delta\rho(-\alpha_u, \tau_{\text{stereo}} - t)$, and the transfer of nuclear density from R to P and back to R implies that $\Delta\rho(\alpha_u, t) < 0$ in the reactant domain ($\alpha_u < 0$), in contrast with $\Delta\rho(\alpha_u, t) > 0$ in the product domain ($\alpha_u > 0$).

Finally, the periodic nuclear flux $F(\alpha_u, t)$ [or the equivalent 1D flux density $j(\alpha_u, t)$] along the umbrella inversion angle α_u during the first cycle ($0 \leq t \leq \tau_{\text{stereo}} = 10.57$ ps) is shown in Figure 5.3(c). In accord with eqn (5.29), the angular profile of the flux is equal to the yield $y(\alpha_u)$, and this is modulated by the sinusoidal time evolution with period τ_{stereo}. As a consequence, the nuclear angular flux has the symmetry relations $F(\alpha_u, t) = F(-\alpha_u, t)$ and $F(\alpha_u, t) = F(\alpha_u, \tau_{\text{stereo}}/2 - t) = -F(\alpha_u, \tau_{\text{stereo}}/2 + t) = -F(\alpha_u, \tau_{\text{stereo}} - t)$. Apparently, the nuclear angular flux $F(\alpha_u, t)$ is positive during the first half cycle ($0 < t < \tau_{\text{stereo}}/2$) when R tunnels along α_u to P, whereas it is negative during the second half cycle ($\tau_{\text{stereo}}/2 < t < \tau_{\text{stereo}}$) when P tunnels back to R. At the switches of the directions, $\mathrm{F}(\alpha_u, t) = 0$ for $t = 0$, $\tau_{\text{stereo}}/2$, τ_{stereo}, $3\tau_{\text{stereo}}/2$, *etc.* In contrast, the "local" maximum and minimum values of the flux $F(\alpha_u, t)$ at umbrella inversion angle α_u are obtained at $t = \tau_{\text{stereo}}/4$, $5\tau_{\text{stereo}}/4$, $9\tau_{\text{stereo}}/4, \ldots$ and at $3\tau_{\text{stereo}}/4$, $7\tau_{\text{stereo}}/4$, $11\tau_{\text{stereo}}/4, \ldots$, respectively.

Quite remarkable is the fact that the "global" maxima of the "forward" flux from R to P, and the minima of the "backward" flux from P to R, occur at

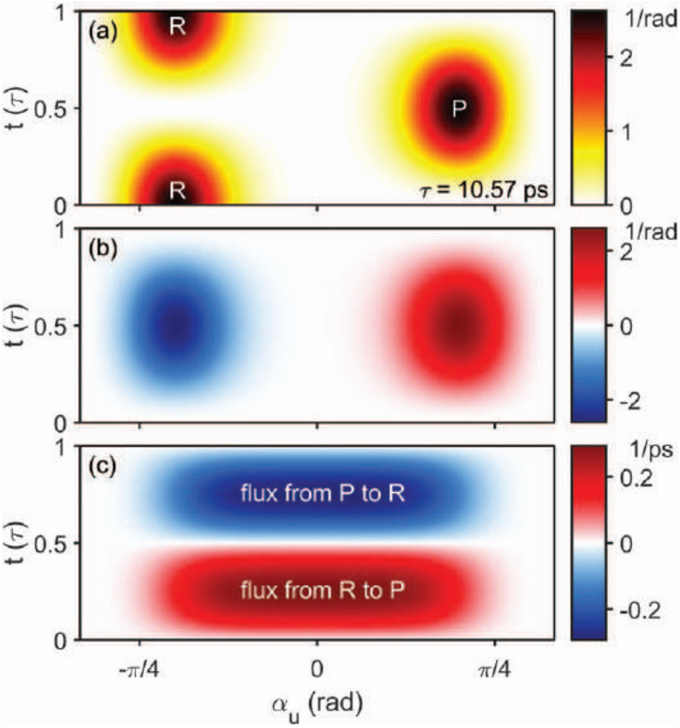

Figure 5.3 Time evolution of the periodic stereomutation of the CHFBr radical by nuclear tunnelling, from the reactant (*R*) *S*-enantiomer to the product (P) *R*-enantiomer along the angle α_u for umbrella inversion, and back, during the first period, $0 \leq t \leq \tau_{\text{stereo}} = 10.57$ ps; compare with Figure 5.1. (a) Nuclear density $\rho(\alpha_u, t)$. The value 0.008 rad^{-1} of $\rho(\alpha_u, t)$ at the planar configuration $(\alpha_u = 0)$ is very small compared to the maximum values 2.622 rad^{-1} close to the potential minima. (b) Difference in the nuclear density $\rho(\alpha_u, t)$ at time t minus the initial density of the reactant, $\rho(\alpha_u, 0) = \rho_R(\alpha_u)$. (c) One-dimensional (1D) nuclear flux $F(\alpha_u, t)$, from R to P and back. At $t = \tau_{\text{stereo}}/2$, the flux changes sign, hence $F(\alpha_u, t = \tau_{\text{stereo}}/2) = 0$. The 1D flux is equal to the 1D nuclear flux density $j(\alpha_u, t)$. The results (a)–(c) are illustrated by color-coded contour plots.

$\alpha_u = 0$, *i.e.* at the potential barrier where the nuclear density is always exceedingly small. Moreover, in the entire domain of the barrier, the values of the flux are just slightly below (above) those maximum (minimum) values – the angular shape of the flux, *i.e.* the yield, has a plateau in the domain of the potential barrier, *cf.* Figure 5.1(b). This result, which may appear paradoxical at first glance, can be rationalized by the following interpretation:[31] the nuclei of the CHFBr radical prefer the two equivalent global minimum structures, either R or P, and they try to avoid the structure of the "transition state" ($\ddagger$) at the potential barrier. However, the radical is prepared initially in the superposition state (5.3) – this is not in an eigenstate, *i.e.* it is non-stationary. Hence quantum mechanics forces the radical to undergo periodic stereomutation from R *via* ‡ to P and then from P *via* ‡ back to R, and so on. Since the nuclei of CHFBr dislike the geometry of the transition state, they make it through ‡ as fast as possible, *i.e.* with maximum velocity. The nuclear flux density may be written as nuclear density times a velocity field.[23,32] The very-high tunnelling velocity thus enables the maximum value of the 1D flux density, or the flux, at the potential barrier, in spite of the very low value of the density.

5.4 Application to Electronic Charge Migration in $HCCBr^{+}$

Let us now switch gears from the rather slow nuclear tunnelling in the typical time domain from picoseconds (ps) to even much longer times,[1] to the ultrafast electronic charge migration in the typical time domain from few hundred attoseconds (as) to few femtoseconds (fs). Our second application of the general quantum theory for the analogy of nuclear tunnelling and electronic charge migration (Section 5.2) is thus to charge migration in the bromo-acetylenic cation, $HCCBr^{+}$. Again, there are several motivations for the choice of this system.

The $HCCBr^{+}$ cation is similar to the $HCCI^{+}$ cation, which serves as a key example. The first joint experimental and theoretical reconstruction and control of charge migration in $HCCI^{+}$ was demonstrated recently by Wörner with partners and coworkers,[15] see also ref. 14. Here we summarize some important details of their reconstruction in order to set up a model that will then allow us to carry out analogous quantum dynamics simulation of charge migration in $HCCBr^{+}$. For this purpose, we centre attention on a specific scenario of their experiments, namely, at first, they orient the neutral linear precursor molecule HCCI along an axis that serves as a laboratory fixed z axis, with the C–I bond pointing into the direction $z \geq 0$. By analogy, we shall assume that $HCCBr^{+}$ is oriented along z, with the origin of the z-coordinate at the C nucleus of the C–Br bond pointing to $z \geq 0$. The generic coordinate "q", which was introduced in Section 5.2, is thus specified as "z", for the present application.

After orientation, an intense laser pulse (maximum intensity closely above 10^{14} W cm^{-2}, wavelength 800 nm, duration about 30 fs, polarization perpendicular to the z-axis) causes tunnel ionization of the neutral precursor, precisely at the selective peak of the laser cycle with maximum electric field strength. The tunnel ionization takes (presumably much) less than 200 as. It prepares the cation in a superposition (5.3) of its electronic ground state ($\mathrm{g} = \tilde{X}^{+}\,{}^{2}\Pi$) and the first excited state ($\mathrm{e} = \tilde{A}^{+}\,{}^{2}\Pi$). For the example of $HCCI^{+}$, the corresponding electronic energy gap is $\Delta E = E_\mathrm{e} - E_\mathrm{g} = 2.23$ eV, at the geometry of the global minimum geometry of the neutral precursor HCCI. Within the next *ca.* 1.7 fs, the electric field changes sign and drives the photo-electron back to the cation. Upon re-collision, the system generates high harmonics that are then used for spectroscopic analysis of the cation.

This allowed the authors of ref. 15 to determine the coefficients in eqn (5.3), with a time resolution of about 100 as. Accordingly, from the perspective of the neutral precursor, the cation is generated with an electron hole centred at the halogen. This can be rationalized because it is easier to photo-detach an electron from a halogen such as iodine or bromine, compared to the hydrogen or carbon atoms of the acetylenic moiety. Changing the perspective from considerations of the electron hole to electrons, the "reactant" cation $HCCI^+$ (and, by our assumption, also $HCCBr^+$) is created with some excess electronic charge in the acetylenic moiety.

The authors of ref. 15 checked carefully that the initial state (5.3) is not contaminated by any other states. This provides a two-state (g, e) scenario of charge migration in the cation, along its *z*-axis, perfectly ready for application of the general theory of Section 5.2. The charge migration proceeds in quasi-field-free environment, because the laser field remains perpendicular to the axis of the cation, such that it cannot induce any further electronic transitions. The authors of ref. 15 then carried out quantum dynamics simulations of the charge migration in $HCCI^+$, starting from the initial state (5.3) and using the model of fixed nuclei. They also checked that the populations of the two states do not change due to any other transitions, *i.e.* the charge migration is adiabatic, in accord with the general theory in Section 5.2, *cf.* eqn (5.8). As a result, they discovered the periodic migration of the electron hole, from the initial location at the iodine atom to the acetylenic moiety, and back. In the case of $HCCI^+$, the period of charge migration is $\tau_{\mathrm{chm}} = h/\Delta E = 1.85$ fs. The generic notation "τ" in Section 5.2 is thus replaced by "τ_{chm}" for the present application to charge migration. In the complementary consideration of the excess electronic charge, it flows from its initial preferential localization in the acetylenic moiety [electronic density $\rho_{\mathrm{R}}(z)$ of the "reactant"] preferably to the halogen atom [electron density $\rho_{\mathrm{P}}(z)$ of the "product"], and back, during one cycle of charge migration with period τ_{chm}.

As résumé of the key ingredients for the present model of $HCCBr^+$, the authors of ref. 15 reconstructed the charge migration in $HCCI^+$ by means of quantum dynamics simulations, *cf.* eqn (5.8), starting from the initial superposition state (5.3) for the two-state scenario. The nuclei were assumed to be frozen during the period $\tau_{\mathrm{chm}} = h/\Delta E = 1.85$ fs, suggesting the model of fixed nuclei.

In addition to the pioneering work of ref. 15, we could reconstruct the flux of the valence electrons along the nuclear axis, during charge migration in $HCCI^+$.[21] For this purpose we employed the same initial state (5.3) and used the same model (two states, fixed nuclei) as in ref. 15. In principle, the total electronic flux should also include the contribution of the core electrons. They travel with the nuclei,[16] however, and since the nuclei are considered to be frozen, the core electrons do not contribute to the electronic flux.

The example of the successful joint experimental and theoretical reconstruction of the electronic charge migration[15] and the electronic flux[21] of the valence electrons in $HCCI^+$ motivates the present analogous quantum dynamics simulation of the charge migration of the valence electrons in

$HCCBr^+$. Accordingly, we employ the two-state model for fixed nuclei. Moreover, we adapt the same methods of *ab initio* quantum chemistry for the calculations of the geometric and energetic properties of $HCCBr^+$ as for $HCCI^+$; for the details, see ref. 33. Specifically, the nuclei of $HCCBr^+$ are frozen in the global minimum geometry of the precursor molecule HCCBr in its ground state $\tilde{X}^+\ {}^1\Sigma^+$, as illustrated in Figure 5.2(a). The corresponding lengths of the H–C, C≡C and C–Br bonds are 1.063 Å, 1.208 Å and 1.798 Å, respectively. The electronic Hamiltonian H in the TISE (5.1) consists of the operators of the kinetic energies of all electrons, and the operators for the Coulomb interactions of all electrons and the fixed nuclei. We also investigated the effects of spin–orbit coupling, but they turn out to be negligible for the present purpose.[33]

The TISE (5.1) is solved for the electronic wave functions Ψ_g and Ψ_e and energies E_g and E_e of the electronic ground state ($g=\tilde{X}^+\ {}^2\Pi$) and the first excited state ($e=\tilde{A}^+\ {}^2\Pi$) at the fixed nuclear geometry. The gap is $\Delta E=E_e-E_g=2.74$ eV. The related period of charge migration is $\tau_{chm}=h/\Delta E=1.51$ fs.

The initial state is constructed as superposition (5.3) of Ψ_g and Ψ_e. For the present purpose, *i.e.* for the demonstration of the analogy of nuclear tunnelling and electronic charge migration, we employ the same coefficients $C_g=C_e=1/\sqrt{2}$ as in Section 5.3, with the same consequences and simplifications, *e.g.* the time shift is equal to zero such that $t'=t$, *etc.*, *cf.* eqn (5.16) and (5.17). As discussed in Section 5.2, this choice yields the most efficient flux; for the present application this means the most efficient charge migration with maximum electronic flux; the present electronic flux in $HCCBr^+$ will, therefore, be more efficient than in the example $HCCI^+$ with the experimentally determined complex and non-equal coefficients, *cf.* ref. 15 and 21. Irrespective of the different coefficients for the initial superposition state (5.3), we still adapt an important property of the example $HCCI^+$, namely, from the perspective of the neutral precursor, it is prepared with electron hole density centred on the halogen, or turning the tables, the excess electron density accumulates in the HCC moiety. Accordingly, we determine the signs of the electronic wave functions Ψ_g and Ψ_e such that the "reactant" and "product" electron densities $\sigma_R(z)$ [eqn (5.18)] and $\sigma_P(z)$ [eqn (5.19)] are prepared with excess valence electron density accumulated in the HCC moiety and at the Br nucleus, respectively; see the discussion after eqn (5.18) and (5.19).

In practice, we first calculate the 3D one-electron densities of the valence electrons in the ground state [$\sigma_g(x, y, z)$] and the excited state [$\sigma_e(x, y, z)$] together with the 3D one-electron density difference

$$\Delta\sigma(x, y, z) = -2N_e \int \Pi' dq_{el}\ \Psi_g(q_{el})\ \Psi_e(q_{el}) \tag{5.34}$$

where "$\int \Pi' dq_{el}$" symbolizes the sum over all electron spins and the integral over the spatial coordinates of all electrons but one, and N_e is the number of valence electrons; compare with eqn (5.20) applied to the present case with equal coefficients, eqn (5.22). Subsequently, the 3D one-electron densities of the valence electrons $\sigma_g(x, y, z)$, $\sigma_e(x, y, z)$ and $\Delta\sigma(x, y, z)$ are integrated over x and y in order to obtain the corresponding 1D axial (z) electron densities of the valence electrons, $\rho_g(z)$, $\rho_e(z)$ and $\Delta\rho(z)$, respectively. The electron yield $y(z)$ can then be calculated according to eqn (5.28),

$$y(z) = -\int_{z_{\min}}^{z} dz'\Delta\rho(z') \tag{5.35}$$

with reasonable choice of the lower integration limit ($\Delta\rho(z) \approx 0$ for $z < z_{\min}$). The axial electron densities of the "reactant" [*i.e.* the density at ($t = 0$) and the "product" (the density at $t = \tau_{\text{chm}}/2$) are then calculated as $\rho_R(z) = \rho_g(z) + \rho_e(z) - \Delta\rho(z)/2$ and $\rho_P(z) = \rho_g(z) + \rho_e(z) + \Delta\rho(z)/2$, compare with eqn (5.18) and (5.19)]. Finally, the time evolution of the electron density $\rho(z, t)$ and the flux $F(z, t)$ are evaluated by the general expressions (5.23), and (5.28) and (5.29) with the substitution $q \to z$ and $t' = t$.

The resulting axial one-electron densities of the valence electrons $\rho_R(z)$ and $\rho_P(z)$ of the "reactant" and "product" cation HCCBr$^+$ are shown in Figure 5.2(a). They are normalized to the number of valence electrons, $N_e = 1 + 4 + 4 + 7 - 1 = 15$. Apparently, $\rho_R(z)$ and $\rho_P(z)$ have similar overall shapes, with two peaks for the local maxima of the electron densities near to the centre of the C≡C bond and at the Br nucleus. These peaks are separated by local minima of the densities in the C–Br bond. Most important for the present purposes, however, are the differences between $\rho_R(z)$ and $\rho_P(z)$. Apparently, the "reactant" $\rho_R(z)$ accumulates slightly more excess electron density in the acetylenic moiety than the "product" $\rho_P(z)$, whereas the "product" $\rho_P(z)$ is more strongly peaked at the bromine nucleus than the "reactant" $\rho_R(z)$. This preparation of $\rho_R(z)$ and $\rho_P(z)$ in HCCBr$^+$ is consistent with the example HCCI$^+$ for the chosen experimental scenario.[14,15] From this result, one may already anticipate that the dominant flux of the excess electron density in HCCBr$^+$ during the first half period $0 < t < \tau_{\text{chm}}/2$ is from the acetylenic moiety to the Br nucleus. This is symbolized by the arrows in the cartoon at the top of Figure 5.2(a).

Figure 5.2(b) shows the difference $\Delta\rho(z) = \rho_P(z) - \rho_R(z)$ of the axial one-electron densities of the "product" minus the "reactant". Essentially, $\Delta\rho(z)$ is negative and positive in the domains of the acetylenic moiety and the Br nucleus, respectively. The corresponding global minima and maxima of $\Delta\rho(z)$ peak at the carbon nucleus of the C–Br bond, and at the Br nucleus, respectively. The switch from dominantly negative to positive values of $\Delta\rho(z)$ occurs in the C–Br bond, near to the local minima of the densities $\rho_P(z)$ and $\rho_R(z)$. In addition, $\Delta\rho(z)$ has several local maxima and minima that are, however, much less pronounced compared to the global extrema. The overall shape of the function $\Delta\rho(z)$ suggests distinguishing the "domains of the reactant and the product" as the domains where $\Delta\rho(z)$ is essentially negative and positive, respectively. The definition of the border z_b between the two domains is somewhat arbitrary, however, due to the small local maxima and minima of $\Delta\rho(z)$. For reference, we set $z_b = 0.50a_0$ – this is the position near to the carbon nucleus of the C–Br bond where $\Delta\rho(z_b) = 0$.

Figure 5.2(b) also has the yield $y(z)$ which is obtained as negative integral of the density difference $\Delta\rho(z)$, *cf.* eqn (3.35). The prominent features of $\Delta\rho(z)$ that are discussed above imply that $y(z)$ is essentially positive, with a plateau type feature in the sub-domain of the C–Br bond which corresponds to the local minima of $\rho_P(z)$ and $\rho_R(z)$ at $z = 1.4a_0$. The global maximum of $y(z)$ is at the border $z = z_b$, which is close to these local minima, but slightly shifted towards the carbon nucleus of the C–Br bond. Close inspection reveals that the yield is negative in the domain well beyond the Br nucleus, albeit with negligibly small absolute values. This is a marginal feature, however, and it is difficult to say whether this is a real phenomenon, or just an artifact due to the fact that the underlying methods of quantum chemistry adapted from ref. 33 are state-of-the-art, but not perfect.

The resulting time evolution of the axial one-electron density $\rho(z, t)$ of the valence electrons of HCCBr$^+$ during the first cycle of charge migration ($0 < t < \tau_{\text{chm}} = 1.51$ fs) is shown in Figure 5.4(a). At first glance, the density

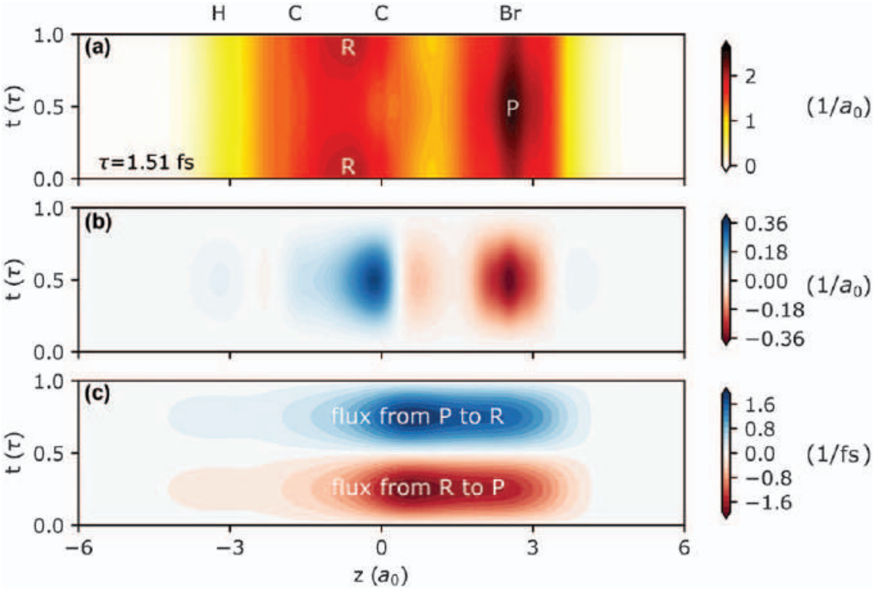

Figure 5.4 Time evolution of the periodic electronic charge migration in the linear HCCBr$^+$ cation along its axis z, during the first period, $0 \leq t \leq \tau_{\text{chm}}$. Initially, the cation is prepared in the "reactant" (R) superposition state $1/\sqrt{2}\ (\Psi_g + \Psi_e)$ of the electronic ground state Ψ_g ($g = \tilde{X}^+\ ^2\Pi$) and the first excited state Ψ_e ($e = \tilde{A}^+\ ^2\Pi$). At $t = \tau_{\text{chm}}/2$, it arrives at the "product" (P) superposition state $1/\sqrt{2}(\Psi_g - \Psi_e)$ (except for an irrelevant overall phase factor). (a) Time evolution of the one-dimensional (1D) electronic density $\rho(z, t)$ of the valence electrons, from R to P and back to R. (b) Difference in the electronic density $\rho(z, t)$ at time t minus the initial density $\rho(z, 0) = \rho_R(z)$. (c) 1D electronic flux $F(z, t)$, equal to the 1D electronic flux density $j(z, t)$. During the time interval $0 < t < \tau_{\text{chm}}/2$ the flux is from R to P. At $t = \tau_{\text{chm}}/2$, it changes direction, hence $F(z,\ t = \tau_{\text{chm}}/2) = 0$. Subsequently from $\tau_{\text{chm}}/2 < t < \tau_{\text{chm}}$, the flux is from P back to R. The results (a)–(c) are illustrated by color-coded contour plots.

appears to be rather robust, with two peaks in the C≡C bond and at the Br nucleus, separated by the local minimum in the centre of the C–Br bond. Close inspection reveals, however, that during the first and second half cycles, a relatively small part of the density flows from the initial accumulation in the C≡C bond to the Br nucleus, and back to the C≡C bond, respectively. It is quite remarkable that this apparent shift of what we may call the "axial excess electron density" proceeds without any significant changes in the overall density at its local minimum at the centre of the C–Br bond. This effect appears more pronounced in Figure 5.4(b) which shows the difference $\Delta\rho(z, t) = \rho(z, t) - \rho_R(z)$ of the axial one-electron density of the valence electrons at time t minus the initial density $\rho(\mathrm{z}, t = 0) = \rho_R(z)$. Obviously, it evolves with temporal symmetry $\Delta\rho(z, t) = \Delta\rho(z, \tau_{\mathrm{chm}} - t)$ such that during the first half cycle, the initial axial excess electron density in the C≡C bond is depleted to the benefit of the density at the Br nucleus, and *vice versa* during the second half cycle, without any significant changes $[\Delta\rho(z \approx 1\ a_0, t) \approx 0]$ of the density $\rho(z, t)$ in a wide range around $z = 1.85a_0$ near to its local minimum. Close inspection also reveals a marginal effect of electron depletion and recovery in the domain beyond the Br nucleus, but as for the discussion of $\Delta\rho(z)$ in Figure 5.2(b), it is not clear whether this is a real, albeit very small effect, or an artifact.

Finally, Figure 5.4(c) documents the time evolution of the axial electronic flux $F(z, t)$. Obviously, it proceeds with robust spatial profile given by the yield $y(z)$ shown in Figure 5.2(b), modulated by the periodic sinusoidal function, with corresponding temporal symmetry $F(z, t) = F(z, \tau_{\mathrm{chm}}/2 - t) = -F(z, \tau_{\mathrm{chm}}/2 + t) = -F(z, \tau_{\mathrm{chm}} - t)$. Accordingly, during the first and second half cycles, the dominant flux of the excess electron density is from the acetylenic moiety *via* the sub-domain of the C–Br bond with minimum density to the Br nucleus, and back, with maximum absolute values $\max|F(z, t)|$ at $z = z_b$ for $t = \tau_{\mathrm{chm}}/4, 3\tau_{\mathrm{chm}}/4, 5\tau_{\mathrm{chm}}/4, 7\tau_{\mathrm{chm}}/4$, *etc.* There are also marginal fluxes in opposite directions, in the domain beyond the Br nucleus, [hardly visible on the colour code scale of Figure 5.4(c)], but, as discussed before, it is not clear whether these are real, albeit negligible effects, or artifacts.

5.5 Comparison of the Results for Stereomutation of CHFBr by Nuclear Tunnelling and for Axial Electronic Charge Migration in HCCBr$^+$

In this section, we compare the results derived in Sections 5.3 and 5.4 for stereomutation of CHFBr by nuclear tunnelling and for axial electronic charge migration in HCCBr$^+$. For this purpose, we inspect the corresponding analogous panels (a), (b), *etc.* of Figures 5.1 and 5.3, and 5.2 and 5.4, respectively, keeping in mind the underlying theory presented in Section 5.2.

As anticipated in the introduction, Figures 5.1(a) and 5.2(a) are entirely different, because they have the cartoons of the nuclear and electronic processes and the corresponding densities of the "reactants" and "products" that are so entirely different. The nuclear and electronic energy gaps ΔE between the levels of the ground and excited nuclear and electronic states that are involved in the processes differ by more than three orders of magnitude. As a consequence, the resulting periods $\tau = h/\Delta E$ also differ by more than three orders of magnitude.

In spite of the enormous qualitative and quantitative differences between the systems and processes illustrated in Figures 5.1(a) and 5.2(a), the rest of the figures reveal impressive analogies. These will be detailed below. For this purpose, we switch back to the generic notation used in Section 5.2, *i.e.* we use the period "τ" and the coordinate "q", instead of the individual "τ_{stereo}" or "τ_{chm}" and "α_u" or "z", respectively. The notation "q_b" means the border between the domains of the reactant (R, $q < q_b$) and the product (P, $q > q_b$), corresponding to the domains "$\alpha_u < 0$" or "$z < z_b$" and "$\alpha_u > 0$" or "$z > z_b$", respectively. When we talk about the "densities" or the "fluxes" (plural!) below, we always mean the corresponding quantities for the two processes: nuclear tunnelling and electronic charge migration.

Close inspection of the remaining Figures 5.1(b) and 5.3 for nuclear tunnelling (Section 5.3) and 5.2(b) and 5.4 for electronic charge migration (Section 5.4) reveals the equivalence of the following phenomena for the two applications.

(i) The density differences $\Delta\rho(q) = \rho_P(q) - \rho_R(q)$ of the reactant (R) and the product (P) are essentially negative in the domain of R, but positive for P, *cf.* Figures 5.1(a) and 5.2(a). The word "essentially" here emphasizes the most prominent properties and disregards the marginal deviations discussed in Section 5.4, and which are actually so small that it is hard to say whether they are real, albeit with entirely negligible effects, or just artifacts.

(ii) The yields $y(q)$ have their maxima at the border q_b between the domains of the reactant and the product. Moreover, the yields have plateaus near to their maxima, *cf.* Figures 5.1(a) and 5.2(a).

(iii) The time evolutions of the densities $\rho(q, t)$ and of the fluxes $F(q, t)$ are periodic, with period τ, *cf.* Figures 5.3 and 5.4.

(iv) The time evolutions of the differences $\Delta\rho(q, t) = \rho(q, t) - \rho(q, t=0)$ of the densities at time t minus the initial densities $\rho(q, t=0) = \rho_R(q)$ have temporal symmetries, $\Delta\rho(q, t) = \Delta\rho(q, \tau - t)$, *cf.* Figures 5.3(b) and 5.4(b).

(v) Likewise, there are temporal symmetries for the fluxes, $F(q, t) = F(q, \tau/2 - t) = -F(q, \tau/2 + t) = -F(q, \tau - t)$, *cf.* Figures 5.3(c) and 5.4(c).

(vi) The density differences $\Delta\rho(q, t)$ are essentially negative in the reactant domains but positive in the product domains. The values of $\Delta\rho(q, t)$ are negligible for values of q close to the borders q_b between the two domains, *cf.* Figures 5.3(b) and 5.4(b). This means that during the full cycles ($0 < t < \tau$), the densities, or part of them, are shifted from R to P, and then back to R, without any significant changes in the densities at the border between R and P. This result for the density differences $\Delta\rho(q, t)$ is of course confirmed by the time evolutions of the densities, *cf.* Figures 5.3(a) and 5.4(a).

(vii) The fluxes $F(q, t)$ are essentially positive, *i.e.* from R along q to P during the first half cycles ($0 < t < \tau/2$) but negative, *i.e.* from P back to R during the second half cycles ($\tau/2 < t < \tau$). They vanish for $t = 0$, $\tau/2$, τ, *etc.* with periodic continuations. At all other times ($t \neq 0$, $\tau/2$, τ, *etc.*), $F(q, t)$ has extreme values at the borders q_b between the reactant and product domains. The absolute maxima and minima of the fluxes are obtained at the borders q_b at times $t = \tau/4$, $3\tau/4$, and then with periodic continuations at $5\tau/4$, $7\tau/4$, *etc.*, *cf.* Figures 5.3(c) and 5.4(c).

(viii) The fluxes $F(q, t)$ have plateaus in the vicinities of their maxima or minima, *cf.* Figures 5.3(c) and 5.4(c).

In brief, all phenomena (i)–(viii) imply that the densities, or part of the densities, are shifted periodically from R to P and then back from P to R, during one cycle with period τ. The processes proceed such that during the first half cycle, P grows at the expense of R, and *vice versa* during the second half cycle, without any significant variations of the densities at the borders q_b between the reactant and product domains. This is achieved by fluxes with plateau-type shapes and maximum or minimum values half-way between R and P, or between P and R.

The similarity of the phenomena (i)–(viii) reveal and document the analogy of the two processes, nuclear tunnelling and electronic charge migration, at least for the quite realistic two-state scenarios we employed in Sections 5.2–5.4.

5.6 Conclusions

We have evaluated the time evolutions of the densities and the fluxes of two different processes of two entirely different model systems and discovered close analogies in the quantum dynamics. The first case study is for periodic stereomutation from the oriented non-linear (*S*)-CHFBr to (*R*)-CHFBr and back to (*S*)-CHFBr by coherent nuclear tunnelling, with period $\tau_\mathrm{stereo} = 10.57$ ps. Here (at least one of) the nuclei move with rather large amplitudes, and the electrons remain in the electronic ground state. The second case is periodic electronic charge migration in the oriented linear $\mathrm{HCCBr^+}$ cation, with much shorter period $\tau_\mathrm{chm} = 1.51$ fs. On this time scale, the nuclei are essentially frozen, and the electrons evolve coherently in the electronic-ground and first-excited states. The analogies of the quantum dynamics are documented in Figures 5.1(b) and 5.3 for nuclear tunnelling, and in Figures 5.2(b) and 5.4 for electronic charge migration, respectively, and they are listed as eight common features (i)–(viii) in Section 5.5.

In the context of this book,[3] we would like to conclude by extending a working hypothesis,[24] namely, the analogies of the quantum dynamics of nuclear tunnelling and electronic charge migration suggest that, not only the stereomutation of CHFBr but also the charge migration in oriented

$HCCBr^+$, share common features of tunnelling. To support this hypothesis, let us first recall (at least) three kinds of quantum mechanical nuclear tunnelling that are documented in the literature. The first and "standard" type of tunnelling is "tunnelling through a potential barrier $V^{\ddagger}$", or briefly "potential tunnelling".[1–3] Here the barrier $V^{\ddagger}$ separates two domains of the molecular system that may be referred to as the domains of the "reactant" (R) and of the "product" (P). The total energy of the system is below the barrier, $E < V^{\ddagger}$. As a consequence, transitions from R to P or from P to R are classically forbidden. Nevertheless, they are allowed by quantum mechanics – "potential tunnelling" is a quantum effect. No doubt, the stereomutation of CHFBr proceeds by potential tunnelling.

The second type of tunnelling is "dynamical tunnelling", discovered by Davis and Heller.[34] As in the case of potential tunnelling, dynamical tunnelling is a quantum effect that enables the transition between two molecular domains even though it is classically forbidden. In this case, however, the classical constraint is quite different from the traditional constraint $E < V^{\ddagger}$, namely, it is a "dynamical constraint." It may arise at higher energies $E > V^{\ddagger}$, and in fact, it may arise even in systems that do not possess any potential barrier at all. In a classical picture, for example, the system may be prepared with specific initial conditions such that it evolves along one of two separate stable periodic orbits that co-exist at the same total energy E. As the name suggests, these orbits are periodic, which means that, in the frame of classical mechanics, the system must stay on its orbit; it must not "hop" to the other periodic orbit. The word "stable periodic orbit" indicates that if one prepares the system in a sufficiently near neighbourhood of the periodic orbit, *e.g.* in a narrow torus about the orbit, it still cannot "hop" into the corresponding torus about the other orbit. In quantum mechanics, the tori about the two different classical periodic orbits correspond to two different wave functions that extend along the orbits. Davis and Heller have shown that if one prepares the molecular system in a wave function that corresponds to one of two separate classical orbits, then it can make a transition to the other wave function that extends along the other orbit, even though this is classically forbidden. This process is called "dynamical tunnelling".[34]

The third kind of tunnelling was discovered by Hashimoto and Takatsuka[35] for systems that possess two separate instable periodic orbits, at the same total energy, in the frame of classical mechanics. The word "instable" indicates that if one prepares the system with initial conditions close to one of the periodic orbits, then it may hop to the neighbourhood of the other orbit. The time evolution of this type of transition has some important characteristic features. Namely, at first, the system cycles close to the initial periodic orbit. Next, after (very!) many such cycles, it makes a sudden hop to the vicinity of the other periodic orbit. Then it continues to cycle about the other periodic orbit, again for many times. This temporal pattern reminds us of the properties of potential tunnelling discussed above, *i.e.* the systems prefer to stay in the domains of R and P for rather long times until they make a sudden transition from R to P, or *vice versa.*[23] Hashimoto and Takatsuka have shown that quantum mechanically, if one prepares the system in the corresponding initial wave function that extends along one of the instable periodic orbits, then its density decreases to the benefit of the density close to the other orbit. This transition occurs without any significant appearance of density in the domains between the two orbits.

The quantum dynamics of the present charge migration in $HCCBr^+$ proceeds in a way that reminds us of the type of dynamical tunnelling discovered by Hashimoto and Takatsuka.[35] For example, the time evolution of the electronic density difference documented in Figure 5.4 is analogous to the time evolution of the nuclear density during dynamical tunnelling, as documented in figure 7 of ref. 35. This leads to our working hypothesis: charge migration in oriented $HCCBr^+$ can be described as dynamical tunnelling. Of course, there are also important differences. Most important: Hashimoto and Takatsuka describe nuclear dynamical tunnelling,[35] whereas the present charge migration would correspond to electronic dynamical tunnelling.

Our working hypothesis is also supported by a re-consideration or re-interpretation of the strikingly different time scales, $\tau_{\text{stereo}} = 10.57$ ps *versus* $\tau_{\text{chm}} = 1.51$ fs. The rather long period τ_{stereo} is for nuclear potential tunnelling. It is well known that the corresponding times for electronic potential tunnelling are much shorter. For example, the preparation of the initial superposition state (5.3) by photo-ionization of the neutral precursor proceeds by electronic potential tunnelling in the time domain below 100 as.[14,15] Likewise, nuclear dynamical tunnelling as discovered by Hashimoto and Takatsuka is a rather slow process in the ps or even much longer time domain. By analogy, electronic dynamical tunnelling should take much shorter times, actually in the sub-fs time domain for the transition in one direction, $\tau_{\text{chm}}/2 = 750$ as.

The present analogy has been discovered for rather simple model systems: they are oriented, they are prepared initially as a superposition of two eigenstates (the ground state and the first-excited states), the quantum dynamics evolve adiabatically, *i.e.* without any transitions between the two states or any others, and they are essentially along one degree of freedom (DOF), without any considerations of the effects of other DOFs that cause decoherence,[36–40] see also ref. 33. It is a challenge to investigate whether the analogy of nuclear tunnelling and electronic charge migration persists in more demanding systems, *i.e.* in molecules that are prepared in a superposition of more than two states, or with diabatic transitions, or with additional significant DOFs, or with competing effects of decoherence.

Acknowledgements

One of us (VS) expresses deep gratitude to his thesis supervisor, Professor H. J. Wörner (ETH Zürich) for stimulating guidance and advice. We also thank Professor K. Takatsuka (The University of Kyoto) for valuable guidance to part of the literature. Generous financial support by the National Key Research Program of China (no. 2017YFA0304203), the program for

Changjiang Scholars and Innovative Research Team (no IRT_17R70), the hundred talent program of Shanxi province, the 111 project (Grant D18001) and the Fund for Shanxi ''1331 Project Key Subjects'' is also gratefully acknowledged. AS is grateful for financial support by an Ambizione grant of the Swiss National Science Foundation.

References

1. F. Hund, *Z. Phys.*, 1927, **43**, 805.
2. C. Fábri, R. Marquardt, A. G. Császár and M. Quack, *J. Chem. Phys.*, 2019, **150**, 014102.
3. S. Kozuch and J. Kästner, *Tunnelling in Molecules – Nuclear Quantum Effects from Bio-to Physical Chemistry*, The Royal Society of Chemistry, London, 2020.
4. H. Eyring, J. Walter and G. E. Kimball, *Quantum Chemistry*, Wiley, New York, ch. 11, 1944.
5. D. J. Diestler, G. Hermann and J. Manz, *J. Phys. Chem. A*, 2017, **121**, 5332.
6. R. Weinkauf, P. Schanen, A. Metsala, E. W. Schlag, M. Bürgle and H. Kessler, *J. Phys. Chem.*, 1996, **100**, 18567.
7. L. S. Cederbaum and J. Zobeley, *Chem. Phys. Lett.*, 1999, **307**, 205.
8. G. L. Yudin, S. Chelkowski, J. Itatani, A. D. Bandrauk and P. B. Corkum, *Phys. Rev. A*, 2005, **72**, 051401.
9. F. Remacle and R. D. Levine, *Proc. Natl. Acad. Sci. U. S. A.*, 2006, **103**, 6793.
10. I. Barth and J. Manz, *Angew. Chem., Int. Ed.*, 2006, **45**, 2962.
11. M. Kanno, H. Kono and Y. Fujimura, *Angew. Chem., Int. Ed.*, 2006, **45**, 7995.
12. S. Chelkowski, G. L. Yudin and A. D. Bandrauk, *J. Phys. B: At., Mol. Opt. Phys.*, 2006, **39**, S409.
13. D. Jia, J. Manz, B. Paulus, V. Pohl, J. C. Tremblay and Y. Yang, *Chem. Phys.*, 2017, **482**, 146.
14. H. J. Wörner, C. A. Arrell, N. Banerji, A. Cannizzo, M. Chergui, A. K. Das, P. Hamm, U. Keller, P. M. Kraus, E. Liberatore, P. Lopez-Tarifa, M. Lucchini, M. Meuwly, C. Milne, J.-E. Moser, U. Rothlisberger, G. Smolentsev, J. Teuscher, J. A. van Bokhoven and O. Wenger, *Struct. Dyn.*, 2017, **4**, 061508.
15. P. M. Kraus, B. Mignolet, D. Baykusheva, A. Rupenyan, L. Horný, E. F. Penka, G. Grassi, O. I. Tolstikhin, J. Schneider, F. Jensen, L. B. Madsen, A. D. Bandrauk, F. Remacle and H. J. Wörner, *Science*, 2015, **350**, 790.
16. T. Bredtmann, D. J. Diestler, S.-D. Li, J. Manz, J. F. Pérez-Torres, W.-J. Tian, Y.-B. Wu, Y. Yang and H.-J. Zhai, *Phys. Chem. Chem. Phys.*, 2015, **17**, 29421.
17. Vít Svoboda, Niraghatam Bhargava Ram, Denitsa Baykusheva, Daniel Zindel, Benjamin Spenger, Manuel Ochsner, Holger Herburger, Jürgen

Stohner, and Hans Jakob Wörner, Femtosecond photoelectron circular dichroism of chemical reactions, Science Advances, submitted, 2020.
18. V. Svoboda, Ph.D. Thesis, ETH Zürich, 2019.
19. M. Born and R. Oppenheimer, *Ann. Phys.(Leipzig)*, 1927, **84**, 457.
20. M. Born and K. Huang, *Dynamical Theory of Crystal Lattices*, Oxford University Press, London, Appendix VIII, 1954, p. 406.
21. H. Ding, D. Jia, J. Manz and Y. Yang, *Mol. Phys.*, 2017, **115**, 1813.
22. J. Manz and K. Yamamoto, *Mol. Phys.*, 2012, **110**, 517.
23. T. Grohmann, J. Manz and A. Schild, *Mol. Phys.*, 2013, **111**, 2251.
24. G. Hermann, C. Liu, J. Manz, B. Paulus, J. F. Pérez-Torres, V. Pohl and J. C. Tremblay, *J. Phys. Chem. A*, 2016, **120**, 5360.
25. C. Liu, J. Manz and Y. Yang, *Phys. Chem. Chem. Phys.*, 2016, **18**, 5048.
26. J. R. Letelier and C. A. Utreras-Días, *Spectrochim. Acta, Part A*, 1997, **53**, 247.
27. R. Meyer and H. H. Günthard, *J. Chem. Phys.*, 1968, **49**, 1510.
28. F. Neese, The ORCA program system, *Wiley Interdiscip. Rev.: Comput. Mol. Sci.*, 2011, **2**, 73.
29. J. M. L. Martin and A. Sundermann, J. Chem. Phys., 2001, **114**, 3408.
30. D. T. Colbert and W. H. Miller, *J. Chem. Phys.*, 1992, **96**, 1982.
31. J. Manz, A. Schild, B. Schmidt and Y. Yang, *Chem. Phys.*, 2014, **442**, 9.
32. M. V. Berry, *Eur. J. Phys.*, 2013, **34**, 1337.
33. D. Jia, J. Manz and Y. Yang, *J. Phys. Chem. Lett.*, 2019, **10**, 4273.
34. M. J. Davis and E. J. Heller, *J. Chem. Phys.*, 1981, **75**, 246.
35. N. Hashimoto and K. Takatsuka, *J. Chem. Phys.*, 1998, **108**, 1893.
36. A. D. Bandrauk, S. Chelkowski, P. B. Corkum, J. Manz and G. L. Yudin, *J. Phys. B: At., Mol. Opt. Phys.*, 2009, **42**, 134001.
37. H. Mineo, S. H. Lin and Y. Fujimura, *Chem. Phys.*, 2014, **442**, 103.
38. C. Arnold, O. Vendrell and R. Santra, *Phys. Rev. A*, 2017, **95**, 033425.
39. M. Vacher, M. J. Bearpark, M. A. Robb and J. P. Malhado, *Phys. Rev. Lett.*, 2017, **118**, 083001.
40. V. Depré, N. V. Golubev and A. I. Kuleff, *Phys. Rev. Lett.*, 2018, **121**, 203002.

CHAPTER 6

Tunnelling and Parity Violation in Chiral and Achiral Molecules: Theory and High-resolution Spectroscopy

MARTIN QUACK* AND GEORG SEYFANG

ETH Zürich, Laboratory for Physical Chemistry, CH-8093 Zürich, Switzerland
*Email: Martin@Quack.ch

6.1 Introduction

Quantum mechanical tunnelling was discovered in 1927 by Friedrich Hund in the context of a discussion of the stereomutation reaction between the enantiomers of chiral molecules. We review here the fundamental new aspects introduced by the discovery of parity violation in 1957 and the subsequent formulation of the standard model of particle physics (SMPP), which led to a radical change in our understanding of the dynamics of stable chiral molecules. We first review the basic theory of parity violation in the framework of the SMPP with the discovery of a new order of magnitude for chiral molecules. We then discuss the conceptual changes for the quantum dynamical tunnelling of achiral, transiently chiral and stable chiral molecules with several current examples. We summarize the current status of the theory. We then outline the concepts for experiments and summarize the current status of experiment.

When Friedrich Hund in 1927[1–3] investigated for chiral molecules the spectroscopic and kinetic consequences of the then-new theory of quantum

Theoretical and Computational Chemistry Series No. 18
Tunnelling in Molecules: Nuclear Quantum Effects from Bio to Physical Chemistry
Edited by Johannes Kästner and Sebastian Kozuch

Published by the Royal Society of Chemistry, www.rsc.org

mechanics as just formulated in terms of the Heisenberg equations of motion[4–6] and the Schrödinger equation, which had been found by Erwin Schrödinger during a skiing holiday in Arosa over the Christmas and New Year holiday 1925/26,[7–13] he discovered a strange phenomenon: For symmetry reasons the ground state wave function as an eigenstate of the Schrödinger equation must have a well-defined "parity" as symmetry with respect to the inversion at the potential maximum in the double-well potential, which could be used in a simple one-dimensional description of the stereomutation reaction interconverting the enantiomers of chiral molecules (Figure 6.1).

More generally this symmetry of parity is related to the inversion of the three spatial coordinates x, y, z, of a physical system (Figure 6.2). Therefore the probability distribution related to the ground state wave function (χ_+ for positive parity in Figure 6.1) had to be delocalized. The first excited state ($-\chi_-$ in Figure 6.1) of negative parity and antisymmetric with respect to inversion would be separated by a small energy interval $\Delta E_\pm = E_- - E_+$ from the ground state. Both eigenstates would have to be considered as achiral. However, a superposition of these states ($\chi_+ + \chi_-$) and ($\chi_+ - \chi_-$) would generate wave functions λ and ρ, localized and chiral, as observed in common experiments of chemistry. These localized states and probability distributions would interconvert λ to ρ and back in a half period of the periodic motion with period τ:

$$t_{\lambda\to\rho} = \tau/2 = h/(2\Delta E_\pm) \tag{6.1}$$

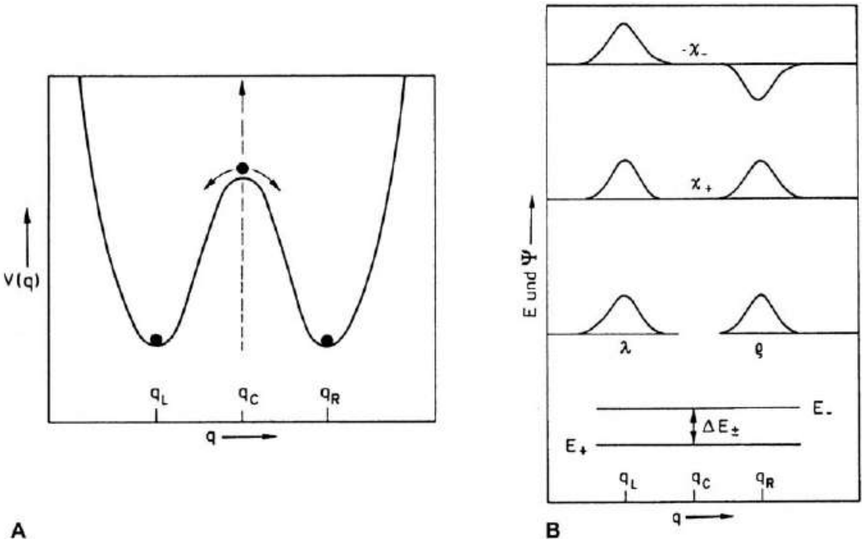

Figure 6.1 The double minimum potential for illustrating symmetry breaking in classical dynamics (A) and parity symmetry, localization and tunnelling in quantum dynamics. Wave functions are shown in (B).
Reproduced from ref. 157 with permission from World Scientific Publishing, Copyright 1995.

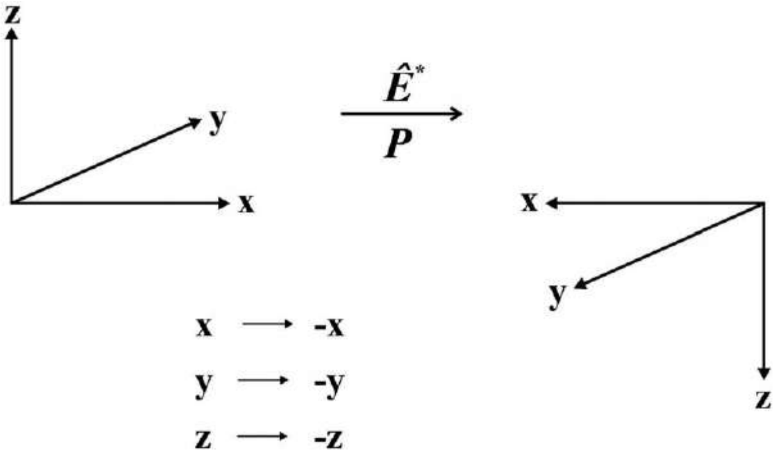

Figure 6.2 Reflection E^* or parity ($\hat{P}$) operation.
Adapted from ref. 36 with permission from John Wiley and Sons, © 2002 WILEY-VCH Verlag GmbH & Co. KGaA, Weinheim.

where h is Planck's constant, although both energies E_+ and E_- were much smaller than the barrier heights considered for chiral molecules. Thus the reaction of this quantum mechanical system could happen at energies below the barrier for reaction, a process impossible, even unthinkable of, in classical mechanics. Later this effect was called tunnelling or the tunnel effect, with the picture of a process that could happen as if there were a "tunnel" through the barrier (see ref. 14 and 15 for more of the history). Hund's description, which is also applicable to achiral molecules such as NH_3, which can be described by a similar double-well potential, has entered the textbooks, and the quantum mechanical tunnel effect has since then been observed in numerous areas of physics and chemistry and has been subject of many books, including the present book[16] (see ref. 17–21 to give just a few examples). In classical mechanics the symmetrical state of the system is located at the maximum of the potential, a point of unstable equilibrium, the stable states at the minima being strictly localized and degenerate, as indicated in Figure 6.1A, very different from the quantum mechanical description.

The discovery of parity violation in 1956/57[22–26] led to consequences for the tunnelling dynamics of chiral molecules that have not yet widely entered the textbooks of chemistry (see, however, ref. 27 and 28). The present brief review deals with these new aspects of tunnelling in chiral molecules as well as related aspects in achiral molecules. Our aim is here to provide a conceptual summary of these phenomena both concerning theoretical and experimental aspects. For more detailed reviews, from which we draw in particular (and in part literally), we refer to ref. 14, 15, 27–32. We shall first briefly outline the theory of parity violation in the framework of the Standard Model of Particle Physics, SMPP, following mainly ref. 27–35.

6.2 Parity Violation in Chiral Molecules in the Framework of the SMPP

6.2.1 Introductory Remarks

In the introduction to his famous paper "Quantum Mechanics of Many Electron Systems" Paul Adrien Maurice Dirac wrote one of the most cited sentences in quantum chemistry:[37]

"The underlying physical laws for the mathematical theory of a large part of physics and the whole of chemistry are thus completely known and the difficulty is only that the exact application of these laws leads to equations much too complicated to be soluble. It therefore becomes desirable that approximate practical methods of applying quantum mechanics should be developed, which can lead to an explanation of complex atomic systems without too much computation".

It is remarkable that the second part of this statement, which forms a reasonable starting point for modern, approximate numerical quantum chemistry and computational chemistry, is only rarely cited. The more frequently cited first sentence with the strong statement about understanding "the whole of chemistry" and the small restriction "the difficulty is only", which claims that the quantum physics of the first half of the 20th century contains all basic knowledge about chemistry, is the one that seems to be liked by many theoretical chemists and physicists. It turns out, however, that this statement is incorrect. There is at least one important part of chemistry, namely stereochemistry and molecular chirality, which can be understood properly only when including the parity-violating weak nuclear force in our quantum chemical theory in the framework of what we have termed "electroweak quantum chemistry",[33,34] completely and fundamentally unknown at the time of Dirac's statement.[37]

Figure 6.3 summarizes the modern view of the origin of the fundamental interactions as publicized on the website of a large accelerator facility (CERN[38]). According to this view, the electromagnetic force, which is included in "Dirac-like" ordinary quantum chemistry, leads to the Coulomb repulsion, say, between two electrons in a molecule by means of photons as field particles. In the picture the two electrons are compared to the ladies on two boats throwing a ball. If we do not see the exchange of the ball, we will observe only the motion of the boats resulting from the transfer of momentum in throwing the ball, and we could interpret this as resulting from a repulsive "force" between the two ladies on the boats. Similarly, we interpret the motion of the electrons resulting from "throwing photons as field particles" as arising from the Coulomb law, which forms the basis of ordinary quantum chemistry. The Coulomb force with the $1/r$ potential energy law is of long range. The other fundamental forces arise similarly, but with other field particles. The strong force with very short range (0.1–1 fm) mediated by the gluons is important in nuclear physics but has only indirect influence in chemistry by providing the structures of the nuclei, which enter as

The forces in nature

Type	Intensity of forces (decreasing order)	Binding particle (field quantum)	Important in
Strong nuclear force	~ 1	Gluons (no mass)	Atomic nucleus
Electro-magnetic force	$\sim 10^{-3}$	Photons (no mass)	Atoms and molecules
Weak nuclear force	$\sim 10^{-5}$	Bosons Z, $W+$, $W-$, (heavy)	Radioactive β-decay, chiral molecules
Gravitation	$\sim 10^{-38}$	Gravitons (?)	Sun and planets, *etc.*

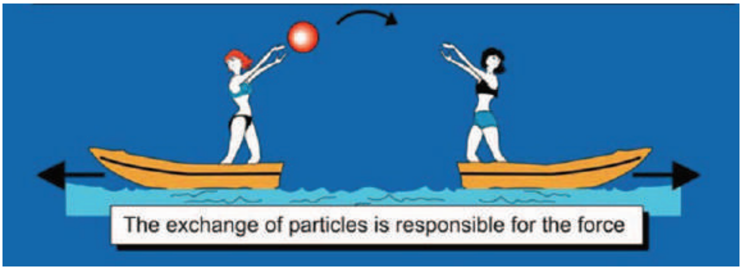

Figure 6.3 Forces in the standard model of particle physics (SMPP) and important effects. This is taken from the CERN website ref. 38, but the importance of the weak interaction for chiral molecules has been added here from our work.
Reproduced from ref. 29 with permission from the Royal Society of Chemistry, in turn, adapted from ref. 38, Public Domain. (We note that, while not referred to in ref. 38, the motif of the lightly dressed ladies throwing balls can be found in a mosaic at Piazza Armerina. Sicily, from the 4th century AD).

parameters in chemistry, but there is otherwise usually no need to retain the strong force explicitly in chemistry. The weak force, on the other hand, is mediated by the $W^{\pm}$and Z^{0} Bosons of very high mass (86.316 and 97.894 Dalton, of the order of the mass of a Rb to Mo nucleus!) and short lifetime (0.26 yoctoseconds $= 0.26 \times 10^{-24}$ s).

This force is thus very weak and of very short range (<0.1 fm) and one might therefore think that, similar to the even weaker gravitational force (mediated by the still hypothetical graviton of spin 2), it should not contribute significantly to the forces between the particles in molecules (nuclei and electrons). Indeed, the weak force, because of its short range, becomes effective in molecules, when the electrons penetrate the nucleus, and then it leads only to a very small perturbation on the molecular dynamics, which ordinarily might be neglected completely.

It turns out, however, that because of the different symmetry groups of the electromagnetic and the electroweak Hamiltonians there arises a fundamentally important, new aspect in the dynamics of chiral molecules, which we therefore have added to the figure from CERN, where this was not originally included, in our Figure 6.3. Indeed, the electromagnetic Hamiltonian commutes with the space inversion or parity operator $\hat{P}$

$$\hat{P}\hat{H} = \hat{H}\hat{P} \tag{6.2}$$

which leads to the consequence that in chiral molecules the delocalized energy eigenstates χ_+ and $-\chi_-$ have well-defined parity and the localized handed states λ and ρ of chiral molecules have exactly the same energy by symmetry (see Section 6.3 for details). Therefore one can also say that the reaction enthalpy $\Delta_R H_0^\varnothing$ for the stereomutation reaction (6.3) between R and S enantiomers of a chiral molecule would be exactly zero by symmetry ($\Delta_R H_0^\varnothing \equiv 0$) a fact originally noted already by van't Hoff[39]

$$\mathrm{R} \leftrightarrows \mathrm{S} \tag{6.3}$$

$$\Delta_R H_0^\varnothing = 0 \text{ (? Van't Hoff) or } \Delta_R H_0^\varnothing = N_A \Delta_{pv} E \text{ (today)}$$

Today, we know, that the electroweak Hamiltonian does not commute with $\hat{P}$

$$\hat{P}\hat{H}_{ew} \neq \hat{H}_{ew}\hat{P} \tag{6.4}$$

and therefore parity is violated leading to a small but non-zero parity-violating energy difference $\Delta_{pv}E$ between enantiomers and thus $\Delta_R H_0^\varnothing \neq 0$ (for example about 10^{-11} J mol^{-1} for a molecule like CHFClBr[40]). We shall discuss in Section 6.3, in more detail, under which circumstances such small effects lead to observable results dominating the quantum dynamics of chiral molecules.

This symmetry violation in chiral molecules is, indeed, the key concept that leads to an interesting interaction between high energy physics and molecular physics and chemistry; indeed also biochemistry.[36,41,42] It results in the following at first perhaps surprising three statements:

1. The fundamentally new physics arising from the discovery of parity violation[22–26] and the consequent electroweak theory in the standard model of particle physics (SMPP)[43–47] leads to the prediction of fundamental new effects in the dynamics of chiral molecules and thus in the realm of chemistry.
2. Molecular parity violation as encoded in eqn (6.2)–(6.4) has possibly (but not necessarily) important consequences for the evolution of biomolecular homochirality in the evolution of life.[28,29,31,32,41,42,48,140]
3. Possible experiments on molecular parity violation open a new window to looking at fundamental aspects of the standard model of high energy physics, and thus molecular physics might contribute to our understanding of the fundamental laws relevant to high energy physics. Indeed, going beyond parity violation and the standard model, molecular chirality may provide a new look at time-reversal symmetry and its violation, in fact the nature of time.[42,110,139,157,161]

It should thus be clear that electroweak quantum chemistry has interesting lessons to tell. A brief history of electroweak quantum chemistry is quickly told. After the discovery of parity violation in 1956/57[22–26] it took about a decade until the possible consequences for chemistry and biology were pointed out by Yamagata in 1966.[48] While his numerical estimates were wrong by many orders of magnitude (as also was a later estimate[49]) and even some of his qualitative reasonings were flawed (see ref. 36), the link between parity violation in high energy physics and the molecular physics of chirality was thus established and repeatedly discussed qualitatively in the 1970s.[50–57]

The first quantitative calculations on molecular parity violation were carried out following the work of Hegström, Rein and Sandars[58,59] and Mason and Tranter[60–67] including several discussions by others in the 1980s.[68–82] Some far-reaching conclusions about consequences for biomolecular homochirality were drawn from some of these early calculations but we know now that none of these early calculations prior to 1995 can be relied on (nor can one retain their conclusions), as they were wrong by orders of magnitude.

Indeed, in 1995, we carefully reinvestigated the calculations of parity-violating energies in molecules and discovered, surprising to many at the time, that an improved theoretical treatment leads to an increase of calculated parity-violating energies by about two orders of magnitude in the benchmark molecules H_2O_2 and H_2S_2.[33–35] This discovery triggered substantial further theoretical[40–42,83–97] and proposals for experimental activity[98–109] and the numerical results were rather quickly confirmed in independent calculations from several research groups, as summarized in Table 6.1. Figure 6.4 provides a graphical survey of the development and Figure 6.5 shows the structures and coordinate definitions for HSSH. Both in Table 6.1 and Figure 6.4, one can see the "big jump" by about a

Table 6.1 Comparison of E_{pv} (in 10^{-20} E_{h}, with $\tau = 45°$) and $\Delta_{\mathrm{pv}}E^{\mathrm{el}} = E_{\mathrm{pv}}(M) - E_{\mathrm{pv}}(P)$ (in 10^{-14} hc cm^{-1}, at $\tau = 90°$) for the molecules HOOH and HSSH computed with various methods. Adapted from ref. 151 with permission from Taylor and Francis, Copyright 2015. See also ref. 29, 30, 36, 111 and 128, and Figure 6.5 for coordinate definitions (schematic). One notes the "big jump" of about a factor 100 occurring in 1995/96.

Method[a] (the year)	E_{pv}(HOOH)	$\Delta_{\mathrm{pv}}E^{\mathrm{el}}$(HOOH)	E_{pv}(HSSH)	$\Delta_{\mathrm{pv}}E^{\mathrm{el}}$(HSSH)
SDE-RHF[62] (1984)	−1.2	−0.03	−135.0	2.0
CIS-RHF[33,34,83,84,128] (1995/6)	−39.7	−5.0	−1654.0	188.1
TDA[86] (1997)	−55.9	−7.0	−1487.7	161.5[b]
CPHF[151] (2015)	−61.38	−2.9	−1865.6	242.0
MC-LR-RPA[35,83,85,128,153] (2000)	−60.88	−2.8	−1913.0	185.0
CASSCF-LR[35,85] (2000)	−45.00	−3.4		
CCSD[151] (2015)	−51.69	−6.4	−2248.6	238.3
ZORA-HF[155] (2005)	−79.30	−3.9	−2350.0	294.5
ZORA-B3LYP[125] (2005)	−65.40	−8.3	−2690.0	290.0
ZORA-BLYP[125] (2005)	−69.30	−9.9	−2750.0	278.3
DC-HF[88] (1999)	−70.60	−4.0	−2077.0	280.0
DC-MP2[154] (2005)	−57.88	−7.3	−2112.0	224.3
DC-CCSD(T)[156] (2000)	−61.20	−8.8	−2110.0	215.1

[a] Note the equivalence, in principle, of methods as given in the parentheses (CIS-RHF, CIS-LR, TDA) and (CPHF, RPA), differences arising only because of slight differences in numerical methods applied in the independent calculations by different authors. In ref. 151 $E_{\mathrm{pv}}(P) - E_{\mathrm{pv}}(M) = \Delta_{\mathrm{pv}}E^{\mathrm{el}}$ was given for H_2O_2 in order to give positive values (see ref. 151 and 159 for an explanation of acronyms).

[b] In principle the TDA value of ref. 86 should be scaled by 75% to give a value of 120× 10^{-14} hc cm^{-1}, see ref. 36 and 84.

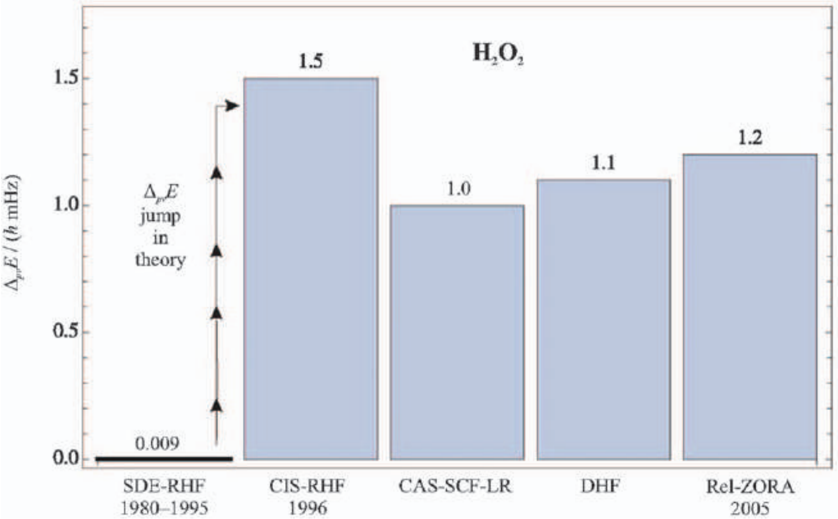

Figure 6.4 Graphical survey of the development of the theory of molecular parity violation with the "big jump" in 1995.
Reproduced from ref. 158 with permission from the Royal Society of Chemistry.

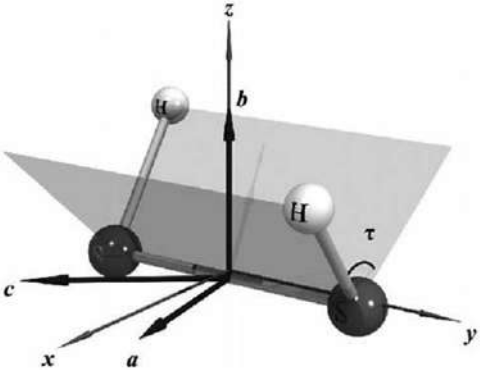

Figure 6.5 Equilibrium structure of HSSH (P-enantiomer) as obtained with the CCSD(T) method and cc-pV5Z basis set shown in the so-called electrostatic reference frame with axes (grey) labelled x, y and z together with the so-called molecular main chiral axes[84] a, b and c (black). The equilibrium structural parameters are $r_e(\text{SS}) = 207.64$ pm, $r_e(\text{SH}) = 134.32$ pm, $\alpha_e(\text{SSH}) = 98.0°$, $\tau_e = 90.72°$.
Adapted from ref. 128 with permission from John Wiley and Sons, © 2004 Wiley Periodicals, Inc., and from ref. 151 with permission from Taylor and Francis, Copyright 2015.

factor of 100 that occurred after 1995 compared to previous values and the consistency of high results afterwards (see also ref. 36 and 111 for some history). While the earlier overoptimistic conclusions on the selection of biomolecular homochirality had to be revised,[36] our work has led to a completely new and much more optimistic outlook on the possibility of doing successful spectroscopic experiments, which are now underway in our own group and others, following several proposed schemes.[27,30,32,98–107,149,152,174–176,181,182] Although no successful experiment has as yet been reported, one may now expect such results in the relatively near future.

In his insightful and enlightening summaries of the status of quantum chemistry in the 1980s Henry F. Schaefer III noted the arrival of what was to be called the ‘‘third age of quantum chemistry’’.[112–114] This age was characterized by the new ability of theoretical quantum chemistry to provide accurate numerical results for chemically relevant species (such as CH_2[115,116]) that could either challenge or overturn apparently established experimental results or else also make reliable predictions for still unavailable but potentially important experimental results. These statements hold true even more today. However, this ‘‘third age of quantum chemistry’’ is entirely based on the Schrödinger–Dirac-like theory including only the electromagnetic force. We might call this ‘‘electromagnetic quantum chemistry’’ (the further development of accurate results for rovibrational energy levels called the ‘‘fourth age’’ also falls in this domain[117]).

In the 1990s, however we introduced the term ‘‘electroweak quantum chemistry’’[33,34] to characterize a theory making quantitatively reliable predictions for phenomena related to fundamental dynamical properties of chiral molecules. In a sense this is a new age for physical stereochemistry. While the predictions appear to be stable and quantitatively reliable from a theoretical point of view, they are ‘‘true predictions’’, as so far there is no experimental result yet available (beyond null results consistent with theory). Thus this new electroweak quantum chemistry still awaits experimental test, and we shall return to this question.

6.2.2 Basic Theory

As we pointed out in the introduction, there was a dramatic change in our quantitative understanding of parity-violating potentials calculated from electroweak quantum chemistry from about 1995.[33,34] One starting point for this was our observation[33] that there were surprisingly large deviations of the older theoretical calculations from simple estimates following an equation proposed by Zel’dovich and coworkers[56]

$$\frac{\Delta_{\mathrm{pv}}E}{h} \cong 10^4 \frac{Z^5}{100^5}\,\mathrm{Hz}. \tag{6.5}$$

This by itself was not such a strong argument, given the complexity of the problem and the many possibilities for compensation of contributions leading to lower values of parity violation than expected from simple estimates. Indeed, we could rationalize such compensations by analysing the calculated parity-violating potentials in terms of a trace of a tensor[33,34] under certain conditions, thus

$$E_{\mathrm{pv}} = E_{\mathrm{pv}}^{XX} + E_{\mathrm{pv}}^{YY} + E_{\mathrm{pv}}^{ZZ}. \tag{6.6}$$

As the three components frequently differ in sign, this explains a certain lowering below the maximum possible values realized for the individual components. However, an even more important observation is related to the RHF wave functions used in the older calculation being really quite inappropriate. Indeed, the simplest improvement of using excited state CIS (configuration interaction singles) wave functions had already introduced an increase in parity-violating potentials by about two orders of magnitude,[33,34,84,85] a result later corroborated by our much improved MC-LR approach[35,85] and further confirmed independently by several other groups as well as in further calculations by our group[86–97] (see also ref. 36, 97 and 111 for some history).

We shall provide here a brief outline of the new theory following ref. 33, 34, 35, 84 and 85 in order to also provide a basic understanding of the limitations and omissions in current approaches (see also ref. 27 and 111 and further references cited therein).

In the framework of the standard model, the relevant parity-violating interaction is mediated by the electrically neutral Z^0 bosons. At molecular energies that are much lower than the energy (corresponding to mc^2) of the Z^0-boson (91.1876 GeV) the contribution of Z^0 becomes virtual.[118–120] This leads at low energies to the Hamiltonian density of the fully relativistic parity-violating electron–neutron interaction of the following form (with $h/2\pi \equiv c \equiv 1$, to simplify notation here, returning to SI units later).

$$\begin{aligned}\hat{H}^{(\mathrm{e}-n)}(x) = {} & \frac{G_\mathrm{F}}{2\sqrt{2}} g_\mathrm{A}(1 - 4\sin^2\Theta_w) j_\mu[\psi^{(\mathrm{el})}(x)] \\ & \times j^\mu_{(\mathrm{ax})}[\psi^{(n)}(x)] + \frac{G_\mathrm{F}}{2\sqrt{2}} j_\mu[\psi^{(n)}(x)] \\ & \times j^\mu_{(\mathrm{ax})}[\psi^{(\mathrm{el})}(x)]\end{aligned} \tag{6.7}$$

with $j^\mu_{(\mathrm{ax})}[\psi(x)]$ involving the familiar γ-matrices[118,119]

$$j^\mu_{(\mathrm{ax})}[\psi(x)] \overset{\mathrm{def}}{=} \Psi^+(x)\gamma^0\gamma^\mu\gamma^5\Psi(x). \tag{6.8}$$

The γ^5 matrix converts the four-vector $j^\mu[\psi(x)]$ into the axial vector $j^\mu_{(\mathrm{ax})}[\psi(x)]$. Similar expressions are obtained for the electron–proton and the electron–electron interactions.[34,120]

In principle, as pointed out in ref. 34, one can use these relativistic equations as a starting point for the theory; relativistic theories of this type have been carried out at different levels of approximation for instance by the group of Barra, Robert and Wiesenfeld (Hückel-type)[68,69,72,73] and four-component relativistic theory by Schwerdtfeger and coworkers.[88,94,95] Omitting the two small components of the bispinors $\Psi^n(x)$ and $\Psi^{\mathrm{el}}(x)$, and thus converting from four component bispinors to two-component spinors following ref. 34, 120–122 one obtains ($\mathrm{i} = \sqrt{-1}$)

$$\begin{aligned}\hat{H}^{(\mathrm{e}-n)}(\boldsymbol{x}) &\\ = \frac{G_{\mathrm{F}}}{4\sqrt{2}\mu c}&\left[-\psi^{\dagger(n)}(\boldsymbol{x})\psi^{(n)}(\boldsymbol{x})\{\psi^{\dagger(\mathrm{el})}(\boldsymbol{x})\boldsymbol{\sigma}(\boldsymbol{P}\psi^{(\mathrm{el})}(\boldsymbol{x})) + (\boldsymbol{P}^{\star}\psi^{\dagger(\mathrm{el})}(\boldsymbol{x}))\boldsymbol{\sigma}\psi^{(\mathrm{el})}(\boldsymbol{x})\}\right.\\ &\left. + \mathrm{i}g_{\mathrm{A}}(1 - 4\sin^2\Theta_{\mathrm{w}})\boldsymbol{P}(\psi^{\dagger(\mathrm{el})}(\boldsymbol{x})\boldsymbol{\sigma}\psi^{(\mathrm{el})}(\boldsymbol{x})\psi^{\dagger(n)}(x))\boldsymbol{\sigma}\psi^{(n)}(\boldsymbol{x})\right]\end{aligned} \tag{6.9}$$

G_{F} is the Fermi constant,[147,159] $\boldsymbol{P}$ the momentum operator, $\boldsymbol{\sigma}$ the doubled spin operator that has as components the familiar 2×2 Pauli matrices, $\boldsymbol{x}$ the spatial coordinate set and μ the reduced mass of the electron. The last term in eqn (6.9) is taken to be small because of the extra prefactor $(1 - 4\ \sin^2\ \Theta_{\mathrm{w}}) \simeq 0.0724$ (depending on the scheme used for the Weinberg parameter[151] and possibly energy dependent) and because of the dependence on neutron (and similarly proton) spin with the tendency of spin compensation in nuclei. The form factor g_{A} (from the strong interaction of the neutron) can be taken as 1.25.[34]

Finally, replacing the neutron density by a delta function because of the contact-like nature of the very short-range weak interaction

$$\Psi^{\dagger(n)}(\boldsymbol{x})\Psi^{(n)}(\boldsymbol{x}) \simeq \delta^3\ (\boldsymbol{x} - \boldsymbol{x}^{(n)}) \tag{6.10}$$

one obtains a Hamilton operator for the electron–neutron interaction

$$\hat{H}^{(\mathrm{e}-n)} = -\frac{G_{\mathrm{F}}}{4\mu c\sqrt{2}}(\boldsymbol{P}\boldsymbol{\sigma}\delta^3(\boldsymbol{x} - \boldsymbol{x}^n) + \delta^3(\boldsymbol{x} - \boldsymbol{x}^n)\boldsymbol{P}\boldsymbol{\sigma}). \tag{6.11}$$

For the electron–proton interaction the Hamiltonian is similarly

$$\hat{H}^{(\mathrm{e-p})} = -\frac{G_{\mathrm{F}}}{4\mu c\sqrt{2}}(1 - 4\sin^2\Theta_{\mathrm{W}}) \cdot (\boldsymbol{P}\boldsymbol{\sigma}\delta^3(\boldsymbol{x} - \boldsymbol{x}^{(\mathrm{p})}) + \delta^3(\boldsymbol{x} - \boldsymbol{x}^{(\mathrm{p})})\boldsymbol{P}\boldsymbol{\sigma}). \tag{6.12}$$

Collecting the terms for neutrons and protons together and defining an electroweak charge Q_a of the nucleus a with charge number Z_a and neutron number N_a

$$Q_a = Z_a\ (1 - 4\ \sin^2\ \Theta_{\mathrm{w}}) - N_a \tag{6.13}$$

one gets an effective electron–nucleus interaction

$$\hat{H}_a^{(\mathrm{e-nucleus})} = -\frac{G_{\mathrm{F}}}{4\mu c\sqrt{2}}Q_a(\boldsymbol{P}\boldsymbol{\sigma}\boldsymbol{\delta}^3(\boldsymbol{x} - \boldsymbol{x}^{(\mathrm{nucleus})}) + \boldsymbol{\delta}^3(\boldsymbol{x} - \boldsymbol{x}^{(\mathrm{nucleus})})\boldsymbol{P}\boldsymbol{\sigma}). \tag{6.14}$$

In addition to the electron–nucleus interaction, one should consider the electron–electron interaction.

$$\hat{H}^{(\mathrm{e-e})} = \frac{G_\mathrm{F}}{2\mu c\sqrt{2}}(1 - 4\sin^2\Theta_\mathrm{W}) \cdot \left\{\delta^3(\boldsymbol{x}^{(1)} - \boldsymbol{x}^{(2)}), (\boldsymbol{\sigma}^{(1)} - \boldsymbol{\sigma}^{(2)}) \cdot (\boldsymbol{P}^{(1)} - \boldsymbol{P}^{(2)})\right\}_+ \\ + \mathrm{i}[\delta^3(\boldsymbol{x}^{(1)} - \boldsymbol{x}^{(2)}), (\boldsymbol{\sigma}^{(1)} \times \boldsymbol{\sigma}^{(2)}) \cdot (\boldsymbol{P}^{(1)} - \boldsymbol{P}^{(2)})]_- \tag{6.15}$$

with obvious notation for the two electrons 1 and 2 in a pair $\{,\}_+$ for the anticommutator and $[,]_-$ for the commutator, used here for brevity.

The electron–electron contribution to the effective parity-violating potential is considered to be small,[34] below 1% of the other contributions, because of the small prefactor and the lack of a corresponding enhancement with Q_a and also because of a compensation of terms from different electron–electron pairs. Thus this term is usually neglected, although one must remember that it really consists of a sum over many electron pairs. Assembling all terms together and introducing the electron spin $\hat{\boldsymbol{s}}$ (with dimension) together with linear momentum $\hat{\boldsymbol{p}}$, the electron mass m_e, and rewriting now everything in consistent SI units throughout, one obtains finally for the electron–nucleus part of the Hamiltonian, using the common symbols and values for the fundamental constants[159]

$$\hat{H}^{(\mathrm{e-nucl})}_{\mathrm{pv1}} = \frac{\pi G_\mathrm{F}}{m_\mathrm{e} hc\sqrt{2}} \sum_{i=1}^{n} \sum_{a=1}^{N} Q_a \{\hat{\boldsymbol{s}}_i \hat{\boldsymbol{p}}_i \delta^3(\vec{r}_i - \vec{r}_a) + \delta^3(\vec{r}_i - \vec{r}_a) \hat{\boldsymbol{s}}_i \hat{\boldsymbol{p}}_i\}. \tag{6.16}$$

We empasize the very small value of the Fermi coupling constant $G_F = 1.43585 \times 10^{-62}$ Jm^3 in SI units. The sums extend over n electrons and N nuclei. This operator can be evaluated in different ways. The simple perturbative sum over states expression in the Breit Pauli approximation for the spin–orbit interaction reads for the parity-violating potential (with $\hat{H}_\mathrm{pv}^{\mathrm{e-nucleus}} \cong \hat{H}_\mathrm{pvl}^{\mathrm{e-nucl}}$)

$$E_\mathrm{pv} = 2\mathrm{Re}\left\{\sum_n \frac{\langle\psi_0|\hat{H}_\mathrm{pv}^{\mathrm{e-nucleus}}|\psi_n\rangle\langle\psi_n|\hat{H}_\mathrm{SO}|\psi_0\rangle}{E_0 - E_n}\right\}. \tag{6.17}$$

The Breit Pauli spin–orbit Hamiltonian $\hat{H}_\mathrm{SO}$ is as usual, here in SI units[151,159]

$$\hat{H}_\mathrm{SO} = \frac{e^2 h^2 \mu_0}{32\pi^3 m_e^2}\left[\sum_{i=1}^{n}\sum_{a=1}^{N} Z_a \frac{\hat{l}_{i,a}\hat{s}_i}{|\vec{r}_a - \vec{r}_i|^3} - \sum_{i=1}^{n}\sum_{j\neq i}^{n} \frac{\hat{l}_{i,j}(\hat{s}_i + 2\hat{s}_j)}{|\vec{r}_i - \vec{r}_j|^3}\right] \tag{6.18}$$

where $\hat{l}_{i,k}$ refers to the orbital angular momentum of electron i with respect to particle number k.

The sum-over-states expression [eqn (6.17)] essentially mixes the electronic ground-state singlet function with excited-state triplets in order to obtain a parity-violating energy expectation value for the true (mixed singlet-triplet) ground state (for a pure singlet this would vanish). However, the sum over states expression, eqn (6.17), when used explicitly, converges slowly for larger molecules. It is well known in the framework of propagator methods[123,124] that the expression in eqn (6.17) is equivalent to the expression from response theory in eqn (6.19)[35,85]

$$E_{\mathrm{pv}} = \langle\langle \hat{H}_{\mathrm{pv}}; \hat{H}_{\mathrm{SO}} \rangle\rangle_{\omega=0} = \langle\langle \hat{H}_{\mathrm{SO}}; \hat{H}_{\mathrm{pv}} \rangle\rangle_{\omega=0}. \tag{6.19}$$

One can say that the parity-violating potential E_{pv} is the response of $\langle\psi_0|\hat{H}_{\mathrm{pv}}|\psi_0\rangle$ to the static ($\omega = 0$) perturbation $\hat{H}_{\mathrm{SO}}$ or *vice versa*. This multiconfiguration linear response approach (MCLR) was derived in ref. 35 and 85, to which we refer for details. It shows much better convergence properties than when evaluating eqn (6.17) directly.

We have given this brief summary of the theory developed in more detail in ref. 33–35 in order to show all the steps of the many successive approximations made. Each of these approximations can be removed when the necessity arises. For instance, if one wishes to describe explicitly hyperfine structure components or NMR experiments one must not neglect the spin-dependent terms and therefore one has to add to the operator of eqn (6.16) a further operator given by eqn (6.20)[35,85], using again anticommutator $\{,\}_+$ and commutator $[,]_-$:

$$\begin{aligned}\hat{H}^{(\mathrm{e-nucl})}_{\mathrm{pv2}} = \frac{\pi G_{\mathrm{F}}}{m_{\mathrm{e}} hc\sqrt{2}} \sum_{i=1}^{n} \Bigg[\sum_{a=1}^{N} & (-\lambda_a)(1 - 4\sin^2\theta_{\mathrm{W}})\{\hat{\boldsymbol{p}}_i \hat{\boldsymbol{I}}_{\boldsymbol{a}}, \delta^3(\vec{r}_i - \vec{r}_a)\}_+ \\ & + (2\mathrm{i}\lambda_a)(1 - 4\sin^2\theta_{\mathrm{W}})(\hat{\boldsymbol{s}}_{\boldsymbol{i}} \times \hat{\boldsymbol{I}}_{\boldsymbol{a}})[\hat{\boldsymbol{p}}_i, \delta^3(\vec{r}_i - \vec{r}_a)]_- \Bigg].\end{aligned} \tag{6.20}$$

Also, sometimes the approximate "theoretical" value of the Weinberg parameter $\sin^2 \Theta_{\mathrm{W}} = 0.25$ is taken, which simplifies the expressions with $(1 - 4 \sin^2 \Theta_{\mathrm{W}}) = 0.0$. However, more generally, the accurate experimental parameter will be used with $(1 - 4 \sin^2 \Theta_{\mathrm{W}}) = 0.0724$[34,159] which may further depend on the energy range considered. Furthermore, one might use the semirelativistic expressions using the Breit Pauli spin–orbit operator (6.18) and the operators for parity violation in eqn (6.16) and (6.20). This should be an excellent approximation for nuclei with maximum charge number $Z_a = 20$ and acceptable up to $Z_a = 40$. However, for more highly charged nuclei one must return to the relativistic eqn(6.7) and from there derive various approximate relativistic expressions, for instance in the four-component Dirac Fock framework[88] or within two-component relativistic approximations.[125] On the other hand, one might also use more approximate treatments such as density functional theory.[96,111,126]

One might also consider investigating explicit "non-virtual" couplings going beyond the use of eqn (6.7) as a starting point, or one might include the electron–electron parity-violating interaction in eqn (6.15) in the calculations. Whether one wishes to invest effort in removing some of the approximations used depends upon one's intuition of whether large improvements are to be expected. At present it seems unlikely that order of magnitude improvements will again be found in the future, although only experiment can give a definitive answer. We think that the currently largest chance for improvement resides in appropriate electronic wave functions that are highly accurate, in particular near the nuclei, and in further effects from molecular structure and motion to be discussed now.

6.2.3 Parity-violating Potential Hypersurfaces and Vibrational Effects

Two qualitative aspects of the structure of parity-violating potentials deserve mentioning. Firstly, similar to the parity conserving electronic potential, the parity-violating potentials are a function of all 3N-6 internal nuclear degrees of freedom in the molecule. Thus, the parity-violating potentials E_{pv} defined by eqn (6.17) or (6.19) define a parity-violating potential hypersurface

$$E_{\mathrm{pv}} = V_{\mathrm{pv}}\ (q_1,\ q_2,\ q_3,\ \ldots\ q_{3N-6}). \tag{6.21}$$

While isolated distortions or individual coordinate displacements have been considered for some time in such calculations (see Figure 6.6 for instance) the true multidimensional aspects have been considered only more recently.[40,91,97,127,128] The spectroscopically observable parity-violating energy differences $\Delta_{\mathrm{pv}}E$ have to be computed as appropriate expectation values of the parity-violating potential in eqn (6.21) for the multidimensional rovibrational state with anharmonically coupled vibrations. This leads to sizeable effects, as was shown recently.[127] However, we know from our work in rovibrational spectroscopy and dynamics of polyatomic molecules[129] that this problem can be handled accurately for not too complex molecules[98–100,129–133,172] and a similar statement applies to the other important dynamical problem: tunnelling (Section 6.3).

A second general aspect of the parity-violating potential arises from the structure of the Hamiltonian in eqn (6.16). Because of the contact-like interaction between electrons and nuclei, the parity-violating potential can be written as a sum of contributions from the individual nuclei

$$V_{\mathrm{pv}}(q_1, q_2, q_3,\ \ldots\ q_{3N-6}) = \sum_{n=1}^{N} V_{\mathrm{pv}}^{\mathrm{a}}(q_1, q_2, q_3,\ \ldots\ q_{3N-6}). \tag{6.22}$$

Because of the approximate Z^5 scaling (see, however, ref. 128) this allows for an easy analysis of calculations and also some rough estimates. Because the electronic wave function generally depends upon the coordinates (q_1, q_2, q_3, … q_{3N-6}) in a very complex fashion, there are, however, no really simple and generally accurate estimates to be expected. However, one can derive certain sets of rules for special cases (see ref. 134 for example). In practice, one has to combine the traditional quantum chemical calculations from the "electromagnetic theory" with the parity-violating potentials from the electroweak theory, as we shall discuss now with emphasis on the symmetry aspects.

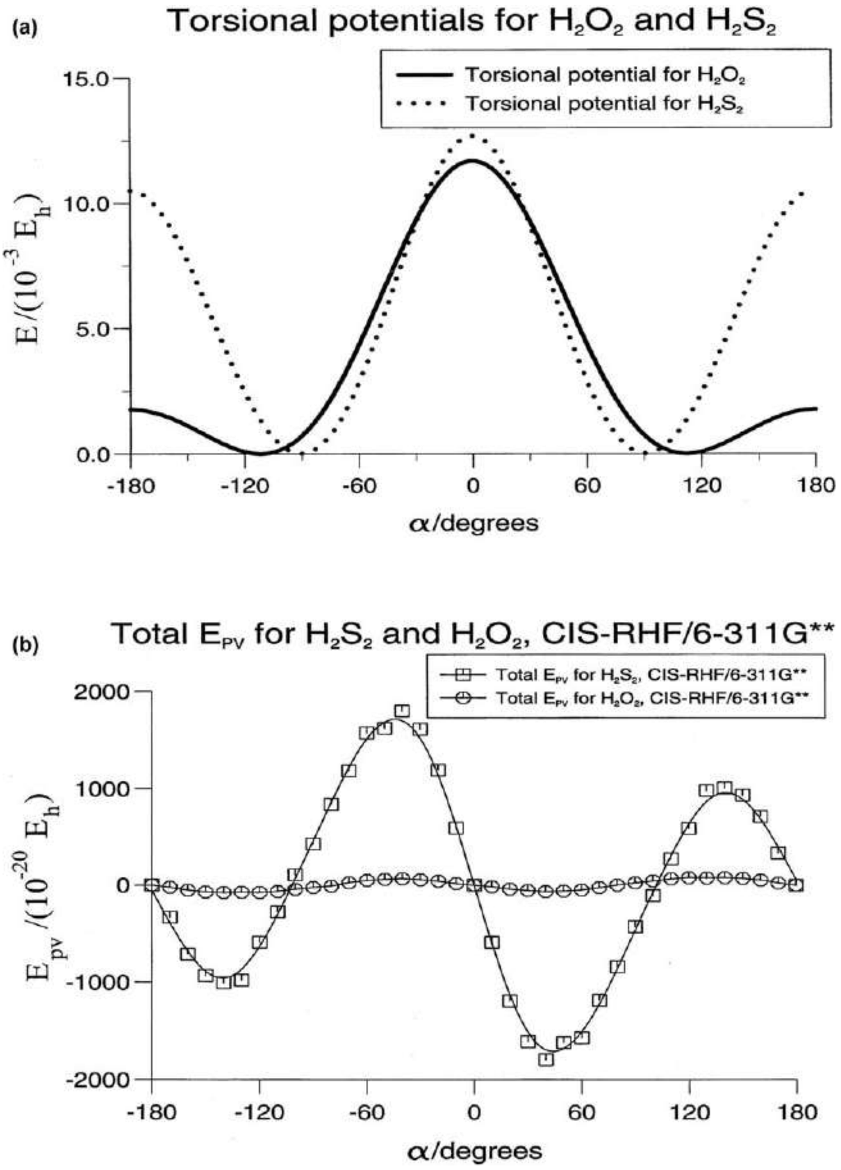

Figure 6.6 Parity conserving and parity-violating potentials for H_2O_2 (a) and H_2S_2 (b). Reproduced from ref. 84 with permission from Elsevier, Copyright 1998.

For visualization as well as for the practical approach on can use as a starting point the Born–Oppenheimer (or adiabatic) potential hypersurface $V(q_1,\ q_2,\ \ldots\ q_s)$ as a function of the set of some generalized internal coordinates $\{q_1,\ q_2,\ q_3\ \ldots\ q_s\}$, where $s = 3N - 6$ is the relevant number of degrees of freedom of a chiral molecule with $N \geq 4$ being the number of nuclei (atoms) of the molecule. This potential is rigorously symmetric upon inversion of the coordinates at the center of mass (parity operation $\hat{P}$ or $\hat{E}^*$)

$$E^* V_{\mathrm{R}}(q_1, q_2, q_2, \ldots q_s) = V_{\mathrm{S}}(\bar{q}_1, \bar{q}_2, \bar{q}_3, \ldots \bar{q}_s) \tag{6.23}$$

with

$$V_{\mathrm{R}}(q_1, q_2, q_2, \ldots q_s) - V_{\mathrm{S}}(\bar{q}_1, \bar{q}_2, \bar{q}_3, \ldots \bar{q}_s) = 0 \tag{6.24}$$

i.e. exactly zero by symmetry. We have indicated by the indices R and S that the inversion E^* transforms an enantiomeric configuration "R" into the corresponding enantiomeric "S" configuration, and the $\bar{q}_i$ indicate the coordinates with the inverted structure.

Of course, the symmetry of the Hamiltonian goes far beyond the Born–Oppenheimer, adiabatic or any other approximation; the exact molecular Hamiltonian $\hat{H}_{\mathrm{em}}$ in electromagnetic theory shows this symmetry. One notes that relevant molecular quantizations and potential energy differences in these potentials are on the order of 100 kJ mol^{-1} corresponding to about 1 eV (covering of course a range of a few orders of magnitude depending on the dynamical process considered).

On the other hand, in electroweak quantum chemistry, one calculates an additional effective "parity-violating" potential $V_{\mathrm{pv}}(q_1, q_2, q_2, \ldots q_s)$, which is antisymmetric under the inversion operation.

$$E^* V_{\mathrm{pvR}}(q_1, q_2, q_2, \ldots q_s) = V_{\mathrm{pvS}}(\bar{q}_1, \bar{q}_2, \bar{q}_3, \ldots \bar{q}_s) = -V_{\mathrm{pvR}}(q_1, q_2, q_2, \ldots q_s) \tag{6.25}$$

Thus one can define for every structure of the chiral molecule a parity-violating energy difference

$$\begin{aligned}\Delta_{\mathrm{pv}}E_{\mathrm{el}}(q_1, q_2, q_3, \ldots q_s) &= V_{\mathrm{pvR}}(q_1, q_2, q_3, \ldots q_s) - V_{\mathrm{pvS}}(\bar{q}_1, \bar{q}_2, \bar{q}_3, \ldots \bar{q}_s)\\ &= 2V_{\mathrm{pvR}}(q_1, q_2, q_3, \ldots q_s).\end{aligned} \tag{6.26}$$

These energy differences are typically very small in absolute value, on the order of 100 aeV or 10^{-11} J mol^{-1} and can be negative or positive depending whether R or S is more stable. They vanish by symmetry for achiral geometries of the molecule. For chiral geometries they satisfy the antisymmetry relation in eqn (6.25). However, even within one set of enantiomeric geometries (say only for the R-isomer) the parity-violating potentials can change sign. Thus there can be, and, indeed, there frequently are, vanishing parity-violating potentials (and $\Delta_{\mathrm{pv}}E_{\mathrm{el}}$) also for *chiral* geometries (see Figure 6.6). This property can be understood by the interpretation of the structure of the parity-violating potential as a trace of a tensor, thus the sum of three components of possibly different signs, but it does not depend on this interpretation.[33,34,84] While well understood, this property spoils any simplistic approach to estimate measurable parity-violating energy differences from theory. They can only be obtained from appropriate theoretical calculation of the parity-violating potential energy hypersurfaces in eqn (6.25) and (6.26) for the relevant set of geometries. Although one can give some simple rules for estimating orders of magnitude of parity-violating potentials, such as the approximate Z^5 scaling with nuclear charge[27,30,33–35,84,85,158] large deviations can occur for individual molecules, for instance if the V_{pv} crosses zero near the chiral equilibrium geometry of the molecule. The chiral molecule 1,3-difluoroallene is such an example.[141,151] Another example is the amino acid alanine, where one has a zero crossing of V_{pv} as a function of a conformational change that is unrelated to enantiomeric structure.[34,92] Thus the actual calculation of the parity-violating potentials by the methods of quantitative electroweak quantum chemistry is necessary, if one wants to obtain accurate results. We do not discuss details here but refer to careful descriptions[27,33–35,40,84,85,88,91–93,96,97,127,128,141–146,151] as an incomplete survey of recent work of this kind.

The parity-violating potentials or parity-violating energy differences $\Delta_{\mathrm{pv}}E_{\mathrm{el}}$ in eqn (6.25) and (6.26) do not correspond to the directly measurable parity-violating energy difference $\Delta_{\mathrm{pv}}E$, for instance in the ground state energy difference between the R and S enantiomers. This is calculated as an expectation value over $\Delta_{\mathrm{pv}}E_{\mathrm{el}}$ in the ground rotational-vibrational (perhaps also hyperfine) state. Thus in practice one uses

$$\hat{H} = \hat{T} + \hat{V}_{\mathrm{R}}(q_1, q_2, q_2, \ldots q_s) \tag{6.27}$$

obtaining ideally

$$\hat{H}\varphi^{(\mathrm{k})}_{\mathrm{evr}} = E^{(\mathrm{k})}_{\mathrm{evr}}\,\varphi^{(\mathrm{k})}_{\mathrm{evr}} \tag{6.28}$$

by solving for the complete rovibronic wave functions $\varphi^{(\mathrm{k})}_{\mathrm{evr}}(q_1, q_2, q_3, \ldots q_s)$ of the electronic ground or some excited state, and if needed including non-adiabatic and hyperfine structural effects. One obtains the desired parity-violating energy differences as expectation values

$$\Delta_{\mathrm{pv}}E^{(\mathrm{k})} = \langle\varphi^{(\mathrm{k})}_{\mathrm{evr}}|\Delta_{\mathrm{pv}}E_{\mathrm{el}}|\varphi^{(\mathrm{k})}_{\mathrm{evr}}\rangle. \tag{6.29}$$

The index "evr" for the internal quantum state of the molecule is considered to include the nuclear spin (hyperfine structure) wave function in molecules possessing nuclei with non-zero spin and in this case the parity-violating Hamiltonian $\hat{H}_{\mathrm{pv}}$ to calculate E_{pv} in eqn (6.17) should include the term $\hat{H}_{\mathrm{pv1}}$ in eqn (6.16) and also the term $\hat{H}_{\mathrm{pv2}}$ from eqn (6.20). Calculations of this type have been presented at various levels of approximation in ref. 40 and 127, for instance. For the rovibrational ground state ($k = 0$) we simply use the symbol $\Delta_{\mathrm{pv}}E$ and for some excited states we use $\Delta_{\mathrm{pv}}E^*$. As a first approximation, one frequently takes $\Delta_{\mathrm{pv}}E_{\mathrm{el}}$ at the equilibrium geometry ($q_1^e, q_2^e, q_3^e, \ldots q_s^e$) in order to estimate $\Delta_{\mathrm{pv}}E$ in the ground state. We have shown, however, that the effects from calculating the correct average by means of eqn (6.29) can be quite large.[127]

We can summarize the theoretical calculation of the parity-violating effects in chiral molecules by stressing again the symmetry aspect. While there is, of course, no current or in the foreseeable future possible technology to calculate quantum chemical energies (say $V_{\mathrm{R}}(q_1, q_2, q_3, \ldots q_s)$ in eqn (6.23) or rovibrational and hyperfine levels, *etc.*) to an accuracy of, say, 100 aeV, which is the order of the electroweak effects, such an accuracy is not needed, because we know that the difference in eqn (6.24) and all similar energy differences derived from ''electromagnetic'' quantum chemistry are exactly zero by symmetry (beyond the Born–Oppenheimer approximation and even including effects from electromagnetic quantum field theory). Thus parity-violating energy differences can be calculated separately and accurately as purely antisymmetric contribution to the effective potentials or level energies, in spite of their extremely small absolute magnitude. In the well-known ''captain and ship'' analogy we can say that we can obtain the weight of the captain alone separately and we do not have to weigh the ship with the captain and then the ship alone and calculate the difference between the two results, which would be impossible in terms of significant accuracy; this direct evaluation of the ''weight of the captain'', corresponding to the parity-violating potential is made possible by symmetry. A similar statement holds for experiments on the effect, to be discussed in Section 6.5 (see also the discussion in ref. 27, 28 and 30).

6.3 The Interplay of Tunnelling and Parity Violation in Chiral Molecules

Having now the ability to calculate accurately and quantitatively the effective parity-violating potentials from electroweak quantum chemistry we can discuss the effects on the quantum dynamics of chiral molecules in relation to tunnelling according to Hund's ''electromagnetic theory''. This is summarized schematically in Figure 6.7, which compares the theoretical situation at the time of Hund, as discussed in the introduction, with the current situation including parity violation in a simple one-dimensional picture of the effective potentials as a function of q.

The one-dimensional ''reaction coordinate'' q relates the two enantiomers and we keep the true multidimensional nature in mind. For reasons of symmetry the eigenstates in the electromagnetic theory will have a well-defined parity and are delocalized. They differ by a tunnelling splitting $\Delta E_{\pm} = E_{-} - E_{+}$ which might be very small. The delocalized eigenstates χ_{+} and $-\chi_{-}$ can be combined to give localized, time-dependent states λ and ρ as discussed in the introduction. We can use χ_{+} and $-\chi_{-}$ also as basis states when introducing the effects from parity violation as a small perturbation. For simplicity, we assume here that both $\Delta E_{\pm}$ and $\Delta_{\mathrm{pv}}E(q_1, q_2, q_3, \ldots q_s)$ are small compared to all the other energy differences between, say, rovibrational levels of the molecule. This allows us to treat the perturbation as a two-level problem, but the treatment can be readily extended to other situations by including more levels. We can distinguish now two limiting situations. In the first case we have

$$|\Delta E_{\pm}| \gg |\Delta_{\mathrm{pv}}E(q_1, \ldots\ldots q_s)|. \tag{6.30}$$

In this limiting case the perturbation will lead only to very small shifts in the energy levels, which remain almost unchanged, as will the tunnelling times in eqn (6.1). The perturbation also leads small ''parity-violating'' admixtures of the opposite parity in the wave functions, whose overall shape will, however, be

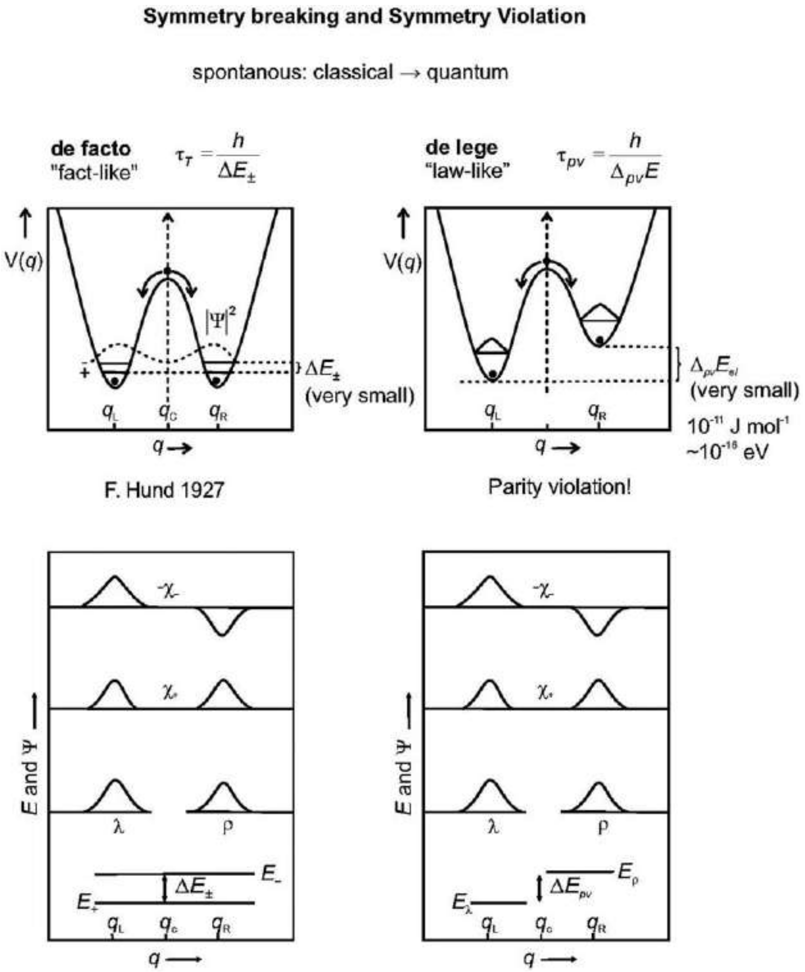

Figure 6.7 Illustration of symmetric and asymmetric double-well potentials for a chiral molecule.
Reproduced from ref. 30 with permission from the Annual Review of Physical Chemistry, Copyright 2008 (see also ref. 149).

essentially unchanged. Thus, in this case the time-dependent eigenstate dynamics and the time-dependent wave packet dynamics will be almost unchanged. This situation applies to transiently chiral molecules to be discussed below. A similar situation applies also to achiral molecules with eigenstates of well-defined parity. The effect of parity violation might still become visible by tiny effects such as changes in the optical selection rules, and a very small optical activity. However, these effects will not be dramatic and not be easily detected. In the other limiting case we have

$$|\Delta_{\mathrm{pv}}E(q_1, \ldots\ldots q_s)| \gg |\Delta E_\pm|. \tag{6.31}$$

This situation applies to stable chiral molecules where $\Delta E_\pm$ can be exceedingly small. In this case one observes a dramatic change. The eigenstates become localized left or right (λ and ρ), that is, the stereomutation times become infinite. While one might say that a change from slow stereomutation tunnelling in, say, a million years to infinite (no tunnelling) is practically irrelevant and not observable in real experiments, there is a second change that is really observable. While in electromagnetic theory the lifetime of the parity eigenstates χ_+ and χ_- are infinite, in electroweak theory the parity eigenstates become in this limit time dependent, evolving with a period

$$\tau_{\mathrm{pv}} = h/\Delta_{\mathrm{pv}}E \tag{6.32}$$

where $\Delta_{\mathrm{pv}}E$ is the energy separation of the energy eigenstates λ and ρ. Within this limit one has also

$$\chi_+ = \frac{1}{\sqrt{2}}(\lambda + \rho) \tag{6.33}$$

$$-\chi_- = \frac{1}{\sqrt{2}}(\lambda - \rho) \tag{6.34}$$

and similarly

$$\lambda = \frac{1}{\sqrt{2}}(\chi_+ - \chi_-) \tag{6.35}$$

$$\rho = \frac{1}{\sqrt{2}}(\chi_+ + \chi_-) \tag{6.36}$$

(see also Figure 6.7). While the superposition principle guarantees that parity eigenstates χ_+ and χ_-can be prepared by superposition of λ and ρ, it turns out that theoretical values of $\Delta_{\mathrm{pv}}E$ such that periods for parity changes happen on a timescale of seconds, which is readily accessible to laboratory experiments.

Some further aspects of the time dependence in the two limits may be useful. The time-dependent Schrödinger equation for the wave function $\Psi(q, t)$ for the isolated molecule with the Hamiltonian $\hat{H}$ is:

$$\mathrm{i}\frac{h}{2\pi}\frac{\partial\Psi(q,t)}{\partial t} = \hat{H}\Psi(q,t) \tag{6.37}$$

with the general solution in terms of eigenfunctions φ_k and energies E_k

$$\hat{H}_k\varphi_k(q) = E_k\varphi_k(q) \tag{6.38}$$

$$\Psi(q,t) = \sum_k c_k\varphi_k \exp(-2\pi\mathrm{i}E_k t/h). \tag{6.39}$$

In the limit of eqn (6.30), where the eigenstates are to an excellent approximation given by χ_+ and χ_-, with energies E_+ and E_-, one thus has for the two-level evolution

$$\Psi(q,t) = \frac{1}{\sqrt{2}}\exp(-2\pi \mathrm{i} E_+ t/h)[\chi_+ + \chi_- \exp(-2\pi \mathrm{i} \Delta E_\pm t/h)] \tag{6.40}$$

with a probability density

$$P(q,t) = \Psi(q,t)\Psi^*(q,t) = |\Psi|^2 = \frac{1}{2}\left|[\chi_+ + \chi_- \exp(-2\pi \mathrm{i}\Delta E_\pm t/h)]\right|^2 \tag{6.41}$$

This describes a structural change of the molecule from left to right during a tunnelling stereomutation.

In the opposite limit of eqn (6.31), where parity violation dominates, the eigenstates φ_k are given by λ and ρ with eigenvalues E_λ and E_ρ to an excellent approximation, and one has for the time-dependent wave function

$$\psi(q,t) = \frac{1}{\sqrt{2}}\exp(-2\pi \mathrm{i} E_\lambda t/h)[\lambda + \rho \exp(-2\pi \mathrm{i} \Delta_{\mathrm{pv}} E t/h)]. \tag{6.42}$$

Now one can follow a change of the parity of the state (or wave function) with time. For $t=0$ in eqn (6.42) one has a state χ_+ of positive parity, eqn (6.33), the probability of finding positive parity is 1 and the probability of finding negative parity is zero. However with increasing time one finds for the state of negative parity the probability

$$p_- = 1 - p_+ = \sin^2(\pi t \Delta_{\mathrm{pv}} E/h). \tag{6.43}$$

From this discussion, it is clear that, for a significant assessment of parity violation in chiral molecules, one has to discuss the role of both parity violation and tunnelling. Only in the limit, where parity violation dominates [eqn (6.31)], will $\Delta_{\mathrm{pv}}E$ be a measurable parity-violating energy difference between the ground-state energies of the localized enantiomers of chiral molecules. In the opposite limit of eqn (6.30), one would simply measure a tunnelling splitting between achiral states of rather well-defined parity. Table 6.2 gives a survey of results for $|\Delta_{\mathrm{pv}}E^{\mathrm{el}}|$ and $|\Delta E_\pm|$ for many molecules, from which the relevant times can be readily calculated as well. Table 6.3 summarizes theoretical results for parity violation in chiral molecules, where the tunnelling splitting is extremely small but has not been calculated quantitatively. However, in any case for all these molecules in Table 6.3 one has the limiting behavior $|\Delta_{\mathrm{pv}}E| \gg |E_\pm|$ corresponding to eqn (6.31) with absolute certainty, whereas for the examples calculated in Table 6.2 this limit applies only to the six molecules ClOOCl, ClSSCl, D_2Te_2, T_2Te_2, HSSSH, and $C_4H_4S_2$. We note here also that the relative differences between $\Delta_{\mathrm{pv}}E^{\mathrm{el}}$ and $\Delta_{\mathrm{pv}}E_0$ (*i.e.* averaged over the vibration-rotation ground-state wave function) are particularly large for molecules that are chiral by isotopic substitution of hydrogen isotopes H, D, and T (see ref. 134 for a discussion).

Table 6.2 Tuning tunnelling and parity violation in a series of molecules (modified and updated after ref. 29, 30 and 135).

Molecule	$\lvert\Delta E_{\mathrm{pv}}^{\mathrm{el}}\rvert/\mathrm{cm}^{-1}$	$\lvert\Delta E_{\pm}\rvert/\mathrm{cm}^{-1}$	Reference
H_2O_2	4×10^{-14}	11	35, 85, 131, 132, 137
D_2O_2	4×10^{-14}	2	35, 85,132
T_2O_2	4×10^{-14}	0.5	138
HSOH	4×10^{-13}	2×10^{-3}	138
DSOD	4×10^{-13}	1×10^{-5}	138
TSOT	4×10^{-13}	3×10^{-7}	138
$HClOH^+$	8×10^{-13}	2×10^{-2}	135
$DClOD^+$	(8×10^{-13})[c]	2×10^{-4}	135
$TClOT^+$	(8×10^{-13})[c]	7×10^{-6}	135
H_2S_2	1×10^{-12}	2×10^{-6}	89
D_2S_2	1×10^{-12}	5×10^{-10}	89
T_2S_2	1×10^{-12}	1×10^{-12}	89
Cl_2O_2	5.75×10^{-13}	6.7×10^{-25}	150–152
Cl_2S_2	1×10^{-12}	$\approx10^{-76}$[a]	90
H_2Se_2	2×10^{-10}[d]	1×10^{-6}	173
D_2Se_2	(2×10^{-10})[c]	3×10^{-10}	173
T_2Se_2	(2×10^{-10})[c]	4×10^{-13}	173
H_2Te_2	3×10^{-9}[b]	3×10^{-8}	135
D_2Te_2	(3×10^{-9})[c]	1×10^{-12}	135
T_2Te_2	(3×10^{-9})[c]	3×10^{-16}	135
HSSSH	1.61×10^{-12}	3.3×10^{-23}	164, 165
$C_4H_4S_2$	1.1×10^{-11}	$<1\times10^{-24}$	162, 166

[a] Extrapolated value.

[b] Calculated in ref. 88 for the P-structure ($r_{\mathrm{TeTe}}=284$ pm, $r_{\mathrm{HTe}}=164$ pm, $\alpha_{\mathrm{HTeTe}}=92^\circ$ and $\tau_{\mathrm{HTeTeH}}=90^\circ$) and the corresponding M-structure. An earlier, very approximate result by Wiesenfeld[73] should be cited as well, giving $\Delta E_{\mathrm{pv}}=8\times10^{-10}\,\mathrm{cm}^{-1}$ for the following structure ($r_{\mathrm{TeTe}}=271.2$ pm, $r_{\mathrm{HTe}}=165.8$ pm, $\alpha_{\mathrm{HTeTe}}=90^\circ$ and $\tau_{\mathrm{HTeTeH}}=90^\circ$).

[c] Not calculated quantitatively, but estimated to be rather similar to the corresponding hydrogen isotopomers.

[d] Calculated in ref. 88 for the P-structure ($r_{\mathrm{HSe}}=145$ pm, $\alpha_{\mathrm{HSeSe}}=92^\circ$ and $\tau_{\mathrm{HSeSeH}}=90^\circ$) and the corresponding M-structure.

Figure 6.8 provides a graphical survey for the transition between the regimes of dominating tunnelling and dominating parity violation, where one can also identify the very approximate "Z^5 scaling law" for a series of hydrides of the chalcogenes[158] (see also ref. 128 for a discussion of the origin and limitations of the scaling law).

Some of the results summarized in Table 6.3 deserve further discussion. The relatively small absolute value of the parity-violating energy difference $\Delta_{\mathrm{pv}}E^{\mathrm{el}}$ at the equilibrium geometry (and also in the ground state) for 1,3-difluoroallene CHF=C=CHF arises because of a transition from positive to negative values of the parity-violating potential $\Delta_{\mathrm{pv}}E^{\mathrm{el}}(\alpha)$ as function of the torsional angle α at a chiral geometry rather near to the equilibrium geometry. The maximum of $\Delta_{\mathrm{pv}}E^{\mathrm{el}}(\alpha)$ would be more than an order of magnitude larger. This type of behaviour is rather frequent and is one of the reasons why simple empirical rules and scaling laws are not sufficient for an accurate estimate of $\Delta_{\mathrm{pv}}E$ in the ground states of chiral molecules. On the other hand the relatively large value of $\Delta_{\mathrm{pv}}E$ for 1,2-dithiine ($C_4H_4S_2$) in

Table 6.3 Parity-violating energy differences $\Delta_{pv}E$ between the ground states (and taken to be sometimes approximately $\Delta_{pv}E^{el}$ at the equilibrium structures) of chiral molecules, for which the tunnelling splitting is extremely small (but not quantitatively calculated, as one has certainly $|\Delta E_{\pm}| \ll |\Delta_{pv}E|$).

Molecule	$\lvert\Delta_{pv}E\rvert/(hc\,cm^{-1})$	Reference
$CHF{=}C{=}CHF$	1.4×10^{-13}	141, 143, 151
$CHF{=}C{=}CHCl$	7×10^{-13}	143, 151
$CHCl{=}C{=}CHCl$	1.1×10^{-12}	143, 151
$PF^{35}Cl^{37}Cl$	2.8×10^{-14}	160
CHFClBr	1.9×10^{-12}	40, 99, 127
CDFClBr	1.9×10^{-12}	127, 163
F-oxirane	1.7×10^{-13}	100, 146, 148
D-oxirane	$(2\times10^{-16})^{c}$	167,183
Cyano-oxirane	1×10^{-13}	93, 168
Cyano-aziridine	1×10^{-13}	93
CHDTOH[a]	3.66×10^{-17}	134
Alanine[b]	$\approx5\times10^{-14}$	34, 33, 92

[a] Value for one of two prominent conformers (see ref. 134).
[b] Very strongly conformer dependent with even sign changes when rotating the –COOH group without changing enantiomeric structure (see ref. 92)
[c] Preliminary estimate, the vibrationally averaged value is larger.

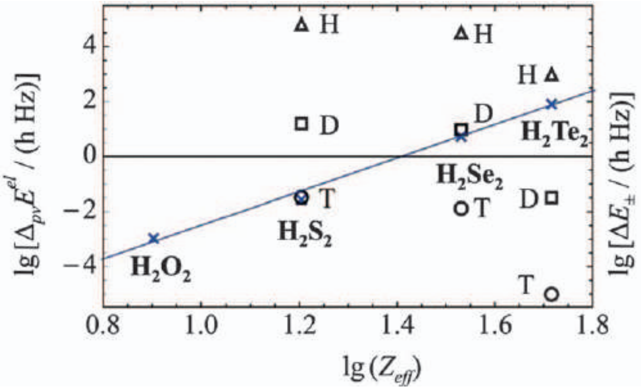

Figure 6.8 Doubly logarithmic representation of the parity-violating energy differences $\Delta_{pv}E^{el}$ (as decadic logarithm, lg, electronic contribution from the parity-violating potential differences) as a function of lg Z_{eff} in the series $^{1,2,3}H–X–X–^{1,2,3}H$ with $X = O$, S, Se, Te and taking $Z_{eff} = Z_X$ as the effective nuclear charge number (crosses '×' for all isotopomers after ref. 158). $\Delta_{pv}E^{el}$ is essentially independent of the hydrogen isotope. This is compared with tunnelling splittings ($\Delta E_{\pm}$) where the dependence on the hydrogen isotope is essential (triangles for H, squares for D, circles for T). The results are from the summary in ref. 27, where the calculations for $\Delta_{pv}E^{el}$ were taken from Berger and Quack (2000)[35] for H_2O_2 and H_2S_2, (also from Bakasov *et al.* (2004)[128]). The results for $\Delta_{pv}E$ H_2Se_2 and T_2Se_2 are from Laerdahl and Schwerdtfeger (1999)[88] and the tunnelling splittings ($\Delta E_{\pm}$ were taken from Quack and Willeke (2003),[138] Gottselig *et al.* (2001),[89] (2003),[173] and (2004).[135] The slope of the straight-line fit is about 4.8, corresponding to about the Z^5_{eff} law (see, however, the discussion in ref. 128).

Table 6.2 corresponds to a value near to the maximum of $\Delta_{pv}E$ as a function of the stereomutation reaction coordinate.

The moderately large value of $\Delta_{pv}E$ for the isotopically chiral molecule $PF^{35}Cl^{37}Cl$ is an example of the fundamentally new isotope effect introduced by the electroweak interaction in isotopically chiral molecules as discussed in more detail in ref. 29, 41 and 160. It arises from the difference of the weak nuclear charges of isotopes in eqn (6.13).[160]

6.4 The Quantum Wavepacket Dynamics in Chiral Molecules Where Either Tunnelling or Parity Violation Dominates

6.4.1 Exact and Approximate Studies of Tunnelling in Prototypical Molecules with Transient Chirality: Hydrogen Peroxide and Ammonia Isotopomers

Figure 6.9 shows the H_2O_2 molecule with the two enantiomers in their equilibrium geometry. This was to our knowledge the first example where a reaction of stereomutation was described on a full-dimensional potential surface with all six internal degrees of freedom[131] and a quantum mechanical treatment with exact DVR methods for the spectroscopic stationary states and the time-dependent wave packet dynamics of the tunnelling process.[132,169] Hydrogen peroxide is well suited as a prototype molecule for such investigations due to the large tunnelling splitting of *ca.* 10 cm^{-1} in the ground state that leads to the result that effectively a quantum dynamics in the spirit of Hund is valid independent of the also existing, but for the dynamics, negligible, parity violation (see below).[33–35] In Table 6.4 the

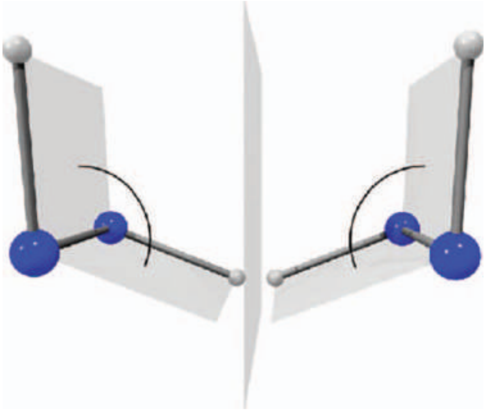

Figure 6.9 H_2O_2 in its two enantiomeric equilibrium geometries, P-enantiomer on the left, M-enantiomer on the right connected by a fast-tunnelling reaction. Reproduced from ref. 161 with permission from Leopoldina, Copyright 1999. See also ref. 131, 132 and 169.

Table 6.4 Tunnelling splittings for H_2O_2 from the numerically exact solution ($\Delta\tilde{\nu}_i^{6D}$), from the quasiadiabatic channel RPH approximation ($\Delta\tilde{\nu}_i^{\mathrm{RPH}}$), and from experiment ($\Delta\tilde{\nu}_i^{\mathrm{exp}}$). T^{6D} is the tunnelling transfer time. Adapted from ref. 132 and 169 with permission from Elsevier, Copyright 1999, 2007. ω_i is the harmonic wave number of the mode i and $\tilde{\nu}_i^{\mathrm{exp}}$ is its experimental fundamental wave number $\tilde{\nu}_i^{\mathrm{6D}}$ exact six-dimensional result from theory on the surface from ref. 131.

i	ω_i/cm^{-1}	$\tilde{\nu}_i^{\mathrm{exp}}$/cm^{-1}	$\tilde{\nu}_i^{6D}$/cm^{-1}	$\Delta\tilde{\nu}_i^{\mathrm{exp}}$/cm^{-1}	$\Delta\tilde{\nu}_i^{6D}$/cm^{-1}	$\Delta\tilde{\nu}_i^{\mathrm{RPH}}$/cm^{-1}	T^{6D}/ps
0	0	0	0	11.4	11.0	11.1	1.5
1	3778	3609.8	3617.7	8.2	7.6	8.4	2.2
2	1453	1395.9	1392.0	(2.4?)	6.1	5.0	2.7
3	889	865.9	850.5	12.0	11.1	10.8	1.5
4	392	254.6	259.3	116	118	120	0.14
5	3762	3610.7	3605.8	8.2	7.4	7.4	2.0
6	1297	1264.6	1236.5	20.5	20.8	21.8	0.8

tunnelling splittings from the numerically exact solution are compared to the approximate results from the quasiadiabatic channel reaction path Hamiltonian (RPH) approach and to experimental results. The strongly mode selective tunnelling times as a function of the excitation of the different degrees of freedom can be recognized. Thus by exciting various vibrational modes, say with a pulsed laser, one can control the stereomutation rates. For example the excitation of the OH-stretching vibrations ν_1 and ν_5 results in a slowing down of the tunnelling process even though the excitation energy is a multiple of the barrier height; it remains an effectively quasiadiabatic process with a slightly modified effective quasiadiabatic channel potential and moment of inertia (''quasi'' tunnelling mass), which is slightly increased by the excitation of an OH-stretching vibration. These two effects together explain qualitatively the slowing down of the process. Similar effects have been found for the inversion motion in the aniline isotopomers (with the chiral isotopomer C_6H_5NHD)[170,171] which shows such a mode-selective ''non-statistical'' tunnelling process with a slowing down after NH-stretching excitation, despite the very high density of states at high excitation in C_6H_5NHD, with good agreement between experimental results and quasiadiabatic channel RPH calculations carried out *ab initio*. While the quasiadiabatic channel RPH treatments have been found to be quite successful in handling multidimensional tunnelling problems, one should bear in mind their approximate nature. The use of ''quasiadiabatic'' in the model is motivated by the approaches of ref. 132, 169, 196 and 207 using an important ''diabatization'' step as compared to the RPH treatment of Miller *et al.*,[208] which might be called rigorously adiabatic. The ''diabatization'' uses the concept of the statistical adiabatic channel model to allow channel potentials of the same symmetry to cross in order to retain their physical nature in terms of the channel wave function.[209] As one might call these crossing ''diabatized'' channels also ''adiabatic'' (with different definitions) we introduced the term quasiadiabatic for them (see ref. 210 for a discussion).

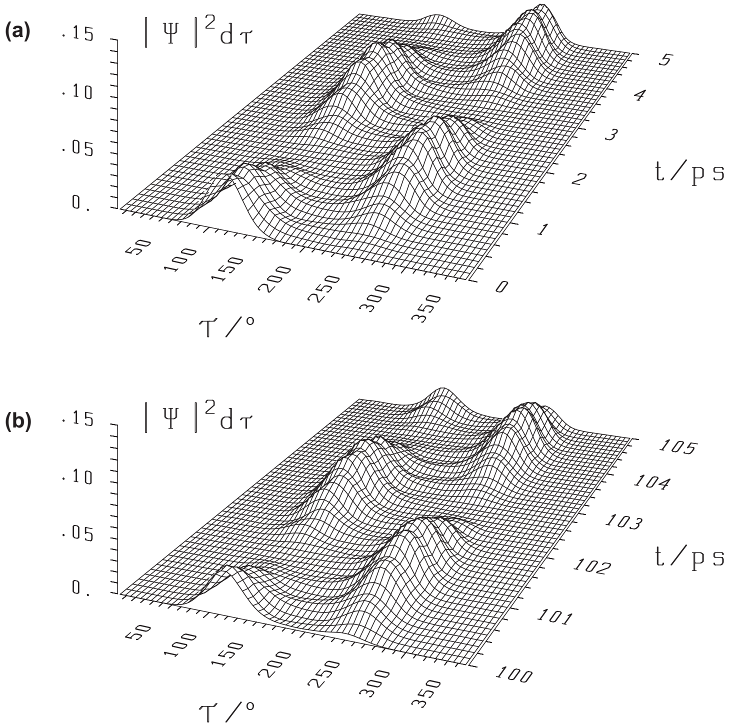

Figure 6.10 Six-dimensional wave packet evolution for H_2O_2 in its lowest quantum states ($i = 0$ in Table 6.4). $|\Psi|^2$ shows the time-dependent probability as a function of the torsional coordinate, where the probability density is integrated over all other coordinates. (a) shows the time interval 0–5 ps and (b) the time interval 100–105 ps with identical initial conditions at $t = 0$ as in (a).[132,169] The migration of the wave packet from the left to the right corresponds to a change from one enantiomer to the other in Figure 6.9.

Figure 6.10 shows as an example the "wave packet dynamics" in the ground state of the H_2O_2 molecule in terms of the six-dimensional quantum mechanical probability density as a function of the torsional angle (integrated over the other five degrees of freedom). One can see the initially, at time $t = 0$, "left"-localized density which shows an approximately Gaussian shape around the equilibrium geometry of the "left" enantiomer and which after 1.5 ps transforms to the "right"-localized wave packet close to the equilibrium geometry of the second ("right") enantiomer.

The detailed full-dimensional analysis of the wave packet dynamics can be used to test the validity of the quasiadiabatic channel-RPH approximation, which turns out to be a remarkably good approximation for this example. Even at high energies one finds indeed quasi-adiabatic tunnelling above the barrier. The different tunnelling velocities for various excitations of different channels in all possible degrees of freedom can be used for a "mode selective'' tunnelling control of the reaction velocity, for instance with the help of laser excitation.[152,172]

As seen from Table 6.4 the excitation of the ''fundamental ν_6'' leads to an enhancement of the tunnelling rate by a factor of 2 while excitation of the torsional mode ν_4 results in an increase in the tunnelling rate by a factor of 10 and the quasiadiabatic channel RPH result is within 5% of the exact result. The time-dependent wave packets from the exact and approximate results are virtually indistinguishable by eye, although the small numerical differences can, of course, be established.[169] The same would be true if one included the parity-violating potentials in the calculation. While rotation was treated approximately in refs. 132,169 in the recent work on tunnelling in ammonia isotopomers all degrees of freedom (vibration and rotation) were treated numerically exactly in a nine-dimensional vibration-rotation-tunnelling calculation.[172] In addition to tunnelling wave packets in the isolated ammonia isotopomers the control of tunnelling rates by well-designed electromagnetic (laser) radiation fields was studied in this work. Figure 6.11 shows the tunnelling enhancement achieved for the chiral isotopomer NHDT, where, with a suitable laser excitation, a transfer time of 40 ps can be obtained compared to a transfer time of 150 ps in the isolated NHDT molecule in its ground state. In addition to this change of the time scale by almost a factor of 4, the minor differences in the shape of the wave packets in the two parts of Figure 6.11 indicate the participation of excited states when including laser excitation.

For a detailed discussion of the fully nine-dimensional tunnelling quantum dynamics of prototype molecule NH_3 and its various deuterium (D), tritium (T), and muonium (Mu) isotopomers under coherent radiative excitation we refer to ref. 172. While ground state tunnelling in ammonia isotopomers is well described by the quasiadiabatic channel reaction path Hamiltonian, there are several excited states where this approximation is insufficient due to strong effects from intramolecular vibrational redistribution,[172,177] which are not included in the ordinary quasiadiabatic channel RPH treatment, although they might, in principle, be included in an extended approach that takes into account such couplings on a case-specific basis.

As can already be seen from the overview in Table 6.2, molecules such as HOOH and NHDT, which are chiral in the equilibrium geometry, but have tunnelling splittings in the ground state on the order of cm^{-1} and have only an exceedingly small effect from parity violation, the tunnelling sublevels have essentially a well-defined parity and the eigenstates are essentially ''achiral'', although they have a small admixture of the ''wrong'' parity and are very slightly optical active. The truly chiral superposition states are short lived (ps to μs, say) and thus one may call these molecules ''transiently chiral'' due to tunnelling, although they would be stable chiral molecules at their minima within classical molecular dynamics. Transiently chiral molecules can show a large optical activity like ordinary chiral molecules, but with a time dependence following the wave packet dynamics. The tunnelling dynamics of transiently chiral molecules is qualitatively similar to the

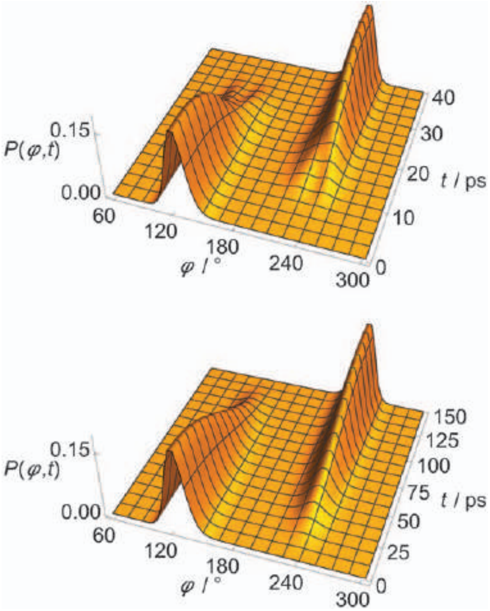

Figure 6.11 Reduced probability density as a function of the inversion coordinate φ and time t for NHDT. The two enantiomeric structures correspond to $\varphi \cong 120^\circ$ and $\varphi \cong 240^\circ$, respectively. The upper and lower panels show reduced probability densities (probability densities integrated over all other coordinates) for the tunnelling enhancement (upper) and field-free (lower) dynamical schemes, respectively. The parameters of the laser pulse are $\tilde{\nu}_0 = 793.5\ \mathrm{cm}^{-1}$, $I_{\mathrm{max}} = 3.15\ \mathrm{GW\,cm}^{-2}$, and $t_{\mathrm{p}} = 40$ ps. Reproduced from ref. 172 with permission from AIP Publishing, Copyright 2019.

tunnelling dynamics of achiral molecules such as NH_3, NHD_2,[172] or phenol[179] as far as parity violation is concerned, which for many applications can be neglected in the quantum dynamics of these molecules, although parity violation leads to some very weak effects also in these cases.

6.4.2 Tunnelling in Chiral Molecules Where Parity Violation Dominates Over Tunnelling

Ordinary stable chiral molecules have lifetimes on the order of at least some days (say $\tau > 10^6$ s) and thus tunnelling splittings of less than $10^{-17}\ \mathrm{cm}^{-1}$, which implies that with typical values of parity-violating energy differences of $|\Delta_{\mathrm{pv}}E| > 10^{-14}\ hc\,\mathrm{cm}^{-1}$ parity violation dominates over tunnelling, eqn (6.31). Therefore the eigenstates are essentially localized in chiral R or S structures (or P and M for axially chiral molecules). This by itself demonstrates the perhaps surprising fact that parity violation is a dominant factor in the quantum dynamics of ordinary chiral molecules.[36,149] Figure 6.12 shows the situation for the molecule Cl-SS-Cl, which has negligible tunnelling in the ground state and up to very high torsional excitation (the highest level shown in Figure 6.12 has torsional quantum number $v_T = 80$, still well below the *trans* barrier for stereomutation, which is calculated to be higher than 5000 cm^{-1} in this molecule). This example shows several features that are frequently

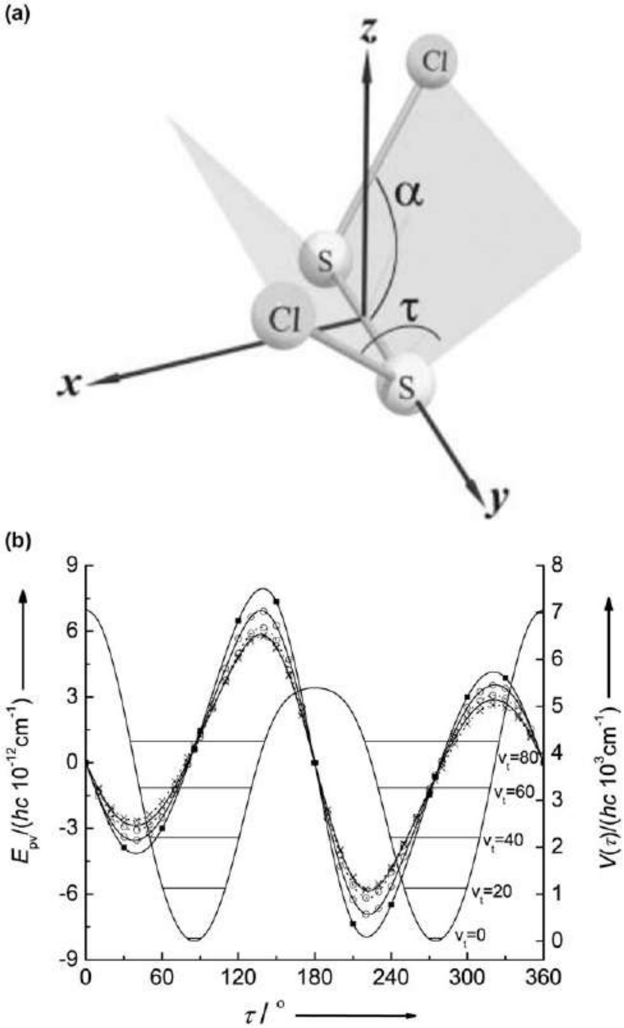

Figure 6.12 (b) Calculated torsional potential (full line, right ordinate scale) and parity-violating potential (left ordinate scale, lines with various symbols for various approximations in the electroweak quantum chemistry[90]) for ClSSCl, where the equilibrium structure and the definition of the torsional angle τ are shown in (a).
Reproduced from ref. 90 with permission from John Wiley and Sons, © 2001 WILEY-VCH Verlag GmbH, Weinheim, Fed. Rep. of Germany, and from ref. 178 with permission from CHIMIA, Copyright 2003 (where one finds a detailed discussion).

encountered. Firstly, there is a strong dependence of the parity-violating potential, which is antisymmetric with respect to inversion at the achiral geometry 180°, upon the torsional angle τ. The parity-violating potential vanishes by symmetry at the achiral planar geometries of the molecule. However, the parity-violating potential also vanishes "accidentally" at some chiral geometries ($\tau \approx 80^\circ$ and 240°). This perhaps at first sight surprising phenomenon is rather frequently observed in the theory of parity violation in chiral molecules and has been discussed in ref. 33, 34, 83 and 84 in terms of the tensor properties of the parity-violating potential. The P enantiomer is stabilized (negative E_{pv}) compared to the M enantiomer for values of $0^\circ < \tau < 80^\circ$ and P is destabilized (positive E_{pv}) compared to M for $80^\circ < \tau < 180^\circ$. Thus, at the equilibrium geometry near $\tau \approx 85^\circ$ the M enantiomer is more stable than the P enantiomer by about $10^{-12}\,\mathrm{cm}^{-1}$. Figure 6.12 shows also the effect using different levels of quantum chemical accuracy in the calculation of the parity-violating potentials. For the optimized equilibrium structures on finds values for the parity violating energy difference in the range $1.14 \leq \Delta_{\mathrm{pv}}E/(\mathrm{hc\,cm}^{-1} * 10^{-12}) \leq 1.62$ at various levels. At the RPA-cc-pvTZ-A level one has at the equilibrium geometry $\Delta_{\mathrm{pv}}E/(\mathrm{hc}) = 1.29 \times 10^{-12}\,\mathrm{cm}^{-1}$. If one calculates the two lowest eigenstates in the effective torsional potential with parity-violating potential included one finds an energy difference $\Delta_{\mathrm{pv}}E/(\mathrm{hc}) = 1.35 \times 10^{-12}\,\mathrm{cm}^{-1}$ between the two lowest states with effectively localized eigenfunctions. If one calculates the expectation value over the parity-violating potential in the ground state wave function in one well and then $\Delta_{\mathrm{pv}}E^{(0)}$ from eqn (6.29) one finds exactly the same values $1.35 \times 10^{-12}\,\mathrm{cm}^{-1}$ as expected.[90]

Finally, one may wish to compare to the tunnelling splitting $\Delta E_{\pm}$ in the hypothetical symmetric potential without parity violation. It turns out that numerical limitations prohibit a direct calculation with, say, the quasiadiabatic channel RPH method, because of the extremely small absolute magnitude of $\Delta E_{\pm}$. Therefore in ref. 90 a scaling and extrapolation method was developed that uses quasiadiabatic channel RPH calculations in a range where they are accurate in scaled torsional potentials

$$V(\tau, f) = fV(\tau) \tag{6.44}$$

with a scaling factor f that reduces the barrier height accordingly. Accurate results for $\Delta E_{\pm}(f)$ with different scaling factors f are then fitted to a three-parameter expression ($\lg = \log_{10}$)

$$\lg|(\Delta E_{\pm}(f)/(\mathrm{hc\ cm}^{-1}))| = P_1 \lg\sqrt{f} + P_2 - P_3\sqrt{f}. \tag{6.45}$$

This gives then a value for $\Delta E_{\pm}$ extrapolated to $f = 1$

$$\Delta E_{\pm}(f = 1) = (\mathrm{hc})10^{P_2 - P_3}\ \mathrm{cm}^{-1}. \tag{6.46}$$

This fit formula is motivated by a WKB approximation result for tunnelling splittings in symmetric double-well potentials $V(x)$.[90,184]

$$\Delta E_{\pm} = (h\omega/\pi)\sqrt{2m\omega a^2/h}\ \exp(-2\pi A S_0/h). \tag{6.47}$$

The terms S_0 and A arise from the WKB theory with the classical angular oscillation frequency ω of the harmonic small amplitude motion around the quadratic well at $x=a$ and $x=-a$, and m is the reduced mass with furthermore:

$$S_0=\int_{-a}^{a}\sqrt{2mV(x)}\,\mathrm{d}x \tag{6.48}$$

$$A=\int_0^a [m\omega/(2mV(x))-1/(a-x)]\mathrm{d}x. \tag{6.49}$$

Scaling of the symmetric double-well potential $V(f,\ x)=f\ V(x)$ results in a classical scaled $\omega(f)=\sqrt{f}\omega(f=1)$. Insertion of $V(f,\ x)$ and $\omega(f)$ into the WKB approximation for $\Delta E_\pm$ gives the ground state tunnelling splitting as a function of the scaling factor f, which can be written in the form of the fit formula with $P_1=3/2$ and $P_2=\lg\left((h\omega/\pi)\sqrt{2m\omega a^2/h}\exp(A)/\mathrm{J}\right)$ and $P_3=2\pi S_0/(h\ \ln 10)$. However, rather than using the "theoretical" values for P_1, P_2, and P_3, which would limit the result to the simple WKB model neglecting details of the potential, the fit includes the properties of the tunnelling dynamics in the real potential by allowing the freely floating parameters to account for the dynamics at least to a reasonable extent. In this way a value of $\Delta E_\pm=(\mathrm{hc})10^{-76}\,\mathrm{cm}^{-1}$ is obtained. Figure 6.13 shows the fit of the equation with the parameters $P_1=1.16(5)$, $P_2=2.59(10)$, and $P_3=78.73(24)$ to numerically calculated ("accurate") points.

Obviously one does not have to know the exact values of the extremely small tunnelling splittings to ascertain the validity of the inequality (6.31).

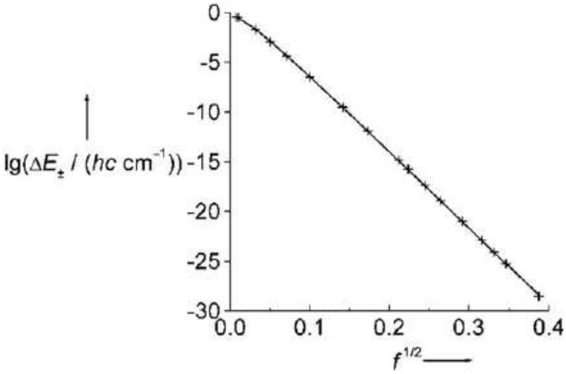

Figure 6.13 Decadic logarithm of the torsional tunnelling splittings $\Delta E_i(f)$ for differently scaled torsional potentials $V(\tau,\ f)=fV(\tau)$ calculated with the quasiadiabatic channel-reaction path Hamiltonian approach (+ for RPH) and fit to eqn (6.45) (line).
Reproduced from ref. 90 with permission from John Wiley and Sons, © 2001 WILEY-VCH Verlag GmbH, Weinheim, Fed. Rep. of Germany.

However, the method presented in ref. 90 can be generally useful in the computation of very small tunnelling splittings. The fitting, interpolation and extrapolation method can be applied to the analysis of many numerically exact multidimensional approaches to tunnelling.

6.4.3 Tunnelling Switching in Chiral and Achiral Molecules

For chiral molecules where in the ground state the tunnelling is effectively suppressed because of the parity-violating asymmetry and the eigenstates are localized essentially near either one or the other potential minimum, one can increase the efficiency of tunnelling by vibrational excitation of modes that promote tunnelling, notably the modes that closely correspond to the reaction coordinate for stereomutation, the torsional mode in HOOH and HSSH and the inversion mode in ammonia NHDT, for example; as already discussed. Thus, at sufficiently high excitation tunnelling will always dominate over parity violation, leading to stereomutation or racemization by tunnelling.[41] This phenomenon has been studied quantitatively for the molecule ClOOCl, which in the vibrational ground state is dominated by parity violation, with therefore localized chiral eigenstates at $v = 0$ (as also seen from Table 6.2).[150–152] The vibration-rotation-tunnelling problem was treated including all vibrational degrees of freedom in the quasiadiabatic channel RPH approximation.[132,136,152] Rotation was treated with a Watson-type Hamiltonian[180] and the WANG program[185] using rotational constants computed from the expectation values in the vibrational states resulting from the quasiadiabatic channel RPH calculations and neglecting the effects of nuclear hyperfine structure. At a torsional level of $v = 10$ the tunnelling splitting is calculated to be about $2 \times 10^{-7}\ \mathrm{cm}^{-1}$, thus dominating by far over the parity violation [$\Delta_{\mathrm{pv}}E \cong (hc)\ 5 \times 10^{-13}\ \mathrm{cm}^{-1}$, about 15% smaller than in the vibrational ground state, computed at the MC-LR RPA/6-311+G(3df) level[152]]. Exciting coherently to $v = 10$ with a 5 μs laser pulse ($\tilde{\nu}_L = 1104.2586\ \mathrm{cm}^{-1}$, $I_{\max} = 30\ \mathrm{MW\,cm}^{-2}$) giving a power broadening of $3.9 \times 10^{-6}\ \mathrm{cm}^{-1}$, much larger than the tunnelling splitting, one generates a highly excited, localized chiral torsional state, which shows field-free tunnelling stereomutation after the laser pulse is switched off. The scheme of excitation is shown in Figure 6.14 and the stereomutation wave packet is shown as probability density in the torsional coordinate (integrated over all other coordinates) in Figure 6.15. This excited state wave packet is comparable to the ground state wave packet shown for HOOH in Figure 6.10. The structure of the probability density is more complicated because of the high torsional excitation, but the effects of parity violation, while included, are not visible on the scale of Figure 6.15. One has essentially a periodic stereomutation motion with a period of about 200 μs, in agreement with eqn (6.1), easily seen in the time range 20–220 μs in the later part of Figure 6.15.

However, when selectively exciting with a narrow bandwidth laser pulse ($\tilde{\nu}_L = 1186.7912\ \mathrm{cm}^{-1}$, $I_{\max} = 0.5\ \mathrm{GW\,cm}^{-2}$, 5 μs) to a tunnelling sublevel at

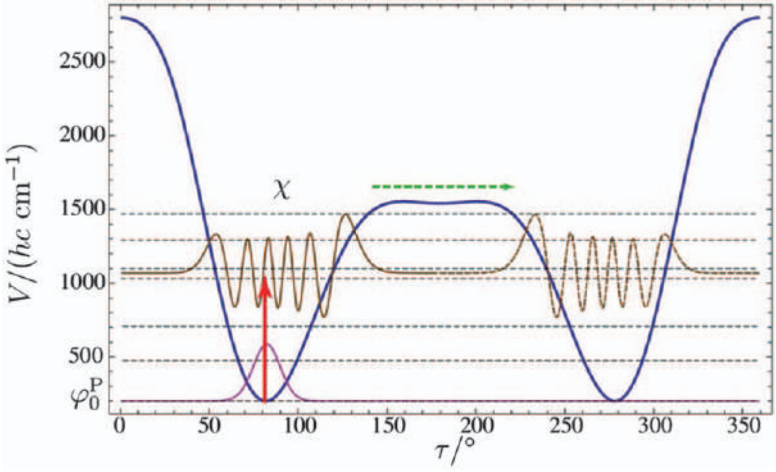

Figure 6.14 Excitation scheme: starting with a chiral ground state, a chiral state $\chi(\nu=10)$ near the barrier is populated after laser irradiation. After the excitation of χ, one expects tunnelling stereomutation (TSM) during field-free evolution, because χ is a superposition of two parity eigenstates.
Reproduced from ref. 152 with permission from American Chemical Society, Copyright 2015.

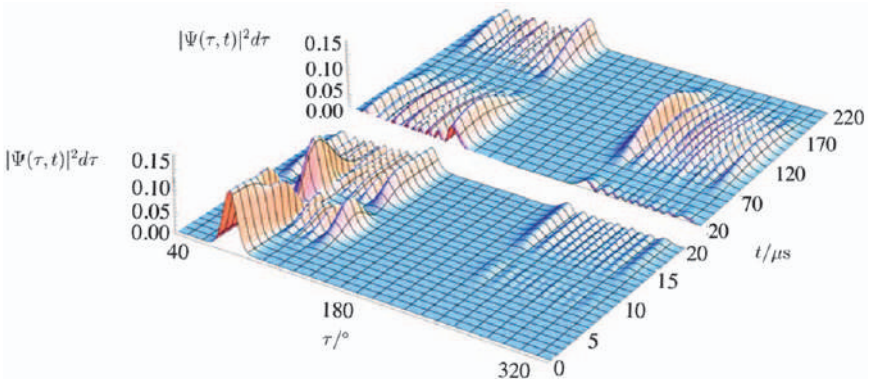

Figure 6.15 Time-dependent wave packet for $0 \leq t \leq 220$ μs with $d\tau = \Delta\tau = 1°$. Early times: wave packet during excitation. After about 15 μs, the laser field is off and field-free evolution starts, which will eventually lead to tunnelling stereomutation (TSM) of the chiral state χ. Later times: wave packet showing TSM during field-free evolution of the molecular state. The period is roughly 200 μs, in accordance with eqn (6.1).
Reproduced from ref. 152 with permission from American Chemical Society, Copyright 2015.

$\mathrm{v_T} = 11$ $(\Delta\tilde{\nu}_{\mathrm{T}} = 1.2 \times 10^{-4}\ \mathrm{cm}^{-1})$ followed by a transfer pulse (593.8252 cm^{-1}, 1.6 MW cm^{-2}, 5 μs) one generates initially a state with well-defined parity after the transfer in $\mathrm{v_T} = 5(\Delta\tilde{\nu}_{\mathrm{T}} = 9.5 \times 10^{-17}\ \mathrm{cm}^{-1})$ where parity violation dominates $(\Delta_{\mathrm{pv}}E = 5.5 \times 10^{-13}(\mathrm{hc})\,\mathrm{cm}^{-1})$. This state will thus slowly change parity following eqn (6.43) giving a population of about 2.5×10^{-7} after some milliseconds for the initially "forbidden" parity, a detectable signal according to the scheme of ref. 41 and 149 and current techniques.[181] The quantum dynamical simulations presented in ref. 152 are the first of their kind treating coherent excitation, vibration-rotation-tunnelling dynamics and electroweak parity violation together and demonstrating experimentally detectable effects. They constitute a realistic simulation of one of the experimental approaches to be discussed in Section 6.5 in more detail.

Tunnelling switching has been identified quantitatively by theory and high-resolution spectroscopy in the achiral molecule *m*-D-phenol, where one has stereoisomers (*syn*-, *anti*-). There it has been proposed for potential use in quantum technology as a molecular quantum switch.[186,187]

Tunnelling switching has also been discussed for partially deuterated or halogenated ethylene isotopomers[157] and recently for the mono deuterated vinyl radical CHD=CH by *ab initio* calculations,[188] see also the review[223] in the current book. A simple stable closed-shell example would be an imine CHD=NH, which also has *syn*- and *anti*-isomers depending upon the relative position of NH with respect to D. The particular property of a quantum switch as compared to a "classical" molecular switch[189] is the possibility of generating the bistructural superposition states of *syn*- and *anti*-isomers, analogous to the bistructural superposition of *R*- and *S*-enantiomers.[41,149,158] For a more detailed discussion of tunnelling motion in asymmetric potentials we refer to general reviews.[14,15] The new concept of bistructural (and possibly multistructural) states in stereochemistry has also been discussed[190] in a broader context of the historical developments of concepts in chemistry. The molecular quantum switch offers many new possibilities for quantum technology, going beyond the quasiclassical molecular switches, which have been so much investigated.

It has also a so far hypothetical importance for a molecular theory of vision and thought including the question of "free will".[42,110]

6.4.4 Tunnelling Stereomutation and Racemization Kinetics in Chiral Molecules

The general problem of tunnelling stereomutation and racemization has been discussed in ref. 41 for the case that either $\Delta E_{\pm}$ or $\Delta_{\text{pv}}E$ or both are very small compared to other energy level spacings, and we briefly summarize the treatment given therein as it provides useful insight. In this case one can treat the kinetics by considering an ensemble of near-degenerate two-level systems. The Hamiltonian matrix has the form (6.50). The eigenvalues for a Hermitian operator (6.51) follow from (6.52).

$$\hat{H} = \begin{pmatrix} H_{11} & H_{12} \\ H_{21} & H_{22} \end{pmatrix} \tag{6.50}$$

$$H_{12}H_{21} = H_{12}H_{12}^{*} = |H_{12}|^2 \tag{6.51}$$

$$E_{1,2} = (H_{11} + H_{22})/2 \pm \frac{1}{2}[(H_{11} - H_{22})^2 + 4|H_{12}|^2]^{1/2} \tag{6.52}$$

If we work in the basis $\chi_\pm$ of states of well-defined parity and introduce $\Delta_{\text{pv}}E$ as a perturbation parameter, one may identify the matrix elements (with real H_{12} and positive $\Delta E_\pm$) in eqn (6.53) and (6.54)

$$\Delta_{\text{pv}}E = 2H_{12} \tag{6.53}$$

$$H_{11} = E_\pm/2 = -H_{22}. \tag{6.54}$$

If $\Delta E_\pm$ is much larger then $\Delta_{\text{pv}}E$, the latter is not a measurable energy difference. If we work in the basis of "left" and "right" handed states λ and ρ one has (positive $\Delta_{\text{pv}}E$), and the eqn (6.55) and (6.56), introducing now $\Delta E_\pm$ as the perturbation (much smaller now than $\Delta_{\text{pv}}E$)

$$H'_{11} = \Delta_{\text{pv}}E/2 = -H'_{22} \tag{6.55}$$

$$\Delta E_\pm = 2H'_{12}. \tag{6.56}$$

The eigenvalues given by eqn (6.57) with respect to the average energy $(E_1 + E_2)/2 = \langle E\rangle \equiv 0$ are obviously the same [$\Delta E_\pm$ and $\Delta_{\text{pv}}E$ are defined as real, positive, eqn (6.57)]. It is immaterial, whether $\Delta_{\text{pv}}E$ or the tunnelling $\Delta E_\pm$ is introduced as "perturbation"

$$E_{1,2} = \langle E\rangle \pm \frac{1}{2}(\Delta E_\pm^2 + \Delta_{\text{pv}}E^2)^{1/2}. \tag{6.57}$$

Eigenvectors for the example of basis χ are given by eqn (6.58) where x and y are defined *via* S [eqn (6.59)] according to eqn (6.60) and (6.61)

$$\boldsymbol{C} = \begin{pmatrix} x & y \\ -y & x \end{pmatrix} \tag{6.58}$$

$$S = (\Delta E_\pm^2 + \Delta_{\text{pv}}E^2)^{1/2} \tag{6.59}$$

$$x^2 = (S + \Delta E_\pm)/(2S) \tag{6.60}$$

$$y^2 = (S - \Delta E_\pm)/(2S) \tag{6.61}$$

The sign of the roots $\sqrt{x^2}$ and $\sqrt{y^2}$ can be taken in various combinations respecting $\boldsymbol{C}^T\boldsymbol{C} = \mathbf{1}$ (S is defined positive). One has by convention $E_1 < E_2$ and $H_{11} < H_{22}$. Figure 6.7 represents the situation [$x = y = 1/\sqrt{2}$, right-hand side of Figure 6.7, and the wave functions are given by eqn (6.33)–(6.36)].

According to the superposition principle (if valid) these states can always be generated. The time evolution is given by the time evolution matrix in eqn (6.62).

$$\boldsymbol{U} = \boldsymbol{C}\begin{pmatrix} \exp(-\mathrm{i}2\pi E_1 t/h) & 0 \\ 0 & \exp(-\mathrm{i}2\pi E_2 t/h) \end{pmatrix}\boldsymbol{C}^{T}. \tag{6.62}$$

The density matrix with the elements $P_{ij} = \langle c_i c_j^* \rangle$ ($\langle\,\rangle =$ average over an appropriate ensemble) has the form given by eqn (6.63) in the basis λ, ρ and the form of eqn (6.64) in the $\chi_\pm$ basis

$$\begin{pmatrix} P_{\mathrm{RR}} & P_{\mathrm{RL}} \\ P_{\mathrm{LR}} & P_{\mathrm{LL}} \end{pmatrix} = \boldsymbol{P}^{\lambda,\rho} \tag{6.63}$$

$$\begin{pmatrix} P_{++} & P_{+-} \\ P_{-+} & P_{--} \end{pmatrix} = \boldsymbol{P}^{\chi_\pm}. \tag{6.64}$$

For the degenerate system (or nearly degenerate system) at any temperature $kT \gg \Delta E$ or S, eqn (6.65) holds

$$\boldsymbol{P}^{\lambda\rho} = \boldsymbol{P}^{\chi_\pm} = \begin{pmatrix} 1/2 & 0 \\ 0 & 1/2 \end{pmatrix}. \tag{6.65}$$

$\boldsymbol{P}$ is invariant under the basis transformation (as any other constant diagonal matrix), also in the many-level case, if $\boldsymbol{H}$ is block diagonal with some constant in each block. A racemic mixture of R and L is identical to a mixture of + and – in terms of any observable ensemble property. A common model for $\boldsymbol{P}$, simplified for the degenerate case, considered as reduced density matrix of the molecule interacting by collisions or otherwise with a thermal bath gives the eqn (6.66) and (6.67), from which the eqn (6.69) and (6.70) can be derived for the relaxation times given by τ_1 and τ_2 with the basis transformation in eqn (6.68).

$$(P_{11} - P_{22}) = (P_{11}^0 - P_{22}^0)\ \exp(-t/\tau_1) \tag{6.66}$$

$$P_{12} = (P_{12}^0\ \exp(-t/\tau_2) \tag{6.67}$$

$$P^{\chi_\pm} = \boldsymbol{C}\boldsymbol{P}^{\lambda,\rho}\boldsymbol{C}^{T} \tag{6.68}$$

$$\tau_1^{\chi_\pm} = \tau_2^{\lambda,\rho} \tag{6.69}$$

$$\tau_2^{\chi_\pm} = \tau_1^{\lambda,\rho}. \tag{6.70}$$

Here we have made use of the reality of P in the case of a degenerate model, because $E_{1,2}$ can be set to zero without loss of generality. To within this approximation, the assignment of "phase" or "population" relaxation times τ_1 and τ_2 is arbitrary in the two-level problem. One can get a "case C" (ref. 41) type relaxation behaviour in this limit with apparent irreversible racemization.

When the density of rovibronic and hyperfine states becomes very large, the two-level approximation breaks down and one can obtain "true" irreversible relaxation according to a Pauli master equation (case B of ref. 211) as discussed in more detail in ref. 41. When averaging over a large number of levels as appropriate for intramolecular stereomutation kinetics of polyatomic molecules at higher excitation, with either thermal or some other statistical non-thermal populations, one obtains relaxation-like behavior following eqn (6.3) with rate constants k_{RS} and k_{SR}, written explicitly for the elementary steps

$$\mathrm{R} \rightarrow \mathrm{S} \text{ rate constant } k_{SR} \tag{6.70}$$

$$\mathrm{S} \rightarrow \mathrm{R} \text{ rate constant } k_{RS}. \tag{6.71}$$

Different from tunnelling stereomutation of isolated levels, which is oscillatory in time, eqn (6.70) and (6.71) describe a relaxation towards a stationary state, possibly microcanonical or thermal equilibrium, depending on the situation. In the general case, however, this relaxation is not simply a first-order kinetics with detailed balance as in an ordinary chemical system. This simple behavior is reached in the limit of ‘‘case B’’ and a thermal initial population. We refer to ref. 41, 42, 211 and 217 for further discussion and to ref. 169 for a simulation showing how statistical averaging arises for the special case of HOOH. We note here that, in principle, either oscillatory- or relaxation-like behavior in isolated molecules showing stereomutation could be observed by measuring the time-dependent structure, say by the techniques of ref. 212–214. The alternative would be to measure time-dependent optical activity, Raman optical activity or vibrational circular dichroism,[215] although such experiments have not yet been carried out on isolated molecules. In a historical context, it is of interest that the very first observation and quantitative kinetic analysis was by a measurement of time-dependent optical activity, albeit not in an isolated molecule nor for an elementary reaction but rather for a catalysed reaction in solution[216] (see ref. 178 for a discussion of the history). Indeed, Wilhelmy seems to have been the first to formulate a first-order rate equation and integrate it to get the exponential behavior as described by eqn (6.72) and (6.73) for the time-dependent concentrations c_R and c_S of the R and S enantiomers:

$$-\frac{\mathrm{d}c_R}{\mathrm{d}t} = +\frac{\mathrm{d}c_S}{\mathrm{d}t} = k_{SR}c_R - k_{RS}c_S \tag{6.72}$$

$$c_R(t) - c_S(t) = [c_R(t_0) - c_S(t_0)] \exp[-(k_{RS} + k_{SR})(t - t_0)]. \tag{6.73}$$

For a discussion of the emergence of this behaviour starting from the Schrödinger equation see ref. 41, 42, 211 and 217.

6.5 Spectroscopic Approaches Towards Tunnelling and Parity Violation in Chiral Molecules

A variety of experimental approaches to detect parity violation in chiral molecules has been proposed. One can find a summary of these in ref. 27, 29, 30, 32, 36, 41, 158, 171 and 176. However, it seems that so far only two of

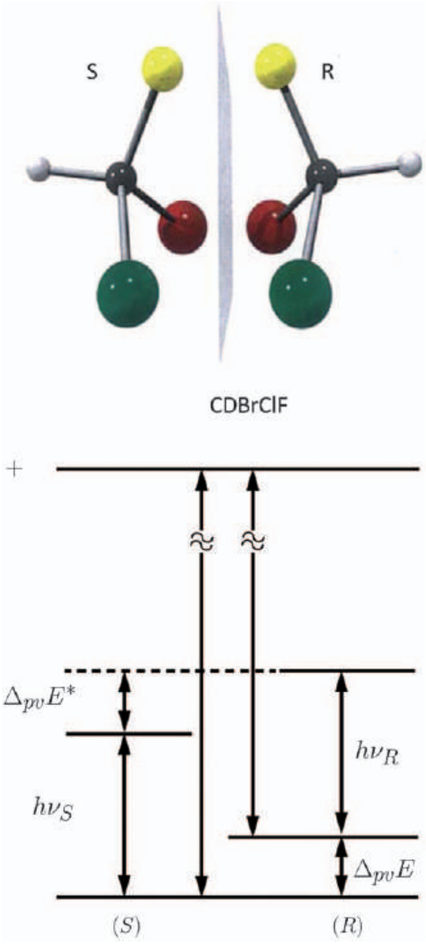

Figure 6.16 Scheme for energy levels and experiments. One notes that $\Delta\nu_{\mathrm{pv}} = \nu_{\mathrm{R}} - \nu_{\mathrm{S}} = (\Delta_{\mathrm{pv}}E^* - \Delta_{\mathrm{pv}}E)/h$ in this scheme.
Reproduced from ref. 29 with permission from the Royal Society of Chemistry, and from ref. 36 with permission from John Wiley and Sons, © 2002 WILEY-VCH Verlag GmbH & Co. KGaA, Weinheim.

these approaches are actively pursued in actual experiments, which may be successful in the foreseeable future, and we restrict our discussion to these, referring to the more complete reviews as mentioned for the larger number of further approaches.

The basic concepts of the current experimental approaches can be understood with the energy level scheme presented in Figure 6.16.

In the first scheme, originally proposed by Letokhov,[51,52] one attempts to measure the frequency difference between spectroscopic transitions, say, in the infrared rotation-vibration spectrum of the separate R and S enantiomers. CHFClBr was an early IR-laser spectroscopic example[51,52] pursued further in the IR and microwave ranges in ref. 98 and 99 where, by analysis of the spectrum of CHFClBr in the CO_2 laser range, a number of coincidences with laser lines were suggested for ultrahigh-resolution spectroscopy. This provided the starting point for the subsequent study in ref. 101, 102 and 174. Of course other spectral ranges might be studied as well, for instance NMR.[72,73] This "Letokhov-scheme" for spectroscopic experiments has two main disadvantages, see ref. 36 and 41 and the critical summary[176] and references cited in ref. 175. Firstly, one cannot derive the parity-violating energy difference $\Delta_{pv}E$, but only the difference of such differences in different states $(\Delta_{pv}E^* - \Delta_{pv}E)$. Secondly one has to obtain enantio-pure samples for the two enantiomers.

In ref. 41 and 149 a scheme was proposed that avoids both of these disadvantages and can derive $\Delta_{pv}E$ and $\Delta_{pv}E^*$ separately. It makes use of transitions to an intermediate excited state of well-defined parity (labelled + in Figure 6.16) that can result either from tunnelling switching or from an excited electronic state that is planar or quasiplanar as for 1,3-difluoroallene. The scheme is outlined in Figure 6.17.

This allows then for a spectroscopic selection of states of well-defined parity. In a second step, in the scheme of Figure 6.17 one prepares a state of well-defined parity in the ground state (or some other low energy state n), which satisfies the condition

$$\Delta_{pv}E^{(n)} \gg \Delta E_{\pm}^{(n)}. \tag{6.74}$$

The parity selection arises from the electric-dipole selection rule connecting levels of different parity. Thus, if in the first step one has selected a state of some given parity, in the second step one prepares a state of the opposite parity. Such a state is a superposition of the energy eigenstates of the two enantiomers separated by $\Delta_{pv}E$ and therefore shows a periodic time evolution with a period given by eqn (6.32). In such a state parity evolves in time due to parity violation and parity is not a constant of the motion. The probability of finding a given parity (p^+ for positive parity and p^- for negative parity) is given by eqn (6.43).

In the third step, the initially "forbidden" population of negative parity $p^-(t)$ is probed very sensitively, for example by resonantly enhanced multiphoton ionization (REMPI). This is possible because the line spectra of positive and negative parity isomers are different, with lines that are well separated at high resolution (Figure 6.17 and ref. 181). In this fashion it is not necessary to wait for a whole period, but it is sufficient to probe the initial time evolution at very early times. The sensitivity in the probe step determines, in essence, how small a value of $\Delta_{pv}E$ can be measured. In a recent proof of principle experiment with a current experimental set up in our laboratory on the achiral molecule ammonia, NH_3, it was estimated that an energy difference as small as 100 aeV should be measurable with the existing current experiment.[181] The original proposal[149] of 1986 assumed population transfer using pulse shaping or chirp by rapid adiabatic passage.

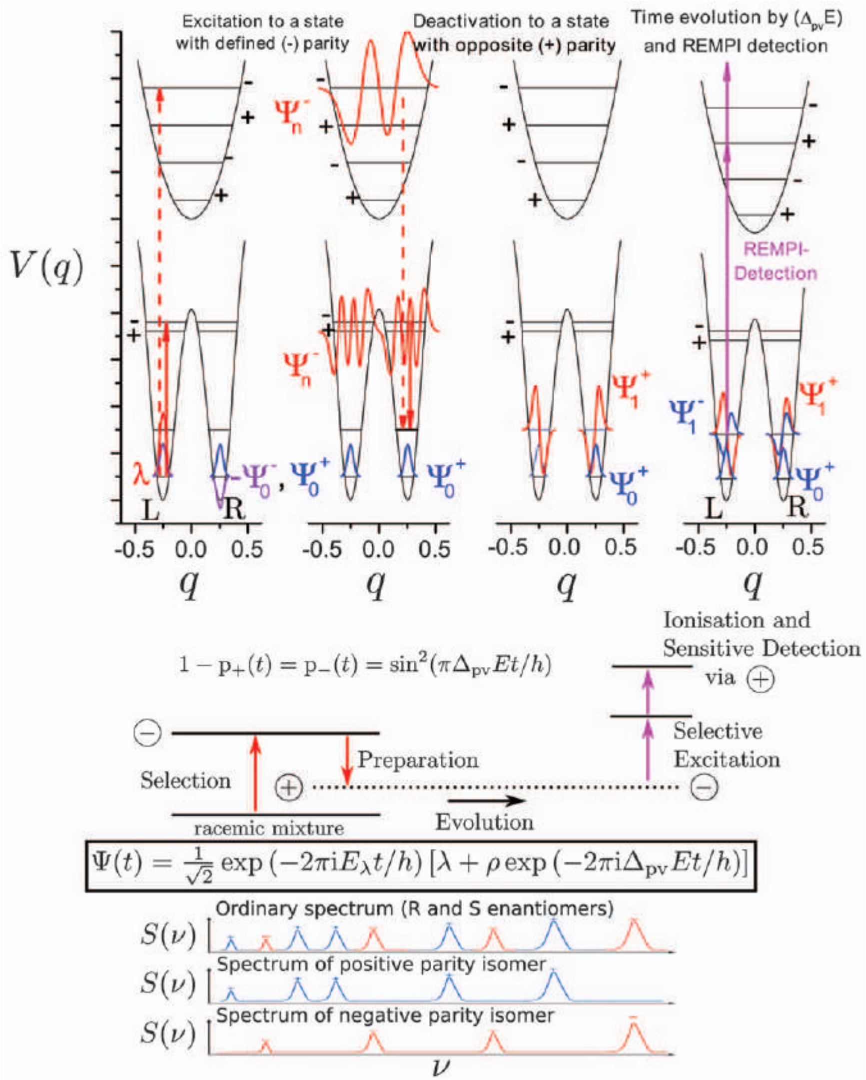

Figure 6.17 Scheme of the preparation and detection steps for the time-resolved experiment to measure $\Delta_{pv}E$. Top: the transitions to the intermediate states are indicated together with the corresponding wave functions for an excited state with well-defined parity close to the barrier of a double minimum potential (full line) or an achiral electronically excited state (dashed line) as an intermediate. The right-hand part shows the sensitive detection step with REMPI. Middle: summary scheme for the three steps. Bottom: the spectra of the normal enantiomers (top) and of the selected positive (blue) and negative (red) parity isomers.
Adapted from ref. 32, 181 and 182 with permission from AIP Publishing, Copyright 2014, 2015, 2019, and from ref. 149 with permission from Elsevier, Copyright 1986.

It is clear, however, that also that the elegant method of stimulated Raman adiabatic passage (STIRAP) as developed later in ref. 194 is an ideal technique for generating population transfer in a well-controlled fashion.[182]

The major current and future challenges are related to the much greater complexity of the rovibrational-tunnelling spectra of chiral molecules as compared to the test molecule NH_3 with its very well-known spectra. However, first spectroscopic investigations on three candidate molecules proved promising (1,2-dithiine $C_4H_4S_2$ and trisulfane HSSSH as well as 1,3-difluoroallene, see Table 6.3). The current cw-OPO laser systems (coupled to a frequency comb) cover only spectral ranges above about 2500 cm^{-1} in the infrared. This limits the choice of molecules. Further development in laser technology, for instance of quantum cascade lasers with power and resolution meeting our needs in the future, might make other molecules accessible, for instance the simpler molecule ClOOCl, for which complete theoretical simulations of the experiment have been achieved already, as discussed in Section 6.4.3.

While the experiment to measure $\Delta_{pv}E$ might have appeared impossible when it was first proposed in 1986,[149] the current outlook on a successful experiment is excellent. Indeed, provided that adequate funding for the continuation of the current project is guaranteed and required spectroscopic analyses can be completed, most significant results can be expected for any of two possible outcomes:

1. Either one finds experimentally the theoretically predicted values for $\Delta_{pv}E$, then one can analyze the results of the precision experiments in terms of the standard model (SMPP) in a range not yet tested by previous experiments.
2. Or else one finds values for $\Delta_{pv}E$ different from the theoretical predictions. This then will lead to a fundamental revision of current theories for $\Delta_{pv}E$ with the potential also for new physics.

In addition, the experimental results will have implications for our understanding the evolution of biomolecular homochirality.[29,31,32,36]

To conclude a note may be useful here on other experiments in physics, and in particular atomic and molecular physics. Indeed, parity violation as discovered in nuclear and particle physics[22–26] has been considered to be rather well understood in the framework of the standard model of particle physics (SMPP) and high energy physics.[43–47,218,219] There have been also successful experiments in atomic spectroscopy (see ref. 220 and 221 and references cited therein) following the early proposals in ref. 121 and 122. There have been also extensive proposals to study parity violation in diatomic molecules, including quite early ones,[222] although until today no successful experiments demonstrating the effect in diatomic molecules have been reported in spite of extensive efforts with null results. We refer to the detailed recent review[221] with some emphasis on experiments on atoms and diatomic molecules.

In agreement with the aim of the present book,[16] our focus has been here entirely on parity violation and its interplay with tunnelling in chiral molecules. Beyond the interest in providing new concepts for physical-chemical stereochemistry, there is also a fundamental aspect in chiral molecules making them rather special in the context of parity violation in atomic and molecular physics in general. Indeed, the strength of parity-violating effects is expected to become large whenever the separation of eigenstates of different parity in the electromagnetic Hamiltonian (say, $\Delta E_{\pm}$) becomes comparable to the absolute value of the coupling matrix element V_{pv} connecting the states with the parity-violating electroweak force or when $|V_{\mathrm{pv}}|$ is even much larger than $|\Delta E_{\pm}|$

$$|\Delta E_{\pm}| \cong |V_{\mathrm{pv}}|. \tag{6.75}$$

While in atoms, and diatomic and some achiral polyatomic molecules one can find states with different parity lying rather close, it is the case of chiral molecules with very slow tunnelling, where the degeneracy becomes almost perfect with $\Delta E_{\pm} \cong 0$, and thus the effect of parity violation is maximum. Experiments of parity violation in atoms have been successful only for heavy atoms, where the theoretical analysis is subject to great uncertainty,[27,220] and no experiment on light atoms are expected in the near future. In contrast our experiment on chiral molecules as described here has an experimentally proven sensitivity to test parity violation in molecules containing nuclei no heavier than chlorine, thus testing parity violation in a new low-energy range.[149,181,182] This is a great advantage compared to the experiments on frequency shifts,[174,224] which might sometime in the future be successful for molecules with heavy transition metal atoms and the like, where large effects are predicted. However, the theoretical analysis will be then subject to even greater uncertainty than for heavy atoms. Thus while such experiments still have interest for chemistry, they are not likely to go beyond what has been achieved in experiments on atoms in terms of a fundamental analysis. In fact the experiment on measuring $\Delta_{\mathrm{pv}}E$ through time-dependent parity seems to be the only one at present with an accuracy that is sufficient to test this sector of physics at low energy with light nuclei.

6.6 Concluding Remarks

To conclude we shall address a fundamental aspect related to the concept of the "potential function", which appears in the usual discussions of tunnelling. Indeed, at first sight it may seem that the concept of "tunnelling" necessarily involves the existence of such a potential function. A closer look shows, however, that things are not quite as simple. We shall start here by considering tunnelling within the quasiadiabatic channel reaction path Hamiltonian and "quasiadiabatic above-barrier tunnelling". In vibrationally excited states of HOOH the wave functions show a tunnelling sublevel structure and tunnelling wave packet dynamics as given by the effective one-dimensional quasiadiabatic channel potential, although their energy is high above the barrier in the multidimensional Born–Oppenheimer surface.

One might then be tempted to say that it is not a ''true'' tunnelling process, as it results from an approximate model. However, the ''exact'' six-dimensional vibration-tunnelling calculation on the complete hypersurface shows about the same level structure and wave packet dynamics as the approximate calculations, and therefore one must conclude that the full quantum dynamics shows ''tunnelling behavior'' even above the barrier. This has led us to introduce the concept of quasiadiabatic channel above barrier tunnelling of importance also in other contexts.[196]

It is furthermore also true that the tunnelling sublevel structure and dynamics at energies below the six-dimensional saddle point result from an approximation. Without the Born–Oppenheimer approximation the ''Born–Oppenheimer potential barriers and saddle points'' disappear. If one treats hydrogen peroxide or other molecules with Born–Oppenheimer barriers ''exactly'' by means of quantum dynamics of a collection of the electrons and nuclei in the molecule, the ''true'' potential arises in essence from the Coulomb interaction of these particles in a very high dimensional space (for instance 60 dimensions for HOOH). However, even then, without any Born–Oppenheimer barriers to tunnel through, the ''exact'' quantum dynamics will show very much the same sublevel structure and tunnelling dynamics as is described by the approximate theory and confirmed by experiment. This suggests a new definition of quantum tunnelling dynamics that does not depend on the concept of potential barriers, as we have pointed out already in the context of the definition of the ''molecular symmetry group'' of non-rigid molecules.[27,195,198] While Longuet-Higgins has, indeed, motivated this group by the existence of high Born–Oppenheimer potential barriers separating symmetrically equivalent isomers and thereby generating systematically degenerate level structures,[197] we pointed out that in a rigorous discussion the symmetry groups should not be defined by an approximation but rather by the induced representation corresponding to the degenerate sublevels, which one can define from an exact theory without any approximation and also by experiment (ref. 27, 195, 198 and references therein). When the perfect degeneracy is lifted by tunnelling leading to observable tunnelling splittings, one can consider this effect, then, as the breaking of an approximate symmetry without having to refer to tunnelling through potential barriers from the Born–Oppenheimer approximation. Thus, the tunnel effect in molecules can be understood as a quantum dynamical phenomenon without making reference to approximate concepts such as Born–Oppenheimer potential hypersurfaces. One can say, however, that the Born–Oppenheimer approximation, and also the quasiadiabatic channel reaction path Hamiltonian with their effective potentials, provide us with simple models[190] that allow us, in the first place, to qualitatively understand the phenomena and, in the second place, to compute the phenomena approximately without too much effort (see also the general discussion by Roald Hoffmann[191] on qualitative understanding *versus* computation). The discussion can be continued similarly at an even deeper level: from the standard model of particle physics we understand even the Coulomb potential as not being a ''fundamental preexisting'' potential but rather as arising from photons as field particles mediating the electromagnetic interaction, as discussed in Section 6.2. Similarly the parity-violating interaction leading to the slight asymmetry effect in the effective potential, as illustrated in Figures 6.6 and 6.7 arises from the Z-bosons as field particles mediating the weak interaction between electrons and nuclei (or protons, neutrons, quarks, *etc.*). The small effective ''parity-violating potential'' (really an extra effective potential hypersurface that is antisymmetric with respect to inversion and should not at all be interpreted as a ''Born–Oppenheimer hypersurface'') arises from an approximation in carrying out the computation in electroweak quantum chemistry.[27] While there would be no need to make the approximation, it nevertheless corresponds to a useful model that allows us to understand the small symmetry violation and to practically compute it with feasible effort. Conceptually, however, exact tunnelling dynamics in this effective asymmetric potential should be understood on the basis of the quantum sublevel structure arising from the symmetry breaking removal of a degeneracy, which can be observed by experiment or could also be derived from an exact theory without making any reference to the parity-violating potential hypersurface, nor to the Born–Oppenheimer surface for that matter.

A brief note is also useful concerning the role of relativistic effects. As is well known, these are important for the dynamics of electron motion whenever the heavier elements are involved in the molecules considered. These effects can be calculated by relativistic quantum chemistry[192,199,205] and can lead, indeed, to dramatic changes in the effective Born–Oppenheimer potential barriers for tunnelling. Once these effects are included, the tunnelling motion of atoms and molecules can be computed and understood in very much the same way using the Schrödinger equation, as discussed for non-relativistic potentials. If the molecules move at relativistic speeds, one has to consider the changes in the definition of time that is then to be measured by an atomic clock moving at relativistic speed.[42,110,204] Indeed, molecular tunnelling systems such as ammonia can be, and have been, used as molecular clocks, and one has the well-understood (and in fact experimentally observed) relativistic effects, such as an atomic and molecular ''twin paradox'' discussed by Einstein.[193] Further considerations arise when considering violations of time-reversal symmetry and possibly a hypothetical violation of CPT symmetry[42,178,200–204,206] and we refer to ref. 27, 157 and 158, where one can also find a discussion of fundamental aspects of the definition of time and of the ''42 open problems'', some of which are related to tunnelling.

Acknowledgements

We gratefully acknowledge support, help from and discussions with Ziqiu Chen, Csabá Fabri, Karen Keppler, Roberto Marquardt, Frédéric Merkt, Eduard Miloglyadov, Robert Prentner, Jürgen Stohner, Martin Willeke, and Gunther Wichmann as well as financial support from ETH Zürich, the laboratory of Physical Chemistry and an Advanced Grant of the European

Research Council ERC, as well as the COST project MOLIM. This publication is based on a lecture (San Diego, ACS August 2019) and dedicated to HF Schaefer III on the occasion of his 75th birthday.

References

1. F. Hund, *Z. Phys.*, 1927, **43**, 788.
2. F. Hund, *Z. Phys.*, 1927, **43**, 805.
3. F. Hund, *Z. Phys.*, 1927, **40**, 742.
4. W. Heisenberg, *Z. Physik*, 1925, **33**, 879.
5. W. Heisenberg, *Die Physikalischen Prinzipien der Quantentheorie*, Hirzel Verlag, Leipzig, 1980.
6. P. A. M. Dirac, *The Principles of Quantum Mechanics*, 4th edn, Clarendon Press, Oxford, 1958.
7. E. Schrödinger, *Ann. Phys.*, 1926, **81**, 109.
8. E. Schrödinger, *Ann. Phys.*, 1926, **79**, 361.
9. E. Schrödinger, *Ann. Phys.*, 1926, **79**, 489.
10. E. Schrödinger, *Ann. Phys.*, 1926, **80**, 437.
11. E. Schrödinger, *Naturwissenschaften*, 1926, **14**, 664.
12. M. Quack, *Bunsenmagazin*, 2012, **14**, 181.
13. W. J. Moore, *Schrödinger, Life and Thought*, Cambridge Univ. Press, Cambridge, 1989, p. 195.
14. G. Seyfang and M. Quack, *Nachr. Chemie*, 2017, **66**, 307.
15. M. Quack and G. Seyfang, Atomic and molecular tunnelling processes in chemistry, Chapter 7 in *Time Dependent Quantum Dynamics and Spectroscopy*, ed. R. Marquardt and M. Quack, Elsevier, Amsterdam, 2020.
16. J. Kästner and S. Kozuch, *Quantum Mechanical Tunneling*, Royal Society of Chemistry, 2020.
17. R. K. Allemann and N. S. Scrutton, *Quantum Tunneling in Enzyme-catalysed Reactions*. RSC Publishing, Cambridge, 2009.
18. B. P. Bell, *The Tunnel Effect in Chemistry*, Chapman and Hall, London, 1980.
19. G. Herzberg, *Molecular Spectra and Molecular Structure: II. Infrared and Raman Spectra*, Van Nostrand, New York, 1943.
20. G. Herzberg, *Molecular Spectra and Molecular Structure: III. Electronic Spectra and Electronic Structure of Polyatomic Molecules*, Van Nostrand, New York, 1966.
21. M. Quack and F. Merkt, *Handbook of High-Resolution Spectroscopy*, John Wiley, Chichester, New York, 2011.
22. T. D. Lee and C. D. Yang, *Phys. Rev.*, 1956, **104**, 254.
23. C. S. Wu, E. Ambler, R. W. Hayward, D. D. Hoppes and R. P. Hudson, *Phys. Rev.*, 1957, **105**, 1413.
24. J. I. Friedman and V. Telegdi, *Phys. Rev.*, 1957, **105**, 1681.
25. H. Schopper, *Phil. Mag.*, 1957, **2**, 710.
26. R. L. Garwin, L. M. Lederman and M. Weinrich, *Phys. Rev.*, 1957, **105**, 1415.

27. M. Quack, Fundamental symmetries and symmetry violations from high resolution spectroscopy, in *Handbook of High Resolution Spectroscopy*, ed. M. Quack and F. Merkt, Wiley, Chichester, New York, 2011, vol. 1, ch. 18, pp. 659.
28. *Symmetrie und Asymmetrie in Wissenschaft und Kunst, Nova Acta Leopoldina NF*, ed. M. Quack and J. Hacker, 2016, vol. 127, No. 412, p. 7 (preface to book with a total of 275 pages and contributions by several authors in English and German).
29. M. Quack, Electroweak quantum chemistry and the dynamics of parity violation in chiral molecules, in *Modelling Molecular Structure and Reactivity in Biological Systems, Proc. 7th WATOC Congress, Cape Town January 2005*, ed. K. J. Naidoo, J. Brady, M. J. Field, J. Gao and M. Hann, Royal Society of Chemistry, Cambridge, 2006, pp. 3–38.
30. M. Quack, J. Stohner and M. Willeke, *Ann. Rev. Phys. Chem.*, 2008, **59**, 741.
31. M. Quack, Molecular Parity Violation and Chirality: The Asymmetry of Life and the Symmetry Violations of Physics, in *Quantum Systems in Chemistry and Physics: Progress in Methods and Applications, Proceedings of QSCP XVI, Kanazawa 11 to 17 September 2011", Series Title: "Progress in Theoretical Chemistry and Physics*, ed. K. Nishikawa, J. Maruani, E. Brändas, G. Delgado-Barrio and P. P. Piecuch, Springer Verlag , 2012, ch. 3, pp. 47–76.
32. M. Quack, *Adv. Chem. Phys.*, 2014, **157**, 249.
33. A. Bakasov, T. K. Ha and M. Quack, Ab initio calculation of molecular energies including parity-violating interactions, in *Chemical Evolution, Physics of the Origin and Evolution of Life, Proc. of the 4th Trieste Conference (1995)*, ed. J. Chela-Flores and F. Raulin, Kluwer Academic Publishers, Dordrecht, 1996, p. 287.
34. A. Bakasov, T. K. Ha and M. Quack, *J. Chem. Phys.*, 1998, **109**, 7263.
35. R. Berger and M. Quack, *J. Chem. Phys.*, 2000, **112**, 3148.
36. M. Quack, *Angew. Chem., Int. Ed. Engl.*, 2002, **41**, 4618–4630.
37. P. A. M. Dirac, *Proc. R. Soc. London, A*, 1929, **123**, 714.
38. CERN, Webseite http://doc.cern.ch//archive/electronic/cern/others/PHO/photodi/9809005.jpeg, Bildnummer CERN AC_Z04_V25/B/1992.
39. J. H. van't Hoff, *La chimie dans l'espace*, ed. B. M. Bazendijk, Rotterdam, reprinted in ed. and C. Bourgeois, Sur la dissymétrie moléculaire, Coll. Epistème, Paris, 1986, 1887.
40. M. Quack and J. Stohner, *Phys. Rev. Lett.*, 2000, **84**, 3807.
41. M. Quack, *Angew. Chem., Int. Ed. Engl.*, 1989, **28**, 571. *Angew. Chem.*, 1989, **101**, 588.
42. M. Quack, Time and time reversal symmetry in quantum chemical kinetics, in *Fundamental World of Quantum Chemistry, a Tribute to the Memory of Per Olof Löwdin*, ed. E. J. Brändas and E. S. Kryachko, Kluver Publ., Dordrecht, 2004, vol. 3, pp. 423.
43. S. L. Glashow, *Nucl. Phys.*, 1961, **22**, 579.
44. S. Weinberg, *Phys. Rev. Letters*, 1967, **19**, 1264.

45. A. Salam, *Proceedings of the 8th Nobel Symposium*, Almkvist und Wiksell, Stockholm, 1968, p. 367.
46. M. J. G. Veltman, *Rev. Mod. Phys.*, 2000, **72**, 341.
47. G. 't Hooft, *Rev. Mod. Phys.*, 2000, **72**, 333.
48. Y. Yamagata, *J. Theor. Biol.*, 1966, **11**, 495.
49. A. S. Garay and P. Hrasko, *J. Mol. Evol.*, 1975, **6**, 77.
50. D. W. Rein, *J. Mol. Evol.*, 1974, **4**, 15.
51. V. S. Letokhov, *Phys. Lett. A*, 1975, **53**, 275.
52. O. N. Kompanets, A. R. Kukudzhanov, V. S. Letokhov and L. L. Gervits, *Opt. Commun.*, 1976, **19**, 414.
53. E. Arimondo, P. Glorieux and T. Oka, *Opt. Commun.*, 1977, **23**, 369.
54. L. Keszthelyi, *Phys. Lett. A*, 1977, **64**, 287.
55. L. Keszthelyi, *Orig. Life Evol. Biosph.*, 1977, **8**, 299.
56. B. Y. Zeldovich, D. B. Saakyan and I. I. Sobelman, *JETP Lett.*, 1977, **25**, 94.
57. R. A. Harris and L. Stodolsky, *Phys. Lett. B*, 1978, **78**, 313.
58. D. W. Rein, R. A. Hegström and P. G. H. Sandars, *Phys. Lett. A*, 1979, **71**, 499.
59. R. A. Hegström, D. W. Rein and P. G. H. Sandars, *J. Chem. Phys.*, 1980, **73**, 2329.
60. S. F. Mason and G. E. Tranter, *J. Chem. Soc. Chem. Comm*, 1983, 117.
61. S. F. Mason and G. E. Tranter, *Chem. Phys. Lett.*, 1983, **94**, 34.
62. S. F. Mason and G. E. Tranter, *Mol. Phys.*, 1984, **53**, 1091.
63. S. F. Mason, *Nature*, 1984, **311**, 19.
64. G. E. Tranter, *Mol. Phys.*, 1985, **56**, 825.
65. G. E. Tranter, *Chem. Phys. Lett.*, 1985, **121**, 339.
66. G. E. Tranter, *Chem. Phys. Lett.*, 1985, **115**, 286.
67. G. E. Tranter, *Nature*, 1985, **318**, 172.
68. A. L. Barra, J. B. Robert and L. Wiesenfeld, *Phys. Lett. A*, 1986, **115**, 443.
69. A. L. Barra, J. B. Robert and L. Wiesenfeld, *BioSystems*, 1987, **20**, 57.
70. D. K. Kondepudi, *BioSystems*, 1987, **20**, 75.
71. A. J. Macdermott, G. E. Tranter and S. B. Indoe, *Chem. Phys. Lett.*, 1987, **135**, 159.
72. A. L. Barra, J. B. Robert and L. Wiesenfeld, *Europhys. Lett.*, 1988, **5**, 217.
73. L. Wiesenfeld, *Mol. Phys.*, 1988, **64**, 739.
74. P. Jungwirth, L. Skala and R. Zahradnik, *Chem. Phys. Lett.*, 1989, **161**, 502.
75. A. J. Macdermott and G. E. Tranter, *Chem. Phys. Lett.*, 1989, **163**, 1.
76. A. J. Macdermott and G. E. Tranter, *Croat. Chem. Acta*, 1989, **62**, 165.
77. O. Kikuchi and H. Wang, *Bull. Chem. Soc. Jpn.*, 1990, **63**, 2751.
78. O. Kikuchi, H. Wang, T. Nakano and K. Morihashi, *Theochem.-J. Mol. Struct.*, 1990, **64**, 301.
79. J. Chela-Flores, *Chirality*, 1991, **3**, 389.
80. A. Salam, *J. Mol. Evol.*, 1991, **33**, 105.
81. A. Salam, *Phys. Lett. B*, 1992, **288**, 153.
82. O. Kikuchi and H. Kiyonaga, *Theochem-J. Mol. Struct.*, 1994, **118**, 271.

83. A. Bakasov, T. K. Ha and M. Quack, *Chimia*, 1997, **51**, 559.
84. A. Bakasov and M. Quack, *Chem. Phys. Lett.*, 1999, **303**, 547.
85. R. Berger and M. Quack, *Proc. 37th IUPAC Congress*, Berlin, 1999, vol. 2, p. 518.
86. P. Lazzeretti and R. Zanasi, *Chem. Phys. Lett.*, 1997, **279**, 349.
87. R. Zanasi and P. Lazzeretti, *Chem. Phys. Lett.*, 1998, **286**, 240.
88. J. K. Laerdahl and P. Schwerdtfeger, *Phys. Rev. A*, 1999, **60**, 4439.
89. M. Gottselig, D. Luckhaus, M. Quack, J. Stohner and M. Willeke, *Helv. Chim. Acta*, 2001, **84**, 1846.
90. R. Berger, M. Gottselig, M. Quack and M. Willeke, *Angew. Chem., Int. Ed.*, 2001, **40**, 4195, (*Angew. Chem.*, 2001, **113**, 4342).
91. M. Quack and J. Stohner, *Z. Phys. Chem.*, 2000, **214**, 675. *Proc. 12th Symp. on Atomic and Surface Physics and related Topics*, ed. D. Bassi and P. Tosi, Folgaria, Trento, 2000, PR-11, pp. 1–4.
92. R. Berger and M. Quack, *ChemPhysChem*, 2000, **1**, 57.
93. R. Berger, M. Quack and G. S. Tschumper, *Helv. Chim. Acta*, 2000, **83**, 1919.
94. J. K. Laerdahl, P. Schwerdtfeger and H. M. Quiney, *Phys. Rev. Lett.*, 2000, **84**, 3811.
95. J. K. Laerdahl, R. Wesendrup and P. Schwerdtfeger, *ChemPhysChem*, 2000, **1**, 60.
96. A. C. Hennum, T. Helgaker and W. Klopper, *Chem. Phys. Lett.*, 2002, **354**, 274.
97. M. Quack and J. Stohner, *Chirality*, 2001, **13**, 745.
98. A. Beil, D. Luckhaus, R. Marquardt and M. Quack, *Faraday Discuss.*, 1994, **99**, 49.
99. A. Bauder, A. Beil, D. Luckhaus, F. Müller and M. Quack, *J. Chem. Phys.*, 1997, **106**, 7558.
100. H. Hollenstein, D. Luckhaus, J. Pochert, M. Quack and G. Seyfang, *Angew. Chem., Int. Ed. Engl.*, 1997, **36**, 140, (*Angew. Chem.*, **109**, 136).
101. C. Daussy, Premier test de très haute précision de violation de la parité dans le spectre de la molécule chirale CHFClBr, Thèse, Université Paris 13, Villetaneuse, Paris Nord, 1999.
102. C. Daussy, T. Marrel, A. Amy-Klein, C. T. Nguyen, C. J. Bordé and C. Chardonnet, *Phys. Rev. Lett.*, 1999, **83**, 1554.
103. J. Crassous and A. Collet, *Enantiomer*, 2000, **5**, 429.
104. M. J. M. Pepper, I. Shavitt, P. V. R. Schleyer, M. N. Glukhovtsev, R. Janoschek and M. Quack, *J. Comput. Chem.*, 1995, **16**, 207.
105. M. Quack, *Faraday Discuss.*, 1994, 389.
106. R. Berger, *Phys. Chem. Chem. Phys.*, 2003, **5**, 12.
107. A. S. Lahamer, S. M. Mahurin, R. N. Compton, D. House, J. K. Laerdahl, M. Lein and P. Schwerdtfeger, *Phys. Rev. Lett.*, 2000, **85**, 4470.
108. H. Buschmann, R. Thede and D. Heller, *Angew. Chem., Int. Ed.*, 2000, **39**, 4033.
109. P. Frank, W. Bonner and R. N. Zare, in *Chemistry for the 21st Century*, ed. E. Keinan and I. Schechter, Wiley-VCH, Weinheim, 2001, ch. 11, p. 175.

110. M. Quack, Zeit und Zeitumkehrsymmetrie in der molekularen Kinetik. Schriftliche Fassung des Vortrages am 7. Symposium der Deutschen Akademien der Wissenschaften, Berlin-Brandenburgische Akademie der Wissenschaften Berlin, Zeithorizonte in der Wissenschaften, 31.10. und 1.11.2002, ed. D. Simon, De Gruyter, Berlin, 2004, p. 125.
111. M. Quack and J. Stohner, *Chimia*, 2005, **59**, 530.
112. H. F. Schaefer III, *Quantum Chemistry. The Development of ab initio Methods in Molecular Electronic Structure Theory*, Clarendon Press, Oxford, 1984.
113. H. F. Schaefer, *Chimia*, 1989, **43**, 1.
114. W. G. Richards, *Nature*, 1979, **278**, 507.
115. C. F. Bender and H. F. Schaefer III, *J. Am. Chem. Soc.*, 1970, **92**, 4984.
116. C. F. Bender and H. F. Schaefer III, *J. Am. Chem. Soc.*, 1972, **94**, 6888.
117. A. G. Császár, C. Fábri, T. Szidarovszky, E. Mátyus, T. Furtenbacher and G. Czakó, *PhysChemChemPhys*, 2012, **14**, 1085.
118. N. N. Bogoljubov and D. V. Shirkov, *Quantum Fields, Benjamin/Cummings, Reading, Massachusetts etc.*, 1983.
119. N. N. Bogoljubov and D. V. Shirkov, *Introduction to the Theory of Quantized Fields*, Wiley, New York *a.o.*, 1980.
120. A. Bakasov, T. K. Ha and M. Quack, Parity-violating potentials for molecules and clusters, in *Proceedings of the Symposium on Atomic and Surface Physics and Related Topics, SASP 98, Going/Kitzbühel, Austria*, ed. A. Hansel and W. Lindinger, Institut für Ionenphysik der Universität Innsbruck, 1998, p. 4.
121. M. A. Bouchiat and C. Bouchiat, *J. Phys.*, 1974, **35**, 899.
122. M. A. Bouchiat and C. Bouchiat, *J. Phys.*, 1975, **36**, 493.
123. J. Linderberg and Y. Öhrn, *Propagators in Quantum Chemistry*, Academic Press, London, 1973.
124. O. Vahtras, H. Agren, P. Jorgensen, H. J. A. Jensen, T. Helgaker and J. Olsen, *J. Chem. Phys.*, 1992, **96**, 2118.
125. R. Berger and C. van Wüllen, *J. Chem. Phys.*, 2005, **122**, 134316.
126. P. Schwerdtfeger, T. Saue, J. N. P. van Stralen and L. Visscher, *Phys. Rev. A*, 2005, **71**, 012103.
127. M. Quack and J. Stohner, *J. Chem. Phys.*, 2003, **119**, 11228.
128. A. Bakasov, R. Berger, T. K. Ha and M. Quack, *Int. J. Quantum Chem.*, 2004, **99**, 393.
129. M. Quack, *Annu. Rev. Phys. Chem.*, 1990, **41**, 839.
130. M. Quack, Molecular femtosecond quantum dynamics between less than yoctoseconds and more than days: Experiment and theory in Femtosecond Chemistry, in *Proc. Berlin Conf. Femtosecond Chemistry, Berlin (March 1993)*, ed. J. Manz and L. Woeste, Verlag Chemie, Weinheim, 1995, ch. 27, p. 781.
131. B. Kuhn, T. R. Rizzo, D. Luckhaus, M. Quack and M. A. Suhm, *J. Chem. Phys.*, 1999, **111**, 2565.
132. B. Fehrensen, D. Luckhaus and M. Quack, *Chem. Phys. Lett.*, 1999, **300**, 312.

133. D. Luckhaus and M. Quack, Gas Phase Kinetics Studies, in *Encyclopedia of Chemical Physics and Physical Chemistry*, ed. J. H. Moore and N. Spencer, IOP Publishing, Bristol, 2001, vol. 2, (Methods), ch. B. 2.5, p. 1871.
134. R. Berger, M. Quack, A. Sieben and M. Willeke, *Helv. Chim. Acta*, 2003, **86**, 4048.
135. M. Gottselig, M. Quack, J. Stohner and M. Willeke, *Int. J. Mass Spectrom.*, 2004, **233**, 373.
136. B. Fehrensen, D. Luckhaus and M. Quack, *Z. Phys. Chem.*, 1999, **209**, 1.
137. W. B. Olson, R. H. Hunt, B. W. Young, A. G. Maki and J. W. Brault, *J. Mol. Spectrosc.*, 1988, **127**, 12.
138. M. Quack and M. Willeke, *Helv. Chim. Acta*, 2003, **86**, 1641.
139. M. Quack, *Chimia*, 2001, **55**, 753.
140. M. Quack, *Philos. Trans. Roy. Soc. London*, 1990, **A 332**, 203.
141. M. Gottselig and M. Quack, *J. Chem. Phys.*, 2005, **123**, 84305.
142. J. K. Laerdahl and P. Schwerdtfeger, *Phys. Rev. A*, 1999, **60**, 4439.
143. L. Horný and M. Quack, *Faraday Discuss.*, 2011, **150**, 152.
144. P. Lazzeretti, R. Zanasi and F. Faglioni, *Phys Rev E*, 1999, **60**, 871.
145. R. Berger, Parity-violation effects in molecules, in *Relativistic Electronic Structure Theory, Vol. Part 2*, ed. P. Schwerdtfeger, Elsevier, Amsterdam, 2004, ch. 4, pp. 188–288.
146. R. Berger, M. Quack and J. Stohner, *Angew. Chem., Int. Ed.*, 2001, **40**, 1667, (*Angew. Chem.*, **113**, 1716).
147. E. Fermi, *Z. Physik*, 1934, **89**, 522.
148. F. Hobi, R. Berger and J. Stohner, *Mol. Phys.*, 2013, **111**, 2345.
149. M. Quack, *Chem. Phys. Lett.*, 1986, **132**, 147.
150. M. Quack and M. Willeke, *J. Phys. Chem. A*, 2006, **110**, 3338.
151. L. Horný and M. Quack, *Mol. Phys.*, 2015, **113**, 1768.
152. R. Prentner, M. Quack, J. Stohner and M. Willeke, *J. Phys. Chem. A*, 2015, **119**, 12805.
153. R. Berger, *J. Chem. Phys.*, 2008, **129**, 154105.
154. J. N. P. van Stralen, L. Visscher, C. V. Larsen and H. J. A. Jensen, *Chem. Phys.*, 2005, **311**, 81.
155. R. Berger, N. Langermann and C. vanWüllen, *Phys. Rev.*, 2005, **A 71**, 042105.
156. J. Thyssen, J. K. Laerdahl and P. Schwerdtfeger, *Phys. Rev. Lett.*, 2000, **85**, 3105.
157. M. Quack, *Die Symmetrie von Zeit und Raum und ihre Verletzung in molekularen Prozessen in Jahrbuch 1990-1992 der Akademie der Wissenschaften zu Berlin, W. de Gruyter*, Verlag, Berlin, 1993, pp. 467, (printed version of the 8th public academy lecture, Berlin 4.10.1990); there exists also a slightly changed English version: M. Quack, The symmetries of time and space and their violation in chiral molecules and molecular processes, pp. 172, in *Conceptual Tools for Understanding Nature. Proc. 2nd Int. Symp. of Science and Epistemology Seminar, Trieste April 1993*, ed. G. Costa, G. Calucci and M. Giorgi, World Scientific Publ., Singapore, 1995.

158. M. Quack, *Faraday Disc*, 2011, **150**, 533.
159. E. R. Cohen, T. Cvitas, J. G. Frey, B. Holmström, K. Kuchitsu, R. Marquardt, I. Mills, F. Pavese, M. Quack, J. Stohner, H. L. Strauss, M. Takami and A. Thor, *Quantities, Units and Symbols in Physical Chemistry*, 3rd edn, 2007.
160. R. Berger, G. Laubender, M. Quack, A. Sieben, J. Stohner and M. Willeke, *Angew. Chem.*, 2005, **117**, 3689, (*Angew. Chem., Int. Ed.* (*Engl.*), 2005, **44**, 3623).
161. M. Quack, *Nova Acta Leopoldina*, 1999, **81**(Neue Folge (No. 314)), 137.
162. S. Albert, I. Bolotova, Z. Chen, C. Fábri, L. Horný, M. Quack, G. Seyfang and D. Zindel, *Phys. Chem. Chem. Phys.*, 2016, **18**, 21976.
163. S. Albert, K. Keppler, V. Boudon, P. Lerch and M. Quack, *J. Mol. Spect*, 2017, **337**, 105.
164. S. Albert, I. Bolotova, Z. Chen, C. Fábri, M. Quack, G. Seyfang and D. Zindel, *Phys. Chem. Chem. Phys.*, 2017, **19**, 11738.
165. C. Fábri, L. Horný and M. Quack, *ChemPhysChem*, 2015, **16**, 3584.
166. S. Albert, F. Arn, I. Bolotova, Z. Chen, C. Fábri, G. Grassi, P. Lerch, M. Quack, G. Seyfang, A. Wokaun and D. Zindel, *J. Phys. Chem. Lett.*, 2016, **7**, 3847.
167. S. Albert, Z. Chen, K. Keppler, P. Lerch, M. Quack, V. Schurig and O. Trapp, *Phys. Chem. Chem. Phys.*, 2019, **21**, 3669.
168. S. Albert, P. Lerch, K. Keppler and M. Quack, *Proceedings of the 20th Symposium on Atomic, Cluster and Surface Physics 2016 (SASP 2016), Davos, Switzerland, 7 to 12 February 2016*, ed. J. Stohner and Ch. Yeretzian, Innsbruck University Press (IUP), Innsbruck, 2016, pp. 165–168.
169. B. Fehrensen, D. Luckhaus and M. Quack, *Chem. Phys.*, 2007, **338**, 90.
170. M. Hippler, E. Miloglyadov, M. Quack and G. Seyfang, Mass and isotope selective infrared spectroscopy, in *Handbook of High Resolution Spectroscopy*, ed. M. Quack and F. Merkt, Wiley, Chichester, New York, 2011, vol. 2, ch. 28, pp. 1069.
171. S. Albert, P. Lerch and M. Quack, *Proceedings of the 20th Symposium on Atomic, Cluster and Surface Physics 2016 (SASP 2016), Davos, Switzerland, 7 to 12* February 2016, ed. J. Stohner and Ch. Yeretzian, Innsbruck University Press (IUP), Innsbruck, 2016, p. 169.
172. C. Fábri, R. Marquardt, A. Császár and M. Quack, *J. Chem. Phys.*, 2019, **150**, 014102.
173. M. Gottselig, M. Quack and M. Willeke, *Israel J. Chem.*, 2003, **43**, 353.
174. S. K. Tokunaga, C. Stoeffler, F. Auguste, A. Shelkovnikov, C. Daussy, A. Amy-Klein, C. Chardonnet and B. Darquié, *Mol. Phys.*, 2013, **111**, 2363.
175. M. Schnell and J. Küpper, *Farad. Discuss. Chem. Soc*, 2011, **150**, 33.
176. M. Quack, *Farad. Discuss. Chem. Soc*, 2011, **150**, 123.
177. R. Marquardt, M. Quack, J. Thanopulos and D. Luckhaus, *J. Chem. Phys.*, 2003, **118**, 643.
178. M. Quack, *Chimia*, 2003, **57**, 147.
179. S. Albert, P. Lerch, R. Prentner and M. Quack, *Angew. Chem. Intl. Ed.*, 2013, **52**, 346, (*Angew. Chem.*, **125**, 364).

180. J. K. G. Watson, in *Vibrational Spectra and Structure*, ed. J. R. Durig, Elsevier, Amsterdam, vol. 6, 1978, p. 1.
181. P. Dietiker, M. Miloglyadov, M. Quack, A. Schneider and G. Seyfang, *J. Chem. Phys.*, 2015, **143**, 244305.
182. E. Miloglyadov, M. Quack, G. Seyfang, G. Wichmann, Chapter A.2.3 Precision Experiments for Parity Violation in Chiral Molecules: the Role of STIRAP 11–13, 51–52 in K. Bergmann, H.-C. Nägerl, C. Panda, G. Gabrielse, E. Miloglyadov, M. Quack, G. Seyfang, G. Wichmann, S. Ospelkaus, A. Kuhn, S. Longhi, A. Szameit, P. Pirro, B. Hillebrands, X.-F. Zhu, J. Zhu, M. Drewsen, W. K. Hensinger, S. Weidt, T. Halfmann, H.-L. Wang, G. Sorin Paraoanu, N. V. Vitanov, J. Mompart, T. Busch, T. J. Barnum, D. D. Grimes, R. W. Field, M. G. Raizen, E. Narevicius, M. Auzinsh, D. Budker, A. Pálffy, C. H. Keitel, *J. Phys. B: At., Mol. Opt. Phys.* 2019, **52**, 202001.
183. S. Albert, Z. Chen, K. Keppler, C. Manca Tanner, M. Quack, V. Schurig, J. Stohner and O. Trapp, *Chimia*, 2019, **73**, 615, and to be published.
184. A. Garg, *Am. J. Phys.*, 2000, **68**, 430.
185. D. Luckhaus and M. Quack, *Mol. Phys.*, 1989, **68**, 745.
186. C. Fábri, S. Albert, Z. Chen, R. Prentner and M. Quack, *Phys. Chem. Chem. Phys.*, 2018, **20**, 7387.
187. S. Albert, Z. Chen, C. Fábri, P. Lerch, R. Prentner and M. Quack, *Mol. Phys.*, 2016, **114**, 2751.
188. J. Smydke, C. Fábri, C. Sarka and A. Császár, *Phys. Chem. Chem. Phys.*, 2019, **21**, 3453.
189. *Molecular Switches*, ed. B. L. Feringa and W. R. Browne, Wiley-VCH Verlag GmbH & Co. KGaA, 2nd edn, 2011.
190. M. Quack, *European Review*, 2014, **22**, S 50.
191. R. Hoffmann, *J. Mol. Struct.*, 1998, **424**, 1.
192. M. Reiher and A. Wolf, *Relativistic Quantum Chemistry: The Fundamental Theory of Molecular Science*, 1st edn, Wiley-VCH, Weinheim, 2009.
193. A. Einstein, *Grundzüge der Relativitätstheorie*, Vieweg, Braunschweig, 1922.
194. U. Gaubatz, P. Rudecki, S. Schieman and K. Bergman, *J. Chem. Phys.*, 1990, **92**, 5363.
195. M. Quack, *J. Chem. Phys.*, 1985, **82**, 3277.
196. M. Quack and M. Suhm, *J. Chem. Phys.*, 1991, **95**, 28.
197. H. C. Longuet-Higgins, *Mol. Phys.*, 1963, **6**, 445.
198. M. Quack, *Mol. Phys.*, 1977, **34**, 477.
199. R. Mastalerz and M. Reiher, Relativsitic Electronic Structure Theory for Molecular Spectroscopy, in *Handbook of High Resolution Spectroscopy*, ed. M. Quack and F. Merkt, Wiley, Chichester, 2011, vol. 1, p. 405.
200. M. Quack, *Chem. Phys. Lett.*, 1994, **231**, 421.
201. M. Quack, *J. Mol. Struct.*, 1993, **292**, 171.
202. G. Gabrielse, *Nova Acta Leopoldina, NF*, 2016, **127**(412), 91, (see ref. 28).
203. H. Fritsch, *Nova Acta Leopoldina, NF*, 2016, **127**(412), 75, (see ref. 28).
204. M. Quack, *Nova Acta Leopoldina, NF*, 2016, **127**(412), 119, (see ref. 28).
205. P. Pyykkö, *Chem. Rev.*, 2012, **112**, 371.

206. ALPHA Collaboration, *Nature*, 2020, **578**, 375, (M. Ahmadi, *et al.*).
207. B. Fehrensen, D. Luckhaus and M. Quack, *Z. Phys. Chem.*, 1999, **300**, 312.
208. W. H. Miller, N. C. Handy and J. E. Adams, *J. Chem. Phys.*, 1980, **72**, 99.
209. M. Quack and J. Troe, *Ber. Bunsenges. Phys. Chem.*, 1974, **78**, 240.
210. M. Quack and J. Troe, Statistical Adiabatic Channel Models, in *Encyclopedia of Computational Chemistry*, ed. P. von Ragué Schleyer, N. Allinger, T. Clark, J. Gasteiger, P. A. Kollman, H. F. Schaefer III and P. R. Schreiner, John Wiley and Sons, 1998, vol. 4, p. 2708.
211. M. Quack, *J. Chem. Phys.*, 1978, **69**, 1282.
212. H. Feldmann, D. Kella, E. Malkin, E. Miklazky, Z. Vager, J. Zajfman and R. Naaman, *J. Chem. Soc. Farad. Trans*, 1990, **86**, 2469.
213. P. Herwig, K. Zawatzky, M. Grieser, O. Heber, B. Jordon-Thaden, C. Krantz, O. Novotny, R. Repnow, V. Schurig, D. Schwalm, Z. Vager, A. Wolf, O. Trapp and H. Kreckel, *Science*, 2013, **342**, 1084.
214. M. Pitzer, R. Berger, J. Stohner, R. Dörner and M. Schöffler, *Chimia*, 2018, **72**, 384.
215. L. Barron, *Molecular Light Scattering and Optical Activity*, 2nd edn, Cambridge University Press, 2004.
216. L. Wilhelmy, *Poggendorfs Ann.*, 1850, **81**, 413 and 419.
217. M. Quack, *Adv. Chem. Phys.*, 2014, **157**, 97.
218. L. Hoddeson, L. Brown, M. Riordan and M. Dresden, *The Rise of the Standard Model: A History of Particle Physics from 1964 to 1979*, Cambridge University Press, 1997.
219. *60 Years of CERN, Experiments and Discoveries*, ed. H. Schopper and L. Di Lella, World Scientific, Singapore, 2015.
220. S. C. Bennet and C. E. Wieman, *Phys. Rev. Lett.*, 1999, **82**, 2484.
221. R. Berger and J. Stohner, *WIREs Comp. Mol. Sci*, 2019, **9**(3), e1396.
222. M. K. Kozlov and L. N. Labzowski, *J. Phys. B: At., Mol. Opt. Phys.*, 1995, **28**, 1933.
223. A. Császár and C. Fábri, From Tunnelling Control to Controlling Tunnelling, in *Quantum Mechanical Tunneling*, ed. J. Kästner and S. Kozuch, Royal Society of Chemistry, 2020, pp. 146–166.
224. A. Cournol, M. Manceau, M. Pierens, L. Lecordier, D. B. A. Tran, R. Santagata, B. Argence, A. Goncharov, O. Lopez, M. Abgrall, Y. Le Coq, R. Le Targat, H. Alvarez Martinez, W. L. Lee, D. Xu, P. E. Pottie, R. J. Hendricks, T. E. Wall, J. M. Bieniewska, B. E. Sauer, M. R. Tarbutt, A. Amy Klein, S. K. Tokunaga and B. Darquié, *Quantum Electron.*, 2019, **49**, 288–292.

CHAPTER 7

Instanton Theory to Calculate Tunnelling Rates and Tunnelling Splittings

VIKTOR ZAVERKIN AND JOHANNES KÄSTNER*

Institute for Theoretical Chemistry, University of Stuttgart, Pfaffenwaldring 55, 70569 Stuttgart, Germany
*Email: kaestner@theochem.uni-stuttgart.de

7.1 Introduction

The prediction of tunnelling rate constants and tunnelling splittings of vibrational levels is vital for the understanding of tunnelling processes in chemistry. There is a whole zoo of methods available; several are reviewed in this book. One such method is instanton theory, which is the focus of this chapter. It describes quantum effects such as quantum tunnelling using a semiclassical approximation to the quantum movement of particles. Semiclassical instanton theory can, in terms of accuracy and computational effort, be classified somewhere between the semiclassical approaches with assumptions on the tunnelling path (multidimensional tunnelling methods), which are described in Chapter 8 of this book, and full quantum dynamics, described in Chapter 10.

Historically, instanton theory was derived several times, more or less independently. In the late 1960s initial versions were proposed[1,2] in the view of the imaginary free-energy approach,[3–5] followed by approaches based on transition state theory in the 1970s.[3,6,7] In the last decade, the theory was derived from first principles.[8] In general, it is based on similar assumptions as transition state theory, like the omission of recrossing events of the barrier.

Theoretical and Computational Chemistry Series No. 18
Tunnelling in Molecules: Nuclear Quantum Effects from Bio to Physical Chemistry
Edited by Johannes Kästner and Sebastian Kozuch

Published by the Royal Society of Chemistry, www.rsc.org

To characterize quantum transitions in full detail, one would have to solve Schrödinger's equation with techniques like wave-packet dynamics or proper scattering boundary conditions to obtain the state-to-state differential and integral cross sections, as well as the scattering matrix S. In many cases, detailed knowledge of cross sections is not necessary, especially if the quantity of interest is merely a thermal rate constant. The average over all cross sections for a given energy E results in the cumulative reaction probability $N(E)$.[6] From that, one can obtain the thermal rate constant $k(T)$ at a given temperature T by

$$k(T) = \frac{1}{2\pi\hbar\, Q_{\mathrm{RS}}} \int_{-\infty}^{\infty} N(E) \exp(-E/k_{\mathrm{B}}T)\, \mathrm{d}E. \tag{7.1}$$

Here, $\hbar$ is the reduced Planck's constant, Q_{RS} is the canonical partition function of the reactant state and k_{B} is Boltzmann's constant. Instanton theory can be used to obtain Q_{RS} and $k(T)$ directly, or it can be applied to obtain $N(E)$. Both approaches are discussed in this chapter. Besides semiclassical instanton theory, which is closely related to ring-polymer molecular dynamics (RPMD),[9,10] as also discussed in recent review papers,[11–13] there is an instanton-like theory that omits the definition of the tunnelling path and is referred to as quantum instanton theory.[14,15] It uses the quantum Boltzmann operator rather than its semiclassical approximation and locates dividing surfaces rather than tunnelling paths.

7.2 Theory

There are several ways to approach instanton theory, and some of them have been explored independently by different researchers in the past. Here, we adopt a derivation that is close to transition state theory (TST). Instanton theory can, just like in TST, be applied to bimolecular and unimolecular reactions. Bimolecular processes correspond to scattering phenomena. Unimolecular reactions can be seen as a metastable state that decays without back reaction, *e.g.* a molecule that splits into two fragments that separate without ever meeting again.

7.2.1 Imaginary Free-energy Approach

The decay of such a metastable quantum state can be described by assigning a complex energy to the state, with a small imaginary part:[16]

$$E = E_{\mathrm{D}} - i\frac{\Gamma\hbar}{2}. \tag{7.2}$$

Here, E_{D} is the real-valued part of the energy and $-\Gamma\hbar/2$ is the imaginary part. A wave function associated with such an energy can still solve the time-independent Schrödinger equation. Complex eigenvalues are possible if the wave function is non-zero at the boundaries.[17,18] That is, for example, the case for a particle leaving the reactant well as an outgoing plane wave. With a time-independent Hamiltonian $\mathscr{H}$ and Schrödinger's equation

$$\frac{\partial\Psi}{\partial t} = -\frac{i}{\hbar}\mathscr{H}\Psi, \tag{7.3}$$

the time propagation of the wave function is $\Psi(t) = \exp(-i\mathscr{H}t/\hbar)\Psi(0)$. Inserting eqn (7.2) the resulting survival probability is

$$|\Psi(t)|^2 = \mathrm{e}^{-\Gamma t}|\Psi(0)|^2. \tag{7.4}$$

That means, eqn (7.2) describes the first-order decay with a rate constant Γ, or, *vice versa*, the decay rate of a metastable state can be derived from the imaginary part of its energy

$$\Gamma = -\frac{2}{\hbar}\mathrm{Im}(E). \tag{7.5}$$

To arrive at a canonical, *i.e.* thermally averaged, rate constant k, the Boltzmann average of eqn (7.5) is taken and the rate constant is related to the free energy F of the system,[4]

$$k = -\frac{2}{\hbar}\mathrm{Im}(F). \tag{7.6}$$

With $F = -1/k_\mathrm{B}T \ln(Q)$ the rate constant is

$$k = \frac{2k_\mathrm{B}T}{\hbar}\mathrm{Im}(\ln Q) = \frac{2k_\mathrm{B}T}{\hbar}\arctan\left(\frac{\mathrm{Im}\,Q}{\mathrm{Re}\,Q}\right) \approx \frac{2k_\mathrm{B}T}{\hbar}\frac{\mathrm{Im}\,Q}{\mathrm{Re}\,Q}, \tag{7.7}$$

where the last relation holds for $\mathrm{Im}\,Q \ll \mathrm{Re}\,Q$. In practice, it turns out that the instanton, *i.e.* the equivalent of a transition state, has an imaginary partition function, while the reactant state's partition function is real-valued.

In summary, the imaginary free-energy approach allows the calculation of thermal rate constants from the imaginary part of the free energy of a system. The next step is to calculate the partition function.

7.2.2 Partition Functions

Partition functions are calculated *via* Feynman's path integral formulation, since this will turn out beneficial for the following derivations. As a pre-requisite we assume perfect separability of the partition function into vibrational, rotational, and translational contributions. Firstly, we deal with the vibrational contribution.

The partition function can be derived from the similarity between the Schrödinger propagator $\exp(-i\mathscr{H}t/\hbar)$ and the Boltzmann operator $\exp(-\mathscr{H}/k_\mathrm{B}T)$. A partition function can be obtained by propagating a state onto itself over a "time" $t = -i\tau$, where $\tau = \hbar/k_\mathrm{B}T$, which is referred to as Euclidean time. While this expression, indeed, has the dimensionality of a time, it is imaginary. Replacing the time t by the imaginary time $-i\tau$ is referred to as Wick rotation. We consider Feynman paths $x(\tau)$ in configuration space. Since we propagate a state onto itself, the paths are closed, *i.e.* $x(\tau = 0) = x(\tau = \hbar/k_\mathrm{B}T)$. This results in the expression for the partition function[19]

$$Q = \int \mathscr{D}\mathbf{x} \exp\left[-\frac{1}{\hbar}\int_0^{\frac{\hbar}{k_\mathrm{B}T}}\left[\frac{m}{2}\left(\frac{\partial x}{\partial \tau}\right)^2 + V(x(\tau))\right]\,\mathrm{d}\tau\right]. \tag{7.8}$$

With boldface **x** we denote paths in configurational space, $\mathscr{D}\mathbf{x}$ represents an integral over all possible closed paths **x** of period $\hbar/k_BT$, m is the mass of the atoms, and x is a point in configurational space, *i.e.* the coordinates of all atoms of an atomic structure. Here we consider rotational, translational, and vibrational degrees of freedom, so x is a vector of length D for $D/3$ atoms. $V(x)$ is the potential energy, the electronic energy given by the Born–Oppenheimer approximation. The term $\frac{m}{2}\left(\frac{\partial x}{\partial \tau}\right)^2$ is a kinetic energy, which can be simplified to $\frac{1}{2}\left(\frac{\partial y}{\partial \tau}\right)^2$ if mass-weighted coordinates $y=\sqrt{m}x$ are used. With the definition of the Euclidean action

$$S_E[\mathbf{y}]=\int_0^{\frac{\hbar}{k_BT}}\left[\frac{1}{2}\left(\frac{\partial y}{\partial \tau}\right)^2+V(y(\tau))\right]\mathrm{d}\tau, \tag{7.9}$$

eqn (7.8) simplifies to $Q=\int\mathscr{D}\mathbf{y}\exp(-S_E/\hbar)$. For a practical solution of the integral in eqn (7.8), the integral along τ and the integral over all paths have to be approximated.

The integral over τ defining the Euclidean action S_E is approximated by a discretisation of $x(\tau)$ into P segments of equal length in τ, $\Delta\tau=\frac{\hbar}{k_BTP}$. With the replacement of the derivative by finite differences eqn (7.9) turns into

$$S_E(\mathbf{y})=\sum_{k=1}^{P}\left(\frac{|y_{k+1}-y_k|^2}{2(\Delta\tau)^2}+V(y_k)\right)\Delta\tau. \tag{7.10}$$

Here, y_k is a vector of all coordinates of one replica of our system, *i.e.* a vector with D components. The vector **y**, which represents the whole discretised path, is obtained by concatenating all y_k to result in a vector with PD components. The closure of the path is ensured by $y_{P+1}:=y_1$. With that, $S_E(\mathbf{y})$ is a regular function rather than the functional $S_E[\mathbf{y}]$, which depends on the continuous function $y(\tau)$. This discretisation of τ is also called the time-slicing approximation. With that, the integral over all paths, which was given rather formally as $\mathscr{D}\mathbf{y}$, is now replaced as $\int\mathscr{D}\mathbf{y}\rightarrow\int\frac{1}{\sqrt{m^{PD}}}\mathrm{d}^{PD}y$. The factor $\sqrt{m^{PD}}$ will be omitted in the next discussion since it has no influence on the resulting expression of the reaction-rate constant. Thus, the discretization turns the integral over all paths into a standard multidimensional integral over all components of all replicas along the path.

The discretised integral over all paths can be approximated numerically. One way to do so is by molecular dynamics, as done in ring-polymer molecular dynamics (RPMD),[9] reviewed in ref. 10. Here, we take a different approach: we approximate the integral by the so-called steepest-descent, or stationary-phase, or semiclassical approximation,[20] and solve the resulting integral analytically. In general, we search for solutions to the equation of motions (see below) that extremise the action, *i.e.* those solutions for which the action is stationary. However, the kinetic energy as well as the potential energy are bounded from below. Thus, there is a path $\mathbf{y}_{\mathrm{min}}$ that minimises S_{E} and, therefore, has the highest statistical weight. This path will be the dominant contribution to Q in eqn (7.8) and is called an instanton. In the steepest-descent approximation, the integral over all paths is approximated by integrating over $\mathbf{y}_{\mathrm{min}}$ and its immediate surroundings. The Euclidean action S_{E} is expanded in a Taylor series around $\mathbf{y}_{\mathrm{min}}$. The first derivative, $\partial S_{\mathrm{E}}/\partial\mathbf{y}$ vanishes, since $\mathbf{y}_{\mathrm{min}}$ is a minimum of $S_{\mathrm{E}}(\mathbf{y})$. The remaining terms are

$$S_{\mathrm{E}}(\mathbf{y}) = S_{\mathrm{E}}(\mathbf{y}_{\mathrm{min}}) + \frac{1}{2}(\mathbf{y}-\mathbf{y}_{\mathrm{min}})^T \left.\frac{\partial^2 S_{\mathrm{E}}}{\partial \mathbf{y}^2}\right|_{\mathbf{y}=\mathbf{y}_{\mathrm{min}}} (\mathbf{y}-\mathbf{y}_{\mathrm{min}}) + \mathcal{O}((\mathbf{y}-\mathbf{y}_{\mathrm{min}})^3). \quad (7.11)$$

With the abbreviation $S''_{\mathrm{E}} := \left.\frac{\partial^2 S_{\mathrm{E}}}{\partial \mathbf{y}^2}\right|_{\mathbf{y}=\mathbf{y}_{\mathrm{min}}}$ and using only harmonic terms the expression for the partition function results in

$$Q = \int_{-\infty}^{\infty} \exp[-S_{\mathrm{E}}(\mathbf{y}_{\mathrm{min}})/\hbar - \tfrac{1}{2}(\mathbf{y}-\mathbf{y}_{\mathrm{min}})^T S''_{\mathrm{E}}(\mathbf{y}-\mathbf{y}_{\mathrm{min}})/\hbar]\, \mathrm{d}^{PD}y. \quad (7.12)$$

This is a multidimensional Gaussian integral with the solution

$$Q = \sqrt{\frac{(2\pi\hbar)^{PD}}{\det S''_{\mathrm{E}}}} \exp[-S_{\mathrm{E}}(\mathbf{y}_{\mathrm{min}})/\hbar]. \quad (7.13)$$

More generally, one can formulate Q as the exponential of the Euclidean action multiplied by a fluctuation factor F, which describes the quantum fluctuations around the instanton path:

$$Q = F \exp[-S_{\mathrm{E}}(\mathbf{y}_{\mathrm{min}})/\hbar]. \quad (7.14)$$

These equations allow the calculation of partition functions in practical applications. The path $\mathbf{y}_{\mathrm{min}}$ minimises the Euclidean action, *i.e.* it solves

$$\frac{\partial S_{\mathrm{E}}}{\partial y_k} = \left(\frac{k_{\mathrm{B}}TP}{\hbar}\right)^2 (-y_{k-1} + 2y_k - y_{k+1}) + \frac{\partial V(y_k)}{\partial y_k} \overset{!}{=} 0, \quad (7.15)$$

in the discretised version, or

$$\frac{\delta S_{\mathrm{E}}}{\delta y} = -\frac{\mathrm{d}^2 y(\tau)}{\mathrm{d}\tau^2} + \frac{\partial V(y(\tau))}{\partial y} \overset{!}{=} 0. \quad (7.16)$$

for the continuous formulation, derived from eqn (7.9). Especially from the last expression, an important property of the instanton path can be deduced. Eqn (7.16) essentially states that the gradient of the potential energy equals the second derivative of the mass-weighted coordinates with respect to time, *i.e.* mass times acceleration. That is Newton's second law in the negative potential energy. Thus, $\mathbf{y}_{\mathrm{min}}$, the instanton path, is a classical closed trajectory (classical periodic orbit) on the upside-down potential energy surface. Such a classical trajectory has a constant total energy E_b. The instanton path has two turning points and re-traces itself. At the turning points, the kinetic energy of the instanton trajectory is zero. Thus, the potential energies of these points have to be equal. The total energy E_b is sometimes referred to as the tunnelling energy of the respective instanton.

7.2.3 Instanton Paths

There are different types of paths that fulfil eqn (7.15). The trivial solution corresponds to the reactant state: all replicas of the path are located in the same minimum of the potential energy surface $V(y)$. In this case, S''_{E} can be readily calculated. For large P the resulting partition function approaches that of a multidimensional quantum harmonic oscillator. This is not surprising, since we have approximated the potential energy surface in the vicinity of the path by that of a harmonic oscillator.

To describe tunnelling, a trajectory associated with the classical transition state has to be found. Indeed, a path with all replicas located at any stationary point of the potential energy surface, like a first-order saddle point, fulfils eqn (7.15). However, starting from saddle points, S_{E} can be lowered at low enough temperature by extending the path until it fulfills eqn (7.15). Such extended paths are suitable instanton paths and are unique for each temperature.

An instanton path can be regarded as the semiclassical tunnelling path with the highest statistical weight among all possible tunnelling paths at a given temperature. It generally differs from the minimum-energy path, the intrinsic reaction coordinate (IRC), by cutting corners; a short tunnelling path has a higher tunnelling probability. Thus, the most likely tunnelling path will be shorter than the minimum-energy path at the expense of a somewhat higher energy along the path. The instanton path typically does not proceed through the saddle point on the potential energy surface, see Figure 7.1.[21] This relates to other multidimensional semiclassical approaches to calculate tunnelling rates, discussed in Chapter 4 of this book. There, the paths also cut corners in order to increase the tunnelling probability. However, *ad hoc* assumptions are required by these methods to construct the path, while the instanton path is always defined by the stationary-action principle, *i.e.* eqn (7.15).

7.2.4 Rate Constants

In extended instanton paths, one eigenvalue of the matrix S''_{E} must be zero; it corresponds to cyclic exchange of the indices of the replicas or, in other words, it corresponds to time-translation invariance of Euclidean action S_{E}. Its associated eigenmode is the tangent to the instanton path. Integration along that eigenmode must be excluded from eqn (7.12), but can be handled by other means, *e.g.*, the Faddeev–Popov trick.[22] That eigenmode has one node. Consequently, there must be one lower (negative) eigenvalue. Its associated eigenmode corresponds to the movement of the whole instanton

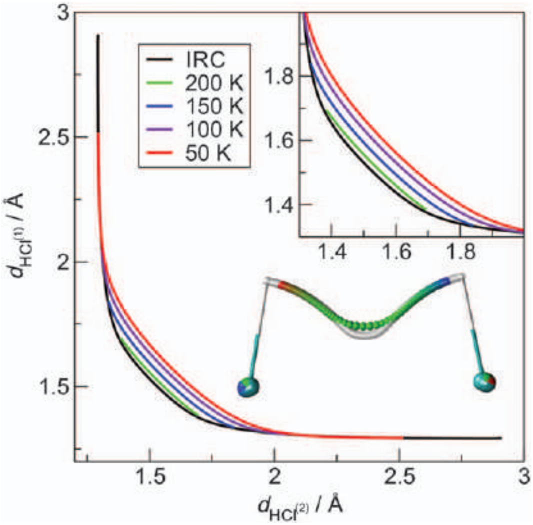

Figure 7.1 Corner cutting in the reaction of HCl + Cl → Cl + HCl; the Cl–H distances are reduced during the tunnelling process. At low temperature, the corner cutting leads to a significant reduction of the total path length. The illustration of the molecular system shows the classical intrinsic reaction coordinate (IRC, white path) and the instanton at 50 K (from red to green to blue).
Reproduced from ref. 21 with permission from the Royal Society of Chemistry.

path towards the reactant or product region. This directly corresponds to the transition mode in classical transition state theory. Integration along that eigenmode in eqn (7.12) is only possible after an appropriate analytic continuation.[1,22] It results in the partition function of the instanton becoming imaginary. Putting all these pieces together, we arrive at an expression for the rate constant in canonical instanton theory:

$$k_{\mathrm{inst}} = \frac{2k_{\mathrm{B}}T}{\hbar}\frac{\operatorname{Im} Q_{\mathrm{inst}}}{Q_{\mathrm{RS}}} = \underbrace{\sqrt{\frac{\prod_{\ell=1}^{PD}\lambda_\ell^{\mathrm{RS}}}{\prod_{\ell=2}^{PD}|\lambda_\ell^{\mathrm{inst}}|}}\sqrt{\frac{S_0 k_{\mathrm{B}} TP}{2\pi\hbar^2}}}_{F_{\mathrm{inst}}/F_{\mathrm{RS}}}\exp[-\Delta S_{\mathrm{E}}/\hbar]. \tag{7.17}$$

Here, $\lambda_\ell^{\mathrm{RS}}$ refers to the eigenvalues of S_{E}'' of the reactant, $\lambda_\ell^{\mathrm{inst}}$ to those of the instanton, $\Delta S_{\mathrm{E}} = S_{\mathrm{E}}(\mathbf{y}_{\mathrm{inst}}) - S_{\mathrm{E}}(\mathbf{y}_{\mathrm{RS}})$, and

$$S_0 = \frac{k_{\mathrm{B}}TP}{\hbar}\sum_{k=1}^{P}|y_{k+1} - y_k|^2. \tag{7.18}$$

S_0 can be interpreted as twice the kinetic-energy contribution to the Euclidean action as defined in eqn (7.10). It is a measure of the length of the path. If r is the arc length along the instanton path in mass-weighted coordinates, S_0 can also be calculated as

$$S_0 = \sqrt{8}\int_{r_a}^{r_b} \sqrt{V(r) - E_b}\,\mathrm{d}r. \tag{7.19}$$

This is twice the barrier penetration integral (or action integral), denoted θ in Chapter 4 or the quantity approximated by s in Chapter 12.

The way of calculating the fluctuation factor F in eqn (7.17) is sometimes referred to as determinant method because the whole determinant of the Hessian of the Euclidean action is used. There are alternative ways to calculate F. In some cases, they may be numerically advantageous, which is why we briefly mention them here without derivation.

The steepest-descent approximation may be used first for all replicas but one, followed by another steepest-descent approximation for that replica (pinning point).[13,23] Alternatively, the steepest-descent approximation may be done directly from eqn (7.1) to approximate the integral over E rather than from eqn (7.8) to approximate the integral over x or y, as done in eqn (7.12). The steepest descent in E leads to[6,24]

$$F = \prod_{i=1}^{D} \frac{1}{2\sinh(u_i/2)} \tag{7.20}$$

where u_i are called stability parameters. For an instanton the mode along the reaction path has to be treated separately.[25] For a Feynman path collapsed to a minimum on the PES or for a model system in which the vibrational modes perpendicular to the instanton path do not couple to the vibrations along the path, the stability parameters directly refer to the vibrational frequencies *via* $u_i = \hbar\omega_i/k_\mathrm{B}T$. However, in any real molecule, vibrations are coupled. In that case, the u_i may be obtained from the eigenvalues of the monodromy matrix.[24,26–29] Since this is numerically unstable for low temperatures, different schemes and approximations, which generally allow the calculation of u_i with sufficient accuracy for molecules with about a dozen or more atoms, have been suggested.[6,29–32] These methods, however, are beyond the scope of this chapter.

7.2.5 Unimolecular and Bimolecular Cases

The derivation of the canonical instanton rate constant has so far concentrated on the partition function of the instanton, the transition-state equivalent. The partition function of the reactant is also required to calculate the rate constant. Since the modes orthogonal to the instanton path were treated in the harmonic approximation, it makes sense to do the same for the reactant state.

In case of a unimolecular reaction, the reactant state is a single molecule, just like the instanton. For N atoms, there are $D = 3N - 6$ (or $D = 3N - 5$ for linear molecules) vibrational modes. The partition function for a D-dimensional quantum harmonic oscillator is

$$Q_{\mathrm{HO}} = F_{\mathrm{HO}} = \prod_{i=1}^{D} \frac{1}{2\sinh(\hbar\omega_i/2k_{\mathrm{B}}T)}. \tag{7.21}$$

However, in the instanton expression, we used a finite number of replicas P. To make use of error compensation it is beneficial to use an equivalent finite-P expression for the vibrational partition function of the reactant as well:

$$Q_{\mathrm{RS}} = (2\pi\hbar)^{\frac{PD}{2}} \prod_{\ell=1}^{PD} \frac{1}{\sqrt{\lambda_{\ell,\mathrm{RS}}}} \exp\left[-S_{\mathrm{E}}(\mathbf{y}_{\mathrm{RS}})/\hbar\right]. \tag{7.22}$$

The eigenvalues $\lambda_\ell^{\mathrm{RS}}$ of the Hessian matrix S''_{E} of the reactant state can directly be calculated from the Hessian of the potential energy.[33]

Rotations are generally treated by assuming perfect separability between vibrational and rotational motion using the J-shifting approach.[34] Rotation is included by using the $J=0$ partition function calculated above, multiplied by the partition function of a suitable rigid rotor. The rotor geometry of the reactant state is its minimum geometry. For the instanton, one can assume a super molecule comprised of all replicas, each weighted with $1/P$. Alternatively, the product of the rotational partition functions of all replicas can be used. Usually the former approach is used. Classical or quantum rigid rotor approaches can be used for the rotational partition function. The ratio of the translational partition functions of the reactant and the instanton is unity for unimolecular processes. With these approximations, the thermal rate constant is calculated directly without considering the decay probabilities of individual quasi-bound states of the reactant. This approach generally works fairly well.

To demonstrate the capabilities of instanton theory, we compare calculated rate constants to experimental ones, namely the decay of methylhydroxycarbene to acetaldehyde. Experimentally, half-lives ($\tau_{\frac{1}{2}} = \ln 2/k$) of 66 ± 5, 196 ± 4, and 251 ± 2 min were found[35] at 11 K in Ar, Kr, and Xe matrices, respectively. The corresponding calculated half-life is 171 min,[36] which is in good agreement with the experimental data. Unimolecular instanton rate constants usually become temperature independent at low temperature. This corresponds to tunnelling from one quantum state, the ground state of the reactant molecule.

To calculate thermal rate constants of bimolecular reactions, the partition functions of both reactants need to be considered. Their vibrational and rotational contributions are handled just like for the unimolecular case. By contrast, the ratio of the translational partition functions has to be calculated. Since the relative translation of the reactants is not quantised, the classical expression of the partition function can be used. Here, error

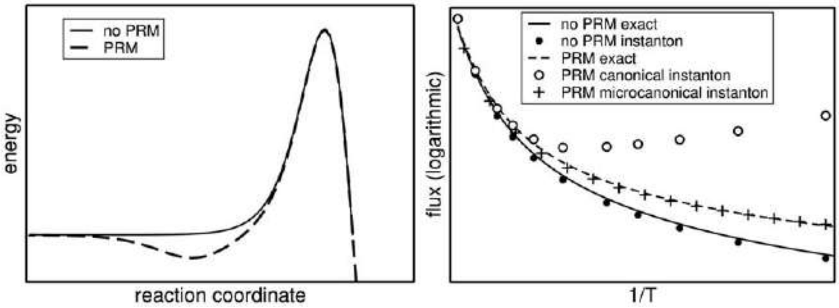

Figure 7.2 Flux through a potential with and without pre-reactive minimum (PRM). Left: potential, right: flux.

cancellation cannot be exploited as efficiently as in the unimolecular case. Three rotational and three translational modes of the reactant change into six vibrational modes of the transition states. Thus, more replicas are sometimes needed to converge the results.

To show the degree of accuracy that can be achieved, we compare rate constants for the gas-phase reaction $H_2 + OH \rightarrow H_2O + H$ calculated with instanton theory and with the multiconfigurational time-dependent Hartree approach (MCTDH) discussed in Chapter 10 of this book. Both were obtained with the NN1 potential energy surface.[37] Details of the calculations are given in ref. 38 for instanton theory and ref. 39 for MCTDH. A graph comparing the rate constants is given in Figure 10.7. Between 200 K and 150 K the rate constants of MCTDH and instanton theory differ by less than 20%.

There is an additional issue with bimolecular rate constants in canonical instanton theory. The potential energy surfaces of many bimolecular systems exhibit a pre-reactive potential minimum, see Figure 7.2. Such a minimum may be caused by van der Waals interactions between the molecules. At low pressure, the molecules will generally not thermalise in this shallow minimum but rather dissociate. However, canonical instanton theory assumes thermal equilibration throughout the whole reaction path. That means, the instanton will, at low temperature, reach into the pre-reactive potential well and describe the tunnelling out of this well. Since the well is energetically lower than the asymptotic reactant state of separated molecules, the resulting rate constants are overestimated and, in fact, diverge to high values for low temperatures.[40]

One way to resolve such a dilemma is to adopt a microcanonical approach to instanton theory. In this approach the cumulative reaction probability $N(E)$ is calculated and used in eqn (7.1) rather than its thermal average. The underlying microcanonical theory is rather different[6,24,29,31,41,42] from canonical instanton theory, since the derivation using partition functions, as done in eqn (7.6) and (7.7), is no longer appropriate. However, the outcome is similar to an algorithmic point of view. To calculate $N(E)$, one has to find an instanton with the energy of its turning points E_b being equal to E. Then, $N(E)$ is given by[6]

$$N(E) = \sum_{k=1}^{\infty} (-1)^{k-1} \exp[-kS_0(E_b)/\hbar] \times \prod_{i=1}^{D-1} \frac{1}{2\sinh(ku_i(E_b)/2)}. \qquad (7.23)$$

Thus, in order to calculate $N(E)$ instantons at different energies E_b have to be found and their stability parameters u_i have to be calculated. It is much easier, however, to optimise an instanton for a given temperature rather than for a given energy E_b. Thus, generally, a set of pre-defined temperatures is chosen such that an approximately evenly distributed set of energies results. These are then used for the thermal average in eqn (7.1) with a canonical ensemble appropriate for the reactant state.

The effects of a microcanonical treatment are visualised in Figure 7.2 for a simple one-dimensional example. We calculated the flux rather than the rate constant, because it is independent of the reactant state. An Eckart potential was chosen as an example for a PES without a pre-reactive minimum (PRM), since for this potential the exact analytic quantum flux is known. The exact flux was furthermore calculated by back-propagation of a transmitted wave function, which agrees very well with the exact flux (not shown). Back-propagation can also be used for the potential with a PRM. For the potential without PRM (solid lines in Figure 7.2), thermal instanton rate constants match those of the exact solution quite accurately. With a PRM, the canonical instanton flux is accurate at high temperature (to the left of the right-hand graph) but deviates strongly from the back-propagation results at low temperature, when the instanton starts to spread into the PRM. The flux calculated *via* a microcanonical instanton approach (plus signs) is accurate over the whole temperature range.

7.2.6 Tunnelling Splittings

The splitting of vibrational levels in molecules with two or more symmetry-equivalent minima on the PES is caused by tunnelling between these minima. Just like the tunnelling reaction between different minima, such tunnelling processes can be described using instanton theory.[43–50] While the temperature has a direct meaning in canonical instanton theory, the tunnelling splitting Δ is obtained for the limit of $T \to 0$.

$$\Delta = \lim_{T\to 0} 2\hbar \sqrt{\frac{S_0}{4\pi\hbar}} \sqrt{\frac{\det S''_\mathrm{E}(\mathrm{min})}{\det S''_\mathrm{E}(\mathrm{inst})}} \exp[-S_0/2\hbar] \qquad (7.24)$$

with S''_E calculated at one of the minima and at the instanton path connecting these minima, respectively. Eqn (7.24) is applicable to the splitting of the vibrational ground state. Splitting of excited states are available *via* extensions of the theory.[47]

Compared to rate constants, tunnelling splittings can be measured with much higher accuracy. This reduces the applicability of instanton theory for tunnelling splittings due to its intrinsic error. However, valuable insight could still be obtained in certain cases.[51]

7.3 Implementation and Practical Use

Here we will discuss which steps have to be taken to calculate rate constants or tunnelling splittings using instanton theory for realistic small- to medium-sized molecules (*i.e.* up to maybe 30 atoms). The largest number of atoms for which an instanton calculation has been performed was, to the authors' knowledge, 78 active atoms.[52] However, fewer active atoms are generally sufficient, since the tunnelling motion often concentrates on rather few atoms. The description provided here is meant to be generally applicable, but follows the authors' implementation in the open-source DL-FIND code.[53] Rate constants are typically required at a series of temperatures, while for tunnelling splittings, the limit to zero temperature is required. Here we will not discuss technical details of the implementation.

The initial step is generally to locate a saddle point on the potential energy surface with standard saddle-point search algorithms. Using transition state theory, an initial estimate of the rate constant can be obtained. Additionally, the crossover temperature T_c can be obtained from the absolute value of the imaginary vibrational frequency ω_b

$$T_\mathrm{c} = \frac{\hbar\ \omega_b}{2\pi k_\mathrm{B}}. \tag{7.25}$$

Above this temperature, the instanton is in general collapsed to a point. Below T_c, it spreads out and the canonical instanton theory as described above can be applied. The crossover temperature is also a qualitative estimate below which temperature tunnelling contributes significantly to the rate constant. From eqn (7.25) it is clear that for any reaction with a barrier frequency larger than about 1300 cm^{-1}, atom tunnelling will play a significant role at room temperature. This estimate is valuable to decide if instanton calculations are actually necessary.

The next step is to optimise an instanton path at one chosen temperature. A temperature close to, but below T_c is typically a good choice. An appropriate initial guess for the instanton path is to spread the images along the unstable vibrational mode of the saddle point.[54] To optimise the instanton, the gradient of the Euclidean action, eqn (7.15), is minimised. To achieve that, the gradient at each replica along the instanton path is calculated in each optimisation step. The breakthrough of instanton theory as a generally applicable tool to calculate rate constants in chemistry and surface science came when it was realised that the search for an instanton path is a saddle-point search problem.[55,56] It turned out that re-using the Hessians of the saddle point or previous instanton rate calculations at different temperatures yields a quadratically converging optimisation algorithm for instanton paths.[33,54] Therefore, the path search is typically no longer the time-critical step in instanton calculations (the subsequent Hessian calculations are time critical instead).

Once an instanton path is found which fulfils eqn (7.15) to a sufficient degree the instanton rate constant can be calculated. This can be done by using eqn (7.17) or by calculating the fluctuation factor F using eqn (7.20). In either case, the Hessians of the potential energy with respect to the coordinates of all atoms in all replicas have to be calculated. While all replicas can be treated in parallel it is still rather time consuming in general.

Now the process can be repeated for lower temperatures. The converged instanton path serves as starting point for the subsequent path search. The resulting rate constants have to be converged with respect to P. The lower the temperature, the more replicas are generally required. Sometimes, several hundreds are used. Especially on potential energy surfaces which contain intrinsic numerical noise, as those obtained on-the-fly from electronic structure calculations, the convergence of the path search at very low temperature may be impeded. It turns out that subsequent instanton searches at different temperatures lead to many repeated energy, gradient, and Hessian calculations at very similar structures. This is enhanced by many replicas accumulating close to the reactant-state minimum at low temperature. Approaches to re-distribute the replicas have been proposed.[33,57] However, a local interpolation or approximation of the potential energy surface, which has been done with different machine-learning approaches,[58–61] seems to be more promising.

Canonical instanton theory can only be applied below the crossover temperature T_c. Close to T_c, the rate constant is overestimated by up to a factor of two. In many cases, especially if one attempts to calculate kinetic isotope effects in biological systems,[52] the contribution of tunnelling around that temperature is important. One way to extend instanton theory to the full temperature range is to employ microcanonical instanton theory. However, extensions of canonical instanton theory to higher temperature were proposed.[27,62–65] Such corrections are recommended for all instanton rate constants close to T_c and enable a smooth continuation to higher temperatures.

It must be stressed that instanton theory, especially in its semiclassical formulation discussed here, is an approximative method. It has an intrinsic error compared to exact quantum theories. However, that error is generally rather small compared to any error caused by the underlying potential energy surface. The computational requirements of instanton path searches and calculations of the rate constants often restrict the choice of the electronic structure method. Since repeated Hessian calculations at rather similar geometries are required to calculate instanton rate constants, as mentioned above, machine learning techniques are increasingly used to approximate these.[58–61] However, dual-level schemes, which have been applied successfully in computational chemistry, can also be used in instanton rate calculations. In practice it works quite well, as demonstrated for a number of cases.[66] The basic assumption is that a fast but inaccurate electronic structure method can reproduce geometries quite well, while it may fail at reproducing exact energies. Thus, such a fast method is used for locating the instanton geometry, while a more accurate and computationally more expensive method is used to calculate the energies along the path. This approach significantly reduces the number of energy calculations and avoids all gradient calculations with the more accurate method.

7.4 Conclusions

Overall, instanton theory is a promising compromise between accuracy and computational efficiency. Canonical instanton theory can be used to calculate thermal rate constants below T_c. Corrections are required close to T_c; computationally efficient extensions are available above it. Microcanonical instanton theory can be applied over the whole temperature range and is preferable for low-pressure gas-phase rate constants at low temperature. Tunnelling splittings of vibrational levels can be obtained. The advantages of instanton theory have led to a sharp increase in its use in chemistry, biochemistry, astrochemistry, materials science, surface science and related fields, as well as increased availability of standard codes in the last decade.

Acknowledgements

This work was financially supported by the Deutsche Forschungsgemeinschaft (DFG, German Research Foundation) under Germanys Excellence Strategy EXC-2075 390740016 and the European Union's Horizon 2020 research and innovation programme (grant agreement No. 646717, TUNNELCHEM).

References

1. J. S. Langer, *Ann. Phys.*, 1967, **41**, 108.
2. J. S. Langer, *Ann. Phys.*, 1969, **54**, 258–275.
3. C. G. Callan Jr. and S. Coleman, *Phys. Rev. D*, 1977, **16**, 1762.
4. I. Affleck, *Phys. Rev. Lett.*, 1981, **46**, 388–391.
5. V. A. Benderskii, D. E. Makarov and C. A. Wight, *Adv. Chem. Phys.*, 1994, **88**, 55.
6. W. H. Miller, *J. Chem. Phys.*, 1975, **62**, 1899.
7. S. Coleman, *Phys. Rev. D*, 1977, **15**, 2929.
8. J. O. Richardson, *J. Chem. Phys.*, 2016, **144**, 114106.
9. I. R. Craig and D. E. Manolopoulos, *J. Chem. Phys.*, 2005, **122**, 084106.
10. S. Habershon, D. E. Manolopoulos, T. E. Markland and T. F. Miller, *Annu. Rev. Phys. Chem.*, 2013, **64**, 387–413.
11. J. Kästner, *WIREs Comput. Mol. Sci.*, 2014, **4**, 158.
12. J. Meisner and J. Kästner, *Angew. Chem., Int. Ed.*, 2016, **55**, 5400–5413.
13. J. O. Richardson, *Int. Rev. Phys. Chem.*, 2018, **37**, 171–216.
14. W. H. Miller, Y. Zhao, M. Ceotto and S. Yang, *J. Chem. Phys.*, 2003, **119**, 1329.
15. J. Vaníček, W. H. Miller, J. F. Castillo and F. J. Aoiz, *J. Chem. Phys.*, 2005, **123**, 054108.
16. G. Gamow, *Z. Phys.*, 1928, **51**, 204.
17. A. Bohm, M. Gadella and G. B. Mainland, *Am. J. Phys.*, 1989, **57**, 1103.

18. R. de la Madrid and M. Gadella, *Am. J. Phys.*, 2002, **70**, 626.
19. R. Feynman and A. Hibbs, *Quantum Mechanics and Path Integrals*, MacGraw Hill, New York, 1975.
20. W. H. Miller, *J. Chem. Phys.*, 1971, **55**, 3146–3149.
21. J. Meisner, M. N. Markmeyer, M. U. Bohner and J. Kästner, *Phys. Chem. Chem. Phys.*, 2017, **19**, 23085–23094.
22. H. Kleinert, *Path Integrals in Quantum Mechanics, Statistics, Polymer Physics, and Financial Markets*, World Scientific, 5th edn, 2009.
23. S. C. Althorpe, *J. Chem. Phys.*, 2011, **134**, 114104.
24. S. Chapman, B. C. Garrett and W. H. Miller, *J. Chem. Phys.*, 1975, **63**, 2710.
25. R. G. Littlejohn, *J. Math. Phys.*, 1990, **31**, 2952–2977.
26. M. C. Gutzwiller, *J. Math. Phys.*, 1971, **12**, 343–358.
27. M. Kryvohuz, *J. Chem. Phys.*, 2011, **134**, 114103.
28. M. Ceotto, *Mol. Phys.*, 2012, **110**, 547–559.
29. A. Löhle and J. Kästner, *J. Chem. Theory Comput.*, 2018, **14**, 5489–5498.
30. J. O. Richardson, *J. Chem. Phys.*, 2015, **143**, 134116.
31. S. R. McConnell, A. Löhle and J. Kästner, *J. Chem. Phys.*, 2017, **146**, 074105.
32. P. Winter and J. O. Richardson, *J. Chem. Theory Comput.*, 2019, **15**, 2816–2825.
33. J. B. Rommel and J. Kästner, *J. Chem. Phys.*, 2011, **134**, 184107.
34. J. M. Bowman, *J. Phys. Chem.*, 1991, **95**, 4960–4968.
35. P. R. Schreiner, H. P. Reisenauer, D. Ley, D. Gerbig, C.-H. Wu and W. D. Allen, *Science*, 2011, **332**, 1300.
36. J. Kästner, *Chem. – Eur. J.*, 2013, **19**, 8207–8212.
37. J. Chen, X. Xu, X. Xu and D. H. Zhang, *J. Chem. Phys.*, 2013, **138**, 154301.
38. J. Meisner and J. Kästner, *J. Chem. Phys.*, 2016, **144**, 174303.
39. R. Welsch, *Angew. Chem., Int. Ed.*, 2018, **57**, 13150–13153.
40. S. Álvarez-Barcia, M.-S. Russ, J. Meisner and J. Kästner, *Faraday Discuss.*, 2016, **195**, 69–80.
41. J. O. Richardson, *Faraday Discuss.*, 2016, **195**, 49–67.
42. J. O. Richardson, *J. Chem. Phys.*, 2018, **148**, 200901.
43. Z. Smedarchina, W. Siebrand and M. Z. Zgierski, *J. Chem. Phys.*, 1995, **103**, 5326.
44. V. A. Benderskii, E. V. Vetoshkin, L. von Laue and H. P. Trommsdorff, *Chem. Phys.*, 1997, **219**, 143–160.
45. C. S. Tautermann, A. F. Voegele, T. Loerting and K. R. Liedl, *J. Chem. Phys.*, 2002, **117**, 1962.
46. C. S. Tautermann, A. F. Voegele, T. Loerting and K. R. Liedl, *J. Chem. Phys.*, 2002, **117**, 1967.
47. G. V. Mil'nikov and H. Nakamura, *J. Chem. Phys.*, 2005, **122**, 124311.
48. G. Mil'nikov and H. Nakamura, *Phys. Chem. Chem. Phys.*, 2008, **10**, 1374–1393.
49. J. O. Richardson and S. C. Althorpe, *J. Chem. Phys.*, 2009, **131**, 214106.
50. J. O. Richardson and S. C. Althorpe, *J. Chem. Phys.*, 2011, **134**, 054109.

51. J. O. Richardson, C. Pérez, S. Lobsiger, A. A. Reid, B. Temelso, G. C. Shields, Z. Kisiel, D. J. Wales, B. H. Pate and S. C. Althorpe, *Science*, 2016, **351**, 1310–1313.
52. J. B. Rommel, Y. Liu, H.-J. Werner and J. Kästner, *J. Phys. Chem. B*, 2012, **116**, 13682.
53. J. Kästner, J. M. Carr, T. W. Keal, W. Thiel, A. Wander and P. Sherwood, *J. Phys. Chem. A*, 2009, **113**, 11856–11865.
54. J. B. Rommel, T. P. M. Goumans and J. Kästner, *J. Chem. Theory Comput.*, 2011, **7**, 690.
55. A. Arnaldsson, Ph.D. thesis, University of Washington, 2007.
56. S. Andersson, G. Nyman, A. Arnaldsson, U. Manthe and H. Jónsson, *J. Phys. Chem. A*, 2009, **113**, 4468.
57. D. M. Einarsdóttir, A. Arnaldsson, F. Óskarsson and H. Jónsson, *Lecture Notes in Computer Science*, **vol. 7134**, 2012, p. 45.
58. A. M. Cooper, P. P. Hallmen and J. Kästner, *J. Chem. Phys.*, 2018, **148**, 094106.
59. G. Laude, D. Calderini, D. P. Tew and J. O. Richardson, *Faraday Discuss.*, 2018, **212**, 237–258.
60. S. R. McConnell and J. Kästner, *J. Comput. Chem.*, 2019, **40**, 866–874.
61. A. M. Cooper and J. Kästner, *J. Phys. Chem. A*, 2019, **123**, 9061–9068.
62. M. Kryvohuz and R. A. Marcus, *J. Chem. Phys.*, 2012, **137**, 134107.
63. M. Kryvohuz, *J. Chem. Phys.*, 2013, **138**, 244114.
64. Y. Zhang, J. B. Rommel, M. T. Cvitaš and S. C. Althorpe, *Phys. Chem. Chem. Phys.*, 2014, **16**, 24292–24300.
65. S. McConnell and J. Kästner, *J. Comput. Chem.*, 2017, **38**, 2570–2580.
66. J. Meisner and J. Kästner, *J. Chem. Theory Comput.*, 2018, **14**, 1865–1872.

CHAPTER 8

Semiclassical Multidimensional Tunnelling Calculations

DONALD G. TRUHLAR

Department of Chemistry, Chemical Theory Center, and Minnesota
Supercomputing Institute, University of Minnesota, 207 Pleasant St. SE,
Minneapolis, MN 55455-0431, USA
Email: truhlar@umn.edu

8.1 Introduction

Quantum mechanical tunnelling is one of the earliest studied phenomena that is qualitatively different in quantum mechanics and classical mechanics. It was first proposed for electrons by Hund in his studies of electrons or atoms penetrating a potential barrier,[1–3] by several others in molecular and solid-state physics,[3] and most famously by Gamow in the context of the escape of α particles from the nucleus,[3–6] but it was slow to be widely appreciated in chemical kinetics. In a broad review of general and physical chemistry in 1932, it was stated[7] that "Chemical differences between hydrogen and diplogen [as the authors called deuterium] are to be expected on theoretical grounds for several reasons, but the dominating factor is likely to be the smaller half-quantum of zero-point energy possessed by diplogen in virtue of its greater mass." Notably there is no mention of tunnelling in this generalization. A similar review in 1934 has large sections on deuterium and kinetics, but tunnelling is again not mentioned.[8] The role of tunnelling in chemical reactions seems to have first been speculated by Applebey and Ogden in 1936[9] and discussed more fully by Bell at a Faraday Discussion in 1938,[10] who advanced it as a possible cause of nonlinear

---

Theoretical and Computational Chemistry Series No. 18
Tunnelling in Molecules: Nuclear Quantum Effects from Bio to Physical Chemistry
Edited by Johannes Kästner and Sebastian Kozuch

Published by the Royal Society of Chemistry, www.rsc.org

Arrhenius plots. His discussion, however, takes no cognizance of transition state theory, and he discusses tunnelling as a one-dimensional phenomenon governed by the raw potential energy surface, an oversimplification that continued to be made by many workers for many decades into the future. Bell stated, ''So far no evidence has been produced that directly demonstrates the presence of the 'tunnel effect.'' At the same Faraday Discussion, Wigner[11] explained how tunnelling could lead to a leveling out of Arrhenius plots at low temperature, leading to a smaller pre-exponential factor, but concluded that ''apart from reactions involving H, the tunneling effect cannot be made responsible at ordinary temperatures for any large decrease of the temperature independent factor.''

Nevertheless, there was valuable theoretical work on tunnelling in the 1930s. Already, in 1932, Wigner[12] showed how classical transition state theory, with the transition state at the saddle point, could be quantized to the lowest order, $O(\hbar^2)$, in $\hbar$, including the leading term due to tunnelling. And Bell, in 1933,[13] derived the tunnelling probability for a one-dimensional Eckart barrier and concluded that calculations in the literature on ortho-para conversion in hydrogen were ''probably in error'' due to neglect of tunnelling. Bell said ''The barrier is treated as one-dimensional. This is permissible, since there is in general a definite direction of approach of two reacting molecules for which the activation energy is a minimum,'' which is generally not a good approximation, as discussed below. He also said ''It is concluded that a quantum-mechanical treatment is necessary for any reaction involving the motion of a hydrogen atom or proton, while heavier atoms may be considered to behave classically,'' which is very true as a general rule, noting that general rules usually have some exceptions (and indeed there are some ''exceptional'' cases of non-hydrogenic tunnelling), although it took decades before the community routinely took this into account.

Moving ahead in time, I note a 1970 review on proton transfer reactions, where Caldin said ''The question is not whether tunnelling occurs, but whether it is detectable.'' In the same article Caldin said, ''The first definite indication that the tunnel effect was significant in controlling the rate of a reaction in solution was published in 1956'' by Bell *et al.*[14] in their study of the deuterium kinetic isotope effect in the base-catalyzed bromination of 2-carbethoxycyclopentanone. Caldin also concluded that ''The tunnel effect is by now the likeliest interpretation of the evidence on several reactions,'' with which I agree. However, he added ''It remains true that such reactions appear to be exceptional and that in most proton-transfer reactions the tunnelling corrections can probably be ignored,'' with which I disagree. In my opinion, theoretical work has now established that it is most likely that any hydrogen-atom transfer or proton transfer with a barrier of about 5 kcal mol^{-1} or higher is probably dominated by tunnelling at room temperature and below (and often too much higher temperatures), and the burden of proof in interpreting experiments on such reactions should shift from ''Is there any evidence of tunnelling?'' to asking if there is any reason to doubt that the reaction is dominated by tunnelling, since that is the usual finding when such reactions are examined with modern theoretical analysis. The goal of this chapter is to review the methods used to calculate tunnelling probabilities realistically.

8.2 Theory

In 1970, LeRoy *et al.*[15] showed that the tunnelling probability for realistic shapes of potential energy barriers could differ significantly from tunnelling by an Eckart barrier or the even simpler parabolic approximation. The inadequacy of an Eckart barrier is also discussed in other papers.[16,17] Nevertheless, one still sees papers in the current literature using the approximation of an Eckart barrier. However, in order to obtain a more accurate tunnelling probability, it is necessary not just to use a realistic shape of the potential energy barrier, but also to go beyond the one-dimensional tunnelling model to obtain an effective potential or an ensemble of effective potentials.

Johnston and Rapp[18] were the first to try to include multidimensional effects in tunnelling, and Johnston described their method as resulting from "several bold assumptions about the appropriate tunnelling path or paths."[19] This is very stimulating work, but the method itself is not quantitative and is only of historical interest.

Attempts to treat quantum mechanical tunnelling more accurately were held back by two factors: (i) the lack of appreciation of how to include quantum effects in transition state theory so that one could test predictions against experimental rate constants and kinetic isotope effects (or accurate theoretical results, when they became available) and (ii) insufficient knowledge of potential energy surfaces. The first impediment involved understanding what we now call quasiclassical transition state theory. Quasiclassical transition state theory refers to calculating all partition functions quantum mechanically but treating the reaction coordinate (which does not appear in the transition state partition function because it is the degree of freedom missing in the transition state) classically; quantizing the partition functions of bound modes was done already by Wigner in 1932[12] and was assumed in Eyring's classic paper of 1935.[20] A convenient name for the set of modes excluding the reaction coordinate is the "modes transverse to the reaction coordinate", and we can say that Eyring quantized the transverse modes.

The above-mentioned papers dealt with canonical transition state theory, *i.e.*, the evaluation of rate constants for a canonical ensemble characterized by a temperature. To treat tunnelling rigorously one needs at least a microcanonical theory where the dynamics are calculated for each total energy (which is a parameter in the time-independent Schrödinger equation) and then thermally averaged. More specifically one must ask the question of what reaction probabilities are implied by quasiclassical transition state theory, and then one could ask how to modify these reaction probabilities by including energy-dependent tunnelling probabilities. It was shown, first partially[21,22] and then more completely,[23] that transition state theory corresponds to an adiabatic treatment of all motions except the reaction coordinate; adiabaticity in this context means that their quantum numbers are conserved as the system proceeds along the reaction path (where the reaction coordinate measures progress along the reaction path). In fact, it was later shown that a calculation assuming such adiabaticity leads to microcanonical variational transition state theory, in which the transition state dividing surface is chosen to minimize the flux through the transition state for each total energy, rather than conventional transition state theory, where the transition state dividing surface is located at the saddle point.[24,25]

It is conventional to add tunnelling to transition state theory by multiplying by a transmission coefficient that makes up for the simplifications inherent in quasiclassical transition state theory. In general there can be several contributions to the transmission coefficient, including the correction for the breakdown of the equilibrium assumption of transition state theory, correction for the breakdown of the no-recrossing approximation of transition state theory (*i.e.*, that the net flux through the transition state dividing surface is equal to the one-way flux, which in classical mechanics would mean that trajectories do not recross the transition state dividing surface), and correction for the classical treatment of the reaction coordinate. One can consider the overall transmission coefficient to be a product of three correction factors corresponding to these effects.[26] The third factor is called the tunnelling transmission coefficient, and it is the one of primary interest here. The tunnelling transmission coefficient may be defined as the ratio of the reaction rate calculated when reaction-coordinate motion is treated quantum mechanically to that calculated when it is treated classically. The considerations in the previous paragraph imply that the tunnelling correction to transition state theory should involve barrier heights determined by adding zero point energy in modes transverse to the reaction coordinate to the potential energy surface along reaction paths. The simplest general version of such a theory is as follows. One starts by calculating a steepest descents path down from the saddle (both toward reactants and toward products) in isoinertial coordinates, which are coordinates scaled so that the reduced mass is the same in all directions.[16,25] We call such a path the minimum-energy path[25] (MEP); it is also often called the intrinsic reaction coordinate[27] (IRC, although a more semantically correct name would be intrinsic reaction path). One usually then makes (often only implicitly) the ground-state tunnelling approximation, which is simply that the tunnelling transmission coefficient is calculated for ground-state reactions but used for all reactions, even those that do not emanate from the ground state of the reactants. For reaction from the ground state, one adds the local zero point energy in transverse modes all along the path, which replaces the potential energy barrier by the vibrationally adiabatic ground-state barrier. [The potential energy along the reaction path is the Born–Oppenheimer potential along that path and is called $V_{\mathrm{MEP}}(s)$; the highest point of $V_{\mathrm{MEP}}(s)$ occurs at the saddle point, and subtracting the value at reactants yields what is called classical barrier height. The barrier maximum on the ground-state vibrationally adiabatic potential curve, which is called $V_{\mathrm{a}}^{\mathrm{G}}(s)$, is not necessarily at the saddle point, and the barrier height, again obtained by subtracting the value at reactants, may be greater or smaller than the classical barrier height.] Given the vibrationally adiabatic barrier, one then calculates the tunnelling as if the reaction path were rectilinear, which is an approximation since the reaction path is curved and the kinetic energy operator is different in curvilinear coordinates. This simple scheme, first reported in 1971,[16] has been called by several names, such as the vibrationally adiabatic zero-curvature approximation, the vibrationally adiabatic ground-state approximation, and the minimum-energy-path adiabatic approximation; I here call it the zero-curvature tunnelling (ZCT) approximation, which is a name for it that we have used in many papers since 1991.

Note that although the ZCT approximation involves a one-dimensional tunnelling calculation, it is actually a multidimensional tunnelling approximation because the vibrationally adiabatic potential used along the reaction path involves contributions from the transverse modes. Furthermore, these contributions vary with the distance *s* along the reaction path. If the reaction coordinate were separable, as assumed in quasiclassical transition state theory, these contributions would, by the definition of separability, be independent of *s*. Hence the tunnelling transmission coefficient corrects not just for quantum effects but for non-separability. (Whereas the tunnelling transmission coefficient corrects for quantal non-separability, one may consider that the recrossing transmission coefficient, which is the second factor mentioned above, corrects for classical non-separability since trajectories would not recross the dividing surface if the reaction coordinate were separable.)

The second impediment to progress in tunnelling theory for chemical kinetics began to disappear when accurate calculations of the $H + H_2$ potential energy surface finally appeared. Early work on the potential energy surface for this reaction was clouded by the question of whether there was a single symmetric barrier or two asymmetric barriers on either side of a well sometimes called "Lake Eyring"; predictions of asymmetric saddle points persisted as late as 1967, as reviewed elsewhere.[28] Nevertheless, the Porter–Karplus surfaces of 1964,[29] with a collinear symmetric saddle point, correctly became accepted as qualitatively correct. Another important advance critical to the development of accurate methods for quantum mechanical tunnelling was the calculation of accurate quantum mechanical rate constants for the collinear $H + H_2$ reaction, which is a two-dimensional problem.[30] These rate constants now allowed the testing of approximate tunnelling methods against accurate quantum mechanics in more than one dimension. One immediately found that ZCT tunnelling is inaccurate, leading to rate constants underestimated by factors of 19 and 3.4 at 200 and 300 K, respectively. This was a serious impasse for theory, and it was argued that it was due either to the breakdown of the adiabatic approximation or the assumption of zero curvature.[30] (We now know that the latter is the chief culprit.)

The impasse began to be resolved in 1977 when Marcus and Coltrin[31] proposed a new tunnelling path for collinear $H + H_2$. This path corresponded to a path along the vibrational turning points on the concave side of the reaction path, and they justified this path based on a semiclassical argument (the Wentzel–Kramers–Brillouin (WKB) approximation) in which the decay of the probability density $|\psi|^2$ in a classically forbidden region is $e^{-2\theta}$ where θ is an action integral given by

$$\begin{aligned}\theta &= \int_{\text{tunnelling region}} \mathrm{d}\xi \left|p_{\xi,\text{eff}}\right| \\ \theta &= \int_{\text{tunnelling region}} \mathrm{d}\xi \sqrt{2\mu(E - V_{\text{eff}}(\xi))}\end{aligned} \tag{8.1}$$

where ξ measures distance (in the isoinertial coordinate system) along the tunnelling path, $p_{\xi,\text{eff}}$ is the ξ-component of the effective momentum, μ is the reduced mass to which the isoinertial coordinates are scaled, E is the energy, and $V_{\text{eff}}(\xi)$ is the effective potential. Since $V_{\text{eff}}(\xi) > E$ in a tunnelling region, $p_{\xi,\text{eff}}$ is imaginary, and this is an imaginary-action integral. The semiclassical argument is basically that any path within the zero-point vibrational amplitude (transverse to the MEP) has the same effective potential for tunnelling, namely the ground-state vibrationally adiabatic potential curve, also called $V_a^G(s)$. Therefore, in isoinertial coordinates, the path with the least exponential decay, *i.e.*, the dominant path, is the shortest path, *i.e.* (for smooth MEPs with smoothly changing local zero-point energy), the path is along the concave-side vibrational turning points. Later work showed that it is best to calculate the tunnelling along such a dominant path rather than averaging over many paths within the width of the vibrational wave packet.[32] The Marcus–Coltrin path was generalized to treat the $H + H_2$ reaction in the real three-dimensional world,[33] and again good results were obtained.

Because this approach involves a path on the concave side of the reaction path, it may be called a corner-cutting tunnelling approximation. Path curvature in classical mechanics leads to a system veering to the convex side of the path, as occurs at the first turn of a bobsled run. The direction of the effect gets turned around in quantum tunnelling, leading to motion on the concave side of the MEP. This is sometimes called the quantum bobsled effect.

Two technical issues needed to be resolved to make the method practical and accurate for general polyatomic reactions. First, the distance to the vibrational turning point sometimes exceeds the distance at which curvilinear coordinates attached to the reaction path become multivalued. This was solved[34] by reformulating the theory in terms of an effectively reduced mass so that the integration is carried out along the MEP instead of along the actual dominant tunnelling path:

$$\begin{aligned}\theta &= \int_{\text{tunnelling region}} \mathrm{d}s \left|p_{s,\text{eff}}\right| \\ \theta &= \int_{\text{tunnelling region}} \mathrm{d}s \sqrt{2\mu_{\text{eff}}(s)(E - V_a^G(s))}\end{aligned} \tag{8.2}$$

where μ_{eff} is smaller than μ in regions where the reaction path is curved. Because the tunnelling path can lie in a region where the coordinate system based on the MEP is multivalued, the actual tunnelling path is not well defined in this method, but μ_{eff} is well defined and is formulated such that eqn (8.1) and (8.2) give the same result in the limit where the MEP has small curvature; in such a limit the concave side vibrational turning point is in the region describable by the curvilinear coordinates based on s. However, μ_{eff} is also defined such that it remains well defined and smooth in all cases and is generally applicable.[34]

The three-dimensional $H + H_2$ reaction has three transverse vibrational modes, but the curvature (which is a vector) has only a single nonzero component because the reaction path is collinear and so it never curves into the bending coordinate directions. The reaction path of a general polyatomic reaction, though, has multidimensional curvature. The second technical issue to be resolved in turning the Marcus–Coltrin idea into a general scheme concerned the physically correct calculation of the amount of corner cutting when there is multidimensional reaction path curvature. When this was done properly,[35,36] the method was called the centrifugal-dominant small-curvature semiclassical adiabatic ground-state approximation, but the shorter name of small-curvature tunnelling (SCT) approximation soon replaced the long one.

Marcus and Coltrin had pointed out that their physical model would break down for the common mass combination where a hydrogen or proton tunnels between two massive molecular subsystems,[31] and later Babamov and Marcus[37,38] (following earlier qualitative considerations by Marcus[39]) presented another approximation designed to treat the transfer of a hydrogen atom or proton between two heavier particles in a collinear reaction using polar coordinates. In order to understand why a different treatment is needed for this case, it is useful to consider what the potential energy surface and MEP for a bimolecular atom transfer reaction look like when plotted in isoinertial coordinates. Figure 8.1 illustrates the key points. On the left we see that the reaction valley and the product valley are perpendicular when plotted *vs.* the bond distances of the forming and breaking bonds. However, this is not the case in isoinertial coordinates. The angle between the reactant valley and the product valley in isoinertial coordinates is called the skew angle β, and for a reaction of the form $A + BC \rightarrow AB + C$, where A, B, and C are atoms, molecules, or molecular fragments (B is a hydrogen atom or a proton for the cases of most interest here) it is given by

$$\beta = \arccos\lfloor m_A m_C / m_{AB} m_{BC} \rfloor \tag{8.3}$$

where m_X is the mass of X. We see that $\beta = 60^\circ$ for the case of equal masses (center panel of Figure 8.1), but it gets very small ($\cos\beta \approx 1$) when $m_B \ll m_A$ and $m_B \ll m_C$ (rightmost panel of Figure 8.1). Figure 8.1 shows that a large skew angle corresponds to low curvature of the MEP, and a small skew angle corresponds to large curvature of the MEP. With this in mind, it is also useful to review the motivation for using isoinertial coordinates. If we did not use isoinertial coordinates, the reduced mass in eqn (8.1) would be a function of the location on the curvilinear tunnelling path. To find the optimized tunnelling path, one would have to find the best compromise of a

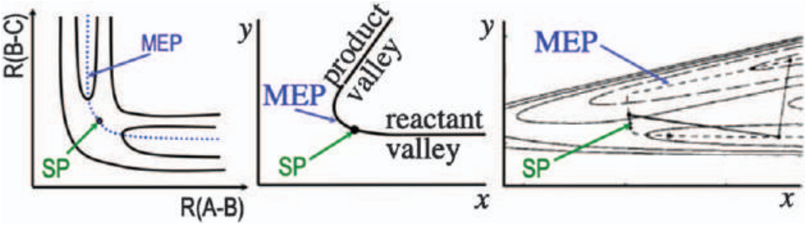

Figure 8.1 Three views of the potential energy contours and minimum energy path (MEP) for $A+BC \rightarrow AB+C$ reactions. The saddle point (SP) is also labeled. Left: plotted *vs.* the lengths of the forming and breaking bonds. Center: plotted *vs.* two mass-scaled coordinates (x and y) for the case where A, B, and C have the same mass. Right: plotted *vs.* two mass-scaled coordinates (x and y) for the case where the mass of B is much less than the masses of A and C. The right-hand plot is for an exothermic reaction, and it also shows two possible straight-line paths along which tunnelling might occur.

path with small reduced mass (to minimize the radicand), a path with a low barrier (also to minimize the radicand), and a short path (to minimize the length of the interval over which the integration is carried out). When we use isoinertial coordinates, all paths have the same reduced mass and we just need a compromise of low barrier and short path. In the small-curvature limit, any path shortening due to cutting the corner more than the outer vibrational turning point of the vibration transverse to the reaction path would involve an increase in effective potential that would outweigh the advantage of a shorter path, and in this way we arrive at the SCT tunnelling approximation. When the skew angle is small, one can obtain a much shorter path by severe corner cutting because the product valley is close to the reactant valley. This is illustrated by the nearly vertical path in the right panel of Figure 8.1. In the limit of large reaction-path curvature, the distance criterion totally dominates, and the optimum tunnelling path should be a straight line from the reactant valley to the product one.

In our own work, we developed a method to treat the large-curvature limit for general polyatomic reactions by using straight-line tunnelling paths as motivated above. Early versions were called the large-curvature ground-state method,[40–45] and the theory achieved its final form in version 4. The version 4 approximation[46] (LCG4) is called the large-curvature tunnelling (LCT) approximation. It differs from SCT in three key ways: (1) The tunnelling path is not restricted to the region inside the ground-state vibrational amplitude where one may use the vibrationally adiabatic potential curve, and large-curvature approximations use a diabatic effective potential in the region beyond the outer turning points of the transverse vibrational motion. (2) A given tunnelling path need not conserve the transverse vibrational quantum numbers, but rather a system beginning in the ground vibrational state of the reactants may tunnel into excited vibrational states of the product (when the reaction is considered in the exothermic or thermoneutral direction).

(3) The tunnelling, even for a given initial and final vibrational state, is not dominated by a single tunnelling path for each energy but rather there is an average over a sequence of tunnelling paths, each starting somewhere on the MEP in the reactant valley and proceeding along a straight line to a point (determined by a quantization criterion) on the MEP in the product valley. Plots showing examples of large-curvature tunnelling paths for tunnelling from the ground state of reactants into either the ground state or excited vibrational states of the product are available in previous papers.[43,44,47]

Two points about curvature of the reaction path can be emphasized. First of all, it is not the skew angle alone that determines the effect of reaction-path curvature on tunnelling because the skew angle is a global characteristic of the path. The key issue is how big is the curvature in the region of the barrier, and an exothermic reaction may have the barrier very early where the reaction path is not yet very curved. In such a case, the effect of curvature on the tunnelling may be small or negligible. For bimolecular hydrogen-transfer or proton-transfer reactions, the region of largest curvature tends to be where the forming bond is about half made and the breaking bond is about half broken; this is also the region where thermoneutral and nearly thermoneutral reactions have their barriers and also where intrinsic barriers tend to be largest (the intrinsic barrier for a symmetric reaction is the same as the barrier; the intrinsic barrier for a non-thermoneutral reaction is the barrier in the exoergic direction) and hence where tunnelling effects can be most significant. The second point to be made is that it is not as easy to guess the curvature for unimolecular reactions as it is for concerted bimolecular ones,[48] because the skew angle in a bimolecular reaction is calculated from the cosine of the angle between the relative translation of the reactants and the relative translation of the products, but the directions of entrance and exit for a unimolecular reaction are very case specific.

Because the LCT approximation requires more extensive calculations than the SCT approximation, it was originally much more expensive, but now efficient interpolation algorithms are available to make it very affordable.[49,50]

While the SCT and LCT formalisms represent two limiting cases, both of them seem to be accurate for intermediate curvature, so they cover all possible cases. A simple procedure to cover all cases is simply to perform both kinds of calculation and choose whichever gives a larger tunnelling probability.[51] When this is done for each value of the energy the result is called microcanonical optimized multidimensional tunnelling (μOMT).[52]

In classical mechanics, Hamilton's principle states that solving the equations of motion are equivalent to finding the least-action path.[53] Eqn (8.1) shows that the dominant tunnelling path is the one with the least imaginary action, and this may be considered an analytic continuation of Hamilton's principle to complex momenta (the classical momentum is imaginary or complex when the classical kinetic energy is negative, as it would be in a tunnelling region where the potential energy is greater than the total energy). It is natural to ask if this can be used to obtain a more general approximation to the tunnelling probability than the small-curvature and large-curvature limiting approximations discussed above. In a sense, this is done by classical S matrix theory, where one calculates a trajectory in imaginary time with complex coordinates and momenta,[54] but this is impractical for real systems because it is hard to make the trajectory satisfy the correct real boundary conditions. However, one can find a variational approximation to the tunnelling trajectory by finding the least-imaginary-action path from among a sequence of paths that satisfy the correct boundary conditions. One major problem that needs to be solved in such an approach is determining the individual components of the complex momentum since the action integral involves $\mathbf{p} \cdot d\mathbf{q}$, where $\mathbf{q}$ is a vector of coordinates, and therefore we need the components of $\mathbf{p}$ in order to calculate the exponential decay. This was accomplished by using the same kind of diabatic model as used in the LCT method, and this results in a least-action ground-state tunnelling approximation that is also called the least-action tunnelling (LAT) approximation.[55,56] Usually we expect that the LAT approximation is not needed, and it is sufficient to use the μOMT approximation, but in a set of cases where it was applied to polyatomic reactions,[57] namely the reaction of CF_3 with CH_4, CD_3H, and CD_4, it did give kinetic isotope effects in consistently better agreement with experiment. Least-action tunnelling approximations have also been proposed by Taketsugu and Hirao[58] and Tautermann *et al.*[59]

It has not been emphasized so far, but the tunnelling transmission coefficient also includes quantum mechanical effects on reaction-coordinate motion when the energy exceeds the effective barrier height. Just as a quantum mechanical system shows non-classical transmission across a barrier at energies below the barrier top, it also shows non-classical reflection for energies above the barrier top (this may be thought of as a diffraction effect). The situation is particularly clear for a parabolic barrier (*i.e.*, a purely quadratic barrier), where the quantum results can be obtained analytically. If $P(E)$ is the transmission probability at energy E, and $V_{\max}$ is the maximum potential energy of the parabolic barrier, one finds[17]

$$P(E) = \frac{1}{1 + e^{2\theta}}, E < V_{\max} \tag{8.4}$$

$$P(V_{\max}) = 0.5, \tag{8.5}$$

$$P(V_{\max} + \Delta) = 1 - P(V_{\max} - \Delta),\ \Delta > 0. \tag{8.6}$$

For non-parabolic barriers, the probability is not necessarily 0.5 at the barrier top, and these equations do not hold precisely; nevertheless, they are enforced in all of our tunnelling approximations discussed above with $V_{\max}$ replaced by the maximum of $V_a^G(s)$. This maximum is called V_a^{AG}. Note that eqn (8.4) reduces to the WKB approximation, $e^{-2\theta}$, when θ is large. Replacing $e^{-2\theta}$ by $1/(1 + e^{2\theta})$ is called parabolic uniformization; it can also be derived by phase integral methods.[60]

Equations (8.4)–(8.6) show that the effect of tunnelling is to broaden the reaction threshold. Although the semiclassical tunnelling approximations we are discussing here correspond to reactions emanating in the ground state (when the reaction is considered in the exothermic or thermoneutral direction), this broadening actually occurs at all reaction thresholds (where each threshold is associated with a quantized energy level of the transition state).[61–65] The broadening may be understood as energy–time uncertainty broadening because the transition state energy level has a finite lifetime. The amount of broadening at each threshold may be understood quantitatively in terms of the lifetime of a quantum mechanical resonance state associated with the reaction threshold, and this lifetime may be correlated with the width of the barrier on the vibrationally adiabatic potential energy curve. The ground-state approximation that we have made may be recast in this language as the assumption that the broadening is the same at all thresholds. It is not, but this assumption can still be used to get useful tunnelling transmission coefficients.

Note that if we used eqns (8.4) and (8.5), and if we assumed no tunnelling, *i.e.*, if we set $\theta = 0$, the probability of passage through the transition state dividing surface would be a Heaviside function rising from 0 to 1 at $E = V_{\mathrm{max}}$; that is, the rate would be controlled by $V_{\mathrm{a}}^{\mathrm{AG}}$ rather than by $V_{\mathrm{a}}^{\mathrm{G}}(s)$ at the saddle point, as in conventional transition state theory. Since the low-temperature limit of variational transition state theory has the variational transition state at the maximum of $V_{\mathrm{a}}^{\mathrm{G}}(s)$ rather than at the saddle point, the correct inclusion of tunnelling in transition state theory is more consistent with variational transition state theory than with conventional transition state theory. The fact that the variational transition sate is not exactly at the maximum of $V_{\mathrm{a}}^{\mathrm{G}}(s)$ at finite temperature leads to a small consistency factor called the classical adiabatic ground-state correction,[42,66a] or the consistency may be enforced by using improved canonical variational theory (ICVT),[42,50] but these are small effects and the technical details need not concern us here.

Another point worth mentioning is that the transmission coefficient is not necessarily larger for deuterium-substituted system than for a protium system, in contrast to what one would find if tunnelling were one-dimensional. The simplest-to-understand example of the counterintuitive case occurs as a special case for the common situation where the zero point effects make the vibrationally adiabatic ground-state barrier height smaller than the classical barrier height because the zero-point energy of the transition state is smaller than the zero-point energy of the reactants. Then, for a small classical barrier, the vibrationally adiabatic barrier might be low but above the zero-point energy of reactants for deuterium transfer but even lower and below the zero-point energy of reactants for protium transfer. So there would be tunnelling for deuterium but not for protium. Further discussion of this counterintuitive case is given elsewhere.[66b]

8.3 Validation

The methods described above (ZCT, SCT, LCT, μOMT, and LAT) have been widely tested against exact quantum mechanical solutions of the Schrödinger equation for the rate constants of many collinear atom–diatom reactions and a few three-dimensional atom–diatom reactions, and they have also been widely used for more complicated reactions where they can be compared to experiment. The tests against exact quantum mechanics are direct tests of the accuracy of the calculated rate constant that are of special interest because the transmission coefficients and the accurate quantum mechanical rate constants are calculated for the same potential energy surface, so the comparison is not compounding the error due to the difference in the surfaces with the error due to the semiclassical tunnelling calculation. However, since the comparisons are done for the rate constant, they also test the underlying transition state theory to which the tunnelling transmission coefficient is applied. For the tests reported here the underlying transition state theory is anharmonic ICVT.

We summarized a series of such tests comparing k_{approx} and k_{acc} (where k_{approx} is the approximate rate constant computed by ICVT with the given tunnelling transmission coefficient, and k_{acc} is the accurate quantum mechanical rate constant) in a review article.[67] The tests include up to 52 collinear and three-dimensional rate constants for various atom–diatom reactions at each temperature (the precise number for each temperature is in Table 8.1). In order to allow the errors to be averaged without bias toward overestimates or underestimates and without cancellation of errors between overestimates and underestimates, test results were averaged in terms of positive percentage error, where positive percentage error is defined, for example, such that it is +50% when k_{approx} and k_{acc} differ by a factor of 1.5 (in contrast to the signed percentage error, which is +50% when $k_{\text{approx}}/k_{\text{acc}} = 1.5$ but −33% when $k_{\text{acc}}/k_{\text{approx}} = 1.5$). The logarithmically averaged positive percentage errors are shown in Table 8.1.

Table 8.1 shows that we obtain the best results with the LAT approximation and that the results are only ever so slightly less accurate on average with μOMT. Table 8.1 also shows that the results are greatly improved as compared to ZCT when one includes reaction-path curvature, as in all four of the methods to the right of ZCT. This is an especially important result when one considers that essentially all one-dimensional tunnelling results in the literature may be considered to be approximations to ZCT.

The results at 200 K are especially striking because the error without tunnelling is very large; an average positive percentage error of 1600% corresponds to an underestimate of the rate constant by a factor of 17, whereas

Table 8.1 Average positive percentage error in multidimensional tunnelling calculations for collinear and three-dimensional atom–diatom reactions.[a]

T (K)	*N*[b]	No tunnelling	ZCT	SCT	LCT	μOMT	LAT
200	41	1576	332	63	49	41	40
250	44	488	167	43	32	28	28
300	52	273	116	34	24	23	21
400	53	124	75	36	22	21	20
600	41	45	33	21	18	17	16

[a] From Table 77 of ref. 67.

[b] *N* is the number of comparisons to exact results at this temperature; this is limited by the number of exact rate constants available for comparison.

an average positive percentage error of 40% corresponds to an error of a factor of 1.4. The error is particularly large because the 41 tests of the semiclassical theory at 200 K are dominated by hydrogen transfers; the 41 cases at 200 K include 23 protium transfers (17 collinear and six 3D), 11 transfers of muonium, deuterium, or tritium (10 collinear and one 3D), and seven transfers of a halogen (4 collinear and three 3D).

The improvement continues up to higher temperatures. For example, the average positive percentage errors at 300 K in Table 8.1 correspond to errors by a factor of 3.7 for no tunneling, 2.2 for ZCT, 1.3 for SCT, and 1.2 for LCT, μOMT, or LAT. This illustrates a general point, namely that the LCT method (and therefore also the μOMT and LAT methods) has better across-the-board accuracy than the SCT method. Neverthelesss, the much simpler SCT method is usually good enough; its average error is higher mainly because it can greatly underestime the tunnelling in cases with very small skew angles.[67]

After the review article, a unique opportunity arose to the test multidimensional semiclassical tunnelling methods against an accurate quantum mechanical rate constant (for a given potential energy surface) for a polyatomic reaction,[68,69] in particular the reaction $H + CH_4 - H_2 + CH_3$, for which accurate quantum mechanical rate constants were obtained by very difficult calculations.[70] (Actually, the accurate quantum calculations for this case, unlike those used for tests described above, do involve an approximation, namely that rotation and vibrations are separable. That assumption is also made in the calculations to which we compare, so it does not affect the validity of the comparison.) The ICVT/μOMT calculations were found to agree with the accurate quantum ones within 22% (maximum error) over the full range of temperatures from 200 to 1000 K, over which the rate constants vary by eight orders of magnitude.[69]

8.4 Extensions

In applications to molecules that have torsions, the transition state may have several conformations with only small barriers between them. For such a case we developed multipath variational transition state theory where one includes tunnelling along the lowest-energy path through each conformation of the transition state.[71,72]

In addition to gas-phase reactions discussed so far, the multidimensional semiclassical tunnelling methods have also been used for diffusion at gas–solid interfaces,[73–76] for bulk diffusion and transport from a gas–solid interface to the bulk,[76] for reactions in solid matrices,[77] for the reactions in liquid-phase solutions, and for enzyme-catalyzed reactions.[78–87]

For solid-state reactions, it is important to pay special attention to the low-temperature limit. In the low-temperature limit, all the reaction is in the exothermic direction and it proceeds from the lowest energy state of the reactants. Therefore the rate constant becomes independent of temperature. This is easily accommodated in the semiclassical theory by considering tunnelling only at the quantized energies of the reactants.[73–77]

For reactions in liquids and enzymes, the number of minimum energy paths may become essentially uncountable and one must use statistical methods, in particular potentials of mean force, rather than an unaveraged potential energy surface, to calculate the reaction rate.[88–91] If implicit solvation models are used to calculate the free energies of the reacting solute, one does not have a minimum energy path, but one can calculate a minimum free energy path, and by making a practical approximation called the canonical mean shape zero-order (CMS-0) approximation, the tunnelling probabilities may be calculated using the potential of mean force rather than the potential energy surface.[88] The potential of mean force is also called the free energy surface.[92,93]

However, if the solvent is treated explicitly by molecular dynamics simulation with weighted histogram analysis[94] (WHAM) of the free energy, one may employ a liquid-state multipath tunnelling approximation by selecting a statistical sample of paths from the variational transition state slice through the WHAM free energy profile along the reaction coordinate. This is called ensemble-averaged variational transition state theory, and it has been applied successfully to many enzyme reactions.[78–84] A key finding is that the tunnelling transmission coefficient can depend strongly on ensemble averaging.[95,96]

8.5 Concluding Remarks

Computational details of the methods discussed above are given elsewhere.[42,97–99]

The present review has focussed on the development of semiclassical multidimensional tunnelling methods that are available in the Polyrate[100] and Pilgrim[101] computer programs. Reviews of recent work on tunnelling effects in chemistry are available elsewhere.[83,102–108]

Abbreviations

CMS-0	Canonical mean shape zero-order
ICVT	Improved canonical variational theory
LAT	Least-action tunnelling
LCT	Large-curvature tunnelling
MEP	Minimum-energy path
μOMT	Microcanonical optimized multidimensional tunnelling
SCT	Small-curvature tunnelling
WHAM	Weighted histogram analysis method
WKB	Wentzel–Kramers–Brillouin
ZCT	Zero-curvature tunnelling

Acknowledgments

This work was supported in part by the U.S. Department of Energy, Office of Basic Energy Sciences under Award DE-SC0015997.

References

1. F. Hund, Zur Deutung der Molekelspektren. I, *Z. Phys.*, 1927, **40**, 742–764.
2. F. Hund, Zur Deutung der Molekelspektren. III, *Z. Phys.*, 1927, **43**, 805–846.
3. E. Merzbacher, The early history of quantum tunneling, *Phys. Today*, 2002, **55**(8), 44–49.
4. G. Gamow, The quantum theory of nuclear disintegration, *Nature*, 1928, **122**, 805–806.
5. E. U. Condon, Tunneling – How it all started, *Am. J. Phys.*, 1978, **46**, 319–323.
6. M. Razavy, *Quantum Theory of Tunneling*, World Scientific, Singapore, 2003, pp. 2–4.
7. R. P. Bell, E. J. Bowen, C. N. Hinshelwood, H. W. Thompson and J. H. Wolfenden, General and physical chemistry, *Annu. Rep. Prog. Chem.*, 1933, **30**, 13–81.
8. R. P. Bell, E. J. Bowen, N. V. Sidgwick, H. W. Thompson and L. A. Woodward, General and physical chemistry, *Analyst*, 1934, **31**, 13–93.
9. M. P. Applebey and G. Ogden, The electrolytic preparation of deuterium and the separation coefficient α, *J. Chem. Soc.*, 1936, **1936**, 163–168.
10. R. P. Bell, The kinetics of proton transfer reactions, *Trans. Faraday Soc.*, 1938, **34**, 229–236.
11. E. Wigner, The transition state method, *Trans. Faraday Soc.*, 1938, **34**, 29–41.
12. E. Wigner, Über das Überschreiten von Potentialschwellen bei chemischen Reaktione, *Z. Phys. Chem. B*, 1932, **19**, 203–216.
13. R. P. Bell, The application of quantum mechanics to chemical kinetics, *Proc. R. Soc. London, Ser. A*, 1933, **139**, 466–474.
14. R. P. Bell, J. A. Fendley and J. R. Hulett, The hydrogen isotope effect in the bromination of 2-carbethoxycyclopentanone, *Proc. R. Soc. London, Ser. A*, 1956, **A235**, 453–468.
15. R. J. Le Roy, K. A. Quickert and D. J. Le Roy, Permeability of one-dimensional potential barriers, *Trans. Faraday Soc.*, 1970, **66**, 2997–3006.
16. D. G. Truhlar and A. Kuppermann, Exact tunneling calculations, *J. Am. Chem. Soc.*, 1971, **93**, 1840–1851.
17. B. C. Garrett and D. G. Truhlar, Semiclassical tunneling calculations, *J. Phys. Chem.*, 1979, **83**, 2921–2926.
18. H. S. Johnston and D. Rapp, Large tunnelling corrections in chemical reaction rates. II, *J. Am. Chem. Soc.*, 1961, **83**, 1–9.
19. H. S. Johnston, *Gas Phase Reaction Rate Theory*, The Ronald Press, New York, 1966, pp. 191–196.
20. H. Eyring, The activated complex in chemical reactions, *J. Chem. Phys.*, 1935, **3**, 107–115.
21. M. A. Eliason and J. O. Hirshflelder, General collision theory treatment for the rate of bimolecular, gas phase reactions, *J. Chem. Phys.*, 1959, **30**, 1426–1436.
22. R. A. Marcus, On the Theory of Chemical-Reaction Cross Sections. II. Application to the $H + H_2$ Reaction, *J. Chem. Phys.*, 1967, **46**, 959–966.

23. D. G. Truhlar, The Adiabatic Theory of Chemical Reactions, *J. Chem. Phys.*, 1970, **53**, 2041–2044.
24. B. C. Garrett and D. G. Truhlar, Generalized Transition State Theory. Classical Mechanical Theory and Applications to Collinear Reactions of Hydrogen Molecules, *J. Phys. Chem.*, 1979, **83**, 1052–1079.
25. B. C. Garrett and D. G. Truhlar, Generalized Transition State Theory. Quantum Effects for Collinear Reactions of Hydrogen Molecules, *J. Phys. Chem.*, 1979, **83**, 1079–1112.
26. M. Garcia-Viloca, J. Gao, M. Karplus and D. G. Truhlar, How Enzymes Work: Analysis by Modern Rate Theory and Computer Simulations, *Science*, 2004, **303**, 186–195.
27. K. Fukui, The path of chemical reactions – The IRC approach, *Acc. Chem. Res.*, 1981, **14**, 363–368.
28. D. G. Truhlar and R. E. Wyatt, $H + H_2$: Potential Energy Surfaces and Elastic and Inelastic Scattering, *Adv. Chem. Phys.*, 1977, **36**, 141–204.
29. R. N. Porter and M. Karplus, Potential Energy Surface for H_3, *J. Chem. Phys.*, 1964, **40**, 1105–1115.
30. D. G. Truhlar and A. Kuppermann, Exact and Approximate Quantum Mechanical Reaction Probabilities and Rate Constants for the Collinear $H + H_2$ Reaction, *J. Chem. Phys.*, 1972, **56**, 2232–2252.
31. R. A. Marcus and M. E. Coltrin, A new tunneling path for reactions such as $H + H_2 \rightarrow H_2 + H$, *J. Chem. Phys.*, 1977, **67**, 2609–2613.
32. R. T. Skodje, D. G. Truhlar and B. C. Garrett, Vibrationally Adiabatic Models for Reactive Tunneling, *J. Chem. Phys.*, 1982, **77**, 5955–5976.
33. B. C. Garrett and D. G. Truhlar, Reliable *Ab Initio* Calculation of a Chemical Reaction Rate and a Kinetic Isotope Effect: $H + H_2$ and $D + D_2$, Reliable *Ab Initio* Calculation of a Chemical Reaction Rate and a Kinetic Isotope Effect: $H + H_2$ and $D + D_2$, *Proc. Natl. Acad. Sci. U. S. A.*, 1979, **76**, 4755–4759.
34. R. T. Skodje, D. G. Truhlar and B. C. Garrett, A General Small-Curvature Approximation for Transition-State-Theory Transmission Coefficients, *J. Phys. Chem.*, 1981, **85**, 3019–3023.
35. D.-h. Lu, T. N. Truong, V. S. Melissas, G. C. Lynch, Y.-P. Liu, B. C. Garrett, R. Steckler, A. D. Isaacson, S. N. Rai, G. C. Hancock, J. G. Lauderdale, T. Joseph and D. G. Truhlar, Polyrate 4: A New Version of a Computer Program for the Calculation of Chemical Reaction Rates for Polyatomics, *Comput. Phys. Commun.*, 1992, **71**, 235–262.
36. Y.-P. Liu, G. C. Lynch, T. N. Truong, D.-h. Lu, D. G. Truhlar and B. C. Garrett, Molecular Modeling of the Kinetic Isotope Effect for the [1,5]-Sigmatropic Rearrangement of *cis*-1,3-Pentadiene, *J. Am. Chem. Soc.*, 1993, **115**, 2408–2415.
37. V. K. Babamov and R. A. Marcus, Dynamics of Hydrogen Atom and Proton Transfer Reactions. Symmetric Case, *J. Chem. Phys.*, 1981, **74**, 1790–1798.
38. V. K. Babamov, V. Lopez and R. A. Marcus, Dynamics of Hydrogen Atom and Proton Transfer Reaction. Nearly Degenerate Asymmetric Case, *J. Chem. Phys.*, 1983, **78**, 5621–5628.

39. R. A. Marcus, Theories of Electrode Kinetics, in *Physicochemical Hydrodynamics: B. G. Levich Festschrift*, ed. D. B. Spalding, Advance Publications, London, 1977, pp. 473–482.
40. B. C. Garrett, D. G. Truhlar, A. F. Wagner and T. H. Dunning, Jr., Variational Transition State Theory and Tunneling for a Heavy-Light-Heavy Reaction using an *Ab Initio* Potential Energy Surface. $^{37}Cl + H(D)^{35}Cl \rightarrow H(D)^{37}Cl + {}^{35}Cl$, *J. Chem. Phys.*, 1983, **78**, 4400–4413.
41. D. K. Bondi, J. N. L. Connor, B. C. Garrett and D. G. Truhlar, Test of Variational Transition State Theory with a Large-Curvature Tunneling Approximation Against Accurate Quantal Reaction Probabilities and Rate Coefficients for Three Collinear Reactions with Large Reaction-Path Curvature: Cl + HCl, Cl + DCl, Cl + MuCl, *J. Chem. Phys.*, 1983, **78**, 5981–5989.
42. D. G. Truhlar, A. D. Isaacson and B. C. Garrett, Generalized Transition State Theory, in *Theory of Chemical Reaction Dynamics*, ed. M. Baer, CRC Press, Boca Raton, FL, **vol. 4**, 1985, pp. 65–137.
43. B. C. Garrett, N. Abusalbi, D. J. Kouri and D. G. Truhlar, Test of Variational Transition State Theory and the Least-Action Approximation for Multidimensional Tunneling Probabilities Against Accurate Quantal Rate Constants for a Collinear Reaction Involving Tunneling in an Excited State, *J. Chem. Phys.*, 1985, **83**, 2252–2258.
44. M. M. Kreevoy, D. Ostović, D. G. Truhlar and B. C. Garrett, Phenomenological Manifestations of Large-Curvature Tunneling in Hydride Transfer Reactions, *J. Phys. Chem.*, 1986, **90**, 3766–3774.
45. B. C. Garrett, T. Joseph, T. N. Truong and D. G. Truhlar, Application of the Large-Curvature Tunneling Approximation to Polyatomic Molecules: Abstraction of H or D by Methyl Radical, *Chem. Phys.*, 1989, **136**, 271–284.
46. A. Fernandez-Ramos and D. G. Truhlar, Improved Algorithm for Corner Cutting Calculations, *J. Chem. Phys.*, 2001, **114**, 1491–1496.
47. T. Albu, J. C. Corchado and D. G. Truhlar, Molecular Mechanics for Chemical Reactions. A Standard Strategy for Using Multi-Configuration Molecular Mechanics for Variational Transition State Theory with Optimized Multidimensional Tunneling, *J. Phys. Chem. A*, 2001, **105**, 8465–8487.
48. D. G. Truhlar, Discussion, *J. Chem. Soc., Faraday Trans.*, 1994, **90**, 1740–1743.
49. D. G. Truhlar, J. C. Corchado, J. Espinosa-Garcia and A. Fernandez-Ramos, Interpolated Algorithms for Large-Curvature Tunneling Calculations, *J. Phys. Chem. A*, 2002, **106**, 4957–4960.
50. A. Fernández-Ramos and D. G. Truhlar, A New Algorithm for Efficient Direct Dynamics Calculations of Large-Curvature Tunneling and Its Application to Radical Reactions with 9–15 Atoms, *J. Chem. Theory Comput.*, 2005, **1**, 1063–1078.
51. D. G. Truhlar, D.-h. Lu, S. C. Tucker, X. G. Zhao, A. Gonzàlez-Lafont, T. N. Truong, D. Maurice, Y.-P. Liu and G. C. Lynch, Variational Transition State Theory with Multidimensional Semiclassical Ground-State

Transmission Coefficients: Applications to Secondary Deuterium Kinetic Isotope Effects in Reactions Involving Methane and Chloromethane, *ACS Symp. Ser.*, 1992, **502**, 16–36.

52. Y.-P. Liu, D.-h. Lu, A. Gonzàlez-Lafont, D. G. Truhlar and B. C. Garrett, Direct Dynamics Calculation of the Kinetic Isotope Effect for an Organic Hydrogen-Transfer Reaction, Including Corner-Cutting Tunneling in 21 Dimensions, *J. Am. Chem. Soc.*, 1993, **115**, 7806–7817.
53. L. D. Landau and E. M. Lifshitz, *Mechanics*, Pergamon, Oxford, 1960, p. 2.
54. T. F. George and W. H. Miller, Classical S-matrix theory of reactive tunneling: Linear $H + H_2$ collisions, *J. Chem. Phys.*, 1972, **57**, 2458–2467.
55. B. C. Garrett and D. G. Truhlar, A Least-Action Variational Method for Calculating Multi-dimensional Tunneling Probabilities for Chemical Reactions, *J. Chem. Phys.*, 1983, **79**, 4931–4938.
56. R. Meana-Pañeda, D. G. Truhlar and A. Fernández-Ramos, Least-Action Tunneling Transmission Coefficient for Polyatomic Reactions, *J. Chem. Theory Comput.*, 2010, **6**, 6–17.
57. R. Meana-Pañeda, D. G. Truhlar and A. Fernández-Ramos, Direct Dynamics Implementation of the Least-Action Tunneling Transmission Coefficient. Application to the $CH_4/CD_3H/CD_4 + CF_3$ Abstraction Reactions, *J. Chem. Theory Comput.*, 2010, **6**, 3015–3025.
58. T. Taketsugu and K. Hirao, A least-action variational method for determining tunneling paths in multidimensional system, *J. Chem. Phys.*, 1997, **107**, 10506–10514.
59. C. S. Tautermann, A. F. Voegele, T. Loerting and K. R. Liedl, The optimal tunneling path for the proton transfer in malonaldehyde, *J. Chem. Phys.*, 2002, **117**, 1962–1966.
60. R. A. Marcus, Generalization of Activated-Complex Theory. III. Vibrational Adiabaticity, Separation of Variables, and a Connection with Analytical Mechanics, *J. Chem. Phys.*, 1965, **43**, 1598–1605.
61. D. C. Chatfield, R. S. Friedman, D. G. Truhlar, B. C. Garrett and D. W. Schwenke, Global Control of Suprathreshold Reactivity by Quantized Transition States, *J. Am. Chem. Soc.*, 1991, **113**, 486–494.
62. D. C. Chatfield, R. S. Friedman, D. G. Truhlar and D. W. Schwenke, Quantum-Dynamical Characterization of Reactive Transition States, *Faraday Discuss. Chem. Soc.*, 1991, **91**, 289–304.
63. R. S. Friedman and D. G. Truhlar, Chemical Reaction Thresholds are Resonances, *Chem. Phys. Lett.*, 1991, **183**, 539–546.
64. D. C. Chatfield, R. S. Friedman, D. W. Schwenke and D. G. Truhlar, Control of Chemical Reactivity by Quantized Transition States, *J. Phys. Chem.*, 1992, **96**, 2414–2421.
65. D. C. Chatfield, R. S. Friedman, S. L. Mielke, G. C. Lynch, T. C. Allison, D. G. Truhlar and D. W. Schwenke, Computational Spectroscopy of the Transition State, in *Dynamics of Molecules and Chemical Reactions*, ed. R. E. Wyatt and J. Z. H. Zhang, Marcel Dekker, New York, 1996, pp. 323–386.

66. (a) B. C. Garrett, D. G. Truhlar, R. S. Grev and A. W. Magnuson, Improved Treatment of Threshold Contributions in Variational Transition State Theory, *J. Phys. Chem.*, 1980, **84**, 1730–1748; (b) J. Ho, J. Zheng, R. Meana-Pañeda, D. G. Truhlar, E. J. Ko, G. P. Savage, C. M. Williams, M. L. Coote and J. Tsanaktsidis, Chloroform as a Hydrogen Atom Donor in Barton Reductive Decarboxylation Reactions, *J. Org. Chem.*, 2013, **78**, 6677–6687.
67. T. C. Allison and D. G. Truhlar, Testing the Accuracy of Practical Semiclassical Methods: Variational Transition State Theory with Optimized Multidimensional Tunneling, in *Modern Methods for Multidimensional Dynamics Computations in Chemistry*, ed. D. L. Thompson, World Scientific, Singapore, 1998, pp. 618–712.
68. J. Pu, J. C. Corchado and D. G. Truhlar, Test of Variational Transition State Theory with Multidimensional Tunneling Contributions Against an Accurate Full-dimensional Rate Constant Calculation for a Six-Atom System, *J. Chem. Phys.*, 2001, **115**, 6266–6267.
69. J. Pu and D. G. Truhlar, Validation of Variational Transition State Theory with Multidimensional Tunneling Contributions Against Accurate Quantum Mechanical Dynamics for $H + CH_4 \rightarrow H_2 + CH_3$ in an Extended Temperature Interval, *J. Chem. Phys.*, 2002, **117**, 1479–1481.
70. F. Huarte-Larrañaga and U. Manthe, Vibrational excitation in the transition state: The $CH_4 + H \rightarrow CH_3 + H_2$ reaction rate constant in an extended temperature interval, *J. Chem. Phys.*, 2002, **116**, 2863–2869.
71. T. Yu, J. Zheng and D. G. Truhlar, Multipath Variational Transition State Theory. Rate Constant of the 1,4-Hydrogen Shift Isomerization of the 2-Cyclohexylethyl Radical, *J. Phys. Chem. A*, 2012, **116**, 297–308.
72. J. Zheng and D. G. Truhlar, Multi-path Variational Transition State Theory for Chemical Reaction Rates of Complex Polyatomic Species: Ethanol + OH Reactions, *Faraday Discuss.*, 2012, **157**, 59–88.
73. J. G. Lauderdale and D. G. Truhlar, Diffusion of Hydrogen, Deuterium, and Tritium on the (100) Plane of Copper: Reaction-Path Formulation, Variational Transition State Theory, and Tunneling Calculations, *Surf. Sci.*, 1985, **164**, 558–588.
74. S. E. Wonchoba and D. G. Truhlar, Effect of Phonon Coupling on Hydrogen Tunneling Rates at Gas-Surface Interfaces, *J. Chem. Phys.*, 1993, **99**, 9637–9651.
75. S. E. Wonchoba, W.-P. Hu and D. G. Truhlar, Surface Diffusion of H on Ni(100). Interpretation of the Transition Temperature, *Phys. Rev. B*, 1995, **51**, 9985–10002.
76. S. E. Wonchoba and D. G. Truhlar, General Potential-Energy Function for H/Ni and Dynamics Calculations of Surface Diffusion, Bulk Diffusion, Subsurface-to-Surface Transport, and Absorption, *Phys. Rev. B*, 1996, **53**, 11222–11241.
77. P. S. Zuev, R. S. Sheridan, T. V. Albu, D. G. Truhlar, D. A. Hrovat and W. T. Borden, Carbon Tunneling from a Single Quantum State, *Science*, 2003, **299**, 867–870.

78. C. Alhambra, J. Corchado, M. L. Sánchez, M. Garcia-Viloca, J. Gao and D. G. Truhlar, Canonical Variational Theory for Enzyme Kinetics with the Protein Mean Force and Multidimensional Quantum Mechanical Tunneling Dynamics. Theory and Application to Liver Alcohol Dehydrogenase, *J. Phys. Chem. B*, 2001, **105**, 11326–11340.
79. Q. Cui and M. Karplus, Quantum Mechanics/Molecular Mechanics Studies of Triosephosphate Isomerase-Catalyzed Reactions: Effect of Geometry and Tunneling on Proton-Transfer Rate Constants, *J. Am. Chem. Soc.*, 2002, **124**, 3093–3124.
80. D. G. Truhlar, J. Gao, M. Garcia-Viloca, C. Alhambra, J. Corchado, M. L. Sanchez and T. D. Poulsen, Ensemble-Averaged Variational Transition State Theory with Optimized Multidimensional Tunneling for Enzyme Kinetics and Other Condensed-Phase Reactions, *Int. J. Quantum Chem.*, 2004, **100**, 1136–1152.
81. J. Pang, S. Hay, N. S. Scrutton and M. J. Sutcliffe, Deep tunnelling dominates the biologically important hydride transfer reaction from NADH to FMN in morphinone reductase, *J. Am. Chem. Soc.*, 2008, **130**, 7092–7097.
82. J. Ruiz-Pernía, M. Garcia-Viloca, S. Bhattacharyay, J. Gao, D. G. Truhlar and I. Tuñon, Critical Role of Substrate Conformational Change in the Proton Transfer Process Catalyzed by 4-Oxalocrotonate Tautomerase, *J. Am. Chem. Soc.*, 2009, **131**, 2687–2698.
83. D. G. Truhlar, Tunneling in Enzymatic and Nonenzymatic Hydrogen Transfer Reactions, *J. Phys. Org. Chem.*, 2010, **23**, 660–676.
84. D. G. Truhlar, Transition State Theory for Enzyme Kinetics, *Arch. Biochem. Biophys.*, 2015, **582**, 10–17.
85. Y. Kim, B. K. Mai and S. Park, VTST/MT studies of the catalytic mechanism of C–H activation by transition metal complexes with $[Cu_2(\mu\text{-}O_2)]$, $[Fe_2(\mu\text{-}O_2)]$ and Fe(IV)–O cores based on DFT potential energy surfaces, *J. Biol. Inorg. Chem.*, 2017, **22**, 321–338.
86. K. Świderek, K. Arafet, A. Kohen and V. Moliner, Benchmarking quantum Mechanics/Molecular mechanics (QM/MM) methods on the thymidylate synthase-catalyzed hydride transfer, *J. Chem. Theory Comput.*, 2017, **13**, 1375–1388.
87. M. Delgado, S. Görlich, J. E. Longbotham, N. S. Scrutton, S. Hay, V. Moliner and I. Tuñón, Convergence of Theory and Experiment on the Role of Preorganization, Quantum Tunneling, and Enzyme Motions into Flavoenzyme-Catalyzed Hydride Transfer, *ACS Catal.*, 2017, **7**, 3190–3198.
88. D. G. Truhlar, Y.-P. Liu, G. K. Schenter and B. C. Garrett, Tunneling in the Presence of a Bath: A Generalized Transition State Theory Approach, *J. Phys. Chem.*, 1994, **98**, 8396–8405.
89. Y.-Y. Chuang, C. J. Cramer and D. G. Truhlar, Interface of Electronic Structure and Dynamics for Reactions in Solution, *Int. J. Quantum Chem.*, 1998, **70**, 887–896.

90. C. J. Cramer and D. G. Truhlar, Implicit Solvation Models: Equilibria, Structure, Spectra, and Dynamics, *Chem. Rev.*, 1999, **99**, 2161–2200.
91. G. K. Schenter, B. C. Garrett and D. G. Truhlar, Generalized Transition State Theory in Terms of the Potential of Mean Force, *J. Chem. Phys.*, 2003, **119**, 5828–5833.
92. Y. Kim, J. R. Mohrig and D. G. Truhlar, Free Energy Surfaces for Liquid-Phase Reactions and Their Use to Study the Border Between Concerted and Nonconcerted α,β-Elimination Reactions of Esters and Thioesters, *J. Am. Chem. Soc.*, 2010, **132**, 11071–11082.
93. S. J. Klippenstein, V. Pande and D. G. Truhlar, Chemical Kinetics and Mechanisms of Complex Systems: A Perspective on Recent Theoretical Advances, *J. Am. Chem. Soc.*, 2014, **136**, 528–546.
94. S. Kumar, J. M. Rosenberg, D. Bouzida, R. H. Swendsen and P. A. Kollman, The weighted histogram analysis method for free-energy calculations on biomolecules. I. The method, *J. Comput. Chem.*, 1992, **13**, 1011–1021.
95. J. Pu, J. Gao and D. G. Truhlar, Multidimensional Tunneling, Recrossing, and the Transmission Coefficient for Enzymatic Reactions, *Chem. Rev.*, 2006, **106**, 3140–3169.
96. L. Masgrau and D. G. Truhlar, The Importance of Ensemble Averaging in Enzyme Kinetics, *Acc. Chem. Res.*, 2015, **48**, 431–438.
97. C. F. Jackels, Z. Gu and D. G. Truhlar, Reaction-Path Potential and Vibrational Frequencies in Terms of Curvilinear Internal Coordinates, *J. Chem. Phys.*, 1995, **102**, 3188–3201.
98. A. Fernandez-Ramos, B. A. Ellingson, B. C. Garrett and D. G. Truhlar, Variational Transition State Theory with Multidimensional Tunneling, *Rev. Comput. Chem.*, 2007, **23**, 125–232.
99. J. L. Bao and D. G. Truhlar, Variational Transition State Theory: Theoretical Framework and Recent Developments, *Chem. Soc. Rev.*, 2017, **46**, 7548–7596.
100. J. Zheng, J. L. Bao, R. Meana-Pañeda, S. Zhang, B. J. Lynch, J. C. Corchado, Y.-Y. Chuang, P. L. Fast, W.-P. Hu, Y.-P. Liu, G. C. Lynch, K. A. Nguyen, C. F. Jackels, A. Fernandez Ramos, B. A. Ellingson, V. S. Melissas, J. Villà, I. Rossi, E. L. Coitiño, J. Pu, T. V. Albu, A. Ratkiewicz, R. Steckler, B. C. Garrett, A. D. Isaacson, and D. G. Truhlar, Polyrate – version 2017-C (University of Minnesota, Minneapolis, MN, 2018), https://comp.chem.umn.edu/polyrate/
101. (a) D. Ferro-Costas, D. G. Truhlar and A. Fernández-Ramos, Pilgrim – version 2.0; University of Minneapolis, Minnesota, MN, USA and Universidade de Santiago de Compostela, Santiago, Spain, 2019, https://comp.chem.umn.edu/pilgrim and https://github.com/daferro/Pilgrim; (b) D. Ferro-Costas, D. G. Truhlar and A. Fernández-Ramos, Pilgrim: A Thermal Rate Constant Calculator and a Chemical Kinetics Simulator, *Comput. Phys. Commun.*2020, **256**, 107457.

102. J. Kästner, Theory and simulation of atom tunneling in chemical reactions, *WIREs Comput. Mol. Sci.*, 2014, **4**, 158–168.
103. W. T. Borden, Reactions that involve tunneling by carbon and the role that calculations have played in their study, *WIREs Comput. Mol. Sci.*, 2016, **6**, 20–46.
104. À. González-Lafont and J. M. Lluch, Kinetic isotope effects in chemical and biochemical reactions: physical basis and theoretical methods of calculation, *WIREs Comput. Mol. Sci.*, 2016, **6**, 584–603.
105. E. M. Greer, K. Kwon, A. Greer and C. Doubleday, Thermally activated tunneling in organic reactions, *Tetrahedron*, 2016, **72**, 7357–7373.
106. J. Meisner and J. Kästner, Atom Tunneling in Chemistry, *Angew. Chem., Int. Ed.*, 2016, **55**, 5400–5413.
107. P. R. Schreiner, Tunneling Control of Chemical Reactions: The Third Reactivity Paradigm, *J. Am. Chem. Soc.*, 2017, **139**, 15276–15283.
108. J. O. Richardson, Perspective: Ring-polymer instanton theory, *J. Chem. Phys.*, 2018, **148**, 200901.

CHAPTER 9

The Calculation of Tunnelling Splittings Illustrated on Malonaldehyde

DAVID FERRO-COSTAS AND ANTONIO FERNÁNDEZ-RAMOS*

Centro Singular de Investigación en Química Biolóxica e Materiais
Moleculares (CIQUS); Universidade de Santiago de Compostela, 15706,
Santiago de Compostela, Spain
*Email: qf.ramos@usc.es

9.1 Introduction

Descriptions of the tunnelling effect are almost as old as quantum mechanics. As early as 1927 Hund applied the Schrödinger equation to a problem in which quantum mechanical tunnelling made its first appearance, namely the inversion of ammonia.[1] To describe this umbrella vibration he constructed a one-dimensional (1D) double-well potential consisting of two identical parabolas joined by a finite barrier. The wavefunctions of such individual wells have a non-zero (although usually small) probability of penetrating the barrier. To solve the Schrödinger equation, Hund adopted harmonic oscillator wavefunctions centered in each of the two wells. These two stationary wavefunctions overlap in the classically forbidden region, creating a coherent oscillation between the two wells.

Unfortunately, the analytical solution of the Schrödinger equation is only possible for simple potentials, therefore, it is convenient to devise an approximation that allows writing explicit expressions for the wavefunction even though they will be approximate. A very popular and useful

---

Theoretical and Computational Chemistry Series No. 18
Tunnelling in Molecules: Nuclear Quantum Effects from Bio to Physical Chemistry
Edited by Johannes Kästner and Sebastian Kozuch

Published by the Royal Society of Chemistry, www.rsc.org

methodology is the well-known Wentzel, Kramers and Brillouin (WKB) or semiclassical (sometimes also called quasi-classical) approximation,[2] which was developed in 1926 and that works well when certain variables with action units (energy×time) are much larger than Planck's constant h. Because the WKB wavefunction is proportional to the imaginary exponential of the classical action [$\exp(\mathrm{i}S/\hbar)$, where S is the action and $\hbar = h/2\pi$], it is convenient to use path integrals.[3] In the quantum regime, the sum over paths is dominated by the most probable of the paths, which is obtained as a compromise between paths of varying length and width. This path is the one that minimizes the action and is usually called the *instanton* path.[4,5]

Tunnelling splittings can also be calculated using quantum dynamics approaches as, for instance, the multi-configuration time-dependent Hartree (MCTDH) method[6–8] or the recent path integral molecular dynamics implementation.[9]

The purpose of this chapter is to review a representative set of methods reported in the literature for the calculation of proton and deuterium tunnelling splittings and compare their results with observed splittings. Section 9.2 is dedicated to semiclassical methods, *i.e.*, to the WKB and instanton approximations. To keep this task tractable we focus on a single molecule, malonaldehyde (Sections 9.3–9.6), which is widely used as a touchstone for tunnelling calculations, and we also restrict ourselves mostly to the vibrational ground-state level (Sections 9.4 and 9.5). Splitting of excited vibrational levels offers a wide field for debate, so it is briefly discussed in Section 9.6. Section 9.7 outlines the main conclusions.

9.2 Semiclassical Methods

9.2.1 The WKB Approximation

The WKB approximation makes use of the solution provided in 1925 by the English mathematician Harold Jeffreys,[10] so sometimes the WKB approximation is referred as WKBJ or JWKB.[2] Jeffreys provided an analytical formula to a second-order differential equation similar to the Schrödinger equation (previous to the appearance of this equation!) for a particle of mass m with energy E moving in a general potential $V(x)$. The solution (the wavefunction) is of the type

$$\psi(x) \simeq \frac{1}{\sqrt{p(x)}} \exp\left[\pm \frac{i}{\hbar} \int^{x} p(x)\mathrm{d}x\right] \tag{9.1}$$

where $p(x)$ is the momentum of the particle, which is given by

$$p(x) = \sqrt{2m[E - V(x)]} \tag{9.2}$$

Notice that eqn (9.1) is a plane-wave wavefunction and, therefore, provides the exact quantum mechanical solution when the potential is constant, *i.e.*, when $k'(x) = \frac{1}{\hbar}\frac{\mathrm{d}p(x)}{\mathrm{d}x} = 0$ (notice that $k(x) = \frac{1}{\hbar}p(x)$). It remains a good approximation when $k'(x)$ is negligible, or being more precise, when $|k'(x)| \ll [k(x)]$.[2]

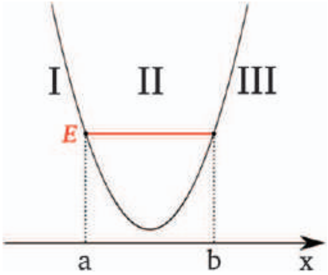

Figure 9.1 Particle with energy E moving in a one-well potential $V(x)$. The turning points a and b separate region II (classically allowed) from regions I and III (classically forbidden).

In the case of a particle moving in the potential well of Figure 9.1 with energy E, in which the classical accessible region II corresponds to $a \leq x \leq b$ where a and b are the classical turning points, the wavefunction is oscillatory. Regions I and III are classically forbidden and the wavefunction is a decreasing real exponential. The trickier part in the WKB formulation is that the wavefunction of eqn (9.1) diverges at the turning points but we need a well-behaved function over the three regions. This is achieved through the so-called *connection formulas* or *connection rules*. It can be shown that the wavefunctions for the three regions can be written as

$$\psi(x) = \begin{cases} \dfrac{C'}{2\sqrt{|p(x)|}} \exp\left[-\dfrac{1}{\hbar}\displaystyle\int_x^a |p(x)|\mathrm{d}x\right] & x \in \mathrm{I}; \\ \dfrac{C'}{\sqrt{p(x)}} \cos\left[\displaystyle\int_a^x p(x)\mathrm{d}x - \dfrac{\pi}{4}\right] = \dfrac{C}{\sqrt{p(x)}} \cos\left[\displaystyle\int_x^b p(x)\mathrm{d}x + \dfrac{\pi}{4}\right] & x \in \mathrm{II}; \\ \dfrac{C}{2\sqrt{|p(x)|}} \exp\left[-\dfrac{1}{\hbar}\displaystyle\int_b^x |p(x)|\mathrm{d}x\right] & x \in \mathrm{III}. \end{cases} \tag{9.3}$$

The two cosine functions of eqn (9.3) have to be the same throughout region II and should connect with regions I and III. Thus, $C = (-1)^n C'$, and the sum of the phases of the two equations must be an integer multiple of π, in such a way that

$$\frac{1}{\hbar}\int_a^b p(x)\mathrm{d}x - \frac{\pi}{2} = n\pi \tag{9.4}$$

or for a periodic orbit going back and forth between the a and b turning points

$$\frac{1}{2\pi\hbar}\oint p(x)\mathrm{d}x = n + \frac{1}{2} \tag{9.5}$$

where $\oint p(x)\mathrm{d}x = 2\int p(x)\mathrm{d}x$. Notice that eqn (9.4) and (9.5) correspond to the well-known Bohr-Sommerfeld quantum condition of the old quantum theory.

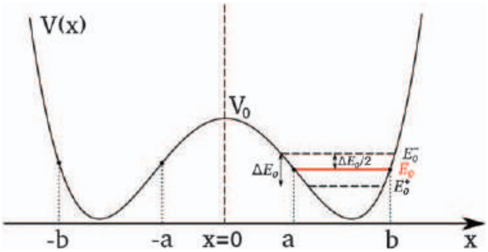

Figure 9.2 Particle with energy E_0 moving in a double-well potential $V(x)$. The splitting of this energy level and the turning points are also indicated.

Let us now consider the case of a particle with energy E_0 in the right-side well of a symmetric double-well potential that has a barrier height V_0 located at $x = 0$, as the one depicted in Figure 9.2. The motion of the particle in the interval $a \leq x \leq b$ is well described by the region II wavefunction of eqn (9.3), $\psi_{\text{II}}(x)$, which we now call $\psi_0(x)$. If we assume that the probability of passing through the barrier is negligible, the normalization constant C can be determined by the relation

$$\int_a^b |\psi_0(x)|^2 \mathrm{d}x = \frac{1}{2} C^2 \int_a^b \frac{\mathrm{d}x}{p(x)} = 1 \tag{9.6}$$

where we have substituted the oscillating $\cos^2()$ function by its averaged value, that is, $\frac{1}{2}$. The integral of the r.h.s. is proportional to the period of motion in the well, T_0, and $\omega_0 = \dfrac{2\pi}{T_0}$ is the frequency at the well, so C can be obtained. Similarly, it is possible to define a wavefunction in the left well, $\psi_0(-x)$, in such a way that the contribution of this function in the right well is very small. When we take into account the small tunnelling probability the E_0 level splits into two levels E_0^+ and E_0^- whose corresponding wavefunctions are described by a linear combination of the one-well wavefunctions. The symmetric $(+)$ combination is given by

$$\psi_0^+ = \frac{1}{\sqrt{2}} [\psi_0(-x) + \psi_0(x)] \tag{9.7}$$

whereas the antisymmetric $(-)$ combination is given by

$$\psi_0^- = \frac{1}{\sqrt{2}} [\psi_0(-x) - \psi_0(x)] \tag{9.8}$$

Notice that at $x = 0$, $\psi_0^+(0) = \sqrt{2}\psi_0(0)$ and $\dfrac{\mathrm{d}\psi_0^+(0)}{\mathrm{d}x} = 0$. The two Schrödinger equations resulting from the two energy levels E_0 and E_0^+ with wavefunctions $\psi_0(x)$ and ψ_0^+, respectively, can be combined to find the difference in energy between the two levels. Thus,

$$E_0 - E_0^+ = \frac{\hbar^2}{m} \psi_0(0) \psi_0'(0). \tag{9.9}$$

In the same manner:

$$E_0^- - E_0 = \frac{\hbar^2}{m}\psi_0(0)\psi_0'(0) \tag{9.10}$$

Therefore, the tunnelling splitting ΔE_0 is given by

$$\Delta E_0 = E_0^- - E_0^+ = \frac{2\hbar^2}{m}\psi_0(0)\psi_0'(0), \tag{9.11}$$

and

$$E_0^{\mp} = E_0 \pm \frac{\Delta E_0}{2}. \tag{9.12}$$

Eqn (9.11) is analogous to the Herring formula[11–13] given below, in which ψ_0 is not necessarily semiclassical:

$$\Delta E_0 = \frac{2\hbar^2}{m}\frac{\psi_0(0)\psi_0'(0)}{\int_0^\infty \mathrm{d}x|\psi_0(x)|^2}. \tag{9.13}$$

The denominator of eqn (9.13) normalizes the wavefunction.

Finally, taking into account that $\psi_0'(0) = \frac{mv_0}{\hbar}\psi_0(0)$, where $v_0 = \sqrt{\frac{2}{m}(V_0 - E_0)}$, the tunnelling splitting is

$$\Delta E_0 = \frac{\hbar\omega_0}{\pi}\exp\left[\frac{1}{\hbar}\int_{-a}^{a}|p(x)|\mathrm{d}x\right]. \tag{9.14}$$

The integral of eqn (9.14) is usually called the imaginary action integral, which for given energy is

$$\theta(E) = \int_{-a}^{a}|p(x)|\mathrm{d}x = \int_{-a}^{a}\sqrt{2m(V(x) - E)}\mathrm{d}x. \tag{9.15}$$

This integral should not be mistaken for the classical action integral, $S_\mathrm{C}(E)$, which appears in eqn (9.4) and is given by

$$S_\mathrm{C}(E) = \int_a^b p(x)\mathrm{d}x = \int_a^b \sqrt{2m(E - V(x))}\mathrm{d}x. \tag{9.16}$$

The classical action integral for a periodic trajectory that makes k passes back and forth in the well is

$$\Phi(E) = 2kS_\mathrm{C}(E). \tag{9.17}$$

The expression of eqn (9.14) is the same as the one deduced by Miller using the periodic orbit theory.[14] In particular, Miller obtained that the tunnelling splitting is given by

$$\Delta E_0 = \frac{\exp\left[-\frac{1}{\hbar}\theta(E_0)\right]}{\pi\frac{\mathrm{d}S_\mathrm{C}(E_0)}{\mathrm{d}E}} \tag{9.18}$$

where $\frac{\mathrm{d}S_\mathrm{C}(E_0)}{\mathrm{d}E} = [\hbar\omega_0]^{-1}$.

The imaginary action integral is related to the tunnelling transmission probability by the well-known Gamow formula:[15]

$$P(E_0) \simeq \exp\left[-\frac{2}{\hbar}\theta(E_0)\right]. \tag{9.19}$$

The probability of eqn (9.19) is usually called the primitive WKB probability and it works well if the tunnelling probability is small, as we have assumed in the derivation. If this assumption is not valid (for instance, for energies near the top of the barrier), the exact or uniform WKB transmission probability for any energy E below the potential barrier is:[16]

$$P(E) = \frac{1}{1 + \exp\left[\frac{2}{\hbar}\theta(E_0)\right]}. \tag{9.20}$$

9.2.2 Semiclassical Instanton

Another methodology that is especially suited for tunnelling calculations is based on path integral methods.[3] This formulation of quantum mechanics generalizes the action principle of classical mechanics and it is ideal for the search of the least-action path in classically forbidden regions of the potential. The motion of a particle between an initial point $x_i(0)$ and a final point $x_\text{f}(t_0)$ in the interval of time t_0 can be described by the time evolution operator (also called propagator), which is expressed through the time independent Hamiltonian $\mathscr{H}$ as

$$\langle x_\text{f}|\mathrm{e}^{-i\mathscr{H}t_0/\hbar}|x_i\rangle = N\int[Dx(t)]\mathrm{e}^{\frac{i}{\hbar}S[x(t)]} \tag{9.21}$$

where N is a normalization constant and $[Dx(t)]$ indicates the sum over all possible paths weighted by the factor $\mathrm{e}^{\frac{i}{\hbar}S[x(t)]}$, $S[x(t)]$ being the action defined through the Lagrangian, $\mathscr{L}(x,\dot{x}) = \frac{1}{2}m\dot{x}^2 - V(x)$, and given by

$$S[x(t)] = \int_0^{t_0}\mathscr{L}(x,\dot{x})\mathrm{d}t. \tag{9.22}$$

At this point it is convenient to introduce imaginary time by making the substitution $it = \tau$ (also called Wick rotation) in eqn (9.21), because it transforms oscillating exponentials into decreasing ones. At the same time the connection between quantum mechanics and statistical mechanics is achieved through the relation between the imaginary time of the propagator $it_0/\hbar$ and the inverse temperature $\beta = (k_\text{B}T)^{-1}$, that is, $\beta = it_0/\hbar = \tau_0/\hbar$ where k_B is Boltzmann's constant. In this way the propagator is transformed into the density matrix

$$\rho(x_\text{f},\, x_i;\beta) = \langle x_f|\mathrm{e}^{-\beta\mathscr{H}}|x_i\rangle, \tag{9.23}$$

where $e^{-\beta\mathscr{H}}$ is usually called the Boltzmann operator. The incorporation of imaginary time also transforms $\dot{x} \to i\dot{x}$, $V(x) \to -V(x)$ and $E \to -E$ in such a way that the Lagrangian becomes the Hamiltonian and

$$-iS[x(t)] = S_{\mathrm{E}}[x(\tau)] = \int_0^{\beta\hbar} \mathscr{H}(x,\dot{x})\mathrm{d}\tau = \int_{-\beta\hbar/2}^{\beta\hbar/2} \mathscr{H}(x,\dot{x})\mathrm{d}\tau \qquad (9.24)$$

where $S_{\mathrm{E}}[x(\tau)]$ is called the Euclidean action (the change in the limits of the integral indicates that in one case the motion is initiated at time $\tau = 0$, whereas in the other case at time $-\tau/2$). Therefore, the density matrix is given by

$$\rho(x_f, x_i; \beta) = N\int [Dx(\tau)]\mathrm{e}^{-\frac{1}{\hbar}S_{\mathrm{E}}[x(\tau)]}. \qquad (9.25)$$

The classical motion of the particle in real time is like the classical motion in imaginary time with the inverted potential,[17] which is exactly the situation we encounter here (Figure 9.3). Therefore, running trajectories in imaginary time involves paths through the tunnelling region, that is, trajectories through a classically forbidden region. In the semiclassical limit ($\hbar \to 0$), which is the classical path approximation for the matrix elements of the Boltzmann operator, the primitive WKB tunnelling probability is recovered.[18] In this limit, the propagator will be dominated by the stationary points of the action. To search for these "characteristic values" of the action let us start with the expression for the thermal rate constant, k, which is given by

$$kZ_0 = \frac{1}{2\pi\hbar}\int P(E)\mathrm{e}^{-\beta E}\mathrm{d}E \qquad (9.26)$$

where Z_0 is the reactant partition function and $P(E)$ is the reaction probability. Eqn (9.26) contains two competing factors, namely the Boltzmann factor and the reaction probability.[19] At low temperatures, tunnelling will be the main contribution to the integral and the reaction probability can be replaced by the primitive WKB probability. Thus, at a given β value, the integral will be dominated by a narrow band of levels around a single energy

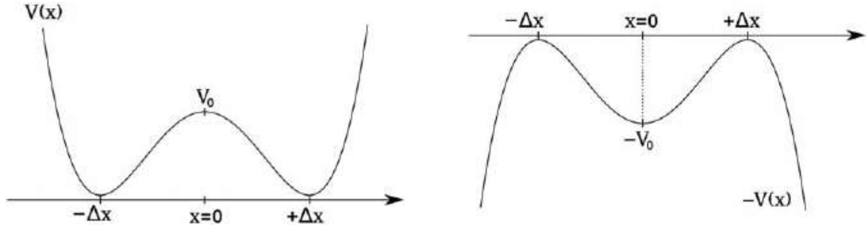

Figure 9.3 Double-well potential, before (left) and after (right) the switch to imaginary time.

level $E^*(\beta)$, so we can apply the steepest-descent method[20] to the integral to give

$$kZ_0 \approx \frac{1}{\hbar\sqrt{2\pi}}\left[\left(\frac{d^2W(E)}{dE^2}\right)_{E=E^*}\right]^{-1/2}\exp\left\{-\left[\frac{W(E^*)}{\hbar}+\beta E^*\right]\right\} \tag{9.27}$$

where we have used $W(E)=2\theta(E)$. The search for an extremum involves

$$\frac{d}{dE^*}\left[W(E^*)+\beta\hbar E^*\right]=0 \tag{9.28}$$

leading to

$$\beta\hbar=-\frac{dW(E^*)}{dE^*} \tag{9.29}$$

and because the orbit is periodic

$$\beta\hbar=\Theta(E^*)=2\int_{-a}^{a}\frac{dx}{\sqrt{V(x)-E^*}} \tag{9.30}$$

where $\Theta(E^*)$ is the period in imaginary time in the upside-down potential and E^* is determined by eqn (9.30). Also,

$$\left(\frac{d^2W(E)}{dE^2}\right)_{E=E^*}=\frac{d\Theta(E^*)}{dE^*}. \tag{9.31}$$

The action at energy E^* is given by[19]

$$S_I(\beta)=W(E^*)+\beta\hbar E^* \tag{9.32}$$

and taking into account that for a classical trajectory[21]

$$2S_C(E)=S[x(t)]+Et \tag{9.33}$$

the analogous equation in imaginary time is

$$W(E)=S_E[x(\tau)]-\beta\hbar E \tag{9.34}$$

and, therefore

$$S_I(\beta)=S_E[x_I(\tau)]. \tag{9.35}$$

The thermal rate constant of eqn (9.27) can be rewritten as

$$kZ_0 \approx \frac{1}{\hbar\sqrt{2\pi}}\left[\frac{d\Theta(E^*)}{dE^*}\right]^{-1/2}e^{-S_I(\beta)/\hbar}. \tag{9.36}$$

The l.h.s of eqn (9.35) represents the so-called *instanton* action. It is the overall result of tunnelling along numerous paths of varying length and energy, which can be replaced by tunnelling along a single trajectory, called the *instanton* or *bounce* path. The instanton exists only below a given temperature called the cross-over temperature $T_c = \hbar\omega^*/2\pi k_B$, where ω^* is the absolute value of the imaginary frequency at the top of the barrier. This path, $x_I(\tau)$, has the characteristic that, at any temperature, it minimizes the Euclidian action, and therefore it is an extremal trajectory in imaginary time of period $\hbar\beta$ in the inverted potential.[4,19,22,23] In other words, the extremum in the Euclidean action leads to

$$\frac{\delta S_E}{\delta x} = \frac{d^2[x_I(\tau)]}{d\tau^2} + \frac{dV[x_I(\tau)]]}{dx} = 0 \tag{9.37}$$

with the boundary condition $x_I(\tau + \hbar\beta) = x_I(\tau)$. The differential eqn (9.37) produces two types of solutions, the trivial ones for the minima and the transition state, and a non-trivial one, the instanton solution. The first one leads to a minimum of the action but the transition state and the instanton are saddle points of the Euclidean action. The instanton solution prevails at low temperatures, *i.e.*, at temperatures lower than T_c, whereas the transition state dominates at temperatures above the cross-over temperature.

Although the instanton action dominates at low temperatures, there are small fluctuations about the instanton path $\delta x(\tau)$ that can be incorporated in a prefactor (also called pre-exponential factor). Deviations in the path translate into deviations in the action and the latter is expanded up to quadratic terms (the lowest term in the expansion), so the action for a path given by $x(\tau) = x_I(\tau) + \delta x(\tau)$ is given by

$$S[x(\tau)] = S_I + \frac{1}{2}\int_0^{\hbar\beta} d\tau\, \delta x(\tau)\left\{-\partial_\tau^2 + \frac{d^2V[x_I(\tau)]}{dx^2}\right\}\delta x(\tau) \tag{9.38}$$

where ∂_τ^2 is the second derivative operator. The differential equation inside the integral of eqn (9.38) can be solved using the appropriate basis of eigenfunctions. The result, after diagonalization, is a set of eigenvalues that can be integrated independently. The integral is a Gaussian and can be easily taken. The density matrix is given by

$$\langle x_f|e^{-\beta\mathscr{H}}|x_i\rangle = N\left[\det\left(-\partial_\tau^2 + \frac{d^2V[x_I(\tau)]}{dx^2}\right)\right]^{-1/2} e^{-S_I/\hbar} \tag{9.39}$$

where the determinant is another way of representing the product of eigenvalues. However, because of translational invariance of the instanton trajectory one of the eigenvalues is zero and needs special treatment.[22]

At this moment it is interesting to introduce the partition function as the trace of the $e^{-\beta\mathscr{H}}$ operator. Specifically, the thermal rate constant that uses the ImF method[24–26] is defined as

$$k = 2\beta^{-1}\frac{\text{Im}\,Z}{Z_0} = \frac{2}{\hbar}\text{Im}\,F \tag{9.40}$$

which results in

$$k = \sqrt{\frac{S_0}{2\pi\hbar}} \left[\frac{\det'\left(-\partial_\tau^2 + \frac{\mathrm{d}^2 \mathrm{V}[x_\mathrm{I}(\tau)]}{\mathrm{d}x^2}\right)}{\det(-\,\partial_\tau^2 + \omega_0^2)} \right]^{-1/2} \mathrm{e}^{-S_\mathrm{I}/\hbar} \tag{9.41}$$

where the determinant in the numerator represents the product of the eigenvalues excluding the zero value. The action S_0 is

$$S_0 = \int_{-\Delta x}^{\Delta x} \sqrt{2V(x)}\mathrm{d}x. \tag{9.42}$$

Notice that the partition function of reactants is given by

$$Z_0 = [\det(-\partial_\tau^2 + \omega_0^2)]^{-1/2} \tag{9.43}$$

where ω_0 is the frequency at the bottom of the potential well $V(x)$. Following Benderskii,[27] similarly to the rate constant and in the limit $\beta \to \infty$, it is possible to obtain the tunnelling splitting as

$$\Delta E_0 = \sqrt{\frac{2S_k}{\pi\hbar}} \left[\frac{\det'\left(-\partial_\tau^2 + \frac{\mathrm{d}^2 V[x_\mathrm{I}(\tau)]}{\mathrm{d}x^2}\right)_\mathrm{kink}}{\det(-\partial_\tau^2 + \omega_0^2)} \right]^{-1/2} \mathrm{e}^{-S_\mathrm{k}/\hbar} \tag{9.44}$$

or in a compact way as

$$\Delta E_0 = \mathscr{A} \mathrm{e}^{-S_\mathrm{k}/\hbar} \tag{9.45}$$

where $\mathscr{A}$ is the pre-exponential factor given by

$$\mathscr{A} = \sqrt{\frac{2S_\mathrm{k}}{\pi\hbar}} \left[\frac{\det'\left(-\partial_\tau^2 + \frac{\mathrm{d}^2 V[x_\mathrm{I}(\tau)]}{\mathrm{d}x^2}\right)_\mathrm{kink}}{\det(-\partial_\tau^2 + \omega_0^2)} \right]^{-1/2} \tag{9.46}$$

and the action S_k is the Euclidean action evaluated when $\beta \to \infty$ over the instanton trajectory as

$$S_\mathrm{k} = S_\mathrm{E}[x_\mathrm{I}(\tau)] = \int_{-\infty}^{\infty} \mathscr{H}(x_\mathrm{I}, \dot{x}_\mathrm{I})\mathrm{d}\tau \tag{9.47}$$

or it can be also evaluated from eqn (9.42). The trajectory can move between $-\Delta x$ and Δx (a 'kink'), and back between Δx and $-\Delta x$ (an 'anti-kink'); in fact any extremal or instanton trajectory includes a given integer number n of kink–anti-kink passes. The tunnelling splitting can be calculated from a single kink using eqn (9.44) since the particle usually passes long periods of time at rest in ±Δx (the minima) so the kinks can be considered independent from each other. Eqn (9.44) can be written as a function of the instanton trajectory by doubling the kink, which also involves doubling the eigenvalues in the pre-exponential factor. Thus,

$$\Delta E_0 = \sqrt{\frac{S_\mathrm{I}(0)}{\pi\hbar}} \left[\frac{\det''\left(-\partial_\tau^2 + \dfrac{\mathrm{d}^2 V[x_\mathrm{I}(\tau)]}{\mathrm{d}x^2}\right)_\mathrm{I}}{\det(-\partial_\tau^2 + \omega_0^2)} \right]^{-1/4} \mathrm{e}^{-S_\mathrm{I}(0)/2\hbar} \tag{9.48}$$

where in this case the pre-exponential factor is evaluated by removing the two zero eigenvalues. Tunnelling splittings are calculated in the limit when $\beta \to \infty$, that is, when the temperature reaches the absolute zero ($T = 0$ K). Therefore, it is common to write the instanton action as $S_\mathrm{I}(T = 0)$ or simply like in eqn (9.48) as $S_\mathrm{I}(0)$.

Mil’nikov and Nakamura[28–30] exploited the connection between the WKB approximation and instanton theory, which allowed them to evaluate in an easy manner the determinants of the pre-exponential factor. For a symmetric double-well potential, the wavefunction in one of the wells [for instance, of the left well (L)] can be written as

$$\phi_\mathrm{L}(x) = \exp\left(-\frac{1}{\hbar} W_0 - W_1\right) \tag{9.49}$$

where the substitution of eqn (9.49) into the Shrödinger equation leads to two differential equations that allow obtaining W_0 and W_1. In particular,

$$W_0 = \int_{-\Delta x}^{x} p_0(z)\mathrm{d}z \tag{9.50}$$

and

$$W_1 = \int_{-\Delta x}^{x} \frac{\mathrm{d}z}{p_0(z)} \left(\frac{\partial^2 W_0}{\partial z^2} - \frac{2E_0}{\hbar} \right) \tag{9.51}$$

where $p_0(x) = \sqrt{2V(x)}$ and E_0 is the ground-state vibrational energy. Assuming that the potential is harmonic in the vicinity of the minima and making use of the Herring equation [eqn (9.13)], the tunnelling splitting is

$$\Delta E_0 = \hbar\omega_0 \sqrt{\frac{4\omega_0}{\pi\hbar}}\, p_0(0) \mathrm{e}^{-2W_1(x=0)} \mathrm{e}^{-S_0/\hbar} \tag{9.52}$$

where S_0 is given by eqn (9.42) and $W_1(x = 0)$ is evaluated at the top of the barrier. Eqn (9.51) can be written as a function of the instanton period using an equation similar to eqn (9.30), *i.e.*, writing the period as $\tau = \int dz/p_0(z)$. It leads to

$$W_1(x=0) = \frac{1}{2}\int_{-\infty}^{0} d\tau[A(\tau) - A(-\infty)] \tag{9.53}$$

where $A \equiv dp_0/dx$ and if $\tau \to \infty$ then $x \to -\Delta x$. If the potential is assumed harmonic at $\pm\Delta x$ then $V(x \to \pm\Delta x) \simeq \frac{1}{2}\omega_0^2(x \pm \Delta x)^2$, and the momentum $p_0(x \to \pm\Delta x) = \omega_0(x \pm \Delta x)$ with $A(\to\infty) = \omega_0 = 2E_0/\hbar$.

In the above discussion about semiclassical methods (WKB and the instanton) we have mainly concentrated our efforts in 1D systems. Notice that the tunnelling splitting calculated by the semiclassical eqn (9.14) is equivalent to that evaluated by eqn (9.48) and (9.52) for 1D tunnelling.[28,31,32] These equations are key when moving to multidimensional systems. For instance, the uniform tunnelling probability expression of eqn (9.20) is regularly used when incorporating quantum effects in variational transition state theory.[33] These quantum effects are multidimensional because the action integral of eqn (9.15) includes couplings between the reaction coordinate and the rest of the vibrational normal modes. This is the case of the small-curvature tunnelling probability that incorporates such couplings in the mass of the tunnelling particle.[34] For instance, this approach has been used by Brown *et al.*[35] to calculate the tunnelling splitting for the ammonia inversion. Other options allow calculating the action along some previously prescribed path, as for instance along the linear reaction path (LRP),[36–38] or searching for the least action path.[39–41]

The multidimensional tunnelling splitting by means of instanton theory can be evaluated from eqn (9.48) but to locate an extremum in the Euclidean action is now harder, because the search should be performed in a multidimensional space. In the multidimensional case, additionally to the $\mathscr{A}$ prefactor (also called longitudinal and whose presence is due to the zero eigenvalue), a transverse pre-exponential factor $\mathscr{B}_t$ appears due to the increase in dimensionality. The transverse prefactor has no influence in the longitudinal prefactor, so they can be factorized.[42] The resulting expression for calculating the tunnelling splitting is

$$\Delta E_0 = \mathscr{B}_t \Delta E_0^{1\mathrm{D}} \tag{9.54}$$

where ΔE_0^{1D} is calculated, for instance, from eqn (9.48) but with a search for the instanton action in the full configuration space.

Mil'nikov and Nakamura[28–30] solve this problem by working out the similarities between WKB and instanton in a multidimensional framework. Other researchers were able to develop general procedures to search for instanton trajectories thanks to the connection between instantons, Feynman path integrals and ring polymer dynamics.[43–46]

An alternative approximation for the calculation of tunnelling splittings, which avoids trajectory calculations, is the approximated instanton method developed by Smedarchina *et al.*[47–49] In this approach $\mathscr{B}_t$ is treated within the adiabatic approximation and the multidimensional action is evaluated without explicit search for the instanton path.

9.3 Malonaldehyde

Malonaldehyde (3-hydroxy-2-propenal, MA), illustrated in Figure 9.4, is a planar molecule that[50] "has a symmetrical double minimum potential surface with a relatively low barrier between the two minima so that rapid tunnelling occurs between the two asymmetric forms of malonaldehyde". MA is a planar molecule of C_s symmetry with a C_{2v} transition state.

Table 9.1 lists the normal-mode frequencies[51] of the two types of stationary points, that is, the equilibrium and the saddle-point structures. For the former, the symmetry of normal-mode frequencies is A' for the in-plane modes and A'' for the out-of-plane modes, respectively. At the saddle point, the in-plane modes have A_1 or B_2 symmetries, and the out-of-plane modes may have A_2 or B_1 symmetries.

In 1981, Wilson *et al.* used microwave spectroscopy to measure the tunnelling splitting of MA and its deuterated species and obtained values of ~21 and ~3 cm^{-1}, respectively.[53] Some of the authors later refined the values to 21.58 and 2.91 cm^{-1}, respectively,[53] which we treat hereafter as the values to be matched by theory. They also performed 1D tunnelling calculations, estimating a barrier height for proton transfer of about 6.6 kcal mol^{-1}.

The tunnelling in MA takes place within an OHO hydrogen bond: the proton is exchanged between two oxygen atoms. The tunnelling coordinate is thus an OH-stretching vibration. As shown in Table 9.1, this is the highest-frequency vibration in the molecule. While the proton tunnels from one side

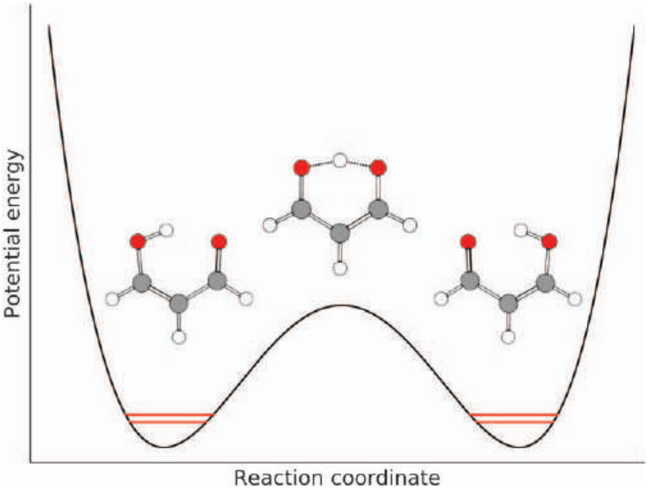

Figure 9.4 Double-well potential representing the stationary points (equilibrium and saddle point) of malonaldehyde.

Table 9.1 Labeling of the equilibrium i' and their corresponding saddle-point j normal modes. Frequencies (in cm^{-1}) taken from ref. 51. The description of the normal modes and the symmetry of the saddle-point normal modes are also indicated.

i'	$\omega_{i'}$	Description	j	ω_j	Symmetry
1′	255	Out-of-plane ring deformation	1	366	A2
2′	271	O···O stretch	4	627	A1
3′	399	Out-of-plane ring deformation	2	395	B1
4′	501	In-plane ring deformation	3	569	B2
5′	787	Out-of-plane C–H bend	5	788	B1
6′	878	Out-of-plane O–H bend	12	1339	B1
7′	885	In-plane ring deformation	6	943	A1
8′	982	C–C stretch	9	1064	A1
9′	1017	Out-of-plane C–H bend	8	1059	A2
10′	1043	Out-of-plane C–H bend	7	1016	B1
11′	1100	In-plane C–H bend	10	1099	B2
12′	1268	In-plane C–H bend	13	1361	A1
13′	1402	In-plane C–H bend	11	1319	B2
14′	1407	In-plane O–H bend	17	1896	A1
15′	1463	In-plane C–H bend	14	1492	B2
16′	1629	O–H bend; C=C/C=O stretch	15	1604	B2
17′	1702	C=C/C=O stretch	16	1626	A1
18′	2996	C–H stretch	19	3109	A1
19′	3181	C–H stretch	18	3109	B2
20′	3223	C–H stretch	20	3244	A1
21′	3371	OH stretch	0	1384 *i*	B2

to the other, the other atoms will also tend to be displaced. The tunnelling will thus not be so simple as that in ammonia mentioned in Section 9.1, where the low-frequency inversion is basically 1D. This complexity is readily appreciated if we consider the transition state of the tunnelling process, also illustrated in Figure 9.4 and Table 9.1. Clearly the changes in position and frequency are not limited to a single mode.

In the following sections, we will discuss various attempts to deal with this problem, roughly following a historical path. The reported proton and deuterium tunnelling splittings and their ratio are collected in Table 9.2.

9.4 Early Calculations

9.4.1 Eckart Potential

Bicerano *et al.*[54] modeled the proton transfer by a 1D Eckart potential with a barrier height of 8.0 kcal mol^{-1} and, using an expression of the form of eqn (9.14), obtained a tunnelling splitting of 40 cm^{-1} for H and 3 cm^{-1} for D transfer. While the values are in the right ballpark, as shown in Table 9.2, they fail in one important aspect: they yield the wrong H/D ratio, *viz.* 13.3 against the experimental value of 7.42. Since the same potential is used for both isotopes, it is clear that the 1D treatment is unable to simulate the complexity of the proton transfer process. In fact, the MP2 theoretical

Table 9.2 Ground-state tunnelling splittings of malonaldehyde obtained by diverse theoretical methods. Experiment is indicated in bold numbers in the first row. V_0 (in kcal mol^{-1}) is the difference in energy between the equilibrium and the saddle point configurations.

Ref.	Year	Method	V_0	Level	$\Delta E_0(H)$	$\Delta E_0(D)$	Ratio
52	**1981**	**Experiment**	—		∼21	∼3	7
53	**1984**	**Experiment**	—		**21.58**	**2.91**	**7.4**
54	1983	1D Eckart, WKB	8.0	CISD(DC)//HF/DZ	40	∼3	∼13
				Scaled freq. by 10%	18	≲1	≈18
57	1986	RSH, QMC	4.3	HF with fitted V_0	60	—	—
			6.8	HF with fitted V_0	17	—	—
60	1989	3D RSH, QMC	7.1	SCF-MCPF	9	0.7	12.9
61	1990	2D QMC	7.81	HF/3-21G	1.54	—	—
			4.98	HF/3-21G+ZPE	10.6	—	—
78	1992	2D QCT	4.98	From ref. 61	4.01	—	—
79	1992	2D Tunnelling matrix	4.98	From ref. 61	8.2	0.3	27.3
31	1993	2D SC instanton	4.98	2D-PES with model param.	13	—	—
47	1995	MD (in-plane NM) SC AIM	10.3	HF/6-31+G**	19.7	2.6	7.6
80	1994	MD (in-plane NM) QCT	10.0	Experimental data of ref. 52 and 116	24.5	—	—
81	1995	MD QCT	10.0	Experimental data of ref. 52 and 116	21.8	5.2	4.3
28	2001	MD instanton	10.0	From ref. 81	57.7	8.63	6.7
91	2001	MD (in-plane NM) QCT	3.62	Fit to MP2/6-31G(d, p)	21.4	—	—
		MD QCT			13.9	12.7	1.1
90	2002	3D QMC	3.8	B1LYP/6-311++G(d, p)	42.3	15.3	2.8
			4.0	PM3/MAIS-SRP	24.3	5.3	4.6
40	2002	WKB	4.4	Scaled B3LYP/6-31+G(d)	24.7	1.6[76]	15.4
93	2003	MD instanton	3.81	CCSD(T)/(a)pVTZ	21.2	3.0	7.1
82	2003	RPH + anharmonic effects	2.90	B3LYP/TZ2P	58	—	—
97	2004	MCTDH	3.62	From ref. 91	25	—	—
83	2004	RPH harmonic	3.62	Fit to MP2/6-31G(d, p)	38	6	6.3
	2004	RPH + anharmonic effects			15	—	—
84	2006	RSH	3.62	MP2/6-31G(d, p)	11	—	—
98	2007	MD quantum Monte Carlo	3.62	From ref. 91	25.7 ± 0.3	3.21 ± 0.09	8.0
89	2008	DMC	4.09	Fit to CCSD(T)/apV5Z//apVTZ	21–22 ± 2–3	2–3 ± 2–3	—

Table 9.2 (*Continued*)

Ref.	Year	Method	V_0	Level	$\Delta E_0(H)$	$\Delta E_0(D)$	Ratio
103	2008	1D Q_{im}	4.09	From ref. 89	25.9	4.6	5.6
102	2009	MD (NEO) QMC	3.62	MP2/6-31G(d, p)	24.5	—	—
92	2011	MD QCT	3.62	MP2/6-31G(d, p)	54.5	5.2	10.5
45	2011	MD ring polymer instanton	10.0	From ref. 81	51	7.5	6.8
99	2011	MCTDH	4.09	From ref. 89	23.4	—	—
100	2011	MCTDH	4.09	From ref. 89	23.8	—	—
73	2012	RIM	4.08	W1BD/MC-QCID/3	25.2	3.4	7.4
106	2012	RPH	—	CCSD(T)//MP2/6-311++G**	21.6	2.8	7.7
107	2014	iMDH QMC	4.08	From ref. 73	25.4	3.2	7.9
88	2014	DMC	4.03	Fit to CCSD(T)(F12*)/def2-TZVPP	21.0	3.2	6.6
9	2016	PIMD	4.03	From ref. 88	20.6	—	—
95	2016	RPIM	4.09	From ref. 89	25	3.4	7.4
101	2016	MCTDH	4.09	From ref. 89	24.5	—	—
105	2017	2D Q_{im}	4.09	From ref. 89	18.49	2.74	6.7
96	2018	PIMD	4.03	From ref. 88	19.3	—	—

calculations of Frisch *et al.*[55] predict a substantial skeletal rearrangement between the equilibrium structures and the transition state, indicating the multidimensionality of the transfer. In addition, this work shows the importance of including electronic correlation in the electronic structure calculations in order to obtain reliable proton transfer barrier heights. In particular, the single-point MP4 calculations yield a barrier height of 4.3 kcal mol^{-1} rather lower than the value of 8.0 kcal mol^{-1} used by Bicerano.

9.4.2 The Reaction Surface Hamiltonian

Carrington and Miller[56,57] developed a reaction surface Hamiltonian (RSH), as an extension of the reaction path Hamiltonian[58] (RPH), in which two coordinates are treated as large-amplitude motions or "reaction-like coordinates". In the case of MA, these coordinates were the O–H and the O···H distances (see Figure 9.5). The RSH for the $3N$ coordinates (N is the number of atoms) can be expressed in a rigorous manner as a function of the two reaction coordinates $\mathbf{r} = (r_1, r_2)$, the normal mode coordinates $\mathbf{Q} \equiv \{Q_k\}$, $k = 1, \ldots, 3N-8$ and their conjugated momenta ($\mathbf{P}_r$, $\mathbf{P}_Q$)

$$\mathscr{H}(\mathbf{r}, \mathbf{P}_r, \mathbf{Q}, \mathbf{P}_Q) = \frac{1}{2}[\mathbf{P}_r\,\mathbf{P}_Q]\begin{bmatrix} \mathbf{G}_{rr} & \mathbf{G}_{rQ} \\ \mathbf{G}_{Qr} & \mathbf{G}_{QQ} \end{bmatrix}\begin{bmatrix} \mathbf{P}_r \\ \mathbf{P}_Q \end{bmatrix} + V(\mathbf{r}) + \frac{1}{2}\mathbf{Q}\mathbf{L}^{\dagger}\mathbf{F}\mathbf{L}\mathbf{Q} \tag{9.55}$$

where the first term in the r.h.s of eqn (9.55) is the kinetic energy as a function of different Wilson **G**-matrix elements; $V(\mathbf{r})$ is the two-dimensional potential generated by progressing along the two **r** coordinates and optimizing the rest of the $3N-8$ internal coordinates; **F** is the force constants matrix and **L** the transformation matrix that diagonalizes it. The Hamiltonian can be expanded in terms $\mathscr{H} = \mathscr{H}_0 + \mathscr{H}_1 + \mathscr{H}_2 + \cdots$ but usually only the zero-order term is considered, and therefore

$$\mathscr{H}(\mathbf{r}, \mathbf{P}_r, \mathbf{Q}, \mathbf{P}_Q) \approx \mathscr{H}_0(\mathbf{r}, \mathbf{P}_r, \mathbf{Q}, \mathbf{P}_Q) = \mathscr{H}_r(\mathbf{r}, \mathbf{P}_r) + \mathscr{H}_{\text{vib}}(\mathbf{Q}, \mathbf{P}_Q; \mathbf{r}) \tag{9.56}$$

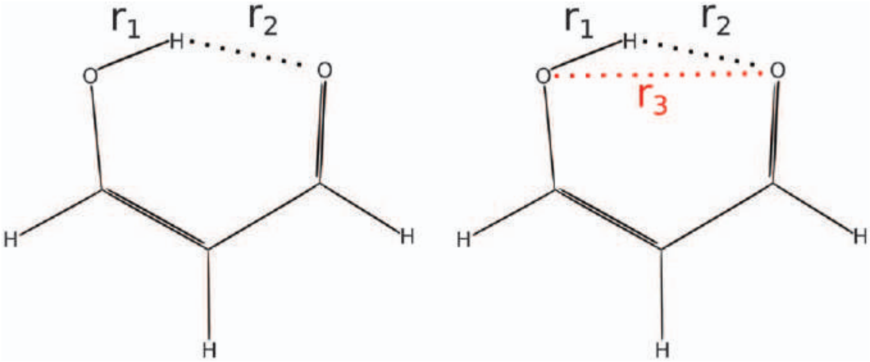

Figure 9.5 Reaction coordinates considered in the works of Carrington and Miller[56,57] (left) and Shida *et al.*[60] (right).

where

$$\mathscr{H}_r(\mathbf{r},\mathbf{P}_r)=\frac{1}{2}\mathbf{P}_r\mathbf{G}^0_{rr}\mathbf{P}_r+V(\mathbf{r}) \tag{9.57}$$

and

$$\mathscr{H}_{\text{vib}}(\mathbf{Q},\mathbf{P}_Q;\mathbf{r})=T(\mathbf{Q},\mathbf{P}_Q;\mathbf{r})+\frac{1}{2}\mathbf{Q}\mathbf{L}(\mathbf{r})^{\dagger}\mathbf{F}(\mathbf{r})\mathbf{L}(\mathbf{r})\mathbf{Q} \tag{9.58}$$

where $T(\mathbf{Q},\mathbf{P}_Q;\mathbf{r})$ is a kinetic energy term. The $(3N-8)\times(3N-8)$ $\mathbf{L}(\mathbf{r})$ matrix is chosen in such a way that diagonalizes the force constants $\mathbf{F}(\mathbf{r})$ matrix. This can be performed by a standard **FG** procedure,[59]

$$\mathbf{L}(\mathbf{r})^{\dagger}\mathbf{F}(\mathbf{r})\mathbf{L}=\boldsymbol{\omega}(\mathbf{r})^2 \tag{9.59}$$

where $\boldsymbol{\omega}(\mathbf{r})$ are the $3N-8$ normal mode frequencies at each value of the $\mathbf{r}$ coordinates. Additionally, the diagonalization yields $T(\mathbf{Q},\mathbf{P}_Q;\mathbf{r})=\frac{1}{2}\mathbf{P}_Q\mathbf{P}_Q$. Quantum mechanical calculations can be carried out on a two-dimensional surface Hamiltonian by assuming that the remaining $3N-8$ normal modes follow the reaction surface adiabatically. The resulting Hamiltonian is given by

$$\mathscr{H}(\mathbf{r},\mathbf{P}_r)=\frac{1}{2}\mathbf{P}_r\mathbf{G}^0_{rr}\mathbf{P}_r+V(\mathbf{r})+\left[\mathbf{n}+\frac{1}{2}\right]\hbar\boldsymbol{\omega}(\mathbf{r}) \tag{9.60}$$

where $\mathbf{G}^0_{rr}$ is the 2×2 Wilson $\mathbf{G}$ matrix built at a given position of the two $\mathbf{r}$ coordinates; $\mathbf{n}$ is a vector with the vibrational quantum numbers. In the vibrationally adiabatic ground-state approximation $\mathbf{n}=\mathbf{0}$ and the quantum mechanical calculations are carried out using a potential of the type

$$V_{\text{ad}}(\mathbf{r})=V(\mathbf{r})+\frac{1}{2}\sum_{k=1}^{3N-8}\hbar\omega_k(\mathbf{r}). \tag{9.61}$$

Miller and Carrington[57] stated that "Even at the zeroth-order level, though, it is important that the dynamics of the two reaction surface modes are treated exactly, so that if it is indeed true that only these two degrees of freedom are strongly involved in the process of interest, then even this zeroth-order description can be quite accurate and the perturbative corrections truly small." However, despite the beauty of this groundbreaking approach the tunnelling splitting was greatly overestimated (60 cm^{-1}) for reasons that are not entirely clear, since the barrier of 4.3 kcal mol^{-1} is close to the most recent and accurate values and the O···O contribution, which is known to be positive, was neglected.

Indeed, when Shida *et al.*[60] redefined the RSH approach as a function of Cartesian coordinates and incorporated the O···O distance as the third reaction coordinate (see Figure 9.5), they obtained much smaller splittings, namely 9 and 0.7 cm^{-1}, for H and D transfer, respectively. They also explored the deviation of the tunnelling path from the minimum energy path (MEP), *i.e.*, they obtained the expectation value path (EVP). This path is a compromise between the MEP, which is energetically the most favorable path but so long as to yield a vanishing splitting, and the linear-reaction path (LRP). However, the 1D tunnelling splitting along the EVP turned out to be only 0.3 cm^{-1}. The authors claimed that this was a proof of the necessity of a multidimensional approach.

The above statement was also supported by additional calculations designed to study the influence of the vibrational excitation of the lowest frequency mode (the O···O stretching) on the tunnelling splitting using the three-dimensional potential. This excitation substantially increased the tunnelling splitting with respect to the ground-state value. The fact that the O···O stretching motion enhances tunnelling makes sense since it creates intermittently shortened transfer distances for the proton. As a result, it is clear that this mode plays an important role in the proton transfer process in MA and indeed in all hydrogen-bonded systems. Bosch *et al.*[61] reached a similar conclusion when applying the method of Makri and Miller[62] to a model incorporating a reaction coordinate, represented by the O–H stretch, coupled to a harmonic bath, which in this case was represented by the O···O motion.

9.4.3 Instantons

These earlier results showed that vibrational modes other than the tunnelling mode can affect the tunnelling splitting. Benderskii *et al.*[63] modeled the proton transfer by a two-parabola potential for a colinear atom–diatom heavy-light-heavy system (A–H···A). This simple model allows building a two-dimensional (2D) Hamiltonian that includes the A–H bond cleavage (the reaction coordinate) and the A···A symmetric stretching motion, as the coupled transverse mode. Making an analogy with MA, while the tunnelling mode, labeled x, is of course antisymmetric (B_2 type), in this model the transverse mode is symmetric and labeled y_s (A_1 type). The coupling between the two vibrational modes was taken to be linear in the transverse-mode coordinate. For this Hamiltonian, it is possible to solve the instanton equation and analyze the effect of the transverse mode on the instanton action and thereby on the tunnelling splitting. This effect of the symmetrically coupled transverse mode depends on the strength of the coupling, measured as the displacement Δy_s between one of the minima and the saddle point. It also depends on the magnitude of its frequency ω_s with respect to the scaling frequency $\Omega = \sqrt{U_0}/\Delta x$, where U_0 is the barrier height along the linear reaction path and $\pm\Delta x$ is the location of the minima. If the symmetric heavy-heavy motion is a low-frequency mode (LF), *i.e.*, if $\omega_\text{s}/\Omega \ll 1$, it can be treated within the "sudden" approximation (also known as "fast-flip" or "frozen-bath" approximation).

The symmetric mode then contributes to the 2D instanton action as:

$$S_\text{I}^\text{2D}(0) = \frac{S_\text{I}^\text{1D}(0)}{1 + \delta_\text{s}(0)} \tag{9.62}$$

where the argument in all variables of eqn (9.62) indicates that the temperature is set to $T = 0$ K; $S_{\mathrm{I}}^{1\mathrm{D}}(0)$ is the 1D instanton action, which can be calculated from eqn (9.47), and $\delta_{\mathrm{s}}(0)$ is the contribution of the symmetric mode, whose magnitude is proportional to the coupling between the two normal modes.

The coupling decreases the action integral and therefore enhances tunnelling, thus increasing the tunnelling splitting. In this case, the tunnelling path tends to be much shorter than the MEP, and in general very far away from it. Notice that the value of $\delta_{\mathrm{s}}(0)$ is independent of the shape of the potential entering the 1D action.

On the other hand, if ω_{s} is a high-frequency (HF) mode, that is, if $\omega_{\mathrm{s}}/\Omega \gg 1$, the transverse mode follows the motion along the reaction coordinate adiabatically and the effect is like having a motion in a 1D potential with an effective mass that increases the mass of the tunnelling particle. The effect is like moving the 1D instanton trajectory towards longer and less energetic paths, such as the MEP, and thus decreases the splitting. In this case,

$$S_{\mathrm{I}}^{2\mathrm{D}}(0) = S_{\mathrm{I}}^{1\mathrm{D}}(m_{\mathrm{eff}};\, 0). \tag{9.63}$$

Antisymmetric transverse modes, labeled as y_a, do not affect the tunnelling splitting in this model unless they have the same symmetry as the reaction coordinate at the transition state, in which case their coupling is of the type $C_a x y_a$, where C_a is the coupling constant of mode y_a. These modes create a damping effect on tunnelling by reducing the splitting by a Franck–Condon factor, F_a,[62,64]

$$\Delta E_0 = \Delta E_0^{1\mathrm{D}} F_a \tag{9.64}$$

where $\Delta E_0^{1\mathrm{D}}$ is the 1D tunnelling splitting with no coupling. Inspection of the effect of antisymmetric modes ω_a over tunnelling showed that if $\omega_a/\Omega \ll 1$ the antisymmetric mode contributes to the Franck–Condon factor of the form:

$$F_a \approx \mathrm{e}^{-\delta_a(0)} \tag{9.65}$$

where $\delta_a(0)$ includes the coupling between the reaction coordinate and the antisymmetric mode. Thus, it contributes to the action as

$$S_{\mathrm{I}}^{2\mathrm{D}(0)} \approx S_{\mathrm{I}}^{1\mathrm{D}(0)} + \delta_{\mathrm{a}}^{(0)}. \tag{9.66}$$

In the case that $\omega_a/\Omega \gg 1$ the antisymmetric mode contributes to the effective mass. Explicit expressions for $C_{a,s}$, $\delta_{a,s}$ and m_{eff} are given in the next subsection as a function of parameters that can be obtained from electronic structure calculations.

The analysis of the impact of the symmetric and antisymmetric normal-modes on the instanton action, as well as their classification depending on the magnitude of their frequency, was an important breakthrough in the understanding of the multidimensional nature of tunnelling splittings. Benderskii and Makarov[31] calculated the instanton action for a 2D model potential, which included O–H as a reaction coordinate and O···O as the symmetric linearly coupled mode to it. They obtained a tunnelling splitting of 13 cm^{-1} assuming adiabatic and linear reaction path barrier heights of

4.98 and 18.01 kcal mol^{-1}, respectively. Since the adiabatic barrier was later found to be closer to 4 kcal mol^{-1}, the calculated splitting reflects favorably on the accuracy of the method.

9.4.4 The Approximate Instanton Method

Smedarchina *et al.*[47] used these results of Benderskii and coworkers[31,42,63] to develop the approximate instanton method (AIM)[48,49] as a general procedure to calculate proton tunnelling splittings in molecules and complexes. To this end they formulated the first multidimensional Hamiltonian capable of including all transverse modes linearly coupled to the tunnelling mode. Contrary to earlier approaches, it is generated in terms of the mass-weighted Cartesian coordinates of the saddle point $\{x, \mathbf{y}\}$, which is the structure of highest symmetry, in which the tunnelling mode is imaginary. Hence the name imaginary-mode Hamiltonian (iMDH). It assumes the following general form:

$$\begin{aligned}\mathscr{H} &= -\frac{\hbar^2}{2}\frac{\partial^2}{\partial x^2} - \frac{\hbar^2}{2}\sum_i \frac{\partial^2}{\partial y_i^2} + V(x,\mathbf{y})\,;\\ V(x,\mathbf{y}) &= V(x) + \frac{1}{2}\sum_i \omega_i^2 y_i^2 - x^2\sum_s C_s y_s - x\sum_a C_a y_a,\end{aligned} \tag{9.67}$$

where $V(x)$ is a double-minimum potential that connects the two minima at $x = \pm\Delta x$, and subscripts s and a indicate modes that are, symmetric and antisymmetric with respect to reflection in the plane $x = 0$, that is, in-plane modes that are displaced between the minima and transition state structures, as shown in Figure 9.6. The magnitude of the displacement is given by

$$\Delta y_j = |\mathbf{x}^{\ddagger} - \mathbf{x}_{\mathrm{EQ}}|\mathbf{L}_j^{\ddagger} \tag{9.68}$$

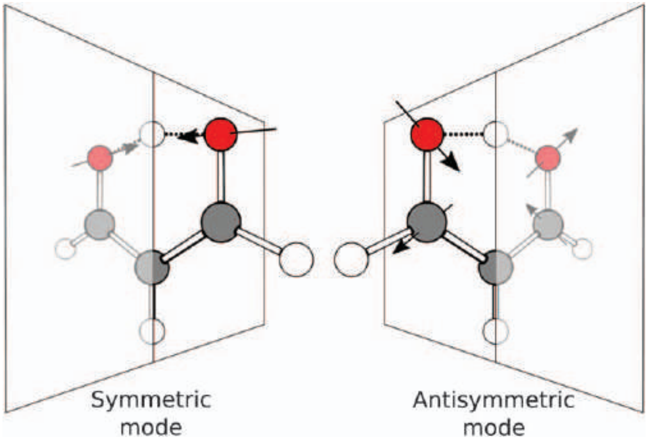

Figure 9.6 Representation of the dividing plane together with symmetric and antisymmetric normal modes.

where $\mathbf{x}^{\ddagger}$ and $\mathbf{x}_{\mathrm{EQ}}$ are the mass-weighted Cartesian coordinates of the saddle point and equilibrium configurations, respectively. Because mass-weighted Cartesian coordinates are a type of rectilinear coordinates, we consider that a given normal mode j at the saddle point is linearly displaced if $\Delta y_j > 0$. In fact, only in-plane modes are linearly displaced between the two configurations, and the coupling constants are a function of these displacements, which are given by

$$C_s = \omega_s^2 \Delta y_s / \Delta x^2; \quad C_a = \omega_a^2 \Delta y_a / \Delta x. \tag{9.69}$$

For the reaction coordinate, Δx is calculated from

$$\Delta x = \; |\mathbf{x}^{\ddagger} - \mathbf{x}_{\mathrm{EQ}}|\mathbf{L}_F^{\ddagger} \tag{9.70}$$

where the eigenvector $\mathbf{L}_F^{\ddagger}$ $(F = 3N - 6)$ corresponds to the mode with imaginary frequency at the saddle point.

Instead of working with the Hamiltonian of eqn (9.67), it is convenient to operate with the vibrational adiabatic potential $V_{\mathrm{ad}}(x)$, which is obtained by the condition

$$\frac{\partial V(x, \mathbf{y})}{\partial \mathbf{y}} = 0 \tag{9.71}$$

leading to the following Hamiltonian

$$\begin{aligned} \mathscr{H} = &- \frac{\hbar^2}{2} \frac{\partial^2}{\partial x^2} - \frac{\hbar^2}{2} \sum_i \frac{\partial^2}{\partial y_i^2} + V_{\mathrm{ad}}(x) \\ &+ \frac{1}{2} \sum_s \omega_s^2 (y_s - C_s x^2 / \omega_s^2)^2 + \frac{1}{2} \sum_a \omega_a^2 (y_a - C_a x / \omega_a^2)^2. \end{aligned} \tag{9.72}$$

The vibrationally adiabatic potential can be directly obtained from electronic structure calculations. It also has the advantage that the vibrational correction to the potential is exactly the factor introduced by the B_t transverse prefactor of eqn (9.54) when such a factor is treated within the adiabatic approximation. Therefore the potential between the reactant and the saddle point (which for instance, could be the minimum-energy path), is projected using eqn (9.70) and is transformed into the vibrational adiabatic potential when the zero-point energy is added. Usually, a quartic potential is used for the calculation of tunnelling splittings within the AIM and therefore

$$V_{\mathrm{ad}}(x) = V_{\mathrm{ad}}^0 \left[1 - \left(\frac{x}{\Delta x} \right)^2 \right]^2 \tag{9.73}$$

where V_{ad}^0 is the vibrational adiabatic barrier height. The adiabatic approximation, which is also adopted in RPH and RSH, assumes that the reaction coordinate corresponds to a slow motion when compared with the rest of vibrational degrees of freedom. This assumption is questionable in proton transfer reactions, because the reaction coordinate mainly corresponds to the O–H stretching in the equilibrium structure. Therefore, in AIM the adiabatic approximation is only applied to the evaluation of the transverse prefactor and the high-frequency modes in the multidimensional instanton action.

The multidimensional tunnelling splitting in AIM is given by

$$\Delta E_0 = \frac{\omega_0}{\pi} e^{S_I(0)/2\hbar} \tag{9.74}$$

where ω_0 is the frequency at the bottom of the well (see for instance ref. 49 for more details). The multimensional instanton action is calculated from the 1D instanton action taking into account its equivalence with the WKB expression. To this 1D action, the symmetric and antisymmetric couplings are added in a similar way as in eqn (9.62) and (9.66) assuming that couplings are additive. The result is:

$$S_I(0) = \frac{W(m_{\text{eff}}; E_0)}{1 + \sum_s^{\text{LF}} \delta_s(0)} + \alpha_s \sum_a^{\text{LF}} \delta_a(0) \tag{9.75}$$

where the action equals

$$W(m_{\text{eff}}; E_0) = 2\int_{-x_0}^{x_0} \sqrt{2m_{\text{eff}}(V_{\text{ad}}(x) - E_0)}\,\text{d}x \tag{9.76}$$

where $\pm x_0$ are the classical turning points at energy $E_0 = \hbar\omega_0/2$. The effective mass on the 1D instanton action is given by[63,65]

$$m_{\text{eff}} = m_0 + \sum_a^{\text{HF}} \Delta m_a + 4x^2 \sum_s^{\text{HF}} \Delta m_s \tag{9.77}$$

being m_0 the mass of the tunnelling particle and

$$\Delta m_s = (C_s/\omega_s^2)^2; \quad \Delta m_a = (C_a/\omega_a^2)^2. \tag{9.78}$$

The parameters $\delta_{a,s}$ are given by

$$\delta_s(0) = \frac{1}{4}\frac{\omega_0}{\omega_s}\left(\frac{C_s \Delta x}{\Omega^2}\right)^2; \quad \delta_a = 2\left(\frac{\Delta y_a}{a_0}\right)^2 \tag{9.79}$$

where $a_0 = (\hbar/\omega_a)^{1/2}$ is the zero-level amplitude of mode y_a and α_s is a parameter smaller than unity that takes into account the effect of the symmetric coupling on the antisymmetric one. Notice that in the work of Smedarchina *et al.* ω_0 and $W(m_{\text{eff}}; E_0)$ are usually referred to as Ω_0 and $S_1^0(m_{\text{eff}}; E_0)$, respectively. All the required parameters can be extracted from the structures and Hessians of the two stationary points when the quartic potential is used to evaluate the 1D potential.

The calculated H/D splittings obtained by AIM were 19.7/2.6 cm^{-1} for the *ab initio* calculated potential and 27.4/3.5 cm^{-1} for a quartic potential, by far the best estimates reported at the time.

Given the approximate nature of the procedure and the low level of the potentials (HF/6-31+G**), this agreement may look entirely fortuitous, but the same method gave equally good agreement for splittings of ground and excited levels of larger molecules and complexes such as tropolone,[66] 9-hydroxyphenalenone[67] and the formic acid dimer,[68] which included levels for which the splitting was not known in advance.

AIM presents some interesting features: (i) it provides a clear physical picture about the nature of the contribution of the transverse modes by hindering (antisymmetric) or promoting (symmetric) tunnelling; (ii) it is multidimensional and includes couplings of the type $C_s x^2 y_s$ between the reaction coordinate and the symmetric modes and of the type $C_a x y_a$ between the reaction coordinate and antisymmetric modes; (iii) the explicit evaluation of the multidimensional instanton path is avoided, because the instanton action is approximated by eqn (9.75); (iv) all the couplings and displacements appearing in iMDH can be obtained from electronic structure calculations; and (v) the potential energy surface can be generated with information exclusively from the minima and the transition state. The characteristics of the AIM method allowed the theoretical calculation of the tunnelling splittings in a wide variety of "large" systems apart from those already mentioned: calix[4]arenes,[69] 2-pyridone·2-hydroxypyridine,[70,71] benzoic acid dimer,[68] and porphycene,[72] which due to their size could not be studied by other multidimensional methods.

As a drawback, in AIM the contribution of the modes depends on the value of the normal-mode frequency and the modes need to be classified within the "sudden" (LF modes) or "adiabatic" (HF modes) approximations.

In a later development, this method was modified to allow for a wider range of coupled-mode frequencies. In the "rainbow" version (RIM),[73,74] this was achieved by separating the Euclidian action into adiabatic and non-local terms. The adiabatic term incorporates the coupled modes through a renormalization of barrier height and reduces the dynamics to a 1D problem involving only the tunnelling coordinate. The non-local term is more involved but since it is smaller than the adiabatic term it can be treated as a "perturbation". This replaces the search for the Euclidean action by a direct evaluation.

The rainbow approximation was designed to bridge the gap between the sudden and adiabatic regimes. Many refinements were introduced, including high-level structure and force-field calculations, that yielded an adiabatic barrier of 4.08 kcal mol^{-1} for MA. However, the resulting H/D splittings of 25.2/3.4 cm^{-1} remained close to the earlier AIM results.

9.4.5 Least-action Tunnelling Path

The quest for the "best" tunnelling path on the reaction swath (the region of the PES between the MEP and the LRP) of MA in a similar fashion as the least-action path[39,41] was attempted by Tautermann *et al.*[40,75] These authors performed B3LYP/6-31+G(d) geometry optimizations and CCSD(T)/cc-aug-pVDZ single-point calculations over the MP2 geometries, which gave a barrier height of 4.4 kcal mol^{-1}. Under the above prescriptions the optimal tunnelling path was closer to the MEP than to the LRP and the calculated H-transfer tunnelling splitting was 24.7 cm^{-1}. Later, a value of 1.6 cm^{-1} was reported for the D-transfer tunnelling splitting.[76] The splittings were calculated with a 1D semiclassical expression derived by Garg,[32] which combined some features of the WKB formulation with the 1D instanton action.

Despite the good result for proton transfer, the isotope effect, which should be relatively more accurate, was overestimated by a factor of 2, indicating that the vibrational coupling was not treated properly by the method.

9.4.6 "Semiclassical" Trajectory Simulations

A different multidimensional approach pioneered by Makri and Miller[77] consists in the implementation of semiclassical methods within the framework of classical trajectories. Trajectories are propagated in one of the wells (in the classical allowed region) but each time the trajectory hits a turning point (a point with no momentum in the tunnelling coordinate), the tunnelling amplitude is computed following a previously prescribed tunnelling direction. In particular, the cumulative tunnelling amplitude factor has the form

$$S(t) = \sum_n h(t - t_n)\mathrm{e}^{-\theta(t_n)} \tag{9.80}$$

where t_n is the time at which the trajectory hits a turning point; and $h(t - t_\mathrm{n})$ is the step function, which is zero if $(t - t_n) \leq 0$ and unity otherwise. The imaginary action integral is calculated in a similar manner as the one of eqn (9.15)

$$\theta(t_n) = \frac{1}{\hbar}\int_0^{\zeta_n} \mathrm{d}\zeta\sqrt{2m(V(\zeta) - E_n)} \tag{9.81}$$

but E_n is the energy at the turning point and ζ_n is the length of the path. The tunnelling splitting is calculated as the time derivative of an average of the cumulative tunnelling amplitude over an ensemble of classical trajectories

$$\Delta E_0 = 2\hbar\frac{\mathrm{d}}{\mathrm{d}t}\langle S(t)\rangle. \tag{9.82}$$

Bosch *et al.*[78] ran classical trajectories on a 2D PES of MA that included the O–H stretching as the reaction coordinate and the O$\cdots$O stretching as the motion coupled to it. The trajectory was considered that hit a turning point when the momentum along the x coordinate was zero. The action integral was evaluated along the LRP, *i.e.*, along the x coordinate. The model yielded a tunnelling splitting of 4.01 cm^{-1} for a barrier height of 4.98 kcal mol^{-1} along the MEP and of 18.01 kcal mol^{-1} along the LRP. The splitting increased to 5.97 cm^{-1} when the tunnelling path was optimized. The result improved to a value of 8.20 cm^{-1} when Bosch *et al.*[79] constructed a 2D Hamiltonian and obtained the tunnelling amplitude from a 2×2 tunnelling matrix; and the "exact" direct diagonalization results of the 2D PES[61] led to a tunnelling splitting of 10.6 cm^{-1}. The above results seem to indicate the "semi"-classical trajectories method underestimates the tunnelling amplitudes.

Thompson and coworkers built a global PES, which initially involved only in-plane motions[80] but later on also included out-of-plane motions,[81] to study the tunnelling splitting of MA using eqn (9.82). For the first study, the authors reported a value of 24.5 cm^{-1}, which is in close agreement with the experimental result. The result was even closer to experiment in the second study, with a reported value of 21.8 cm^{-1}, suggesting a modest negative contribution of coupling with out-of-plane modes. For the evaluation of the action integral "straight-line paths parallel to the equilibrium O–O distance vector" were chosen. However, the method yielded a value of 5.2 cm^{-1} for the deuterium tunnelling splitting, underestimating the isotope effect by a factor close to 2, which suggests that the vibrational coupling is not well handled. This suggestion is supported by the observation that application to vibrational excited levels led to unsatisfactory results (see for instance table II and Figure 9.4 of ref. 81 and the experimental values of Table 9.3).

9.5 Recent Calculations

9.5.1 Global and Semi-global Potential Energy Surfaces

Subsequent multidimensional instanton calculations by others (see Section 5.2) pointed towards inaccuracies in Thompson's PES as the source of artificially large splittings, so new PESs based on *ab initio* calculations were built. From 2003 to 2006, Tew *et al.*[82–84] built potential energy surfaces for MA able to support the variational configuration interaction approximation[85,86] from which rotational and vibrational energy levels can be obtained. This methodology was implemented in the MULTIMODE program.[87] The potentials generated by the variational configuration interaction were employed in combination with the reaction path Hamiltonian[58] or the reaction surface Hamiltonian.[56] The results range from the 58 cm^{-1} for a B3LYP/TZ2P calculation, which presents a barrier height of 2.90 kcal mol^{-1}, to the 15 cm^{-1} obtained at the MP2/6-31G(d, p) level with a barrier height of 3.62 kcal mol^{-1}. These PESs were superseded by a semi-global potential function,[88] which involved electronic structure calculations performed at the CCSD(T)(F12*)/def2-QZVPP level over CCSD(T)(F12*)/def2-TZVPP geometries. The reported barrier height for this level of theory is 4.03 kcal mol^{-1}. Wang *et al.*[89] also developed a PES based on highly accurate CCSD(T) calculations (with a barrier height of 4.09 kcal mol^{-1}) and basis-set-limit extrapolation of energies for MA, reporting 4.04 kcal mol^{-1} as their most accurate barrier height.

Instead of generating a global PES, Babić *et al.*[90] built a three-dimensional PES that included the donor, the acceptor and the transferred atom, the remaining degrees of freedom being treated as a "bath" of harmonic oscillators. The authors claimed that the B1LYP/6-311++G(d, p) barrier height of 3.7 kcal mol^{-1} was close enough to the CCSD(T)/cc-aug-pVTZ value of 3.9 kcal mol^{-1} to model the reduced 3D PES for a subsequent diagonalization of the Hamiltonian. A semiempirical PM3 PES with specific reaction parameters was fitted to give a barrier of 4.0 kcal mol^{-1}. The reported H/D splittings were 42.3/15.3 cm^{-1} for the DFT and 24.3/5.3 cm^{-1} for the semiempirical PES, respectively, values that fail to reproduce the observed isotope effect. This also casts some doubt on the claim that the out-of-plane motion of the transferred H atom has a strong damping effect on the tunnelling.

The same criticism applies to the application by Yagi *et al.*[91] of the semiclassical simulation methodology by Makri and Miller. These simulations were carried out on a global potential energy surface built from electronic structure calculations at the MP2/6-31G(d, p) level, with a proton transfer barrier of 3.62 kcal mol^{-1}. These authors found an even stronger damping effect of the out-of-plane modes on the tunnelling splitting than Thompson and coworkers, namely, a reduction of the splitting from 21.4 cm^{-1} for the potential without out-of-plane modes to 13.9 cm^{-1} for the one that included them. However, since the calculated deuterium splitting of 12.7 cm^{-1} greatly underestimates the isotope effect, this conclusion cannot be trusted. The same applies to more recent calculations of Ootani and Taketsugu[92] who also carried out MP2/6-31G(d, p) calculations but performed *ab initio* molecular dynamics simulations instead of fitting the data to an analytical PES. The reported H/D tunnelling splittings had values of 54.5/5.2 cm^{-1}, respectively, both of which are far off the mark.

One of the problems of the simulation with classical trajectories lays in the difficulty of finding the most probable tunnelling path inside the barrier; typically, 1D paths such as the linear reaction path are chosen, an oversimplification that counts as a serious drawback of this method. More successful applications of the PES of Yagi are described in Section 5.3.

9.5.2 Multidimensional Instanton and Path Integrals

The appearance of global analytical PESs made it possible to perform multidimensional instanton calculations, as well as computationally expensive quantum calculations, which could not be possible otherwise. Thompson's PES, although inaccurate in some aspects, since it was based on limited experimental information on malonaldehyde, contributed to this advance.

For instance, Mil'nikov and Nakamura[28] using this PES reported a splitting of 58 cm^{-1} and a H/D ratio of 6.7. In particular, these authors were the first to devise a multidimensional instanton method based on the procedure described in eqn (9.49)–(9.53) that involved:[93] "(i) an efficient method of finding instanton trajectories in multidimensional space, (ii) an efficient way of evaluating pre-exponential factors, and (iii) canonical invariance of the theory." However, the results were handicapped by the inaccuracies in the PES. In 2003, Mil'nikov *et al.*[93] performed CCSD(T) calculations with the cc-pVTZ basis set for H and C atoms and aug-cc-pVTZ basis set for oxygen, which led to a barrier height of 3.81 kcal mol^{-1}. They reported H/D splittings of 21.2/3.0 cm^{-1}, in very good agreement with experiment. The method of Mil'nikov and Nakamura has been recently simplified by Eraković *et al.*[94] by using an approach that avoids expensive matrix diagonalizations. The tunnelling splitting of 50.7 cm^{-1} on Thompson's PES, in the same line as previous calculations on this PES, indicates that the approximation is sound.

Richardson and Althorpe[45] also used this PES to perform ring-polymer instanton calculations with full dimensionality; the converged results produced a tunnelling splitting for hydrogen transfer of 51 cm^{-1} and a H/D ratio of 6.8. Cvitaš and Althorpe,[95] employing the most accurate PES of Wang *et al.*,[89] reported H/D tunnelling splittings of 25/3.5 cm^{-1} and a ratio of 7.4, in good agreement with experiment.

Mátyus *et al.*[9] made use of the density matrix, which can be written as a complete set of eigenvalues E_n and eigenstates ψ_n of the molecular Hamiltonian as

$$\rho(\mathbf{x},\mathbf{x}';\beta) = \sum_n \psi_n^*(\mathbf{x})\psi_n(\mathbf{x})\mathrm{e}^{-\beta E_n} \tag{9.83}$$

where $\mathbf{x}$ is the set of $3N$ Cartesian coordinates. At very low temperatures, we can assume that the density matrix is well approximated by the two lowest wavefunctions of the double-well potential [one symmetric given by ψ_0^+, as in eqn (9.7), and one antisymmetric given by ψ_0^-, as in eqn (9.8)]. The difference between both wavefunctions is their behaviour when reflected over the plane that passes through the transition state and divides the potential in two halves. We can define a symmetry operator $\hat{P}$ in such a way that $\mathbf{x}' = \hat{P}\mathbf{x} = -\mathbf{x}$. It follows that $\psi_0^+(\mathbf{x}') = \psi_0^+(\mathbf{x})$ and $\psi_0^-(\mathbf{x}') = -\psi_0^-(\mathbf{x})$. The tunnelling splitting can be then calculated as the ratio

$$\frac{\rho(\mathbf{x},\hat{P}\mathbf{x};\beta)}{\rho(\mathbf{x},\mathbf{x};\beta)} \approx \frac{|\psi_0^+(\mathbf{x})|^2\mathrm{e}^{-\beta E_0^+} + |\psi_0^-(\mathbf{x})|^2\mathrm{e}^{-\beta E_0^-}}{|\psi_0^+(\mathbf{x})|^2\mathrm{e}^{-\beta E_0^+} - |\psi_0^-(\mathbf{x})|^2\mathrm{e}^{-\beta E_0^-}} = \tanh\left(\frac{1}{2}\Delta E_0[\beta - \bar{\beta}(\mathbf{x})]\right) \tag{9.84}$$

where $\Delta E_0 = E_0^- - E_0^+$ and

$$\bar{\beta}(\mathbf{x}) = \frac{2}{\Delta E_0}\log\left|\frac{\psi_0^-(\mathbf{x})}{\psi_0^+(\mathbf{x})}\right|. \tag{9.85}$$

The tunnelling splitting is obtained from eqn (9.84) and the density matrices are obtained from path integral molecular dynamics.[9] The calculated value is 20.6 cm^{-1}.

Very recently, Vaillant *et al.*[96] performed a new path-integral molecular dynamics simulation that included a Langevin thermostat, where the integration along the instanton path provided a suitable reaction coordinate. A tunnelling splitting of 19.3 cm^{-1} was reported and the authors claim that the new method can also deal with very small tunnelling splittings. However, a discrepancy of about 10% was found when comparing this value to the diffusion Monte Carlo result on the same PES.[88] The absence of deuterium data prevents a definitive assessment of these methods.

9.5.3 Quantum Dynamics

The PES of Yagi *et al.* was employed by Manthe and coworkers[97,98] to perform rigorous full-dimensional quantum dynamic calculations using two different approaches: the multiconfigurational time-dependent Hartree (MCTDH) and the diffusion Monte Carlo based projection operator imaginary time spectral evolution (POITSE) methods. The first method produced a hydrogen splitting of 25 cm^{-1} and the second H/D splittings of 25.7 ± 0.3 and 3.21 ± 0.09 cm^{-1}. Later MCTDH calculations by Schröder *et al.*,[99] employing the PES developed by Wang *et al.*,[89] obtained a value of 23.4 cm^{-1}. In fact, Wang *et al.* also carried out their own quantum dynamics calculations by means of the unbiased "fix-mode" diffusion Monte Carlo method, which yielded H/D tunnelling splittings that bracketed the experimental results with an error of about 2–3 cm^{-1}. This PES was also employed by Hammer and Manthe[100] who performed elaborated multilayer MCTDH calculations that yielded (along with many excited-level splittings discussed in Section 9.6) a splitting of 23.8 cm^{-1}, a value that is virtually the same as the 24.5 cm^{-1} splitting resulting from the time-independent quantum mechanical calculations performed by Wu *et al.*[101] The diffusion Monte Carlo calculations performed on the PES of Mizukami *et al.*[88] led to H/D tunnelling splittings of 21.0/3.2 cm^{-1}.

The MP2/6-31G(d, p) level was also utilized by Hazra *et al.*[102] together with the nuclear-electronic orbital method and combined with vibronic coupling theory. The reported ground-state tunnelling splitting of 24.5 cm^{-1} is in good agreement with experiment. The authors indicated that one symmetric mode (the O···O stretching) and two antisymmetric modes (corresponding to C–C and C–O vibrations) are strongly coupled to the proton transfer reaction coordinate, in good agreement with the AIM results displayed in Section 9.4.4. Unlike previous researchers, Hazra *et al.* indicated that the out-of-plane modes have little effect on the tunnelling splitting. Apart from this uncertainty, it appears that full-dimensional quantum dynamics calculations performed over global potential energy surfaces can reproduce the tunnelling splitting of MA with an error not exceeding 10%.

9.5.4 The Revival of Approximate Methods

Larger systems, as for instance 9-hydroxyphenalenone, have been studied spectroscopically. However, full quantum dynamics calculations on these systems are unfeasible at the moment. Therefore, it is important to continue to develop methods able to identify and extract the most relevant physical effects that influence the tunnelling splittings. In this scenario, semiclassical methods and quantum methods using reduced dimensionality can fill up the gap in the transition toward large systems. An example is the Q_{im}-Hamiltonian developed by Bowman and coworkers,[103,104] which is given by

$$\mathscr{H}_{Q_{\mathrm{im}}} = -\frac{\hbar^2}{2}\frac{\partial^2}{\partial Q_{\mathrm{im}}^2} + V(Q_{\mathrm{im}}) \tag{9.86}$$

where $V(Q_{\mathrm{im}})$ is the fully relaxed potential for a given Q_{im}, where Q_{im} is the mode with imaginary frequency at the transition state. The Hamiltonian of eqn (9.86) can be solved using a 1D prescription or it can incorporate other modes within the vibrationally adiabatic ground state approximation $V_{\mathrm{ad}}(Q_{\mathrm{im}})$

$$\mathscr{H}_{Q_{\mathrm{im}}} = -\frac{\hbar^2}{2}\frac{\partial^2}{\partial Q_{\mathrm{im}}^2} + V_{\mathrm{ad}}(Q_{\mathrm{im}}) \tag{9.87}$$

where

$$V_{\mathrm{ad}}(Q_{\mathrm{im}}) = V(Q_{\mathrm{im}}) + \frac{1}{2}\sum_{k}^{3N-7} \omega_k(Q_{\mathrm{im}}). \tag{9.88}$$

Notice that the vibrational adiabatic potential of eqn (9.88) is of the same type as the one employed in RSH [see eqn (9.61)], although for the latter the sum runs over $3N-8$ instead of $3N-7$ modes because it operates with a reaction surface instead of a reaction path.

The model can be extended easily by adding coupled modes to this effectively 1D potential. Although the path described by Q_{im} shares with the MEP the barrier height, it may be substantially narrower than the path along the MEP, as it corresponds to the projection of the MEP onto this path. In this sense the coordinate Q_{im} shares with AIM the way in which the reaction coordinate is calculated [see eqn (9.70)]. A comparison between the Hamiltonian of eqn (9.87) and the RPH of Miller *et al.*[58] in the absence of coupling (zero-curvature) shows that the former is more adequate to describe the tunnelling splitting. Thus, the reported tunnelling splittings for H/D transfer in MA are 25.9/4.6 cm^{-1} with the Q_{im} approach and 0.30/0.10 cm^{-1} with the RPH.[103] The tunnelling splittings changed to 18.49/2.74 cm^{-1} when a second normal mode, namely the O···O, was incorporated in the Q_{im} Hamiltonian.[105] This is unusual, since in all previous studies addition of direct coupling to this mode increased the splitting. For instance, in the case of the RPH, the zero-curvature splittings are increased by incorporating the coupling between the reaction coordinate and the transverse modes in the kinetic energy as an effective mass and Coriolis type of couplings in the potential energy.[106]

The use of the imaginary mode as the reaction coordinate was introduced in AIM, the method discussed in Section 9.4.4. This Hamiltonian, based on the normal mode coordinates of the transition state, is the iMDH of eqn (9.67) and (9.72). The quantization of such a Hamiltonian is straightforward but requires the incorporation of a mass-dependent coordinate in the kinetic energy.[107] It is given by eqn (9.72) but $\mathscr{T}_x = -\frac{\hbar^2}{2}\partial^2/\partial x^2$, the kinetic energy along the reaction coordinate, is substituted by

$$\mathscr{T}_x = -\frac{\hbar^2}{2}\frac{\partial}{\partial x}\frac{1}{m(x)}\frac{\partial}{\partial x}. \tag{9.89}$$

The expression of the effective mass $m(x)$ is the same as the one of eqn (9.77). The effective mass incorporates all the high-frequency symmetric and antisymmetric modes, only the linearly coupled (in y) low-frequency modes add dimensionality to the Hamiltonian because the low frequency uncoupled modes are incorporated as a vibrationally adiabatic correction to the 1D potential $V(x)$.

For the case of MA, the coupling constants show that there is one symmetric mode strongly coupled to the reaction coordinate (the O···O stretching) and another symmetric mode weakly coupled to it. This 3D calculation leads to tunnelling splittings of 25.4/3.2 cm^{-1} for the H/D transfer. These results show that quantum Hamiltonians with reduced dimensionality can be very useful to calculate tunnelling splittings in larger systems. In fact, the Q_{im} path method[108] and the reduced dimensionality imaginary mode Hamiltonian[109] were both able to reproduce the tunnelling splittings in a molecule as large as porphycene.

9.6 State-selected Tunnelling Splittings

Thus far we have only discussed tunnelling splitting of the zero-point level, but have found that, in order to obtain accurate results, it is necessary to deal properly with the molecular vibrations and their coupling. This problem becomes more acute if one of the coupled levels is excited. On the other hand, measurements of splitting of vibrationally excited levels open a new window on vibrational coupling in molecules with a tunnelling mode. Some of the first calculations on state-selected tunnelling splittings involving proton transfer reactions were performed by Smedarchina *et al.*[66,67] using the AIM approximation, and by Takada and Nakamura[110] using WKB theory.

Benderskii *et al.*,[111] using a full-dimensional Hamiltonian similar to the one of eqn (9.72), were able to evaluate state-selected tunnelling splittings for malonaldehyde. The symmetric, antisymmetric and the out-of-plane-modes, which they called gated, linear and squeezed, respectively, were incorporated by expanding the potential in power series of the coordinates. For the squeezed modes, which are missing from eqn (9.72) the coupling is of the type x^2y^2. The state-selected tunnelling splittings are solved by applying a perturbative instanton approach[112] to the Hamiltonian. The results reported for the first vibrational excited state tunnelling splitting of every normal mode showed that upon excitation most of the modes exhibit enhancing effects with respect to the ground state value. However, a look at the experimental results

Table 9.3 Labeling of the equilibrium and their corresponding saddle-point normal modes as indicated by the Dushinsky matrix coefficients $g_{i'j}$.[51] Frequencies (in cm^{-1}) are taken from refs 51/113. The magnitude $\delta\Delta_{i',0}$ (in cm^{-1}) represents the experimental difference between the excited state and ground-state tunnelling splittings, as taken from refs 117–120. The selection rule that applies in each case is also listed.

i'	$\omega_{i'}$	j	ω_j	Symmetry	$g_{i'j_1}$	$g_{i'j_2}$	$\delta\Delta_{i',0}$	Rule
$1'$	255/269	1	366/346	A2	$g_{1'1}=-0.91$	$g_{1'2}=-0.40$	-16 to -13	V(1, 2)
$2'$	271/295	4	627/609	A1	$g_{2'4}=-0.94$	$g_{2'0}=-0.23$	$+35$	II
$3'$	399/383	2	395/394	B1	$g_{3'2}=0.91$	$g_{3'1}=-0.39$	-7	V(2, 1)
$4'$	501/522	3	569/573	B2	$g_{4'3}=-0.98$	$g_{4'17}=0.15$	-7	III
$5'$	787/761	5	788/750	B1	$g_{5'5}=0.99$	$g_{5'8}=-0.12$	-2 to -1	IV
$6'$	878/888	12	1339/1322	B1	$g_{6'12}=0.90$	$g_{6'7}=0.36$	-19 to -17	V(12, 7)
$7'$	885/897	6	943/958	A1	$g_{7'6}=0.95$	$g_{7'4}=-0.24$	$+5$	II
$8'$	982/996	9	1064/1074	A1	$g_{8'9}=-0.93$	$g_{8'10}=-0.23$	-8	V(9, 10)
$9'$	1017/998	8	1059/998	A2	$g_{9'7}=0.90$	$g_{9'12}=-0.38$	—	V(7, 12)
$10'$	1043/1023	7	1016/995	B1	$g_{10'8}=0.96$	$g_{1'7}=-0.23$	—	IV
$11'$	1100/1105	10	1099/1101	B2	$g_{11'10}=0.94$	$g_{11'9}=-0.17$	-5	V(10, 9)
$12'$	1268/1281	13	1361/1405	A1	$g_{12'11}=-0.62$	$g_{12'13}=-0.61$	-14	V(11, 13)
$13'$	1402/1419	11	1319/1340	B2	$g_{13'11}=0.70$	$g_{13'13}=-0.59$	-22	V(11, 13)
$14'$	1407/1394	17	1896/1894	A1	$g_{14'17}=0.62$	$g_{14'0}=0.48$	$+47$	I
$15'$	1463/1490	14	1492/1472	B2	$g_{15'14}=0.79$	$g_{15'16}=0.37$	-22	V(14, 16)
$16'$	1629/1647	15	1604/1620	B2	$g_{16'15}=0.78$	$g_{16'17}=-0.47$	-1	III
$17'$	1702/1714	16	1626/1618	A1	$g_{17'16}=-0.85$	$g_{17'14}=0.44$	-15	V(16, 14)
$18'$	2996/3197	19	3109/3127	A1	$g_{18'19}=0.70$	$g_{18'18}=0.70$	$0/-19$	V(18, 19)
$19'$	3181/3021	18	3109/3141	B2	$g_{19'18}=0.70$	$g_{19'19}=-0.68$	$0/-19$	V(19, 18)
$20'$	3223/3251	20	3244/3227	A1	$g_{20'20}=0.98$	$g_{20'19}=0.14$	0	II
$21'$	3371/3251	0	$1384i/1253i$	B2	$g_{0'0}=0.81$	$g_{0'17}=-0.42$	—	I

of Table 9.3, which were unavailable at that time, shows that there are many modes that reduce the splitting upon excitation. Therefore, it remains to be established whether this perturbative approach can deal with relatively strong coupling, which is normally encountered in systems of practical interest where experimental data are available.

At present, the amount of available measurements of this type is very limited, but they have led to some interesting new insights.[117–120] In Table 9.3 we show the results of recent experiments on MA, presented in the form of differences between the splitting of selected excited levels and the ground level.

To get insight into the effect of the state-selected excitations over the tunnelling splitting, Siebrand *et al.*[51] developed a series of selection rules based on the transition state normal-mode symmetry and on the coefficients of the Dushinsky matrix, which is calculated as

$$\mathbf{G} = (\mathbf{L}^{\ddagger})^{\dagger}\,\mathbf{L} \tag{9.90}$$

where $(\mathbf{L}^{\ddagger})^{\dagger}$ is the transpose matrix of the transition state eigenvectors and $\mathbf{L}$ is the matrix of the equilibrium structure eigenvectors. The frequencies listed in Table 9.3 are taken from Siebrand *et al.*[51] and from Wu,[113] who employed the PES developed by Wang *et al.*[89] in 2008. In fact, eqn (9.90) indicates that any transition state normal-mode j can be expanded in terms of i' modes of the equilibrium structure.

$$|j\rangle = \sum_{i} g_{ji'}|i'\rangle \tag{9.91}$$

or *vice versa*

$$|i'\rangle = \sum_{j} g_{i'j}|j\rangle. \tag{9.92}$$

A given mode i' at the equilibrium configuration will preserve its characteristics and will have a one-to-one relation to a specific j mode if $|g_{i'j}| \sim 1$. In these cases the symmetry of the normal mode decides the effect of the excitation over the splitting leading to the following four rules:

- Rule I: Excitation of the tunnelling mode increases the tunnelling splitting.
- Rule II: Excitation of a symmetric mode increases the tunnelling splitting.
- Rule III: Excitation of an antisymmetric mode other than the tunnelling mode decreases the tunnelling splitting.
- Rule IV: Excitation of an undisplaced mode has no effect on the tunnelling splitting.

As shown in Table 9.3 there are several modes that meet rules I–IV, but there are situations in which $|g_{i'j}|$ is substantially smaller than unity, indicating that the i' mode is strongly coupled to another mode. In those cases the following rule applies:

- Rule V: Excitation of any mode that interchanges with any other mode during the tunnelling event, such that their combination is antisymmetric, decreases the tunnelling splitting.

Rule V applies to pairs of modes strongly mixed and in that case overrules rules II–IV. If we denote those pairs at the equilibrium structure as (i'_1, i'_2) and at the transition state as (j_1, j_2), they will be characterized by coefficients

$$|g_{i'_1 j_1}| \simeq |g_{i'_2 j_1}| \quad \text{or} \quad |g_{i'_2 j_2}|\,; \tag{9.93}$$

$$|g_{i'_1 j_2}| \simeq |g_{i'_2 j_2}| \quad \text{or} \quad |g_{i'_2 j_1}| \tag{9.94}$$

subject to the condition $|g_{i'_1 j_1}|^2 + |g_{i'_1 j_2}|^2 \sim 1$. Table 9.3 shows several pairs of these modes, *i.e.*, pairs for which $A_1 \otimes B_2 = B_2$ or $A_2 \otimes B_1 = B_2$. The reduction of the splitting or the drag imposed on the tunnelling proton will be proportional to the mixing of the modes. The classification of the modes following the selection rules is given in Figures 9.7 and 9.8.

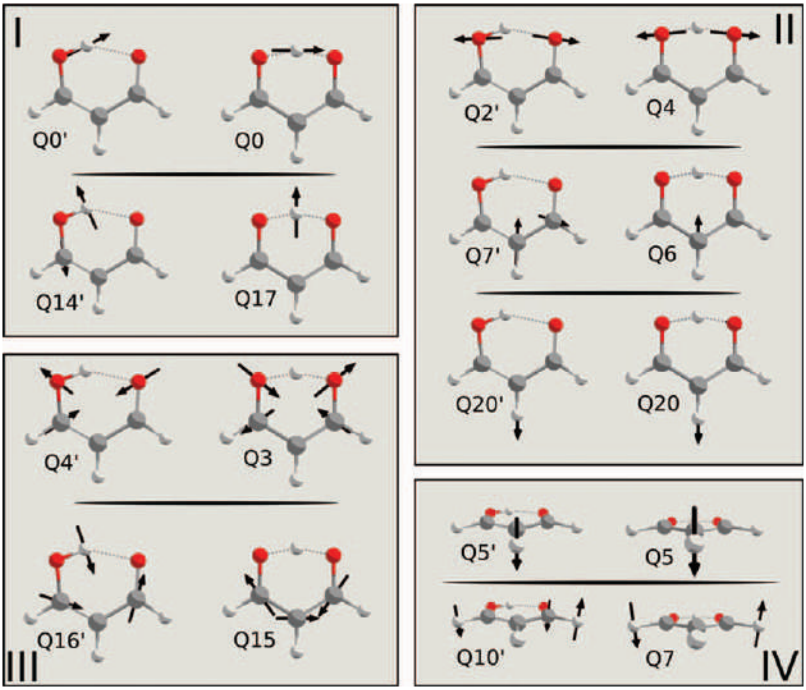

Figure 9.7 Correlation between equilibrium and saddle point normal modes which obey rules I–IV. Numbering as in Table 9.1.

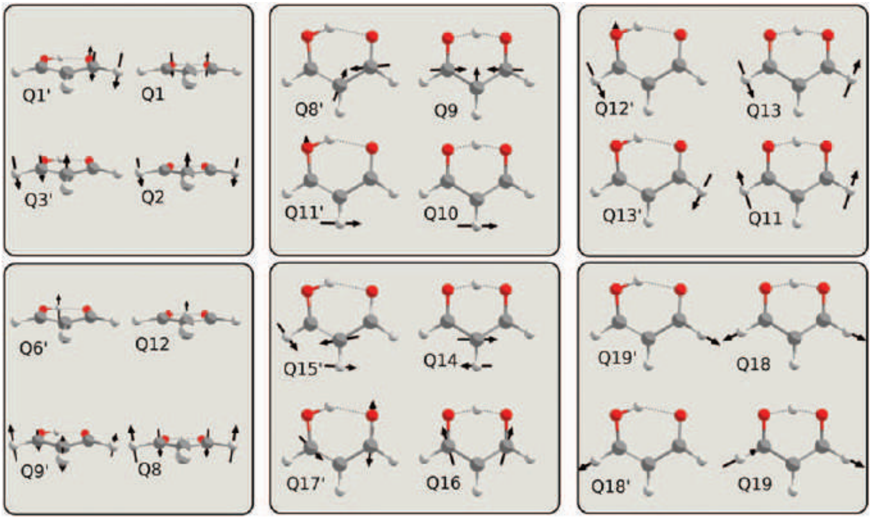

Figure 9.8 Same as Figure 9.7 but for rule V.

The normal modes that under excitation increase the tunnelling splitting correspond to modes that follow rules I–II. The MCTDH results of Hammer and Manthe[114] and the Q_{im} results of Wang and Bowman[115] and Wu[113] reproduce satisfactorily the excitation of modes that correspond to ''almost'' pure A_1 symmetric modes (Q2′ and Q7′) or that have an important component of the reaction coordinate (Q14′), as indicated in Figure 9.9.

The theoretical prediction of the excitation of the out-of-plane modes or of in-plane-modes that are strongly coupled is more involved. For these modes, there is a marked difference between the results of Hammer and Manthe, which are close to experiment in the frequency region where their calculations converged, and the ones of the other authors, who greatly underestimate the reductions in the splitting. In the case of the out-of-plane modes the Q_{im} method of Wang and Bowman predicts no change in the tunnelling splitting, as shown in Figure 9.10, because these modes are not linearly displaced. However, inspection of Table 9.3 shows that modes Q1′ and Q6′ increase substantially in frequency between the equilibrium and saddle-point configurations, implying a strong quadratic coupling, so that rule IV breaks down. Therefore, the excitation of one of these modes increases the effective barrier for tunnelling with respect to the ground-state barrier, having a suppressing effect on the tunnelling splitting. Taking into account this adiabatic correction the Q_{im} predicts a decrease in the tunnelling splitting upon excitation of Q1′ and Q6′ of 2 and 9 cm^{-1}, respectively. These arguments do not work in high-frequency coupled modes as Q15′ or Q17′. The results using the Q_{im} method improve when these modes are explicitly included in the diagonalization of the Hamiltonian (see Figure 9.10).[113] These new calculations are a clear improvement, but do not measure up to the state-selected tunnelling splittings calculated by Hammer and Manthe, although their results were limited to low frequencies.

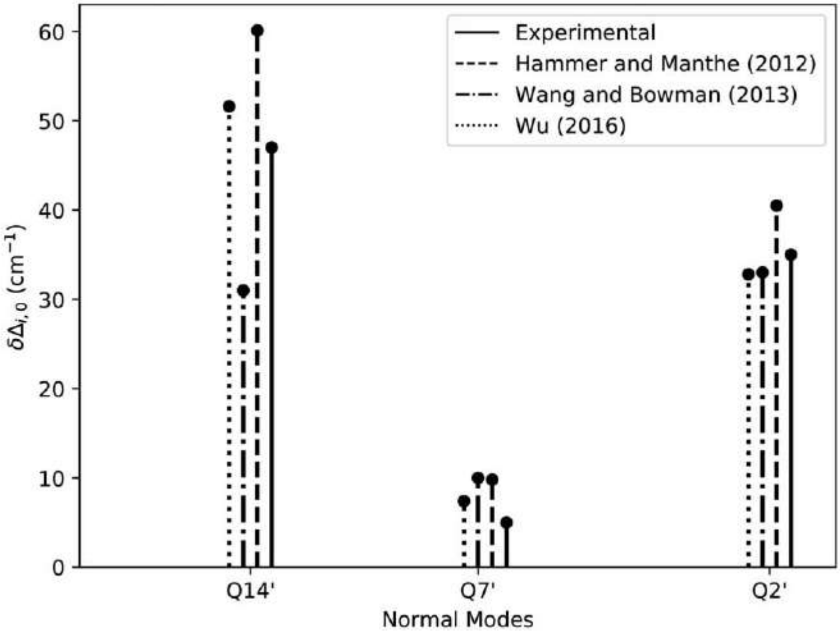

Figure 9.9 Variation of the tunnelling splitting with respect to the ground-state value for modes obeying rules I–II.

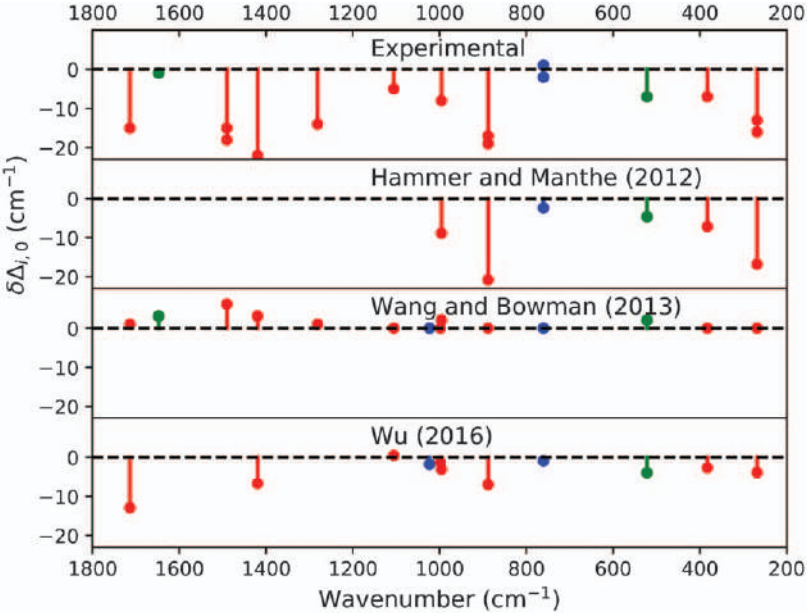

Figure 9.10 Variation of the tunnelling splitting with respect to the ground-state value for modes obeying rule III (green), rule IV (blue), and rule V (red).

The above discussion shows that some important steps have been taken towards the prediction of state-selected tunnelling splittings; however, a complete theoretical description of this phenomenon seems still far off.

9.7 Conclusion

As the results in Table 9.2 indicate, the accurate calculation of ground-level tunnelling splittings of simple molecules such as MA is achievable but requires a large computational effort. If we require an accuracy of ±10% for splittings and ±10% for H/D isotope effects, only a few of the reported calculations pass muster and most of these are of recent dates. This implies that extension of the calculations to larger molecules will require the development of new methods, in particular approximation methods that are both tractable and reliable. The same holds *a fortiori* for the calculation of state-selected splittings. On the other hand, there remain lots to learn about the interaction between vibrations in molecules with large-amplitude modes.

Funding

Financial support from the Consellería de Cultura, Educación e Ordenación Universitaria (Axuda para Consolidación e Estructuración de unidades de investigación competitivas do Sistema Universitario de Galicia, Xunta de Galicia ED431C 2017/17 & Centro singular de investigación de Galicia acreditación 2019-2022, ED431G 2019/03) and the European Union (European Regional Development Fund -ERDF), is gratefully acknowledged.

Abbreviations

AIM	Approximate instanton method
DMC	Diffusion Monte Carlo
iMDH	Imaginary mode Hamiltonian
LRP	Linear reaction path
MCTDH	Multiconfigurational time-dependent Hartree method
MD	Multidimensional method
MEP	Minimum energy path
NEO	Nuclear-electronic orbital method
NM	Normal mode
QCT	"Quasiclassical" trajectories as described by Makri and Miller
Q_{im}	Imaginary-frequency normal-mode method
QMC	Quantum mechanical method
PIMD	Path integral molecular dynamics
RIM	"Rainbow" instanton approximation
RPIM	Ring-polymer instanton method
RPH	Reaction path Hamiltonian
RSH	Reaction surface Hamiltonian
SC	Semi-classical approximation
WKB	Semi-classical Wenzel–Kramer–Brillouin approximation

Acknowledgements

The authors are indebted to Zorka Smedarchina and Willem Siebrand from the National Research Council of Canada for their encouragement and wise comments, which have greatly improved the manuscript. DF-C thanks Xunta de Galicia for financial support through a postdoctoral grant.

References

1. F. Hund, Zur Deutung der Molekelspektren III, *Z. Phys.*, 1927, **43**, 805–826.
2. N. Fröman and P. O. Fröman, *JWKB Approximation. Contributions to the Theory*, North-Holland Publishing Company, Amsterdam, 1965.
3. R. P. Feynmann and A. R. Hibbs, *Quantum Mechanics and Integrals*, McGraw-Hill Book Company, Inc., New York, 1965.
4. S. Coleman, *The whys of Subnuclear Physics*, Plenun Press, New York, 1979.
5. M. Paranjape, *The Theory and Applications of Instanton Calculations*, Cambridge University Press, Cambridge, UK, 2018.
6. H.-D. Meyer, U. Manthe and L. S. Cederbaum, The multi-configurational time-dependent Hartree approach, *Chem. Phys. Lett.*, 1990, **165**, 73–78.
7. H.-D. Meyer, F. Gatti and G. A. Worth, *Multidimensional Quantum Dynamics*, Wiley-VCH, 2009.
8. U. Manthe, The multi-configurational time-dependent Hartree approach revisited, *J. Chem. Phys.*, 2015, **142**, 244109.
9. E. Mátyus, D. J. Wales and S. C. Althorpe, Quantum tunneling splittings from path-integral molecular dynamics, *J. Chem. Phys.*, 2016, **144**, 114108.
10. H. Jeffreys, On certain approximate solutions of linear differencial equations of the second order, *Proc. London Math. Soc.*, 1925, **s2–23**, 428–436.
11. L. D. Landau and E. M. Lifshitz, *Quantum Mechanics: Non-relativistic Theory*, Pergamon Press, 3rd edn, **vol. 3**, 1977.
12. C. Herring, Critique of the Heitler-London method of calculating spin couplings at large distances, *Rev. Mod. Phys.*, 1962, **34**, 631–645.
13. H. Dekker, Coherent tunneling: On the level splitting of local ground states in bistable potential, *Phys. Lett.*, 1986, **114A**, 295–297.
14. W. H. Miller, Periodic orbit description of tunneling in symmetric and asymmetric double-well potentials, *J. Chem. Phys.*, 1979, **83**, 960–963.
15. G. Gamow, Zur Quantentheorie des Atomkernes, *Z. Phys.*, 1928, **51**, 204–212.
16. E. C. Kemble, *The Fundamental Principles of Quantum Mechanics with Elementary Applications*, McGraw-Hill Book Company, Inc., New York, 1st edn, 1937.
17. W. H. Miller, Classical path approximation for the Boltzmann density matrix, *J. Chem. Phys.*, 1971, **55**, 3146–3149.

18. W. H. Miller and T. F. George, Analytic continuation of classical mechanics for classically forbidden collision processes, *J. Chem. Phys.*, 1972, **56**, 5668–5681.
19. W. H. Miller, Semiclassical limit of quantum mechanical transition state theory for nonseparable systems, *J. Chem. Phys.*, 1975, **62**, 1899–1906.
20. M. Chaichian and A. Demichev, *Path Integrals in Physics. Volumen I: Stochastic Processes and Quantum Mechanics*, Taylor & Francis, Bristol and Philadelphia, 2001.
21. K. C. Gutzwiller, Phase-integral approximation in momentum space and the bound states of an atom, *J. Math. Phys.*, 1967, **8**, 1979–2000.
22. S. Coleman, Fate of the false vacuum: Semiclassical theory, *Phys. Rev. D*, 1977, **15**, 2929.
23. A. I. Vainshtein, V. I. Zakharov, V. A. Novikov and M. A. Shifman, ABC of instantons, *Sov. Phys. Usp.*, 1982, **25**, 195–215.
24. I. Affleck, Quantum-statistical metastability, *Phys. Rev. Lett.*, 1981, **46**, 388–391.
25. J. Ankerhold, *Quantum Tunneling in Complex Systems: The Semiclassical Approach*, Springer-Verlag, Freiburg, Germany, **vol. 224**, 2007.
26. J. O. Richardson, Derivation of instanton rate theory from first principles, *J. Chem. Phys.*, 2016, **144**, 114106.
27. V. Benderskii, D. E. Makarov and C. A. Wight, Chemical dynamics at low temperatures, *Adv. Chem. Phys.*, 1994, **88**, 1.
28. G. V. Mil'nikov and H. Nakamura, Practical implementation of the instanton theory for the ground-state tunneling splitting, *J. Chem. Phys.*, 2001, **115**, 6881–6897.
29. G. Mil'nikov and H. Nakamura, Tunneling splittings and decay of metastable states in polyatomic molecules: invariant instanton theory, *Phys. Chem. Chem. Phys.*, 2008, **10**, 1374–1393.
30. H. Nakamura and G. Mil'nikov, *Quantum Mechanical Tunneling in Chemical Physics*, CRC Press, Boca Raton, FL, 2013.
31. V. A. Benderskii and D. E. Makarov, Quantum chemical dynamics in two dimensions, *Chem. Phys.*, 1993, **170**, 275–293.
32. A. Garg, Tunnel splittings for one-dimensional potential wells revisited, *Am. J. Phys.*, 2000, **68**, 430–437.
33. A. Fernández-Ramos, A. Ellingson, B. C. Garrett and D. G. Truhlar, Variational transition state theory, *Rev. Comput. Chem.*, 2007, **23**, 125–262.
34. R. T. Skodje, D. G. Truhlar and B. C. Garrett, Vibrationally adiabatic models for reactive tunneling, *J. Chem. Phys.*, 1982, **77**, 5955–5976.
35. F. B. Brown, S. C. Tucker and D. G. Truhlar, Semiclassical reaction-path methods applied to calculate the tunneling splitting in ammonia, *J. Chem. Phys.*, 1985, **83**, 4451–4455.
36. W. H. Miller, B. A. Ruf and Y.-T. Chang, A diabatic reaction path hamiltonian, *J. Chem. Phys.*, 1988, **89**, 6298–6304.
37. B. C. Garrett, T. Joseph, T. N. Truong and D. G. Truhlar, Application of the large-curvature tunneling approximation to polyatomic molecules:

abstraction of H or D by methyl radical, *Chem. Phys.*, 1989, **136**, 271–293.

38. A. Fernández-Ramos and D. G. Truhlar, Improved algorithm for corner-cutting tunneling calculations, *J. Chem. Phys.*, 2001, **114**, 1491–1496.
39. B. C. Garrett and D. G. Truhlar, A least-action variational method for calculating multidimensional tunneling probabilities for chemical reactions, *J. Chem. Phys.*, 1983, **79**, 4931–4938.
40. C. S. Tautermann, A. F. Voegele, T. Loerting and K. R. Liedl, The optimal tunneling path for the proton transfer in malonaldehyde, *J. Chem. Phys.*, 2002, **117**, 1962–1966.
41. R. Meana-Pañeda, D. G. Truhlar and A. Fernández-Ramos, Least-action transmission coefficient for polyatomic reactions, *J. Chem. Theory Comput.*, 2010, **6**, 6–17.
42. V. A. Benderskii, D. E. Makarov, D. L. Pastur and P. G. Grirevich, Preexponential factor of the rate constant of low-temperature chemical reactions. Fluctuational width of tunneling channels and stability frequencies, *Chem. Phys.*, 1992, **161**, 51–61.
43. S. C. Althorpe, On the equivalence of two commonly used forms of semiclassical instanton theory, *J. Chem. Phys.*, 2011, **134**, 114104.
44. J. B. Rommel and J. Kästner, Adaptive integration grids in instanton theory improve the numerical accuracy at low temperature, *J. Chem. Phys.*, 2011, **134**, 184107.
45. J. O. Richardson and S. C. Althorpe, Ring-polymer instanton method for calculating tunneling splittings, *J. Chem. Phys.*, 2011, **134**, 054109.
46. J. Meisner, J. B. Rommel and J. Kästner, Kinetic isotope effects calculated with the instanton method, *J. Comput. Chem.*, 2011, **32**, 3456–3463.
47. Z. Smedarchina, W. Siebrand and M. Z. Zgierski, An instanton approach to intramolecular hydrogen exchange: Tunneling splittings in malonaldehyde and the hydrogenoxalate anion, *J. Chem. Phys.*, 1995, **103**, 5326–5334.
48. W. Siebrand, Z. Smedarchina, M. Z. Zgierski and A. Fernández-Ramos, Proton tunnelling in polyatomic molecules: a direct-dynamics instanton approach, *Int. Rev. Phys. Chem.*, 1999, **18**, 5–41.
49. Z. Smedarchina, A. Fernández-Ramos and W. Siebrand, Software news and updates - DOIT: A program to calculate thermal rate constants and mode-specific tunneling splittings directly from quantum-chemical calculations, *Int. J. Phys. Chem*, 2001, **22**, 787–801.
50. W. F. Rowe, Jr., R. W. Duerst and E. B. Wilson, The intramolecular hydrogen bond in malonaldehyde, *J. Am. Chem. Soc.*, 1976, **98**, 4021–4023.
51. W. Siebrand, Z. Smedarchina and A. Fernández-Ramos, Communication: Selection rules for tunneling splitting of vibrationally excited levels, *J. Chem. Phys.*, 2013, **139**, 021101.
52. S. L. Baughcum, R. W. Duerst, W. F. Rowe, Z. Smith and E. B. Wilson, Microwave spectroscopic study of malonaldehyde (3-hydroxy-2-

propenal). 2. Structure, dipole moment, and tunneling, *J. Am. Chem. Soc.*, 1981, **103**, 6296–6303.

53. S. L. Baughcum, Z. Smith, E. B. Wilson and R. W. Duerst, Microwave spectroscopic study of malonaldehyde. 3. Vibration-rotation interaction and one-dimensional model for proton tunneling, *J. Am. Chem. Soc.*, 1984, **106**, 2260–2265.
54. J. Bicerano, H. F. Schaefer III and W. H. Miller, Structure and tunneling dynamics of malonaldehyde. A theoretical study, *J. Am. Chem. Soc.*, 1983, **105**, 2550–2553.
55. M. J. Frisch, A. C. Scheiner, H. F. Schaefer and J. S. Binkley, The malonaldehyde equilibrium geometry: A major structural shift due to the effects of electron correlation, *J. Chem. Phys.*, 1985, **82**, 4194–4198.
56. T. Carrington and W. H. Miller, Reaction surface Hamiltonian for the dynamics of reactions in polyatomic systems, *J. Chem. Phys.*, 1984, **81**, 3942–3949.
57. T. Carrington and W. H. Miller, Reaction surface description of intramolecular hydrogen atom transfer in malonaldehyde, *J. Chem. Phys.*, 1985, **84**, 4364–4370.
58. W. H. Miller, N. C. Handy and J. E. Adams, Reaction path hamiltonian for poliatomic molecules, *J. Chem. Phys.*, 1980, **72**, 99–112.
59. E. B. Wilson, Jr., J. C. Decius and P. C. Cross, *Molecular Vibrations*, Dover Publications, Inc., New York, 1955.
60. N. Shida, P. F. Barbara and J. E. Almlöf, A theoretical study of multidimensional nuclear tunneling in malonaldehyde, *J. Chem. Phys.*, 1989, **91**, 4061–4072.
61. E. Bosch, M. Moreno, J. M. Lluch and J. Bertrán, Bidimensional tunneling dynamics of malonaldehyde and hydrogenoxalate anion. A comparative study, *J. Chem. Phys.*, 1990, **93**, 5685–5692.
62. N. Makri and W. H. Miller, Basis set methods for describing the quantum mechanics of a ‘‘system’’ interacting with a harmonic bath, *J. Chem. Phys.*, 1987, **86**, 1451–1457.
63. V. A. Benderskii, V. I. Goldanskii and D. E. Makarov, Low-temperature chemical reactions. Effect of symmetrically coupled vibrations in collinear exchange reactions, *Chem. Phys.*, 1991, **154**, 407–424.
64. V. K. Babamov, Intramolecular hydrogen atom tunneling. Analytical solution for linear coupling to a low-frequency bath, *Chem. Phys. Lett.*, 1994, **217**, 254–260.
65. Z. Smedarchina, A. Fernández-Ramos and M. A. Ríos, A comparison of two methods for direct tunneling dynamics: Hydrogen exchange in the glycolate anion as a test case, *J. Chem. Phys.*, 1997, **106**, 3956–3964.
66. Z. Smedarchina, W. Siebrand and M. Z. Zgierski, Mode specific hydrogen tunneling in tropolone: An instanton approach, *J. Chem. Phys.*, 1996, **104**, 1203–1212.
67. A. Fernández-Ramos, Z. Smedarchina, M. Zgierski and W. Siebrand, Mode-specific tunneling splittings in 9-hydroxyphenalenone:

Comparison of two methods for direct tunneling dynamics, *J. Chem. Phys.*, 1998, **109**, 1004–1013.

68. Z. Smedarchina, A. Fernandez-Ramos and W. Siebrand, Tunneling dynamics of double proton transfer in formic acid and benzoic acid dimers, *J. Chem. Phys.*, 2005, **122**, 134309.
69. A. Fernández-Ramos, Z. Smedarchina and F. Pichierri, Proton tunneling in calixarenes: a theoretical investigation, *Chem. Phys. Lett.*, 2001, **343**, 627–632.
70. Z. Smedarchina, W. Siebrand, A. Fernández-Ramos and E. Martínez-Núñez, New interpretation of ground- and excited-state tunneling splitting in 2-pyridone·2-hydroxypyridine, *Chem. Phys. Lett.*, 2004, **386**, 396–402.
71. J. R. Roscioli, D. W. Pratt, Z. Smedarchina, W. Siebrand and A. Fernández-Ramos, Proton transfer dynamics via high resolution spectroscopy in the gas phase and instanton calculations, *J. Chem. Phys.*, 2004, **120**, 11351–11354.
72. Z. Smedarchina, M. F. Shibl, O. Kühn and A. Fernández-Ramos, The tautomerization dynamics of porphycene and its isotopomers - Concerted versus stepwise mechanisms, *Chem. Phys. Lett.*, 2007, **436**, 314–321.
73. Z. Smedarchina, W. Siebrand and A. Fernández-Ramos, The rainbow instanton method: A new approach to tunneling splitting in polyatomics, *J. Chem. Phys.*, 2012, **137**, 224105.
74. Z. Smedarchina, W. Siebrand and A. Fernández Ramos, Zero-point tunneling splittings in compounds with multiple hydrogen bonds calculated by the rainbow instanton method, *J. Phys. Chem. A*, 2013, **117**, 11086–11100.
75. C. S. Tautermann, A. F. Voegele, T. Loerting and K. R. Liedl, An accurate semiclassical method to predict ground-state tunneling splittings, *J. Chem. Phys.*, 2002, **117**, 1967–1974.
76. C. S. Tautermann, A. F. Voegele and K. R. Liedl, The ground-state tunneling splitting of various carboxylic acid dimers, *J. Chem. Phys.*, 2004, **120**, 631–637.
77. N. Makri and W. H. Miller, A semiclassical tunneling model for use in classical trajectory simulations, *J. Chem. Phys.*, 1989, **91**, 4026–4036.
78. E. Bosch, M. Moreno and J. M. Lluch, A semiclassical simulation for tunneling dynamics of malonaldehyde and hydrogenoxalate anion, *Chem. Phys.*, 1992, **159**, 99–107.
79. E. Bosch, M. Moreno and J. M. Lluch, Tunneling dynamics in isotopically substituted malonaldehyde. Comparison between symmetric and asymmetric species, *J. Am. Chem. Soc.*, 1992, **114**, 2072–2076.
80. Y. Guo, T. D. Sewell and D. L. Thompson, A full-dimensional semiclassical calculation of vibrational mode selectivity in the tunneling splitting in a planar model of malonaldehyde, *Chem. Phys. Lett.*, 1994, **224**, 470–475.
81. T. D. Sewell, Y. Guo and D. L. Thompson, Semiclassical calculations of tunneling splitting in malonaldehyde, *J. Chem. Phys.*, 1995, **103**, 8557–8565.

82. D. P. Tew, N. C. Handy, S. Carter, S. Irle and J. Bowman, The internal coordinate path Hamiltonian; application to methanol and malonaldehyde, *Mol. Phys.*, 2003, **101**, 3513–3525.
83. D. P. Tew, N. C. Handy and S. Carter, The vibrations and tunnelling of malonaldehyde on a Møller–Plesset surface, *Mol. Phys.*, 2004, **102**, 2217–2226.
84. D. P. Tew, N. C. Handy and S. Carter, A reaction surface Hamiltonian study of malonaldehyde, *J. Chem. Phys.*, 2006, **125**, 084313.
85. S. Carter, J. M. Bowman and L. B. Harding, Ab initio calculations of force fields for H_2CN and ClHCN and vibrational energies of H_2CN, *Spectrochim. Acta A*, 1997, **53**, 1179–1188.
86. S. Carter, J. Culik and J. M. Bowman, Vibrational self-consistent field method for many-mode systems: A new approach and application to the vibrations of CO adsorbed on Cu(100), *J. Chem. Phys.*, 1997, **107**, 10458–10469.
87. J. M. Bowman, S. Carter and X. Huang, MULTIMODE: a code to calculate rovibrational energies of polyatomic molecules, *Int. Rev. Phys. Chem.*, 2003, **22**, 533–549.
88. W. Mizukami, S. Habershon and D. P. Tew, A compact and accurate semi-global potential energy surface for malonaldehyde from constrained least squares regression, *J. Chem. Phys.*, 2014, **141**, 144310.
89. Y. Wang, B. J. Braams, J. M. Bowman, S. Carter and D. P. Tew, Full-dimensional quantum calculations of ground-state tunneling splitting of malonaldehyde using an accurate ab initio potential energy surface, *J. Chem. Phys.*, 2008, **128**, 224314.
90. D. Babić, S. D. Bosanac and N. Došlić, Proton transfer in malonaldehyde: a model three-dimensional study, *Chem. Phys. Lett.*, 2002, **358**, 337–343.
91. K. Yagi, T. Taketsugu and K. Hirao, Generation of full-dimensional potential energy surface of intramolecular hydrogen atom transfer in malonaldehyde and tunneling dynamics, *J. Chem. Phys.*, 2001, **115**, 10647–10655.
92. Y. Ootani and T. Taketsugu, Ab Initio Molecular Dynamics Approach to Tunneling Splitting in Polyatomic Molecules, *J. Comput. Chem.*, 2011, **33**, 60–65.
93. G. V. Mil'nikov, K. Yagi, T. Taketsugu, H. Nakamura and K. Hirao, Tunneling splitting in polyatomic molecules: Application to malonaldehyde, *J. Chem. Phys.*, 2003, **119**, 10–13.
94. M. Eraković, C. L. Vaillant and M. T. Cvitaš, Instanton theory of ground-state tunneling splittings with general paths, *J. Chem. Phys.*, 2020, **152**, 084111.
95. M. T. Cvitaš and S. C. Althorpe, Locating instantons in calculations of tunneling splittings: The test case of malonaldehyde, *J. Chem. Theory Comput.*, 2016, **12**, 787–803.

96. C. L. Vaillant, D. J. Wales and S. C. Althorpe, Tunneling splittings from path-integral molecular dynamics using a Langevin thermostat, *J. Chem. Phys.*, 2018, **148**, 234102.
97. M. D. Coutinho-Neto, A. Viel and U. Manthe, The ground state tunneling splitting of malonaldehyde: Accurate full dimensional quantum dynamics calculations, *J. Chem. Phys.*, 2004, **121**, 9207–9210.
98. A. Viel, M. D. Coutinho-Neto and U. Manthe, The ground state tunneling splitting and the zero point energy of malonaldehyde: A quantum Monte Carlo determination, *J. Chem. Phys.*, 2007, **126**, 024308.
99. M. Schröder, F. Gatti and H.-D. Meyer, Theoretical studies of the tunneling splitting of malonaldehyde using the multiconfiguration time-dependent Hartree approach, *J. Chem. Phys.*, 2011, **134**, 234307.
100. T. Hammer and U. Manthe, Intramolecular proton transfer in malonaldehyde: Accurate multilayer multi-configurational time-dependent Hartree calculations, *J. Chem. Phys.*, 2011, **134**, 224305.
101. F. Wu, Y. Ren and W. Bian, The hydrogen tunneling splitting in malonaldehyde: A full-dimensional time-independent quantum mechanical method, *J. Chem. Phys.*, 2016, **145**, 074309.
102. A. Hazra, J. H. Skone and S. Hammes–Schiffer, Combining the nuclear-electronic orbital approach with vibronic coupling theory: Calculation of the tunneling splitting for malonaldehyde, *J. Chem. Phys.*, 2009, **130**, 054108.
103. Y. Wang and J. M. Bowman, One-dimensional tunneling calculations in the imaginary-frequency, rectilinear saddle-point normal mode, *J. Chem. Phys.*, 2008, **129**, 121103.
104. E. Kamarchik, Y. Wang and J. Bowman, Reduced-dimensional quantum approach to tunneling splittings using saddle-point normal coordinates, *J. Phys. Chem. A*, 2009, **113**, 7556–7562.
105. F. Wu and Y. Ren, Primary and secondary isotope effect on tunnelling in malonaldehyde using a quantum mechanical scheme, *Mol. Phys.*, 2017, **115**, 1700–1707.
106. Y. Yang, X. Liu, M. Meuwly, L. Xiao and S. Jia, Harmonic bath averaged Hamiltonian: An efficient tool to capture quantum effects of large systems, *J. Phys. Chem. A*, 2012, **116**, 11134–11139.
107. A. Fernández-Ramos, Z. Smedarchina and W. Siebrand, Multidimensional Hamiltonian for tunneling with position-dependent mass, *Phys. Rev. E*, 2014, **90**, 033306.
108. Z. Homayoon, J. M. Bowman and F. A. Evangelista, Calculations of mode-specific tunneling of double-hydrogen transfer in porphycene agree with and illuminate experiment, *J. Phys. Chem. Lett.*, 2014, **5**, 2723–2727.
109. Z. Smedarchina, W. Siebrand and A. Fernández-Ramos, Tunneling splitting in double-proton transfer: Direct diagonalization results for porphycene, *J. Chem. Phys.*, 2014, **141**, 174312.
110. S. Takada and H. Nakamura, Effects of vibrational excitation on multidimensional tunneling: General study and proton tunneling in tropolone, *J. Chem. Phys.*, 1995, **102**, 3977–3992.

111. V. A. Benderskii, E. V. Vetoshkin, I. S. Irgibaeva and H. P. Trommsdorff, Tunneling splittings in vibrational spectra of non-rigid molecules IX. Malonaldehyde and its isotopomers as a test case for fully coupled multidimensional tunneling dynamics, *Chem. Phys.*, 2000, **262**, 393–422.
112. V. A. Benderskii, E. V. Vetoshkin, S. Y. Grebenshchikov, L. von Laue and H. P. Trommsdorff, Tunneling splitting in vibrational spectra of non-rigid molecules. I. Perturbative instanton approach, *Chem. Phys.*, 1997, **219**, 119–142.
113. F. Wu, Quantum mechanical investigation of mode-specific tunneling upon fundamental excitation in malonaldehyde, *J. Phys. Chem. A*, 2016, **120**, 3849–3854.
114. T. Hammer and U. Manthe, Iterative diagonalization in the state-averaged multi-configurational time-dependent Hartree approach: Excited state tunneling splittings in malonaldehyde, *J. Chem. Phys.*, 2012, **136**, 054105.
115. Y. Wang and J. M. Bowman, Mode-specific tunneling using the Q_{im} path: Theory and an application to full-dimensional malonaldehyde, *J. Chem. Phys.*, 2013, **139**, 154303.
116. Z. Smith, E. B. Wilson and R. W. Duerst, The infrared spectrum of gaseous malonaldehyde (3-hydroxy-2-propenal), *Spectrochim. Acta A*, 1983, **39A**, 1117–1129.
117. C. Duan and D. Luckhaus, High resolution IR-diode laser jet spectroscopy of malonaldehyde, *Chem. Phys. Lett.*, 2004, **391**, 129–133.
118. T. N. Wassermann, D. Luckhaus, S. Coussan and M. A. Suhm, Proton tunneling estimates for malonaldehyde vibrations from supersonic jet and matrix quenching experiments, *Phys. Chem. Chem. Phys.*, 2006, **8**, 2344–2348.
119. N. O. B. Lüttschwager, T. N. Wassermann, S. Coussan and M. A. Suhm, Periodic bond breaking and making in the electronic ground state on a sub-picosecond timescale: OH bending spectroscopy of malonaldehyde in the frequency domain at low temperature, *Phys. Chem. Chem. Phys.*, 2010, **12**, 8201–8207.
120. N. O. B. Lüttschwager, T. N. Wassermann, S. Coussan and M. A. Suhm, Vibrational tuning of the hydrogen transfer in malonaldehyde – a combined FTIR and Raman jet study, *Mol. Phys.*, 2013, **111**, 2211–2227.

CHAPTER 10

Quantum-dynamical Calculation of Rate Constants in Polyatomic Reactions Employing the Quantum Transition State Concept

RALPH WELSCH

Center for Free-Electron Laser Science, Deutsches Elektronen-Synchrotron,
Notkestr. 85, 22607 Hamburg, Germany
Email: ralph.welsch@desy.de

10.1 Introduction

Throughout this chapter, we consider basic bimolecular reactions of the form $\mathrm{A} + \mathrm{BC} \rightarrow \mathrm{AB} + \mathrm{C}$. The basic observable that links macroscopic variation of concentration or partial pressures to the microscopic domain of molecular collisions is the *thermal rate constant*, $k(T)$. Macroscopically, it links the change of the product concentration, [AB], to the concentration of the reactants, [A] and [BC]:

$$\frac{\mathrm{d}[\mathrm{AB}]}{\mathrm{d}t} = k(T)[\mathrm{A}][\mathrm{BC}]. \tag{10.1}$$

Microscopically, in particular in the gas phase, it can be understood in terms of scattering events. Each reaction is essentially a collision of two

---

Theoretical and Computational Chemistry Series No. 18
Tunnelling in Molecules: Nuclear Quantum Effects from Bio to Physical Chemistry
Edited by Johannes Kästner and Sebastian Kozuch

Published by the Royal Society of Chemistry, www.rsc.org

molecules which results in a rearrangement of the bonds of the two molecules and a transfer of one group (B in the example above) from one molecule to the other. This is called *reactive scattering* and has to be distinguished from elastic collisions and inelastic collisions without rearrangement that result in rotational and/or vibrational excitation or de-excitation. For any given initial ro-vibrational state of the reactants and a given total energy of the system, a probability for a reactive scattering event, *i.e.*, a *reaction probability*, can be obtained. The sum of all these reaction probabilities is known as the *cumulative reaction probability* (CRP) and is denoted as $N(E)$. The thermal average of the CRP then gives the thermal rate constant:

$$k(T) = \frac{1}{2\pi Q_{\mathrm{r}}(T)} \int_{-\infty}^{\infty} \mathrm{d}E\, \mathrm{e}^{-E/k_{\mathrm{B}}T} N(E), \tag{10.2}$$

where $Q_{\mathrm{r}}(T)$ is the partition function of the reactants. *Microcanonical rate constants* $k(E)$ can be obtained from the CRP by weighing with the density of states of the reactants $\rho_{\mathrm{r}}(E)$:

$$k(E) = \frac{1}{2\pi\rho_{\mathrm{r}}(E)} N(E). \tag{10.3}$$

One can obtain the CRP and therefore the rate constants by calculating each reaction probability individually.[1] However, if the reaction occurs through a barrier, then the possibility of overcoming that barrier determines the CRP and any information about the asymptotic states is irrelevant. Therefore, the CRP and rate constants can be obtained in a *direct* way by simulations of the transient dynamics in the barrier or transition state region.

In this chapter, we will introduce an exact, convenient and efficient theory to directly calculate thermal and microcanonical rate constants for reactions crossing a barrier as sketched in Figure 10.1. The approach is termed the *quantum transition state concept* and is based on generalized *flux correlation functions*. To this end, we will introduce a convenient way to define *reaction channels*. If the total energy or temperature is reasonably small, there is only

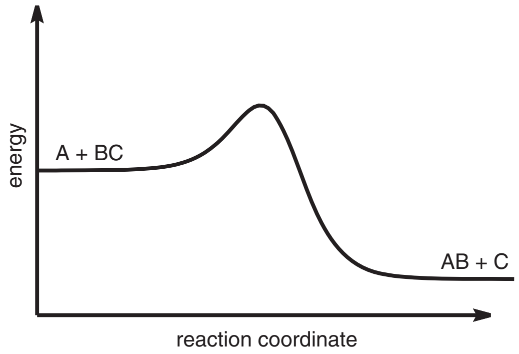

Figure 10.1 Sketch of the energy profile of a general $A + BC \rightarrow AB + C$ reaction proceeding *via* a potential energy barrier.

a small number of relevant channels and thus the transient dynamics can be obtained by short-time propagation of a small number of wavepackets representing the different channels. As only short-time propagation is required within the quantum transition state concept, one can employ efficient and exact quantum dynamics approaches like the *multiconfigurational time-dependent Hartree* (MCTDH) approach, to obtain the exact thermal rate constant of polyatomic reactions.

The chapter is organized into three parts. The first part consists of Sections 10.2 and 10.3. In this part, the basic theory underpinning the calculation of thermal rate constants is briefly reviewed. This includes basic scattering theory and flux correlation functions (Section 10.2). Furthermore, the efficient evaluation of thermal rate constants employing the quantum transition state concept is introduced (Section 10.3). The second part introduces several numerical techniques to solve the time-dependent Schrödinger equation, which is required to numerically evaluate the flux correlation functions introduced before. This part includes the description of the standard wavepacket approach (Section 10.4) and the more advanced multiconfigurational time-dependent Hartree approach (Section 10.5). Both, the first and second part can be read independently, if one is only interested in the basic theory and the quantum transition state concept or if one is only interested in the more technical details of quantum dynamics simulations and the MCTDH approach. In the third part (Section 10.6), the methodology introduced in this chapter is exemplified for prototypical tri-, tetra- and six-atomic reactions.

10.2 Theory of Thermal Rate Constant Calculations

In this section, we will look at the aforementioned reaction $A + BC \rightarrow AB + C$ and the associated rate constant $k(T)$ in two different, but connected, theoretical ways and review some basic theory. The first approach will be based on microscopic scattering theory and the second one is based on flux correlation functions. Only a brief overview of each approach can be given and the reader is referred to ref. 2–7 for more details.

10.2.1 Scattering Theory

The fundamental and overarching quantity of scattering theory is the *scattering* or *S-matrix* with elements $S_{\text{if}}(E)$.[3] It gives the transition amplitudes leading from some quantum state of the system i to another quantum state f at a fixed total energy E. For our chemical reaction, i will be the direct product of the ro-vibrational states of the molecules A and BC, which are infinitely separated and have a relative velocity defined by the remaining energy $E_{\text{coll}} = E - E_{\text{A}} - E_{\text{BC}}$, which is also termed *collision energy*. Consequently, f is the direct product of the ro-vibrational state of AB and C, which are again infinitely separated and have a relative velocity defined by the remaining energy $E_{\text{k,rel}} = E - E_{\text{AB}} - E_{\text{C}}$. Any transition probability from a reactant state i to a product state f is given as the square of the appropriate S-matrix element, *i.e.*, $p_{i\rightarrow f}(E) = |S_{if}(E)|^2$. The transition probabilities include non-reactive cases, *e.g.*, inelastic collisions exciting or de-exciting rotational or vibrational motion without bonds being broken and formed. In the remainder of this chapter, we exclusively consider reactive scattering events and thus we will always talk about *reaction probabilities* instead of the more general transition probabilities.

The S-matrix can be defined employing Møller operators $\Omega_\pm$[3]

$$S_{if} = \langle \Psi_f^- | \Psi_i^+ \rangle = \langle \Psi_f | \Omega_-^\dagger \Omega_+ | \Psi_i \rangle. \tag{10.4}$$

with

$$\Omega_\pm = \lim_{t\rightarrow\mp\infty} \mathrm{e}^{i\hat{H}t} \mathrm{e}^{-i\hat{H}_0 t}, \tag{10.5}$$

where $\hat{H}$ is the full Hamiltonian and $\hat{H}_0$ is the asymptotic free Hamiltonian. The action of a Møller operator on an initial state is that it first propagates backwards (forwards) to $t = -\infty$ $(t = +\infty)$ using the free Hamiltonian $\hat{H}_0$ and then propagates forwards (backwards) to $t = 0$. The resulting states are the scattering states at $t = 0$ and are denoted by

$$\Psi^\pm = \Omega_\pm \Psi = \Omega_\pm (\chi\, g^\pm) \tag{10.6}$$

where χ is the direct product of the ro-vibrational states of the reactant or product molecules and $g^\pm$ are free wavepackets with incoming and outgoing momenta in the scattering coordinate, respectively. In other words, the Møller operator Ω_+ maps an initially $(t = -\infty)$ free state to its corresponding scattering state at $t = 0$, which evolved under the action of the full Hamiltonian that includes the interaction of both reaction partners. Similarly, the Møller operator Ω_- maps a scattering state at $t = 0$ onto its corresponding final free (*i.e.*, with non-interacting products) state in the infinite future $(t = +\infty)$. Therefore the overlap $\langle \Psi_f^- | \Psi_f^+ \rangle$, *i.e.*, the transition amplitude of an incoming scattering state at $t = 0$ to an outgoing scattering state at $t = 0$, can be understood as the transition amplitude from an initial state $\Psi_i = \chi_i\, g^+$ with quantum numbers i to a final state $\Psi_f = \chi_f\, g^-$ with quantum numbers f. One can now define the *scattering operator*[3]

$$\hat{S} = \Omega_-^\dagger \Omega_+. \tag{10.7}$$

The energy-resolved S-matrix elements belonging to states with well-defined energy are then obtained as

$$S_{if}(E) = \langle \Psi_{f,E}^- | \Psi_{i,E}^+ \rangle. \tag{10.8}$$

Energy-normalized scattering states can be constructed by a linear combination of wave packets[5]

$$\Psi_{i,E}^+ = \frac{1}{2\pi\Delta^+(E)} \int_{-\infty}^{\infty} \mathrm{d}t\ \mathrm{e}^{iEt}\, \mathrm{e}^{-i\hat{H}t} \Phi_i^+ \tag{10.9}$$

where the wavepackets

$$\Phi_i^+(R, r) = \chi_i(r) g^+\ (R) \tag{10.10}$$

are products of eigenstates of the internal Hamiltonian χ_n and a wavepacket, $g^+(R)$, in the reaction coordinate located in the asymptotic region with incident momentum and the normalization coefficients[5]

$$\Delta^+(E) = \langle \Psi_E^+(R) | \Phi^+(R) \rangle = \sqrt{\frac{m}{2\pi k}} \int e^{ikR} g^+(R)\ dR, \tag{10.11}$$

where m is the corresponding mass and k the wavenumber with $E = \frac{k^2}{2m}$. S-matrix elements can be obtained efficiently by a correlation function expression as[5]

$$S_{i,f}(E) = \frac{1}{2\pi \Delta^+(E) \Delta^-(E)} \int_{-\infty}^{\infty} dt\ e^{iEt} \langle \Phi_f^- | e^{-i\hat{H}t} | \Phi_i^+ \rangle. \tag{10.12}$$

Given the full knowledge of the scattering matrix, one can obtain the CRP as sum over all reaction probabilities:

$$N(E) = \sum_i \sum_f p_{i \to f}(E) = \sum_i \sum_f \left| S_{if}(E) \right|^2, \tag{10.13}$$

and from the CRP, the thermal and microcanonical rate constants can be obtained as given in eqn (10.2) and (10.3).

10.2.2 Flux Correlation Functions

The calculation of the full scattering matrix is cumbersome and also superfluous if the sole purpose is to obtain rate constants. The rate constants only depend on the dynamics around the barrier and not on the specific dynamics in the asymptotic regions. We will introduce a theory that allows for the ''direct'' calculation of thermal or microcanonical rate constants. It was originally introduced employing formal scattering theory.[6–8] However, we will introduce it in a more intuitive way.[9]

Let us consider a thermal ensemble of reactants. They can be described by the density matrix[9]

$$\rho_r = \frac{1}{Q_r(T)} e^{-\beta \hat{H}/2} (1 - h)\ e^{-\beta \hat{H}/2}, \tag{10.14}$$

$$Q_r(T) = \mathrm{tr}(e^{-\beta \hat{H}/2} (1 - h)\ e^{-\beta \hat{H}/2}), \tag{10.15}$$

where h is a function defined in terms of a *dividing (hyper)surface*, which discriminates between reactants and products. h equals unity on the product side of the dividing surface and zero on the reactant side. Therefore, h is a projector onto the product geometries and $(1-h)$ projects onto reactant geometries. Please note that the ordering of the Boltzmann operator and the projector is not important here as any reaction is only a weak perturbation of the overall thermal equilibrium.[9] If the reaction is a strong perturbation of the thermal equilibrium the definition of a thermal rate constant is not valid. The time evolution of the system described by the density matrix in eqn (10.14) reads

$$\rho_\mathrm{r}(t) = \mathrm{e}^{-i\hat{H}t}\rho_\mathrm{r}\ \mathrm{e}^{i\hat{H}t}. \tag{10.16}$$

The amount of product at time t is calculated as the time-dependent expectation value of the projector onto the products, h, and reads

$$\langle h\rangle(t) = \mathrm{tr}(h\rho_\mathrm{r}(t)) \tag{10.17}$$

$$= \frac{1}{Q_\mathrm{r}(T)}\mathrm{tr}(\mathrm{e}^{-i\hat{H}t}\mathrm{e}^{-\beta\hat{H}/2}(1-h)\ \mathrm{e}^{-\beta\hat{H}/2}\mathrm{e}^{i\hat{H}t}h) \tag{10.18}$$

$$= \frac{1}{Q_\mathrm{r}(T)}C_\mathrm{s}(t), \tag{10.19}$$

where we have inserted eqn (10.14) and (10.16) into eqn (10.17), used the cyclic property of the trace and defined the position–position or side–side correlation function $C_\mathrm{s}(t)$

$$C_\mathrm{s}(t) = \mathrm{tr}((1-h)\ \mathrm{e}^{i(\hat{H}t+i\beta\hat{H}/2)}\ h\mathrm{e}^{-i(\hat{H}t+i\beta\hat{H}/2)}). \tag{10.20}$$

The rate at which product is formed is

$$\frac{\mathrm{d}}{\mathrm{d}t}\langle h\rangle(t) = \frac{1}{Q_\mathrm{r}(T)}\frac{\mathrm{d}}{\mathrm{d}t}C_\mathrm{s}(t) \tag{10.21}$$

$$= \frac{1}{Q_\mathrm{r}(T)}\mathrm{tr}\left((1-h)\frac{\mathrm{d}}{\mathrm{d}t}\left\{\mathrm{e}^{i(\hat{H}t+i\beta\hat{H}/2)}h\mathrm{e}^{-i(\hat{H}t-i\beta\hat{H}/2)}\right\}\right) \tag{10.22}$$

$$= \frac{1}{Q_\mathrm{r}(T)}\mathrm{tr}\left((1-h)\mathrm{e}^{i(\hat{H}t+i\beta\hat{H}/2)}i(\hat{H}h-h\hat{H})\ \mathrm{e}^{-i(\hat{H}t-i\beta\hat{H}/2)}\right) \tag{10.23}$$

$$= \frac{1}{Q_\mathrm{r}(T)}\mathrm{tr}\left((1-h)\mathrm{e}^{i(\hat{H}t+i\beta\hat{H}/2)}\hat{F}\mathrm{e}^{-i(\hat{H}t-i\beta\hat{H}/2)}\right) \tag{10.24}$$

$$= \frac{1}{Q_\mathrm{r}(T)}C_\mathrm{f,s}(t), \tag{10.25}$$

where we have used the definition of the flux operator $\hat{F} = i[\hat{H}, h]$ and defined the flux–position or flux–side correlation function $C_\mathrm{f,s}(t)$. The flux–side correlation function can also be cast into the following form[9]

$$C_\mathrm{f,s}(t) = \mathrm{tr}(\hat{F}\mathrm{e}^{i(\hat{H}t+i\beta\hat{H}/2)}\ h\mathrm{e}^{-i(\hat{H}t-i\beta\hat{H}/2)}). \tag{10.26}$$

To obtain the experimentally observed rate constant, *i.e.*, a continuous rate at which the products are formed, one has to damp the fluctuations caused by the initial preparation of the system by taking the long-time limit of eqn (10.21). The rate constant is obtained as

$$k(T) = \lim_{t\to\infty} \frac{\mathrm{d}}{\mathrm{d}t} \langle h \rangle (t) = \frac{1}{Q_\mathrm{r}(T)} \lim_{t\to\infty} C_{\mathrm{f,s}}(t). \tag{10.27}$$

In practice, the long-time limit is reached once the flux–side correlation function shows a prolonged plateau. A flux–flux correlation function[9]

$$C_\mathrm{f}(t) = \frac{\mathrm{d}}{\mathrm{d}t} C_{\mathrm{f,s}}(\mathrm{t}) = \mathrm{tr}\left(\hat{F}\mathrm{e}^{i(\hat{H}t+i\beta\hat{H}/2)}\ \hat{F}\mathrm{e}^{-i(\hat{H}t+i\beta\hat{H}/2)}\right), \tag{10.28}$$

can be used to obtain thermal rate constants as

$$k(T) = \frac{1}{Q_\mathrm{r}(T)} \int_0^\infty \mathrm{d}t\, C_f(t). \tag{10.29}$$

A convenient formula for calculating the CRP[9] is derived by employing the identity

$$\mathrm{e}^{i(Ht+i\beta H/2)} = \int_{-\infty}^{\infty} \mathrm{d}E\ \mathrm{e}^{i(Et+i\beta E/2)}\delta(\hat{H}-E) \tag{10.30}$$

and inserting it into a slightly rewritten form of eqn (10.29) to find

$$\begin{aligned}
k(T) &= \frac{1}{2Q_\mathrm{r}(T)} \int_{-\infty}^{\infty} \mathrm{d}t\ \mathrm{tr}\left(\hat{F}\mathrm{e}^{i(\hat{H}t+i\beta\hat{H}/2)}\hat{F}\mathrm{e}^{-i(\hat{H}t+i\beta\hat{H}/2)}\right) \\
&= \frac{1}{2Q_\mathrm{r}(T)} \int_{-\infty}^{\infty} \mathrm{d}t \int_{-\infty}^{\infty} \mathrm{d}E \int_{-\infty}^{\infty} \mathrm{d}E' \mathrm{e}^{-\beta(E+E')/2} \mathrm{e}^{-i(E-E)t} \mathrm{tr}\left(\hat{F}\delta(\hat{H}-E')\hat{F}\delta(\hat{H}-E)\right) \\
&= \frac{\pi}{Q_\mathrm{r}(T)} \int_{-\infty}^{\infty} \mathrm{d}E \int_{-\infty}^{\infty} \mathrm{d}E' \delta(E-E') \mathrm{e}^{-\beta(E+E')/2} \mathrm{tr}\left(\hat{F}\delta(\hat{H}-E')\hat{F}\delta(\hat{H}-E)\right) \\
&= \frac{\pi}{Q_\mathrm{r}(T)} \int_{-\infty}^{\infty} \mathrm{d}E\ \mathrm{e}^{-\beta E} \mathrm{tr}\left(\hat{F}\delta(\hat{H}-E)\hat{F}\delta(\hat{H}-E)\right),
\end{aligned} \tag{10.31}$$

where we have performed the time integral to give

$$\int_{-\infty}^{\infty} \mathrm{d}t\, \mathrm{e}^{-i(E-E')t} = 2\pi\delta(E-E'). \tag{10.32}$$

Comparing with eqn (10.2) gives

$$N(E) = 2\pi^2 \mathrm{tr}(\hat{F}\delta(\hat{H}-E)\hat{F}\delta(\hat{H}-E)). \tag{10.33}$$

It is important to note that all formulas for obtaining rate constants, *i.e.*, eqn (10.27), (10.29) and (10.33), are independent of the specific choice of the dividing surface in h as they always employ the limit of $t\to\infty$.

10.2.3 Connection to Transition State Theory

The generalized flux–flux correlation function of eqn (10.33) will be the basic equation that we will use to efficiently obtain exact thermal rate constants from quantum dynamics simulations. Before we go ahead, we will deepen our understanding of the flux–side correlation functions by considering its connection to the well known classical *transition state theory* (TST). The classical limit of the trace is the phase space integral[9]

$$\mathrm{tr}(\ldots) \Rightarrow \frac{1}{(2\pi\hbar)^f}\int \mathrm{d}^f x_0 \int \mathrm{d}^f p_0 \; \ldots\,. \tag{10.34}$$

The thermal weight $\mathrm{e}^{-\beta\hat{H}}$ is given by $\mathrm{e}^{-\beta H} = \mathrm{e}^{-\beta E(\mathbf{x}_0,\mathbf{p}_0)}$, where H is the classical Hamiltonian of the system and $E(\mathbf{x}_0,\mathbf{p}_0)$ is the energy of a trajectory starting at the phase-space point $(\mathbf{x}_0,\mathbf{p}_0)$. The flux through a dividing surface at $t=0$ is[9]

$$\int_{\substack{\text{dividing}\\\text{surface}}} \mathrm{d}^{f-1}\mathbf{x}_{\mathrm{DS}}\,\delta(\mathbf{x}(0)-\mathbf{x}_{\mathrm{DS}})\,\mathbf{e}\cdot\dot{\mathbf{x}}(0) \tag{10.35}$$

where $\mathbf{e}$ denotes a unit vector orthogonal to the dividing surface and pointing towards the products, and the integration is performed over the full dividing surface. Hence, only trajectories starting at the dividing surface need to be considered. The factor $\mathrm{e}^{i\hat{H}t}h\mathrm{e}^{-i\hat{H}t}$ determines whether the system is on the product side or on the reactant side of the dividing surface at a given time t. Classically, this can be translated to whether the trajectory $\mathbf{x}(t)$ is on the product or reactant side of the dividing surface at time t and we find[9]

$$\mathrm{e}^{i\hat{H}t}h\mathrm{e}^{-i\hat{H}t} \Rightarrow h(\mathbf{x}(t)). \tag{10.36}$$

The classical analog to

$$k(T) = \frac{1}{Q_{\mathrm{r}}(T)}\lim_{t\to\infty} C_{\mathrm{f,s}}(t) \tag{10.37}$$

reads

$$k(T) = \frac{1}{(2\pi\hbar)^f Q_{\mathrm{r}}(T)}\int_{\substack{\text{dividing}\\\text{surface}}} \mathrm{d}^{f-1}\mathbf{x}_0 \int \mathrm{d}^f\mathbf{p}_0\;\mathbf{e}\cdot\dot{\mathbf{x}}(0)\mathrm{e}^{-\beta E(\mathbf{x}_0,\mathbf{p}_0)}\lim_{t\to\infty} h(\mathbf{x}(t)). \tag{10.38}$$

The *dynamical factor*, $\lim_{t\to\infty} h(\mathbf{x}(t))$, contains all the information about the dynamics and it only depends on the asymptotic $(t\to\infty)$ value of the trajectories. The rate constant can be obtained by taking into account all possible trajectories pinned on the dividing surface at $t=0$, weighted by their Boltzmann weight and initial momentum and the long-time limit of the dynamical factor, *i.e.*, counting only trajectories that end up as products.

Let us now consider a few representative trajectories as sketched in Figure 10.2. Please note, that the trajectories in Figure 10.2 are sketched and

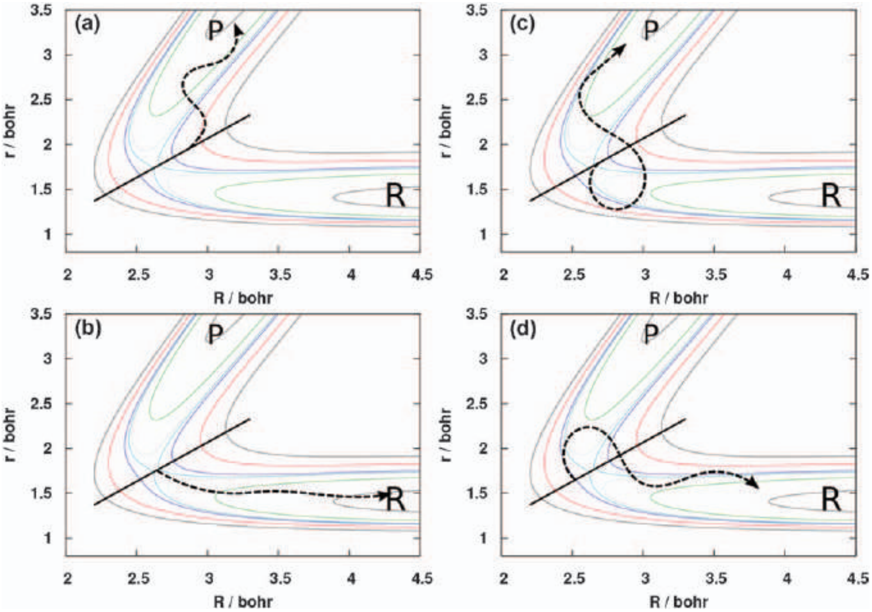

Figure 10.2 Sketch of different reactive (a), (c) and non-reactive (b), (d) trajectories. The two trajectories sketched in (a) and (b) directly proceed towards products (**P**) and reactants (**R**) respectively, while the trajectories sketched in (c) and (d) start off in a different direction and then recross the dividing surface. An illustration of a potential energy surface is given by its contour lines. The dividing surface is indicated as a thick, black line.

are for illustrative purposes only. In typical low-dimensional systems one would find only few recrossing trajectories. In Figure 10.2 the reactant and product asymptotic area are indicated by **R** and **P**, respectively. The two trajectories shown in panel (a) and (b) are "direct", *i.e.*, they start off towards the reactants and products, respectively, and continue on towards the reactants or products. Trajectory (a) ends up in the reactant asymptotic area and thus does not contribute to the dynamical factor, while trajectory (b) ends up in the product asymptotic area and thus contributes to the dynamical factor. The other two trajectories in Figure 10.2, panels (c) and (d), do not continue on their initial direction, but turn around and do recross the dividing surface. The trajectory starting towards the reactant region shown in panel (c) ends up in the product asymptotic area and contributes to the rate, while the trajectory starting off towards the products, ends up in the reactant asymptotic area and does not contribute to the rate. The calculation of the dynamical factor is the most costly step of the classical thermal rate constant simulation as it requires a long propagation of the trajectories. Therefore, approximations exist to simplify rate constant calculations. The most well known is transition state theory (TST). In TST it is assumed that a trajectory that starts towards the products, *i.e.*, with $\mathbf{e} \cdot \dot{\mathbf{x}}(0) > 0$, will end up as a product, and trajectory starting towards the reactants, *i.e.*, with $\mathbf{e} \cdot \dot{\mathbf{x}}(0) < 0$, will end up as a reactant. Any recrossing is neglected and the dynamical factor is approximated as

$$\lim_{t\to\infty} h(\mathbf{x}(t)) = \begin{cases} 1, & \text{if } \mathbf{e}\cdot\dot{\mathbf{x}}(0) > 0 \\ 0, & \text{if } \mathbf{e}\cdot\dot{\mathbf{x}}(0) < 0. \end{cases} \tag{10.39}$$

In TST, two types of trajectories are counted wrongly. First, all trajectories starting towards the products but ending up as reactants (*e.g.*, as shown in Figure 10.2d) are falsely counted and increase the TST rate compared to the exact classical rate. Trajectories starting towards the reactants, but ending up as products are not counted and also increase the TST rate compared to the exact classical rate, as these trajectories would have a negative weight in the exact classical rate. Therefore, the TST rate is a strict upper bound of the exact classical rate constant.

10.3 Quantum Transition State Concept

The quantum transition state concept (QTSC) is based on flux correlation functions (see Section 10.2.2). The QTSC results in a numerically efficient and conceptually appealing way to obtain rate constants. To understand the QTSC, we need to have a closer look at the flux operator and its eigenvalues, which will be covered first. After deriving the working equations of the QTSC and discussing how to treat overall rotational motion, we will consider the interpretation of the resulting reaction dynamics in terms of *natural reaction channels* and give a short outlook on how the QTSC can be extended to yield state-to-state cross sections in a very efficient way. Additional details can be found in ref. 2 and 9–11.

10.3.1 Thermal Flux Operator

We start by investigating the flux operator in more detail by focusing on a one-dimensional system. The flux operator reads[10]

$$\hat{F} = i[\hat{H}, h(x-x_0)] = i\left[\frac{\hat{p}^2}{2m}, h(x-x_0)\right] \tag{10.40}$$

$$= \frac{-i}{2m}\left(\frac{\partial^2}{\partial x^2} h(x-x_0) - h(x-x_0)\frac{\partial^2}{\partial x^2}\right) \tag{10.41}$$

$$= \frac{-i}{2m}\left(\frac{\partial}{\partial x}\delta(x-x_0) + \delta(x-x_0)\frac{\partial}{\partial x} + h(x-x_0)\frac{\partial^2}{\partial x^2} - h(x-x_0)\frac{\partial^2}{\partial x^2}\right) \tag{10.42}$$

$$= \frac{1}{2m}\left(\hat{p}\delta(x-x_0) + \delta(x-x_0)\hat{p}\right) \tag{10.43}$$

$$= \frac{1}{2m}\left(\hat{p}|x_0\rangle\langle x_0| + |x_0\rangle\langle x_0|\hat{p}\right), \tag{10.44}$$

where $|x_0\rangle$ are states localized at the dividing surface position x_0. The image of $\hat{F}$ spans the two-dimensional space $\{|x_0\rangle,\ \hat{p}|x_0\rangle\}$. Therefore, $\hat{F}$ only has two non-vanishing eigenvalues and is of rank two. $\hat{F}$ is purely imaginary as both $\hat{H}$ and $h(x-x_0)$ are real and $\hat{F}$ contains an additional factor i. $\hat{F}$ is also hermitian:

$$\hat{F}^{\dagger} = \frac{1}{2m}(\hat{p}|x_0\rangle\ \langle x_0| + |x_0\rangle\ \langle x_0|\hat{p})^{\dagger} \tag{10.45}$$

$$= \frac{1}{2m}\left(\langle x_0|^{\dagger}\ |x_0\rangle^{\dagger}\hat{p}^{\dagger} + \hat{p}^{\dagger}\ \langle x_0|^{\dagger}|x_0\rangle^{\dagger}\right) \tag{10.46}$$

$$= \frac{1}{2m}(|x_0\rangle\ \langle x_0|\hat{p} + \hat{p}|x_0\rangle\langle x_0|) \tag{10.47}$$

$$= \hat{F}. \tag{10.48}$$

Thus, the eigenvalues of $\hat{F}$ form a pair with the same absolute value, but opposite signs and the corresponding eigenvectors are complex conjugates of each other. The flux operator is singular since neither $|x_0\rangle$ nor $\hat{p}|x_0\rangle$ are elements of a Hilbert space. The eigenvalues are unbound and employing the flux operator in numerical calculations is not possible. One way to circumvent this problem is to employ a modified flux operator with a limited momentum spectrum.[13,14] The corresponding eigenfunctions $f_{\pm}(x)$ and eigenvalues $f_{\pm}$ can be derived analytically and read[13]

$$f_{\pm}(x) = \frac{1}{\sqrt{2}}\left(\sqrt{\frac{p_{\max}}{\pi}}\frac{\sin(p_{\max}x)}{p_{\max}x} \pm i\sqrt{\frac{3p_{\max}}{\pi}}\frac{p_{\max}x\cos(p_{\max}x) - \sin(p_{\max}x)}{(p_{\max}x)^2}\right), \tag{10.49}$$

$$f_{\pm} = \pm\frac{p_{\max}^2}{2\pi\sqrt{3}}, \tag{10.50}$$

respectively. If the maximum momentum $p_{\max}$ is larger than any physically relevant momentum, *i.e.*, large enough to cover the full range of relevant collision energies at a given temperature, the results for any physical observable will be independent of the choice of $p_{\max}$.

Another way to remove the singularity from the flux operator, and the way we will follow for the rest of this chapter, is to employ the thermal flux operator[15]

$$\hat{F}_T = \mathrm{e}^{-\hat{H}/2kT}\hat{F}\mathrm{e}^{-\hat{H}/2kT}. \tag{10.51}$$

The thermal flux operator is regular and has similar properties as the flux operator.[15,16] It is purely imaginary, hermitian and in one dimension it only has two non-vanishing eigenvalues $f_{T,\pm}$ with

$$f_{T,+} = -f_{T,-}, \tag{10.52}$$

$$|f_{T,+}\rangle = |f_{T,-}\rangle^{*}. \tag{10.53}$$

We can write the thermal flux operator as

$$\hat{F}_T = \mathrm{e}^{-\hat{H}/2kT} \frac{1}{2m} (\hat{p}|x_0\rangle \; \langle x_0| + |x_0\rangle \; \langle x_0|\hat{p}) \; \mathrm{e}^{-\hat{H}/2kT} \tag{10.54}$$

and see that the thermal flux eigenstates span the two-dimensional space $\{\mathrm{e}^{-\hat{H}/2kT} \; |x_0\rangle\}$, $\{\mathrm{e}^{-\hat{H}/2kT}\hat{p}|x_0\rangle\}$.

More insight into the thermal flux operator can be gained by considering a separable, multidimensional Hamiltonian:

$$\hat{H}(x,\mathbf{Q}) = \hat{H}_\mathrm{r}(x) + \hat{H}_\perp(\mathbf{Q}), \tag{10.55}$$

where $\hat{H}_\mathrm{r}$ is a one-dimensional Hamiltonian describing the motion along the reaction coordinate and $\hat{H}_\perp$ is the Hamiltonian that describes the bound motion in the remaining (orthogonal) degrees of freedom. Dividing the thermal flux operator into two components we obtain

$$\hat{F}_T = \mathrm{e}^{-\hat{H}/2kT}\mathrm{e}^{-\hat{H}_\perp/2kT} i \left([\hat{H}_\mathrm{r}, h(x - x_0)] + \underbrace{[\hat{H}_\perp, h(x - x_0)]}_{=0} \right) \mathrm{e}^{-\hat{H}_\mathrm{r}/2kT}\mathrm{e}^{-\hat{H}_\perp/2kT} \tag{10.56}$$

$$= \mathrm{e}^{-\hat{H}_\perp/kT} (\mathrm{e}^{-\hat{H}_\mathrm{r}/2kT} i[\hat{H}_\mathrm{r}, h(x - x_0)] \; \mathrm{e}^{-\hat{H}_\mathrm{r}/2kT}). \tag{10.57}$$

Each eigenstate of $\hat{H}_\perp$ gives rise to a pair of non-vanishing eigenstates of $\hat{F}_T$, carries the weight of the thermal population of the corresponding $\hat{H}_\perp$ eigenstate and the jth eigenvalue pair of $\hat{F}_T$ is $f_{T,+}\mathrm{e}^{-E_{\perp,j}/kT}$ and $f_{T,-}\mathrm{e}^{-E_{\perp,j}/kT}$, where $f_{T,+}$ and $f_{T,-}$ are the eigenvalues of the thermal flux operator associated with $\hat{H}_\mathrm{r}$. If the thermal energy is small compared to the vibrational spacing, which is often true, there is only a small number of significant eigenvalues of $\hat{F}_T$. The above analysis was done for a separable system, but one can expect similar results for non-separable systems and it was found in many systems that the number of significant thermal flux eigenvalues is small.

As an illustrative example, the contours of the probability density of the eigenstate pairs of the thermal flux operator corresponding to the lowest and second-lowest eigenvalues for the co-linear $\mathrm{D} + \mathrm{H}_2 \rightarrow \mathrm{DH} + \mathrm{H}$ reaction are displayed in Figure 10.3. The coordinates r and R refer to the H_2 distance and the distance of D to the center of mass of H_2, respectively. The contour lines of the potential energy surface are shown as thin lines, while the contour lines of the thermal flux eigenstates are shown as thick lines. The first eigenfunction can be identified as the ground state as it does not show any nodes. The second eigenfunction shows a node along the symmetric stretching coordinate (the nodal plane is indicated by a thick red line) and thus can be interpreted as the first vibrationally excited state. It can also be seen that the probability maxima of the eigenstates do not sit on top of the

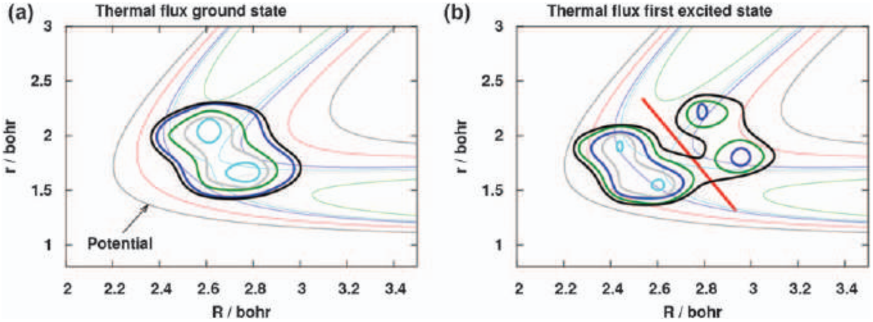

Figure 10.3 Contour plot (thick lines) of the probability density of the first two pairs of thermal flux eigenstates for the co-linear $D+H_2 \rightarrow DH+H$ reaction. The nodal line of the second pair of thermal flux eigenstates is indicated as thick red line. The potential energy surface contour is shown as thin lines.

barrier, but are displaced towards the reactant and product asymptotic areas due to the thermal weighting.

10.3.2 Working Equations

To evaluate the flux-corrlation function using the thermal flux operator we employ the spectral representation

$$\hat{F}_T = \sum_{f_T} |f_T\rangle f_T \langle f_T| \tag{10.58}$$

and insert it into the flux correlation function to obtain the CRP as[17,18]

$$N(E) = 2\pi^2 \mathrm{tr}(\hat{F}\delta(\hat{H}-E)\hat{F}\delta(\hat{H}-E)) \tag{10.59}$$

$$= 2\pi^2 \mathrm{e}^{2E/\mathrm{kT}} \mathrm{tr}(\hat{F}_T\delta(\hat{H}-E)\hat{F}_T\delta(\hat{H}-E)) \tag{10.60}$$

$$= 2\pi^2 \mathrm{e}^{2E/kT} \sum_{f_T}\sum_{f'_T} f_T f'_T \langle f_T|\delta(\hat{H}-E)|f'_T\rangle\langle f'_T|\delta(\hat{H}-E)|f_T\rangle \tag{10.61}$$

$$= \frac{1}{2}\mathrm{e}^{2E/kT} \sum_{f_T}\sum_{f'_T} f_T f'_T \left|\int_0^\infty \mathrm{d}t\; \mathrm{e}^{iEt}\langle f_T|\mathrm{e}^{-i\hat{H}t}|f'_\mathrm{T}\rangle\right|. \tag{10.62}$$

The CRP is obtained from a real-time propagation of the thermal flux eigenstates and thus only a small number of wavepackets need to be propagated. Formally, the integration goes to $t \rightarrow \infty$, but the integrand goes to zero as the overlap of an (initial) thermal flux eigenstate with any time-propagated thermal flux eigenstate vanishes. As the thermal flux eigenstates are localized in the transition state area, and run downhill into the reactant and product asymptotic areas, this overlap vanishes quickly and the calculation of the CRP converges fast with respect to the propagation time t. The wavepacket propagation typically has to be done only for some tens of femtoseconds. The thermal rate constant is obtained using eqn (10.2).

Eqn (10.59) can be modified by replacing only one of the flux operators in the correlation function with a thermal flux operator and obtain[13]

$$N(E) = 2\pi^2 \mathrm{tr}(\hat{F}\delta(\hat{H}-E)\hat{F}\delta(\hat{H}-E)) \tag{10.63}$$

$$= 2\pi^2 \mathrm{e}^{E/\mathrm{kT}} \mathrm{tr}(\hat{F}_T\delta(\hat{H}-E)\hat{F}\delta(\hat{H}-E)) \tag{10.64}$$

$$= 2\pi^2 \mathrm{e}^{E/kT} \sum_{f_T} f_T \langle f_T|\delta(\hat{H}-E)\hat{F}\delta(\hat{H}-E)|f_T\rangle \tag{10.65}$$

$$= \frac{1}{2}\mathrm{e}^{E/kT} \sum_{f_T} f_T \int_0^\infty \mathrm{d}t_1 \int_0^\infty \mathrm{d}t_2 \ \mathrm{e}^{iEt_1}\mathrm{e}^{-iEt_2} \langle f_T|e^{i\hat{H}t_2}\hat{F}\mathrm{e}^{-i\hat{H}t_1}|f_T\rangle. \tag{10.66}$$

While in the previous case of eqn (10.59) we had to take into account all cross-correlation terms, but only for one time index, we now take the two-time correlation of each thermal flux eigenstate individually to obtain the CRP.

10.3.3 Overall Rotational Motion

Thus far, we implicitly only discussed internal (*i.e.*, vibrational) motion in the thermal flux eigenstates and restricted ourselves to vanishing total angular momentum ($J = 0$). This is important when discussing the number of thermal flux eigenstates relevant at a given temperature. The spacing between rotational energy levels is typically much smaller than the thermal energy available. Many rotational (or ro-vibrational) states are populated and the number of relevant thermal flux eigenstates increases dramatically and therefore, the computational effort to obtain the CRP increases also.

One way to circumvent the need to treat the full overall rotation motion is to employ the *J-shifting* approximation.[19] In the J-shifting approximation, one assumes that the overall rotational motion and the internal motion are separable and thus the partition functions for the overall rotation and the remaining motion factorize. Therefore, one only calculates the thermal rate constant for vanishing total angular momentum and introduces the contributions due to overall rotation by employing the rotational partition function at the transition state, $Q^{\ddagger}_{\mathrm{rot}}(T)$. The full rate constant is obtained as[19]

$$k(T) = Q^{\ddagger}_{\mathrm{rot}}(T)k_{J=0}(T). \tag{10.67}$$

The assumption of (nearly) separable rotational motion is often reasonable for direct reactions as the time scale of rotations, several picoseconds, is much larger than the time scale of the barrier crossing, typically a few tens of femtoseconds. For linear transition states, the rotation around the linear axis occurs on the time scale of the reaction process and thus has to be treated explicitly and only the rotation perpendicular to the linear axis is assumed to be separable resulting in the *modified J-shifting* approximation.[17]

Yet, there are also ways to accurately incorporate overall rotational motion in the QTSC simulations. The overall wavefunction depends on the internal degrees of freedom Q_{int} and the three Euler angles α, β, and γ and can be expanded employing Wigner rotation matrices D^J_{MK} as[20]

$$\Psi(Q_{\text{int}}, \alpha, \beta, \gamma) = \sum_{J=0}^{\infty} \sum_{M=-J}^{J} \sum_{K=-J}^{J} \Psi(Q_{\text{int}}, 0, 0, 0) D^J_{MK}(\alpha, \beta, \gamma), \tag{10.68}$$

where J denotes the total angular momentum quantum number, M the quantum number associated with the projection of the total angular momentum on a space-fixed axis, and K the quantum number associated with the projection of the total angular momentum on a body-fixed axis. As J and M are good quantum numbers, we can re-write eqn (10.68) as

$$\Psi_{JM}(Q_{\text{int}}, \alpha, \beta, \gamma) = \sum_{K=-J}^{J} \Psi_{JK}(Q_{\text{int}}, 0, 0, 0) D^J_{MK}(\alpha, \beta, \gamma). \tag{10.69}$$

One can now separate the contributions due to each Ψ_{JM} and obtain the overall rate constant as a sum of $k_{JM}(T)$ components. This can still be simplified. The M quantum number describes the orientation of the system in the laboratory frame, but the rate constant is independent of this orientation, and the value of $k_{JM}(T)$ does not depend on M. This results in a $(2J+1)$-fold degeneracy to obtain

$$k(T) = \sum_J (2J+1) k_J(T). \tag{10.70}$$

Often $k_J(T)$ for a few representative values of J are obtained and the other values are interpolated. Yet, to calculate any $k_J(T)$, one needs to treat all relevant K-components of the overall wavefunction $\Psi_{JK}(\mathbf{Q}_{\text{int}}, 0, 0, 0)$, which is often all $(2J+1)$ components. Therefore, the number of relevant thermal flux eigenstates is multiplied by all relevant K-components that are treated for a given J.

To avoid the use of a large number of thermal flux eigenstates, one can employ a statistical evaluation of the trace in the flux correlation function. We employ statistical functions[13,21]

$$|\phi_j\rangle = \sum_l (-1)^{\alpha_l(j)} |\chi_l\rangle, \tag{10.71}$$

where $\alpha_l(j)$ denotes an integer random number and $|\chi_l\rangle$ are suitable basis functions employed in the respective degree of freedom (DOF). The statistical wave functions satisfy the completeness relation

$$\begin{aligned} \lim_{M\to\infty} \frac{1}{M} \sum_{j=1}^{M} |\phi_j\rangle\langle\phi_j| &= \lim_{M\to\infty} \frac{1}{M} \sum_{j=1}^{M} \sum_m \sum_n (-1)^{\alpha_m(j)} (-1)^{\alpha_n(j)} |\chi_m\rangle\langle\chi_n| \\ &= \sum_m |\chi_m\rangle\langle\chi_m| = 1 \end{aligned} \tag{10.72}$$

as

$$\lim_{M\to\infty}\frac{1}{M}\sum_{j=1}^{M}(-1)^{\alpha_m(j)}(-1)^{\alpha_n(j)}=\delta_{mn}. \tag{10.73}$$

We now re-write the flux operator as

$$\hat{F}=\lim_{M\to\infty}\frac{1}{M}\sum_{j=1}^{M}|\phi_j\rangle\langle\phi_j|\hat{F}', \tag{10.74}$$

where $\hat{F}'$ no longer depends on the coordinate treated with the statistical approach. If the Hamiltonian is separable and the basis functions $|\chi_l\rangle$ are eigenfunctions of the corresponding Hamiltonian, a single sample is sufficient to obtain the full trace required as all samples yield equal results. If the degrees of freedom to be treated statistically are only weakly correlated to the other degrees of freedom, this approach is very efficient. Rotations and vibrations are often approximately separable and the presented scheme is particularly efficient for treating rotations.

Now we can define a set of M statistical thermal flux operators as

$$\hat{F}_T^j=\mathrm{e}^{-\frac{\hat{H}}{2kT}}\hat{F}|\phi_j\rangle\ \langle\phi_j|\ \mathrm{e}^{-\frac{\hat{H}}{2kT}}, \tag{10.75}$$

with $j=1,\ \ldots\ ,M$. The corresponding working equations for a CRP calculation read

$$N(E)=\lim_{M\to\infty}\frac{1}{M}\sum_{j=1}^{M}\frac{1}{2}\mathrm{e}^{E/kT}\sum_{f_T^{(j)}}f_T^{(j)}\int_0^\infty \mathrm{d}t_1\int_0^\infty \mathrm{d}t_2\ \mathrm{e}^{iEt_1}\mathrm{e}^{-iEt_2}\langle f_T^{(j)}|\mathrm{e}^{i\hat{H}t_2}\hat{F}\mathrm{e}^{-i\hat{H}t_1}|f_T^{(j)}\rangle, \tag{10.76}$$

where $f_T^{(j)}$ and $|f_T^{(j)}\rangle$ are the eigenvalues and eigenfunctions of $\hat{F}_T^j$.

10.3.4 Natural Reaction Channels

The thermal flux eigenstates can be interpreted as the vibrational states of the activated complex and each thermal flux eigenstate pair forms a reaction channel which contributions to the overall rate constant can be calculated by taking each summand in eqn (10.66) individually. Yet, these contributions depend strongly on the choice of the dividing surface. Please note, that the overall rate constant does not depend on the choice of the dividing surface. Nonetheless, there is a rigorous way to define *natural reaction channels* that are independent of the choice of the dividing surface. The natural reaction channels and their associated *natural reaction probabilities* can be defined by a singular value decomposition of the S-matrix.[22,23] To this end, the S-matrix is written as

$$S_{if}(E)=\sum_k U_{f,k}(E)s_k(E)V_{i,k}(E)^*, \tag{10.77}$$

where

$$\sum_f U_{f,k}(E)U^{*}_{f,l}(E) = \delta_{kl}, \tag{10.78}$$

$$\sum_i V_{i,k}(E)V^{*}_{i,l}(E) = \delta_{kl} \tag{10.79}$$

are the left- and right-singular vectors, respectively, and the $s_k(E)$ are called singular values, which are real and positive. The natural reaction probabilities are defined as $p_k(E) = |s_k(E)|^2$. The CRP can then be calculated as

$$N(E) = \sum_i \sum_f \left|S_{if}(E)\right|^2 = \sum_k p_k(E). \tag{10.80}$$

In other words, each non-vanishing singular value $s_k(E) > 0$ gives rise to a particular natural reaction channel, which is uniquely defined due to the uniqueness of the SVD. Initial state-selected reaction probabilities can be calculated from the SVD decomposition as

$$p_i(E) = \sum_f \left|S_{if}(E)\right|^2 = \sum_k p_k(E)\left|V_{i,k}(E)\right|^2. \tag{10.81}$$

The factors $|V_{i,k}(E)|^2$ describe the transition probability from a given initial state *i* into the *k*th natural reaction channel and $p_k(E)$ again give the reaction probability for the specific natural reaction channel. The natural reaction probabilities defined through the SVD decomposition can be directly identified with the eigen reaction probabilities of a rigorously defined reaction probability operator.

The natural reaction probabilities can be computed within the quantum transition state concept and without requiring any knowledge of the asymptotic states. A transformed S-matrix is decomposed as

$$\tilde{S}_{l_r,l_p}(E) = \sum_k \tilde{U}_{l_p,k}(E) s_k(E) \tilde{V}^{*}_{l_r,k}(E), \tag{10.82}$$

which has the same singular values as $S_{if}(E)$, but a much smaller dimension as l_r and l_p are limited by the number of relevant thermal flux eigenvalues. The transformed matrix is defined as

$$\tilde{S}_{l_r,l_p}(E) = d_{l_r}^{(r,+)}(E) d_{l_p}^{(p,-)}(E) \sum_{f_T^j} f_T^j \frac{\mathrm{e}^{E/kT}}{2\pi} \mathbf{B}_{j,l_p}^{(p,-)}{*}(E)\mathbf{B}_{j,l_r}^{(r,+)}(E), \tag{10.83}$$

where $d_l^{a,s}$ and $\mathbf{B}_{j,l}^{(a,s)}$ are the eigenvalues and eigenvectors of a generalized flux matrix

$$\mathscr{F}_{j,j'}^{(a,s)}(E) = 2\pi \langle f_T^j | \delta(\hat{H} - E)\, \hat{F}_a^s \delta(\hat{H} - E) | f_T^{j'} \rangle \tag{10.84}$$

with the flux operator $\hat{F}_a^s$ located towards the reactant $(a=r)$ or product $(a=p)$ asymptotic area and only considers components with incoming $(s=+)$ or outgoing $(s=-)$ momenta in the reaction coordinate R:

$$\hat{F}_a^{\pm} = \frac{1}{2}(h(\pm\hat{p}_R)\hat{F}_a + \hat{F}_a h(\pm\hat{p}_R)). \tag{10.85}$$

For details of the computation interested readers are referred to ref. 22.

10.3.5 Beyond Rate Constants

While the QTSC was introduced for the efficient calculation of rate constants circumventing the need for the full scattering matrix, it has been shown that the QTSC can be used to obtain the full scattering matrix of polyatomic systems in a very efficient way. These extensions of QTSC are briefly discussed here and all details can be found in ref. 24–27.

To obtain quantities depending on initial and/or final states, we need to obtain information on the dynamics into the reactant and/or product asymptotic areas. Yet, to obtain a numerically efficient approach, we have chosen to place the dividing surfaces in the transition state region. However, the formulas for obtaining CRPs or thermal rate constants are independent of the choice of the dividing surface. If we obtain the rate constants as in eqn (10.63), *i.e.*, with only employing one thermal flux operator, we have the freedom to move the location of the second dividing surface, while retaining the numerical advantage of a small number of wavepackets. To obtain initial-state selected reaction probabilities, we place this second dividing surface into the reactant asymptotic area and denote the associated flux operator as $\hat{F}_{\text{reac}}$. We introduce a projection operator on the initial state with quantum number $\mathbf{n}_r$, *i.e.*, the ro-vibrational state of the reactants $|\chi_{\mathbf{n}_r}\rangle$, $\hat{P}_{\mathbf{n}_r} = |\chi_{\mathbf{n}_r}\rangle\langle\chi_{\mathbf{n}_r}|$. The resulting flux correlation function reads[28–31]

$$p_{\mathbf{n}_r}(E) = 2\pi^2 e^{E/kT}\,\mathrm{tr}(\hat{F}_T\delta(\hat{H}-E)\hat{P}_{\mathbf{n}_r}\hat{F}_{\text{reac}}\delta(\hat{H}-E)) \tag{10.86}$$

and we obtain the working equation as

$$p_{\mathbf{n}_r}(E) = \frac{1}{2}e^{E/kT}\sum_{f_T} f_T\int_0^{\infty} dt_1 \int_0^{\infty} dt_2\; e^{iEt_1} e^{-iEt_2}\langle f_T|e^{i\hat{H}t_2}|\chi_{\mathbf{n}_r}\rangle\langle\chi_{\mathbf{n}_r}|\hat{F}_{\text{reac}}\; e^{-i\hat{H}t_1}|f_T\rangle. \tag{10.87}$$

Now, the propagation has to be carried out for longer times, *i.e.*, until the wavepackets passed through the dividing surface located in the reactant asymptotic area. As we always compute overlaps with initial states located in the reactant asymptotic area, we can remove any parts of the wavepackets that move into the product asymptotic area from the simulation. This can be done employing imaginary absorbing potentials.

To obtain state-to-state quantities new, generalized flux correlation functions had to be derived[24,26] and the corresponding working equations read

$$
\begin{aligned}
p_{\mathbf{n}_r \to \mathbf{n}_p}(E) = {} & \frac{1}{4\pi^2} \mathrm{e}^{2E/kT} \sum_{f_T} \sum_{f'_T} f_T f'_T \\
& \times \int_0^\infty \mathrm{d}t_1 \; \mathrm{e}^{-iEt_1} \langle \phi_p^- \chi_{\mathbf{n}_p} | \mathrm{e}^{-i\hat{H}t_1} | f'_T \rangle^* \int_0^\infty \mathrm{d}t_2 \; \mathrm{e}^{iEt_2} \langle \phi_p^- \chi_{\mathbf{n}_p} | \mathrm{e}^{-i\hat{H}t_2} | f_T \rangle \\
& \times \int_0^\infty \mathrm{d}t_3 \; \mathrm{e}^{-iEt_3} \langle \phi_r^+ \chi_{\mathbf{n}_r} | \mathrm{e}^{-i\hat{H}t_3} | f_T \rangle^* \int_0^\infty \mathrm{d}t_4 \; \mathrm{e}^{iEt_4} \langle \phi_r^+ \chi_{\mathbf{n}_r} | \mathrm{e}^{-i\hat{H}t_4} | f'_T \rangle,
\end{aligned}
\tag{10.88}
$$

where ϕ_r^+ and ϕ_p^- are one-dimensional incoming (+) and outgoing (−) wavefunctions located in the reactant and product asymptotic area and depending only on the respective scattering coordinate.

One can see that each integral can be obtained independently and only requires overlap of propagated thermal flux eigenstates with reactant product states. The propagation towards the asymptotic areas are decoupled and the dynamics into the respective other asymptotic area can be removed from the simulation. The full scattering matrix can be obtained from two simulations. In the first simulation, only the dynamics into the reactant asymptotic area is considered and all dynamics towards the product asymptotic area is blocked by imaginary absorbing potentials. In the second simulation, only the dynamics into the product asymptotic area is considered and all dynamics towards the reactant asymptotic area is blocked by imaginary absorbing potentials. The two individual simulations are more efficient than a full simulation taking both asymptotic areas into account simultaneously. This is because there exists no good coordinate system simultaneously describing reactants and products efficiently. Within the QTSC framework, one can choose a dedicated reactant coordinate system for the simulation towards the reactant asymptotic area and a dedicated product coordinate system for the simulation towards the product asymptotic area. Similar formulas have been derived for integral and differential cross sections.[26]

10.4 Numerical Quantum Dynamics: Standard Wave Packets

In order to obtain thermal rate constants from rigorous quantum dynamics calculations, we need to obtain suitable initial wave packets (*i.e.*, thermal flux eigenstates) and propagate them in time solving the time-dependent Schrödinger equation (TDSE)

$$
i\frac{\partial}{\partial t}\psi(\mathbf{x},t) = \hat{H}\psi(\mathbf{x},t). \tag{10.89}
$$

This section introduces the standard approach to solve the TDSE by expanding the wavepackets in a time-independent basis. In the next section, we will introduce the more efficient multiconfigurational time-dependent Hartree (MCTDH) approach. MCTDH is well suited to calculate rate constants of polyatomic systems exactly.

For everything presented in this and the next section, we assume that the potential energy surface of the specific system is available in an suitable form that can be evaluated efficiently. Recent years have seen a lot of progress in obtaining potential energy surfaces in such forms and the interested reader is referred to reviews in this area.[32–34]

10.4.1 Wavefunction Representations

Wavepackets are represented in a finite, time-independent basis $\phi_n(\mathbf{x})$[35–37]

$$\psi(\mathbf{x},t)=\sum_{n=1}^{N} A_n(t)\phi_n(\mathbf{x}) \tag{10.90}$$

with equations of motion (EOM) for the time-dependent expansion coefficients $A_n(t)$ a set of linear, first-order differential equations

$$i\frac{\partial}{\partial t}A_n(t)=\sum_{m=1}^{N} H_{nm}A_m(t), \tag{10.91}$$

with $H_{nm}=\langle\phi_n|\hat{H}|\phi_m\rangle$ the matrix representation of the Hamiltonian. Different representations are used to evaluate the terms of the Hamiltonian. A basis representation is used to evaluate the kinetic energy and simple, well-known terms of the potential energy, while the remaining potential energy is evaluated employing a grid representation.[35]

Consider a Hamiltonian of the form

$$\hat{H}=\hat{H}_0+\hat{V}, \tag{10.92}$$

with well-known eigenstates and energies of $\hat{H}_0$:$|\phi_n\rangle$ and E_n. Representing the wavefunction $|\psi\rangle$ in this basis

$$|\psi\rangle=\sum_n c_n|\phi_n\rangle, \tag{10.93}$$

we evaluate the matrix elements of $\hat{H}_0$ as

$$\langle\phi_n|\hat{H}_0|\phi_m\rangle=E_n\delta_{nm} \tag{10.94}$$

and the action of $\hat{H}_0$ on the wavefunction as

$$\langle\phi_n|\hat{H}_0|\psi\rangle=E_nc_n. \tag{10.95}$$

Using grid point states $|X_n\rangle$ to represent the wavefunction

$$|\psi\rangle=\sum_n k_n|X_n\rangle, \tag{10.96}$$

and evaluating matrix elements of $\hat{V}$ as

$$\langle X_n|V|X_m\rangle = V(x_n)\delta_{nm} \tag{10.97}$$

and action of $\hat{V}$ on the wavefunction as

$$\langle X_n|\hat{V}|\psi\rangle = V(x_n)k_n. \tag{10.98}$$

We rewrite the Hamiltonian in a spectral representation as

$$\hat{H} = \sum_k |\phi_k\rangle E_k\langle\phi_k| + \sum_k |X_k\rangle V(x_k)\ \langle X_k|. \tag{10.99}$$

and employing the transformation between both representations, we can evaluate the matrix elements

$$\langle\phi_n|\hat{H}|\phi_m\rangle = E_n\delta_{nm} + \sum_k \langle\phi_n|X_k\rangle\ V(x_k)\ \langle X_k|\phi_m\rangle, \tag{10.100}$$

$$\langle X_n|\hat{H}|X_m\rangle = \sum_k \langle X_n|\phi_k\rangle\ E_k\langle\phi_k|X_m\rangle + V(x_n)\delta_{nm}, \tag{10.101}$$

and the action of the Hamiltonian as

$$\langle\phi_n|\hat{H}|\psi\rangle = E_n c_n + \sum_k \langle\phi_n|X_k\rangle\ V(x_n)\ \sum_j \langle X_k|\phi_j\rangle c_j, \tag{10.102}$$

$$\langle X_n|\hat{H}|\psi\rangle = \sum_k \langle X_n|\phi_k\rangle\ E_k\sum_j \langle\phi_k|X_j\rangle k_j + V(x_n)k_n. \tag{10.103}$$

The two most used approaches to define the dual representation schemes are the discrete variable representation (DVR)[38–40] and the fast Fourier transformation (FFT) approach.[41]

The basis transformation can be written as a matrix multiplication transforming the vector $\mathbf{c} = \{c_j\}$ into $\mathbf{k} = \{k_j\}$. $\mathbf{k} = \mathbf{U}\mathbf{c}$, with the matrix elements $U_{mn} = \langle X_m|\phi_n\rangle$. The numerical cost of the basis transformation scales with the number of basis functions squared. Assuming the same number of basis functions N in each of the f DOFs, the basis transformation scales as N^2f. This can be reduced if we can write the full basis or grid as a direct product of one-dimensional basis functions or grid points. In this case, we can write

$$\phi_{n=(n_1,n_2,\ldots,n_f)}(x_1, x_2, \ldots, x_f) = \phi^{(1)}_{n_1}(x_1)\cdot\phi^{(2)}_{n_2}(x_2)\ \ldots\ \phi^{(f)}_{n_f}(x_f), \tag{10.104}$$

$$|X_{m=(m_1,m_2,\ldots,m_f)}\rangle = |X^{(1)}_{m_1}\rangle|\ X^{(2)}_{m_2}\rangle\ldots|X^{(f)}_{m_f}\rangle. \tag{10.105}$$

The transformation matrix elements $\langle X_m|\phi_n\rangle$ factorize to give

$$\langle X_m|\phi_n\rangle = \langle X^{(1)}_{m_1}\ |\ \phi^{(1)}_{n_1}\rangle\cdot\langle X^{(2)}_{m_2}\ |\ \phi^{(2)}_{n_2}\rangle\ \ldots\langle X^{(f)}_{m_f}\ |\phi^{(f)}_{n_f}\rangle. \tag{10.106}$$

The transformation can be calculated for each DOF individually:

$$\begin{aligned}\langle X_m|\psi\rangle &= \mathbf{k} = k_{m_1,m_2,\ldots,m_f}\\ &= \left(\sum_{n_1}\left\langle X_{m_1}^{(1)} \mid \phi_{n_1}^{(1)}\right\rangle\left(\sum_{n_2}\left\langle X_{m_2}^{(2)} \mid \phi_{n_2}^{(2)}\right\rangle \ldots \left(\sum_{n_f}\left\langle X_{m_f}^{(f)} \mid \phi_{n_f}^{(f)}\right\rangle c_{n_1,n_2,\ldots,n_f}\right) \ldots\right)\right).\end{aligned} \tag{10.107}$$

The ith sum in eqn (10.107) scales like $N \cdot N^f$ and the overall cost is $\left(\sum_{i=1}^{f} N\right) \cdot N^f = fN^{f+1}$.

10.4.1.1 Discrete Variable Representation

In DVR optimally localized grid points are obtained by diagonalizing the position operator in the given basis representation:

$$\langle\phi_n|\hat{x}|\phi_m\rangle = \sum_j \langle\phi_n|X_j\rangle x_j \langle X_j|\phi_m\rangle. \tag{10.108}$$

The eigenstates $|X_j\rangle$ are the grid point states and the eigenvalues x_j the corresponding grid points. $\langle\phi_n|X_j\rangle$ defines the transformation from the grid to the basis representation. The DVR representation is optimal in the sense that it minimizes the localization criterion, *i.e.*, given any possible basis $|\xi_n\rangle$,

$$\sum_n (\langle\xi_n|x^2|\xi_n\rangle - \langle\xi_n|x|\xi_n\rangle^2) \tag{10.109}$$

is minimized by the DVR grid, $|\xi_n\rangle = |X_n\rangle$.

The corresponding evaluation of the potential energy integrals

$$\langle\phi_n|\hat{V}|\phi_m\rangle = \sum_j \langle\phi_n|X_j\rangle V(x_j) \langle X_j|\phi_m\rangle \tag{10.110}$$

can be obtained as a Gaussian quadrature for bases $|\phi_n\rangle$ consisting of orthogonal polynomials multiplied by a weight function. For vibrational degrees of freedom, harmonic oscillator eigenfunctions are often used while Legendre polynomials are employed for angular coordinates. Other options are possible and schemes that employ eigenfunctions of system-specific H_0 Hamiltonians can be used. As potential energy surfaces are typically less structured than wavefunctions, it is sufficient to have the same number of grid points as basis functions as the truncation error in the basis representation is larger than the Gaussian quadrature error.

10.4.1.2 Fast Fourier Transformation Representation

One can also employ the fast Fourier transformation (FFT) to mediate the basis-to-grid transformation. The FFT representation utilizes N evenly,

Δx-spaced grid points within a given interval $[x_s, x_e]$. The grid points in coordinate space are connected to grid points in the momentum space interval $\left[p_s, p_s + \frac{2\pi}{\Delta x}\right]$ *via* a discrete Fourier transformation:

$$|X_m\rangle = \frac{1}{\sqrt{N}} \sum_{n=0}^{N-1} e^{ip_n x_m} |P_n\rangle, \tag{10.111}$$

$$|P_n\rangle = \frac{1}{\sqrt{N}} \sum_{m=0}^{N-1} e^{-ip_n x_m} |X_m\rangle. \tag{10.112}$$

The FFT provides a numerically efficient implementation of this transformation as it scales like $N \log N$.

The Fourier transformation assumes that the wavefunction is $x_e - x_s$-periodic in coordinate space and $\frac{2\pi}{\Delta x}$-periodic in momentum space, respectively. Converged results can be obtained if the wavefunction either vanishes at and outside of the set boundaries of the position and momentum grid or if it truly obeys the assumed periodicity.

10.4.2 Time Propagation

We will turn our attention to special integration schemes to solve the TDSE. Please note, that any general-purpose integration schemes like Runge–Kutta could be used, but the two methods discussed below are more efficient for the type of problems we discuss here.

10.4.2.1 Split Operator Propagator

The first method is the split operator scheme.[42] It utilizes the dual representation from the last section. We use eqn (10.92), (10.99) and the Trotter formula to find for the propagator

$$e^{-i\hat{H}\Delta t} = e^{-i\hat{V}\Delta t/2} e^{-i\hat{H}_0\Delta t} e^{-i\hat{V}\Delta t/2} + \mathcal{O}(\Delta t^3). \tag{10.113}$$

We evaluate each part in its respective spectral representation

$$\begin{aligned} e^{-i\hat{H}\Delta t} = &\left(\sum_k |X_k\rangle\ e^{-iV(x_k)\Delta t/2} \langle X_k|\right)\left(\sum_k |\phi_k\rangle\ e^{-iE_k\Delta t} \langle \phi_k|\right) \\ &\left(\sum_k |X_k\rangle\ e^{-iV(x_k)\Delta t/2} \langle X_k|\right) + \mathcal{O}(\Delta t^3) \end{aligned} \tag{10.114}$$

to obtain a second order, short time integrator. To evaluate $(\Sigma_k |X_k\rangle\ e^{-iV(x_k)\Delta t/2}\ \langle X_k|)$, we utilize the coordinate representation, while the basis representation is utilized to evaluate $(\Sigma_k |\phi_k\rangle\ e^{-iE_k\Delta t}\ \langle \phi_k|)$. This can be done efficiently, as the operators are diagonal in the respective representations. Between these evaluations, we transform the wavefunction between the two representations. Repeating propagations along a small timestep Δt allows propagation for any period of time T required

$$e^{-i\hat{H}T} = \prod_{n=1}^{T/\Delta t} e^{-i\hat{V}\Delta t/2} e^{-i\hat{H}_0\Delta t} e^{-i\hat{V}\Delta t/2} + \mathcal{O}(\Delta t^2). \tag{10.115}$$

The split operator scheme offers several advantageous properties. It is unitary, as each exponential operator is unitary, and strictly conserves the norm of the wavefunction and it shows good long-time stability. However, the split operator approach is a low order method and very small timesteps Δt are needed to obtain highly accurate results.

10.4.2.2 Short Iterative Lanczos Propagator

To overcome the shortcomings of the split operator scheme, higher-order approaches should be used. These schemes are often based on polynomial expansions of the propagator:

$$e^{-i\hat{H}\Delta t} = \sum_{n=0}^{N} c_n(\Delta t)\hat{H}^n + \mathcal{O}(\Delta t^{N+1}). \tag{10.116}$$

The action of the propagator on the wavefunction is computed using a recursion:

$$\psi_n = a_n\hat{H}\psi_{n-1} + \sum_{j=0}^{n-1} b_{n,j}\psi_j, \tag{10.117}$$

with a_n, $b_{n,j}$ coefficients predetermined by the integration scheme. When orthogonal polynomials are employed, the above relation can be reduced to a three-point recursion relation, *i.e.*, $b_{n,j} = 0$ for $j < n - 2$. One particular approach is the short iterative Lanczos (SIL) propagator,[43] but other schemes, *e.g.*, based on Chebychev polynomials, are widely used as well.[44]

The SIL propagator uses a short polynomial expansion, where N is typically chosen as 10 or less. Within the Lanczos scheme, the Hamilton is represented in the Krylov space comprised of $\{\psi, \hat{H}\psi, \hat{H}^2\psi, \ldots, \hat{H}^N\psi\}$. The resulting "model" Hamiltonian matrix H_{kry} is tridiagonal and can be efficiently diagonalized to obtain

$$H_{\mathrm{kry}}\chi_j = E_{\mathrm{kry},j}\chi_j, \tag{10.118}$$

where the eigenvalues $E_{\mathrm{kry},j}$ quickly converge to the real eigenvalues E_j. The eigenvalues and eigenstates are used to propagate the wavefunction as

$$e^{-i\hat{H}\Delta t}\psi = \sum_{j=1}^{N+1} \chi_j e^{-iE_{\mathrm{kry},j}\Delta t}\langle\chi_j|\psi\rangle + \mathcal{O}(\Delta t^{N+1}). \tag{10.119}$$

As for the split operator scheme, the SIL propagator is unitary and provides long-time stability, but at an increased accuracy due to the order of the error being much higher. Δt is chosen such that $\Delta t/N$ is around the inverse spectral range of $\hat{H}$.

10.4.3 Obtaining Eigenstates

Thermal flux eigenstates can be obtained using the iterative Lanczos scheme we briefly touched on in the last section.[45] There only low-order expansions were employed, while higher orders are required to obtain the desired number of eigenstates.

To obtain the eigenstates of an operator $\hat{O}$, which in our case is the thermal flux operator, we start with some (arbitrary) initial wave function ψ_0 and then obtain a sequence of wave functions ψ_m, $m = 1, \ldots, M$ as

$$\psi_m = \mathcal{N}\left(\hat{O}\psi_{m-1}\sum_{j=0}^{m-1}\langle\psi_j|\hat{O}|\psi_{m-1}\rangle\psi_j\right) \tag{10.120}$$

where $\mathcal{N}$ is a normalization factor obtained by requiring $\langle\psi_m|\psi_m\rangle = 1$. If $\hat{O}$ is Hermitian the matrix elements $\langle\psi_j|\hat{O}|\psi_{m-1}\rangle$ vanish for $i < m-2$ and we obtain a simple three-point recursion relation for ψ_m. The operator $\hat{O}$ is then represented in this basis, which gives a tridiagonal matrix that can be diagonalized efficiently by standard methods. The eigenvalues of the tridiagonal matrix converge to the eigenvalues of $\hat{O}$ with increasing the Lanzcos order M.

For the case of the calculation of thermal rate constants, we have to apply the thermal flux operator $\hat{O} = \hat{F}_T = \mathrm{e}^{-\hat{H}/2kT}\hat{F}\mathrm{e}^{-\hat{H}/2kT}$ on the Lanczos wavefunctions. As the application of $\mathrm{e}^{-\hat{H}/kT} = \mathrm{e}^{-\beta\hat{H}}$ is the same as propagating in imaginary time for $t = -i\hbar\beta$, we can utilize the propagation schemes introduced above. Therefore, we have to propagate in imaginary time for $-i\dfrac{\hbar}{2kT}$, apply the flux operator $\hat{F}$ and again propagate in imaginary time for $-i\dfrac{\hbar}{2kT}$ to perform one Lanczos iteration.

Please note, that the same approach can also be used to obtain the (vibrational) eigenstates of a Hamiltonian. In that case, it is efficient to diagonalize the Boltzman operator $\mathrm{e}^{-\beta\hat{H}}$ (instead of $\hat{H}$) and again employ imaginary-time propagation within the Lanczos iterations.

10.5 Numerical Quantum Dynamics: Multiconfigurational Time-dependent Hartree

The wavepacket approach introduced in the last section can be used for tri- to tetratomic systems, but the calculations become cumbersome as memory requirement and computational time increase exponentially with system size. More efficient approaches are needed to treat larger systems. Among the most successful ones is the multiconfigurational time-dependent Hartree (MCTDH) approach. MCTDH and specific extensions that are relevant to the calculation of thermal rate constants are presented. The MCTDH approach has been reviewed several times and the interested reader is refered to ref. 12 and 46–49.

10.5.1 Time-dependent Basis and Equations of Motion

The ansatz of the wavefunction is written as[50,51]

$$\Psi(x_1, \dots, x_f, t) = \sum_{j_1=1}^{n_1} \cdots \sum_{j_f=1}^{n_f} A_{j_1\dots j_f}(t) \prod_{k=1}^{f} \phi_{j_k}^{(k)}(x_k, t) \tag{10.121}$$

where $\phi_{j_k}(x_k, t)$ are time-dependent basis functions, called *single-particle functions* (SPFs) and $A_{j_1\cdots j_f,(t)}$ expansion coefficients on this basis. The SPFs are represented in a time-independent basis $\{\chi_j^k(x_k)\}$:

$$\phi_{j_k}^{(k)}(x_k, t) = \sum_{i_k=1}^{N_k} A_{j_k;\, i_k}^{(k)}(t)\chi_{i_k}^{k}(x_k). \tag{10.122}$$

One can use FFT and DVR schemes as described in Section 10.4.1. The Dirac–Frenckel time-dependent variational principle

$$\left\langle \delta\psi \middle| i\frac{\partial}{\partial t} - \hat{H} \middle| \Psi \right\rangle = 0 \tag{10.123}$$

is employed to obtain EOMs of the expansion coefficients and the SPFs. In the original implementation of MCTDH the following gauge condition is used[50]

$$i\left\langle \phi_n^{(k)} \middle| \frac{\partial}{\partial t} \middle| \phi_m^{(k)} \right\rangle = \left\langle \phi_n^{(k)} | \hat{h}_k | \phi_f^{(k)} \right\rangle, \tag{10.124}$$

where $\hat{h}_k$ are hermitian, one-particle operators. This reflects that the EOMs are invariant with respect to unitary transformations of the SPF basis. The original MCTDH derivation removes the resulting redundancy and requires

$$i\left\langle \phi_n^{(k)} \middle| \frac{\partial}{\partial t} \middle| \phi_m^{(k)} \right\rangle = 0, \tag{10.125}$$

$$\langle \phi_n^{(k)} | \phi_m^{(k)} \rangle = \delta_{nm}. \tag{10.126}$$

Further details on the derivation and recent improvements are described in ref. 52. The final EOMs read[50]

$$i\frac{\partial}{\partial t} A_{l_1\dots l_f}(t) = \sum_{j_1=1}^{n_1} \cdots \sum_{j_f=1}^{n_f} \langle \phi_{l_1}^{(1)} \dots \phi_{l_f}^{(f)} | \hat{H} | \phi_{j_1}^{(1)} \dots \phi_{j_f}^{(f)} \rangle A_{j_1\dots j_f}(t), \tag{10.127}$$

$$i\frac{\partial}{\partial t}\phi_n^{(k)}(x_k,t)=(1-\hat{P}_k)\sum_l \rho_{nl}^{(k)^{-1}}\sum_j \langle\psi_l^{(k)}|\hat{H}|\psi_j^{(k)}\rangle\phi_j^{(k)}, \tag{10.128}$$

with

$$\hat{P}_k=\sum_j |\phi_j^{(k)}\rangle\ \langle\phi_j^{(k)}|, \tag{10.129}$$

the projector onto the space spanned by the SPF,

$$\rho_{nl}^{(k)}=\langle\phi_n^{(k)}|\phi_l^{(k)}\rangle, \tag{10.130}$$

the single-particle density matrix and

$$\langle\hat{H}\rangle_{lj}^{(k)}=\langle\psi_l^{(k)}|\hat{H}/\psi_j^{(k)}\rangle \tag{10.131}$$

the matrix of the mean-field operators acting on coordinate x_k, which utilizes the single-hole functions

$$|\psi_j^{(k)}\rangle=\psi_j^{(k)}\ (x_1,\ldots,x_{k-1},x_{k+1},\ldots,x_m) \tag{10.132}$$

$$=\sum_{j_1}\cdots\sum_{j_{k-1}}\sum_{j_{k+1}}\cdots\sum_{j_f}A_{j_1,\ldots,j_{k-1},j,j_{k+1},\ldots,j_f}(t)$$

$$\phi_{j_1}^{(1)}(x_1,t)\cdots\phi_{j_{k-1}}^{(k-1)}(x_{k-1},t)\phi_{j_{k+1}}^{(k+1)}(x_{k+1},t)\cdots\phi_{j_f}^{(f)}(x_f,t). \tag{10.133}$$

We see that the EOM for the expansion coefficients [eqn (10.127)] is similar to eqn (10.91) for the standard approach. Yet, we see that the EOMs for the SPFs are more involved than the EOMs for $A_{l_1\cdots l_f}$. MCTDH gains its numerical efficiency, compared to the standard wavepacket approach, by employing an optimized set of time-dependent expansion functions, such that the basis sizes n_i can be chosen much smaller than N_i. Assuming the same SPF and primitive basis set sizes for each DOF, $n_1=n_2=\ldots n_f=n$ and $N_1=N_2=\ldots N_f=N$, we see that the propagation of the $A_{l_1\cdots l_f}$ coefficients scales like fn^{f+1} (see Section 10.4.1). The numerical effort due to the motion of the SPFs scales like fnN^2. For larger systems, the n^{f+1} is the leading contribution. Thus, both the standard approach and MCTDH scale exponentially, but the actual cost increases much slower in MCTDH. The savings in MCTDH are roughly $\left(\frac{N}{n}\right)^{f+1}$. Typically, N is in the order of 100, while n is often smaller than 10.

10.5.1.1 Time Propagation

The coupled, non-linear differential equations presented in eqn (10.127) and (10.128) can be integrated using general, all-purpose integrators. However, more efficient schemes exploiting the structure of the MCTDH EOMs have been developed. We introduce the idea underlying these approaches.

For more details, see ref. 53 and 54. For the propagation, three different types of operations are required:

1. Calculation of matrix elements and mean-field matrices at t_0, $H_{lj}(t_0)$, $\langle\hat{H}\rangle^{(k)}_{lj}(t_0)$, $\rho^{(k)}_{nl}(t_0)$.
2. Action of $H_{lj}(t_0)$ on $A_{l_1\cdots l_f(t)}$ to solve eqn (10.127).
3. Action of $(1-\hat{P}_k)\Sigma_l\rho^{(k)-1}_{nl}(t_0)\sum_j\langle\hat{H}\rangle^{(k)}_{lj}(t_0)$ on $\phi^{(k)}_j$ to solve eqn (10.128).

The different objects present in the MCTDH EOMs evolve on different timescales. The mean-field matrices and matrix elements evolve on the slowest timescale and can be considered constant during the propagation of the other two. Hence this family of MCTDH integration schemes is called *constant mean field* (CMF) approaches. To integrate for Δt, operation 1 has to be performed once, while operations 2 and 3 might be performed several times. To integrate the $A_{l_1\cdots l_f(t)}$ coefficients, one can employ special integration schemes, *e.g.*, the ones discussed in Section 10.4.2. The differential equations of the SPFs are non-linear and thus all purpose integration schemes, *e.g.*, the Bulirsch–Stoer method,[55] are typically used here.

For step 1, we need the matrix elements of the Hamiltonian in the SPF basis, H_{lj}. In particular, we need to calculate f-dimensional integrals of the form

$$\langle\phi^{(1)}_{l_1}\cdots\phi^{(f)}_{l_f}|\hat{H}|\phi^{(1)}_{j_1}\cdots\phi^{(f)}_{j_f}\rangle. \tag{10.134}$$

As the SPFs are time-dependent and of complicated form, it is not possible to directly employ any of the schemes introduced in Section 10.4.1 for treating such integrals. The original MCTDH approach requires the Hamiltonian to be a sum of products of one-particle operators, *i.e.*,

$$\hat{H}=\sum_{n=1}^{S}c_n\prod_{k=1}^{f}\hat{h}^{(k)}_n, \tag{10.135}$$

where $\hat{h}^{(k)}_n$ only acts on the kth DOF. The integral factorizes into one-dimensional integrals

$$\langle\phi^{(1)}_{l_1}\ldots\phi^{(f)}_{l_f}|\hat{H}|\phi^{(1)}_{j_1}\ldots\phi^{(f)}_{j_f}\rangle=\left\langle\phi^{(1)}_{l_1}\ldots\phi^{(f)}_{l_f}\middle|\sum_{n=1}^{S}c_n\prod_{k=1}^{f}\hat{h}^{(k)}_n\middle|\phi^{(1)}_{j_1}\ldots\phi^{(f)}_{j_f}\right\rangle \tag{10.136}$$

$$=\sum_{n=1}^{S}c_n\prod_{k=1}^{f}\left\langle\phi^{(k)}_{l_k}\middle|\hat{h}^{(k)}_n\middle|\phi^{(k)}_{j_k}\right\rangle. \tag{10.137}$$

Typical kinetic energy operators and model potentials are of this *"sum of products"* form. However, general potential energy surfaces have to be refitted to match this structure.[56–59] A way to treat general potential energy surfaces using a DVR-like approach will be discussed in Section 10.5.3.

10.5.2 Useful Extensions of MCTDH

Several extensions of the MCTDH approach exist that are particularly helpful for the calculation of thermal rate constants and that allow for an increased numerical efficiency of the simulations.

10.5.2.1 State-averaging

One extension is the state-averaged MCTDH.[60] A set of W MCTDH wavefunctions is expanded in the same SPF basis, but with different top-level A coefficients:

$$\Psi_w(x_1, \ldots, x_f, t) = \sum_{j_1=1}^{n_1} \cdots \sum_{j_f=1}^{n_f} A_{w;j_1 \ldots j_f}(t) \prod_{k=1}^{f} \phi_{j_k}^{(k)}(x_k, t) \quad w = 1, \ldots, W. \tag{10.138}$$

This approach results in a SPF basis that is an optimized averaged description of the W wavefunctions. It has been shown that the SPF basis size does not increase significantly when several wavefunctions are combined in this scheme and thus the state-averaged MCTDH approach has a reduced numerical cost compared to standard MCTDH. The SPF integration has to be done once. This extension is useful for thermal rate constant calculations as we have to obtain and propagate several thermal flux eigenstates. This can be done in a single simulation instead of W different simulations.

10.5.2.2 Mode Combination

Thus far, the SPFs have been written as functions of a single DOF. However, they can be functions of any number of DOFs.[61–63] To this end, the f physical DOFs are combined into d logical DOFs, $q_1, \ldots, q_d$, with dimensionality $d_1, \ldots, d_d$. The corresponding wavefunction ansatz reads

$$\Psi(q_1, \ldots, q_d, t) = \sum_{j_1=1}^{n_1} \cdots \sum_{j_d=1}^{n_d} A_{j_1 \ldots j_d}(t) \prod_{k=1}^{d} \phi_{j_k}^{(k)}(q_k, t), \tag{10.139}$$

$$\phi_{j_k}^{(k)}(q_k, t) = \phi_{j_k}^{(k)}(x_{\alpha_k+1}, \ldots, x_{\alpha_k+d_k}, t) \tag{10.140}$$

$$= \sum_{i_1=1}^{N_{\alpha_k+1}} \cdots \sum_{i_{d_k}=1}^{N_{\alpha_k+d_k}} A^{(k)}_{j_k; i_1, \ldots, i_{d_k}}(t) \cdot \chi^{k}_{i_1, \ldots, i_{d_k}}(x_{\alpha_k+1}, \ldots, x_{\alpha_k+d_k}) \tag{10.141}$$

with $\alpha = \sum_{i=1}^{k-1} d_i$. For simplicity, we assume that the χs are functions of all primitive coordinates within a given logical coordinate, but in general it can also be a direct product basis. This approach is called "mode combination".

10.5.2.3 Multi-layer MCTDH

The MCTDH approach can be viewed as a two-layer approach. The first layer consists of the $A_{l_1 \dots l_f}$ coefficients while the second layer consists of the expansion coefficients for the SPFs, $A_{j_k;i_k}^{(k)}$. Similarly, the standard wavepacket approach can be viewed as a single-layer approach. The structure of such wave function expansions can be conveniently visualized employing tree diagrams.[64] Some example diagrams for a three-dimensional system are given in Figure 10.4. In these diagrams, a filled circle represents a set of A coefficients and each line represents a logical or physical DOF represented by the A coefficient on top of it with the number next to it denoting the number of basis functions employed. The top line represents the overall wavefunction. Consequently, the diagram for the standard approach (Figure 10.4a) consists of a single filled circle representing the A coefficients given in eqn (10.90) and three lines representing the three physical DOFs and each DOF represented by N basis functions. The standard MCTDH wavefunction representation (Figure 10.4b) consists of four filled circles. The top one represents the top-layer A_{l_1,l_2,l_3} coefficients, while the other three represent the $A_{j_k;i_k}^{(k)}$ coefficients used in the SPF expansions. For each DOF, n SPFs are used. Each SPF function is one-dimensional and is represented by N basis functions. Panel c of Figure 10.4 displays the tree diagram of a mode combination MCTDH wave function. The physical DOFs x_2 and x_3 are combined into a logical DOF q_2. Therefore, only two filled circles are present on the second layer, but one of them is two-dimensional, *i.e.*, has two lines attached to its bottom.

These diagrams will be useful to discuss a very powerful extension of MCTDH, termed *multilayer* (ml) MCTDH.[64–67] One can view any

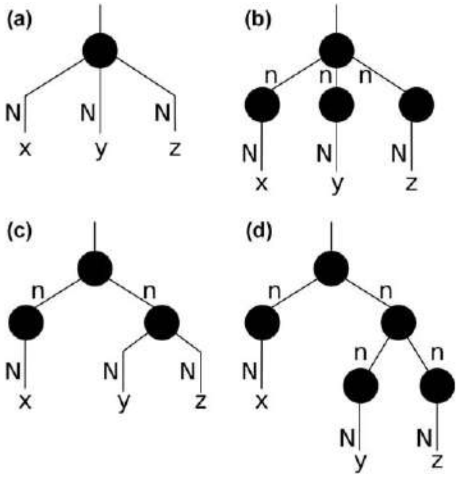

Figure 10.4 Tree-like representation of different wavefunction expansions. A circle represents a set of A coefficients and a line a logical or physical coordinate. (a) Standard wave [eqn (10.141)]. (b) Standard MCTDH expansion [eqn (10.121)]. (c) Mode combination MCTDH [eqn (10.141)]. (d) Multi-layer MCTDH [eqn (10.144)].

multidimensional SPF as a wavefunction, which is treated within the MCTDH scheme, *i.e.*, expanded in a time-dependent basis. The ansatz for a three-layer MCTDH wavefunction reads

$$\Psi_w(x_1^1, \ldots x_d^1, t) = \sum_{j_1=1}^{n_1} \cdots \sum_{j_d=1}^{n_d} A^1_{w\,;j_1\ldots j_d}(t) \prod_{k=1}^{d} \phi^{1\,;k}_{j_k}(x_k^1, t), \tag{10.142}$$

$$\phi_p^{1\,;k}(x_k^1, t) = \phi_p^{1\,;k}(x_1^{2\,;k}, \ldots, x_{d_k}^{2\,;k}, t) = \sum_{j_1=1}^{n_{k,1}} \cdots \sum_{j_p=1}^{n_{k,d_k}} A^{2\,;k}_{p\,;j_1\ldots j_{d_k}}(t) \prod_{l=1}^{d_k} \phi^{2\,;k,l}_{j_l}(x_l^{2\,;k}, t), \tag{10.143}$$

$$\phi_p^{2\,;k,\lambda}(x_\lambda^{2\,;k}, t) = \sum_{j=1}^{N_\alpha} A^{3\,;k\,;\lambda}_{p\,;j}(t)\chi_j^\alpha(x_\lambda^{2\,;k}), \tag{10.144}$$

$$\text{with } \alpha = \lambda - \sum_{i=1}^{k-1} d_i. \tag{10.145}$$

We have changed the notation for the logical DOFs from q back to x, but include the index of the layer they are associated with. All SPFs and A coefficients carry an index denoting the layer they are in. Figure 10.4d depicts the tree diagram for a three-layer MCTDH wavefunction. Similar to the mode combination wavefunction, only two filled circles are present in the second layer. However, there is a third layer added which consists of two filled circles representing the expansion of the multidimensional SPF. These SPFs are one-dimensional and expanded in a time-independent basis of size N.

Please note, that this can be done recursively until each DOF is expanded in a time-independent basis. The (near) optimal choice for combining DOFs in this scheme, *i.e.*, the topology of the tree, is an active area of research.

10.5.3 Correlation DVR

The standard MCTDH approach requires the Hamiltonian to be in a "sum of products" form, but most potential energy surfaces used in accurate rate constant calculations are not in this form. Often the potential is refit to match this structure. However, there is another possibility to factorize the potential integral, which is based on the DVR approach introduced in Section 10.4.1. The DVR approach can be generalized to a time-dependent DVR (TDDVR) approach.[51,68] Within the MCTDH framework one would then evaluate the potential energy integrals on time-dependent grids associated with the time-dependent basis spanned by the SPFs. The time-dependent grid points $q_{m_k}(t)$ are obtained by diagonalizing the position operator matrix in the SPF basis[69]

$$\langle \phi_{l_k}^{(k)}(t)|\hat{x}_k|\phi_{j_k}^{(k)}(t)\rangle = \sum_{m_k} \langle \phi_{l_k}^{(k)}(t)|Q_{m_k}(t)\rangle\ q_{m_k}(t)\langle Q_{m_k}(t)|\phi_{j_k}^{(k)}(t)\rangle. \tag{10.146}$$

Employing this scheme within the MCTDH framework can lead to large numerical errors. The reason for that is the small size of the SPF basis. The reason for the success of the DVR approach is that the wavefunction shows more structure than the potential and, therefore, any quadrature errors in the evaluation of the potential integrals is smaller than the error due to the finite representation of the wavefunction. In the MCTDH framework, the A coefficients account for the correlation in the system and the SPF basis size is independent of the separable dynamics. Consequently, the TDDVR grid points are only properly able to treat the parts of the potential that result in correlation. The number of grid points is too small to accurately calculate the integrals over the separable parts of the potential. This can be exemplified for the most extreme case of a completely separable potential $V(x_1,\ldots,x_f) = V_1(x_1) + \ldots + V_f(x_f)$. The dynamics of this system can be described using a single SPF per DOF. The exact potential energy matrix elements read

$$\langle \phi^{(1)}_{l_1} \ldots \phi^{(f)}_{l_f} | \hat{V} | \phi^{(1)}_{j_1} \ldots \phi^{(f)}_{j_f} \rangle = \sum_{n=1}^{f} \langle \phi^{(n)}_{l_n} | V_n | \phi^{(n)}_{j_n} \rangle. \tag{10.147}$$

Within the TDDVR approach the potential energy matrix elements read

$$\langle \phi^{(1)}_{l_1} \ldots \phi^{(f)}_{l_f} | \hat{V} | \phi^{(1)}_{j_1} \ldots \phi^{(f)}_{j_f} \rangle \approx \sum_{n=1}^{f} V_n\left(\langle \phi^{(n)}_{l_n} | \hat{x}_n | \phi^{(n)}_{j_n} \rangle\right), \tag{10.148}$$

which differs from the exact value as $\langle \phi^{(n)}_{l_n} | V_n | \phi^{(n)}_{j_n} \rangle \neq V_n\ (\langle \phi^{(n)}_{l_n} | \hat{x}_n | \phi^{(n)}_{j_n} \rangle)$.

This problem can be circumvented by employing the *correlation DVR* (CDVR) approach,[69] which introduces additional terms to treat the separable parts of the potential exactly. The potential matrix elements in the grid basis are calculated as

$$\begin{aligned} &\langle Q^{(1)}_{l_1} \ldots Q^{(f)}_{l_f} | \hat{V} | Q^{(1)}_{j_1} \ldots Q^{(f)}_{j_f} \rangle \\ &\quad = V(q^{(1)}_{l_1}, \ldots, q^{(f)}_{l_f}) \delta_{l_1 j_1} \ldots \delta_{l_f j_f} + \sum_{k=1}^{f} \langle Q^{(k)}_{l_k} | \Delta V(q^{(1)}_{l_1}, \ldots, q^{(k-1)}_{l_{k-1}}, \\ &\quad\quad \times x_k, q^{(k+1)}_{l_{k+1}}, \ldots, q^{(f)}_{l_f}) | Q^{(1)}_{j_1} \rangle \delta_{l_1 j_1} \ldots \delta_{l_{k-1} j_{k-1}} \delta_{l_{k+1} j_{k+1}} \ldots \delta_{l_f j_f} \end{aligned} \tag{10.149}$$

with

$$\begin{aligned} &\langle Q^{(k)}_{l_k} | \Delta V(q^{(1)}_{l_1}, \ldots, q^{(k-1)}_{l_{k-1}}, x_k, q^{(k+1)}_{l_{k+1}}, \ldots, q^{(f)}_{l_f}) | Q^{(k)}_{j_k} \rangle \\ &\quad = \langle Q^{(k)}_{l_k} | V(q^{(1)}_{l_1}, \ldots, q^{(k-1)}_{l_{k-1}}, x_k, q^{(k+1)}_{l_{k+1}}, \ldots, q^{(f)}_{l_f}) | Q^{(k)}_{j_k} \rangle - V(q^{(1)}_{l_1}, \ldots, q^{(f)}_{l_f}) \delta_{l_k, j_k}. \end{aligned} \tag{10.150}$$

The first part on the right hand side of eqn (10.149) is the original TDDVR result and the second part describes the correction. To evaluate the potential

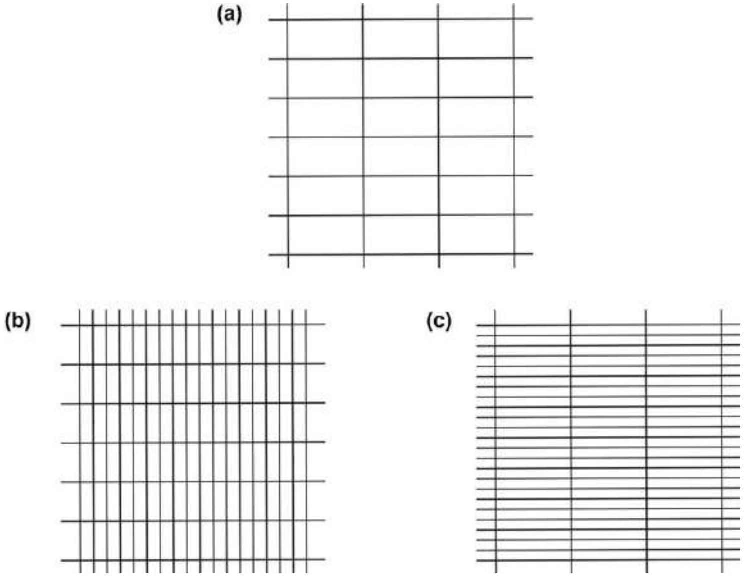

Figure 10.5 Sketch of the CDVR grids for a two-dimensional problem. (a) The small TDDVR grid. (b), (c) The two CDVR correction grids.

energy integrals, $f+1$ grids are employed. A grid with $n=\prod_{l=1}^{f} n_l$ grid points and f correction grids with $N_k \prod_{l=1,l\neq k}^{f} n_l$ grid points. For a two-dimensional problem, this is schematically shown in Figure 10.5. Panel a shows the small TDDVR grid with four and seven grid points in the DOFs. Panels b and c display the two CDVR correction grids. In panel b, the four time-dependent grid points are replaced by 18 time-independent grid points, while the seven time-dependent grid points are unchanged. In panel c, the four time-dependent grid points are kept and the seven are replaced by 24 time-independent grid points. To obtain the full potential energy matrix, one has to evaluate the potential on these three grids. The CDVR scheme solves the separable problem discussed before exactly. The correction terms read

$$\begin{aligned}&\langle Q^{(k)}_{l_k}|\Delta V(q^{(1)}_{l_1},\ldots,q^{(k-1)}_{l_{k-1}}, x_k, q^{(k+1)}_{l_{k+1}},\ldots,q^{(f)}_{l_f})|Q^{(k)}_{j_k}\rangle\\ &\quad=\langle Q^{(k)}_{j_k}|V_k(x_k)|Q^{(k)}_{j_k}\rangle - V_k(q^{(k)}_{j_k})\delta_{l_k,j_k}\end{aligned} \tag{10.151}$$

and there we obtain

$$\begin{aligned}\langle\phi^{(1)}_{l_1}\ldots\phi^{(f)}_{l_f}|\hat{V}|\phi^{(1)}_{j_1}\ldots\phi^{(f)}_{j_f}\rangle &\approx \sum_{k=1}^{f} V_k(q^{(k)}_{l_k})\delta_{l_k,j_k}+\\ &\sum_{k=1}^{f}(\langle Q^{(k)}_{l_k}|V_k(x_k)|Q^{(k)}_{j_k}\rangle - V_k(q^{(k)}_{j_k})\delta_{l_k,j_k})\\ &\delta_{l_1,j_1}\ldots\delta_{l_{k-1},j_{k-1}}\delta_{l_{k+1},j_{k+1}}\ldots\delta_{l_f,j_f},\end{aligned} \tag{10.152}$$

which is the exact result given in eqn (10.148). Please note that this scheme is not significantly more expensive than the standard approach as any potential values required for the correction terms have to be calculated for the mean-field potential matrix elements required to propagate the SPFs. The CDVR approach favorably combines with the state-averaged MCTDH as most of the potential calls are due to the SPF basis and thus do not have to be repeated for each wavepacket. The CDVR approach can be combined with ml-MCTDH. Details on this are found in ref. 66, 70, and 71.

10.5.4 Eigenstate Calculations within MCTDH

Utilizing the state-averaged MCTDH a simple strategy based on successive applications of an operator, *e.g.*, $\hat{F}_T$, and Gram–Schmidt orthogonalization can be used to obtain eigenstates.[12,60] We use a set of N orthonormal trial wavefunctions $\{\psi_n,\ n=1,\ldots,N\}$, the current approximate eigenstates, which are iteratively refined to obtain the N lowest eigenstates. Within each iteration, we first calculate the eigenstates of $\hat{F}_T$ within the basis of our current approximate eigenstates. This is done by applying $\hat{F}_T$ to the set of approximate eigenstates to get $\{\hat{F}_T\psi_n,\ n=1,\ldots,N\}$, and diagonalizing the matrix $F_{n,n'}=\langle\psi_n|\hat{F}_T\psi_{n'}\rangle$ as

$$F_{n,n'}=\sum_{j=1}^{N}U_{nj}f_jU^{*}_{n'j}. \tag{10.153}$$

The eigenvectors U_j are sorted according to the ascending magnitude of the eigenvalues f_j to improve convergence. The set $\{\hat{F}_T\psi_n,\ n=1,\ldots,\ N\}$ is transformed into the basis given by U to give

$$\phi_j=\sum_{n=1}^{N}U_{nj}\hat{F}_T\psi_n. \tag{10.154}$$

We orthonormalize the transformed wavefunctions $\{\phi_n,\ n=1,\ldots,N\}$ employing the Gram–Schmidt procedure to obtain a new set of approximate eigenstates. This procedure is repeated until convergence.

One can also employ the Lanczos scheme within the MCTDH context using some modifications.[12,72] This modified Lanczos scheme can be combined with state-averaged approach. Details on this approach are found in ref. 60, 73, and 74. Please note, that there are also other ways to obtain eigenstates within the MCTDH framework. They are discussed in ref. 75 and 76.

10.5.5 Statistical Approaches for Calculating Rotational Motion and Partition Functions

Statistical wave functions $\Psi^{(j)}$ for the efficient treatment of overall rotational motion can be obtained in two ways within the MCTDH framework. One can either randomize the top-layer A coefficients employing a random phase[77]

$$\Psi^{(j)}(x_1, \ldots, x_f) = \sum_{j_1=1}^{n_1} \cdots \sum_{j_f=1}^{n_f} \mathrm{e}^{\mathrm{i}\theta_{j_1,\ldots,j_f}(j)} \prod_{k=1}^{f} \phi_{j_k}^{(k)}(x_k, t), \tag{10.155}$$

with $\theta_{j_1,\ldots,j_f}(j)$ random numbers in the interval $[0, 2\pi]$, or one can randomize the A coefficients of the bottom-layer SPF as[10,13,21]

$$\phi_{j_k}^{(k)}(x_k) = \sum_{i_k=1}^{N_k} (-1)^{\alpha_{i_k}(j)} \chi_{i_k}^{k}(x_k), \tag{10.156}$$

with $\alpha_{i_k}(j)$ a random integer and the initial wavefunction is taken to be a Hartree product of the statistical SPFs, *i.e.*, the top-layer A coefficient is $A_{j_1\ldots j_f}=1$, if $j_1=j_2=\ldots=j_f=1$ and $A_{j_1\ldots j_f}=0$ otherwise. Tests have shown that the latter approach converges significantly faster and it is used here.[78] For the case of overall rotational motion, we employ Wigner rotation matrices $|JMK\rangle$ as basis functions and obtain the statistical wavefunction as[10,13,21]

$$|\phi_{\mathrm{rot}}^{(j)}\rangle = \sum_{J=0}^{J_{\max}} \sum_{K=-\mathrm{Min}(J,K_{\max})}^{\mathrm{Min}(J,K_{\max})} (-1)^{\alpha_{J,K}(j)} \sqrt{2J+1}|JKM\rangle, \tag{10.157}$$

with $\alpha_{J,K}(j)$ random integers and the quantum number M chosen arbitrarily. The statistical wavefunctions can also be used to obtain the partition function of the reactants.[79]

The statistical error in each case converges to zero as $\frac{1}{\sqrt{M}}$. The efficiency of the convergence is governed by its variance. For the case of the partition function it reads[80]

$$\sigma^2 = \lim_{M\to\infty} \frac{1}{M} \sum_{j=1}^{M} |\langle \Psi^{(j)}|\mathrm{e}^{-\beta\hat{H}_{\mathrm{R}}}|\Psi^{(j)}\rangle - \mathrm{tr}(\mathrm{e}^{-\beta\hat{H}_{\mathrm{R}}})|^2 \tag{10.158}$$

$$= \sum_{n\neq m} |\langle \chi_n|\mathrm{e}^{-\beta\hat{H}_{\mathrm{R}}}|\chi_m\rangle|^2 + \langle \chi_n|\mathrm{e}^{-\beta\hat{H}_{\mathrm{R}}}|\chi_m\rangle^2, \tag{10.159}$$

which is only dependent on the off-diagonal matrix elements in the chosen basis. For separable overall Hamiltonians and $|\chi_{l_k}\rangle$ chosen as eigenfunctions of the separable parts, a single sample ($M=1$) is sufficient for convergence, but also for correlated systems the number of samples is typically small if good coordinate systems and well-suited basis functions are chosen.

10.6 Examples

We will close this chapter by giving a few examples of reactions that have been treated with the approach introduced. We will consider three reactions, a tri-, tetra-, and six-atomic reaction, respectively. We will focus on results obtained employing potential energy surfaces (PES) that are based on highly accurate electronic structure calculations, and that were fit with high accuracy. For each example, we will highlight different aspects, *e.g.*, the accurate treatment of spin–orbit coupling, the accuracy of the J-shifting approximation or considerations regarding ml-MCTDH and different PES.

10.6.1 $Cl + H_2 \rightarrow HCl + H$

The results summarized here have been published in ref. 81 and 82. The $Cl + H_2 \rightarrow HCl + H$ reaction has been an important benchmark reaction to study the effects of spin-orbit coupling on the reactivity.

10.6.1.1 Treatment of Spin–Orbit Coupling

There are several different ways to account for spin–orbit coupling. The exact treatment of spin–orbit coupling requires the PES to be fitted including spin–orbit coupling. The spin–orbit split PESs can be used in the dynamical simulation and the splitting of the initial states has to be included in the partition function. The corresponding partition function then reads

$$Q_{\text{reac}}^{\text{elec}} = 2 + \mathrm{e}^{-\Delta E/kT}, \tag{10.160}$$

with ΔE the asymptotic spin–orbit splitting of the atomic Cl. Yet, most PES do not employ spin–orbit coupling explicitly and its effects on the dynamics cannot be accounted for. However, the effect on the reactant partition function can be described. Given that the spin–orbit coupling is important only asymptotically and quenched in the interaction region, this treatment is justified. In this case, the asymptotic PES corresponds to the average energy of the spin–orbit split states and the partition function has to be taken as

$$Q_{\text{reac}}^{\text{elec}} = 2\mathrm{e}^{\Delta E/3kT}\mathrm{e}^{+-2\Delta E/3kT}. \tag{10.161}$$

In ref. 82, the validity of this approach is tested for the $Cl + H_2$ reaction. A PES that accurately includes spin–orbit splitting is employed (the CWad PES) and consequently eqn (10.163) is used in the reactant partition function. These results are compared to older work[81] that employed a PES without inclusion of spin–orbit splitting (the BW2 PES) and that used eqn (10.164) in the reactant partition function. The resulting rate constants are given in Figure 10.6. The results for both surfaces agree very well with each other and also with experimental results. To quantify the error due to neglecting the spin–orbit coupling in the dynamical simulation, the ratio of the thermal rate constants obtained with the BW2 PES and the CWad PES is given on the top-right of Figure 10.6. The error is below 5%, even at temperatures as low as 200 K. This error is within the convergence error of the full simulations. Please note that it is important to always consider if the employed PES is constructed with or without explicitly including spin–orbit coupling and use the appropriate formula for inclusion of the spin–orbit splitting in the reactant partition function.

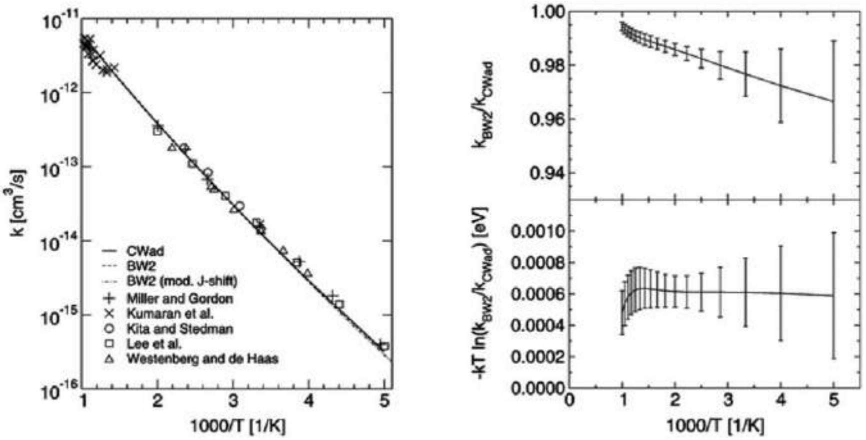

Figure 10.6 Left: thermal rate constants obtained with (CWad) and without (BW2) explicit treatment of spin–orbit coupling. Different experimental results are given as symbols. Right: ratio of thermal rate constants obtained without and with explicit treatment of spin–orbit coupling (upper panel). The energy difference corresponding to this ratio is displayed in the lower panel. The error bars referr to the error from the statistical treatment of the rotational motion (see Section 10.5.5).
Reproduced from ref. 82 with permission from the PCCP Owner Societies.

10.6.2 $H_2 + OH \rightarrow H_2O + H$

The reaction of H_2 and OH is the main route for water formation in the interstellar medium. It is also the benchmark tetratomic reaction and has been studied for decades using accurate theoretical approaches. We will focus on recent results that not only use the approaches detailed in this chapter, but were also the first rigorous thermal rate constant simulations to employ modern, high-level PES for this system. The details are given in ref. 83–85.

The thermal rate constants between 700 K and 150 K are shown in Figure 10.7. and compared to different experimental results and harmonic TST (see Section 10.2.2). In the high-temperature regime, TST gives relatively good rate constants as both the classical and no-recrossing approximations are reasonable here. Towards lower temperature, *i.e.*, below 500 K, the TST rates dramatically underestimate the experimental and QTSC results due to neglecting recrossing and tunnelling. The rigorous QTSC results agree very well with the experimental results.

10.6.2.1 The J-shifting Approximation

In Section 10.3.3 we introduced the J-shifting approximation. It is widely used in accurate and approximate thermal rate constant simulations. Older work suggested that this approximation is not good for the $H_2 + OH$ reaction as rate constant differ by a factor of two at 300 K between close-coupling and J-shifting simulations.[92] In Figure 10.8, we show thermal rate constants

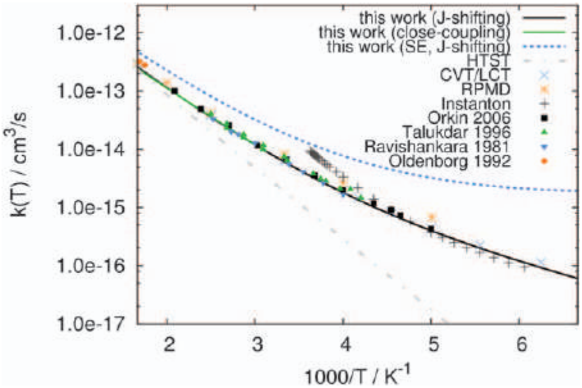

Figure 10.7 Thermal rate constants $k(T)$ in $\mathrm{cm}^3\,\mathrm{s}^{-1}$ for the $H_2 + OH$ reaction. Accurate results on the NN1 and SE PESs are given as black line and blue dots. Experimental results are given as filled symbols,[86–89] TST as grey dash-dotted line,[90] semi-empirically corrected TST as blue crosses,[90] RPMD as orange stars,[91] and instanton results as black crosses.[90]
Reproduced from ref. 84 with permission from John Wiley and Sons, © 2018 Wiley-VCH Verlag GmbH & Co. KGaA, Weinheim.

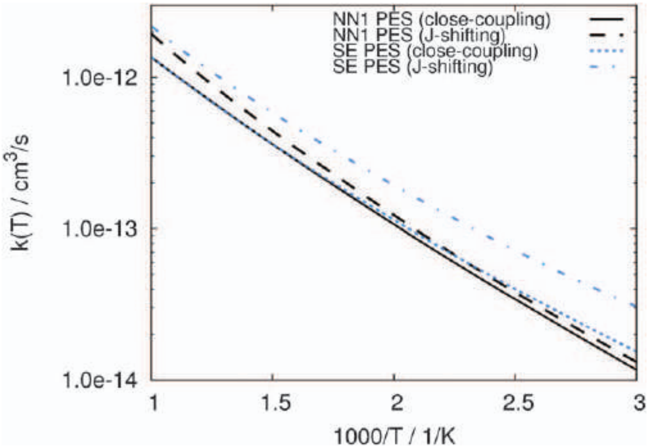

Figure 10.8 Thermal rate constants $k(T)$ in $\mathrm{cm}^3\,\mathrm{s}^{-1}$ for the $H_2 + OH$ reaction. Rigorous close-coupling results and J-shifting results on both the NN1 and SE PESs are given.
Reproduced from ref. 83 with permission from AIP Publishing, Copyright 2018.

obtained with rigorous close-coupling simulations and with the J-shifting approximation for both the old, semi-empirical Schatz–Elgersma (SE) PES[93] and the new, high-level neural network (NN1) PES.[94] The results obtained on the SE PES show the same errors of the J-shifting approximation as the older work. In contrast, both rigorous close-coupling and J-shifting rate constants calculated for the NN1 PES only deviate by up to 20% at 300 K.

It was previously discussed that the fit of the SE PES deviates from the *ab initio* data, in particular around the transition state. This results in large differences of the moments of inertia associated with the transition state on the PES and in the *ab initio* calculations. The moments of inertia are integral to the J-shifting approximation and these deviations result in the breakdown of the J-shifting approximation on the SE PES. Due to the better fit in the NN1 PES, the transition state is reproduced better and the rotational motion can be separated well, resulting in reasonable J-shifting results.

10.6.3 $H+CH_4 \rightarrow H_2+CH_3$

The $H+CH_4$ reaction is considered the benchmark six-atomic reaction. It has attracted a large amount of work, including several full-dimensional calculations of the rate constant. While the first of these calculations had to use a less accurate, semi-empirical PES,[95] the past ten years have seen several rigorous simulations employing highly accurate PES.[96–98] The results presented here were originally published in ref. 23 and 99–101.

10.6.3.1 *Multilayer MCTDH Considerations*

As discussed in Section 10.5.2, the ml-MCTDH is a useful approach for the propagation of high-dimensional wavepackets. In ref. 99, the efficiency of the ml-MCTDH approach for the calculation of thermal rate constants of $H+CH_4$ has been investigated. As the main purpose of this study was to investigate the efficiency of the ml-MCTDH approach, a cheap, semi-empirical PES and transition state normal modes were employed. The convergence of thermally weighted $N(E)$ for a particular ml-MCTDH wave function is shown in Figure 10.9 and Table 10.1. Exact results are obtained

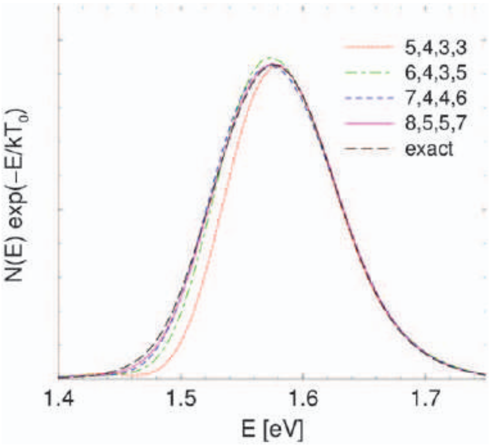

Figure 10.9 Thermally weighted $N(E)$ at 300 K for the JG-PES. See ref. 99 for details. Reproduced from ref. 99 with permission from AIP Publishing, Copyright 2012.

Table 10.1 Wall time, *i.e.*, elapsed real time, and thermal rate constant at 300 K of different basis sets. See ref. 99 for details. Reproduced from ref. 99 with permission from AIP Publishing, Copyright 2012.

n_1, n_2, n_3, n_4	Wall time	Factor	k/k_{exact} at 300 K
5, 4, 3, 3	134 min	1.00	0.894
6, 4, 3, 5	241 min	1.80	0.982
7, 4, 4, 6	419 min	3.13	0.997
8, 5, 5, 7	905 min	6.77	0.997
EXACT	3383 min	25.25	1.00

with single-layer MCTDH employing over 230 000 top-level configurations. Fast convergence of the ml-MCTDH results with respect to the basis set size is found. A set of only $7 \times 4 \times 4 \times 6 = 672$ top-level configurations is sufficient to converge the rate constant within less than 1% and for convergence of about 10%, a factor of about two fewer configurations is required. The speed-up gained by the ml-MCTDH approach is apparent when comparing the simulation times on a single-core AMD Opteron 850 processor with 2.4 GHz, which is also shown in Table 10.1. Speed-ups of about an order of magnitude can be obtained within reasonable convergence criteria.

10.6.3.2 Comparing Different PES

For the accurate theoretical description of a reaction process the PES is of crucial importance. Several PES have been published based on high-level *ab initio* calculations but using very different fitting or interpolating techniques. Here, we will compare the results of thermal rate constant calculations on these different PES. The different PES are constructed using Shepard interpolation (WWM, ZFWCZ, m-ZFWCZ, ZFWCZ-WM), permutationally invariant polynomials (ZBB3) or high-dimensional feed-forward neural networks (XCZ). Apart from the accuracy of the fit or interpolation of these PES, there is another issue to be considered when doing high-dimensional rate constant calculations employing the QTSC and MCTDH. In Section 10.5.3 we discussed the CDVR approach, which employs time-dependent grids and requires billions of PES evaluations. The relative cost of evaluating the PES introduced above is 6 (WWM), 66 (ZBB3), 230 000 (ZFWCZ), 10 (ZFWCZ-WM), and 3 (XCZ) compared to the semi-empirical JG PES. Figure 10.10 presents the thermal rate constant calculated on the different PES. For comparison, several experimental results are also given. Good agreement between the theoretical and experimental results is obtained. The spread of experimental results is bigger than the differences between the results for different PES. In particular, the newest PES (XCZ, ZFWCZ-WM) agree nearly perfectly with each other.

10.6.3.3 Natural Reaction Channels

In Section 10.3.4, the interpretation of CRPs with respect to natural reaction channels was discussed. Ref. 23 presents the decomposition of the CRP of

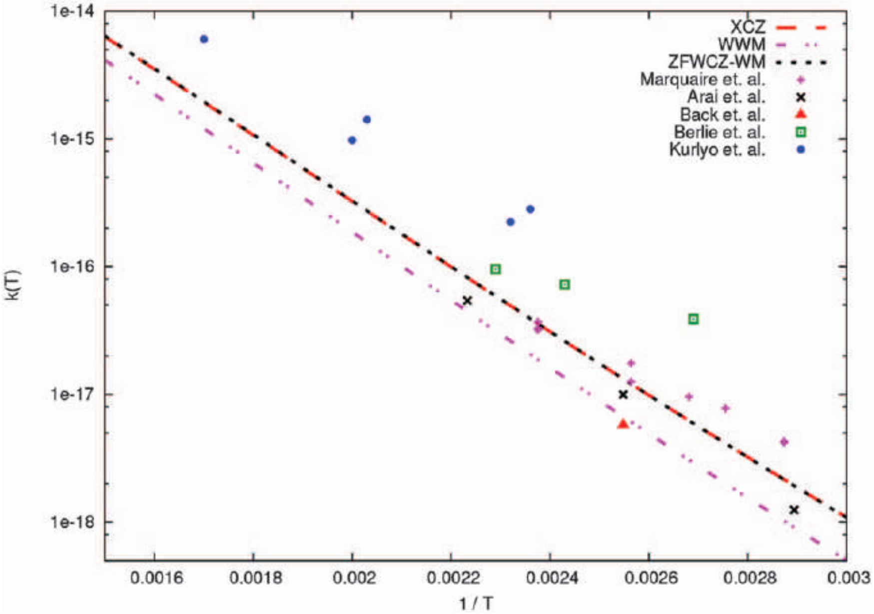

Figure 10.10 Thermal rate constants for different PESs. Experimental data[102–106] are shown as symbols.
Reproduced from ref. 101 with permission from AIP Publishing, Copyright 2015.

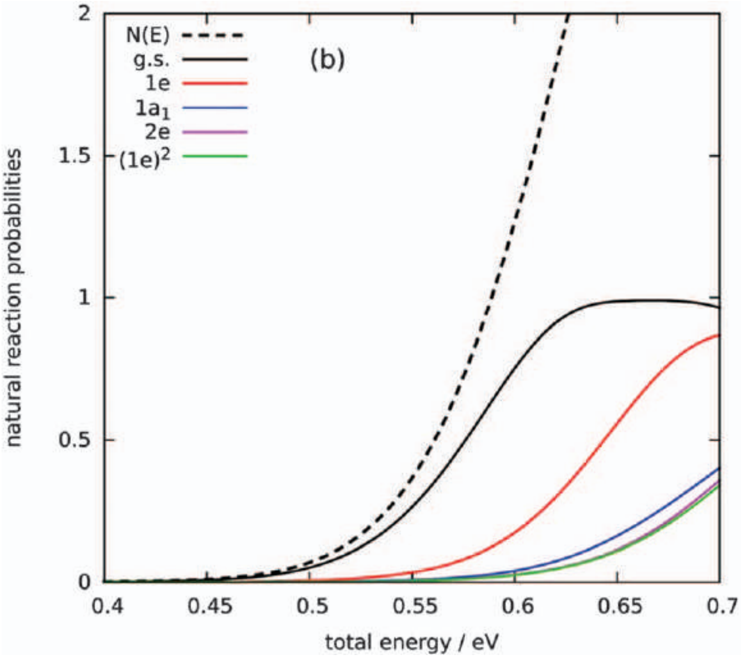

Figure 10.11 CRP and associated natural reaction probabilities for the $H+CH_4$ reaction. Reproduced from ref. 23 with permission from the Royal Society of Chemistry.

the $H + CH_4$ reaction into its natural reaction channels, which is shown in Figure 10.11. At low energies, close to the threshold, the reaction proceeds exclusively through the natural reaction channel associated with the ground vibrational state of the activated complex. At energies about 0.05 eV higher, the two degenerate channels associated with the $H–H–CH_3$ bending motion start to contribute. This is consistent with the harmonic excitation energy of this mode of 534 cm^{-1}. At even higher energies the CH_3 umbrella mode, the $H–CH_3$ bending mode and the first overtone of the $H–H–CH_3$ bending mode start to contribute.

Acknowledgements

I am grateful to Uwe Manthe, Johannes Kästner, Gerd Schiffel, and Fermín Huarte-Larrañaga for many discussions and collaboration. I thank Roman Ellerbrock and Caroline Arnold for many helpful comments on the manuscript.

References

1. B. Zhao and H. Guo, State-to-state quantum reactive scattering in four-atom systems, *Wiley Interdiscip. Rev.: Comput. Mol. Sci.*, 2017, **7**(3), e1301.
2. A. Fernández-Ramos, J. A. Miller, S. J. Klippenstein and D. G. Truhlar, Modeling the Kinetics of Bimolecular Reactions, *Chem. Rev.*, 2006, **106**(11), 4518–4584.
3. J. R. Taylor, *Scattering Theory: The Quantum Theory of Nonrelativistic Collisions*, Courier Corporation, 2006.
4. J. J. Sakurai and E. D. Commins, *Modern Quantum Mechanics*, revised edn, AAPT, 1995.
5. D. J. Tannor and D. E. Weeks, Wave packet correlation function formulation of scattering theory: The quantum analog of classical S-matrix theory, *J. Chem. Phys.*, 1993, **98**(5), 3884–3893.
6. W. H. Miller, Quantum Mechanical Transition State Theory and a New Semiclassical Model for Reaction Rate Constants, *J. Chem. Phys.*, 1974, **61**, 1823.
7. W. H. Miller, S. D. Schwartz and J. W. Tromp, Quantum Mechanical Rate Constants for Bimolecular Reactions, *J. Chem. Phys.*, 1983, **79**, 4889.
8. T. Yamamoto, Quantum Statistical Mechanical Theory of the Rate of Exchange Chemical Reactions in the Gas Phase, *J. Chem. Phys.*, 1960, **33**, 281.
9. F. Huarte-Larrañaga and U. Manthe, Thermal Rate Constants for Polyatomic Reactions: First Principles Quantum Theory, *Z. Phys. Chem.*, 2007, **221**, 171–213.
10. U. Manthe, Reaction Rates, in *Methods in Reaction Dynamics*, ed. Jakubetz W., Springer Berlin Heidelberg, Berlin, Heidelberg, 2001, pp. 167–193.

11. U. Manthe, Accurate Calculations of Reaction Rates: Predictive Theory Based on a Rigorous Quantum Transition State Concept, *Mol. Phys.*, 2011, **109**, 1415–1426.
12. *Multidimensional Quantum Dynamics: MCTDH Theory and Applications*, ed. Meyer H. D., Gatti F. and Worth G. A., Wiley-VCH, Weinheim, 2009.
13. F. Matzkies and U. Manthe, Accurate Reaction Rate Calculations Including Internal and Rotational Motion: A Statistical Multi-Configurational Time-Dependent Hartree Approach, *J. Chem. Phys.*, 1999, **110**, 88–96.
14. T. Seideman and W. H. Miller, Calculation of the cumulative reaction probability via a discrete variable representation with absorbing boundary conditions, *J. Chem. Phys.*, 1992, **96**, 4412.
15. T. J. Park and J. Light, Quantum Flux Operators and Thermal Rate Constant: Collinear $H + H_2$, *J. Chem. Phys.*, 1988, **88**(8), 4897–4912.
16. E. Pollak, The symmetrized quantum thermal flux operator, *J. Chem. Phys.*, 1997, **107**(1), 64–69.
17. F. Matzkies and U. Manthe, A Multi-Configurational Time-Dependent Hartree Approach to the Direct Calculation of Thermal Rate Constants, *J. Chem. Phys.*, 1997, **106**, 2646.
18. F. Matzkies and U. Manthe, Accurate Quantum Calculations of Thermal Rate Constants Employing MCTDH: $H_2 + OH \rightarrow H + H_2O$ and $D_2 + OH \rightarrow D + DOH$, *J. Chem. Phys.*, 1998, **108**, 4828–4836.
19. J. M. Bowman, Reduced Dimensionality Theory of Quantum Reactive Scattering, *J. Phys. Chem.*, 1991, **95**, 4960–4968.
20. C. F. Curtiss, J. O. Hirschfelder and F. T. Adler, The Separation of the Rotational Coordinates From the N-Particle Schroedinger Equation, *J. Chem. Phys.*, 1950, **18**, 1638–1642.
21. F. Matzkies and U. Manthe, Combined Iterative Diagonalization and Statistical Sampling in Accurate Reaction Rate Calculations: Rotational Effects in $O + HCl \rightarrow OH + Cl$, *J. Chem. Phys.*, 2000, **112**, 130–136.
22. U. Manthe and R. Ellerbrock, S-matrix Decomposition, Natural Reaction Channels, and the Quantum Transition State Approach to Reactive Scattering, *J. Chem. Phys.*, 2016, **144**(20), 204119.
23. R. Ellerbrock and U. Manthe, Natural reaction channels in $H + CHD_3 \rightarrow H_2 + CD_3$, *Faraday Discuss.*, 2018, **212**, 217–235.
24. R. Welsch, F. Huarte-Larranaga and U. Manthe, State-to-State Reaction Probabilities within the Quantum Transition State Framework, *J. Chem. Phys.*, 2012, **136**(6), 064117.
25. R. Welsch and U. Manthe, Thermal Flux Based Analysis of State-to-State Reaction Probabilities, *Mol. Phys.*, 2012, **110**(9–10), 703–715.
26. U. Manthe and R. Welsch, Correlation Functions for Fully or Partially State-Resolved Reactive Scattering Calculations, *J. Chem. Phys.*, 2014, **140**(24), 244113.
27. R. Welsch and U. Manthe, Loss of Memory in $H + CH_4 \rightarrow H_2 + CH_3$ State-to-State Reactive Scattering, *J. Phys. Chem. Lett.*, 2015, **6**(3), 338–342.

28. F. Huarte-Larrañaga and U. Manthe, Calculating Initial-State-Selected Reaction Probabilities from Thermal Flux Eigenstates: A Transition-State-Based Approach, *J. Chem. Phys.*, 2005, **123**, 204114.
29. U. Manthe, Calculation of Initial State-Selected Reaction Probabilities by a Minimal Number of Wavepackets, *Chem. Phys. Lett.*, 1995, **241**, 497–501.
30. R. Welsch and U. Manthe, Communication: Ro-vibrational Control of Chemical Reactivity in $H + CH_4 \rightarrow H_2 + CH_3$: Full-Dimensional Quantum Dynamics Calculations and a Sudden Model, *J. Chem. Phys.*, 2014, **141**(5), 051102.
31. R. Welsch and U. Manthe, The Role of the Transition State in Polyatomic Reactions: Initial State-Selected Reaction Probabilities of the $H + CH_4 \rightarrow H_2 + CH_3$ Reaction, *J. Chem. Phys.*, 2014, **141**(17), 174313.
32. B. Jiang, J. Li and H. Guo, Potential Energy Surfaces from High Fidelity Fitting of Ab Initio Points: the Permutation Invariant Polynomial-Neural Network Approach, *Int. Rev. Phys. Chem.*, 2016, **35**(3), 479–506.
33. C. Qu, Q. Yu and J. M. Bowman, Permutationally invariant potential energy surfaces, *Annu. Rev. Phys. Chem.*, 2018, **69**, 151–175.
34. S. Manzhos, R. Dawes and T. Carrington, Neural network-based approaches for building high dimensional and quantum dynamics-friendly potential energy surfaces, *Int. J. Quantum Chem.*, 2015, **115**(16), 1012–1020.
35. U. Manthe, *Quantum Molecular Dynamics with Wave Packets, Quantum Simulations of Complex Many-Body Systems: From Theory to Algorithms*, Lecture Notes-Jülich: John von Neumann Institute for Computing, 2002, pp. 361–375.
36. D. H. Zhang and H. Guo, Recent advances in quantum dynamics of bimolecular reactions, *Annu. Rev. Phys. Chem.*, 2016, **67**, 135–158.
37. B. Jackson, Time-dependent wave packet approach to quantum reactive scattering, *Annu. Rev. Phys. Chem.*, 1995, **46**(1), 251–274.
38. D. O. Harris, G. G. Engerholm and W. D. Gwinn, Calculation of Matrix Elements for 1-Dimensional Quantum-Mechanical Problems and Application to Anharmonic Oscillators, *J. Chem. Phys.*, 1965, **43**, 1515.
39. A. S. Dickinson and P. R. Certain, Calculation of Matrix Elements for One-Dimensional Quantum-Mechanical Problems, *J. Chem. Phys.*, 1968, **49**, 4209.
40. J. C. Light, I. P. Hamilton and J. V. Lill, Generalized Discrete Variable Approximation in Quantum-Mechanics, *J. Chem. Phys.*, 1985, **82**, 1400–1409.
41. D. Kosloff and R. Kosloff, A Fourier Method Solution for the Time-Dependent Schrodinger-Equation as a Tool in Molecular-Dynamics, *J. Comput. Phys.*, 1983, **52**, 35–53.
42. M. D. Feit, J. A. Fleck and A. Steiger, Solution of the Schrodinger-Equation by a Spectral Method, *J. Comput. Phys.*, 1982, **47**, 412–433.
43. T. J. Park and J. C. Light, Unitary Quantum Time Evolution by Iterative Lanczos Reduction, *J. Chem. Phys.*, 1986, **85**, 5870–5876.

44. H. Tal-Ezer and R. Kosloff, An Accurate and Efficient Scheme for Propagating the Time-Dependent Schrodinger-Equation, *J. Chem. Phys.*, 1984, **81**, 3967–3971.
45. M. C. M. O'Brien and S. N. Evangelou, Calculation of Absorption-Band Shapes in Dynamic Jahn-Teller Systems by the Use of the Lanczos-Algorithm, *J. Phys. C: Solid State Phys.*, 1980, **13**, 611–623.
46. F. Gatti, B. Lasorne, H. D. Meyer and A. Nauts, *Applications of Quantum Dynamics in Chemistry*, Springer, **vol. 98**, 2017.
47. H. D. Meyer and G. A. Worth, Quantum Molecular Dynamics: Propagating Wavepackets and Density Operators Using the Multiconfiguration Time-Dependent Hartree Method, *Theor. Chem. Acc.*, 2003, **109**, 251–267.
48. H. Wang, Multilayer Multiconfiguration Time-Dependent Hartree Theory, *J. Phys. Chem. A*, 2015, **119**(29), 7951–7965.
49. U. Manthe, Wavepacket dynamics and the multi-configurational time-dependent Hartree approach, *J. Phys.: Condens. Matter*, 2017, **29**(25), 253001.
50. H. D. Meyer, U. Manthe and L. S. Cederbaum, The Multi-Configurational Time-Dependent Hartree Approach, *Chem. Phys. Lett.*, 1990, **165**, 73–78.
51. U. Manthe, H. D. Meyer and L. S. Cederbaum, Wave-Packet Dynamics within the Multiconfiguration Hartree Framework: General Aspects and Application to NOCl, *J. Chem. Phys.*, 1992, **97**, 3199–3213.
52. U. Manthe, The Multi-Configurational Time-Dependent Hartree Approach Revisited, *J. Chem. Phys.*, 2015, **142**(24), 244109.
53. M. H. Beck and H. D. Meyer, An Efficient and Robust Integration Scheme for the Equations of Motion of the Multiconfiguration Time-Dependent Hartree (MCTDH) Method, *Z. Phys. D: At., Mol. Clusters*, 1997, **42**, 113–129.
54. U. Manthe, On the Integration of the Multi-Configurational Time-Dependent Hartree (MCTDH) Equations of Motion, *Chem. Phys.*, 2006, **329**, 168–178.
55. W. H. Press, S. A. Teukolsky, W. T. Vetterling and B. P. Flannery, *Numerical Recipes*, Cambridge University Press, 1992.
56. A. Jäckle and H. D. Meyer, Product Representation of Potential Energy Surfaces, *J. Chem. Phys.*, 1996, **104**, 7974–7984.
57. D. Peláez and H. D. Meyer, The Multigrid POTFIT (MGPF) Method: Grid Representations of Potentials for Quantum Dynamics of Large Systems, *J. Chem. Phys.*, 2013, **138**(1), 014108.
58. F. Otto, Multi-Layer Potfit: An Accurate Potential Representation for Efficient High-Dimensional Quantum Dynamics, *J. Chem. Phys.*, 2014, **140**(1), 014106.
59. M. Schröder and H. D. Meyer, Transforming high-dimensional potential energy surfaces into sum-of-products form using Monte Carlo methods, *J. Chem. Phys.*, 2017, **147**(6), 064105.

60. U. Manthe, The State Averaged Multiconfigurational Time-Dependent Hartree Approach: Vibrational State and Reaction Rate Calculations, *J. Chem. Phys.*, 2008, **128**, 064108.
61. M. Ehara, H. D. Meyer and L. S. Cederbaum, Multiconfiguration Time-Dependent Hartree (MCTDH) Study on Rotational and Diffractive Inelastic Molecule-Surface Scattering, *J. Chem. Phys.*, 1996, **105**, 8865–8877.
62. A. Raab, G. A. Worth, H. D. Meyer and L. S. Cederbaum, Molecular Dynamics of Pyrazine after Excitation to the S(2) Electronic State Using a Realistic 24-Mode Model Hamiltonian, *J. Chem. Phys.*, 1999, **110**, 936–946.
63. M. H. Beck, A. Jäckle, G. A. Worth and H. D. Meyer, The Multiconfiguration Time-Dependent Hartree (MCTDH) Method: a Highly Efficient Algorithm for Propagating Wavepackets, *Phys. Rep.*, 2000, **324**, 1–105.
64. U. Manthe, A Multilayer Multiconfigurational Time-Dependent Hartree Approach for Quantum Dynamics on General Potential Energy Surfaces, *J. Chem. Phys.*, 2008, **128**, 164116.
65. H. Wang and M. Thoss, Multilayer Formulation of the Multiconfiguration Time-Dependent Hartree Theory, *J. Chem. Phys.*, 2003, **119**, 1289–1299.
66. U. Manthe, Layered Discrete Variable Representations and Their Application within the Multiconfigurational Time-Dependent Hartree Approach, *J. Chem. Phys.*, 2009, **130**, 054109.
67. O. Vendrell and H. D. Meyer, Multilayer Multiconfiguration Time-Dependent Hartree Method: Implementation and Applications to a Henon-Heiles Hamiltonian and to Pyrazine, *J. Chem. Phys.*, 2011, **134**, 044135.
68. E. Sim and N. Makri, Time-dependent discrete variable representations for quantum wave packet propagation, *J. Chem. Phys.*, 1995, **102**, 5616.
69. U. Manthe, A Time-Dependent Discrete Variable Representation for (Multiconfiguration) Hartree Methods, *J. Chem. Phys.*, 1996, **105**, 6989–6994.
70. R. van Harrevelt and U. Manthe, Degeneracy in Discrete Variable Representations: General Considerations and Application to the Multiconfigurational Time-Dependent Hartree Approach, *J. Chem. Phys.*, 2004, **121**, 5623–5628.
71. R. van Harrevelt and U. Manthe, Multidimensional Time-Dependent Discrete Variable Representations in Multiconfiguration Hartree Calculations, *J. Chem. Phys.*, 2005, **123**, 064106.
72. U. Manthe and F. Matzkies, Iterative Diagonalization within the Multi-Configurational Time-Dependent Hartree Approach: Calculation of Vibrationally Excited States and Reaction Rates, *Chem. Phys. Lett.*, 1996, **252**, 71–76.
73. T. Hammer and U. Manthe, Iterative Diagonalization in the State-Averaged Multi-Configurational Time-Dependent Hartree Approach:

Excited State Tunneling Splittings in Malonaldehyde, *J. Chem. Phys.*, 2012, **136**, 054105.

74. R. Wodraszka and U. Manthe, Iterative Diagonalization in the Multi-Configurational Time-Dependent Hartree Approach: Ro-Vibrational Eigenstates, *J. Phys. Chem. A*, 2013, **117**, 7246.
75. M. H. Beck and H. D. Meyer, Extracting accurate bound-state spectra from approximate wave packet propagation using the filter-diagonalization method, *J. Chem. Phys.*, 1998, **109**(10), 3730–3741.
76. H. D. Meyer, F. L. Quere, C. Leonard and F. Gatti, Calculation and Selective Population of Vibrational Levels with the Multiconfiguration Time-Dependent Hartree (MCTDH) Algorithm, *Chem. Phys.*, 2006, **329**, 179–192.
77. M. Nest and R. Kosloff, Quantum dynamical treatment of inelastic scattering of atoms at a surface at finite temperature: The random phase thermal wave function approach, *J. Chem. Phys.*, 2007, **127**(13), 134711.
78. U. Lorenz and P. Saalfrank, Comparing thermal wave function methods for multi-configuration time-dependent Hartree simulations, *J. Chem. Phys.*, 2014, **140**(4), 044106.
79. U. Manthe and F. Huarte-Larrañaga, Partition Functions for Reaction Rate Calculations: Statistical Sampling and MCTDH Propagation, *Chem. Phys. Lett.*, 2001, **349**, 321–328.
80. T. Westermann, R. Brodbeck, A. B. Rozhenko, W. W. Schoeller and U. Manthe, Photodissociation of Methyl Iodide Embedded in a Host-Guest Complex: A Full Dimensional (189D) Quantum Dynamics Study of CH_3I@resorc[4]arene, *J. Chem. Phys.*, 2011, **135**, 184102.
81. U. Manthe, W. Bian and W. Werner, Quantum-Mechanical Calculation of the Thermal Rate Constant for the $H_2 + Cl \rightarrow H + HCl$ Reaction, *Chem. Phys. Lett.*, 1999, **313**, 647–654.
82. U. Manthe, G. Cappecchi and H. J. Werner, The Effect of Spin-Orbit Coupling on the Thermal Rate Constant of the $H_2 + Cl \rightarrow H + HCl$ Reaction, *Phys. Chem. Chem. Phys.*, 2004, **6**, 5026–5030.
83. R. Welsch, Rigorous Close-Coupling Quantum Dynamics Calculation of Thermal Rate Constants for the Water Formation Reaction of $H_2 + OH$ on a High-Level PES, *J. Chem. Phys.*, 2018, **148**, 204304.
84. R. Welsch, Low Temperature Thermal Rate Constants for the Water Formation Reaction $H_2 + OH$ from Rigorous Quantum Dynamics Calculations, *Angew. Chem., Int. Ed.*, 2018, **130**, 13334.
85. R. Welsch, Kinetic Isotope Effects in the Water Forming Reaction $H_2/D_2 + OH$ from Rigorous Close-Coupling Quantum Dynamics Simulations, *Phys. Chem. Chem. Phys.*, 2019, **21**, 17054.
86. A. Ravishankara, J. Nicovich, R. Thompson and F. Tully, Kinetic Study of the Reaction of Hydroxyl with Hydrogen and Deuterium From 250 to 1050 K, *J. Phys. Chem.*, 1981, **85**(17), 2498–2503.

87. R. K. Talukdar, T. Gierczak, L. Goldfarb, Y. Rudich, B. M. Rao and A. Ravishankara, Kinetics of Hydroxyl Radical Reactions with Isotopically Labeled Hydrogen, *J. Phys. Chem.*, 1996, **100**(8), 3037–3043.
88. R. Oldenborg, G. Loge, D. Harradine and K. Winn, Kinetic Study of the Hydrogel + Hydrogen Reaction from 800 to 1550 K, *J. Phys. Chem.*, 1992, **96**(21), 8426–8430.
89. V. L. Orkin, S. N. Kozlov, G. A. Poskrebyshev and M. J. Kurylo, Rate Constant for the Reaction of OH with H_2 between 200 and 480 K, *J. Phys. Chem. A*, 2006, **110**(21), 6978–6985.
90. J. Meisner and J. Kästner, Reaction Rates and Kinetic Isotope Effects of H2 + OH → H2O + H, *J. Chem. Phys.*, 2016, **144**(17), 174303.
91. J. Castillo and Y. Suleimanov, A Ring Polymer Molecular Dynamics Study of the $OH + H_2$ (D_2) Reaction, *Phys. Chem. Chem. Phys.*, 2017, **19**(43), 29170–29176.
92. U. Manthe and F. Matzkies, Rotational Effects in the $H_2 + OH \rightarrow H + H_2O$ Reaction Rate: Full-Dimensional Close-Coupling Results, *J. Chem. Phys.*, 2000, **113**, 5725–5731.
93. G. C. Schatz and H. Elgersma, A Quasi-Classical Trajectory Study of Product Vbrational Distributions in the $OH + H_2 \rightarrow H_2O + H$ Reaction, *Chem. Phys. Lett.*, 1980, **21**, 73.
94. J. Chen, X. Xu, X. Xu and D. H. Zhang, A Global Potential Energy Surface for the $H_2 + OH \leftrightarrow H_2O + H$ Reaction Using Neural Networks, *J. Chem. Phys.*, 2013, **138**(15), 154301.
95. F. Huarte-Larrañaga and U. Manthe, Full Dimensional Quantum Calculations of the $CH_4 + H \rightarrow CH_3 + H_2$ Reaction Rate, *J. Chem. Phys.*, 2000, **113**, 5115–5118.
96. T. Wu, H. J. Werner and U. Manthe, First-Principles Theory for the $H + CH_4 \rightarrow H_2 + CH_3$ Reaction, *Science*, 2004, **306**, 2227–2229.
97. R. van Harrevelt, G. Nyman and U. Manthe, Accurate Quantum Calculations of the Reaction Rates for $H/D + CH_4$, *J. Chem. Phys.*, 2007, **126**, 084303.
98. G. Nyman, R. van Harrevelt and U. Manthe, Thermochemistry and Accurate Quantum Reaction Rate Calculations for $H_2/HD/D_2 + CH_3$, *J. Phys. Chem. A*, 2007, **111**, 10331–10334.
99. R. Welsch and U. Manthe, Reaction Dynamics with the Multi-Layer Multi-Configurational Time-Dependent Hartree Approach: $H + CH_4 \rightarrow H_2 + CH_3$ Rate Constants for Different Potentials, *J. Chem. Phys.*, 2012, **137**(24), 244106.
100. R. Welsch and U. Manthe, Fast Shepard Interpolation on Graphics Processing Units: Potential Energy Surfaces and Dynamics for $H + CH_4 \rightarrow H_2 + CH_3$, *J. Chem. Phys.*, 2013, **138**(16), 164118.
101. R. Welsch and U. Manthe, Full-Dimensional and Reduced-Dimensional Calculations of Initial State-Selected Reaction Probabilities Studying the $H + CH_4 \rightarrow H_2 + CH_3$ Reaction on a Neural Network PES, *J. Chem. Phys.*, 2015, **142**(6), 064309.

102. P. M. Marquaire, A. G. Dastidar, K. C. Manthorne and P. D. Pacey, Electron Spin Resonance Study of the Reaction of Hydrogen Atoms With Methane, *Can. J. Chem.*, 1994, **72**, 600.
103. M. R. Berlie and D. J. LeRoy, Kinetics of the Reaction $H + CH_4 = CH_3 + H_2$, *Can. J. Chem.*, 1954, **32**, 650.
104. R. A. Back and D. V. D. Auwera, The Mercury-Photosensitized Decomposition of Methane, *Can. J. Chem.*, 1962, **40**, 2339.
105. M. J. Kurlyo, G. A. Hollinden and R. B. Timmons, WSR Study of the Kinetic Isotope Effect in the Reaction of H and D Atoms With CH_4, *J. Chem. Phys.*, 1970, **52**, 1773.
106. H. Arai, S. Nagai, K. Matsuda and M. Hatada, Effect of Irradiation Temperature on the Radiolysis of Methane, *Radiat. Phys. Chem.*, 1981, **17**, 151.

CHAPTER 11

Eigenstate Approaches for High Resolution Spectroscopy of Tunnelling in Small Molecular Systems

P. BRYAN CHANGALA*[a] AND JOSHUA H. BARABAN*[b]

[a] JILA, Department of Physics, University of Colorado, Boulder, CO 80309, United States; [b] Department of Chemistry, Ben-Gurion University of the Negev, Beer-Sheva 8410501, Israel
*Emails: bryan.changala@colorado.edu; jbaraban@bgu.ac.il

11.1 Introduction

Although the term ‘‘tunnelling’’ can imply a dynamic, time-dependent process, the phenomenon is equally well described in an eigenstate picture. Here two zeroth-order wavefunctions on either side of a barrier overlap *via* the classically forbidden region, leading to an interaction represented by a ‘‘tunnelling’’ matrix element between two zeroth-order basis states. The resulting energy level shifts and mixing have observable spectroscopic consequences in the frequency domain, alongside the more frequently considered dynamical effects. Oftentimes these observables can lead more directly to information about the molecular Hamiltonian, making this approach highly complementary to time-domain approaches that monitor the tunnelling rate explicitly.

Here we outline the time-independent perspective on tunnelling by illustration with two model limiting cases. The remainder of the chapter

Theoretical and Computational Chemistry Series No. 18
Tunnelling in Molecules: Nuclear Quantum Effects from Bio to Physical Chemistry
Edited by Johannes Kästner and Sebastian Kozuch

Published by the Royal Society of Chemistry, www.rsc.org

describes our preferred *ab initio* eigenstate methods for treating tunnelling in molecular systems, along with examples from the literature.

11.1.1 Symmetric Double Minimum

A special tunnelling case occurs in symmetric systems, where identical and therefore exactly degenerate copies of a molecule exist and interact (see also Chapter 9). Ammonia (NH_3) is perhaps the most famous example in this category, where in its trigonal pyramidal structure the nitrogen atom can be located either above or below the plane defined by the three hydrogen atoms. These two identical instances $|1\rangle$ and $|2\rangle$ of the NH_3 molecule are then coupled along the symmetric umbrella deformation, ν_2, into the symmetric and anti-symmetric eigenstates $|+\rangle$ and $|-\rangle$, respectively: $|+/-\rangle = \frac{|1\rangle}{\sqrt{2}} \pm \frac{|2\rangle}{\sqrt{2}}$. The energy difference $E_+ - E_-$ or tunnelling splitting is equivalent to the $|1\rangle$ to $|2\rangle$ inversion frequency (when divided by Planck's constant, h). For example, in the ground rovibrational state of ammonia, this inversion splitting is 24 GHz.[1] The symmetric double minimum case is important not only because it tends to exhibit large tunnelling splittings, due to the quasi-first-order[†] effect of the tunnelling matrix element on the degenerate basis states, but also because the Hamiltonian and eigenspectrum are relatively simple, compared to the more general case.

11.1.2 General Asymmetric Case

Generally, two minima of a potential energy surface need not be related by symmetry, but the zeroth-order eigenstates of the isolated potential wells can still interact by tunnelling mechanisms. The resulting energy level patterns are then significantly more complex; each zeroth-order state is no longer guaranteed one dominant partner with which it interacts straightforwardly *via* quasi-first-order perturbation theory, for example. Understanding the final eigenspectrum in terms of tunnelling requires evaluating interaction matrix elements between the two sets of zeroth-order states and using second-order perturbation theory to obtain shifts from the zeroth-order energies.

Tunnelling problems in real molecules can comprise *both* asymmetric and symmetric tunnelling mechanisms simultaneously. This occurs when the permutation of identical but not necessarily symmetry-equivalent nuclei is mediated by the presence of an intermediate, distinct isomer. In such a situation the eigenspectrum will exhibit both types of effects: (1) the quasi-first-order tunnelling splittings typical of the symmetric case, superimposed upon (2) the asymmetric case perturbations between the two isomers. An example of such a case, S_1 acetylene, is given in Section 11.3.4 below.

[†] By "quasi-first-order", we mean that the effect of the off-diagonal matrix element eventually manifests as a first-order perturbation theory correction to the energies, despite initially appearing to be a second-order effect. This is due to the necessary diagonalization of the degenerate subspace, which shifts the matrix element onto the diagonal.

Due to the rich complexity of these systems, highly accurate computational methods that can guide spectroscopic studies towards an eventually experimentally based effective Hamiltonian are extremely useful.

11.2 Computational Methods

Ab initio frequency-domain approaches are often based on the time-independent Schrödinger equation (SE) for the total molecular Hamiltonian. Under the Born–Oppenheimer approximation,[2] which is accurate for all cases considered here, one need only solve an effective nuclear motion SE,

$$H_\mathrm{n}|\psi_n\rangle = [T_\mathrm{n} + V]|\psi_n\rangle = E|\psi_n\rangle, \tag{11.1}$$

which describes rovibrational motion on an adiabatic potential energy surface (PES) V, a function of the $3N-6$ internal coordinates. In polyatomic molecules, this is a high-dimensional, many-body problem. Its solution is especially complex for non-rigid, multiwell systems that exhibit extreme anharmonicity and large-amplitude nuclear motion. Such difficulties are inevitable for molecules in which tunnelling dynamics are important. Automated ‘‘black box’’ tools, such as those based on standard vibrational perturbation theory,[3,4] are simply inadequate for these types of systems. The development of accurate and efficient alternative methods to tackle them remains a challenge.

This section provides an overview of the computational methods we use to understand, predict, and interpret the rovibronic spectroscopic signatures of tunnelling in small- to medium-sized molecules. These tools span both variational and perturbative approaches. The former involves iterative eigensolvers combined with sparse direct-product grid representations of the nuclear motion Hamiltonian, which is a relatively well-established technique for high accuracy spectroscopic calculations.[5–7] For systems that are too large to treat with this approach, we have developed a version of rovibrational perturbation theory based on curvilinear vibrational mean-field theory.[8] Both of these approaches require two key pieces: a numerically exact kinetic energy operator (KEO) for general curvilinear coordinates and a reliable PES fitted to high-accuracy electronic energies.

11.2.1 Direct-product Discrete Variable Representation Grids and Iterative Eigensolvers

The most general way to compute the spectrum of a rovibrational Hamiltonian is *via* variational methods.[6,9] In this approach, wavefunctions are represented as linear combinations of a set of basis functions. The matrix representation of the Hamiltonian operator in this basis set is diagonalized to compute its eigenvalues (energies) and eigenvectors (wavefunctions). By systematically increasing the size of the basis set, numerically exact energies and wavefunctions can be converged. The calculation is limited only by the size of the Hamiltonian matrix one can build and diagonalize; as such, appropriate choices for coordinates and efficient basis sets are crucial.

The most straightforward basis set for multi-dimensional wavefunctions is a direct product of one-dimensional basis functions for each vibrational degree of freedom.[5,6] These take the general form

$$\Phi_{i_1 i_2 \cdots i_n}(\vec{q}) = \phi^{(1)}_{i_1}(q_1)\phi^{(2)}_{i_2}(q_2)\cdots\phi^{(n)}_{i_n}(q_n), \tag{11.2}$$

where each vibrational coordinate q_k, $k = 1\ldots n$, has its own independent set of 1D basis functions $\phi^{(k)}_{i_k}(q_k)$. The desired many-body wavefunctions are represented as an n-index sum over the direct product basis,

$$\Psi(\vec{q}) = \sum_{i_1}\sum_{i_2}\cdots\sum_{i_n} c_{i_1 i_2 \cdots i_n}\phi_{i_1 i_2 \cdots i_n}(\vec{q}), \tag{11.3}$$

where the coefficients $c_{i_1 i_2 \cdots i_n}$ are equal to the components of the eigenvectors of the Hamiltonian matrix. As the number of basis functions $\phi^{(k)}_{i_k}$ for each coordinate approaches completeness in 1D, so does the many-dimensional direct-product basis.

The challenge with this simple approach is that the number of direct-product basis functions grows exponentially with the number of coordinates. For example, each 1D basis set typically needs a minimum of 10 functions for accurate results, yielding a total of 10^n direct-product basis functions. A five-atom molecule, such as CH_4, has $n = 3N - 6 = 9$ internal coordinates, so its minimum basis set contains 10^9 functions. Most importantly, the Hamiltonian operator in this basis is a $10^9 \times 10^9$ matrix, which would require about 10^{10} gigabytes of memory to store on a computer. Even if this were possible, direct diagonalization methods of $m \times m$ matrices scale as $\mathcal{O}(m^3)$ and are impractical for such large matrices. Furthermore, only the lowest energy eigenvalues are typically desired, which represent a very small fraction of the complete eigenvalue spectrum of the Hamiltonian matrix. Calculating the entire set of eigenvalues is therefore a vast waste of resources.

The problem of calculating and storing the Hamiltonian matrix is avoided by using iterative diagonalization methods,[10–12] in particular the Lanczos algorithm,[13] which is applicable to Hermitian matrices. Iterative methods focus the computational effort on calculating the lowest energy eigenvalues and not the entire unnecessary spectrum. They also require only that one calculate the Hamiltonian matrix-vector product, $w = Hv$, where v is an arbitrary vector of basis function coefficients. The key point is that matrix-vector products (MVPs) can be calculated without the explicit construction of the matrix H itself. This drastically reduces the memory requirements, making the direct-product basis approach viable. We forgo a detailed discussion of iterative diagonalization algorithms here.[6,14] We most often employ the so-called thick-restart Lanczos method, details of which can be found in ref. 15.

In general, the efficiency of iterative techniques is determined by the cost of MVPs with the Hamiltonian. Discrete variable representation (DVR) basis sets[16–19] are an essential tool for reducing the computational expense of this step. DVRs are coordinate-representation basis functions that are highly localized about discrete values (*i.e.* grid points) of the coordinate variable.[18] A fundamental property of DVRs is that matrix representations of scalar functions are approximately diagonal,

$$\int \mathrm{d}q\ \phi_i{}^*(q) f(q) \phi_j(q) \approx \delta_{ij} f(q_i), \tag{11.4}$$

where ϕ_i (ϕ_j) is the DVR basis function centered on grid point q_i (q_j). This diagonal approximation is related to Gaussian quadrature of integrals, and the associated error rapidly decreases as the number of DVR basis functions (*i.e.* the number of grid points) increases.[18]

Using DVR basis sets with iterative diagonalization is advantageous for two reasons. First, the diagonal property results in a highly sparse Hamiltonian matrix with a small fraction of non-zero matrix elements. (Coordinate derivative operators result in off-diagonal matrix elements, but these derivatives appear in the KEO as products of at most two distinct coordinates. Therefore, off-diagonal matrix elements only occur between DVR basis functions that differ by two or fewer grid index values.) Second, these matrix elements can be calculated without performing expensive integrals. The only information needed is the values of the PES and KEO coefficients at the DVR grid points. These properties make MVPs and iterative diagonalization simple and efficient. Additional techniques such as spectral transformations[12,20,21] and symmetry-adapted Lanczos[22] can further improve the computational efficiency.

The above discussion focuses on the pure vibrational problem ($J = 0$). Rotations are easily included by attaching a set of rotational basis functions to each DVR grid point. That is, the rovibrational basis is a direct product between the vibrational DVR functions and a single set of rotational basis functions. (We usually employ symmetric top functions quantized along one of the molecule-fixed axes.) Apart from modifying the Hamiltonian MVP routine to account for rotational and rovibrational terms in the KEO, the iterative diagonalization algorithm is essentially unchanged. Both the size of the combined rovibrational direct-product basis and the cost of MVPs scale linearly as $2J + 1$.

11.2.2 Rovibrational Perturbation Theory Based on Curvilinear Vibrational Mean-field Theory

Although iterative techniques and DVRs make direct-product-basis variational calculations orders of magnitude more efficient than direct matrix construction and diagonalization, their cost still scales exponentially with the number of coordinates, limiting them to small molecules of up to four or five atoms. (We note that recent advances[14,23,24] have substantially pushed this dimensionality limit for some cases. Other approaches such as contracted basis techniques[25–27] are also important for addressing this issue.) For medium-sized molecules, it is advantageous to use approximate methods that are even more efficient while retaining enough accuracy to be useful for spectroscopy.

One of the most popular approximate methods is second-order vibrational perturbation theory (VPT2).[3,4,28] The zeroth-order description in VPT2 is a set of uncoupled harmonic oscillator vibrations and rigid-top rotations. Perturbative corrections from anharmonicity and rotation–vibration coupling are used to generate anharmonic vibrational frequencies and effective rotational parameters. Although VPT2 is based on the formally exact Watson Hamiltonian,[29] it relies on rectilinear normal coordinates and single-reference Eckart embedding.[30] This renders it best suited for molecules that undergo small harmonic displacements from a single, well-defined equilibrium configuration. VPT2 thus fails for floppy or highly anharmonic molecules and is fundamentally incapable of treating tunnelling between multiple PES wells.[4,8]

For a perturbative treatment to be successful, it is crucial to construct a zeroth-order picture that accurately reflects the large-amplitude, highly anharmonic vibrational motion associated with tunnelling. We base our approach on vibrational self-consistent field theory (VSCF)[31–34] and second-order vibrational Møller–Plesset perturbation theory (VMP2).[35,36] VMP2 corrects a zeroth-order VSCF mean-field wavefunction for vibrational correlation effects using Rayleigh–Schrödinger perturbation theory, in analogy to electronic structure MP2.[37] While VSCF-based methods were originally developed for the rectilinear Watson Hamiltonian, they have since been applied to a variety of curvilinear coordinate systems.[38–44] We have extended the curvilinear VSCF/VMP2 approach by accounting for the rotational and rotation–vibration coupling terms of the nuclear motion Hamiltonian.[8] Rotational and rovibrational effective Hamiltonians are then calculated by applying a second-order contact, or Van Vleck, transformation[45] to the zeroth-order VSCF Hamiltonian.

The zeroth-order VSCF wavefunction ansatz is a Hartree product for the n vibrational coordinates,

$$\Psi_0(\vec{q}) = \psi_1(q_1)\psi_2(q_2)\cdots\psi_n(q_n), \tag{11.5}$$

or in ket notation,

$$|\Psi_0\rangle = |1\rangle|2\rangle\cdots|n\rangle = \prod_k |k\rangle. \tag{11.6}$$

Variational optimization of $|\Psi_0\rangle$ leads to a 1D Schrödinger equation for each degree of freedom,

$$\hat{h}_k|k\rangle = \varepsilon_k|k\rangle, \tag{11.7}$$

where

$$\hat{h}_k = \left(\prod_{l\neq k}\langle l|\right) H_\mathrm{v} \left(\prod_{l\neq k}|l\rangle\right) \tag{11.8}$$

is the one-body Hamiltonian for vibrational coordinate k, computed by averaging the full vibrational Hamiltonian H_v over the other degrees of freedom $l \neq k$. As in other mean-field theories, this set of equations is solved iteratively until self-consistency is reached. We use underlying DVR basis sets for each of these 1D problems.

Second-order vibrational Møller–Plesset perturbation theory (VMP2) is used to correct the VSCF wavefunction $|\Psi_0\rangle$. The VMP2 energy is computed using standard Rayleigh–Schrödinger perturbative corrections,

$$E_0^{\text{VMP2}} = E_0^{(0)} + E_0^{(2)}, \tag{11.9}$$

$$E_0^{(0)} = \langle \Psi_0 | H_\text{v} | \Psi_0 \rangle, \tag{11.10}$$

$$E_0^{(2)} = \sum_{|\nu\rangle \neq |\Psi_0\rangle} \frac{|\langle \Psi_0 | H_\text{v} | \nu \rangle|^2}{E_0^{(0)} - E_\nu^{(0)}}, \tag{11.11}$$

where the second-order sum is over virtual excitation wavefunctions $|\nu\rangle$ formed from higher-energy eigenfunctions of the one-body problems, eqn (11.7). (These form a direct-product basis set that completely spans the one-body functional space.) The zeroth-order wavefunction $|\Psi_0\rangle$ is not necessarily the ground state. Excited vibrational states can be targeted equally well.

This approach provides approximate wavefunctions and energies for the pure vibrational Hamiltonian $H_\text{v} = T_\text{v} + V$, where T_v is the vibrational KEO. To calculate rovibrational states with $J > 0$, one must consider the full nuclear motion Hamiltonian $H_\text{n} = H_\text{v} + T_\text{r} + T_\text{rv}$, which contains additional KEO terms for rotational motion (T_r) and rotation–vibration coupling (T_rv). These terms are typically several orders of magnitude smaller than the vibrational part of the Hamiltonian and therefore may be folded into the perturbative treatment. This procedure is formally carried out with a contact or Van Vleck transformation,[45] with the final product being a rotational or rovibrational effective Hamiltonian for the vibrational state of interest.[46–48] The detailed working equations for this process in the VMP2 framework can be found in ref. 8.

The basic contact transformation procedure works well when individual vibrational states are well-separated in energy and only interact weakly with each other. Large-amplitude tunnelling motion, however, results in closely spaced vibrational states separated by energy differences often of the same magnitude as rotational excitations. This can lead to non-perturbative, resonant rotation–vibration tunnelling interactions. In this case, the resonantly interacting states can be grouped together into a multistate block. The contact transformation eliminates coupling between this enlarged block and the rest of the rovibrational manifold, resulting in a multistate effective Hamiltonian. This effective Hamiltonian accurately treats the non-perturbative interactions among the resonant vibrational states. We will see an example of multistate effective Hamiltonians in the section below about tunnelling *gauche*-butadiene.

11.2.3 Kinetic Energy Operators

Relative to rectilinear coordinates, which form the basis of the Eckart–Watson Hamiltonian,[29] curvilinear coordinates provide an improved treatment of molecular vibrations and large-amplitude tunnelling motion. These benefits come at the cost of a significantly more complex analytical form of the nuclear motion KEO.[49–52] However, the use of DVR basis functions, which require only numerical evaluation of the KEO instead of closed-formed analytical expressions, obviates these drawbacks.[53–59]

We follow the usual Podolsky approach to derive a general curvilinear KEO.[56,57,60] The curvilinear coordinate system for an N-atom molecule is defined by specifying the Cartesian positions $\vec{x}_i$ of each nucleus $i=1\ldots N$ in a body-fixed, center-of-mass frame as a function of n internal vibrational coordinates q_k, $k=1\ldots n$. For full-dimensional problems, $n=3N-6$, although one can also consider reduced-dimension models that use only a subset $n<3N-6$ of the available degrees of freedom. The n internal coordinates are collectively denoted as $\vec{q}$. The body-frame Cartesian position functions $\vec{x}_i(\vec{q})$ generate an associated metric tensor $\mathbf{g}$, an $(n+3)\times(n+3)$ symmetric matrix with elements given by

$$g_{kl}=\sum_i^N m_i \partial_k \vec{x}_i \cdot \partial_l \vec{x}_i, \tag{11.12}$$

$$g_{\alpha l}=\sum_i^N m_i (\hat{e}_\alpha \times \vec{x}_i) \cdot \partial_l \vec{x}_i, \tag{11.13}$$

$$g_{\alpha\beta}=\sum_i^N m_i (\hat{e}_\alpha \times \vec{x}_i) \cdot (\hat{e}_\beta \times \vec{x}_i). \tag{11.14}$$

k, l, *etc.* are vibrational indices taking values $1\ldots n$, and α, β, γ are rotational indices, taking values x, y, and z (*i.e.* the three body-fixed axes). $\hat{e}_\alpha$ is a unit vector parallel to the body-fixed α axis, and m_i is the mass of the ith atom.[‡] The metric determinant is $g=\det(\mathbf{g})$ and the metric inverse is $\mathbf{G}=\mathbf{g}^{-1}$.

Using these quantities, the rovibrational KEO can then be written as

$$T=T_\mathrm{v}+T_\mathrm{r}+T_\mathrm{rv}, \tag{11.15}$$

which includes a vibrational term,

$$T_\mathrm{v}=\frac{\hbar^2}{2}\sum_{kl} g^{-1/4}\partial_k^\dagger G_{kl} g^{1/2} \partial_l g^{-1/4}, \tag{11.16}$$

a rotational term,

$$T_\mathrm{r}=\frac{-\hbar^2}{4}\sum_{\alpha\beta} G_{\alpha\beta}\left[\frac{iJ_\alpha}{\hbar},\frac{iJ_\beta}{\hbar}\right]_+, \tag{11.17}$$

and a rotation–vibration coupling term,

$$T_\mathrm{rv}=\frac{-\hbar^2}{2}\sum_{k\gamma}(-\partial_k^\dagger G_{k\gamma}+G_{k\gamma}\partial_k)\frac{iJ_\gamma}{\hbar}, \tag{11.18}$$

where the operator J_α is the body-frame projection of the total angular momentum $\mathbf{J}$ along the α-axis. (The Hermitian conjugate derivatives $\partial_k^\dagger$ act to the

---

[‡] We use atomic (rather than nuclear) masses in all calculations, as is the standard approach under the Born–Oppenheimer approximation. We note, however, that the issue of atomic *vs.* nuclear masses can be subtle,[61,62] especially for ionic systems.[63]

left.) Matrix elements of this KEO are calculated using the volume element $dq_1 dq_2 \cdots dq_n$,[60] *i.e.* the normalization convention is

$$\int \cdots \int dq_1 \cdots dq_n \psi^*(\vec{q})\psi(\vec{q}) = 1. \tag{11.19}$$

The above form of the KEO is convenient for the iterative direct-product DVR grid approach. Matrix elements of complicated expressions such as $g^{-1/4}\partial_k^\dagger G_{kl} g^{1/2} \partial_l g^{-1/4}$ are simple to evaluate by repeated insertion of the truncated identity operator and use of the diagonal-DVR approximation.[56]

For the VSCF-based methods, it turns out to be useful to push the derivative operators appearing in T_v to the edges of each term (*i.e.* ∂_k all the way to right and $\partial_k^\dagger$ to the left). Doing so rearranges T_v into an equivalent form,[43,44]

$$T_\mathrm{v} = \frac{\hbar^2}{2}\sum_{kl} \partial_k^\dagger G_{kl} \partial_l + \frac{\hbar^2}{2}\sum_{l}(U_l \partial_l + \partial_l^\dagger U_l) + V_T, \tag{11.20}$$

where the single-derivative coefficients are

$$U_l = -\frac{1}{4}\sum_{k}\left(\frac{\partial_k g}{g}\right) G_{kl}, \tag{11.21}$$

and the kinetic pseudo-potential is

$$V_T = \frac{\hbar^2}{32}\sum_{kl}\left(\frac{\partial_k g}{g}\right)\left(\frac{\partial_l g}{g}\right) G_{kl}. \tag{11.22}$$

The determinant derivative is conveniently evaluated using the relation $(\partial_k g)/g = \mathrm{tr}(\mathbf{G}\partial_k \mathbf{g})$.

Matrix element integrals of the various terms in the KEO, such as G_{kl}, U_l, and V_T, as well as the PES, must be computed between Hartree product basis states. These terms in general depend on all n internal coordinates, leading to very high-dimensional integrals. For example, molecules as large as butadiene, considered below, would require 24-dimensional sums, which are impractical to compute. A common method to address this problem is to expand the various high-dimensional functions in a many-body (or "n-mode") expansion.[34,43] For some scalar function $F(q_1, q_2, \ldots, q_n)$, this expansion is

$$F(q_1, \ldots, q_n) = f_0 + \sum_k f_k(q_k) + \sum_{k<l} f_{kl}(q_k, q_l) + \sum_{k<l<m} f_{klm}(q_k, q_l, q_m) + \cdots, \tag{11.23}$$

where

$$\begin{aligned} f_0 &= F(q_1^\mathrm{ref}, \ldots, q_n^\mathrm{ref}), \\ f_k &= F(q_1^\mathrm{ref}, \ldots, q_k, \ldots, q_n^\mathrm{ref}) - f_0, \\ f_{kl} &= F(q_1^\mathrm{ref}, \ldots, q_k, q_l, \ldots, q_n^\mathrm{ref}) - f_k - f_l - f_0, \\ f_{klm} &= F(q_1^\mathrm{ref}, \ldots, q_k, q_l, q_m. \ldots, q_n^\mathrm{ref}), \\ &\quad - f_{kl} - f_{km} - f_{lm} - f_k - f_l - f_m - f_0, \end{aligned} \tag{11.24}$$

and so on. $(q_1^{\text{ref}},\ldots,q_n^{\text{ref}})$ is a reference geometry about which the expansion is computed. In tunnelling molecules, a single reference geometry may not be appropriate. In this case, large-amplitude coordinates may be ‘‘dereferenced’’ such that the many-body expansion is carried at every DVR grid-point of the dereferenced coordinates. Many-body expansions break up a complicated high-dimensional function into smaller parts of lower dimensionality. By taking the expansion to include all terms up to n-body contributions, the exact original function F is recovered, but nothing is gained. It is often accurate, however, to truncate the expansion at three- or four-body terms, which drastically reduces the dimensionality of the matrix element integrals of F. The small errors introduced by the many-body expansion can be systematically controlled by checking that computed energies are converged with respect to the maximum number of n-body terms.

11.2.4 Coordinate Systems and Body-fixed Frame Embedding

The procedures above allow us to construct the numerically exact KEO for an arbitrary set of internal coordinates $\vec{q}$ and body-fixed frame embedding (implicitly defined by the Cartesian position functions $\vec{x}_i(\vec{q})$). The question remains, how do we choose these coordinates optimally for tunnelling systems?

For iterative direct-product DVR grid calculations, we often use primitive valence coordinates such as internuclear distances, bond angles, and dihedral angles.[51] Simple orthogonal coordinate systems like Jacobi and Radau coordinates are also convenient.[64,65] For reduced-dimension calculations, it is of course necessary to choose coordinates that accurately describe the dynamics of the sub-system of interest. The computational efficiency and accuracy of full-dimensional direct-product grid calculations, however, are not strongly dependent on the choice of coordinates as long as they compactly span the energetically relevant regions of configuration space.

On the other hand, the choice of coordinates is critically important for VSCF-based calculations. In general, one wants to find a coordinate system that minimizes coupling and leads to an approximately separable vibrational Hamiltonian, $H_\text{v}(\vec{q}) \approx h_1(q_1) + h_2(q_2) + \cdots$. This ensures that the VSCF Hartree product is an accurate zeroth-order wavefunction and that the various many-body expansions will be accurate for low expansion orders. For non-tunnelling molecules with a single equilibrium configuration, the ground and lowest excited vibrational states are usually best described with the normal coordinates associated with the PES minimum. These are found by a (curvilinear) harmonic analysis using the classic GF method based on the kinetic energy coupling (G) and force (F) matrices.[66] For tunnelling systems with more than one dynamically accessible minimum, however, we turn to a reaction path (RP) coordinate system.[39,67–71] A RP coordinate system is based on the steepest descent trajectory that connects neighboring minima through intermediate saddle points on the PES. At each point along the steepest descent RP, a modified GF calculation is performed to determine the ‘‘instantaneous’’ normal modes orthogonal to the RP at that position. In this way, the RP coordinate system smoothly interpolates between the different normal mode coordinates associated with each local minimum. It provides an approximately globally separable coordinate system, which is crucial to making VSCF/VMP2 efficient and accurate.

In addition to choosing a coordinate system that minimizes the coupling between different vibrations, VSCF/VMP2 requires that the body-fixed frame embedding results in small rotation–vibration coupling terms T_{rv}. This embedding is defined by how the molecular body-fixed frame is rotated in space for a given value of the internal coordinates $\vec{q}$. For single-well cases, the best choice of embedding is usually the Eckart frame,[30] which eliminates rotation–vibration coupling at the reference equilibrium geometry. Implementing Eckart frame embedding for arbitrary curvilinear Hamiltonians is, in general, a complicated, non-trivial problem.[58,59,72–75] The approach we take is based on the elegant quaternion algebra method recently introduced by Krasnoshchekov *et al.*[76] Briefly stated, for a given Cartesian geometry in a non-Eckart frame $\vec{x}_i$, the corresponding Eckart frame geometry can be found with a rotation,

$$\vec{x}_i^{\,\mathrm{Eckart}} = U(\vec{q})\vec{x}_i, \tag{11.25}$$

where the rotation matrix $U(\vec{q})$ explicitly depends on the curvilinear internal coordinates. This approach permits the usual single-reference Eckart frame embedding, as well as quasi-Eckart embedding based on a moving reference geometry that tracks large-amplitude tunnelling motions.[73] In each of these cases, we automatically evaluate the (first and second) derivatives of $U(\vec{q})$ necessary to construct the numerically exact KEO. Further algorithmic details can be found in ref. 8.

11.2.5 Potential Energy Surfaces

Last, but not least, an accurate potential energy surface based on high-level quantum chemical methods is the foundation for any nuclear motion calculation. We generally rely on single-reference coupled-cluster (CC) theory – in particular its CCSD(T) variant[77] – in combination with the Dunning correlation-consistent basis sets[78] or the atomic natural orbital (ANO) basis sets of Almlöf and Taylor.[79] All electronic structure calculations for our in-house PESs are performed with the CFOUR package.[80]

One advantage of DVR basis sets is that the PES only needs to be numerically evaluated on grid points. The coordinates used to describe the PES are therefore entirely independent of the ‘‘dynamical’’ coordinates used in the nuclear motion calculation itself, providing substantial flexibility in the underlying analytical representation of the PES. A high-dimensional polynomial in some set of internal coordinates is typically fit *via* linear-least-squares to a set of electronic energies. The method of permutationally invariant polynomials (PIPs) is particularly useful for generating surfaces that rigorously enforce nuclear permutation symmetry.[81] We make extensive use of this approach and have developed a suite of tools for constructing, fitting, and coding PIP surfaces combined with automated differentiation.[82,83]

11.3 Examples

The utility of the methods just described is perhaps best appreciated through a few molecular examples from our recent work with several collaborators. These examples span a variety of spectroscopic methods, including pure rotational spectroscopy in the microwave region, rotation–vibration infrared spectroscopy, photoelectron spectroscopy, and electronic spectroscopy *via* laser-induced fluorescence and resonance-enhanced multiphoton ionization.

11.3.1 H_2O_2

Hydrogen peroxide is a famous case of torsional tunnelling, as well as the simplest molecule to exhibit torsional isomerization. As such, there is a significant amount of literature on the subject (most notably by Koput[84–87]), but we would like to draw the reader's attention to ref. 88, where we compared the performance of numerically exact and approximate rovibrational methods in the course of determining a complete semi-experimental equilibrium structure for the first time. Table 11.1 provides a representative comparison for the pure torsional vibrational levels. The results obtained by VMP2 are in excellent agreement with and significantly less expensive than variational methods (the errors introduced by the vibrational approximations are less significant than those inherent in the Born–Oppenheimer PES), which serves as an encouraging benchmark for applying these techniques to tunnelling systems.

H_2O_2 is a good example of the impact that large-amplitude motion has on the structure determination of tunnelling molecules. The "r_0" structure based on directly measured ground state rotational constants has a dihedral angle of 119(1)°. The ground state, however, exhibits significant tunnelling delocalization, and after taking into account the calculated zero-point rotation-vibration effects, the semi-experimental equilibrium structure is corrected to 113.6(3)°.[88] We also note that the zero-point corrections based on standard VPT2 differ by 10–20% relative to variational calculations, demonstrating the importance of such numerically exact rovibrational calculations for tunnelling molecules.

Table 11.1 Pure torsion vibrational levels of H_2O_2, using the (n, τ) labeling convention. Experimentally measured values are compared with numerically exact variational and perturbative VMP2 calculations based on a curvilinear reaction path.

(n, τ)	Experiment[a]	Variational[b]	VMP2[b]
(0, 1)	0	0	0
(0, 4)	11.44	11.01	11.01
(1, 1)	254.55	256.40	256.41
(1, 4)	370.89	371.24	371.26
(2, 1)	569.74	570.32	570.32
(2, 4)	776.12	776.41	776.43

[a] Ref. 89
[b] Ref. 88

11.3.2 CH_3^-

Tunnelling in the methide anion poses a particularly tricky problem because the tunnelling dynamics between the identical trigonal pyramidal structures are inextricably linked to the issue of electron autodetachment at the planar transition state, which resembles the methyl radical. In support of a high-resolution photoelectron spectroscopic study that clearly resolved the umbrella mode tunnelling splittings,[90] we performed reduced dimension direct-product grid DVR calculations, where the computational constraints arose just as much from the need for expensive electronic structure calculations with diffuse basis functions as from the dimensionality. The results matched the experimental tunnelling splittings of CH_3^- and CD_3^- [21(5) and 6(4) cm^{-1}, respectively[90]] to within the measurement uncertainty, despite the challenges that permitted only a limited treatment.

A fundamental issue worth discussing here is the potentially ambiguous meaning of tunnelling barrier values reported in the literature. In other words, effective or reduced dimension tunnelling barriers cannot be compared freely. To illustrate with some specific numbers, the full-dimensional CH_3^- tunnelling barrier height of 386 cm^{-1} is reduced by 10% when dressed for the 4D calculations performed in ref. 90. Even more confusing is that this same value increases to 661 cm^{-1} as a 1D effective barrier, whereas prior theoretical work (that also obtained reasonable agreement with experiment) reported a 1D effective barrier height of 833 cm^{-1}.[91] The explanation for these apparently contradictory results is that tunnelling splittings are sensitively dependent on details of multidimensional potential surfaces that are by definition highly anharmonic. A conceptual reduction to effective barrier heights is a simplification that may be useful, but can definitely be misleading.

11.3.3 *gauche*-Butadiene

The *gauche* conformer of 1,4-butadiene presents a surprising example of tunnelling.[92] Despite needing to twist its heavy atom backbone to move two CH_2 groups past one another in order to interconvert between two enantiomeric forms, the observed tunnelling splitting is comparable in magnitude to light atom tunnelling cases, and the tunnelling remains relatively rapid (~60 ps) even when the molecule is fully deuterated. Similar tunnelling behavior has also been observed recently in the analogous conformer of isoprene,[93] and it appears that this phenomenon may be germane to *cis*-conjugated systems more generally.[94]

From a spectroscopic standpoint, it is interesting that the tunnelling splittings in butadiene were determined not by direct measurement, but rather by effective Hamiltonian fitting of a tunnelling perturbation.[92,95] The possibility of observing transitions between the two tunnelling components and thereby obtaining their energy difference directly was precluded by the symmetry selection rules in this particular pure rotational experiment. However, since the rotational sub-levels of the two components cross at low-J, even a weak Coriolis-mediated tunnelling interaction is sufficient to perturb the spectrum at microwave resolution. Full-dimensional multi-state VMP2 calculations predicted that such a perturbation occurs as a $(J_cJ_a + J_aJ_c)$-type interaction. Indeed, reproducing this portion of the spectrum required and permitted fitting the interaction strength and the tunnelling splitting, which have values for the d_6 isotopologue of 23.4 MHz and 16.5 GHz, respectively.[92] These experimental constants are in excellent agreement with the VMP2 calculations of 23.3 MHz and 17.4 GHz.[92,96]

The issue of tunnelling in *gauche*-butadiene played an important role in the longstanding controversy over its structure. For decades several arguments were advanced based on both theory and experiment in favor of planar or twisted structures for the minor conformer of butadiene. The most direct experimental evidence, obtained by Michl *et al.*[97–100] in polarized infrared matrix studies, indicated that the molecule possessed C_{2v} symmetry and therefore was planar *cis*; on the other hand, increasingly sophisticated electronic structure calculations and gas-phase IR/Raman data all pointed to a substantially non-planar *gauche* structure. In attempting to suggest a resolution to this apparent contradiction, Michl *et al.* raised the hypothetical possibility of rapid tunnelling, which would cause *gauche*-butadiene to display an averaged *cis* C_{2v} structure over the timescale of their measurement. It was not until the experimental observation and determination of the unexpectedly large tunnelling splitting of tens of GHz, aided significantly by the type of *ab initio* calculations described earlier, that this explanation was shown to be correct.

11.3.4 S_1 Acetylene

The first electronically excited singlet state of acetylene is a fascinating model system for studying molecular quantum mechanics and spectroscopy, and a full discussion is beyond the scope of this chapter (see ref. 101 and references therein). Briefly, the $\pi - \pi^*$ excitation from the linear ground state S_0 leads to an excited state S_1 that possesses *trans* and *cis* minima, with a low-barrier isomerization pathway between them *via* a half-linear transition state.

11.3.4.1 cis-trans *Tunnelling and Tunnelling Staggerings*

The first indication of tunnelling in S_1 C_2H_2 came from observation and identification of electronically forbidden transitions into *cis* well states,[102] accompanied by DVR calculations showing qualitatively how tunnelling could permit mixing with *trans* well states and allow these *cis* well states to appear in the S_1–S_0 spectrum.[103] Distortions of the *cis* states' rotational level structure ("*K*-staggerings") were also noted in the experimental data and quantified, but could not be analyzed further at that point in time. Consideration of the multiple possible in-plane and torsional tunnelling pathways between the *trans* and *cis* conformers and their symmetry-related copies[104] provided a framework for understanding the range of potential tunnelling effects. More sophisticated DVR calculations[105] achieved more comprehensive and accurate agreement with experiment. Surprisingly, it was also discovered that decades-old data contained clear evidence of tunnelling staggerings in near-barrier *trans* well states (see Table S2 of ref. 101). Much remains to be done, both experimentally and theoretically, to learn more about molecular tunnelling in this seemingly simple but incredibly rich model system.

11.4 Outlook

This chapter has focused on understanding and predicting the signatures of vibrational tunnelling in frequency domain spectra of small- to medium-sized molecular systems. The *ab initio* methods we use target eigenstates of a ''static'' rovibrational energy level manifold. However, these same spectroscopic tools can be used to address dynamical tunnelling in other scenarios. For example, we are currently exploring complex scaling and related methods in combination with the above curvilinear VMP2 methods to calculate quantum reaction rates, including effects from tunnelling through anharmonic reaction barriers.

Acknowledgements

The work discussed in this chapter represents contributions from many valued collaborators including Marie-Aline Martin-Drumel, Mike McCarthy, Jessica Porterfield, Barney Ellison, Robert Field, Allan Oliveira, Julia Lehman, Carl Lineberger, Anthony Merer, Matt Nava, Sandra Eibenberger, David Patterson, and John Stanton.

References

1. J. P. Gordon, H. J. Zeiger and C. H. Townes, Molecular microwave oscillator and new hyperfine structure in the microwave spectrum of NH_3, *Phys. Rev.*, 1954, **95**(1), 282.
2. M. Born and R. Oppenheimer, Zur Quantentheorie der Molekeln, *Ann. Phys.*, 1927, **389**, 457–484.
3. I. M. Mills, Vibration-Rotation Structure in Asymmetric- and Symmetric-Top Molecules, in *Molecular Spectroscopy: Modern Research*, ed. K. N. Rao and C. W. Mathews, Academic Press, New York, ch. 3.2, 1972, pp. 115–140.
4. V. Barone, Anharmonic vibrational properties by a fully automated second-order perturbative approach, *J. Chem. Phys.*, 2005, **122**, 014108.
5. M. J. Bramley, and T. Carrington. A general discrete variable method to calculate vibrational energy levels of three- and four-atom molecules, *J. Chem. Phys.*, 1993, **99**(11), 8519–8541.
6. T. Carrington, Perspective: Computing (ro-)vibrational spectra of molecules with more than four atoms, *J. Chem. Phys.*, 2017, **146**(12), 120902.

7. A. G. Császár, C. Fábri, T. Szidarovszky, E. Mátyus, T. Furtenbacher and G. Czakó, The fourth age of quantum chemistry: molecules in motion, *Phys. Chem. Chem. Phys.*, 2012, **14**(3), 1085–1106.
8. P. B. Changala and J. H. Baraban, Ab initio effective rotational and rovibrational Hamiltonians for non-rigid systems via curvilinear second order vibrational Møller–Plesset perturbation theory, *J. Chem. Phys.*, 2016, **145**, 174106.
9. J. M. Bowman, T. Carrington and H. D. Meyer, Variational quantum approaches for computing vibrational energies of polyatomic molecules, *Mol. Phys.*, 2008, **106**(16–18), 2145–2182.
10. R. B. Lehoucq, S. K. Gray, D.-H. Zhang and J. C. Light, Vibrational eigenstates of four-atom molecules: a parallel strategy employing the implicitly restarted Lanczos method, *Comput. Phys. Commun.*, 1998, **109**(1), 15–25.
11. H. G. Yu and G. Nyman, A spectral transform Krylov subspace iteration approach to quantum scattering, *Chem. Phys. Lett.*, 1998, **2980**(1–3), 27–35.
12. S. W. Huang and T. Carrington, A new iterative method for calculating energy levels and wave functions, *J. Chem. Phys.*, 2000, **112**, 8765.
13. C. Lanczos, An Iteration Method for the Solution of the Eigenvalue Problem of Linear Differential and Integral Operators, *J. Res. Natl. Bur. Stand.*, 1950, **45**(255), 255–282.
14. T. Carrington, *Using Iterative Eigensolvers to Compute Vibrational Spectra*, John Wiley & Sons, Ltd, 2018, pp. 217–243.
15. K. Wu and H. Simon, Thick-Restart Lanczos Method for Large Symmetric Eigenvalue Problems, *SIAM J. Matrix Anal. Appl.*, 2000, **22**, 602–616.
16. J. V. Lill, G. A. Parker and J. C. Light, Discrete variable representations and sudden models in quantum scattering theory, *Chem. Phys. Lett.*, 1982, **89**(6), 483–489.
17. J. C. Light, I. P. Hamilton and J. V. Lill, Generalized discrete variable approximation in quantum mechanics, *J. Chem. Phys.*, 1985, **82**(3), 1400.
18. J. C. Light and T. Carrington Jr, Discrete-Variable Representations and their Utilization, *Adv. Chem. Phys.*, 2000, **114**, 263.
19. D. T. Colbert and W. H. Miller, A novel discrete variable representation for quantum mechanical reactive scattering via the S-matrix Kohn method, *J. Chem. Phys.*, 1992, **96**, 1982.
20. E. Mátyus and J. Šimunek, and A. G. Császár. On the variational computation of a large number of vibrational energy levels and wave functions for medium-sized molecules, *J. Chem. Phys.*, 2009, **131**(7), 074106.
21. B. Poirier and T. Carrington, Accelerating the calculation of energy levels and wave functions using an efficient preconditioner with the inexact spectral transform method, *J. Chem. Phys.*, 2001, **114**(21), 9254.
22. X.-G. Wang and T. Carrington, A symmetry-adapted method for calculating energy levels with different symmetries from a single set of iterations, *J. Chem. Phys.*, 2001, **114**(4), 1473.

23. A. Leclerc and T. Carrington, Calculating vibrational spectra with sum of product basis functions without storing full-dimensional vectors or matrices, *J. Chem. Phys.*, 2014, **140**(17), 174111.
24. P. S. Thomas, T. Carrington Jr, J. Agarwal and H. F. Schaefer III, Using an iterative eigensolver and intertwined rank reduction to compute vibrational spectra of molecules with more than a dozen atoms: Uracil and naphthalene, *J. Chem. Phys.*, 2018, **149**(6), 064108.
25. P. M. Felker and Z. Bačić, Weakly bound molecular dimers: Intramolecular vibrational fundamentals, overtones, and tunnelling splittings from full-dimensional quantum calculations using compact contracted bases of intramolecular and low-energy rigid-monomer intermolecular eigenstates, *J. Chem. Phys.*, 2019, **151**, 024305.
26. X.-G. Wang and T. Carrington Jr., Using monomer vibrational wavefunctions to compute numerically exact (12D) rovibrational levels of water dimer, *J. Chem. Phys.*, 2018, **148**, 074108.
27. Z. Bacić and J. C. Light, Highly excited vibrational levels of ''floppy'' triatomic molecules: A discrete variable representation—distributed gaussian basis approach, *J. Chem. Phys.*, 1986, **85**(8), 4594–4604.
28. C. Puzzarini, J. F. Stanton and J. Gauss, Quantum-chemical calculation of spectroscopic parameters for rotational spectroscopy, *Int. Rev. Phys. Chem.*, 2010, **29**(2), 273–367.
29. J. K. G. Watson, Simplification of the molecular vibration-rotation Hamiltonian, *Mol. Phys.*, 1968, **15**, 479–490.
30. C. Eckart, Some Studies Concerning Rotating Axes and Polyatomic Molecules, *Phys. Rev.*, 1935, **47**, 552–558.
31. J. M. Bowman, Self-consistent field energies and wavefunctions for coupled oscillators, *J. Chem. Phys.*, 1978, **68**(2), 608–610.
32. J. M. Bowman, The self-consistent-field approach to polyatomic vibrations, *Acc. Chem. Res.*, 1986, **190**(7), 202–208.
33. R. B. Gerber and M. A. Ratner, Self-Consistent-Field Methods for Vibrational Excitations in Polyatomic Systems, *Adv. Chem. Phys.*, 1988, **70**, 97–132.
34. S. Carter, S. J. Culik and J. M. Bowman, Vibrational self-consistent field method for many-mode systems: A new approach and application to the vibrations of CO adsorbed on Cu(100), *J. Chem. Phys.*, 1997, **107**(24), 10458–10469.
35. L. S. Norris, M. A. Ratner, A. E. Roitberg and R. B. Gerber, Møller–Plesset perturbation theory applied to vibrational problems, *J. Chem. Phys.*, 1996, **105**, 11261–11267.
36. O. Christiansen, Møller–Plesset perturbation theory for vibrational wave functions, *J. Chem. Phys.*, 2003, **119**, 5773–5781.
37. C. Møller and M. S. Plesset, Note on an Approximation Treatment for Many-Electron Systems, *Phys. Rev.*, 1934, **460**(7), 618–622.
38. S. Carter and N. C. Handy, The vibrations of H_2O_2, studied by ''multimode,'' with a large amplitude motion, *J. Chem. Phys.*, 2000, **113**, 987–993.

39. J. M. Bowman, X. Huang, N. C. Handy and S. Carter, Vibrational Levels of Methanol Calculated by the Reaction Path Version of MULTIMODE, Using an ab initio, Full-Dimensional Potential, *J. Phys. Chem. A*, 2007, **111**, 7317–7321.
40. T. R. Horn, R. B. Gerber and M. A. Ratner, Vibrational states of very floppy clusters: Approximate separability and the choice of good curvilinear coordinates for $XeHe_2$, I_2He, *J. Chem. Phys.*, 1989, **91**(3), 1813–1823.
41. M. Bounouar and C. Scheurer, The impact of approximate VSCF schemes and curvilinear coordinates on the anharmonic vibrational frequencies of formamide and thioformamide, *Chem. Phys.*, 2008, **347**(1), 194–207.
42. Y. Scribano, D. M. Lauvergnat and D. M. Benoit, Fast vibrational configuration interaction using generalized curvilinear coordinates and self-consistent basis, *J. Chem. Phys.*, 2010, **133**(9), 094103.
43. D. Strobusch and C. Scheurer, Hierarchical expansion of the kinetic energy operator in curvilinear coordinates for the vibrational self-consistent field method, *J. Chem. Phys.*, 2011, **135**, 124102.
44. D. Strobusch and C. Scheurer, The hierarchical expansion of the kinetic energy operator in curvilinear coordinates extended to the vibrational configuration interaction method, *J. Chem. Phys.*, 2011, **135**, 144101.
45. J. H. Van Vleck, On σ-Type Doubling and Electron Spin in the Spectra of Diatomic Molecules, *Phys. Rev.*, 1929, **33**, 467–506.
46. W. Gordy and R. L. Cook, *Microwave Molecular Spectra*, John Wiley & Sons, New York, 3rd edn, 1984.
47. T. J. Lukka and E. Kauppi, Seminumerical contact transformations: From internal coordinate rovibrational Hamiltonian to effective rotational Hamiltonians. Framework of the method, *J. Chem. Phys.*, 1995, **103**(15), 6586.
48. R. W. Field, J. H. Baraban, S. H. Lipoff and A. R. Beck. Effective Hamiltonians for Electronic Fine Structure and Polyatomic Vibrations. in *Handbook of High-Resolution Spectroscopy*, ed. M. Quack and F. Merkt, John Wiley & Sons, Chichester, UK, 2011, p. 1461.
49. X. Chapuisat, A. Nauts and J. P. Brunet, Exact quantum molecular hamiltonians, *Mol. Phys.*, 1991, **72**(1), 1–31.
50. T. J. Lukka, A simple method for the derivation of exact quantum-mechanical vibration-rotation Hamiltonians in terms of internal coordinates, *J. Chem. Phys.*, 1995, **102**, 3945–3955.
51. D. Lauvergnat and A. Nauts, Exact numerical computation of a kinetic energy operator in curvilinear coordinates, *J. Chem. Phys.*, 2002, **116**(19), 8560.
52. J. K. G. Watson, The molecular vibration-rotation kinetic-energy operator for general internal coordinates, *J. Mol. Spectrosc.*, 2004, **228**, 645–658.
53. R. Meyer, Flexible models for intramolecular motion, a versatile treatment and its application to glyoxal, *J. Mol. Spectrosc.*, 1979, **76**, 266–300.

54. M. A. Harthcock and J. Laane, Calculation of kinetic energy terms for the vibrational Hamiltonian: Application to large-amplitude vibrations using one-, two-, and three-dimensional models, *J. Mol. Spectrosc.*, 1982, **91**(2), 300–324.
55. J. Laane, M. A. Harthcock, P. M. Killough, L. E. Bauman and J. M. Cooke, Vector representation of large-amplitude vibrations for the determination of kinetic energy functions, *J. Mol. Spectrosc.*, 1982, **91**, 286–299.
56. E. Mátyus, G. Czakó and A. G. Császár, Toward black-box-type full- and reduced-dimensional variational (ro)vibrational computations, *J. Chem. Phys.*, 2009, **130**(13), 134112.
57. C. Fábri, E. Mátyus and A. G. Császár, Rotating full- and reduced-dimensional quantum chemical models of molecules, *J. Chem. Phys.*, 2011, **134**(7), 074105.
58. C. Fábri, E. Mátyus and A G Császár, Numerically constructed internal-coordinate Hamiltonian with Eckart embedding and its application for the inversion tunnelling of ammonia, *Spectrochim. Acta, Part A*, 2014, **119**, 84–89.
59. V. Szalay, Aspects of the Eckart frame ro-vibrational kinetic energy operator, *J. Chem. Phys.*, 2015, **143**(6), 064104.
60. B. Podolsky, Quantum-Mechanically Correct Form of Hamiltonian Function for Conservative Systems, *Phys. Rev.*, 1928, **32**(5), 812–816.
61. J. K. G. Watson, The isotope dependence of the equilibrium rotational constants in $^1\Sigma$ states of diatomic molecules, *J. Mol. Spectrosc.*, 1973, **45**, 99–113.
62. W. Kutzelnigg, Which masses are vibrating or rotating in a molecule?, *Mol. Phys.*, 2007, **105**(19–22), 2627–2647.
63. M. Mladenović and M. Lewerenz, Comparison of spectroscopic strategies to determine molecular geometries and the impact of nuclear versus atomic masses: the example of HCO^+ and HOC^+, *Mol. Phys.*, 2018, **116**(23–24), 3607–3620.
64. M. Mladenović, Rovibrational Hamiltonians for general polyatomic molecules in spherical polar parametrization. I. Orthogonal representations, *J. Chem. Phys.*, 2000, **112**, 1070.
65. F. Gatti and C. Iung, Exact and constrained kinetic energy operators for polyatomic molecules: The polyspherical approach, *Phys. Rep.*, 2009, **484**(1), 1–69.
66. E. B. Wilson Jr, J. C. Decius and P. C. Cross, *Molecular Vibrations*, Dover, New York, 1980.
67. E. Kraka, Reaction path Hamiltonian and the unified reaction valley approach, *Comput. Mol. Sci.*, 2011, **1**(4), 531–556.
68. A. Nauts and X. Chapuisat, The description of molecular large-amplitude motions in terms of curvilinear coordinates associated with the reaction path, *Chem. Phys.*, 1983, **76**(3), 349–366.
69. W. H. Miller, N. C. Handy and J. E. Adams, Reaction path Hamiltonian for polyatomic molecules, *J. Chem. Phys.*, 1980, **72**, 99.

70. M. Page and J. W. McIver, On evaluating the reaction path Hamiltonian, *J. Chem. Phys.*, 1988, **88**(0), 922.
71. C. F. Jackels, Z. Gu and D. G. Truhlar, Reaction-path potential and vibrational frequencies in terms of curvilinear internal coordinates, *J. Chem. Phys.*, 1995, **102**(8), 3188.
72. V. Szalay, Eckart ro-vibrational Hamiltonians via the gateway Hamilton operator: Theory and practice, *J. Chem. Phys.*, 2017, **146**(12), 124107.
73. D. Lauvergnat, J. M. Luis, B. Kirtman, H. Reis and A. Nauts, Numerical and exact kinetic energy operator using Eckart conditions with one or several reference geometries: Application to HONO, *J. Chem. Phys.*, 2016, **144**(8), 084116.
74. A. Y. Dymarsky and K. N. Kudin, Computation of the pseudorotation matrix to satisfy the Eckart axis conditions, *J. Chem. Phys.*, 2005, **122**(12), 124103.
75. A. Yachmenev and S. N. Yurchenko, Automatic differentiation method for numerical construction of the rotational-vibrational Hamiltonian as a power series in the curvilinear internal coordinates using the Eckart frame, *J. Chem. Phys.*, 2015, **143**(1), 014105.
76. S. V. Krasnoshchekov, E. V. Isayeva and N. F. Stepanov, Determination of the Eckart molecule-fixed frame by use of the apparatus of quaternion algebra, *J. Chem. Phys.*, 2014, **140**(15), 154104.
77. K. Raghavachari, G. W. Trucks, J. A. Pople and M. Head-Gordon, A fifth-order perturbation comparison of electron correlation theories, *Chem. Phys. Lett.*, 1989, **157**(6), 479–483.
78. T. H. Dunning, Gaussian basis sets for use in correlated molecular calculations. I. The atoms boron through neon and hydrogen, *J. Chem. Phys.*, 1989, **90**(2), 1007.
79. J. Almlöf and P. R. Taylor, General contraction of Gaussian basis sets. I. Atomic natural orbitals for first- and second-row atoms, *J. Chem. Phys.*, 1987, **86**(7), 4070.
80. CFOUR, Coupled-Cluster techniques for Computational Chemistry, a quantum-chemical program package by J. F. Stanton, J. Gauss, M. E. Harding, P. G. Szalay with contributions from A. A. Auer, R. J. Bartlett, U. Benedikt, C. Berger, D. E. Bernholdt, Y. J. Bomble, L. Cheng, O. Christiansen, M. Heckert, O. Heun, C. Huber, T.-C. Jagau, D. Jonsson, J. Jusélius, K. Klein, W. J. Lauderdale, F. Lipparini, D. A. Matthews, T. Metzroth, L. A. Mück, D. P. O'Neill, D. R. Price, E. Prochnow, C. Puzzarini, K. Ruud, F. Schiffmann, W. Schwalbach, C. Simmons, S. Stopkowicz, A. Tajti, J. Vázquez, F. Wang, J. D. Watts and the integral packages MOLECULE (J. Almlöf and P.R. Taylor), PROPS (P. R. Taylor), ABACUS (T. Helgaker, H. J. Aa. Jensen, P. Jørgensen, and J. Olsen), and ECP routines by A. V. Mitin and C. van Wüllen. For the current version, see http://www.cfour.de.
81. B. J. Braams and J. M. Bowman, Permutationally invariant potential energy surfaces in high dimensionality, *Int. Rev. Phys. Chem.*, 2009, **28**(4), 577–606.

82. NITROGEN, Numerical and Iterative Techniques for Rovibronic Energies with General Internal Coordinates, a program by P. B. Changala, http://www.colorado.edu/nitrogen.
83. J. Z. Gong, D. A. Matthews, P. B. Changala and J. F. Stanton, Fourth-order vibrational perturbation theory with the Watson Hamiltonian: Report of working equations and preliminary results, *J. Chem. Phys.*, 2018, **149**(11), 114102.
84. J. Koput, On the r_0* structure and the torsional potential function of hydrogen peroxide, *J. Mol. Spectrosc.*, 1986, **115**(2), 438–441.
85. J. Koput, An ab initio study on the equilibrium structure and torsional potential energy function of hydrogen peroxide, *Chem. Phys. Lett.*, 1995, **236**(4), 516–520.
86. J. Koput, S. Carter and N. C. Handy, Potential energy surface and vibrational-rotational energy levels of hydrogen peroxide, *J. Phys. Chem. A*, 1998, **102**(31), 6325–6330.
87. P. Małyszek and J. Koput, Accurate ab initio potential energy surface and vibration-rotation energy levels of hydrogen peroxide, *J. Comput. Chem.*, 2013, **34**(5), 337–345.
88. J. H. Baraban, P. B. Changala and J. F. Stanton, The equilibrium structure of hydrogen peroxide, *J. Mol. Spectrosc.*, 2018, **343**, 92–95.
89. J.-M. Flaud, C. Camy-Peyret, J. W. C. Johns and B. Carli, The far infrared spectrum of H_2O_2. First observation of the staggering of the levels and determination of the cis barrier, *J. Chem. Phys.*, 1989, **91**, 1504.
90. A. M. Oliveira, Y.-J. Lu, J. H. Lehman, P. B. Changala, J. H. Baraban, J. F. Stanton and W. Carl Lineberger, Photoelectron Spectroscopy of the Methide Anion: Electron Affinities of $\cdot CH_3$ and CD_3 and Inversion Splittings of CH_3^- and CD_3^-, *J. Am. Chem. Soc.*, 2015, **137**(40), 12939–12945.
91. W. P. Kraemer, V. Špirko, P.-A. Malmqvist and B. O. Roos, Inversion-vibration energies of CH_3^- and adiabatic electron affinity of CH_3, *J. Mol. Spectrosc.*, 1991, **147**(2), 526–540.
92. J. H. Baraban, M. A. Martin-Drumel, P. B. Changala, S. Eibenberger, M. Nava, D. Patterson, J. F. Stanton, G. B. Ellison and M. C. McCarthy, The molecular structure of *gauche*-1,3-butadiene: Experimental establishment of non-planarity, *Angew. Chem., Int. Ed.*, 2018, **57**, 1821–1825.
93. J. P. Porterfield, J. H. Westerfield, L. Satterthwaite, D. Patterson, P. B. Changala, J. H. Baraban and M. C. McCarthy, Rotational Characterization of the Elusive Gauche Isoprene, *J. Phys. Chem. Lett.*, 2019, **10**(8), 1981–1985.
94. K. B. Wiberg, P. R. Rablen and J. H. Baraban, Butadiene and Heterodienes Revisited, *J. Org. Chem.*, 2018, **83**(15), 8473–8482.
95. M. A. Martin-Drumel, J. H. Baraban, P. B. Changala, J. F. Stanton and M. C. McCarthy, The Hunt for Elusive Molecules: Insights from Joint Theoretical and Experimental Investigations, *Chem. – Eur. J.*, 2019, **25**(30), 7243–7258.
96. P. B. Changala, *High Resolution Infrared Spectroscopy of Complex Polyatomic Molecules*, PhD thesis, University of Colorado Boulder, 2019.

97. C. H. Choi, M. Kertesz, S. Dobrin and J. Michl, Argon-matrix-isolation Raman spectra and density functional study of 1,3-butadiene conformers, *Theor. Chem. Acc.*, 1999, **102**(1), 196–206.
98. B. R. Arnold, V. Balaji, J. W. Downing, J. G. Radziszewski, J. J. Fisher and J. Michl, IR polarization directions in s-trans-1,3-butadiene and the average topochemistry of the s-cis to s-trans photoisomerization in matrix isolation, *J. Am. Chem. Soc.*, 1991, **113**(8), 2910–2919.
99. B. R. Arnold, V. Balaji and J. Michl, Structure of matrix-isolated s-cis-1,3-butadiene from polarized IR spectra: a closer look, *J. Am. Chem. Soc.*, 1990, **112**(5), 1808–1812.
100. J. J. Fisher and J. Michl, s-Cis vs. gauche 1,3-butadiene: evidence for planarity from polarized matrix-isolation IR spectroscopy, *J. Am. Chem. Soc.*, 1987, **109**(4), 1056–1059.
101. J. H. Baraban, P. B. Changala, G. C. Mellau, J. F. Stanton, A. J. Merer and R. W. Field, Spectroscopic characterization of isomerization transition states, *Science*, 2015, **350**(6266), 1338–1342.
102. A. J. Merer, A. H. Steeves, J. H. Baraban, H. A. Bechtel and R. W. Field, Cis-trans isomerization in the S_1 state of acetylene: Identification of cis-well vibrational levels, *J. Chem. Phys.*, 2011, **134**(24), 244310.
103. J. H. Baraban, A. R. Beck, A. H. Steeves, J. F. Stanton and R. W. Field, Reduced dimension discrete variable representation study of *cis–trans* isomerization in the S_1 state of C_2H_2, *J. Chem. Phys.*, 2011, **134**(24), 244311.
104. J. T. Hougen and A. J. Merer, Extended permutation-inversion groups for simultaneous treatment of the rovibronic states of trans-acetylene, cis-acetylene, and vinylidene, *J. Mol. Spectrosc.*, 2011, **2670**(1–2), 200–221.
105. P. B. Changala, J. H. Baraban, J. F. Stanton, A. J. Merer and R. W. Field, Reduced dimension rovibrational variational calculations of the S_1 state of C_2H_2. II. The S_1 rovibrational manifold and the effects of isomerization, *J. Chem. Phys.*, 2014, **140**(2), 024313.

CHAPTER 12

The Tunnelling Flight Time

ELI POLLAK

Chemical and Biological Physics Department, Weizmann Institute of Science,
76100, Rehovoth, Israel
Email: eli.pollak@weizmann.ac.il

12.1 Introduction

The concept of time in quantum mechanics is not trivial. In contrast to position and momentum operators, for which there exists the straightforward commutation relation $[q, p] = i\hbar$, there is no straightforward relation for time and energy. As noted by Pauli[1] this has to do with the fact that the energy is bounded from below, while the coordinate and momentum are not. One may define quantum mechanical time operators, and many people have done so, but there is no unique definition.[2–7] The situation is even more confusing since different definitions give different answers,[8–12] and it is not always clear how to relate them to a specific experiment. An excellent review and presentation of the different definitions of time operators and their properties may be found in two volumes on ‘‘time in quantum mechanics’’ published ten years ago.[13,14]

In this context, a central question that has challenged experiment and theory is how much time does it take to tunnel through a barrier? The tunnelling phenomenon is ubiquitous, being important in physics,[15] chemistry and biology.[16–21] Hydrogen diffusion on surfaces at low temperatures is mainly *via* tunnelling.[22] Proton and hydrogen transfer reactions may be dominated by quantum tunnelling[23] even at room temperature and certainly sufficiently far below it.[24] Heavy atom tunnelling is gaining attention.[25] Yet the tunnelling time has remained particularly elusive.

Theoretical and Computational Chemistry Series No. 18
Tunnelling in Molecules: Nuclear Quantum Effects from Bio to Physical Chemistry
Edited by Johannes Kästner and Sebastian Kozuch

Published by the Royal Society of Chemistry, www.rsc.org

Recent attosecond photoionization experiments of atoms such as helium have accentuated the tunnelling time puzzle.[26] Here, one is concerned with tunnelling in the presence of an external field, which modifies the barrier in time. What is the tunnelling time in this case? How does it depend on the frequency of the modulation? To date, these questions have been discussed in terms of various definitions of quantum time, such as phase delay, imaginary time, dwell time, *etc.*[14,27]

The attosecond experiments have led to contradictory claims. Some find that the tunnelling time vanishes,[28,29] others claim that it is ''short'',[14] and yet others argue that a single tunnelling time cannot be established.[30] The tunnelling time controversy continues to rage. The photoionization experiment has been recently implemented for the hydrogen atom instead of He,[31] this has the advantage that one may analyze the experiment in terms of the numerically exact solution of the time-dependent Schrödinger equation. The conclusion of the authors of ref. 18 was that the tunnelling time vanishes or at least is bounded from above for a few attoseconds. This has been strongly contested in a recent preprint put on ArXiv[32] titled ''Measuring the time a tunnelling atom spends in the barrier'', where the authors note that their experimental results are inconsistent with those that claim such small times for tunnelling.

In this context, one often mentions the Hartman effect,[33] which really should be named the MacColl effect, since the latter discovered it in 1932[34] and Hartman only rediscovered it. The MacColl effect is the observation that the tunnelling time is independent of the width of the barrier through which the particle tunnels. If the tunnelling time is finite and the barrier is sufficiently long, then the MacColl effect predicts that a tunnelling particle would traverse the barrier length with almost infinite speed. Does non-relativistic quantum mechanics lead to a violation of special relativity? Most say no,[35] some say yes.[36] If yes, does this imply that tunnelling must be studied only in a relativistic context?

To answer some of these questions we have, in recent years, taken as a starting point that one should not attempt to formulate time operators but rather use the time-dependent Schrödinger equation as the point of departure.[37,38] In this context, time is a parameter, which gives information on how a wavefunction changes as the time parameter evolves. This change may in principle be measured in a time-of-flight experiment whereby a particle exits a source at the initial time, scatters from a potential and reaches a detector some later time.

This strategy is very different from the Larmor clock class of experiments (see *e.g.* Chapter 20 of ref. 15), pioneered by Baz'[39] and Rybachenko,[40] whereby the barrier region of the potential is coupled to a magnetic field that affects for example a spin degree of freedom of the tunnelling particle, changing its polarization. This change may then be transformed into a time – the Larmor clock time of tunnelling.

A related ''clock'' is devised by coupling the barrier region to a time-dependent field. The time variation of the field provides information on a tunnelling time scale. If the field changes slowly relative to the ''tunnelling time'' the particle will see a frozen potential, while if it changes rapidly the particle will ''feel'' the mean potential. The result of the scattering will depend on the modulation frequency leading to a temporal property of the tunnelling. This is the strategy underlying the so-called Büttiker–Landauer tunnelling time.[41]

Both the Larmor clock and the Büttiker–Landauer "experiments" lead to finite tunnelling times while the tunnelling flight time, as defined and determined in refs 36 and 37, is either found to vanish or is very small. The resolution of this seeming paradox is that the two times measure different properties. The tunnelling flight time is a measure of the time of flight, while the Larmor and Büttiker–Landauer clocks measure an imaginary tunnelling time, as defined first in ref. 42 and is known as the Pollak–Miller time.

The main theme of this review is the tunnelling flight time. In Section 12.2 we will present the theoretical framework leading to the tunnelling flight time. Numerical examples of tunnelling through a symmetric square barrier potential and an asymmetric Eckart barrier potential[43] are presented. The same approach may also be used to investigate flight times in the context of quantum above barrier reflection, this is discussed in Section 12.3. The imaginary time concept and its relation with the Larmor clock are considered in Section 12.4. We end with a discussion in Section 12.5, noting why the vanishing or very small tunnelling flight time does not contradict special relativity. We then point out that although progress has been achieved, there are quite a few open questions remaining – quantum mechanics might still have some additional surprises in store.

12.2 The Tunnelling Flight Time

12.2.1 Preliminaries

The formalism we will use is that of transition path time distributions.[44] The transition path time distribution (TPTD) gives the probability distribution of transition times between two spatial points. The original definition has been given within a classical framework[45,46] and used extensively for example for the study of protein folding[47] and the transition from a folded to an unfolded conformation and *vice versa*.[48]

The quantum mechanical counterpart of the TPTD is a time-correlation function, for example the correlation of an initial state with a final location, considered to be the "screen".[49–51] At least in principle, the quantum TPTD is measurable, for example in single atom time-of-flight experiments.[52] Particles are released from a trap at the initial time,[53] and their time of arrival time at a detector is recorded.

In the context of tunnelling, one considers an incident Gaussian wavepacket, whose mean momentum is well below the barrier top and whose spatial incident width is sufficiently broad such that the probability of transmission at energies above the barrier top is negligible compared to the transmission probability at the incident mean energy. In addition, the incident wavepacket has to be initiated at a distance that is sufficiently far to the left of the barrier (assuming that the particle is scattered with initial positive mean momentum) such that the probability of leakage of density to the transmitted side at the initial time is also much smaller than the transmission probability. These conditions are needed to assure that the wavepacket dynamics reflect pure tunnelling, rather than artefacts resulting from the choice of the initial wavepacket. They imply that the actual numerical computation is not trivial, even though one might be dealing with a system in one dimension.

If one considers only the flight time say in the transmitted direction, it becomes difficult to separate the different contributions to the measured time. The flight time will depend not only on the time spent by the particle as a freely propagating particle, outside the sphere of influence of the potential, there is also a momentum filtering effect. The tunnelling transmission probability is typically exponentially sensitive to the incident energy. The initial state is a wavepacket with different momentum contributions, so that transmission *via* tunnelling will prefer the higher energy components, thus speeding up the transmitted particle.[54,55] This speedup has nothing to do with the tunnelling time itself but has to be estimated to ascertain the true contribution from the tunnelling itself.

The way we have chosen thus far to determine some of these effects is to compare the transmission and reflection tunnelling time distributions. Here too, care must be exercised. The "screen" location, where one measures the reflection times, must be chosen sufficiently to the left of the spatial maximum of the incident wavepacket so that initially the wavepacket does not overlap significantly with the screen. This added condition further complicates the computation, since it implies that the points at which the TPTDs are measured are much further away from the mean incidence position, which also must be far from the region where the potential varies significantly.

12.2.2 Definitions

Thus far, the determination of tunnelling flight times has been limited to scattering on a one-dimensional potential $V(x)$ that goes to a constant asymptotically $(x \to \pm\infty)$ and has a barrier at $x = 0$ with height $V^{\neq}$. The Hamiltonian operator for a particle of mass M with momentum and position operators respectively $\hat{p}$, $\hat{x}$ is

$$\hat{H} = \frac{\hat{p}^2}{2M} + V(\hat{x}). \tag{12.1}$$

The incident wavepacket is chosen to be a coherent state whose coordinate representation is

$$\langle x|\Psi\rangle = \left(\frac{\Gamma}{\pi}\right)^{1/4} \exp\left[-\frac{\Gamma}{2}(x - x_i)^2 + \frac{i}{\hbar} p_i (x - x_i)\right]. \tag{12.2}$$

Γ is the spatial width parameter, the spatial extent of the initial state is $1/\sqrt{\Gamma}$ and the momentum width is $\hbar\sqrt{\Gamma}$.

We first consider an incident wavepacket localized to the left of the potential and moving towards it, so that the initial incident mean momentum p_i is positive. Its magnitude is chosen to be below the barrier height $\left(\frac{p_i^2}{2M} < V^{\neq}\right)$ and the momentum width is such that $\exp\left(-\frac{2MV^{\neq}}{\hbar^2\Gamma}\right) \ll |T(p_i)|^2$, which is the probability of an incident momentum at the barrier energy or higher, is much smaller than the transmission probability $|T(p=\hbar k)|^2$ at the mean incident momentum p_i. We also assume that the mean incident position (x_i) of the wavepacket is such that $\exp\left(-\Gamma x_i^2\right) \ll |T(p_i)|^2$, ensuring that initially there is no meaningful leakage of the wavefunction under the barrier. Since the initial state is a Gaussian wavefunction, the associated transmission ($|T|^2$) and reflection ($|R|^2$) probabilities must be averaged over the incident energy distribution:

$$\begin{aligned} |R_\Psi|^2 &= \int_{-\infty}^{\infty} \mathrm{d}k \frac{|R(k)|^2}{\sqrt{\pi\Gamma}} \exp\left(-\frac{(\hbar k - p_i)^2}{\hbar^2\Gamma}\right), \\ |T_\Psi|^2 &= \int_{-\infty}^{\infty} \mathrm{d}k \frac{|T(k)|^2}{\sqrt{\pi\Gamma}} \exp\left(-\frac{(\hbar k - p_i)^2}{\hbar^2\Gamma}\right). \end{aligned} \tag{12.3}$$

The TPTD may be defined through a density correlation function to find the particle at the point y at time t:

$$C_t(y\,;\,\Psi) = \mathrm{Tr}\left[|\Psi\rangle\langle\Psi| \exp\left(\frac{i\hat{H}t}{\hbar}\right)|y\rangle\langle y| \exp\left(-\frac{i\hat{H}t}{\hbar}\right)\right] = \left|\langle y| \exp\left(-\frac{i\hat{H}t}{\hbar}\right)|\Psi\rangle\right|^2. \tag{12.4}$$

For a free particle, the time integral of this correlation function diverges, since it decays at long times as t^{-1}. In the presence of a potential, the correlation function decays at least as t^{-3}, as shown in ref. 56 and appendix A of ref. 37. This is a consequence of the phenomenon of quantum threshold reflection[57] whereby it is well understood that, at threshold, that is when the incident momentum is very small, the transmission probability vanishes (except for special cases) as p_i^2. The long time limit comes from the very low momentum components so that relative to the free particle, one gains a factor of t^{-2}. This implies that we may define a TPTD as

$$P_t(y\,;\,\Psi) = \frac{C_t(y\,;\,\Psi)}{\int_0^{\infty} \mathrm{d}t C_t(y\,;\,\Psi)}. \tag{12.5}$$

To consider separately the TPTD for reflection and transmission, one divides the TPTD into the respective parts:

$$P_t(y\,;\,\Psi) = |R_\Psi|^2 P_{R,t}(-y\,;\,\Psi) + |T_\Psi|^2 P_{T,t}(y\,;\,\Psi). \tag{12.6}$$

If the particle is incident from the right with negative momentum then one must change the sign of y in eqn (2.6). Due to the long t^{-3} time decay, the mean flight time for the transmitted and reflected particles, defined as:

$$\left\langle t_{R/T,l}(y)\right\rangle = \int_0^{\infty} \mathrm{d}t t P_{R/T,t}(y\,;\,\Psi_l) \tag{12.7}$$

for the particle incident from the left, converges. Similarly, one defines the mean times for the particle incident from the right, except that the sign of y must be inverted.

The TPTD is very similar to the so-called "presence time distribution,"[58] the central difference is that in the TPTD the normalization is over the time interval $[0,\ \infty]$ while in the presence time formulation it is over the time interval $[-\infty,\ \infty]$. Although seemingly a minor issue, it does make a difference. In a time-of-flight experiment, since there is an initial time at which the particle exits the source, the TPTD formulation is the one to be used.

Alternatively, one may define a flux transition path time probability distribution.[59,60] The flux operator at the point y is defined as

$$\hat{F}(y) = \frac{1}{2M}[\hat{p}|y\rangle\langle y| + |y\rangle\langle y|\hat{p}]. \tag{12.8}$$

The flux correlation function at time t is defined analogously to the density time correlation function

$$C_{F,t}(y\,;\,\Psi) = \mathrm{Tr}\left[|\Psi\rangle\langle\Psi| \exp\left(\frac{i\hat{H}t}{\hbar}\right)\hat{F}(y)\exp\left(-\frac{i\hat{H}t}{\hbar}\right)\right]. \tag{12.9}$$

In principle, the flux correlation function is not necessarily everywhere positive and so cannot be used to "measure" the time of flight everywhere. However, in the asymptotic regions where the wavefunction goes as $\exp\left(\pm\frac{i}{\hbar}px\right)$ the flux time distribution will be either only positive or only negative so that there is no difficulty in defining the flux transition time probability distribution

$$P_{F,t}(y \rightarrow \pm\infty) = \frac{C_{F,t}(y\,;\,\Psi)}{\int_0^{\infty}\mathrm{d}t C_{F,t}(y\,;\,\Psi)}. \tag{12.10}$$

Since the flux operator is proportional to the momentum, the long time limit of the flux transition time probability distribution goes as t^{-4}, so that in this case, the variance of the time will also converge. As for the density time distribution, one divides the flux time distribution into a transmitted and reflected part and associates with each a mean transition time.

12.2.3 The Tunnelling Flight Time

The strategy we have used thus far to determine the tunnelling flight time is by comparison of the mean transmission and reflection times. Such a comparison negates the need for any classical dynamics input. Consider first a symmetric barrier potential. One may expect that any difference between the mean transmission and reflection times would reflect the tunnelling flight time, since the reflected particles do not exit the barrier from the right.

There are, though, two complications. One, not a very serious one, is that the exponential tail of the wavefunction penetrating the barrier may contribute equally a small but equal time delay to the transmitted and reflected particles. This is the prediction based on an analysis of Wigner's phase time delay.[61] The second is known as the momentum filtering effect. The momentum dependence of the tunnelling probability goes as $\exp\left[-\frac{(p-p_i)^2}{\hbar^2\Gamma}+\ln\left(|T(p=\hbar k)|^2\right)\right]$. As noted above, to ensure that transmission occurs only *via* tunnelling we assume that $\hbar\sqrt{\Gamma} \ll p_i$ so that minimizing the exponent under this condition implies that the most probable transmitted momentum is slightly larger than the mean incident momentum:

$$p_{\mathrm{mp}} \simeq p_i + \frac{\hbar^2\Gamma}{2}\left[\frac{\mathrm{d}}{\mathrm{d}p}\ln\left(|T(p)|^2\right)\right]_{p=p_i}. \tag{12.11}$$

Since typically, the transmission probability is an exponentially increasing function of the momentum, the excess momentum is positive. The transmitted particles move faster than the reflected ones. This excess momentum depends linearly on the width parameter Γ. As it becomes smaller one may expect that the mean time difference between the reflected and the transmitted particles become smaller. In the limit that it vanishes, the only difference between the two can come from the tunnelling time.

If the potential is asymmetric, there will be large time differences between the reflected and transmitted particles incident from the left and the right, due to the asymptotic potential difference. This too, would mask any contribution from the tunnelling time which, even if finite, would be much smaller. To elucidate the tunnelling time also for asymmetric barriers, we define a mean time difference for particles incident upon the barrier from the left (right) as

$$\Delta t_{\mathrm{l/r}}(\Gamma) = \langle t\rangle_{R,\mathrm{l/r}} - \langle t\rangle_{T,\mathrm{l/r}}. \tag{12.12}$$

Then one defines an overall time difference as the average of the two differences

$$\overline{\Delta t}(\Gamma) = \frac{1}{2}\left[\Delta t_{\mathrm{l}}(\Gamma) + \Delta t_{\mathrm{r}}(\Gamma)\right]. \tag{12.13}$$

With this construct, one has eliminated the time difference due to the free particle motion in the differing asymptotic channels. On the left side of the potential one has particles transmitted from the incident wavepacket to the right and reflected from the incident wavepacket on the left. On the right side one has particles transmitted from the left and reflected from the right. The two possible sources for time differences are the momentum filtering effect and the tunnelling time.

We defined a tunnelling flight time as the mean time difference in the limit that the width $\Gamma \to 0^+$:

$$t_{\mathrm{TFT}} = \lim_{\Gamma \to 0^+} \left[-\overline{\Delta t}(\Gamma) \right]. \tag{12.14}$$

The minus sign is due to the fact that the time difference is between reflected and transmitted particles and we want the residue to reflect a non-negative tunnelling flight time. In this limit, the momentum filtering effect is eliminated.

12.2.4 Numerical Examples – Symmetric Barriers

In the following, we will review results for the density-based transition path time distribution [eqn (12.5)]. First we consider a symmetric Eckart barrier (d is the length scale)

$$V(x) = \frac{V^{\neq}}{\cosh^2\left(\frac{x}{d}\right)}. \tag{12.15}$$

The barrier frequency is ${\omega^{\neq}}^2 = \frac{2V^{\neq}}{Md^2}$ and time is scaled accordingly ($t \to \omega^{\neq} t$). Similarly, one may scale all distances with d and the energy with the barrier height. In the computations shown in Figures 12.1 and 12.2 the barrier height was chosen such that $V^{\neq} = \hbar\omega^{\neq}$, more details may be found in ref. 36.

The reflected and transmitted TPTDs are plotted in Figure 12.1. The initial location of the wavepacket was at -500, the mean incident energy is $V^{\neq}/200$ and the width parameter is 7×10^{-5}. The time distributions are at the "screen" distance of ± 1000. These conditions assure that only tunnelling leads to transmission and there are no initial leakages of the wavefunction to the transmitted region. As expected, the transmitted TPTD is slightly faster than the reflected, but that is all. The distributions are surprisingly similar.

The mean time difference [see eqn (12.12)] is plotted in Figure 12.2 as a function of the width parameter for two different initial energies of the incident Gaussian wavepacket. Note that the time scale at the lower energy is much larger than at the higher incident energy, due to the slower motion in the free particle region. As predicted from eqn (12.11) the mean time difference scales linearly with the spatial width parameter. It vanishes as the

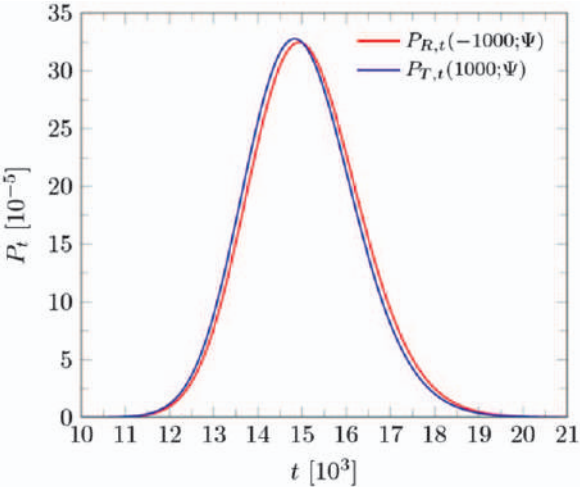

Figure 12.1 The reflected and transmitted TPTDs are plotted for a Gaussian wavepacket incident on a symmetric Eckart barrier. For further details see the text.
Reproduced from ref. 36 with permission from American Chemical Society, Copyright 2017.

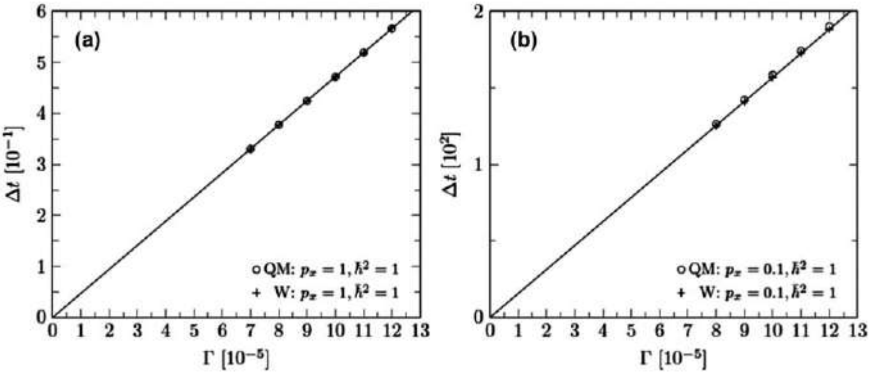

Figure 12.2 The mean time difference between reflection and transmission for scattering from a symmetric Eckart barrier is plotted as a function of the width parameter for two different initial energies of the incident wavepacket. Note the linear dependence and that the time difference vanishes when the width parameter goes to zero irrespective of the incident energy. For further details, see the text.
Reproduced from ref. 36 with permission from American Chemical Society, Copyright 2017.

width parameter goes to zero. This suggests that the tunnelling flight time vanishes or is very small and equal for the reflected and transmitted wavepackets for this specific case of scattering on a symmetric Eckart barrier.

Why do the plots show results only for widths larger than 7×10^{-5}? The reason is numerical; for smaller width parameters one would have to go even farther away from the barrier initially. The integration time becomes long and the accuracy decreases.

It seems though that there is nothing special about the smooth Eckart potential. The same results are found when considering scattering from a square barrier (symmetric) potential:

$$V(x) = V^{\neq}[\theta(x+a) - (x-a)] \tag{12.16}$$

where $\theta(x)$ is the unit step function and $2a$ is the width of the barrier. Using atomic units with unit mass, one finds the results shown in Figure 12.3. Figure 12.3(a) shows the mean time difference for a fixed width of the barrier ($a=1$) but three different barrier heights. In all cases, one finds the same linear dependence and the tunnelling flight time vanishes when the width parameter vanishes. Figure 12.3(b) shows the same result but for a fixed barrier height of unity and different widths of the barrier. (b) confirms that the vanishing tunnelling flight time is independent of the barrier width. (a) shows that it is also independent of the barrier height. Both effects were predicted by MacColl.

As may be seen from Figure 12.3(b), the broader the barrier the larger the slope, that is the filtering effect becomes more pronounced. The broader the barrier the more sensitive is the transmission probability to the incident energy and therefore the filtering effect is stronger. In the deep tunnelling limit, the dependence of the transmission probability on the width goes as

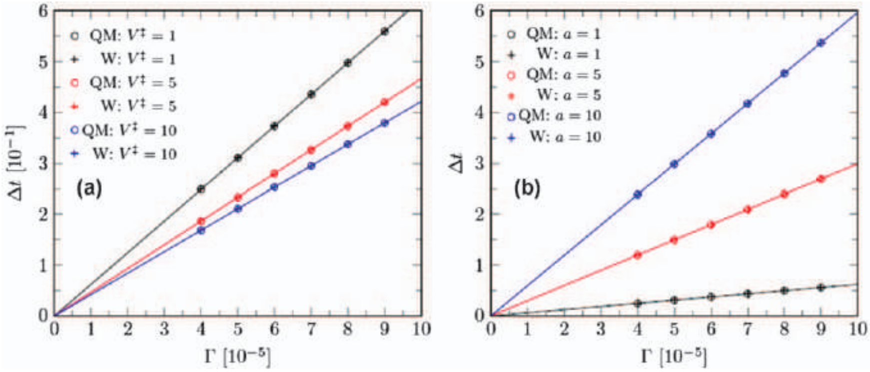

Figure 12.3 The mean time difference between reflection and transmission for scattering from a symmetric square barrier potential is plotted as a function of the width parameter in (a) for different barrier heights at a fixed barrier width ($a=1$) and in (b) for different barrier widths and a fixed barrier height of unity. The notation QM (W) implies that the results were obtained from the numerically exact quantum solution (the classical Wigner approximate solution). In all cases, the TFT difference vanishes. For further details, see the text.
Reproduced from ref. 36 with permission from American Chemical Society, Copyright 2017.

$\exp\left(-\frac{4\sqrt{2M}\sqrt{V^{\neq}-E}}{\hbar}a\right)$ so that the slope of the mean time difference is proportional to the barrier width ($2a$). Similarly, at a fixed barrier width $\left[\frac{\mathrm{d}}{\mathrm{d}p}\ln\left(|T(p)|^2\right)\right]_{p=p_i} \sim \frac{1}{\sqrt{V^{\neq}-E_i}}$ so that as seen in Figure 12.3(a), the slope becomes smaller as the barrier height increases.

12.2.5 Numerical Examples – Asymmetric Barriers

The same phenomena are observed also for the case of an asymmetric Eckart barrier potential:

$$V(x) = V_{-\infty}\left(\frac{1}{1+\exp\left(\frac{x}{b}\right)} + \frac{\kappa\exp\left(\frac{x}{b}\right)}{\left[1+\exp\left(\frac{x}{b}\right)\right]^2}\right). \tag{12.17}$$

The potential goes to the constant $V_{-\infty}$ (chosen to be unity in the computations described below) to the left and vanishes to the right. When the shape parameter κ is between −1 and 1 the potential has the shape of a smooth step potential; it has a barrier for values greater than unity. This dependence is shown in Figure 12.4(a) where the potential is plotted as a function of the distance x for a few different values of κ. Typical reflection and transmission probabilities are plotted in Figure 12.4(b).

A typical example of the time-dependent density for a wavepacket scattered from the left [Figure 12.4(a)] and the right [Figure 12.4(b)] is shown in Figure 12.5. Contours of the density are plotted as a function of the position and the time for $\kappa = 4$. Figure 12.5(c) shows the asymmetric potential as a function of the distance x. The incident energy in both cases is 3/2 (close to the barrier top) and the spatial width parameter $\Gamma = 10^{-2}$. The wavepackets were initiated at $x_i = \pm 50$. The figure is noteworthy for a number of reasons. Note that the incident spatial width is much larger than the distance for which the potential varies noticeably. The wiggles in the center region are a result of the interference between the incident and reflected waves. After collision is over, that is at long times, this interference disappears and the reflected wave function is simply bell shaped. Finally, as expected, the slope is smaller in the right region since the potential is lower and the kinetic energy is higher.

The average flight time difference $\overline{\Delta t}$ [see eqn (12.13)] is plotted *vs.* the spatial width parameter Γ in Figure 12.6. As in the symmetric case, the resulting plot is linear and goes to zero when the width parameter $\Gamma \to 0^+$. Although the results shown in the figure are for a single choice of the shape parameter ($\kappa = 6$) the same results were observed for the five values of ($\kappa = 4, 5, 6, 7, 8$). This seems to indicate that the vanishing tunnelling flight time difference is a property of tunnelling through any simple one-dimensional barrier. The inset in Figure 12.6 shows a blowup of the dependence of the mean flight time difference on the spatial width parameter. Even without extrapolation, a value of

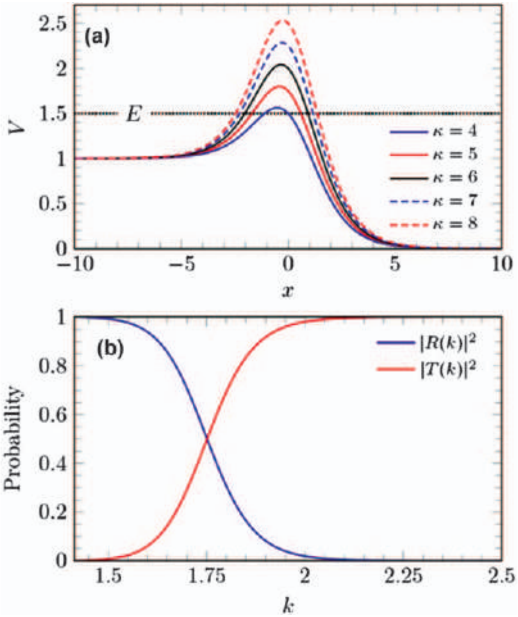

Figure 12.4 The asymmetric Eckart barrier potential is plotted in the top panel for different values of the shape parameter κ. Also shown is the incident energy $E = 3/2$ at which the computations presented in the following figures were carried out. The bottom panel shows the momentum dependence of the reflection and transmission coefficients for $\kappa = 4$. In all cases the length parameter $b = 1$.
Reproduced from ref. 37 with permission from American Chemical Society, Copyright 2018.

10^{-2} for the time difference implies that the speed of crossing the barrier (width ~1) is close to the speed of light (~137 in atomic units = fine structure constant). With a bit more effort one may readily obtain an apparent speed which is larger than allowed by special relativity.

12.2.6 Classical Wigner Dynamics

We have shown that the tunnelling flight time difference vanishes, but this does not “prove” that the tunnelling time is instantaneous. All it shows is that the mean reflection and transmission times are identical. As indicated by analysis of the Wigner time delay it could be that the penetration of the reflected wave into the barrier region is identical to the penetration of the transmitted wave and the two cancel each other out.

To try and shed further light on the tunnelling dynamics it is also instructive to consider an approximate classical Wigner dynamics[62] in which a vanishing tunnelling flight time is inserted by hand, that is for the approximate dynamics we know that the tunnelling flight time vanishes.

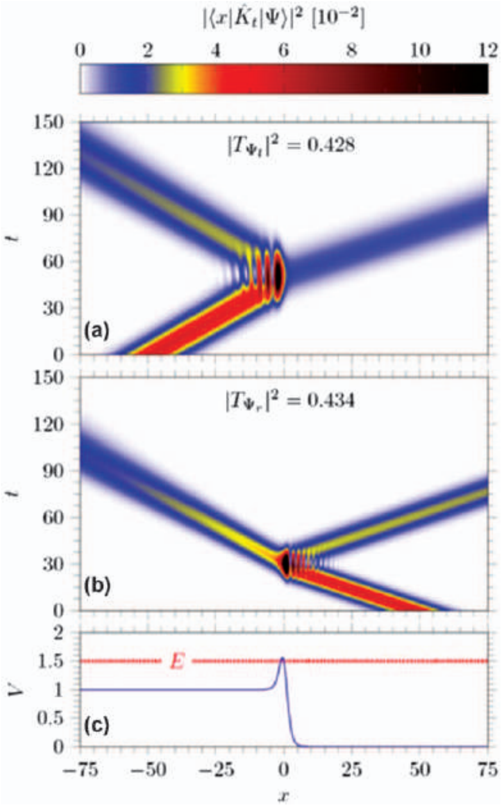

Figure 12.5 The spatio-temporal evolution of a Gaussian wavepacket scattered on an asymmetric Eckart potential. (a) The wavepacket incident from the left, (b) the same for incidence from the right. (c) The spatial dependence of the asymmetric Eckart potential.
Reproduced from ref. 37 with permission from American Chemical Society, Copyright 2018.

If this dynamics accurately reproduces the exact quantum dynamics, this would indicate that one may consider the possibility that the TFT vanishes.

It is well known that any correlation function may be represented in phase space exactly through the Wigner transform[63] of the relevant operators defined as

$$O_w(x,p) = \frac{1}{2\pi\hbar}\int_{-\infty}^{\infty} \mathrm{d}y \exp\left(\frac{ipy}{\hbar}\right)\left\langle x - \frac{y}{2}\middle|\hat{O}\middle|x + \frac{y}{2}\right\rangle \tag{12.18}$$

such that the trace of two operators is exactly given as

$$\mathrm{Tr}\left[\hat{A}\hat{B}\right] = 2\pi\hbar\int_{-\infty}^{\infty} \mathrm{d}p\mathrm{d}x A_{\mathrm{w}}(x,p)B_{\mathrm{w}}(x,p). \tag{12.19}$$

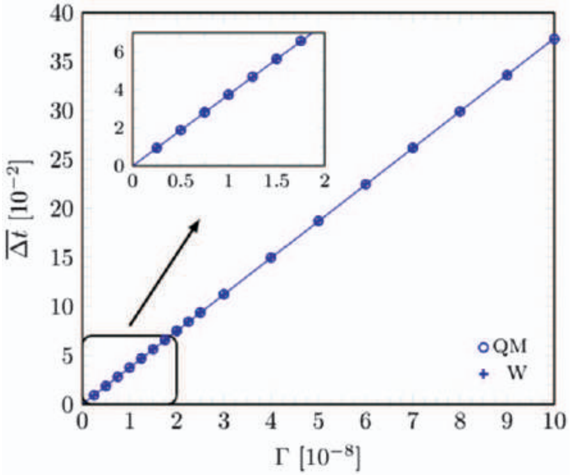

Figure 12.6 The mean flight-time difference as defined in eqn (12.13) is plotted *vs.* the spatial width parameter of the incident coherent state for an asymmetric Eckart barrier. The TPTDs are evaluated at $\pm y = \pm 4 \times 10^5$ (a.u.). For further details see the text.
Reproduced from ref. 37 with permission from American Chemical Society, Copyright 2018.

Consider then the density correlation function given in eqn (12.4). It may be rewritten in Wigner phase space as

$$C_t(y\,;\,\Psi) = 2\pi\hbar\int_{-\infty}^{\infty} \mathrm{d}p\mathrm{d}x\Psi_{\mathrm{w}}(x,p)y_{\mathrm{w}}(x_t,p_t) \tag{12.20}$$

where the Wigner representation of the initial coherent state is the Gaussian

$$\Psi_{\mathrm{w}}(x,p) = \frac{1}{\pi\hbar}\exp\left(-\Gamma(x-x_i)^2 - \frac{(p-p_i)^2}{\hbar^2\Gamma}\right) \tag{12.21}$$

and $y_{\mathrm{w}}(x_t, p_t)$ is the Wigner representation of the Heisenberg time evolved density $\exp\left(\frac{i\hat{H}t}{\hbar}\right)|y\rangle\langle y|\exp\left(-\frac{i\hat{H}t}{\hbar}\right)$. In classical Wigner dynamics,[64] the quantum time evolved density is replaced by its classical counterpart. That is, the Hamiltonian operator is taken to the classical limit, and the initial phase space point x, p is evolved classically to time t. This classical Wigner dynamics is exact for up to quadratic Hamiltonians.

Consider then the classical Wigner dynamics for tunnelling. The incident wavepacket evolves as a free particle until it hits the barrier. Classically it is reflected so that in the classical Wigner approximation, there is no tunnelling through the barrier. The approximation we use is to impose tunnelling on the dynamics as follows. A classical trajectory coming from the left hits the barrier at energy E. The exact quantum transmission probability is $|T(E)|^2$ so we let the trajectory pass through the barrier *instantaneously* to the right side with probability $|T(E)|^2$ and it is reflected at the left turning point with probability $|R(E)|^2 = 1 - |T(E)|^2$. In this way, the classical Wigner dynamics has two important properties. One is that by construction it gives the exact quantum transmission and reflection probabilities. The second property is that by construction, tunnelling through the barrier is instantaneous. The first property assures that this classical Wigner dynamics accounts correctly for momentum filtering. If the resulting flight time is the same as the numerically exact quantum flight time, then we have evidence that perhaps the exact quantum tunnelling flight time vanishes.

Inspection of Figures 12.2, 12.3 and 12.6 shows that each open circle has in it a plus sign, the open circles are the exact quantum result, the plus signs are the results of the classical Wigner approximation. The two results are numerically very close to each other; fitting the data to a linear function one finds that even when the tunnelling probability is $\sim 4\times 10^{-4}$ the two slopes agree with each other with an accuracy of 1% and the relative error becomes orders of magnitude smaller as the tunnelling probability increases.[36,37] These classical Wigner computations lead to two important conclusions. One is that indeed the tunnelling flight time may vanish, since in the classical Wigner computation the reflected part does not penetrate the barrier at all. Second is that at least some aspect of the one-dimensional tunnelling dynamics may be described by an incoherent theory, in the sense that phases of the wavefunction are not important. The classical Wigner approximation as described uses only densities and probabilities; there are no amplitudes within this framework.

12.3 Time and Above-barrier Quantum Reflection

12.3.1 Preliminaries

Above-barrier quantum reflection is the phenomenon by which a particle whose energy is larger than the barrier height finds itself reflected rather than transmitted.[65] This process is different from threshold quantum reflection,[66,67] whereby a quantum particle scattered on an attractive potential is reflected with unit probability (except for special cases). Here, we will consider only above-barrier quantum reflection and refer to it simply as quantum reflection.

The "standard" method by which one considers the above-barrier reflection time is based on Wigner's time delay, also known as the phase time. The reflection or transmission amplitude at a fixed energy may be written as a product of the probability amplitude and a phase

$$X(E) = |X(E)|\exp\left(i\frac{\Phi_X}{\hbar}\right), \quad X = T, R. \tag{12.22}$$

The phase time delay is then defined as

$$\bar{t}_X = \hbar \ \mathrm{Im}\left(\frac{\partial \ln X(E)}{\partial E}\right) = \frac{\partial \Phi_X}{\partial E}, \quad X = T, R. \tag{12.23}$$

It is considered a time delay, since for a free particle it vanishes and the transmission amplitude of a free particle is unity. In the semiclassical limit, it is the difference between the classical flight time of the particle with and without the potential. The time delay and variants of it have been a staple of the community considering the time associated with non-classical effects such as tunnelling and quantum reflection. It has, though, one major philosophical drawback. It is defined at a given energy, through the scattering eigenfunction. The eigenfunction is a stationary solution and so does not display any time dependence. The interpretation comes from the semiclassical limit, where the phase is related to the classical action of the scattered particle at the energy considered. In classical mechanics, the energy derivative of the action is indeed the time, but this is only an analogy. The relevant question should be how does one measure experimentally the time delay especially when the dynamics is dominated by non-classical phenomena such as quantum reflection. In different terms what is the experiment for which the time delay correctly describes the time spent by the quantum particle undergoing some time-dependent change?

In continuation of the consideration of the tunnelling flight time in the previous section, we will review here our recent results[68] which show that the phase time delay concept may fail to describe correctly time of flight experiments probing above barrier reflection, especially when it is dominated by quantum coherence.

In the following, we consider scattering on a symmetric square barrier potential as in eqn (12.16). The reflection and transmission amplitudes are well known:

$$R(k) = \frac{(k^2 - K^2)\sin(2aK)}{2ikK \ \cos(2aK) + (k^2 + K^2)\sin(2aK)} \tag{12.24}$$

$$T(k) = \frac{2ikK \ \exp(-2iak)}{2ikK \ \cos(2aK) + (k^2 + K^2)\sin(2aK)} \tag{12.25}$$

and here the wavevectors are defined as usual:

$$k^2 = \frac{2ME}{\hbar^2}, \quad K^2 = \frac{2M(E - V^{\neq})}{\hbar^2}. \tag{12.26}$$

One notes that the transmission amplitude becomes unity whenever $2aK = n\pi$. This is a result of resonance scattering. The barrier length is $2a$ and an infinite square well with length $2a$ has energy levels whenever its energy $E = \frac{n^2\pi^2\hbar^2}{8Ma^2}$. It is perhaps less appreciated that the observation of the resonance structure depends on the characteristics of the incident wavepacket. For the Gaussian wavepacket, if its initial energy spread is greater than the distance between adjacent resonance states the coherent state averaged transmission probability [eqn (12.3)] will be a smooth monotonically increasing function of the energy. This will occur when

$$\Gamma a^2 \geq \frac{\pi^2}{8}\left(1-\frac{V^{\neq}}{E}\right). \tag{12.27}$$

Only when the initial spatial width is smaller will one observe the resonance oscillations. In other words, for wavepackets, the condition for coherent quantum reflection is that that the incident wavepacket is sufficiently broad in space or equivalently narrow in its momentum distribution so that it can distinguish between adjacent resonance energies.

12.3.2 Phase Times

From the known reflection and transmission amplitudes [eqn (12.24) and (12.25)] and the definition of the phase time one finds that the transmission and reflection phase times associated with the scattering eigenfunction at a given energy are:

$$\bar{t}_{\mathrm{R}} = \frac{\hbar\left(2\alpha\varepsilon(2\varepsilon-1)\sqrt{\varepsilon-1}-\sin\left(2\alpha\sqrt{\varepsilon-1}\right)\right)}{2V^{\neq}\sqrt{\varepsilon(\varepsilon-1)}\left[\sin^2\left(\alpha\sqrt{\varepsilon-1}\right)+4\varepsilon(\varepsilon-1)\right]}, \quad \bar{t}_{\mathrm{T}} = \bar{t}_{\mathrm{R}} - \frac{\alpha\hbar}{2V^{\neq}\sqrt{\varepsilon}} \tag{12.28}$$

where the reduced variables are defined as

$$\alpha = \frac{2a}{\hbar}\sqrt{2MV^{\neq}}, \quad \varepsilon = \frac{E}{V^{\neq}}. \tag{12.29}$$

Interestingly, the difference between the reflected and transmitted phase time $\frac{\alpha\hbar}{2V^{\neq}\sqrt{\varepsilon}} = \frac{a\sqrt{2M}}{\sqrt{E}}$ is just the time it takes a free particle whose energy is E to cross the barrier distance $2a$. Although the individual reflection and transmission phase times display an oscillatory behavior, which reflects the resonance structure, the difference between them is smooth and would seemingly imply that the source of the difference is that the transmitted wave crosses the barrier region only once while the reflected wave crosses it twice.

Since the incident packet is a Gaussian, it is also of interest to study the coherent state averaged phase time delays, defined as

$$\langle \bar{t}_X(p_i)\rangle = \sqrt{\frac{1}{\hbar^2\Gamma}}\int_{-\infty}^{\infty} \mathrm{d}p \exp\left(-\frac{(p-p_i)^2}{\hbar^2\Gamma}\right)\bar{t}_X(p), \quad X = R, T. \tag{12.30}$$

The phase time delays are plotted in Figure 12.7. From the figure one notes that the oscillations in the phase time delays reflect the resonance scattering. The phase time delay maximizes at the resonance positions, reflecting the trapping of the particle in the barrier region due to the

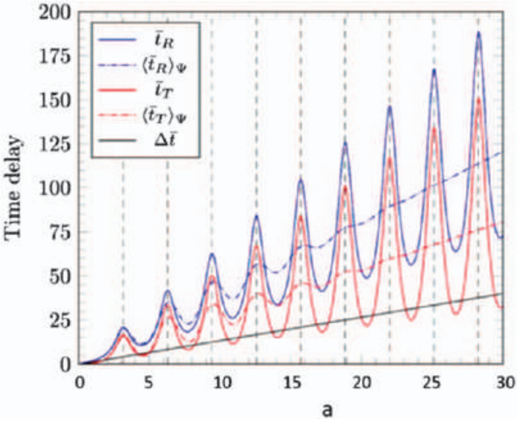

Figure 12.7 The phase time delays for a square barrier with unit height (a.u. throughout) are plotted as a function of the width $2a$ of the square barrier. The incident energy is 1.125. The dashed vertical lines show the location of the resonance energies. $\bar{t}_\mathrm{T}$ and $\bar{t}_\mathrm{R}$ denote the transmitted and reflected time delays as obtained from the phase time [eqn (12.28)] while $\langle\bar{t}_\mathrm{T}\rangle_\Psi$ and $\langle\bar{t}_\mathrm{R}\rangle_\Psi$ denote the numerically evaluated mean transmitted and reflected times as obtained with eqn (12.30). $\Delta\bar{t}$ denotes the difference between the reflected and transmitted time delays. The width of the incident wavepacket is $\Gamma = 2.5\times10^{-4}$. For further details see the text. Reproduced from ref. 63, https://doi.org/10.1103/PhysRev.40.749, with permission from American Physical Society, Copyright 1932.

resonances. Second, as is also obvious from the analytic results, the transmitted and reflected time delays are synchronized; the maxima and minima appear at the same position. Therefore, the difference between them increases linearly with the barrier width. Third, one notes that the coherent state averaged phase time delays oscillate for a narrow barrier, but then the oscillations are damped and the linear increase of the time simply reflects the time delay induced by the slower motion on the barrier. From eqn (12.27) one finds that this transition should occur at $a \simeq 25$, as also seen from the figure. In other words, for barrier widths which are larger than $a = 25$ the dynamics becomes incoherent.

Also in this case of quantum reflection, it is instructive to compare the exact quantum result with a modified classical Wigner approximation. As in the quantum tunnelling case, we consider the density correlation function with an incident state localized to the left of the barrier with positive initial average momentum. In the Wigner phase space, each initial condition is propagated classically until it reaches the location of the first edge of the barrier. Using the step transmission and reflection probabilities, $\left|R_\mathrm{step}\right|^2 = 1 - \left|T_\mathrm{step}\right|^2 = \dfrac{(k-K)^2}{(k+K)^2}$ [with the wave vectors defined as in eqn (12.26)] the trajectory is reflected or transmitted. If transmitted it continues to the right edge of the barrier and, here too, it is either transmitted with probability $|T_\mathrm{step}|^2$ or reflected back, *etc.* Following this scheme, one finds that the mean distance traversed on top of the barrier by the reflected and transmitted particles would be

$$\langle d\rangle_{\mathrm{R}} = \frac{2a}{1+\left|R_{\mathrm{step}}\right|^2}, \quad \langle d\rangle_{\mathrm{T}} = \frac{2a\left(1+\left|R_{\mathrm{step}}\right|^4\right)}{1-\left|R_{\mathrm{step}}\right|^4}. \tag{12.31}$$

The classical Wigner dynamics for the flight-time difference for this trajectory (assuming that the reflected and transmitted screens are symmetrically placed on either side of the barrier) whose energy is E would be

$$\Delta t_{\mathrm{W}}(E) = M\frac{\langle d\rangle_{\mathrm{R}} - \langle d\rangle_{\mathrm{W}}}{\hbar K(E)} = -\frac{2Ma\left|R_{\mathrm{step}}\right|^2}{\hbar K(E)\left(1-\left|R_{\mathrm{step}}\right|^2\right)}. \tag{12.32}$$

If it is negative, the reflected path is shorter than the transmitted path. The quantum flight-time difference as defined in eqn (12.12), the phase time difference $\left(\bar{t}_{\mathrm{R}} - \bar{t}_{\mathrm{T}} - \frac{a\sqrt{2M}}{\sqrt{E}}\right)$, and the Wigner flight-time difference are plotted in Figure 12.8 for a mean energy such that the step potential

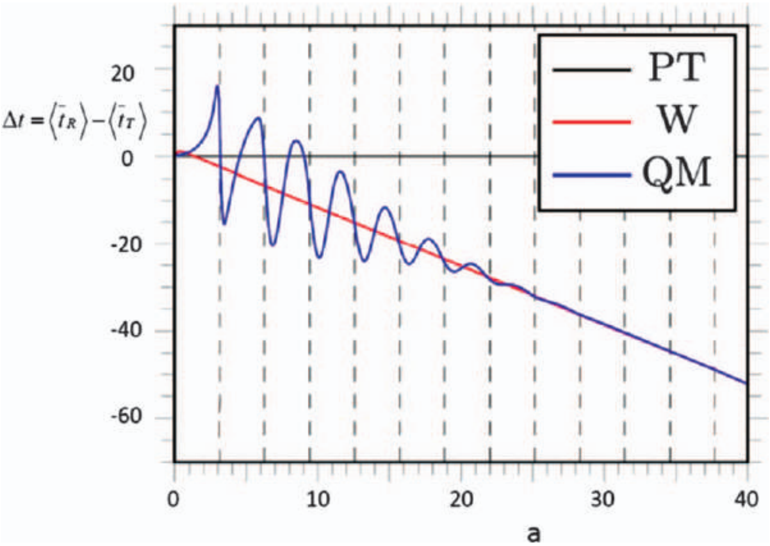

Figure 12.8 The quantum reflection flight-time difference is plotted as a function of the barrier width. $\langle \bar{t}_{\mathrm{T}}\rangle_{\Psi}$ and $\langle \bar{t}_{\mathrm{R}}\rangle_{\Psi}$ denote the mean transmitted and reflected times as obtained with eqn (12.30). QM and W denote the mean times obtained from the numerical exact and classical Wigner approximation respectively while PT stands for the phase time computation. Parameters used are as in Figure 12.7. For further details see the text. Reproduced from ref. 63, https://doi.org/10.1103/PhysRev.40.749, with permission from American Physical Society, Copyright 1932.

reflection probability is $\frac{1}{4}$, as a function of the barrier width. The vertical dashed lines show the barrier resonance locations. The incident energy is 1.125 and the width $\Gamma = 2.5 \times 10^{-4}$. From the figure one notices that the phase time delay is qualitatively incorrect; it is plotted as a constant, since we subtracted from it the difference of the free particle barrier traversal time $\frac{a\sqrt{2M}}{\sqrt{E}}$ to facilitate the plot. The phase time difference would be positive then, not negative. The Wigner theory, which, as for the tunnelling case, is an incoherent theory, is quantitative in the region where the incident wavepacket momentum width is sufficiently broad so as to wipe out the resonance structure. For thinner barriers one finds that the flight-time difference oscillates. This study of the quantum reflection flight-time difference not only reveals the effect of coherence on the flight time but also a qualitative failure of the phase time delay method for estimating the results of time of flight experiments.

12.4 Larmor Time *vs.* Flight Time

12.4.1 Complex Time

As already discussed in the introduction, in quantum mechanics there are many different ways for deducing a "time" associated with a process and these different definitions will give different results. Perhaps the most striking discrepancy is between the experimentally deduced times for photoionization and the Larmor clock times. The former has led to the conclusion that the tunnelling time vanishes or is very small, the latter predict a much longer time. In this section we will argue that the photoionization experiment indeed measures a flight time and, as expected, this flight time either vanishes or is very small. However, the Larmor clock class of experiments essentially measures the Pollak–Miller imaginary time. These two-time scales are different so that there is no real contradiction between them.

As a first step, it is necessary to briefly review the concept of complex time. For this purpose one defines a micro-canonical flux–flux correlation function that correlates the flux measured initially $(t = 0)$ at point x_1 and then the flux measured at point x_2 at some later time t [the quantum flux operator has been given in eqn (12.8)]:

$$\mathrm{C}_{\mathrm{FF},t}(x_1, x_2, t; E) = 2\pi\hbar \mathrm{Tr}[\hat{F}(x_2(t))\hat{F}(x_1(0))]\delta(E - \hat{H}). \qquad (12.33)$$

This correlation function is complex but is real in the classical limit. To simplify, we consider a symmetric potential. As discussed in ref. 69 if one chooses the two points symmetrically on opposite sides of the potential but where the potential vanishes, then the time integral of the correlation function over the time interval $[0, \infty]$ is identical to the transmission probability. More interestingly in the context of the present discussion is that one may take the time average of the imaginary part of the correlation function and this defines the imaginary time

$$t_{\mathrm{Im}}(E) \equiv -\frac{\hbar}{2}\frac{\mathrm{d}\left(\ln|T(E)|^2\right)}{\mathrm{d}E} = \frac{\mathrm{Im}\left[\left[\int_0^\infty \mathrm{d}t t C_{\mathrm{FF}}(-x, x, t; E)\right]\right]}{\int_0^\infty \mathrm{d}t C_{\mathrm{FF}}(-x, x, t; E)}. \tag{12.34}$$

Under suitable definition, taking into account both forward and backward flux, the real part of the time average is identical to the phase time delay.[41] With this construction, one notes that the Wigner formula[70] may be rewritten as a complex time

$$t_T(E) = -i\hbar \frac{\mathrm{d}\ln T(E)}{\mathrm{d}E} \tag{12.35}$$

such that the real part is the phase time delay as in eqn (12.23) and the imaginary part is the imaginary time as in eqn (12.34).

The central question is what is the meaning of this imaginary time, or in different words can it be measured and in what kind of experiment? To answer, one resorts to semiclassics. It is well known that in the deep tunnelling regime the tunnelling transmission probability at an energy E through a barrier whose height is $V^{\neq}$ is given as $|T(E)|^2 \simeq \exp\left[-\frac{\Phi(E)}{\hbar}\right]$ where the action $\Phi(E)$ is the action of the classical periodic orbit moving on the upside-down potential at the energy $V^{\neq} - E$. In classical mechanics the period of the motion is just the energy derivative of the action. We then see that the imaginary time scale is in the semiclassical limit a measure of half of the period of motion on the inverted potential. In the limit of a parabolic barrier with barrier frequency $\omega^{\neq}$ this time is energy independent and equal to $\pi/\omega^{\neq}$. For a square barrier with width $2a$, this time is $\sqrt{\frac{Ma^2}{2(V^{\neq} - E)}}$. It becomes shorter as the energy is lowered. If the barrier is Gaussian shaped, one should expect the imaginary time to be longer as the energy is lowered.

12.4.2 The Larmor Clock

The Larmor clock is based on coupling the barrier potential $V(x)$ to an external magnetic field that vanishes in the region where the potential vanishes. A classical particle with a magnetic moment perpendicular to a uniform magnetic field will precess with a frequency known as the Larmor frequency ω_{L}. Consider then a spin-$\frac{1}{2}$ particle such as an electron scattered off the potential at an incident energy below the barrier top and the spin-polarized upwards in the x direction while the magnetic field coupled to the barrier is in the perpendicular z direction. After tunnelling, the major change in the spin will occur in the z direction[68] implying a precession of the spin due to the tunnelling and the coupling to the magnetic field. If the coupling to the field is weak enough, this precession angle may be inverted into a time by dividing it by the Larmor frequency.[71] The resulting time in the deep tunnelling regime is precisely the imaginary time (see equation 2.20a of ref. 68 and figure 3, $k=1250$, of ref. 72.

The same conclusion holds for other clock schemes, such as employing a time-dependent field in the barrier region, which is the experiment of ref. 32. Why do the clock experiments reveal the imaginary time? Again, the semiclassical context is helpful. The clock is an added degree of freedom, whether a spin, a time-dependent field or a spatial degree of freedom such as a rotation or vibration. Semiclassically, in the weak coupling limit, the classical trajectories that determine the outcome of the scattering event are trajectories that move in imaginary time along the translational coordinate. Within a perturbation theory picture, it is this motion that weakly perturbs the perpendicular degrees of freedom so that they are sensitized to the imaginary time. This is very different from the flight time, which measures the time of flight of the particle and does not need a coupling to other degrees of freedom. It is interesting to note that the tunnelling barrier in the experiment of ref. 32 is a Gaussian, so that when one is not too far from the barrier top one would expect the imaginary time to be rather independent of the incident energy. Indeed, this is what we see in Figure 4c of ref. 32. Within the error bars, the times at energies below the barrier are constant or perhaps slightly increasing, as would be expected for the imaginary time.

The attosecond photoionization experiment does not couple the escaping electron to a different degree of freedom. Rather the attosecond pulse modulates the barrier to ionization in time, thus creating a situation whereby the electron can dissociate by tunnelling. The experiment measures the final kinetic energy of the escaping electron. Theory then showed that this final kinetic energy is compatible with a vanishing flight time through the barrier.[31] The two experiments are different and measure different times; one measures a flight time, the other measures a coupling time to an external degree of freedom. It is impressive that one is able to measure independently these two quantum times which shed light on different aspects of the tunnelling dynamics.

12.5 Discussion

The study of the tunnelling flight time leads to the following conclusions:

1. For scattering through a one-dimensional barrier the tunnelling flight time either vanishes or is very small, independent of the width or height of the barrier, affirming the MacColl effect.
2. Different experiments measure different times. The H and He photoionization experiments measure the flight time. The experiment with a Bose condensate is sensitive to the imaginary time, which provides

information on the shape of the barrier separating the incident and transmitted zones.
3. The phase time delay of Wigner is not always sufficient when considering flight times in the non-classical regimes of scattering.
4. Flight times reveal interesting aspects of quantum reflection. When the incident wavepacket is broader than the barrier, the barrier resonances coherently affect the dynamics leading to an oscillatory flight-time difference between the reflected and transmitted parts of the incident wave packet.

These results are not trivial and raise some further interesting questions. An immediate one is that naively the MacColl effect, according to which the tunnelling flight time is independent of the barrier width, leads to a violation of special relativity, since the ‘‘speed’’ of the tunnelling particle is infinite and not limited by the speed of light. Two answers have been given to this objection. One is that the MacColl effect and its subsequent affirmation is based on non-relativistic Hamiltonian dynamics so that there is nothing that can limit the speed. What is needed is to determine the tunnelling flight time for a relativistic particle. Some efforts have been taken in this direction but they are as of yet, inconclusive.[73–75]

There is an additional aspect. If tunnelling needs a relativistic theory then, perhaps, all the implications of tunnelling on non-relativistic systems need to be rethought? Actually, a violation of special relativity implies the ability to transfer information with a speed faster than light. This is not the case here. Consider the conditions needed to determine the tunnelling flight time. There are two central ones: the amplitude of the incident wave at the barrier must be much smaller than the transmission probability. For the square barrier with width $2a$ this implies that $\Gamma x_i^2 \gg \frac{2a}{\hbar}\sqrt{2M(V^{\neq}-E)}$. The second condition is that the probability for an incident momentum to be higher than the barrier is also much smaller than the transmission probability, this implies $\frac{p_i^2}{\hbar^2\Gamma} \gg \frac{2a}{\hbar}\sqrt{2M(V^{\neq}-E)}$. These two conditions together imply that the center of the incident wavepacket $x_i \gg 2a$. In other words, the distance the particle travels as a free particle is much larger than the barrier width so a vanishing tunnelling flight time will hardly change the overall time of flight which is chosen to be much less than the speed of light.

Other questions abound. What is the tunnelling flight time in multidimensional systems? In tunnelling combined with curve crossing? In dynamic tunnelling as for example between local modes of ABA molecules?[76,77] Due to the fact that in any case the flight time is very small, the usual perturbation theories such as a steepest descent analysis are not obviously sufficient and one must resort to numerical experiments. These are not always easy to implement, given the stringent conditions imposed to assure that one is observing pure tunnelling. This is good news – it implies that there is still much to do and that quantum mechanics might still have a number of surprises waiting for us.

Acknowledgements

I would like to thank Professors Randal Dumont and Aephraim Steinberg, and Dr Tom Rivlin for many discussions. This work has been supported by grants from the Israel Science Foundation and the Minerva Foundation, Munich.

References

1. W. Pauli, *Handb. Phys.*, 1933, **24**, 83.
2. Y. Aharonov and D. Bohm, *Phys. Rev.*, 1961, **122**, 1649.
3. J. Kijowski, *Rep. Math. Phys.*, 1974, **6**, 361.
4. D. Sokolovski, *Proc. R. Soc. A*, 2004, **460**, 1505.
5. E. A. Galapon, *J. Phys. A: Math. Theor.*, 2008, **41**, 455302.
6. J. J. Halliwell, J. Evaeus, J. London and Y. Malik, *Phys. Lett. A*, 2015, **379**, 2445.
7. G. Torres-Vega, *J. Math. Phys.*, 2016, **57**, 122111.
8. E. H. Hauge and J. A. Stovneng, *Rev. Mod. Phys.*, 1989, **61**, 917.
9. R. Landauer, *Ber. Bunsenges. Phys. Chem.*, 1991, **95**, 404.
10. S. Brouard, R. Sala and J. G. Muga, *Phys. Rev. A*, 1994, **49**, 4312.
11. D. Shafir, H. Soifer, B. D. Bruner, M. Dagan, Y. Mairesse, S. Patchkovskii, M. Y. Ivanov, O. Smirnova and N. Dudovich, *Nature*, 2012, **485**, 343.
12. J. Manz, A. Schild, B. Schmidt and Y. Yang, *Chem. Phys.*, 2014, **442**, 9.
13. J. G. Muga, R. S. Mayato and I. Egusquiza, *Lect. Notes Phys.*, 2008, **734**.
14. J. G. Muga, A. Ruschaupt and A. del Campo, *Lect. Notes Phys.*, 2009, **789**.
15. M. Razavy, *Quantum Theory of Tunneling*, World Scientific, Singapore, 2003.
16. V. I. Goldanskii, L. I. Trakhtenberg and V. N. Fleurov, *Tunneling Phenomena in Chemical Physics*, Gordon and Breach, New York, 1989.
17. V. A. Benderskii, D. E. Makarov and C. A. Wight, *Adv. Chem. Phys.*, 1994, **88**.
18. D. Mugnai, A. Ranfagni and L. S. Schulman, *Tunneling and Its Implications*, Adriatico Research Conf., World Scientific, 1996.
19. J. Ankerhold, *Quantum Tunneling in Complex Systems*, Springer Verlag, Berlin, 2007.
20. P. R. Schreiner, H. P. Reisenauer, D. Ley, D. Gerbig, C.-H. Wu and W. D. Allen, *Science*, 2011, **332**, 1300.
21. J. Kaestner, *WIREs Comput. Mol. Sci.*, 2014, **4**, 158.
22. A. P. Jardine, E. Y. M. Lee, D. J. Ward, G. Alexandrowicz, H. Hedgeland, W. Allison, J. Ellis and E. Pollak, *Phys. Rev. Lett.*, 2010, **105**, 136101.
23. J. D. Rodriguez, M. G. Gonzalez, L. Rubio-Lagoa and L. Bañares, *Phys. Chem. Chem. Phys.*, 2014, **16**, 3757.
24. R. J. Shannon, M. A. Blitz, A. Goddard and D. E. Heard, *Nat. Chem.*, 2013, **5**, 745.

25. C. M. Nunes, I. Reva, S. Kozuch, R. J. McMahon and R. Fausto, *J. Am. Chem. Soc.*, 2017, **139**, 17649.
26. A. S. Landsman and U. Keller, *Phys. Rep.*, 2015, **547**, 1.
27. T. Zimmermann, S. Mishra, B. R. Doran, D. F. Gordon and A. S. Landsman, *Phys. Rev. Lett.*, 2016, **116**, 233603.
28. E. A. Galapon, *Phys. Rev. Lett.*, 2012, **108**, 170402.
29. L. Torlina, F. Morales, J. Kaushal, I. Ivanon, A. Kheifetz, A. Zielinski, A. Scrinzi, H. G. Muller, S. Sukiasyan, M. Ivanonv and O. Smirnova, *Nat. Phys.*, 2015, **11**, 503.
30. D. Sokolovski, *Phys. Rev. A*, 2017, **96**, 022120.
31. U. S. Sainadh, H. Xu, X. Wang, A.-T. Noor, W. C. Wallace, N. Douguet, A. Bray, I. Ivanov, K. Bartschat, A. Kheifets, R. T. Sang and I. V. Litvinyuk, *Nature*, 2019, **568**, 75.
32. R. Ramos, D. Spierings, I. Racicot and A. M. Steinberg, *arXiv:1907.13523v1* [physics.atom-ph], 2019.
33. T. E. Hartman, *J. Appl. Phys.*, 1962, **339**, 3427.
34. L. A. MacColl, *Phys. Rev.*, 1932, **40**, 621.
35. H. G. Winful, *Phys. Rep.*, 2006, **436**, 1.
36. H. Aichmann and G. Nimtz, *Found. Phys.*, 2014, **44**, 678.
37. J. Petersen and E. Pollak, *J. Phys. Chem. Lett.*, 2017, **8**, 4017.
38. J. Petersen and E. Pollak, *J. Phys. Chem. A*, 2018, **122**, 3563.
39. A. Baz', *Sov. J. Nucl. Phys.*, 1966, **4**, 182.
40. V. Rybachenko, *Sov. J. Nucl. Phys.*, 1967, **5**, 635.
41. M. Buettiker and R. Landauer, *Phys. Rev. Lett.*, 1982, **49**, 1739.
42. E. Pollak and W. H. Miller, *Phys. Rev. Lett.*, 1984, **53**, 115.
43. J. Linderberg and Y. Őhrn, *Propagators in Quantum Chemistry*, John Wiley & Sons, New York, 2004.
44. G. Hummer, *J. Chem. Phys.*, 2004, **120**, 516.
45. A. M. Berezhkovskii, G. Hummer and S. M. Bezrukov, *Phys. Rev. Lett.*, 2006, **97**, 020601.
46. S. Chaudhury and D. E. Makarov, *J. Chem. Phys.*, 2010, **133**, 034118.
47. K. Neupane, D. A. N. Foster, D. R. Dee, H. Yu, F. Wang and M. T. Woodside, *Science*, 2016, **352**, 239.
48. E. Pollak, *Phys. Chem. Chem. Phys.*, 2016, **18**, 28872.
49. E. Pollak, *Phys. Rev. Lett.*, 2017, **118**, 070401.
50. E. Pollak, *J. Phys. Chem. Lett.*, 2017, **8**, 352.
51. E. Pollak, *Phys. Rev. A*, 2017, **95**, 042108.
52. A. Fuhrmanek, A. M. Lance, C. Tuchendler, P. Grangier, Y. R. P. Sortaisand and A. Browaeys, *New J. Phys*, 2010, **12**, 053028.
53. J. J. Du, W. F. Li, R. J. Wen, G. Li and T. C. Zhang, *Laser Phys. Lett.*, 2015, **12**, 065501.
54. Y. Aharonov, J. Oppenheim, S. Popescu, B. Reznik and W. G. Unruh, *Phys. Rev. A*, 1998, **57**, 4130.
55. R. S. Mayato, D. Alonso and I. L. Egusquiza, *Lect. Notes Phys*, 2008, **734**, 235.
56. G. Muga, *Lect. Notes in Phys.*, 2008, **734**, 31.

57. P. Senn, *Am. J. Phys.*, 1988, **56**, 916.
58. K. Maji, C. K. Mondal and S. P. Bhattacharya, *Int. Rev. Phys. Chem.*, 2007, **26**, 647.
59. R. S. Dumont and T. L. Marchioro II, *Phys. Rev. A*, 1993, **47**, 85.
60. V. Delgado, *Phys. Rev. A*, 1999, **59**, 1010.
61. T. Rivlin, E. Pollak and R. Dumont, work in progress.
62. J. Liu, *Int. J. Quant. Chem.*, 2015, **115**, 657.
63. E. Wigner, *Phys. Rev.*, 1932, **40**, 749.
64. E. J. Heller, *J. Chem. Phys.*, 1976, **65**, 1289.
65. L. Nordhiem, *Z. Phys.*, 1927, **46**, 833.
66. J. E. Lennard-Jones and A. F. Devonshire, *Proc. R. Soc. London, Ser. A*, 1936, **156**, 6.
67. J. Petersen, E. Pollak and S. Miret-Artés, *Phys. Rev. A*, 2018, **97**, 042102.
68. J. Petersen and E. Pollak, *J. Chem. Phys.*, 2018, **148**, 074111.
69. E. Pollak, *J. Chem. Phys.*, 1985, **83**, 1111.
70. E. Wigner, *Phys. Rev.*, 1955, **98**, 145.
71. M. Büttiker, *Phys. Rev. B*, 1983, **27**, 6178.
72. H. M. Krenslin, J. Budczies and K. W. Kehr, *Phys. Rev. A*, 1996, **53**, 3749.
73. S. De Leo and P. P. Rotelli, *Eur. Phys. J. C*, 2007, **51**, 241.
74. S. De Leo, *J. Phys. A: Math. Theor.*, 2013, **46**, 155306.
75. O. del Barco and V. Gasparian, *J. Phys. A: Math. Theor.*, 2011, **44**, 015303.
76. R. T. Lawton and M. S. Child, *Mol. Phys.*, 1979, **37**, 1799.
77. K. Stefanski and E. Pollak, *J. Chem. Phys.*, 1987, **87**, 1079.

Subject Index